Magnetic Machines and Power Electronics for Power MEMS Applications

by

Sauparna Das

M.Eng., Massachusetts Institute of Technology, 2002
B.S., Massachusetts Institute of Technology, 2002

Submitted to the Department of Electrical Engineering and Computer Science
in partial fulfillment of the requirements for the degree of

Doctor of Philosophy

at the

MASSACHUSETTS INSTITUTE OF TECHNOLOGY

September 2005

Signature of Author: _____
Department of Electrical Engineering and Computer Science
August 31, 2005

Certified by: _____
Jeffrey H. Lang
Professor of Electrical Engineering and Computer Science
Thesis Supervisor

Accepted by: _____
Arthur. C. Smith
Chairman, Department Committee on Graduate Students

Magnetic Machines and Power Electronics for Power MEMS Applications

by

Sauparna Das

Submitted to the Department of Electrical Engineering and Computer Science
on August 31, 2005 in Partial Fulfillment of the Requirements
for the Degree of Doctor of Philosophy in Electrical Engineering

ABSTRACT

This thesis presents the modeling, design, and characterization of microfabricated, surface-wound, permanent-magnet (PM) generators, and their power electronics, for use in Watt-level Power MEMS applications such as a microscale gas turbine engine. The generators are three-phase, axial-flux, synchronous machines, comprising a rotor with an annular PM and ferromagnetic core, and a stator with multi-turn surface windings on a soft magnetic substrate. The fabrication of the PM generators, as well as the development of their high-speed spinning rotor test stand, was carried out by collaborators at the Georgia Institute of Technology.

The machines are modeled by analytically solving 2D magneto-quasistatic Maxwell's Equations as a function of radius and then integrating the field solutions over the radial span of the machine to determine the open-circuit voltage, torque and losses in the stator core. The model provides a computationally fast method to determine power and efficiency of an axial-air-gap PM machine as a function of geometry, speed and material properties.

Both passive and active power electronics have been built and tested. The passive power electronics consist of a three-phase transformer and diode bridge rectifier. The active power electronics consist of a switch-mode rectifier based on the boost semi-bridge topology which is used to convert the unregulated AC generator voltages to a regulated 12 V DC without the need for rotor position/speed or stator terminal current/voltage sensing.

At the rotational speed of 300,000 rpm, one generator converts 16.2 W of mechanical power to electrical power. Coupled to the transformer and diode bridge rectifier, it delivers 8 W DC to a resistive load. This is the highest output power ever delivered by a microscale electric generator to date. The corresponding power and current densities of 57.8 MW/m^3 and 6×10^8 A/m^2, respectively, are much higher than those of a macroscale electric generator. At the rotational speed of 300,000 rpm, the generator and switch-mode rectifier delivered 5.5 W DC to a resistive load at a power density three times that of the passive electronics. This Watt-scale electrical power generation demonstrates the viability of scaled PM machines and power electronics for practical Power MEMS applications.

Thesis Supervisor: Jeffrey H. Lang
Title: Professor of Electrical Engineering and Computer Science

ACKNOWLEDGEMENTS

I have the most gratitude for my advisor Jeffrey Lang, whose friendliness, enthusiasm, depth of knowledge and willingness to help made my years as a graduate student a memorable experience. Jeff possesses an amazing ability to explain complex topics in a clear and intuitive manner and he is the one who sparked my interest in electromechanics when I was an undergraduate.

I also thank David Perreault for his help and guidance in the design of the power electronics in this thesis and, James Kirtley for his expertise in electric machinery. Thanks also to Alan Epstein and Stuart Jacobson for leading and organizing the Microengine Project.

I am deeply indebted to David Arnold, Jin-Woo Park, Iulica Zana, Florian Herreault and Preston Galle at the Georgia Institute of Technology who were responsible for the fabrication and experimental set up of the machines presented in this thesis. David Arnold and I have been working together on this project for the past three years and I value the discussions we had on technical subjects as well as on religion, philosophy and life. I thank Mark Allen for giving me the opportunity to gain experience in the clean room at GIT and help fabricate the first generation permanent-magnet machines. Big thanks to Jin-Woo for his help and guidance with the fabrication of the machines. The number of fabrication tricks this man possesses is endless.

Thanks also to Yeun-Ho Joung and David Veazie at Clark Atlanta University for their work on the structural integrity of the permanent-magnet rotors which proved invaluable in achieving high rotational speeds.

I thank Susan Parker for facilitating travel to and from GIT and also Wayne Ryan who made my life a lot easier by teaching me how to use a soldering oven for building my circuit boards.

I wish to thank my mom and dad for their constant love and support during my entire time at MIT. They instilled in me the values and work ethic that enabled me to successfully complete my undergraduate and graduate degrees at this institution.

Funding for this work was provided by the Army Research Laboratory (DAAD19-01-2-0010) under the Collaborative Technology Alliance in Power and Energy program, managed by Mr. John Hopkins (ARL) and Dr. Mukund Acharya (Honeywell). Funding for this work was also provided in part by the Army Research Office (DAAG55-98-1-0292) managed by Dr. Tom Doligalski.

Table of Contents

List of Figures

List of Tables

1 Introduction

1.1 The Microengine Concept

Modern battery technologies have not kept pace with the rising demand for power by portable electronic devices. This problem is most acute for today's soldiers who must carry several batteries to power a host of portable electronic gear such as radios, laser range finders, GPS trackers and night vision cameras. The typical battery employed in the army is the one-time use, $LiSO_2$ BA5590 which provides 170 W-Hr of energy and weighs 2.7 lbs. The army purchases over 350,000 BA5590 at cost of about $100 per battery, which includes a $30 disposal fee [1]. Future soldiers will rely more heavily on electronic gear for combat operations, increasing the demand for portable power. This has led to the need for alternative power sources such as microelectromechanical system-based, or MEMS-based, electric generators that can produce 10–100 W of electrical power. Suitable electric generators could be powered by a variety of prime movers, including liquid flow, pressurized gas, or small combustion engines.

One potential system is a silicon micromachined gas turbine engine [2-5] coupled to an electric generator as shown in Figure 1-1. This "microengine" power generation system has been under development by a number of universities, led by the Massachusetts Institute of Technology (MIT), since 1995, and is one of many new devices in the growing field of Power MEMS. The microengine, no larger than a stack of a few pennies, would be a light weight and refuelable source of energy. The use of silicon micromachining techniques would allow for batch processing, greatly reducing the cost of the engine. Such a device could eliminate the weight, life-cycle costs, and cumbersome logistics associated with conventional batteries while providing high quality electric power.

The use of hydrocarbon fuels in a micro-gas turbine engine presents up to a factor of ten improvement in energy and power density over the best military batteries. Modern batteries typically have energy densities of 100-400 W-hr/kg while advanced fuel cells are targeting 400-700 W-hr/kg. Hydrocarbon fuels, in comparison, have energy densities of 12,000-14,000 W-hr/kg. Even with a chemical-to-electrical efficiency of only 5%, a micro-gas turbine engine would match the energy densities of even the best fuel

cell technology and if they are able to achieve a 10% chemical-to-electrical efficiency then energy densities of up to 1400 W-hr/kg are possible.

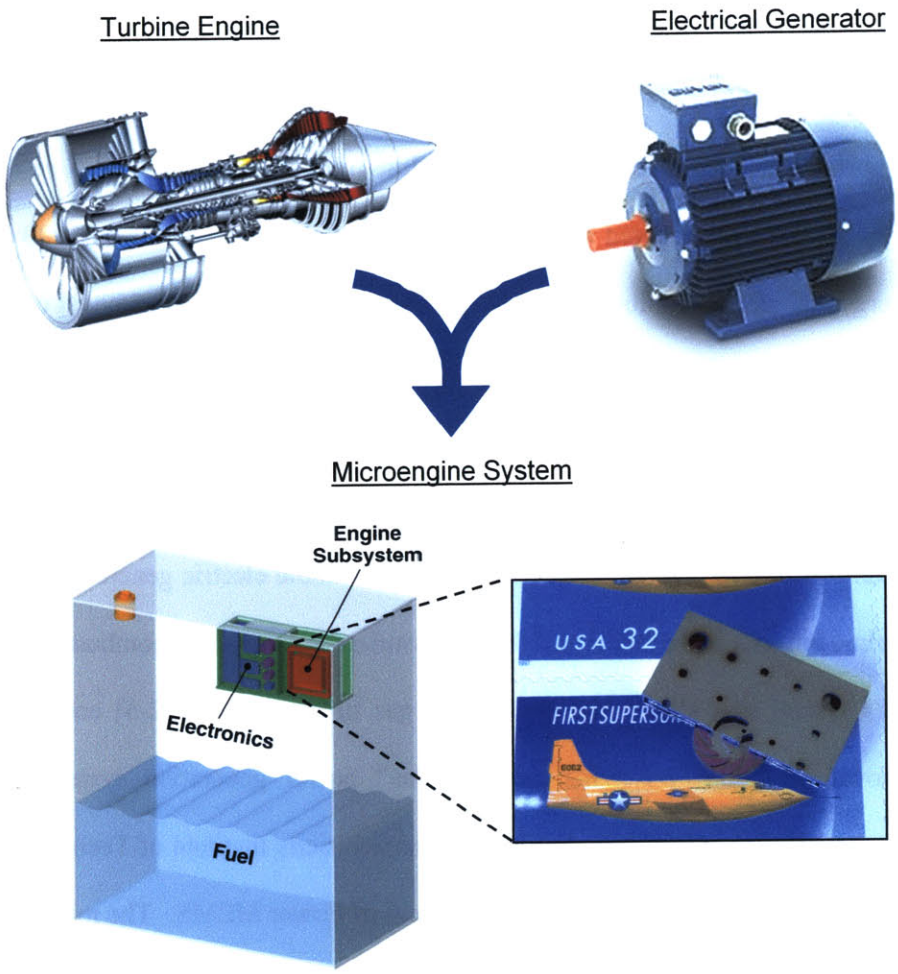

Figure 1-1: Microengine concept.

The micro-gas turbine engine shown in Figure 1-2 is a radial air flow machine and consists of a stack of bonded silicon wafers. A composite, multilevel silicon disk acts as both the compressor and turbine for the microengine, and is supported by gas lubricated air bearings. Micro-bearing rigs have demonstrated the feasibility of stably spinning silicon disks to rotational speeds of 1+ Mrpm and serve as a test bed for the compressor [6,7]. In addition, a microcombustor has been built to verify combustion performance at the microscale [8-10]. Relevant materials research [11-13] and fabrication technology development [14-17] have also been conducted.

This thesis focuses on the modeling and design of microscale magnetic machines and power electronics suitable for generating electric power from the microengine. In particular, induction and permanent-magnet machines are compared in terms of their power density and efficiency within the context of the microengine design constraints. It is found that within the microengine constraints, the surface wound permanent-magnet machine has the highest power density and efficiency. Microscale permanent-magnet machines and both passive and active power electronics have been built and tested with our collaborators at the Georgia Institute of Technology that can generate and deliver 5+ Watts to a load at speeds of 300,000 rpm.

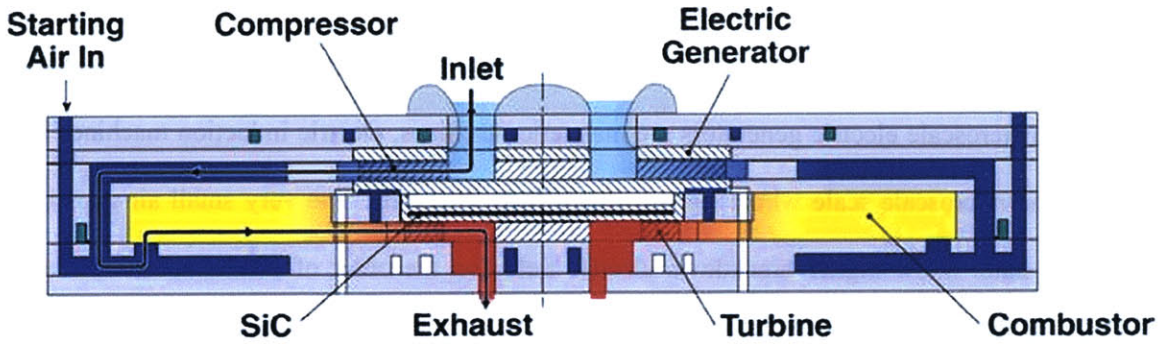

Figure 1-2: Silicon-based, multi-wafer microengine.

1.2 Microscale Electric Generators

The electric generator for the microengine is used to convert the mechanical power of the turbine into electrical energy and must be integrated into the multi-wafer silicon stack. The electric generator's rotor is placed on top of the compressor blades while the generator stator components are integrated into the layers of silicon above the rotor. This places several constraints on any suitable electric generator. First, it must be a planar device with an axial air gap. Second, its fabrication process must be compatible and integratable with the silicon micromachined gas turbine, including the constraint that it operates at high temperatures (~300°C). Last, and most importantly, to achieve the desired output power levels (10–100W), the electrical generator must support high rotor spin (~1 Mrpm) and tip (500 m/s) speeds.

Initial electric generator concepts focused on induction machines. This was due to the initial operating temperature requirement of ~700°C which precluded the use of permanent magnets. Both electric [18-22] and magnetic [23-31] induction machines have been investigated by the MIT Micro-Gas Turbine Engine Project. Within the past year engine models have been developed that indicate that the microengine may be able to maintain a generator operating environment of 300 °C. This meant that permanent magnet (PM) machines using high temperature rare-earth PMs should now also be investigated as possible electric generators. However, the effects of high temperature bonding of rare-earth PMs and the possibility of repoling them must still be investigated.

1.2.1 Electric Induction Machines

The first generators for the Micro-Gas Turbine Engine Project were electric induction machines. Though most macroscale electric generators are magnetic machines, electric induction machines become attractive at the microscale scale where surface area effects dominate. The very small air gaps between the rotor and stator allow higher breakdown electric fields on the order of 10^8 V/m, which drastically increase output power capability. The electric induction generator, shown in Figure 1-3, consists of five fusion bonded silicon wafers. The stator consists of a six phase set of platinum electrodes with 131 pole pairs formed on a thick 20 μm recessed oxide base [18]. The rotor is a thin film of lightly doped polysilicon also residing on a layer of oxide 10 μm thick. The machine has an outer diameter of 3.8 mm and is approximately 1 mm thick. These machines are fabricated using standard CMOS IC processing techniques which make them compatible with the silicon bulk micromachining used in the micro gas turbine as well as the operating temperature requirement.

These machines have produced a peak torque of 0.22 μN-m with a 90 V, 300 kHz excitation as a tethered motor [19]. As spinning motors, these machines demonstrated a peak torque of 3.5 μN-m (309 N-m/m^3) at speeds in excess of 55 krpm, which corresponds to 20 mW (1.8 MW/m^3) of power [20]. Finally, the electric induction machine was tested as a generator and produced 192 μW at 245krpm under a driven excitation at 20 V [21,22]. It has also been able to self-excite and generate power without the

need for external power electronics. At its rated voltage of 300 V and speed of 1 MRPM, the electric induction machine has the potential to generate at most ~1 W and is primarily limited by breakdown and viscous drag in the narrow rotor/stator air gap.

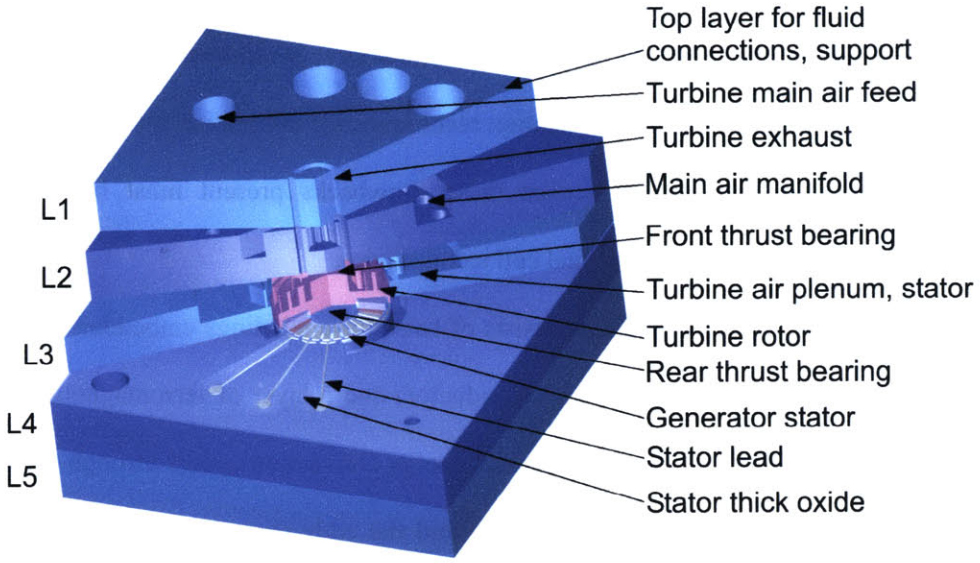

Figure 1-3: 3D section view of the electric induction generator device. The device consists of five silicon layers, fusion bonded together. The electric generator is located in Layers 3 and 4. (Courtesy of Lodewyk Steyn [21,22])

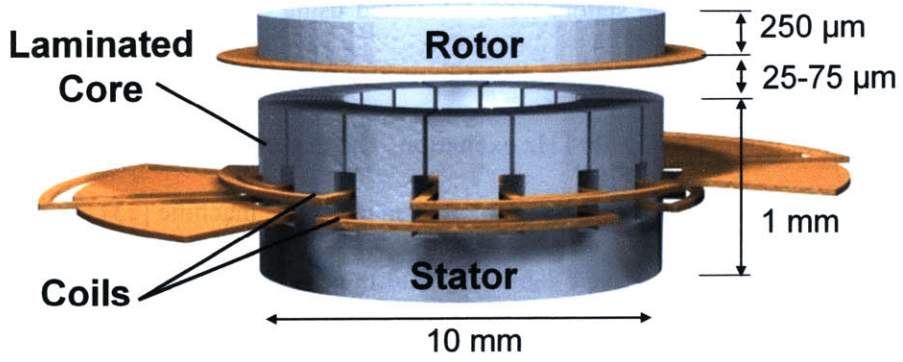

Figure 1-4: Conceptual drawing of an induction machine. (Courtesy of David Arnold, GIT [28])

1.2.2 Magnetic Induction Machines

Magnetic induction machines were developed in parallel with the electric induction machines. Magnetic induction machines offer higher efficiencies as the size and power ratings go up (10 → 100 W).

In addition, these machines can operate at much larger air gaps than their electric counterpart, which greatly reduce windage loss. In fact without the large air gap, an overall engine chemical-to-electrical efficiency of 5% would not be possible. They also operate at lower voltages (1-3 V) and higher currents (2-10 A) and are therefore easier to couple to standard power electronics and loads. Drawbacks to the magnetic induction machine include the use of low structural strength materials (copper, NiFe, CoFeNi) in the rotor and the use of more complex fabrication techniques for integration into the micro-gas turbine engine process flow. However, the challenges these drawbacks present must be overcome if the microengine is to compete with battery and fuel cell technologies.

The planar magnetic induction machine consists of two-phase windings embedded in a slotted stator and a rotor made up of a layer of copper (rotor conductor) and a layer of ferromagnetic material (rotor back iron) as shown in Figure 1-4. Electromechanical energy conversion occurs through the interaction of a traveling magnetic wave in the rotor-stator air gap and the eddy currents induced in the rotor by the traveling wave. The traveling magnetic wave is established through currents in stator phase acting in quadrature.

Initial magnetic induction machines used unlaminated stators [23] because laminated stators were too difficult to fabricate at the time. The stators were fabricated using SU-8 micromolding and multi-level electroplating [24,25]. These first-generation devices were operated as tethered motors and produced a peak torque of 0.3 μN-m using a 6 A_{pk}, 90 kHz excitation. The experimental torque values were an order of magnitude smaller than predicted by analytical models made of the machine [23]. This was because the analytical models assumed the stators were laminated and thus did not account for eddy currents in the stator. This suggests that these eddy currents play a major role in reducing the amount of magnetic flux, generated by the stator currents, coupling the rotor and stator, which was not a surprise. In the end a finite difference time domain model (FDTD) incorporating eddy currents was needed to explain the data [26,27].

The first generation of magnetic induction machines was not compatible with the silicon micromachined gas turbine and could not operate at high temperatures due to the presence of the SU-8

polymer, which melts at 200 °C. The second generation attempted to solve this issue, as well as the eddy current problem, by using stators containing planar Cu coils placed in a three-dimensional, vertically-laminated ferromagnetic core, all supported by a silicon frame [28]. The stator used two highly doped fusion bonded silicon wafers to create the support structure. The silicon was then patterned with SiO_2 and through etched. The laminations were produced by electroplating $Ni_{80}Fe_{20}$ or $Co_{65}Fe_{18}Ni_{17}$ directly on the sides of etched side walls using the highly dope silicon as the seed layer. The core laminations form onion-like concentric rings, where the lamination thickness is approximately one skin depth (~30 μm) to limit eddy current losses. Compared to NiFe, the CoFeNi alloy has similar permeability and resistivity, but has a much higher saturation flux density (higher output power) and higher Curie temperature (higher operating temperature) at the expense of a slight increase in coercivity (larger hysteresis loss) [32].

Referring to Figure 1-4, the rotor is a 250 μm thick ferromagnetic annular ring (10 mm OD, 6mm ID) with a 20 μm thick overlayer of Cu. The Cu extends beyond the magnetic region (12 mm OD, 4 mm ID) to enhance eddy current generation in the rotor for maximum torque. These machines were tested as tethered motors to verify their electromechanical performance and have demonstrated a peak torque of 2.5 μN-m using an 8 A_{pk}, 35 kHz excitation [28]. These machines were never tested as generators.

1.2.3 Permanent Magnet Machines

The permanent-magnet (PM) machines consist of two key components, a rotor with a multi-poled PM and a stator with appropriately designed windings. During operation, the rotating multi-poled PM rotor creates a time-varying magnetic flux in the rotor-stator air gap, which induces AC voltages at the terminals of the stator windings. The PM machines considered in this thesis use an annular permanent magnet mounted on top of a ferromagnetic core. Interior PM machines are not evaluated due to the difficulty of embedding magnets into an electroplated ferromagnetic core.

The PM machine could use the same slotted stator used in induction machines. However, with the use of a suitably thick magnet (500 μm) and high-performance magnetic materials in the rotor and stator

core, the air gap can be made very large (300–500 μm). This allows the stator windings to occupy space in the air gap by placing them on the surface of a flat stator core as shown in Figure 1-5, rather than being embedded in slots and closed over with hats, as in the case of the induction machines.

In a magnetic machine, power conversion occurs through the interaction of the stator currents and rotor flux. In an induction machine, the stator currents also create the rotor flux. The maximum flux that can be produced without saturating the rotor or stator back iron is proportional to the volume of the machine. As the machine is scaled down to the micro level the rotor flux decreases rapidly. The net result is very low electromechanical energy conversion.

Permanent-magnet (PM) synchronous machines offer several advantages over induction machines, especially as the size is reduced [33]. First, the PM creates an independent source of rotor flux that is much larger than what can be produced by an induction machine of the same size, leading to much higher power densities. Second, PM machines are more efficient since there are no eddy currents induced in the rotor, assuming conduction and eddy current losses in the stators are equal.

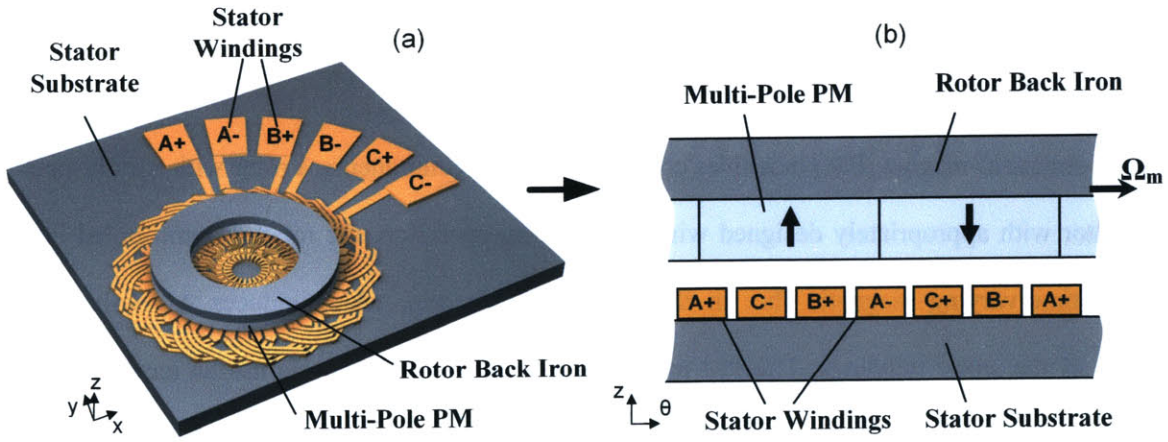

Figure 1-5: Conceptual drawing of a surface wound PM machine: (a) perspective view and (b) cross section. (Courtesy of David Arnold, GIT, [49])

1.2.4 Other Permanent-Magnet Machines in the Literature

Prior work has been done on planar MEMS PM machines. Several axial-air-gap PM motors have been demonstrated [34-38]. Speeds of up to 200 krpm and torques of up to 7.5 μN-m have been achieved [35,36]. Planar, three-phase, synchronous PM motors using magnetic thrust bearings have also been demonstrated [37]. PM generators have also been investigated. One is a turbine generator using a NdFeB PM that has produced 1.1 mW at 30,000 rpm with an air flow of 35 L/min. [39]. The composite turbine/generator rotor was supported by conventional ball-race bearings and measured 1 mm in thickness and 6 mm in diameter. Another has demonstrated high speed rotation (260,000 rpm) by using a combination of air and magnetic bearings [40]. Using an 8 mm diameter $SmCo_5$ rotor, 14.6 mW of power were delivered to a wye-connected resistive load at 58,000 rpm. Using an air powered drill and an 8 mm diameter NdFeB PM the same generator delivered 5 W into a wye-connected resistive load at 380,000 rpm.

The previous work on microscale PM machines for power generation focused solely on the device that performs electromechanical power conversion. This thesis focuses on the complete electric power train starting from the electric generator that does the electromechanical energy conversion to the power electronics that process the power into a usable form for portable power applications as shown in Figure 1-6. In particular, the thesis will present high speed (300,000+ rpm) microscale PM machines and power electronics capable of generating and delivering multi-Watt electric power to a load at a regulated DC output voltage.

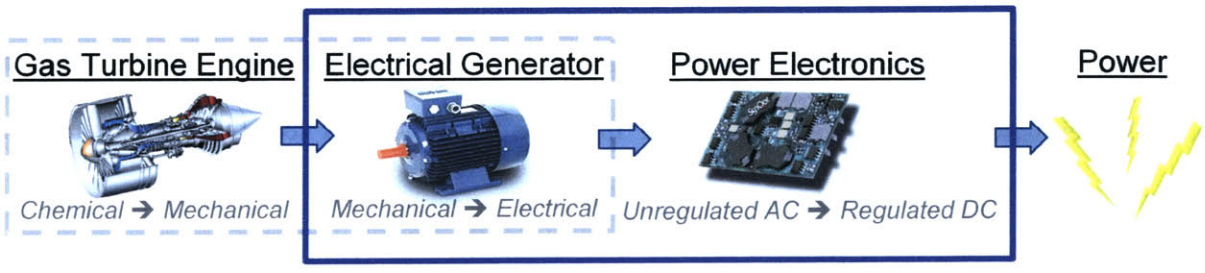

Figure 1-6: Power conversion sequence. The components inside the dashed grey box represent the integrated microengine while components inside the blue box represent the electric power train for the microengine system.

1.3 Thesis Overview and Contributions

This thesis analyzes the performance of planar magnetic induction and permanent-magnet machines at the microscale. The output power capability and efficiency of the machines are compared to determine which machine is the best candidate for power generation within the microengine. To do this, analytical models of the machine are developed to compute open-circuit voltage, torque and various losses. It is found from this comparison that induction machines have poor output power capability and efficiency due to the small number of turns that can be wound on a microfabricated stator which limit the generation of a strong rotor flux. The PM machines, on the other hand, can generate more power and at a higher efficiency due to the independent source of rotor flux produced by the rotor magnet. Comparison is also made between slotted stator and surface wound PM machines. The slotted stator is limited to having only two phases which do not optimally link the flux from the rotor PM. This is due to fabrication constraints of building a slotted magnetic structure from multiple silicon wafers. The surface wound machine can be made with three phases that do optimally link the rotor PM flux and generate higher power at greater efficiency than a PM machine with a slotted stator.

This thesis then presents the modeling, design, and characterization of microfabricated, surface wound, PM generators and power electronics capable of generating Watt-level electric power for use in power MEMS applications such as the micro-gas turbine engine. The generators are three-phase, axial-flux, synchronous machines [41], comprising a rotor with an annular PM and ferromagnetic core and a stator with multi-turn surface windings on a soft magnetic substrate (stator core), as shown in Figure 1-5. Both passive and active power electronics have been built and tested. The passive power electronics consist of a three-phase transformer and diode bridge. The active power electronics consist of a switch-mode rectifier based on the boost semi-bridge topology which is used to convert the generators unregulated AC voltage to a regulated DC voltage of 12 V.

The following chapters detail the scope of the thesis presented above. Chapter 2 discusses the modeling of asynchronous (Induction) and synchronous (PM) magnetic machines with slotted and surface

wound stators. Laminations in the stator and non idealities such as eddy current loss, hysteresis loss and saturation effects are incorporated into the model. Ways of computing relevant machine parameters such as torque, induced voltage, inductance and resistance are also presented. Finally, open-circuit voltage predictions for the surface wound PM machines are verified using finite element analysis (FEA).

Chapter 3 uses the models developed in Chapter 2 to compare the slotted stator induction machine (SLIM), slotted stator PM machine (SLPM) and surface wound PM machine (SWPM) in terms of output power and efficiency as a function of speed, geometry, material properties and input excitation. Electrical performance and fabrication trade offs between slotted and surface wound stators are also discussed. The resulting comparison will show that in terms of power density, efficiency and fabrication simplicity the SWPM is the best design choice for the microengine and will be the focus of the remainder this thesis.

Chapter 4 presents the design, fabrication and testing of the first generation SWPM generator and power electronics. This chapter discusses the choice of dimensions, number of poles and materials selection. The fabrication results of the first generation PM generators are shown along with a discussion of how microfabrication affects generator design. It also presents the stator process flow and rotor magnetization and assembly. The power electronics consists of a three-phase transformer and Schottky diode bridge rectifier. The PM machines are characterized in terms of their phase resistance, inductance and open-circuit voltage. Power generation tests, done in conjunction with colleagues at the Georgia Institute of Technology, with the first generation power electronics are also presented. At a speed of 120,000 rpm, a 2-turn/pole machine demonstrated 2.5 W of mechanical-of-electrical power conversion and delivered 1.1 W to a load resistor. This is the first ever demonstration of Watt level power generation and delivery by a microscale electric machine.

Chapter 5 presents the design, fabrication and testing of the second generation SWPM generator and power electronics. It discusses stator optimization of the number of poles and turns/pole in conjunction with power electronics losses to increase output power capability of the power generation system as a whole. A new stator with concentric windings is presented that has much lower resistance compared to the full pitched windings of the first generation stators. This new stator is characterized in terms of its

circuit parameters and power generation tests, using the first generation power electronics, are shown demonstrating multi-Watt power delivery. One second generation stator, when connected to the transformer and diode bridge, delivered 8 W to a load resistor at a speed of 305,000 rpm. This is the highest output power ever delivered by a power MEMS device to date.

Several switch-mode rectifier topologies are looked at for the second generation power electronics. Two topologies use a three-phase MOSFET bridge rectifier in conjunction with either a continuous-conduction-mode (CCM) boost converter or a discontinuous-conduction-mode (DMC) boost rectifier. Neither of these topologies is chosen because they require seven active devices and gate drives and have large magnetic components. The switch-mode rectifier chosen uses a boost semi-bridge topology operating in DCM. The rectifier is modeled and its losses calculated to predict its efficiency as a function of operating conditions and load. The DCM boost rectifier is built and connected to a first generation stator for initial characterization. Power generation tests with the new optimized stator and switch-mode rectifier are also presented. At a speed of 303,000 rpm the switch-mode rectifier delivers 5.52 W at a regulated output voltage of 12 V.

Finally, Chapter 6 summarizes the thesis, presents conclusions and outlines avenues for future work. Microscale PM machines have been proven capable of spinning at high speeds (100,000+ rpm) and, when connected to the switch-mode rectifier, delivering multi-Watt electric power to a load resistor at a constant DC output voltage emulating the behavior of a battery.

Among the contributions of this thesis are the development of analytical models for axial-flux magnetic machines with surface wound and slotted stators that can be used at any size scale. These models incorporate the effects of saturation, hysteresis, eddy currents and laminations in the rotor and stator core and provide a computationally fast method to determine machine parameters such as open-circuit voltage, inductance and torque. These models have been used to compare induction and PM machines at the microscale.

The fundamental engineering contribution of this thesis is the design and fabrication, in collaboration with colleagues at Georgia Institute of Technology, of the first microscale PM machines to generate

multi-Watt electrical power at rotational speeds in excess of 300,000 rpm. These PM machines are the first to have multi-turn, multi-layer, interleaved coils fabricated using an electroplating process. The stator coils have a total height 200 μm and a minimum feature size of 50 μm. They can operate at current densities of $10^8 - 10^9$ A/m^2 due to the use of flat conductors for the stator coils that are in intimate contact with the surface of the stator core. These current densities are one to two orders of magnitude larger than those found in macroscale PM machines and lead to power densities of up to 60 MW/m^3 which is larger than their macroscale counterparts.

Another important contribution is the design of a compact switch-mode rectifier that can efficiently convert the PM machines' three-phase AC voltages into a regulated 12 V DC output voltage without the need for direct rotor position/speed or stator current/voltage sensing. The rectifier's power stage takes up the same surface area as the stator die, keeping the overall electric power system small. These results demonstrate the viability of scaled PM generators and power electronics for portable power applications.

1.4 Collaboration

This thesis work has been performed in collaboration with David Arnold, Iulica Zana, Jin-Woo Park, Florian Herreault, Preston Galle and Professor Mark Allen at the Georgia Institute of Technology (GIT), and Yeun-Ho Joung and Professor David Veazie at Clark Atlanta University (CAU). GIT was responsible for the rotor PM magnetization process, stator fabrication and spinning rotor test stand assembly for the PM machines. GIT and CAU were responsible for structural integrity analysis and characterization of the PM rotor. The author of this thesis was responsible for the modeling and system level design of the PM machines as well as the design and construction of both the passive and active power electronics. The author was also responsible for the design of the stators for the 1st generation PM machines and took part in the fabrication of the stators. Optimization of the 2nd generation machines was performed using the author's models in conjunction with winding designs developed by GIT. Testing of the generator and power electronics took place at GIT.

2 Modeling

2.1 Overview

This chapter develops models for asynchronous (Induction) and synchronous (PM) planar magnetic machines with slotted and surface wound stators. Surface wound machines are modeled with and without laminations. Because the performance of unlaminated slotted stator machines is so poor [26] slotted stator machines are only modeled with laminations. The machines are modeled analytically so that their performance can be quickly determined as a function of speed, physical dimensions, material properties, and input currents.

Since there are no complicated axial structures such as poles and teeth, the surface wound machines can be modeled as a set of planar continuum layers [42] by solving Maxwell's equations in the Magneto-quasi-static (MQS) domain. The magnetic field intensity, H, and magnetic flux density, B, in the machine due to the rotor PM and stator currents are solved for as a function of radius and then integrated over the radial span of the machine to determine relevant machine parameters such as open-circuit voltage, inductance and torque. This is done in Section 2.2.

The model for the slotted stator magnetic machine consists of two parts. The first part models the machine in the same manner as the surface wound machine to determine the fields due to the rotor magnetization. The slotted stator is treated as two equivalent planar layers, one for the stator slots and one for the base of the stator core. The second part models the rotor and air gap as continuum layers and the stator as a lumped parameter magnetic reluctance circuit to determine the fields due to the stator currents. The rotor continuum model uses the tangential H field at the surface of the stator as a boundary condition to solve for the normal B field at the surface of the stator. The normal B field is integrated over the stator surface to determine the flux over each stator pole. The stator reluctance circuit uses this flux and the phase currents as inputs to determine the tangential H field at the surface of the stator. The full continuum and hybrid continuum/lumped parameter models are combined to determine H and B fields in the

machine as a function of radius. These field solutions are then integrated over the radial span of the machine to determine relevant machine parameters. This is done is Section 2.3.

This general field theory approach is computationally very fast and has been used to model both cylindrical and linear electric machines [43,44]. It can be used for a wide range of planar geometries and is especially useful in determining the effects of air gaps that are on the same order of magnitude as the wavelength of the rotor PM or larger. The field solutions are solved in the spatio-temporal frequency domain, which allows for complicated winding patterns and rotor magnetization profiles to be modeled by decomposing them into their respective Fourier components and then solving for fluxes, voltages, currents, etc., for each harmonic component.

To ease the complexity of this analytical approach, ideal properties are often assumed for the ferromagnetic magnetic materials used in the rotor and stator back irons (e.g. linear B-H relationship, zero conductivity, and no saturation or hysteresis) or in some cases, the effects of the back irons are completely ignored by assuming infinite permeabilities. These approximations are not suitable for the design of high-performance microscale machines, because the effects of the back irons cannot be ignored. The machine model must be able to determine how thin the back irons can be without becoming heavily saturated and thus reducing the total flux. It should also be able to determine hysteresis and eddy current losses in the back irons in order to predict machine efficiency as a function of speed, geometry, and material properties. Thus, saturation, hysteresis, and back iron conductivity must all be accurately accounted.

The models developed in this chapter include methods to accommodate these effects utilizing the full nonlinear B-H relationship. First, an iterative algorithm is used to solve for effective permeabilities for the rotor and stator back irons. Second, the field theory solutions are used to determine hysteresis loss from the back iron's nonlinear B-H curve. The use of effective permeabilities in conjunction with the general field theory approach enables the modeling of machines with nonlinear magnetic materials without resorting to time-consuming numerical methods, while maintaining the computational speed of an analytical model and taking advantage of frequency domain analysis.

This chapter also presents ways of computing relevant machine parameters. The Maxwell Stress Tensor is used to find the pull-in force and torque on the rotor by computing the H fields at the surface of the rotor and integrating the normal and shear stresses over the rotor surface. Use of the Maxwell Stress Tensor also allows the calculation of eddy current losses without the need to calculate current densities or evaluate volume integrals. The field solutions are also used to compute the inductance and open-circuit voltage of a single phase of the machine. Along with a simple approximation for the winding resistance, an equivalent circuit model for PM machines is given in Section 2.2.9.

Finally, verification of the models is presented in Section 2.4. The model for the slotted stator induction machine was verified in [26] for a non-conductive stator. Since the purpose of the laminations is to reduce eddy current effects so that the stators look non conductive, those FEA simulations [26] do not need to be redone. To verify the accuracy of the surface wound machine model, the open-circuit voltage predictions for a PM machine are compared to 3D finite-element analysis (FEA) simulations.

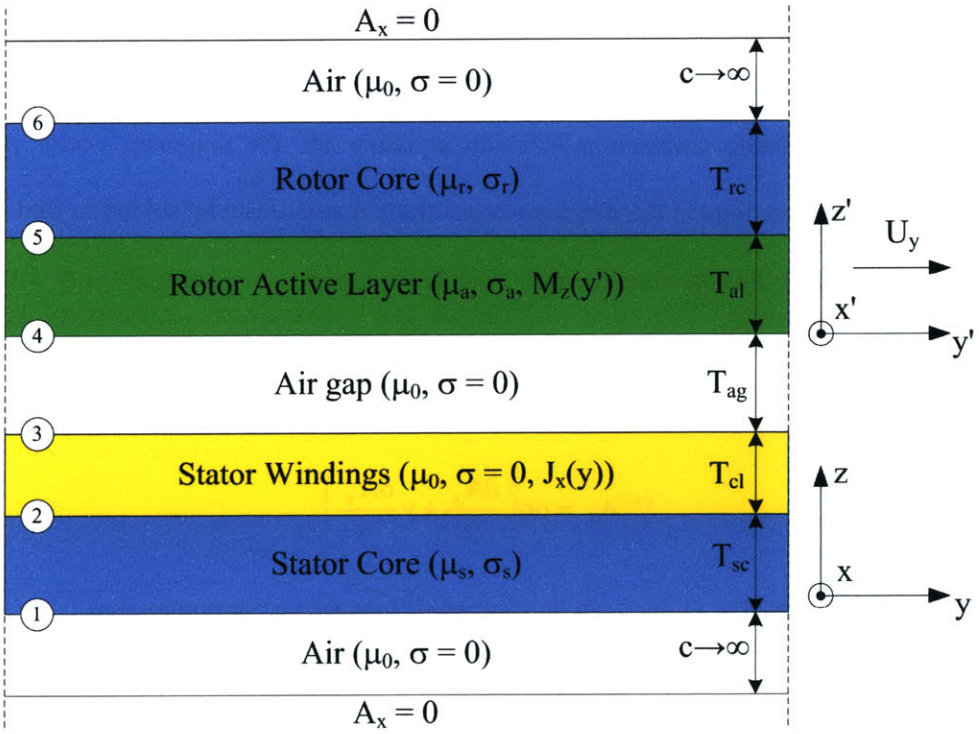

Figure 2-1: The surface wound magnetic machine is modeled as a series of planar continuum layers. The rotor moves in the y direction with velocity U_y. The Vector potential, A_x, is continuous across the interfaces between the layers are designated ① – ⑥.

2.2 Surface Wound Magnetic Machines

The surface wound magnetic machine can be modeled as a set of planar continuum layers since there are no complicated axial structures such as poles and teeth as shown in Figure 2-1. The cylindrical geometry (r, θ, z) of the machine is converted to a Cartesian geometry (x, y, z) by unwrapping the machine and setting

$$r \rightarrow x,\ r\theta \rightarrow y,\ z \rightarrow z. \tag{2-1}$$

The rotor-stator air gap, as well as the space above the rotor and below the stator, are modeled as layers with permeability μ_0 and conductivity $\sigma = 0$. The rotor and stator cores (back iron) are modeled as layers with permeabilities μ_r and μ_s and conductivities σ_r and, σ_s, respectively. The stator windings are modeled as a layer with zero conductivity and permeability μ_0, with an imposed current density distribution $J_x(y,t)$. The effect of proximity eddy currents within the coil layer is modeled separately in section 2.2.10. The rotor *active* layer has a spatially varying magnetization in the axial direction, $M_z(y')$ as well as a permeability μ_a and conductivity σ_a. It can be used to model a PM such as SmCo or NdFeB. The active layer can also model a rotor conductor, such as copper, for induction machines by setting $M_z(y')$ to zero.

A 2D Cartesian coordinate convection-diffusion equation for the magnetic vector potential, A, derived from Maxwell's equations in the magneto-quasi-static domain, can be solved to find the H and B fields due to the rotor active layer at some radius, r [26]. A planar layer moving uniformly with velocity v, will have a vector potential with only one component, A_x. If no magnetization or independent current sources exist in the layer then the convection-diffusion equation for A_x is

$$\nabla^2 A_x = \mu\sigma\left(\frac{\partial A_x}{\partial t} + v\frac{\partial A_x}{\partial y}\right). \tag{2-2}$$

The normal B field and tangential H field can be computed from the vector potential as

$$H_y = \frac{1}{\mu}\frac{\partial A_x}{\partial z}, \tag{2-3}$$

$$B_z = -\frac{\partial A_x}{\partial y}. \tag{2-4}$$

Equation (2-2) governs the behavior of the vector potential in the rotor core, stator core, air gap and regions above the rotor and below the stator, where μ, σ and v will be different for each layer ($v = U_y$ for the rotor core and zero otherwise). Equation (2-2) also governs the vector potential in the rotor active layer for an induction machine as well as an open circuited stator winding layer in the PM machine.

In the moving-coordinate frame of the rotor (x', y', z') (Figure 2-1) the magnetization profile can be decomposed into its Fourier harmonics

$$M_z(y') = \mathrm{Re}\left\{\sum_{n=-\infty}^{\infty} \hat{M}_{zn} e^{-jnky'}\right\}. \tag{2-5}$$

The time-varying field in the stationary coordinate frame is found by substituting $y' = y - U_y t$ into (2-5)

$$M_z(y,t) = \mathrm{Re}\left\{\sum_{n=-\infty}^{\infty} \hat{M}_{zn} e^{jnk(U_y t - y)}\right\}. \tag{2-6}$$

In addition, U_y can be replaced with the linear velocity at radius r, $U_y = \Omega_m r$, where Ω_m is the angular velocity of the rotor in rad/sec. The wave number k is simply P/r, where P is the number of pole pairs. Defining $\omega_m \equiv P\Omega_m$, (2-6) can be rewritten as

$$M_z(y,t) = \mathrm{Re}\left\{\sum_{n=-\infty}^{\infty} \hat{M}_{zn} e^{jn(\omega_m t - ky)}\right\}. \tag{2-7}$$

In addition, the current density in the stator winding layer, J_x, will be function of y and t. The windings on the surface of the stator are arranged so that a traveling magnetic field is created by the winding currents. J_x can be represented in terms of its Fourier harmonics

$$J_x(y,t) = \mathrm{Re}\left\{\sum_{n=-\infty}^{\infty} \hat{J}_{xn} e^{j(\omega_e t - nky)}\right\}, \tag{2-8}$$

where the current in windings is assumed to consist of a single electrical frequency, ω_e. Given the forms of the stator current density distribution and rotor magnetization in Equations (2-7) and (2-8), respectively, the vector potential in the machine will have the following form

$$A_x(y,z,t) = \mathrm{Re}\left\{\sum_{n=-\infty}^{\infty} \hat{A}_{xn}(z) e^{j(m\omega t - nky)}\right\}. \tag{2-9}$$

For each spatial harmonic, the complex amplitudes of the normal B field and tangential H field are now

$$\hat{B}_{zn} = jnk\hat{A}_n, \tag{2-10}$$

$$\hat{H}_{yn} = \frac{1}{\mu}\frac{d\hat{A}_n}{dz}, \tag{2-11}$$

where

$$B_z(y,z,t) = Re\left\{\sum_{n=-\infty}^{\infty}\hat{B}_{zn}(z)e^{j(m\omega t - nky)}\right\}, \tag{2-12}$$

$$H_y(y,z,t) = Re\left\{\sum_{n=-\infty}^{\infty}\hat{H}_{yn}(z)e^{j(m\omega t - nky)}\right\}. \tag{2-13}$$

In Equations (2-9), (2-12) and (2-13) $\omega = \omega_e$ and $m = 1$ for fields generated by stator currents while $\omega = \omega_m$ and $m = n$ for fields generated by the rotor magnetization.

2.2.1 Vector Potentials in Surface Wound Magnetic Machines

Using the continuum model developed in Section 2.2, the vector potential everywhere in the machine can be found. Each layer in Figure 2-1 is the same except for the details of the material properties (μ and σ) and speed. The solution to the convection-diffusion Equation (2-2) for a planar layer with permeability μ, conductivity σ, moving at a constant velocity, v, with no magnetization or independent current density will be examined first. By solving for the A, B and H fields in this planar layer, the field solution for the entire machine can be found by splicing together the solutions of each layer using the appropriate boundary conditions. This approach takes advantage of the fact A, the normal B field and tangential H field are all continuous across the interface of two layers. The strategy will be to find the vector potential at interface of the stator core and windings ②, stator windings and air gap ③, air gap and rotor core ④ and the rotor core and permanent magnet ⑤ as functions of the vector potential at the bottom surface of the stator core, $A_x^{(1)}$ and at the top surface of the rotor core, $\hat{A}_x^{(6)}$. After this has been done $A_x^{(1)}$ and $\hat{A}_x^{(6)}$ due to the magnetization in the rotor, with the stator currents set to zero, will be found and will be denoted

as $A^{(1)}_{x(m)}$ and $\hat{A}^{(6)}_{x(m)}$. Next, $A^{(1)}_{x}$ and $\hat{A}^{(6)}_{x}$ due to the stator current distribution, with the rotor magnetization set to zero, will be determined and will be denoted as $A^{(1)}_{x(J)}$ and $\hat{A}^{(6)}_{x(J)}$. Using the linear superposition of the two separate solutions the vector potential and magnetic fields everywhere in the machine can be found. These field solutions are iterated using different values for the permeability of the rotor and stator cores until the correct effective permeabilities are found so that the B fields in the machine lie on the B-H curves of the core materials used.

Substituting (2-9) into (2-2), the convection-diffusion equation for the magnetic vector potential yields an ordinary differential equation for each harmonic

$$\frac{d^2\hat{A}_{xn}}{dz^2} = \gamma_n^2 \hat{A}_{xn}, \tag{2-14}$$

in a general layer where

$$\gamma_n = \sqrt{n^2k^2 + j\mu\sigma(m\omega - nkv)}. \tag{2-15}$$

The solution to this equation is presented in terms of the complex vector potential amplitudes at the upper (a) and lower (b) boundaries of the planar layer [42], as shown in Figure 2-2. It takes the form

$$\hat{A}_{xn}(z) = \hat{A}^{(b)}_{xn}\frac{\sinh(\gamma_n z)}{\sinh(\gamma_n \Delta)} + \hat{A}^{(a)}_{xn}\frac{\sinh(\gamma_n(\Delta - z))}{\sinh(\gamma_n \Delta)}. \tag{2-16}$$

To simplify the analysis, transfer relations between the complex amplitudes of H, B and A at the upper and lower surfaces of each layer are derived [42]. Figure 2-2 shows a layer of thickness Δ moving in the y direction with constant velocity v and having permeability μ and conductivity σ. The vector potential and/or normal B fields at either the top or bottom surface can be computed from the tangential H on both surfaces using

$$\begin{bmatrix} \hat{A}^{(b)}_{xn} \\ \hat{A}^{(a)}_{xn} \end{bmatrix} = \frac{1}{jnk}\begin{bmatrix} \hat{B}^{(b)}_{zn} \\ \hat{B}^{(a)}_{zn} \end{bmatrix} = \frac{\mu}{\gamma_n}\begin{bmatrix} \coth(\gamma_n\Delta) & \frac{-1}{\sinh(\gamma_n\Delta)} \\ \frac{1}{\sinh(\gamma_n\Delta)} & -\coth(\gamma_n\Delta) \end{bmatrix}\begin{bmatrix} \hat{H}^{(b)}_{yn} \\ \hat{H}^{(a)}_{yn} \end{bmatrix}. \tag{2-17}$$

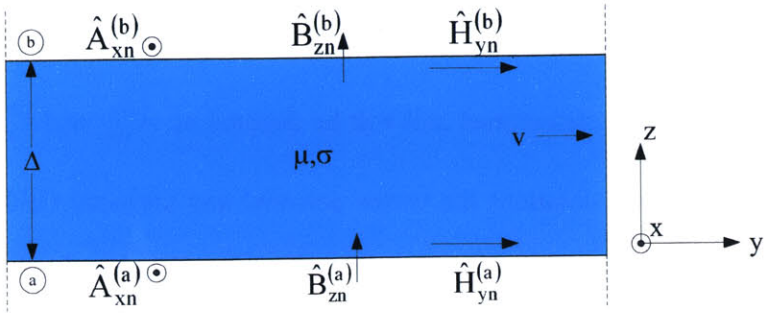

Figure 2-2: Lossy magnetic media of thickness Δ moving in the y direction at a velocity v.

Conversely, the tangential H on either surface can be computed from the vector potential on both surfaces using

$$\begin{bmatrix} \hat{H}_{yn}^{(b)} \\ \hat{H}_{yn}^{(a)} \end{bmatrix} = \frac{\gamma_n}{\mu} \begin{bmatrix} \coth(\gamma_n \Delta) & \dfrac{-1}{\sinh(\gamma_n \Delta)} \\ \dfrac{1}{\sinh(\gamma_n \Delta)} & -\coth(\gamma_n \Delta) \end{bmatrix} \begin{bmatrix} \hat{A}_{xn}^{(b)} \\ \hat{A}_{xn}^{(a)} \end{bmatrix}. \tag{2-18}$$

The transfer relation matrices (2-17) and (2-18) are used to find the vector potential and tangential H at the interfaces of the stator core and windings ②, stator windings and air gap ③, air gap and rotor core ④, and rotor core and PM ⑤, as functions of the vector potential at the bottom surface of the stator core, $A_{xn}^{(1)}$, and at the top surface of the rotor core, $\hat{A}_{xn}^{(6)}$ (Figure 2-1). Referring to Figure 2-1, the vector potential below the stator core at $z = c \rightarrow -\infty$ is 0, and can be written as

$$\hat{A}_{xn}^{(1)} \frac{\sinh(\gamma_{0n}(c+z))}{\sinh(\gamma_{0n} c)}, \tag{2-19}$$

where

$$\gamma_{0n} = \sqrt{n^2 k^2}\,. \tag{2-20}$$

The tangential H field at the bottom surface of the stator core is

$$\hat{H}_{yn}^{(1)} = \hat{A}_{xn}^{(1)} \frac{\gamma_{0n}}{\mu_0} \coth(\gamma_{0n} c) = \frac{\gamma_{0n}}{\mu_0} \hat{A}_{xn}^{(1)}. \tag{2-21}$$

A and H at the interface of the stator core and windings are

$$\hat{A}_{xn}^{(2)} = \frac{\mu_s}{\gamma_{sn}}\left[\coth(\gamma_{sn}T_{sc})\hat{H}_{yn}^{(2)} - \frac{1}{\sinh(\gamma_{sn}T_{sc})}\hat{H}_{yn}^{(1)}\right], \tag{2-22}$$

$$\hat{H}_{yn}^{(2)} = \frac{\gamma_{sn}}{\mu_s}\left[\coth(\gamma_{sn}T_{sc})\hat{A}_{xn}^{(2)} - \frac{1}{\sinh(\gamma_{sn}T_{sc})}\hat{A}_{xn}^{(1)}\right]. \tag{2-23}$$

Substituting the latter into the former yields

$$\hat{A}_{xn}^{(2)} = \frac{\mu_s}{\gamma_{sn}}\left[\left(\frac{\gamma_{sn}}{\mu_s}\left[\coth^2(\gamma_{sn}T_{sc})\hat{A}_{xn}^{(2)} - \frac{\coth(\gamma_{sn}T_{sc})}{\sinh(\gamma_{sn}T_{sc})}\hat{A}_{xn}^{(1)}\right]\right) - \frac{1}{\sinh(\gamma_{sn}T_{sc})}\left(\frac{\gamma_{0n}}{\mu_0}\hat{A}_{xn}^{(1)}\right)\right], \tag{2-24}$$

which simplifies into

$$\hat{A}_{xn}^{(2)} = \left[\frac{\mu_s}{\gamma_{sn}}\frac{\gamma_{0n}}{\mu_0}\sinh(\gamma_{sn}T_{sc}) + \cosh(\gamma_{sn}T_{sc})\right]\hat{A}_{xn}^{(1)}. \tag{2-25}$$

By substituting (2-25) into Equation (2-23), the tangential H field is found to be

$$\hat{H}_{xn}^{(2)} = \left[\frac{\gamma_{sn}}{\mu_s}\sinh(\gamma_{bn}T_{sc}) + \frac{\gamma_{0n}}{\mu_0}\coth(\gamma_{sn}T_{sc})\right]\hat{A}_{xn}^{(1)}. \tag{2-26}$$

This procedure is repeated until the vector potential and tangential H at interfaces ③, ④ and ⑤ are found in terms of $\hat{A}_x^{(1)}$.

The following transfer relation constants are defined for the different layers of the machine:

$$\alpha_{1n} = \frac{\mu_s}{\gamma_{sn}}\frac{\gamma_{0n}}{\mu_0}\sinh(\gamma_{sn}T_{sc}) + \cosh(\gamma_{sn}T_{sc}),\ \alpha_{2n} = \frac{\gamma_{sn}}{\mu_s}\sinh(\gamma_{sn}T_{sc}) + \frac{\gamma_{0n}}{\mu_0}\cosh(\gamma_{sn}T_{sc}) \tag{2-27a}$$

$$\alpha_{3n} = \frac{\mu_0}{\gamma_{0n}}\alpha_{2n}\sinh(\gamma_{0n}T_{cl}) + \alpha_{1n}\cosh(\gamma_{0n}T_{cl}),\ \alpha_{4n} = \frac{\gamma_{0n}}{\mu_0}\alpha_{1n}\sinh(\gamma_{0n}T_{cl}) + \alpha_{2n}\cosh(\gamma_{0n}T_{cl}) \tag{2-27b}$$

$$\alpha_{5n} = \frac{\mu_0}{\gamma_{0n}}\alpha_{4n}\sinh(\gamma_{0n}T_{ag}) + \alpha_{3n}\cosh(\gamma_{0n}T_{ag}),\ \alpha_{6n} = \frac{\gamma_{0n}}{\mu_0}\alpha_{3n}\sinh(\gamma_{0n}T_{ag}) + \alpha_{4n}\cosh(\gamma_{0n}T_{ag}) \tag{2-27c}$$

$$\alpha_{7n} = \frac{\mu_a}{\gamma_{an}}\alpha_{6n}\sinh(\gamma_{an}T_{al}) + \alpha_{5n}\cosh(\gamma_{an}T_{al}),\ \alpha_{8n} = \frac{\gamma_{an}}{\mu_a}\alpha_{5n}\sinh(\gamma_{an}T_{al}) + \alpha_{6n}\cosh(\gamma_{an}T_{al}) \tag{2-27d}$$

Using these constants, the complex amplitudes of the vector potential and tangential H at the interfaces ②, ③, ④, and ⑤ can now be written in terms of $A_{xn}^{(1)}$

$$\hat{A}_{xn}^{(2)} = \alpha_{1n}\hat{A}_{xn}^{(1)},\ \hat{A}_{xn}^{(3)} = \alpha_{3n}\hat{A}_{xn}^{(1)},\ \hat{A}_{xn}^{(4)} = \alpha_{5n}\hat{A}_{xn}^{(1)},\ \hat{A}_{xn}^{(5)} = \alpha_{7n}\hat{A}_{xn}^{(1)} \tag{2-28a}$$

$$\hat{H}_{yn}^{(2)} = \alpha_{2n}\hat{A}_{xn}^{(1)},\ \hat{H}_{yn}^{(3)} = \alpha_{4n}\hat{A}_{xn}^{(1)},\ \hat{H}_{yn}^{(4)} = \alpha_{6n}\hat{A}_{xn}^{(1)},\ \hat{H}_{yn}^{(5)} = \alpha_{8n}\hat{A}_{xn}^{(1)}. \tag{2-28b}$$

The next step is to find the vector potential and tangential H at the same four interfaces in terms of $A_x^{(6)}$. Referring to Figure 2-1, the vector potential above the rotor core at $z = c \rightarrow \infty$ is 0, and can be written as

$$\hat{A}_{xn}^{(6)}\frac{\sinh(\gamma_{0n}(c-z))}{\sinh(\gamma_{0n}c)}. \tag{2-29}$$

The tangential H field at the surface of the rotor core is

$$\hat{H}_{yn}^{(6)} = -\hat{A}_{xn}^{(6)}\frac{\gamma_{0n}}{\mu_0}\coth(\gamma_{0n}c) = -\frac{\gamma_{0n}}{\mu_0}\hat{A}_{xn}^{(6)}. \tag{2-30}$$

A and H at the interface of the rotor core and rotor magnet are

$$\hat{A}_{xn}^{(5)} = \frac{\mu_r}{\gamma_m}\left[\frac{1}{\sinh(\gamma_m T_{rc})}\hat{H}_{yn}^{(6)} - \coth(\gamma_m T_{rc})\hat{H}_{yn}^{(5)}\right], \tag{2-31}$$

$$\hat{H}_{yn}^{(5)} = \frac{\gamma_m}{\mu_r}\left[\frac{1}{\sinh(\gamma_m T_{rc})}\hat{A}_{xn}^{(6)} - \coth(\gamma_m T_{rc})\hat{A}_{xn}^{(5)}\right]. \tag{2-32}$$

Substituting the latter into the former yields

$$\hat{A}_{xn}^{(5)} = \frac{\mu_r}{\gamma_m}\left[\frac{1}{\sinh(\gamma_m T_{rc})}\left(-\frac{\gamma_{0n}}{\mu_0}\hat{A}_{xn}^{(6)}\right) - \left(\frac{\gamma_m}{\mu_r}\left[\frac{\coth(\gamma_m T_{rc})}{\sinh(\gamma_m T_{rc})}\hat{A}_{xn}^{(6)} - \coth^2(\gamma_m T_{rc})\hat{A}_{xn}^{(5)}\right]\right)\right], \tag{2-33}$$

which simplifies into

$$\hat{A}_{xn}^{(5)} = \left[\frac{\mu_r}{\gamma_m}\frac{\gamma_{0n}}{\mu_0}\sinh(\gamma_n T_{rc}) + \cosh(\gamma_n T_{rc})\right]\hat{A}_{xn}^{(6)}. \tag{2-34}$$

By substituting (2-34) into Equation (2-32), tangential H field is found to be

$$\hat{H}_{yn}^{(5)} = -\left[\frac{\gamma_m}{\mu_r}\sinh(\gamma_n T_{rc}) + \frac{\gamma_{0n}}{\mu_0}\coth(\gamma_n T_{rc})\right]\hat{A}_{xn}^{(6)}. \tag{2-35}$$

This procedure is repeated until the vector potential and tangential H at interfaces ②, ③ and ④ are found in terms of $\hat{A}_x^{(6)}$.

The following transfer relation constants are defined for the different layers of the machine:

$$\beta_{1n} = \frac{\mu_r}{\gamma_{rn}}\frac{\gamma_{0n}}{\mu_0}\sinh(\gamma_{rn}T_{rc}) + \cosh(\gamma_{rn}T_{rc}),\ \beta_{2n} = \frac{\gamma_n}{\mu_r}\sinh(\gamma_{rn}T_{rc}) + \frac{\gamma_{0n}}{\mu_0}\cosh(\gamma_{rn}T_{rc}) \tag{2-36a}$$

$$\beta_{3n} = \frac{\mu_a}{\gamma_{an}}\beta_{2n}\sinh(\gamma_{an}T_{al}) + \beta_{1n}\cosh(\gamma_{an}T_{al}),\ \beta_{4n} = \frac{\gamma_{an}}{\mu_a}\beta_{1n}\sinh(\gamma_{an}T_{al}) + \beta_{2n}\cosh(\gamma_{an}T_{al}) \tag{2-36b}$$

$$\beta_{5n} = \frac{\mu_0}{\gamma_{0n}}\beta_{4n}\sinh(\gamma_{0n}T_{ag}) + \beta_{3n}\cosh(\gamma_{0n}T_{ag}),\ \beta_{6n} = \frac{\gamma_{0n}}{\mu_0}\beta_{3n}\sinh(\gamma_{0n}T_{ag}) + \beta_{4n}\cosh(\gamma_{0n}T_{ag}) \tag{2-36c}$$

$$\beta_{7n} = \frac{\mu_0}{\gamma_{0n}}\beta_{6n}\sinh(\gamma_{0n}T_{cl}) + \beta_{5n}\cosh(\gamma_{0n}T_{cl}),\ \beta_{8n} = \frac{\gamma_{0n}}{\mu_0}\beta_{5n}\sinh(\gamma_{0n}T_{cl}) + \beta_{6n}\cosh(\gamma_{0n}T_{cl}) \tag{2-36d}$$

Using these constants, the complex amplitudes of the vector potential and tangential H at interfaces ②, ③, ④, and ⑤ can now also be written as

$$\hat{A}_{xn}^{(5)} = \beta_{1n}\hat{A}_{xn}^{(6)},\ \hat{A}_{xn}^{(4)} = \beta_{3n}\hat{A}_{xn}^{(6)},\ \hat{A}_{xn}^{(3)} = \beta_{5n}\hat{A}_{xn}^{(6)},\ \hat{A}_{xn}^{(2)} = \beta_{7n}\hat{A}_{xn}^{(6)} \tag{2-37a}$$

$$\hat{H}_{yn}^{(5)} = -\beta_{2n}\hat{A}_{xn}^{(6)},\ \hat{H}_{yn}^{(4)} = -\beta_{4n}\hat{A}_{xn}^{(6)},\ \hat{H}_{yn}^{(3)} = -\beta_{6n}\hat{A}_{xn}^{(6)},\ \hat{H}_{yn}^{(2)} = -\beta_{8n}\hat{A}_{xn}^{(6)}. \tag{2-37b}$$

The constants α_{in}, where $|\alpha_{in}| > 1$, describe the exponential decay in the vector potential and tangential H at interface ① due to some source of magnetic field in the layers above it. The constants β_{in}, where $|\beta_{in}| > 1$, describe the decay in the vector potential and tangential H at interface ⑥ due to some source of magnetic field in some layer below. The field distributions in the active layer due to the PM and fields in the coil layer due to the stator currents are governed by their own respective vector potential solutions which are given Sections 2.2.2 – 2.2.5.

Note that for a given excitation source (rotor magnetization or stator current) the vector potential at some interface is written in terms of an α or a β parameter and not both. In other words the two are mutually exclusive. For example the fields due the rotor PM will decay spatially as they move further away from the active layer. Referring to Figure 2-3(a) the fields will decay below the active layer as they move to the air gap, coil layer, and stator core and therefore the α parameters are used for interfaces ② –

④. Since the fields decay in the rotor core which is above the active layer the β parameters are used at interface ⑤. The opposite is true for the fields due to the stator currents in the coil layer as shown in Figure 2-3(b). Due to the symmetry of the machine about the air gap layer, the α parameters are used for interface ② while the β parameters are used for interfaces ③ – ⑤. This summarized in Table 2-1.

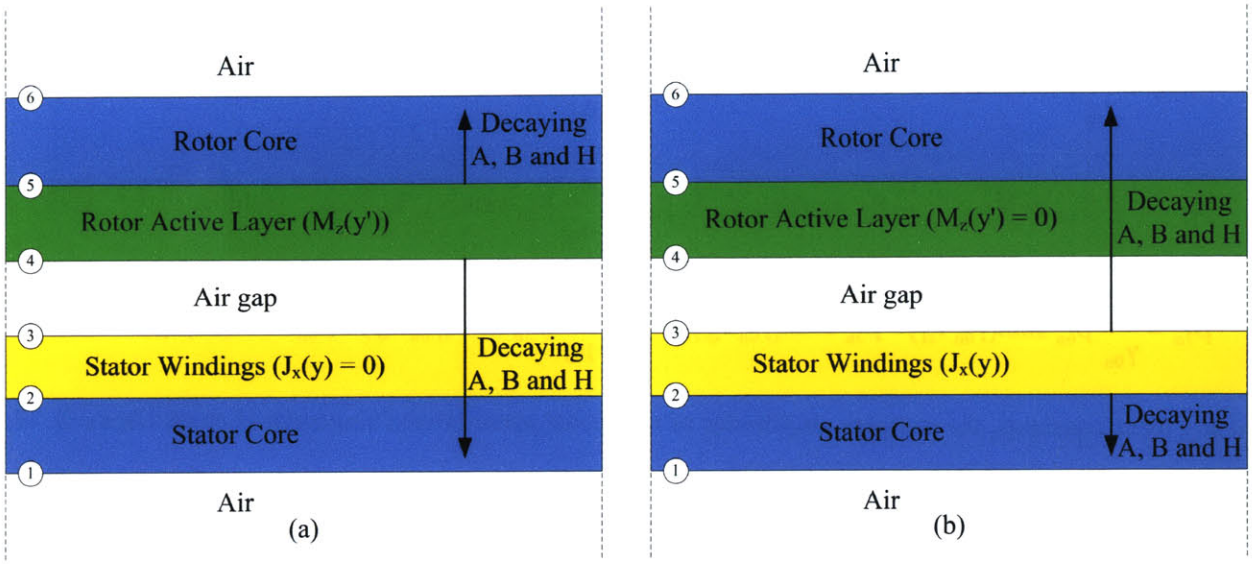

Figure 2-3: Spatially decaying fields due to (a) the rotor PM and (b) the stator currents. When solving for the fields due to one source, the other is set to zero.

Table 2-1: Vector potentials and tangential H at different interface layers due to the rotor PM and stator currents using α and β parameters.

Interface	A_x, H_y due to rotor PM	A_x, H_y due to Stator currents
①	$\hat{A}^{(1)}_{xn(m)}$, $\frac{\gamma_{0n}}{\mu_0}\hat{A}^{(1)}_{xn(m)}$	$\hat{A}^{(1)}_{xn(J)}$, $\frac{\gamma_{0n}}{\mu_0}\hat{A}^{(1)}_{xn(J)}$
②	$\alpha_{1n}\hat{A}^{(1)}_{xn(m)}$, $\alpha_{2n}\hat{A}^{(1)}_{xn(m)}$	$\alpha_{1n}\hat{A}^{(1)}_{xn(J)}$, $\alpha_{2n}\hat{A}^{(1)}_{xn(J)}$
③	$\alpha_{3n}\hat{A}^{(1)}_{xn(m)}$, $\alpha_{4n}\hat{A}^{(1)}_{xn(m)}$	$\beta_{5n}\hat{A}^{(6)}_{xn(J)}$, $-\beta_{6n}\hat{A}^{(6)}_{xn(J)}$
④	$\alpha_{5n}\hat{A}^{(1)}_{xn(m)}$, $\alpha_{6n}\hat{A}^{(1)}_{xn(m)}$	$\beta_{3n}\hat{A}^{(6)}_{xn(J)}$, $-\beta_{4n}\hat{A}^{(6)}_{xn(J)}$
⑤	$\beta_{1n}\hat{A}^{(6)}_{xn(m)}$, $-\beta_{2n}\hat{A}^{(6)}_{xn(m)}$	$\beta_{1n}\hat{A}^{(6)}_{xn(J)}$, $-\beta_{2n}\hat{A}^{(6)}_{xn(J)}$
⑥	$\hat{A}^{(6)}_{xn(m)}$, $-\frac{\gamma_{0n}}{\mu_0}\hat{A}^{(6)}_{xn(m)}$	$\hat{A}^{(6)}_{xn(J)}$, $-\frac{\gamma_{0n}}{\mu_0}\hat{A}^{(6)}_{xn(J)}$

The values for γ_{0n}, γ_{an}, γ_{rn} γ_{sn} will be different for induction and PM machines and are given in table 2-2. In a synchronous machine, such as a PM machine, the electrical frequency of the stator currents, ω_e, equals the angular velocity, ω_m. In an asynchronous machine, such as an induction machine, ω_e can be larger than ω_m (motoring mode) or less than ω_m (generating mode).

Table 2-2: Diffusion constants for different planar layers.

Diffusion Constant	Synchronous Machine	Asynchronous machine
γ_{0n}	$\sqrt{n^2k^2}$	$\sqrt{n^2k^2}$
γ_{an}	$\sqrt{n^2k^2}$	$\sqrt{n^2k^2 + j\mu_a\sigma_a(\omega_e - n\omega_m)}$
γ_{rn}	$\sqrt{n^2k^2}$	$\sqrt{n^2k^2 + j\mu_r\sigma_r(\omega_e - n\omega_m)}$
γ_{sn}	$\sqrt{n^2k^2 + j\mu_s\sigma_s n\omega_m}$	$\sqrt{n^2k^2 + j\mu_s\sigma_s\omega_e}$

2.2.2 Vector Potentials due to the Rotor Magnetization

The vector potential in the machine due to the rotor permanent magnet can now be determined with the aid of the transfer relation constants. For the rotor active layer with magnetization, $M_z(y')$, moving uniformly with velocity U_y the convection-diffusion equation for A_x, derived in appendix A, is

$$\nabla^2 A_x + \mu_a \frac{\partial M_z}{\partial y} = \mu_a \sigma_a \left(\frac{\partial A_x}{\partial t} + U_y \frac{\partial A_x}{\partial y} \right). \tag{2-38}$$

Substituting (2-7) and (2-9) into (2-38), the convection-diffusion equation for the magnetic vector potential yields an ordinary differential equation for each harmonic

$$\frac{d^2 \hat{A}_{xn}}{dz^2} = \gamma_{an}^2 \hat{A}_{xn} + j\mu_a nk \hat{M}_{zn}. \tag{2-39}$$

The particular solution for a PM annulus is

$$\hat{A}_{xnp} = -j\frac{\mu_a nk}{\gamma_{an}^2} \hat{M}_{zn} = -j\hat{A}_{xn(m)}, \tag{2-40}$$

since the magnetization only varies with y and not z. The vector potential in the PM layer is

$$\hat{A}_{xn}(z) = \hat{A}_{xn}^{(b)} \frac{\sinh(\gamma_{an} z)}{\sinh(\gamma_{an} T_{al})} + \hat{A}_{xn}^{(a)} \frac{\sinh(\gamma_{an}(T_{al} - z))}{\sinh(\gamma_{an} T_{al})} - j\hat{A}_{xn(m)}. \tag{2-41}$$

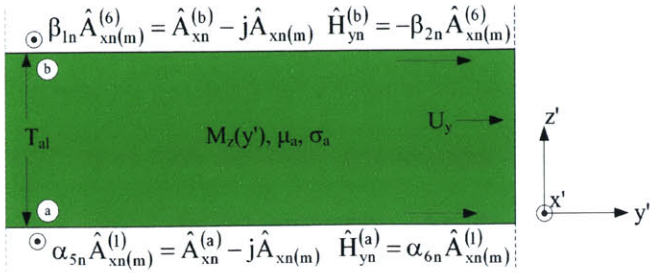

Figure 2-4: Boundary conditions for the rotor PM layer.

The vector potential at the top of the PM can be written in terms of $\hat{A}^{(6)}_{xn(m)}$, while the vector potential at the bottom can be written in terms of $\hat{A}^{(1)}_{xn(m)}$ (Figure 2-4) according to

$$\beta_{1n}\hat{A}^{(6)}_{xn(m)} = \hat{A}^{(b)}_{xn} - j\hat{A}_{xn(m)} \rightarrow \hat{A}^{(b)}_{xn} = \beta_{1n}\hat{A}^{(6)}_{xn(m)} + j\hat{A}_{xn(m)}, \tag{2-42}$$

$$\alpha_{5n}\hat{A}^{(1)}_{xn(m)} = \hat{A}^{(a)}_{xn} - j\hat{A}_{xn(m)} \rightarrow \hat{A}^{(a)}_{xn} = \alpha_{5n}\hat{A}^{(1)}_{xn(m)} + j\hat{A}_{xn(m)}. \tag{2-43}$$

The subscript (m) has been added to denote that the two vector potentials are due to the PM. Similarly, the tangent H field at the top and bottom surfaces of the PM can be expressed as

$$\hat{H}^{(b)}_{yn} = -\beta_{2n}\hat{A}^{(6)}_{xn(m)}, \tag{2-44}$$

$$\hat{H}^{(a)}_{yn} = \alpha_{6n}\hat{A}^{(1)}_{xn(m)}. \tag{2-45}$$

Using transfer relation matrices (2-17) and (2-18), $\hat{A}^{(b)}_{xn}$ and $\hat{A}^{(a)}_{xn}$ can be eliminated leaving the following two equations for $A^{(1)}_x$ and $A^{(6)}_x$

$$\alpha_{6n}\hat{A}^{(1)}_{xn} + \beta_{4n}\hat{A}^{(6)}_{xn} = -j\frac{\gamma_{an}}{\mu_a}\sinh(\gamma_{an}T_{al})\hat{A}_{xn(m)}, \tag{2-46}$$

$$\alpha_{8n}\hat{A}^{(1)}_{xn} + \beta_{2n}\hat{A}^{(6)}_{xn} = -j\frac{\gamma_{an}}{\mu_a}\sinh(\gamma_{an}T_{al})\hat{A}_{xn(m)}. \tag{2-47}$$

Solving (2-46) and (2-47), $\hat{A}^{(1)}_{xn(m)}$ and $\hat{A}^{(6)}_{xn(m)}$ in terms of $\hat{A}_{xn(m)}$ are

$$\hat{A}^{(1)}_{xn(m)} = -j\frac{\gamma_{an}}{\mu_a}\left[\frac{\beta_{4n} - \beta_{2n}}{\alpha_{8n}\beta_{4n} - \alpha_{6n}\beta_{2n}}\right]\sinh(\gamma_{an}T_{al})\hat{A}_{xn(m)}, \tag{2-48}$$

$$\hat{A}^{(6)}_{xn(m)} = -j\frac{\gamma_{an}}{\mu_a}\left[\frac{\alpha_{8n} - \alpha_{6n}}{\alpha_{8n}\beta_{4n} - \alpha_{6n}\beta_{2n}}\right]\sinh(\gamma_{an}T_{al})\hat{A}_{xn(m)}. \tag{2-49}$$

2.2.3 Rotor Magnetization Profile

Rotors using an annular PM as well as discrete PMs will be analyzed as shown in Figure 2-5. For an annular PM the rotor magnetization, impressed using a magnetic poling process, does not abruptly transition between north and south poles; instead, the magnetic remanence smoothly transitions between $+B_r$ and $-B_r$. Normally, in a macroscale machine, discrete PMs are used so this transition region is not present. However, this effect is important because of the small dimensions of the microscale PM machines. Therefore, the annular rotor PM is modeled with a trapezoidal magnetization profile with a linear "transition region" of length c_m, as shown in Figure 2-6. This linear transition is used as a first-order approximation for computational simplicity.

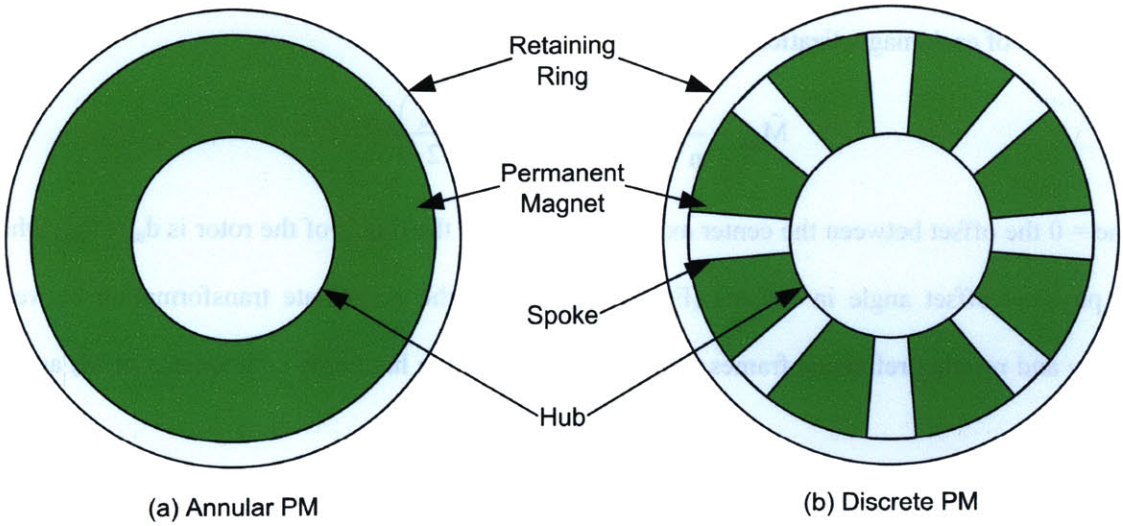

Figure 2-5: Types of PMs used in magnetic machines (a) Annular PM, (b) Discrete PM.

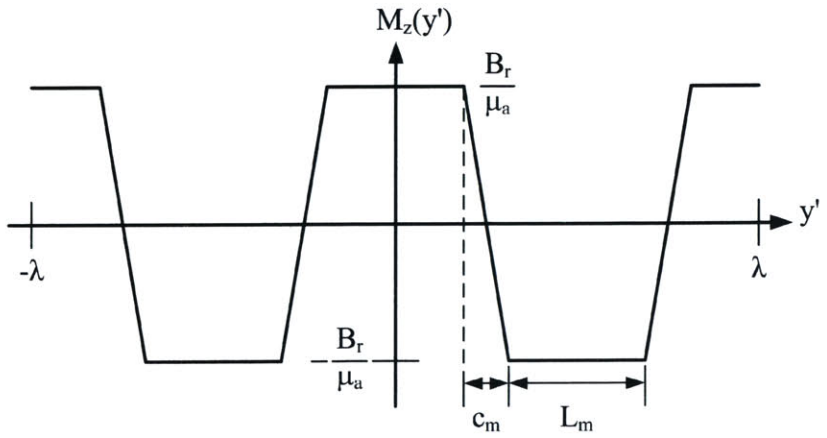

Figure 2-6: Trapezoidal magnetization profile of annular PM. B_r is the remanent flux density of the magnet. c_m is the transition region length.

Due to the even symmetry of the profile shown in Figure 2-6, the Fourier harmonics of the rotor magnetization in Equation (2-7) can be expressed as

$$M_z(y,t) = \mathrm{Re}\left\{ \sum_{n=1,\mathrm{odd}}^{\infty} \hat{M}_{zn} e^{jn(\omega_m t - ky)} \right\}, \tag{2-50}$$

where

$$\hat{M}_{zn} = \frac{1}{\lambda} \int_{\lambda} M_z(y') e^{jnky'} dy . \tag{2-51}$$

Defining the length of region in which the magnetization is uniform, L_m, to be

$$L_m = \frac{\lambda}{2} - c_m = \frac{\pi r}{P} - c_m , \tag{2-52}$$

the magnitude of each magnetization harmonic is

$$\hat{M}_{zn} = \frac{4}{n^2\pi^2} \frac{\lambda}{c_m} \frac{B_r}{\mu_a} \cos\left(nk \frac{L_m}{2} \right) e^{jn\delta_m} . \tag{2-53}$$

At time = 0 the offset between the center axis of Phase A and the d-axis of the rotor is $d_m = \theta_m r$, where θ_m is the physical offset angle in radians (Figure 2-7). Since the coordinate transformation between the stationary and rotating reference frames is $y' = y - d_m - U_y t$, the harmonic components of M_z are shifted by

$$e^{jnk\theta_m r} = e^{jn\frac{P}{r}\theta_m r} = e^{jnP\theta_m} = e^{jn\delta_m} . \tag{2-54}$$

$\delta_m = P\theta_m$ is commonly referred to as the torque angle [41]. Given the magnetization in (2-53) the particular solution to Equation (2-40) is

$$\hat{A}_{xn(m)} = \frac{8}{n\pi} \frac{B_r}{n^2 k^2 c_m} \cos\left(nk \frac{L_m}{2} \right) e^{jn\delta_m} . \tag{2-55}$$

Alternatively, the permanent magnet layer could be composed of discrete "pie" pieces as shown in Figure 2-5. The magnitudes of the magnetization harmonics for this case is

$$\hat{M}_{zn} = \frac{4}{n\pi} \frac{B_r}{\mu_a} \sin\left(nk \frac{L_m}{2} \right) e^{jn\delta_m} . \tag{2-56}$$

Similarly, the particular solution for a discrete PM rotor is

$$\hat{A}_{xn(m)} = \frac{4}{n\pi}\frac{B_r}{nk}\sin\left(nk\frac{L_m}{2}\right)e^{jn\delta_m}. \tag{2-57}$$

Note that L_m can be a function of the radius as is shown in Figure 2-5. The angle spanned by a single pole piece will be some fraction, χ, of π/P. Redefining L_m to be

$$L_m = \chi\frac{\pi r}{P}, \tag{2-58}$$

the magnetization harmonics simplify to

$$\hat{M}_{zn} = \frac{4}{n\pi}\frac{B_r}{\mu_a}\sin\left(\frac{n\pi\chi}{2}\right)e^{jn\delta_m} \tag{2-59}$$

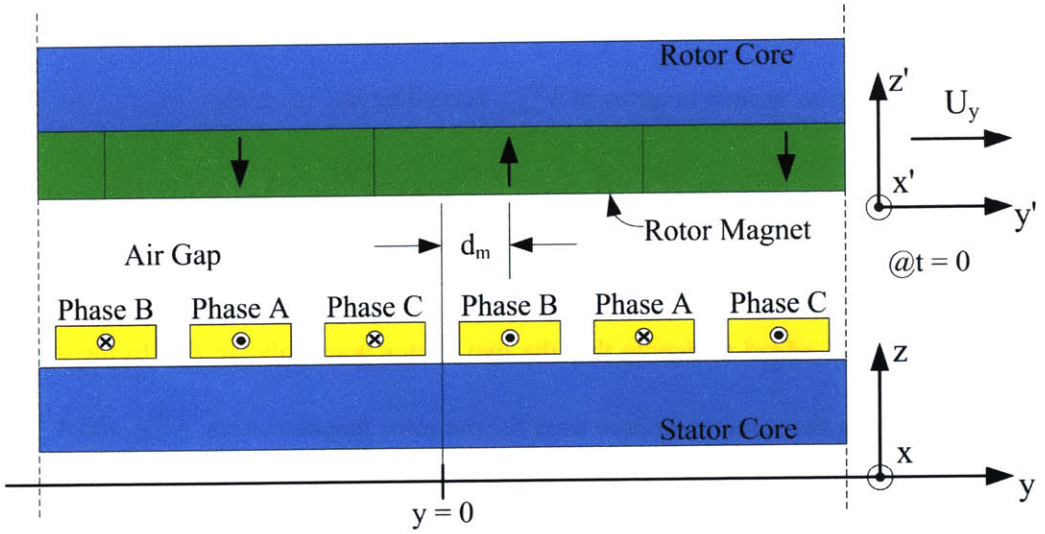

Figure 2-7: PM machine at t = 0 showing an offset of $y = d_m$ between the center axis of phase A and the center of a rotor North Pole.

2.2.4 Vector Potentials due to the Current in the Stator windings

The vector potential in the machine due to the currents in the stator windings can be determined in the same way they were determined from the rotor permanent magnet. For a planar layer with current density distribution, J_x, the governing equation for the vector potential is [45]

$$\nabla^2 A_x = -\mu_0 J_x. \tag{2-60}$$

Following the same procedure in Section 2.2.2, (2-8) and (2-9) are substituted into (2-60) for the magnetic vector potential yielding the following ordinary differential equation for each harmonic

$$\frac{d^2\hat{A}_{xn}}{dz^2} - \gamma_{0n}^2 \hat{A}_{nx} = -\mu_0 \hat{J}_{xn} . \tag{2-61}$$

The resulting particular solution to the vector potential for each harmonic in the stator winding layer is

$$\hat{A}_{xn(J)} = \frac{\mu_0}{\gamma_{0n}^2} \hat{J}_{xn} . \tag{2-62}$$

The vector potential in the stator current layer is

$$\hat{A}_{xn}(z) = \hat{A}_{xn}^{(b)} \frac{\sinh(\gamma_{0n} z)}{\sinh(\gamma_{0n} T_{cl})} + \hat{A}_{xn}^{(a)} \frac{\sinh(\gamma_{0n} (T_{cl} - z))}{\sinh(\gamma_{0n} T_{cl})} + \hat{A}_{xn(J)} . \tag{2-63}$$

The vector potential at the top of the stator current layer can be written in terms of $\hat{A}_{xn(J)}^{(6)}$ while the vector potential at the bottom can be written in terms of $\hat{A}_{xn(J)}^{(1)}$ according to

$$\beta_{5n} \hat{A}_{xn(J)}^{(6)} = \hat{A}_{xn}^{(b)} + \hat{A}_{xn(J)} \rightarrow \hat{A}_{xn}^{(b)} = \beta_{5n} \hat{A}_{xn(J)}^{(6)} - \hat{A}_{xn(J)} , \tag{2-64}$$

$$\alpha_{1n} \hat{A}_{xn(J)}^{(1)} = \hat{A}_{xn}^{(a)} + \hat{A}_{xn(J)} \rightarrow \hat{A}_{xn}^{(a)} = \alpha_{1n} \hat{A}_{xn(J)}^{(1)} - \hat{A}_{xn(J)} . \tag{2-65}$$

The subscript (J) has been added to denote that the two vector potentials are due to the currents in the stator winding. Following the same procedure used for the rotor magnetization, $\hat{A}_{xn(J)}^{(1)}$ and $\hat{A}_{xn(J)}^{(6)}$ in terms of $\hat{A}_{xn(J)}$ are

$$\hat{A}_{xn(J)}^{(1)} = \frac{\gamma_{0n}}{\mu_0} \left[\frac{\beta_{8n} - \beta_{6n}}{\alpha_{4n}\beta_{8n} - \alpha_{2n}\beta_{6n}} \right] \sinh(\gamma_{0n} T_{cl}) \hat{A}_{xn(J)} , \tag{2-66}$$

$$\hat{A}_{xn(J)}^{(6)} = \frac{\gamma_{0n}}{\mu_0} \left[\frac{\alpha_{4n} - \alpha_{2n}}{\alpha_{4n}\beta_{8n} - \alpha_{2n}\beta_{6n}} \right] \sinh(\gamma_{0n} T_{cl}) \hat{A}_{xn(J)} . \tag{2-67}$$

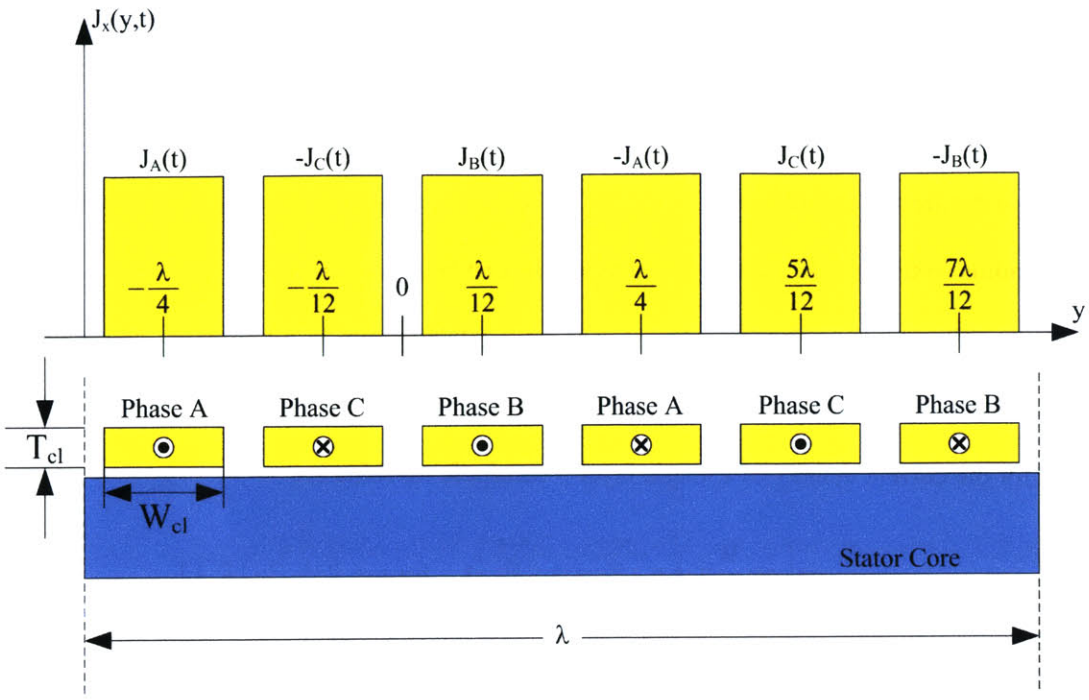

Figure 2-8: Current density distribution for a 1-turn/pole surface wound stator.

2.2.5 Stator current density profile

Like the rotor magnetization, the spatially varying current density in the stator windings can be represented in terms of in Fourier harmonic components according to

$$J_x(y,t) = \mathrm{Re}\left\{\sum_{n=-\infty}^{\infty} \hat{J}_{xn} e^{j(\omega_e t - nky)}\right\}. \tag{2-68}$$

For the 1-turn/pole stator winding shown in Figure 2-8 and where $\lambda = 2\pi r/P$, the complex magnitude of each spatial harmonic is

$$\hat{J}_{xn} = \frac{6}{n\pi}\sin\left(n\pi\frac{W_{cl}}{\lambda}\right)\left[\left(1-(-1)^n\right)J_A(t)e^{-j\frac{n\pi}{2}} + \left(1-(-1)^n\right)J_B(t)e^{j\frac{n\pi}{6}} + \left(1-(-1)^n\right)J_C(t)e^{j\frac{5n\pi}{6}}\right]. \tag{2-69}$$

For a balanced three-phase current excitation the amplitudes of the current density harmonics for the 1-turn/pole machine simplify to

$$\hat{J}_{xn} = \frac{6}{n\pi}\sin\left(n\pi\frac{W_{cl}}{\lambda}\right)e^{-j\frac{n\pi}{2}}J_o, \text{ for } n = 1,-5,\ 7,-11,\ 13\ldots \tag{2-70}$$

The current density in a single radial conductor for a machine with a single winding layer is

$$J_o = \frac{I_o}{W_{cl} T_{cl}}, \tag{2-71}$$

where W_{cl} and T_{cl} are the width and thickness of the stator winding, respectively. Note that W_{cl} can be a function of radius so that windings with variable widths can be modeled.

Machines with more than 1-turn/pole can also be modeled using this approach, where the multiple turns can all reside on a single layer or be stacked onto multiple layers. Referring to Figure 2-9 harmonic amplitudes for the current density of a single layer 2-turn/pole machine are

$$\hat{J}_{xn} = \frac{6}{n\pi} \sin\left(n\pi \frac{W_{cl}}{\lambda} \right) \left(e^{-j\frac{n5\pi}{12}} + e^{-j\frac{n7\pi}{12}} \right) J_o, \text{ for } n = 1,-5, 7,-11, 13\ldots \tag{2-72}$$

For a machine with a double layer winding as depicted in Figure 2-10, the coils are treated as a single conductor and T_{cl} in this case is the sum of the thicknesses of the top coil, bottom coil and via layers. The harmonic amplitudes for this winding pattern is also given by Equation (2-70) where the current density is

$$J_o = \frac{2I_o}{W_{cl} T_{cl}}. \tag{2-73}$$

In general, for a three-phase surface wound machine with P pole pairs, N-turns/pole and κ winding layers the harmonic amplitudes of the current density are

$$\hat{J}_{xn} = \frac{6}{n\pi} \sin\left(n\pi \frac{W_{cl}}{\lambda} \right) J_o \sum_{\substack{\nu=2N'+1 \\ \text{step2}}}^{4N'-1} e^{-j\frac{n\pi}{6N'}\nu}, \text{ for } n = 1,-5, 7,-11, 13\ldots \tag{2-74}$$

and

$$J_o = \frac{\kappa I_o}{W_{cl} T_{cl}}, \tag{2-75}$$

where $N' = N/\kappa$ and T_{cl} is the total height of all κ winding layers. For current density amplitudes given by (2-74) the resulting particular solution to (2-62) is

$$\hat{A}_{xn(J)} = \frac{6}{n\pi} \frac{\mu_0 J_o}{n^2 k^2} \sin\left(n\pi \frac{W_{cl}}{\lambda} \right) \sum_{\substack{\nu=2N'+1 \\ \text{step2}}}^{4N'-1} e^{-j\frac{n\pi}{6N'}\nu}. \tag{2-76}$$

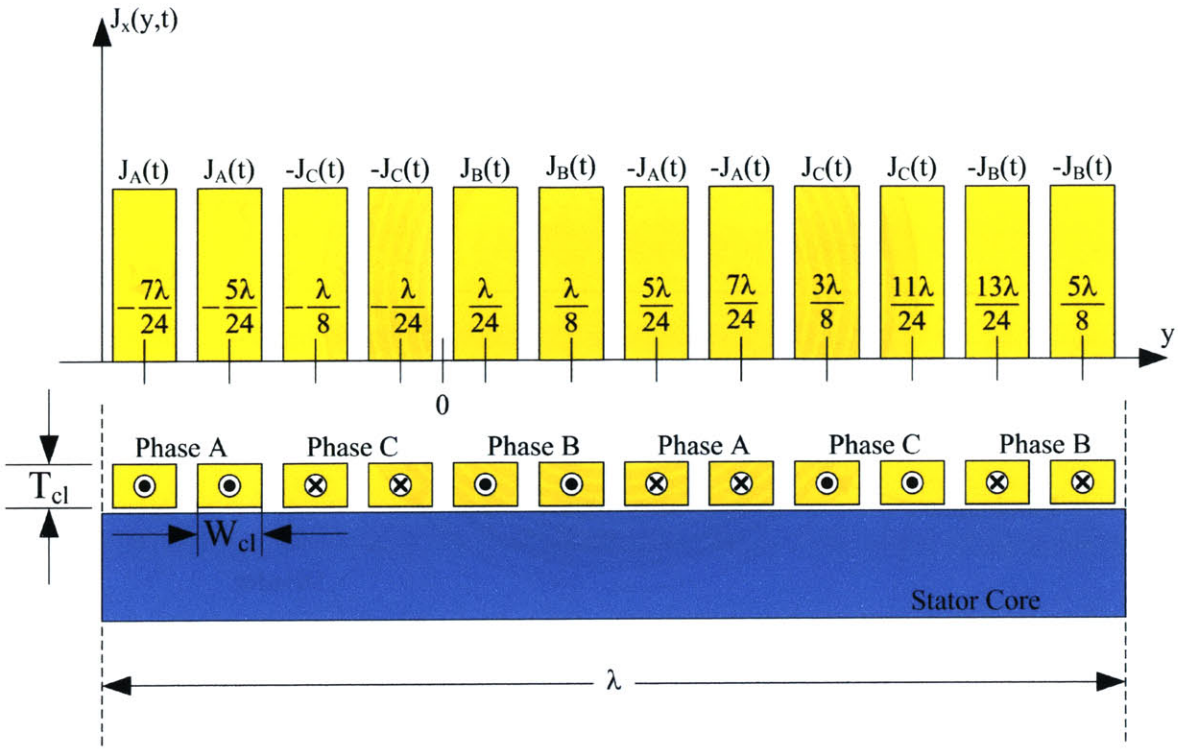

Figure 2-9: Current density distribution for a 2-turn/pole surface wound stator.

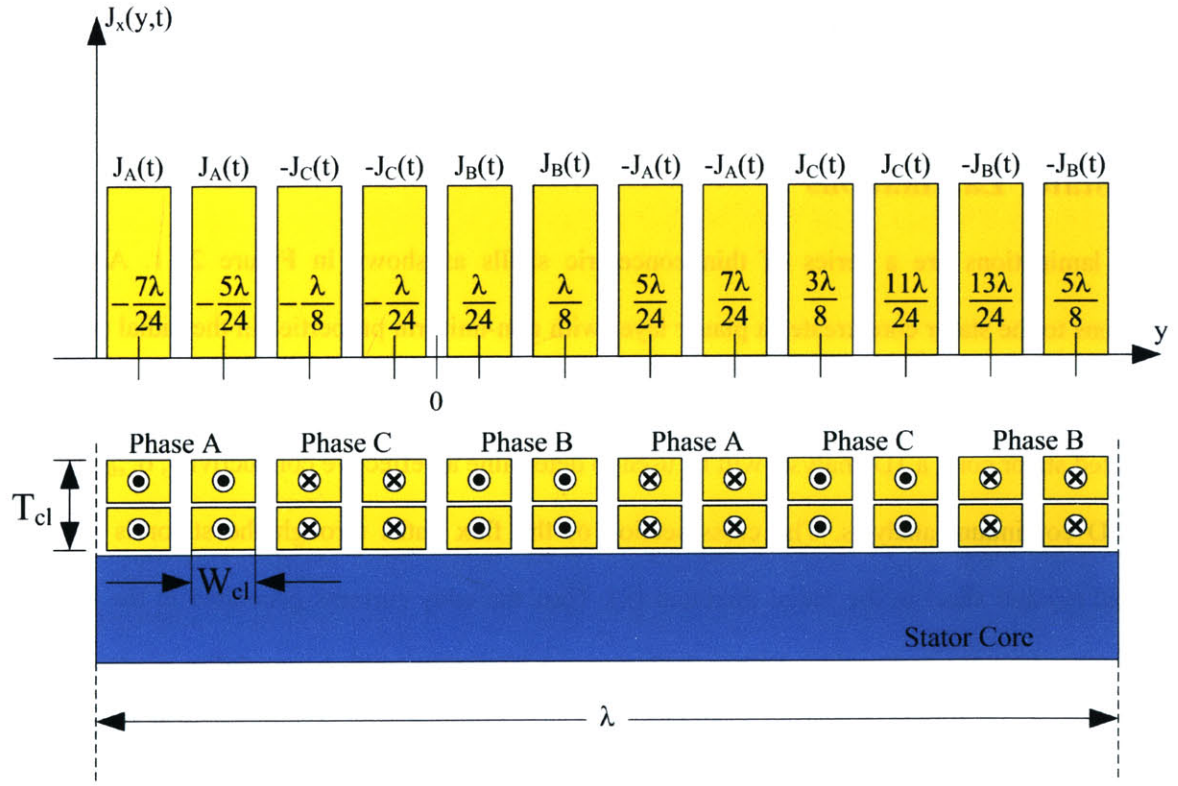

Figure 2-10: Current density distribution for a 4-turn/pole double layer winding.

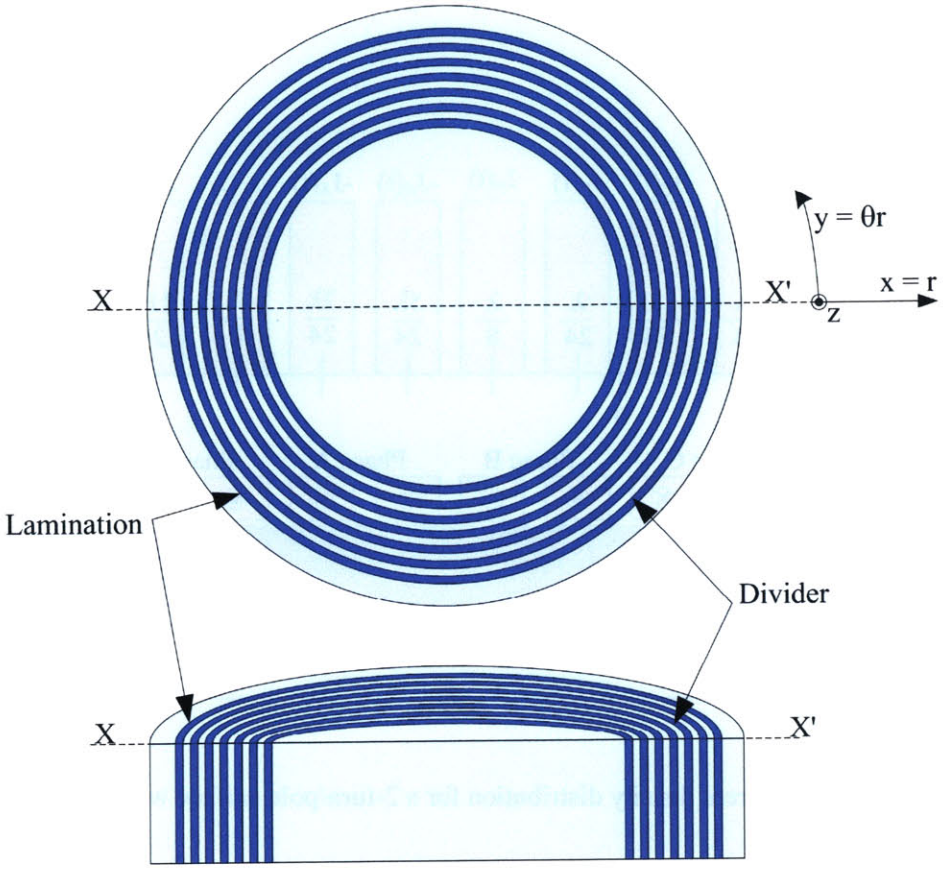

Figure 2-11: Laminated stator for surface wound magnetic machine.

2.2.6 Stator Laminations

The laminations are a series of thin concentric shells as shown in Figure 2-11. Adding these laminations to the stator core creates a planar layer with non-uniform properties in the radial (x) direction which can complicate the field analysis. Rather than solving Maxwell's equations in three dimensions for a laminated stator core, a 1D analysis will be used to determine an effective conductivity, $\sigma_{s,eff}$, to be used in the 2D continuum analysis. The cross section of the flux paths through the stator is long in the azimuthal (y) and short in the radial direction (x). Thus the eddy currents generated in the laminations flow mainly along the y direction. Figure 2-12 shows a lamination with permeability μ, conductivity σ, thickness W and depth T into the page (T >> W). At $x = \pm W/2$, a time varying magnetic field is applied

$$H(t) = \mathrm{Re}\left\{H_0 e^{j\omega t}\right\}. \tag{2-77}$$

The magnetic field inside the lamination will be of the form

$$H_z(y,t) = \mathrm{Re}\left\{\hat{H}_z(y)e^{j\omega t}\right\}. \tag{2-78}$$

$H_z(y,t)$ can be determined by solving the diffusion Equation [45]

$$\frac{\partial^2 H_z}{\partial y^2} = \mu\sigma\frac{\partial H_z}{\partial t}, \tag{2-79}$$

which reduces to following ODE for $\hat{H}_z$

$$\frac{d^2\hat{H}_z}{dy^2} = j\mu\sigma\omega\hat{H}_z. \tag{2-80}$$

Exploiting the even symmetry of the problem, the solution has the following form [46]

$$\hat{H}_z(y) = H_0\frac{\cosh(\alpha y)}{\cosh\left(\alpha\frac{W}{2}\right)}, \tag{2-81}$$

where, $\alpha = \frac{1+j}{\delta}$ and $\delta = \sqrt{\frac{2}{\mu\sigma\omega}}$ is the skin depth for the diffusion of the magnetic field.

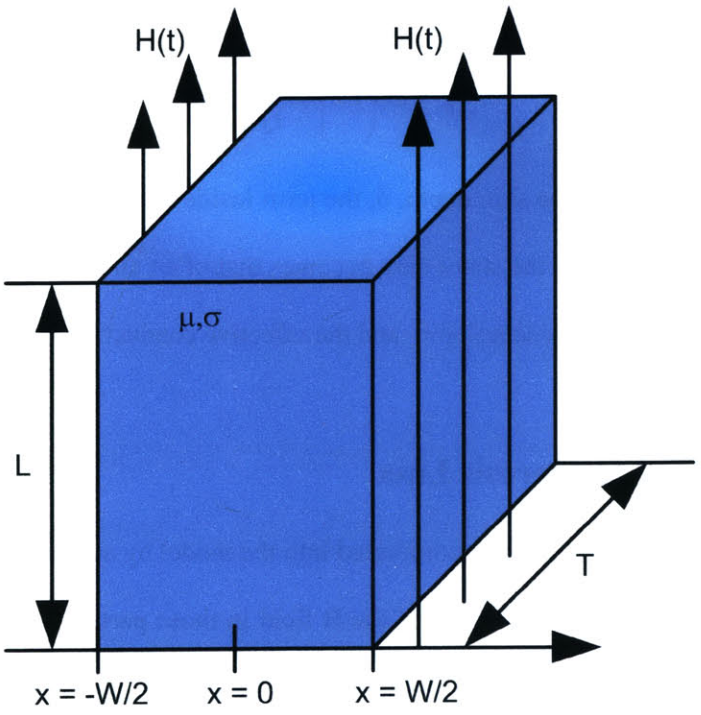

Figure 2-12: Eddy currents in a lamination of thickness W. The lightly shaded region represents minimum flux penetration.

The total flux through this lamination is

$$\hat{\Phi} = \mu T \int_{-W/2}^{W/2} \hat{H}_z(y)dy = \frac{\mu T H_0}{\cosh\left(\alpha \frac{W}{2}\right)} \int_{-W/2}^{W/2} \cosh(\alpha y)dy = \frac{2\mu T H_0}{\alpha} \tanh\left(\alpha \frac{W}{2}\right). \tag{2-82}$$

Equation (2-82) can be rewritten as

$$\hat{\Phi} = \frac{2\mu T H_0}{\alpha} \tanh\left(\alpha \frac{W}{2}\right) \times \frac{W}{W} = (\mu T W) \times \left(\frac{\tanh(Q)}{Q}\right), \tag{2-83}$$

where,

$$Q = \frac{1+j}{2} \frac{W}{\delta}. \tag{2-84}$$

The first term in (2-83) is the flux through the lamination when no eddy currents are present

$$\Phi_0 = \mu T W. \tag{2-85}$$

The second term describes how induced eddy currents reduce the net flux through the lamination. Note that the eddy currents not only decrease the magnitude of the flux but also create a phase lag between the applied MMF and the flux through the lamination because the term is complex. The effective conductivity, $\sigma_{s,eff}$, for the laminated stator core is therefore defined as

$$\sigma_{s,eff} = \sigma_s \left(1 - \left|\frac{\tanh(Q)}{Q}\right|\right). \tag{2-86}$$

As W becomes much larger than the skin depth, δ, the term inside the parenthesis in (2-86) approaches 0 so that $\sigma_{s,eff} \approx \sigma_s$ and the solution in the stator core becomes that of an unlaminated stator. As W becomes much smaller than δ, this term approaches unity and the effective conductivity goes to zero.

2.2.7 Saturation and Hysteresis Loss

Saturation effects in the machine are incorporated into the model by assigning effective permeabilities to the rotor and stator so that the magnitudes of the B field in those parts lie on the core material's B-H curve. The permeability is found iteratively, as shown in Figure 2-13. The procedure starts by assuming an initial value for the permeability in the rotor and stator core, $\mu_{i,1}$, where the i indexes the (r)otor or

(s)tator. Using these values, the magnitudes of the B fields throughout the various parts of the machine are determined using the continuum model (① in Figure 2-13). Once the magnitudes of the B fields are computed, the corresponding H fields are found using the current permeability (② in Figure 2-13),

$$H_{i,1} = \frac{B_{i,1}}{\mu_{i,1}}, \text{ for } i = r, s. \tag{2-87}$$

Since $\mu_{i,1}H_{i,1}$ does not lie on the core material's B-H curve, a new permeability is then computed for each section of the machine (③ in Figure 2-13),

$$\mu_{i,2} = \frac{B(H_{i,1})}{H_{i,1}}. \tag{2-88}$$

The new permeability, $\mu_{i,2}$, is sent back to the machine model, and the B field is recalculated in every section of the machine (④ in Figure 2-13). This process is repeated to find a new H field, $H_{i,2}$, and a new permeability, $\mu_{i,3}$. Solving for the B fields, it is found for the case of Figure 2-13 that using $\mu_{i,3}$, these values lie on the B-H curve (⑤ and ⑥ in Figure 2-13). Therefore, $\mu_{i,3} = \mu_{i,final}$ would be used in the machine model to compute torque and voltages in the machine. In this example convergence is found in only three iterations but in practice it can take up to 20.

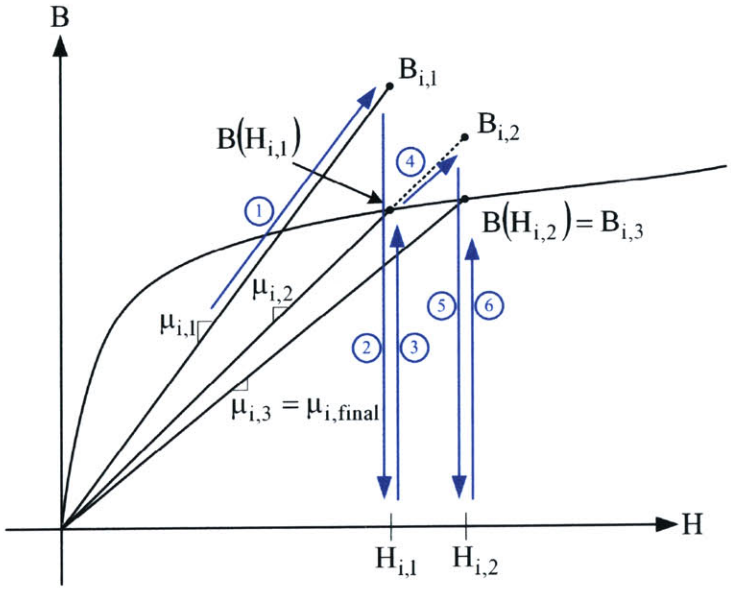

Figure 2-13: Nonlinear B-H curve and linearized approximations to the material permeability.

Since the B fields in the rotor and stator cores vary spatially over one wavelength, a number of different quantities can be sent to the permeability algorithm. The three quantities chosen are the mean, RMS, and peak spatial magnitudes of the B field for each region,

$$B_i = \frac{1}{2\pi}\int_0^{2\pi} B_m^{(j)}(\theta)d\theta, \tag{2-89}$$

$$B_i = \sqrt{\frac{1}{2\pi}\int_0^{2\pi}\left[B_m^{(j)}(\theta)\right]^2 d\theta} \tag{2-90}$$

$$B_i = \max_{\theta}\left(B_m^{(j)}(\theta)\right). \tag{2-91}$$

In (2-89), (2-90) and (2-91), $\theta = \omega_m t - nky$ and $B_m^{(j)}$ is the magnitude of the B field at some interface,

$$B_m^{(j)}(\theta) = \frac{1}{p_f}\sqrt{\left[\mathrm{Re}\left\{\sum_{n=1,odd}^{\infty}\hat{B}_{yn}^{(j)}e^{jn\theta}\right\}\right]^2 + \left[\mathrm{Re}\left\{\sum_{n=1,odd}^{\infty}\hat{B}_{zn}^{(j)}e^{jn\theta}\right\}\right]^2}. \tag{2-92}$$

$B_m^{(j)}$ in the rotor and stator are computed at the bottom surface of the rotor core (j = 5) and top surface of stator core (j = 2), respectively. Note that given the form of (2-92), the RMS of the B fields can be calculated as

$$B_i = \frac{1}{p_f}\sqrt{\frac{1}{2}\sum_{n=1,odd}^{\infty}\left(\left|\hat{B}_{yn}^{(j)}\right|^2 + \left|\hat{B}_{zn}^{(j)}\right|^2\right)}. \tag{2-93}$$

For a stator consisting of laminations of thickness W and separated by dividers of thickness S (Figure 2-14) the B field in the stator core will be higher than in the unlaminated case. This is because the flux from the rotor PM over a radial span of W+S will crowd into a lamination of radial span W since it is much more permeable than the dividers which are non magnetic materials. To account for this effect, a packing factor, p_f, is introduced into Equation (2-92).The packing factor represents the fraction of the core that is taken up by ferromagnetic material and defined to be

$$p_f = \frac{W}{W+S}. \tag{2-94}$$

The rotor core is not laminated since it does not experiences any time varying magnetic fields from the rotor PM and very small magnetic fields from higher order spatial harmonics of the stator currents. Therefore, its packing factor is always 1.

For an unlaminated stator, the fields are evaluated at the middle radius $\frac{1}{2}(R_o - R_i)$. The laminated stator on the other hand is no longer continuous over the radial span of the machine. The iteration procedure is evaluated at the radius of each lamination to determine a permeability, $u_s(r_{lam,i})$, for each stator lamination, where $r_{lam,i}$ is the radius of the i^{th} lamination. Since the field solutions are computed over a continuous radial span, a permeability that varies smoothly with radius, $u_s(r)$, can be computed by interpolating between permeabilities at successive laminations (i.e. between $u_s(r_{lam,i})$ and $u_s(r_{lam,i+1})$).

The predicted open-circuit voltage obtained by using the three different quantities will be compared to FEA simulations to determine which one produces the most accurate result. It will be shown that using the RMS of the B field produces the most accurate results over the range of geometry, material properties and speeds considered in this thesis.

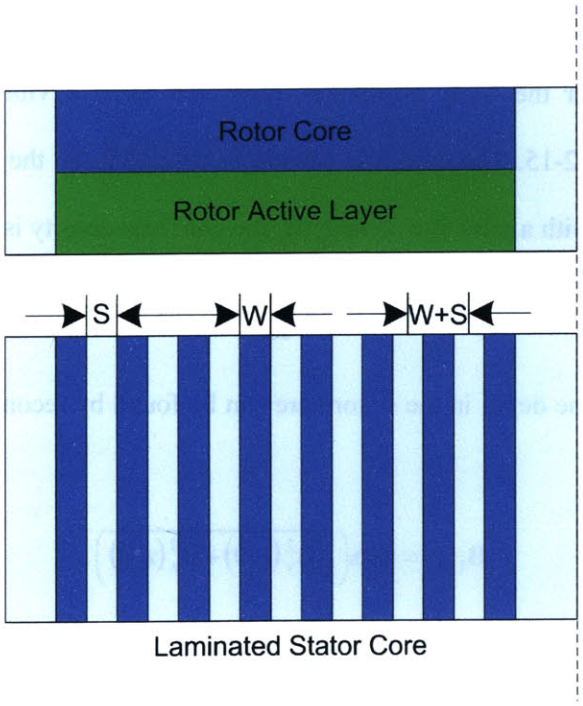

Figure 2-14: Radial view of the laminated stator shows the non-unity packing factor for laminations of thickness W and dividers of thickness S.

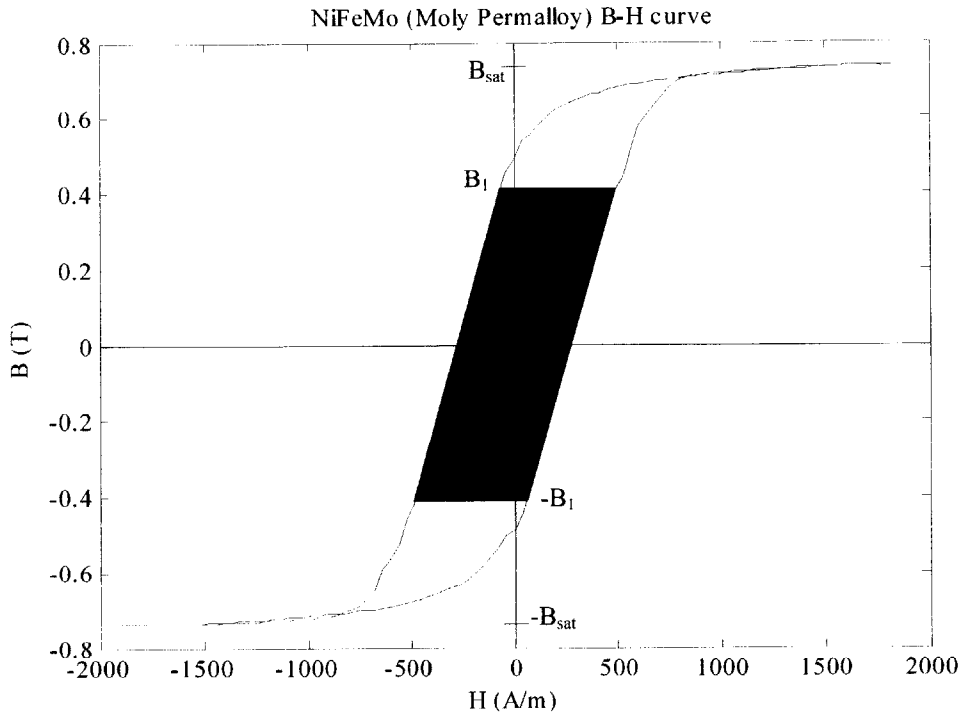

Figure 2-15: B-H loop for Moly Permalloy. The shaded region is the energy dissipated in a cycle for a peak B field of B_1.

The hysteresis loss in the stator core is calculated using the B-H curve of the core material. For example, the B-H curve for the Moly Permalloy, measured using a vibrating sample magnetometer (VSM), is shown in Figure 2-15. The core loss density is defined to be the energy dissipated traversing the B-H loop. For material with a peak flux density B_1 the core loss density is [47]

$$\rho_{core}(B_1) = \int_{-B_1}^{B_1} H(B)dB . \tag{2-95}$$

The peak flux density at some depth in the stator core can be found by reconstructing B_m as a function of z over one period,

$$B_1(z) = \max_{\theta}\left(\sqrt{B_y^2(z,\theta)+B_z^2(z,\theta)}\right), \tag{2-96}$$

where,

$$B_y(z,\theta) = \mathrm{Re}\left\{\mu_s \sum_{n=1,odd}^{\infty}\left(\frac{\gamma_n}{\mu_0}\frac{\sinh(\gamma_{sn}(T_{sc}-z))}{\sinh(\gamma_{sn}T_{sc})}+\alpha_{2n}\frac{\sinh(\gamma_{sn}z)}{\sinh(\gamma_{sn}T_{sc})}\right)\hat{A}^{(1)}_{xn(m)}e^{jn\theta}\right\}, \tag{2-97}$$

$$B_z(z,\theta)=\mathrm{Re}\left\{\sum_{n=1,\mathrm{odd}}^{\infty} jnk\left(\frac{\sinh(\gamma_{sn}(T_{sc}-z))}{\sinh(\gamma_{sn}T_{sc})}+\alpha_{1n}\frac{\sinh(\gamma_{sn}z)}{\sinh(\gamma_{sn}T_{sc})}\right)\hat{A}^{(1)}_{xn(m)}e^{jn\theta}\right\}. \tag{2-98}$$

For an unlaminated stator, (2-96) is evaluated at the middle radius of the machine. For a laminated stator, (2-96) is computed for each lamination, $r_{lam,i}$.

The total core loss is the sum of the total energy dissipated in the stator core times the frequency at which the B-H loop is traversed which for an unlimited stator is

$$P_{core}=\frac{\omega_m}{2\pi}\iiint\rho_{core}(B_1)dV=\frac{\omega_m}{2}\left(R_o^2-R_i^2\right)\int_0^{T_{sc}}\rho_{core}(B_1(z))dz. \tag{2-99}$$

For a laminated stator core with N_{lam} laminations the hysteresis loss is

$$P_{core}=\omega_m W\sum_{i=1}^{N_{lam}} r_{lam,i}\int_0^{T_{sc}}\rho_{core}\left(\frac{1}{p_f}B_1(z)\Big|_{r=r_{lam,i}}\right)dz. \tag{2-100}$$

2.2.8 Torque and Pull-In force

The Maxwell Stress Tensor [46] is used to find the pull-in force and torque on the rotor using the field solutions found for the air gap in the continuum model. Figure 2-16 shows the surface over which the stress tensor is computed. The time averaged force on surface 1 and 3 cancel each other. Surface 4 is assumed to be far away from the surface of the rotor core so that the fields are zero. The time averaged shear forces on the surfaces parallel to the page, which close the surface at the inner and outer radii of the machine, are zero because the magnetic fields lie only on the y-z plane. Therefore, only surface 2 contributes to the time averaged pull-in force and torque. The time average normal and shear stresses at surface 2 are

$$\langle\tau_{zz}\rangle=\frac{\mu_0}{4}\sum_n \mathrm{Re}\left\{\hat{H}^{(4)}_{zn}\hat{H}^{(4)*}_{zn}-\hat{H}^{(4)}_{yn}\hat{H}^{(4)*}_{yn}\right\}=\frac{1}{4}\sum_n \mathrm{Re}\left\{\frac{1}{\mu_0}\hat{B}^{(4)}_{zn}\hat{B}^{(4)*}_{zn}-\mu_0\hat{H}^{(4)}_{yn}\hat{H}^{(4)*}_{yn}\right\}, \tag{2-101}$$

$$\langle\tau_{yz}\rangle=\frac{\mu_0}{2}\sum_n \mathrm{Re}\left\{\hat{H}^{(4)}_{zn}\hat{H}^{(4)*}_{yn}\right\}=\frac{1}{2}\sum_n \mathrm{Re}\left\{\hat{B}^{(4)}_{zn}\hat{H}^{(4)*}_{yn}\right\}. \tag{2-102}$$

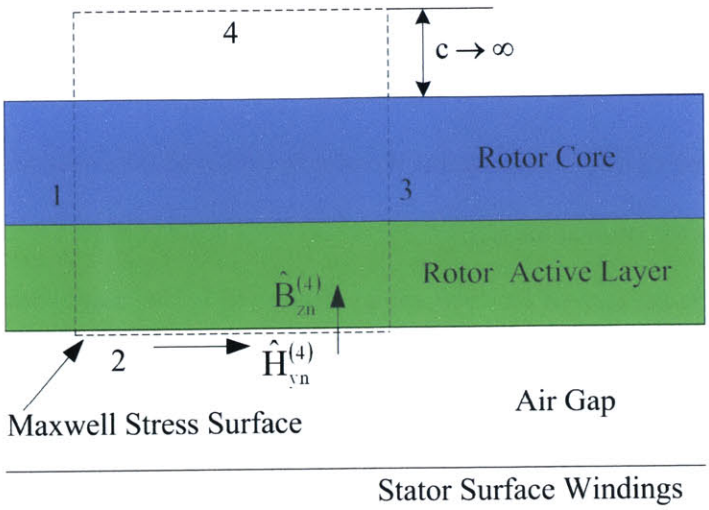

Figure 2-16: Maxwell Stress surface for pull-in force and torque calculations.

The normal B field and tangential H field at the bottom surface of the rotor active layer are

$$\hat{B}_{zn}^{(4)} = jnk\left(\alpha_{5n}\hat{A}_{xn(m)}^{(1)} + \beta_{3n}\hat{A}_{xn(J)}^{(6)}\right), \tag{2-103}$$

$$\hat{H}_{yn}^{(4)} = \alpha_{6n}\hat{A}_{xn(m)}^{(1)} - \beta_{4n}\hat{A}_{xn(J)}^{(6)}. \tag{2-104}$$

Substituting (2-103) and (2-104) into (2-102) gives the shear stress on the rotor due to the rotor magnetization and stator winding currents. They are

$$\left\langle \tau_{yz} \right\rangle = \sum_{n} \mathrm{Re}\left\{ jnk \begin{pmatrix} \alpha_{5n}\alpha_{6n}^{*}\left|\hat{A}_{xn(m)}^{(1)}\right|^{2} - \alpha_{5n}\beta_{4n}^{*}\hat{A}_{xn(m)}^{(1)}\hat{A}_{xn(J)}^{(6)*} \\ + \beta_{3n}\alpha_{6n}^{*}\hat{A}_{xn(J)}^{(6)}\hat{A}_{xn(m)}^{(1)*} - \beta_{3n}\beta_{4n}^{*}\left|\hat{A}_{xn(J)}^{(6)}\right|^{2} \end{pmatrix} \right\}. \tag{2-105}$$

The shear stress Equation (2-105) consists of three components. The first component captures the interaction between the stator currents and the rotor PM,

$$\left\langle \tau_{yz} \right\rangle = \sum_{n} \mathrm{Re}\left\{ jnk\left(- \alpha_{5n}\beta_{4n}^{*}\hat{A}_{xn(m)}^{(1)}\hat{A}_{xn(J)}^{(6)*} + \beta_{3n}\alpha_{6n}^{*}\hat{A}_{xn(J)}^{(6)}\hat{A}_{xn(m)}^{(1)*} \right) \right\}. \tag{2-106}$$

This is the component responsible for electromechanical energy conversion in both motoring and generating modes and is proportional to $-B_r I_o \sin(\delta_m)$. The interaction only occurs if the frequency of the stator currents, ω_e, is equal to the frequency of the voltage induced by the rotor permanent magnet, $\omega_m = P\Omega_m$, and is known as the synchronous torque. When the torque angle is positive, the machine acts as a

generator and when the torque angle is negative, the machine acts as a motor. The peak torque occurs at $\delta_m = \pm\pi/2$. To understand why this is, assume that the Phase A current is $I_o\cos(\omega_m t)$. If $\delta_m = \pi/2$ (generating mode), then flux due to the rotor PM, λ_m, which is proportional to B_r, will lead the Phase A current and will have the form $-\lambda_m\sin(\omega_m t)$. The voltage induced on the terminal of phase A is the time derivative of the PM flux or $-\omega_m\lambda_m\cos(\omega_m t)$ which is in phase with the Phase A current. The time averaged power per phase will be $-\frac{1}{2}\omega_m\lambda_m I_o$.

The second component of Equation (2-105) represents the drag torque on the rotor due to eddy currents in the stator induced by the spinning permanent magnet. This drag is

$$\left\langle \tau_{yz} \right\rangle = \sum_n \mathrm{Re}\left\{ jnk\alpha_{5n}\alpha_{6n}^* \right\} \left| \hat{A}_{xn(m)}^{(1)} \right|^2 . \tag{2-107}$$

This drag torque shows up as eddy current loss and stator core heating. It can be eliminated by using a ferrite (non-conducting) or laminated core.

The final component of the shear stress is the torque due to eddy currents in the rotor induced by the traveling magnetic flux wave generated by the stator currents,

$$\left\langle \tau_{yz} \right\rangle = -\sum_n \mathrm{Re}\left\{ jnk\beta_{3n}\beta_{4n}^* \right\} \left| \hat{A}_{xn(J)}^{(6)} \right|^2 . \tag{2-108}$$

This component is proportional to the square of the stator currents and is the mechanism that generates torque in an induction machine. This torque is a function of the slip frequency of the rotor, $s\omega_e$, where the slip is defined as

$$s = \frac{\omega_e - \omega_m}{\omega_e}, \tag{2-109}$$

and is known as the asynchronous torque. In a synchronous (PM) machine this torque can be generated by higher order spatial harmonics of the traveling magnetic wave generated by the stator currents but will be zero for the fundamental spatial harmonic. In a surface wound machine, this torque is negligible due to the large air gaps even for the fundamental spatial component of the air gap fields, which makes surface wound induction machines a poor choice for electric power generation.

The time averaged stresses are independent of $y = r\theta$ so that the total pull-in force is just 2π times the integral of the normal stress integrated over the radial span of the machine

$$F_{PI} = -2\pi \int_{r=R_i}^{r=R_o} \langle \tau_{zz} \rangle r dr . \tag{2-110}$$

The total torque on the machine can be calculated in a similar matter. The time average torque will 2π times the integral of the radius times the shear stress integrated over the radial span of the machine

$$\text{Torque} = -2\pi \int_{r=R_i}^{r=R_o} \langle \tau_{yz} \rangle r^2 dr . \tag{2-111}$$

Note that the minus sign in front of the integrals in (2-110) and (2-111) is due to the fact that integration is performed over surface 2 which has a normal in the $-\hat{z}$ direction.

2.2.9 Equivalent Circuit Model

Using the Maxwell Stress Tensor to compute the torque, and hence the output power, of machine as a function of stator currents and rotor magnetization is useful for comparing different machines in terms of power density and efficiency. However, to design the complete electric power train it is much more useful to have a circuit model of the generator. The equivalent circuit for a single phase of the balanced PM machine is show in Figure 2-17. It consists of a back EMF source or open-circuit voltage, V_{oc}, due the spinning PM as well as an inductance, L_s, and resistance, R_s, due to the stator windings. The open-circuit voltage and stator inductance can be found using the vector potential solutions to the machine due the rotor magnetization and stator currents, respectively. The resistance is calculated based on the dimensions of radial conductors, and the inner/outer end turns of the stator windings. Only equivalent circuits for PM machines are considered here since induction machines will not be selected in Chapter 3 as the best magnetic machine for electric power generation in the microengine.

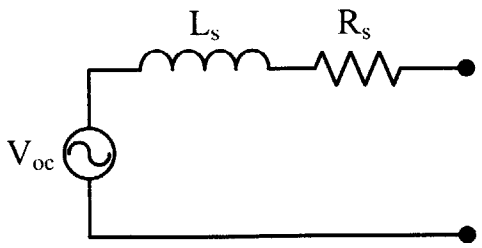

Figure 2-17: Equivalent circuit for a single phase of a PM machine consisting of an open-circuit voltage, V_{oc}, stator winding inductance, L_s, and resistance, R_s.

2.2.9.1 Open-circuit Voltage

The spinning multi-pole PM rotor creates a time-varying flux that induces a voltage, V_{oc}, on each phase of the stator windings governed by Faraday's Law,

$$V_{oc} = \frac{d\lambda_m}{dt}, \tag{2-112}$$

where λ_m is the total flux from the rotor PM linked by a single phase. In order to determine the open-circuit voltage, the axial flux through a single phase of the stator windings must be found. This is achieved by integrating the incremental flux at a given radius over the radial span of the machine. The incremental flux from a single turn can be found by taking the difference between the vector potential [44] of the two radial conductors in that turn (Figure 2-18). For instance, if the radial conductors of phase A of a 1-turn/pole machine spans from $y = y_1$ to $y = y_2$ then the incremental flux in that loop is

$$\hat{\Phi}_{zn,coil(m)} = \int_{y_1}^{y_2} \hat{B}_{zn,coil(m)} e^{-jnky} dy = \hat{A}_{xn,coil(m)} \left(e^{-jnky_1} - e^{-jnky_2} \right), \tag{2-113}$$

where $\hat{A}_{xn,coil(m)}$ is the vector potential evaluated at half the axial thickness of the stator winding layer,

$$\hat{A}_{xn,coil(m)} = \hat{A}^{(1)}_{xn(m)} (\alpha_{1n} + \alpha_{3n}) \frac{\sinh(0.5\gamma_{0n} T_{cl})}{\sinh(\gamma_{0n} T_{cl})}. \tag{2-114}$$

The incremental flux linked by a single phase is P times the flux/pole. From Figure 2-18, the incremental flux/phase in phase A of a 1-turn/pole machine is

$$\hat{\Phi}_{zn,coil(m)} = P\hat{A}_{xn,coil(m)} \left(e^{-jnk\left(-\frac{\lambda}{4}\right)} - e^{-jnk\left(\frac{\lambda}{4}\right)} \right) = 2P\hat{A}_{xn,coil(m)} e^{j\frac{n\pi}{2}}. \tag{2-115}$$

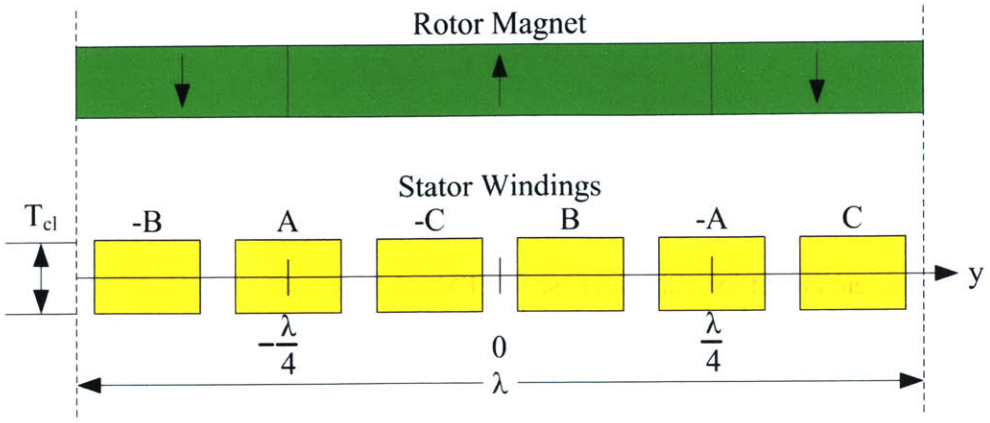

Figure 2-18: Voltage calculation diagram for a 1-turn/pole machine. Flux linked by phase A is equal to the difference in the vector potential between $y = \frac{1}{4}\lambda$ and $y = -\frac{1}{4}\lambda$ evaluated at half the thickness of the stator coils.

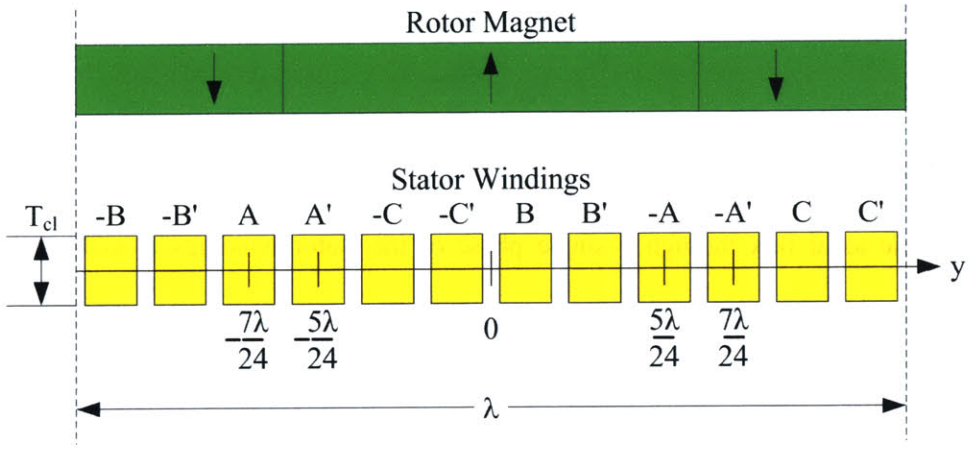

(a) Full Pitch Windings

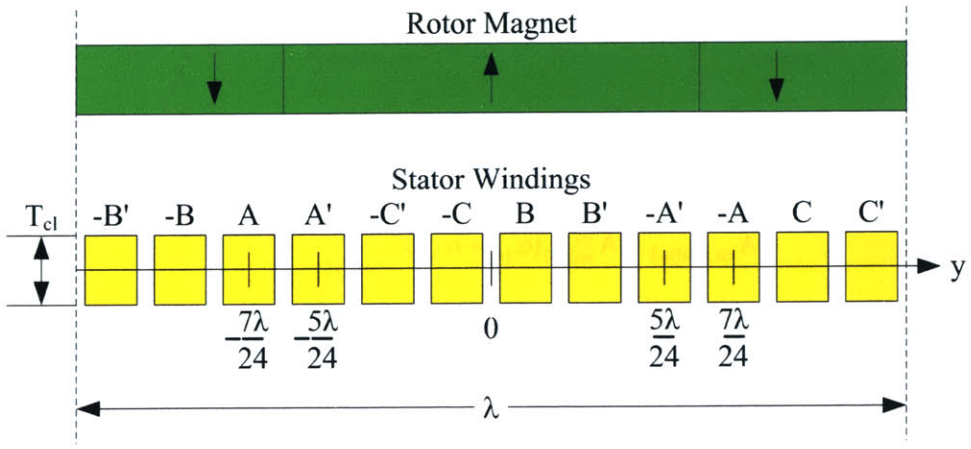

(b) Concentric Windings

Figure 2-19: Voltage calculation diagram for 2-turn/pole machines with (a) full pitch windings and (b) concentric windings. A and –A constitute a single turn while A' and –A' constitute the second turn.

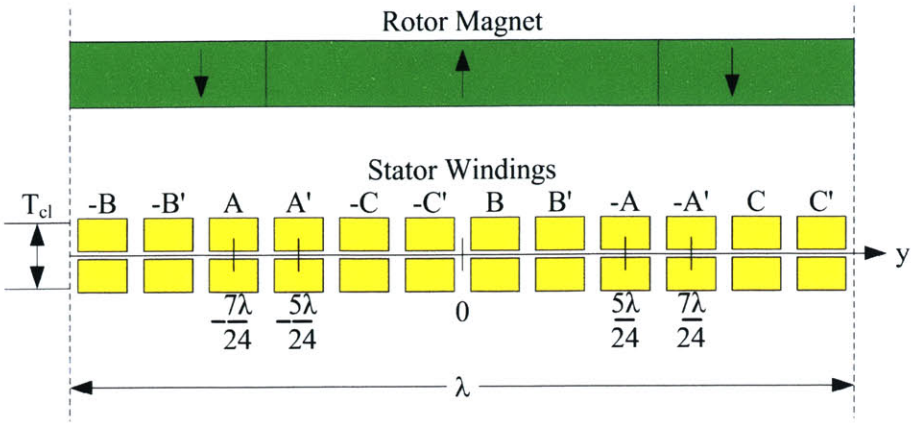

Figure 2-20: Voltage calculation diagram a 4-turn/pole machine with double layer windings. For a machine with a double layer winding, T_{sw} is the sum of the thicknesses of the top and bottom coils.

Machines with more than 1-turn/pole can also be modeled using this approach, where the contributions of each turn are summed to find the incremental flux/pole. The multiple turns can all reside on a single layer or be stacked onto multiple layers [42]. A cross-section of a 2-turn/pole machine is shown in Figure 2-19 for both full pitched and concentric windings. A full pitched winding is one that spans 180 electrical degrees or a half wavelength [41]. Multi-turn concentric windings are made up of long pitched and short pitched windings such as A,-A (long) and A′, -A′ (short) in Figure 2-19(b). The conductors are in the same location for full-pitch and concentric windings and since the flux through the windings is the net difference in vector potentials the incremental flux/phase is the same. Referring to Figure 2-19 for a 2-turn/pole machine with either full-pitch or concentric windings, the incremental flux/phase is

$$\hat{\Phi}_{zn,coil(m)} = P\hat{A}_{xn,coil(m)}\left(e^{-jnk\left(-\frac{7\lambda}{24}\right)} - e^{-jnk\left(\frac{5\lambda}{24}\right)} + e^{-jnk\left(-\frac{5\lambda}{24}\right)} - e^{-jnk\left(\frac{7\lambda}{24}\right)}\right) = 2P\hat{A}_{xn,coil(m)}\left(e^{jn\frac{7\pi}{12}} + e^{jn\frac{5\pi}{12}}\right). \quad (2\text{-}116)$$

This cross section can also be used to model a 4-turn/pole machine that uses two layers of coils with each layer having the same phase sequence as the 2-turn/pole machine (A A′ –C –C′ …) as shown in Figure 2-20. In the case of the 4-turn/pole double winding layer machine, the thickness of the stator winding layer, T_{cl}, is the sum of the thicknesses of the top and bottom coils. For a 4-turn/pole machine using two winding layers, the incremental flux/phase is

$$\hat{\Phi}_{zn,coil(m)} = 4P\hat{A}_{xn,coil(m)}\left(e^{jn\frac{7\pi}{12}} + e^{jn\frac{5\pi}{12}}\right). \tag{2-117}$$

In general, for a three-phase surface wound machine with P pole pairs, N-turns/pole, κ winding layers and $N' = N/\kappa$, the incremental flux/phase is

$$\hat{\Phi}_{zn,coil(m)} = 2\kappa P\hat{A}_{xn,coil(m)} \sum_{\substack{\nu=2N'+1 \\ step2}}^{4N'-1} e^{j\frac{n\pi}{6N'}\nu}. \tag{2-118}$$

Integrating over the radial span of the machine, the total flux linked by a single phase for each harmonic is

$$\hat{\lambda}_{n,coil(m)} = \int_{r=R_i}^{r=R_o} \hat{\Phi}_{zn,coil(m)} dr. \tag{2-119}$$

The harmonic amplitudes of the open-circuit voltage induced by this flux is

$$\hat{V}_{ocn} = \frac{d}{dt}\hat{\lambda}_{n,coil(m)} = jn\omega_m \hat{\lambda}_{n,coil(m)}. \tag{2-120}$$

2.2.9.2 Stator Inductance

The stator inductance can be determined in the same manner as the open-circuit voltage. The total flux generated by the stator currents and linked by a single phase of the machine is found by integrating the incremental flux at a given radius over the radial span of the machine. The incremental flux linked by a single phase is P times the flux/pole. Referring back to Figure 2-18, the incremental flux/phase in phase A of a 1-turn/pole machine is

$$\hat{\Phi}_{zn,coil(j)} = P\hat{A}_{xn,coil(J)}\left(e^{-jnk\left(-\frac{\lambda}{4}\right)} - e^{-jnk\left(\frac{\lambda}{4}\right)}\right) = 2P\hat{A}_{xn,coil(J)}e^{j\frac{n\pi}{2}}. \tag{2-121}$$

where $\hat{A}_{xn,coil(J)}$ is the vector potential due to the stator currents evaluated at half the thickness of the stator winding layer,

$$\hat{A}_{xn,coil(J)} = \left(\alpha_{1n}\hat{A}^{(1)}_{xn(J)} + \beta_{5n}\hat{A}^{(6)}_{xn(J)}\right)\frac{\sinh(0.5\gamma_{0n}T_{cl})}{\sinh(\gamma_{0n}T_{cl})}. \tag{2-122}$$

For the general case of a three-phase surface wound machine with P pole pairs, N-turns/pole, κ winding layers and $N' = N/\kappa$, the incremental flux/phase is

$$\hat{\Phi}_{zn,coil(J)} = 2\kappa P \hat{A}_{xn,coil(J)} \sum_{\substack{\nu=2N'+1 \\ step2}}^{4N'-1} e^{j\frac{n\pi}{6N'}\nu} . \tag{2-123}$$

The stator currents, which have a single temporal frequency (ω_e), generate magnetic fields with multiple spatial harmonics. However, due to the large air gap, the higher order harmonic components are much smaller than the fundamental. Therefore, the flux linked by a winding due to the stator currents is composed of essentially the fundamental component of magnetic field in the air gap. Integrating over the radial span of the machine, the flux linked by a single phase is

$$\hat{\lambda}_{coil(J)} = \int_{r=R_i}^{r=R_o} \hat{\Phi}_{z1,coil(J)} dr . \tag{2-124}$$

Note that this is the flux linkage generated by the sum of the three phase currents. The resulting inductance, L_d, is known as the synchronous inductance [41] and is given by

$$L_d = \frac{Re\{\hat{\lambda}_{coil(J)}\}}{I_o} . \tag{2-125}$$

Phase B and C currents produce a flux linked by phase A that is proportional to the $\cos(\pm 2/3\pi) = -1/2$. Since $i_b + i_c = -i_a$, the sum of the fluxes produced by phase B and C equals half the flux produced by phase A. Phase A will see 1.5 times the flux produced by currents in only phase A. Therefore, the stator phase inductance, L_s, in the single phase model will be

$$L_s = \frac{2}{3I_o} Re\{\hat{\lambda}_{coil(J)}\} . \tag{2-126}$$

2.2.9.3 Stator Resistance

For a surface wound machine the radial conductors of all three phases will occupy the same winding layer. The radial conductors in the same phase are connected by end turns that cross over end turns of the

other phases as depicted in Figure 2-21. The first generation of surface wound stators uses full pitched windings while the second generation stators uses concentric windings.

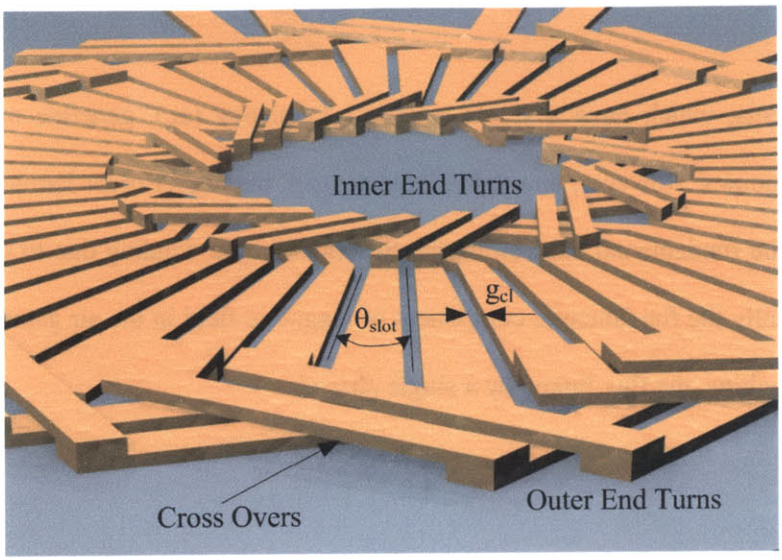

Figure 2-21: Winding pattern for a 2-turn/pole, 8-pole machine. The radial conductors are unlaminated and connected by cross overs.

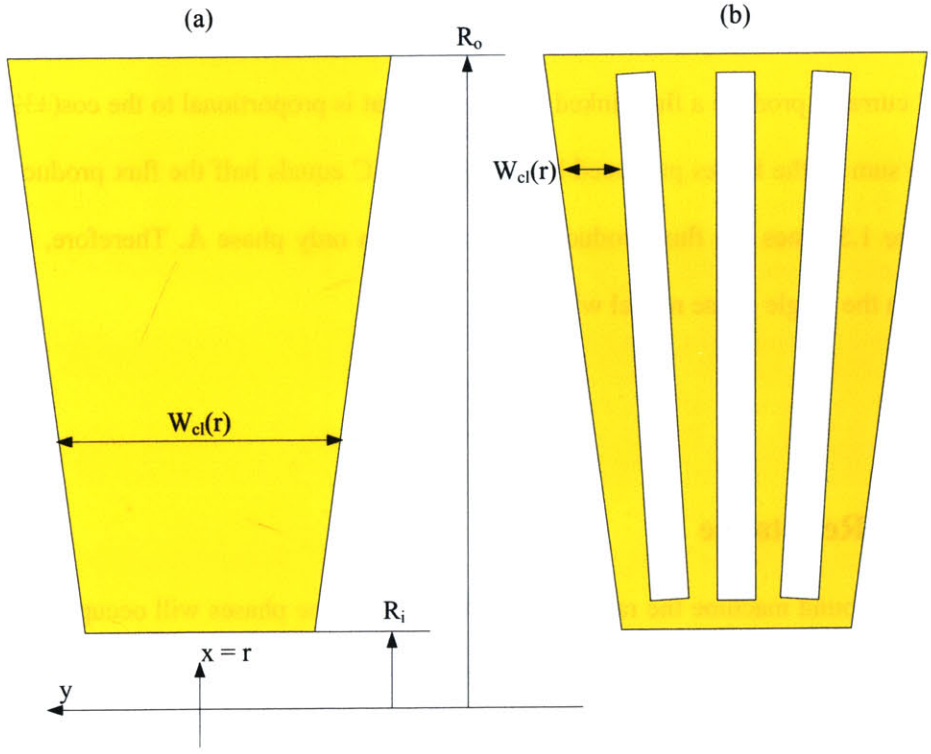

Figure 2-22: Radial Conductors in a single slot (a) unlaminated and (b) laminated.

The radial conductor in each slot can be unlaminated as shown in Figure 2-22(a) or laminated as shown in Figure 2-22(b). Laminated radial conductors can be used to reduce proximity eddy current losses which is discussed in the next section. There are 2PN radial conductors per phase so that the maximum angular span or slot angle for each conductor is

$$\theta_{slot} = \frac{2\pi}{6PN} = \frac{\pi}{3PN}. \tag{2-127}$$

If there are C_{lam} laminations per radial conductor than the width of the laminated conductors is given by

$$W_{cl}(r) = \frac{\pi r}{3PNC_{lam}} - g_{cl}. \tag{2-128}$$

where g_{cl} is the minimum distance between adjacent conductors imposed by fabrication constraints. The resistance of a radial conductor is

$$R_{conductor} = \frac{1}{\sigma_c T_{cl}} \int_{R_i}^{R_o} \frac{dr}{W_{cl}(r)} = \frac{3PNC_{lam}}{\pi\sigma_c T_{cl}} \ln\left(\frac{W_{cl}(R_o)}{W_{cl}(R_i)}\right), \tag{2-129}$$

where T_{cl} is the height of the radial conductor and σ_c is the conductivity of copper. Consequently the resistance of all the radial conductors in a single phase is

$$R_{radial} = \frac{6(PNC_{lam})^2}{\pi\sigma_c T_{cl}} \ln\left(\frac{W_{cl}(R_o)}{W_{cl}(R_i)}\right). \tag{2-130}$$

For full pitched windings, like the one shown in Figure 2-23, the length of all the end turns are the same. The end turns are made of straight conductors that each span $1.5N\theta_{slot}$ radians ($3\theta_{slot}$ radians for the 2-turn/pole machine as shown in Figure 2-23). The length of the outer end turn conductors can be approximated as the hypotenuse of a right triangle,

$$L_{outer} = \sqrt{\left(\frac{3}{2}N\theta_{slot}R_o\right)^2 + (R_{ol} - R_o)^2} = \sqrt{\left(\frac{\pi R_o}{2P}\right)^2 + (R_{ol} - R_o)^2}. \tag{2-131}$$

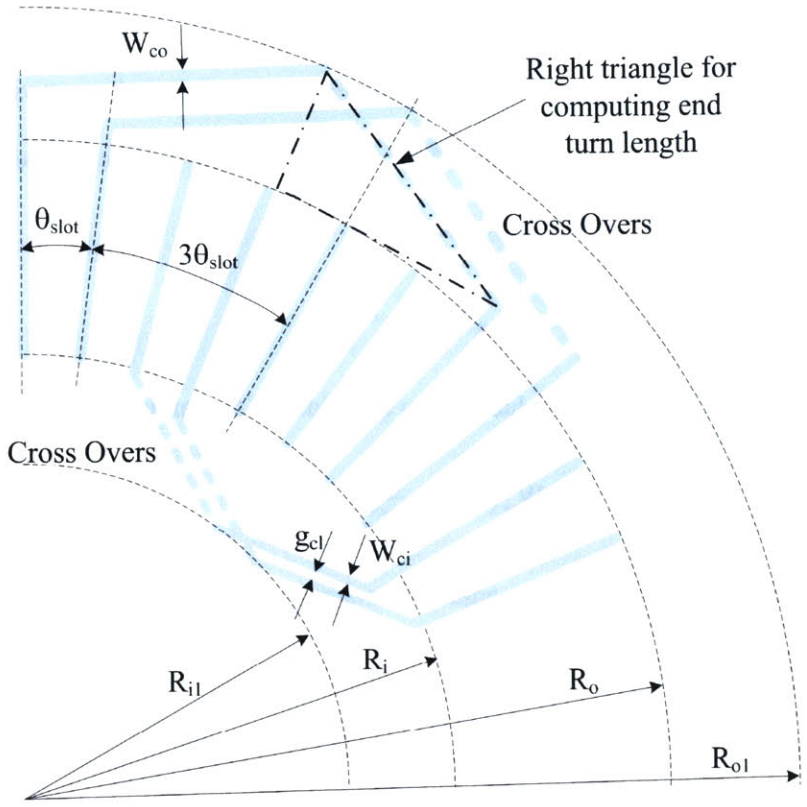

Figure 2-23: End turn connections for a 2-turn/pole full pitched winding.

Since there are two conductors per end turn and NP end turns per phase, the resistance of the outer end turns is

$$R_{outer} = \frac{2NPL_{outer}}{\sigma_c T_{co} W_{co}}, \tag{2-132}$$

where T_{co} and W_{co} are the height and width of the outer end turns, respectively.

The inner end turns are handled in a similar manner. The length of the inner end turn conductors is

$$L_{inner} = \sqrt{\left(\frac{\pi R_i}{2P}\right)^2 + (R_i - R_{i1})^2}\ . \tag{2-133}$$

The corresponding resistance of the inner end turn is

$$R_{inner} = \frac{2NPL_{inner}}{\sigma_c T_{ci} W_{ci}}. \tag{2-134}$$

where T_{ci} and W_{ci} are the height and width of the outer end turns, respectively. The total resistance per phase is $R_{radial} + R_{inner} + R_{outer}$.

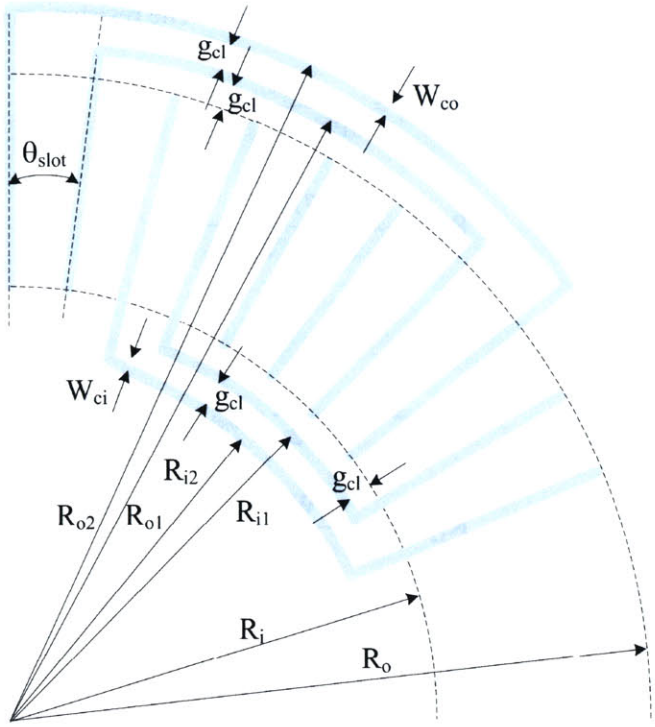

Figure 2-24: End turn connections for a 2-turn/pole concentric winding.

Figure 2-24 shows a 2-turn/pole stator with concentric windings. Each outer end turn has a width W_{co} and is separated from adjacent conductors by a width g_{cl}. The short-pitched and long-pitched outer end turns span angles of $5\theta_{slot}$ and $7\theta_{slot}$, respectively. The resistances of these end turns are

$$R_{outer1} = \frac{5\pi R_{o1}}{3PN\sigma_c T_{co} W_{co}}, \tag{2-135}$$

$$R_{outer2} = \frac{7\pi R_{o2}}{3PN\sigma_c T_{co} W_{co}}, \tag{2-136}$$

where

$$R_{o1} = R_o + \frac{W_{co}}{2} + g_{cl}, \tag{2-137}$$

$$R_{o2} = R_o + \frac{3W_{co}}{2} + 2g_{cl}. \tag{2-138}$$

The resistance per phase of the outer end turns is P times the resistance of the individual end turns

$$R_{outer} = \frac{\pi}{\sigma_c T_{co} W_{co}} \left(\frac{5R_{o1} + 7R_{o2}}{6} \right). \tag{2-139}$$

Similarly, the inner end turns are computed in the same manner. The resistances of the inner end turns are

$$R_{inner1} = \frac{5\pi R_{i1}}{3PN\sigma_c T_{ci} W_{ci}}, \tag{2-140}$$

$$R_{inner2} = \frac{7\pi R_{i2}}{3PN\sigma_c T_{ci} W_{ci}}, \tag{2-141}$$

where

$$R_{i1} = R_i - \frac{W_{ci}}{2} - g_{cl}, \tag{2-142}$$

$$R_{i2} = R_i - \frac{3W_{ci}}{2} - 2g_{cl}, \tag{2-143}$$

and the total resistance per phase of the inner end turn is

$$R_{inner} = \frac{\pi}{\sigma_c T_{co} W_{co}} \left(\frac{5R_{i1} + 7R_{i2}}{6} \right). \tag{2-144}$$

This method can be extended to the general case of an N-turn/pole concentric wounding. If N is even, then will be N/2 short-pitched windings and N/2 long-pitched windings. If N is odd, their will be one full pitched windings, (N-1)/2 short-pitched windings and (N-1)/2 long-pitched windings. The arcs spanned by the n^{th} inner and outer end turns are, respectively,

$$L_{innern} = \frac{[2(N+n)-1]\pi R_{in}}{3PN}, \tag{2-145}$$

$$L_{outern} = \frac{[2(N+n)-1]\pi R_{on}}{3PN}, \tag{2-146}$$

where the radii of the arcs are

$$R_{innern} = R_i - \frac{2n-1}{2} W_{ci} - ng_{coil}, \tag{2-147}$$

$$R_{outern} = R_o + \frac{2n-1}{2} W_{co} + ng_{coil}. \tag{2-148}$$

The total resistance of the inner and outer end turns is then

$$R_{inner} = P\sum_{n=1}^{N}\frac{L_{innern}}{\sigma_c T_{ci} W_{ci}} = \frac{\pi}{\sigma_c T_{ci} W_{ci}}\sum_{n=1}^{N}\frac{[2(N+n)-1]R_{innern}}{3N}, \tag{2-149}$$

$$R_{outer} = P\sum_{n=1}^{N}\frac{L_{outern}}{\sigma_c T_{co} W_{co}} = \frac{\pi}{\sigma_c T_{co} W_{co}}\sum_{n=1}^{N}\frac{[2(N+n)-1]R_{outern}}{3N}. \tag{2-150}$$

The total resistance per phase is $R_{radial} + R_{inner} + R_{outer}$.

2.2.10 Proximity Eddy Current Losses in the Coil Layer

The continuum model of the surface wound machine does not model the stator windings as a layer with conductivity σ_c because it is made up of discrete conductors. There are 6N radial conductors per wavelength of the rotor magnetization and the width of each of these conductors is much smaller than that wavelength. Instead the coil layer is treated as a layer with zero conductivity and impose current density $J_x(y,t)$ in the continuum model. The fields in the machine, due to the stator currents, are computed by solving for the vector potential due to this current distribution.

However, eddy currents within each radial conductor will be present as shown in Figure 2-25(a). These eddy currents are driven by the magnetic fields from the rotor PM and the resulting losses are modeled separately using the field solutions from the continuum model as inputs. The B field from the rotor magnetization is used to compute the induced electric field using Faradays Law. The power dissipation in the radial conductor can then be calculated by integrating the conduction loss density over the volume of the radial conductor. If the losses due these eddy currents are too large, they can be reduced by laminating the radial conductors as shown in Figure 2-25(b). The eddy currents in the conductors will produce their own magnetic fields which retard the flux generated by the rotor magnetization. Ampere's Law is used to compute this retarding B field. So long as this B field is much smaller than the B field due to the rotor PM than the assumption that the conductivity of the coil layer can be ignored in the continuum model will remain valid.

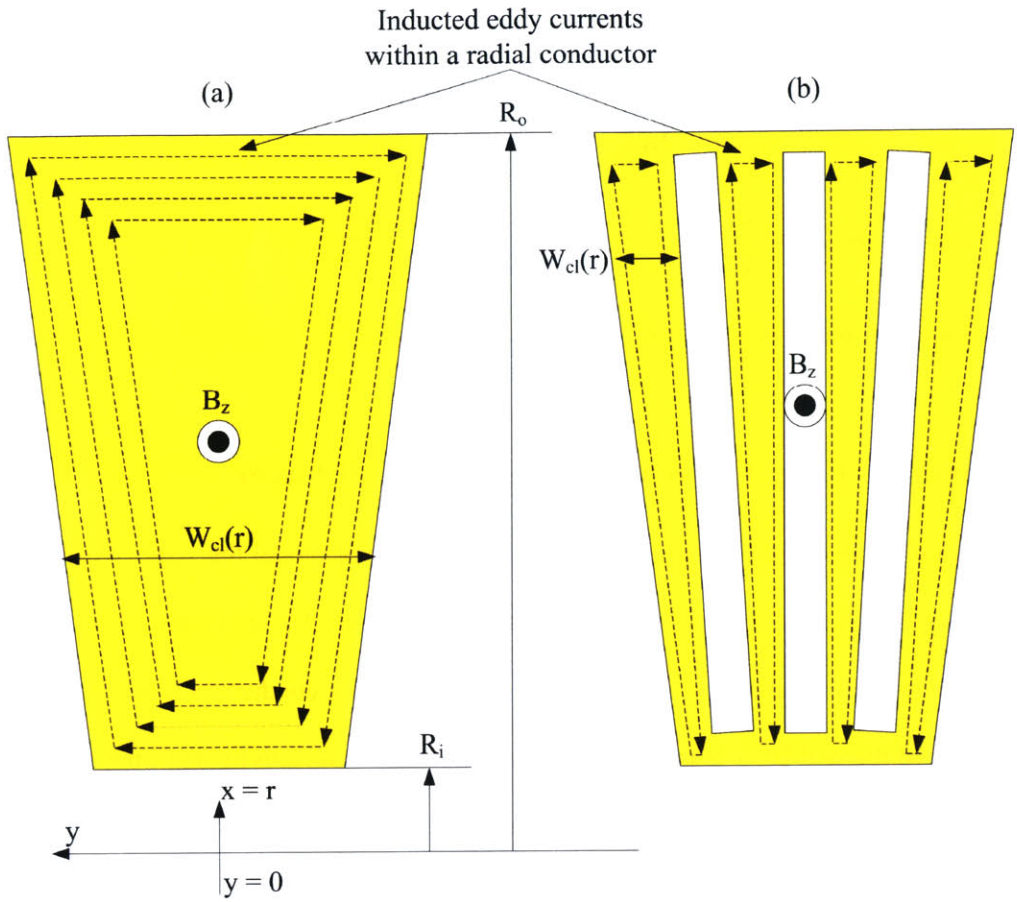

Figure 2-25: Proximity eddy currents in radial conductors (a) unlaminated and (b) laminated.

The induced electric field within a radial conductor can be found using Faradays Law,

$$\oint \bar{E} \cdot d\bar{l} = -\frac{\partial}{\partial t} \int \bar{B} \cdot d\bar{A} . \tag{2-151}$$

The contour for the electric field is assumed to be rectangular and is mainly in the x direction as shown in Figure 2-25. The path lengths in the y direction at the inner and outer radii are assumed to be small with respect to the radial path and are ignored in this analysis. Therefore Equation (2-151), for each harmonic component of the induce electric field, becomes

$$2x\hat{E}_{xn} = -jn\omega_m \hat{B}_{zn,coil(m)} xy , \tag{2-152}$$

where $\hat{B}_{zn,coil(m)}$ is defined in (2-113). The induced electric field is

$$\hat{E}_{xn} = -0.5jn\omega_m \hat{B}_{zn,coil(m)} y . \tag{2-153}$$

The time averaged power loss density in the radial conductor is

$$\left\langle \sigma_c E_{xn}^2(t) \right\rangle_t = \frac{\sigma_c}{2}\left|\hat{E}_{xn}\right|^2 = \frac{\sigma_c}{4}(n\omega_m)^2\left|\hat{B}_{zn,coil(m)}\right|^2 y^2 . \tag{2-154}$$

The loss density increases with the square of the distance from the center of the radial conductor. The power dissipated in the radial conductor for each harmonic component of the B field due to the rotor PM is

$$P_{radn} = 2T_{cl}\int_{R_i}^{R_o}\left(\int_0^{\frac{W_{cl}(r)}{2}} \frac{\sigma_c}{4}(n\omega_m)^2\left|\hat{B}_{zn,coil(m)}\right|^2 y^2 dy\right)dr . \tag{2-155}$$

Evaluating (2-155) gives

$$P_{radn} = \frac{\sigma_c}{96}(n\omega_m)^2\left|\hat{B}_{zn,coil(m)}\right|^2\left(\frac{3PNC_{lam}}{4\pi}\right)T_{cl}\left(W_{cl}(R_o)^4 - W_{cl}(R_i)^4\right). \tag{2-156}$$

There are 6PN radial conductors in a surface wound stator. If each of these conductors has C_{lam} laminations then the total loss due to proximity eddy currents is

$$P_{prox} = \frac{3\sigma_c\omega_m^2}{64\pi}(PNC_{lam})^2 T_{cl}\left[W_{cl}(R_o)^4 - W_{cl}(R_i)^4\right]\sum_{n=1,odd}^{\infty} n^2\left|\hat{B}_{zn,coil(m)}\right|^2 , \tag{2-157}$$

To better understand how this power dissipation scales, assume that width of the radial conductors is taken to be at $r = \frac{1}{2}(R_o - R_i) = R_m$ and is constant over the radial span of the conductor and that g_{cl} is zero. Substituting $P\Omega_m$ for ω_m and revaluating (2-155), the proximity loss will be

$$P_{prox} = (6NC_{lam})\frac{\sigma_c}{96}T_{cl}(R_o - R_i)\left(\frac{\pi R_m}{3NC_{lam}}\right)^3\sum_{n=1,odd}^{\infty}(n\Omega_m)^2\left|\hat{B}_{zn,coil(m)}\right|^2 , \tag{2-158}$$

The proximity effect loss increases with the square of the speed and flux density. However, they scale as the inverse square of the number of turns/pole and number of coil laminations. Increasing N and C_{lam} increases the number of radial conductors but reduces the width of each radial conductor. The power dissipated in each conductor is reduced faster than the increase in the number of total radial conductors because its dissipation scales as the cube of the width while the number of conductors is only linear with N and C_{lam}. Notice, however, that the proximity loss is independent of the number of pole pairs, P.

In order for the zero conductivity assumption for the coil layer used in the continuum model to be valid, the B field generated by these proximity eddy currents should be much smaller than the B fields due to the rotor PM. To find this proximity effect B field, the current through half a radial conductor is computed due the fundamental harmonic of the rotor PM flux. This current is at a maximum at the outer radius where the conductor is widest. Integrating the electric field over half the width of a radial conductor the proximity effect current is

$$\hat{I}_{prox} = \sigma_c T_{cl} \int_0^{\frac{W_{cl}(R_o)}{2}} \hat{E}_{x1} dy = -j \frac{\sigma_c \omega_m}{16} T_{cl} W_{cl}(R_o)^2 \hat{B}_{z1,coil(m)}, \tag{2-159}$$

Figure 2-26 shows how the proximity effect currents are distributed in the windings of phase A. The return path of phase A, denoted as –A, has the opposite proximity current distribution. The peak proximity effect B field can be computed, via Ampere's Law, using the contour in Figure 2-26 and is given by

$$\hat{B}_{prox} = \frac{\mu_0 \hat{I}_{prox}}{(T_{al} + T_{ag} + T_{cl})}, \tag{2-160}$$

The ratio of the proximity B fields to the fundamental of the rotor PM B field is equal to

$$\left| \frac{\hat{B}_{prox}}{\hat{B}_{z1,coil(m)}} \right| = \frac{\mu_0 \sigma_c \omega_m T_{cl} W_{cl}(R_o)^2}{16(T_{al} + T_{ag} + T_{cl})} << 1. \tag{2-161}$$

Equation (2-161) should be no more that 0.05 in order for the continuum model to be valid.

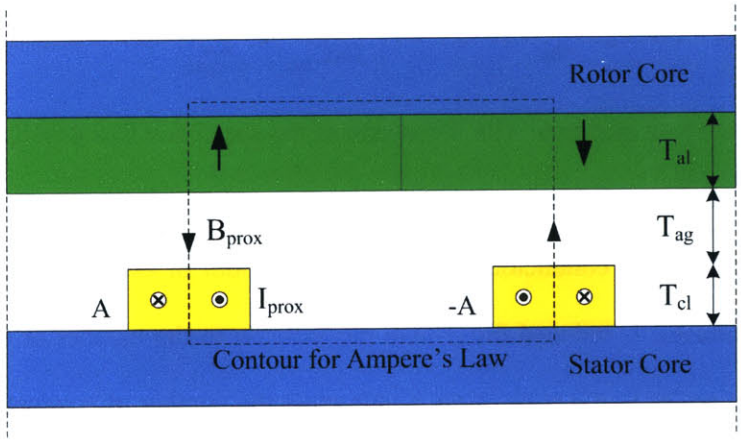

Figure 2-26: Proximity eddy current distribution in a single phase and contour for computing the B field due to these currents.

2.3 Slotted Stator Magnetic Machines

For the slotted stator magnetic machine, one source of magnetic field resides in the rotor active layer. The other source of magnetic field resides in slots covered over with hats. Because of the distinct location of each of these sources the slotted stator magnetic machine consists of two models (Figure 2-27). One model is used for determining the fields in the machine due to the rotor magnetization and a separated model is used to determine the fields due to the stator currents. To model the slotted stator PM machine both models are needed but for the induction machine, the rotor magnetization is zero so only the model that determines the fields due to the stator currents is needed.

To determine the fields due to the rotor magnetization, the continuum model from the surface wound machine is used. The slotted stator is divided into two equivalent layers. The first layer, composed of the stator poles, hats and buried windings, is called the slot layer and replaces the coil layer in the continuum model. This layer has permeability, μ_p, and conductivity, σ_p. The second layer is made up of the stator base and has a permeability, μ_b, and conductivity, σ_b. It replaces the stator core layer in the continuum model. The normal B field at the surface of the stator is used to determine the flux through the pole and base. These fluxes are sent to the iterative algorithm for saturation to determine an effective permeability for the pole, μ_p, and base, μ_b. The stator lamination model for the surface wound machine is used to determine the effective conductivities for the stator layers.

To determine the fields in the machine due to the stator currents the air gap and rotor use the same continuum analysis of the surface wound machine but the stator is modeled as a lumped parameter magnetic reluctance circuit due to its complex slotted structure. This hybrid continuum/lumped parameter model is the same approach used in [26] to model magnetic induction machines. The model used here builds on [26] by incorporating the effects of laminations, saturation, eddy current loss in the stator and hysteresis loss. The rotor continuum model uses the tangential H field at the surface of the stator produced by currents in stator slots as a boundary condition to solve for the normal B field at the surface of the stator. The normal B field is integrated over the stator surface to determine the flux over each stator pole.

The stator reluctance circuit uses this flux and the phase currents as inputs to determine the tangential H field at the surface of the stator. The rotor and stator models are combined to determine H and B fields in the machine as a function of stator currents.

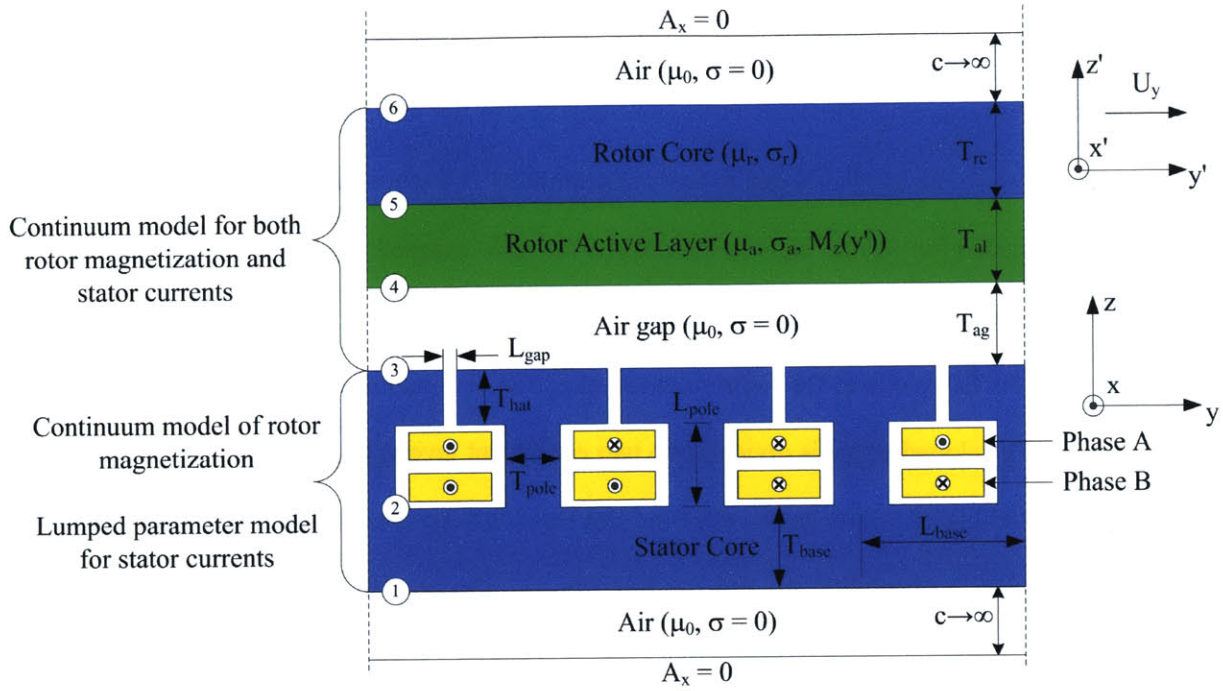

Figure 2-27: The slotted stator magnetic machine model consists of a continuum model for the rotor and air gap and a lumped parameter model for the stator.

2.3.1 Continuum Model for Rotor Magnetization

The slotted stator is divided into two equivalent layers as shown in Figure 2-28. The first layer consists of the stator pole, hat and the buried windings and is will be represented by the stator slot layer. This layer has permeability, μ_p, and conductivity, σ_p. The stator base is treated as a separate layer with permeability, μ_b, and conductivity, σ_b. The β parameters (2-36a) – (2-36c) remain the same but the α parameters, (2-27a) – (2-27b) are modified as follows,

$$\alpha_{1n} = \frac{\mu_b}{\gamma_{bn}} \frac{\gamma_{0n}}{\mu_0} \sinh(\gamma_{bn} T_{sb}) + \cosh(\gamma_{bn} T_{sb}),\ \alpha_{2n} = \frac{\gamma_{bn}}{\mu_b} \sinh(\gamma_{bn} T_{sb}) + \frac{\gamma_{0n}}{\mu_0} \cosh(\gamma_{bn} T_{sb}) \qquad (2\text{-}162a)$$

$$\alpha_{3n} = \frac{\mu_p}{\gamma_{pn}} \alpha_{2n} \sinh(\gamma_{pn} T_{sl}) + \alpha_{1n} \cosh(\gamma_{pn} T_{sl}),\ \alpha_{4n} = \frac{\gamma_{pn}}{\mu_p} \alpha_{1n} \sinh(\gamma_{pn} T_{sl}) + \alpha_{2n} \cosh(\gamma_{pn} T_{sl}) \qquad (2\text{-}162b)$$

The diffusion constants for the stator are also modified and are shown in Table 2-3.

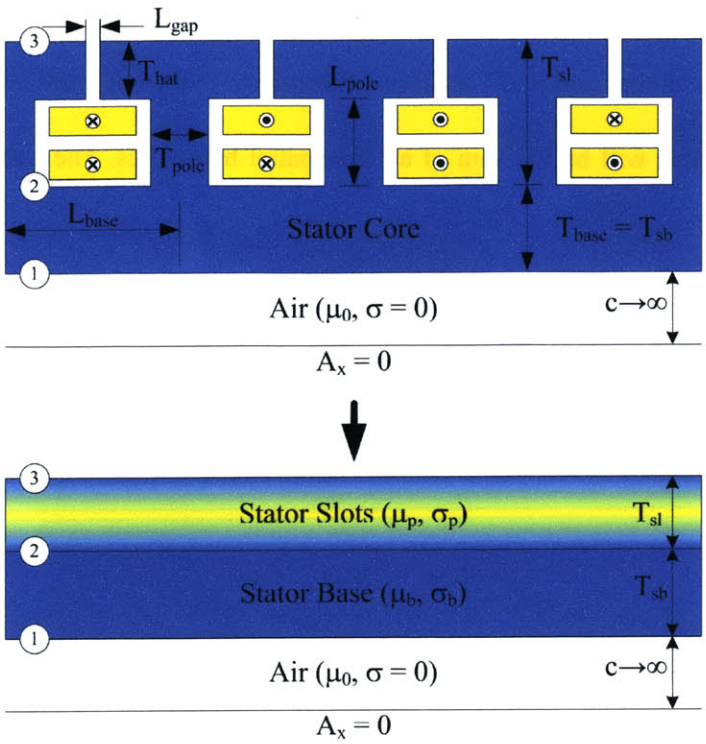

Figure 2-28: The slotted stator is divided into two equivalent layers, one for the slots and one for the stator base.

Table 2-3: Diffusion Constants for Different Planar Layers.

Diffusion Constant	Synchronous Machine	Asynchronous machine
γ_{0n}	$\sqrt{n^2k^2}$	$\sqrt{n^2k^2}$
γ_{an}	$\sqrt{n^2k^2}$	$\sqrt{n^2k^2 + j\mu_a\sigma_a(\omega_e - n\omega_m)}$
γ_{rn}	$\sqrt{n^2k^2}$	$\sqrt{n^2k^2 + j\mu_r\sigma_r(\omega_e - n\omega_m)}$
γ_{pn}	$\sqrt{n^2k^2 + j\mu_p\sigma_p n\omega_m}$	$\sqrt{n^2k^2 + j\mu_p\sigma_p\omega_e}$
γ_{bn}	$\sqrt{n^2k^2 + j\mu_b\sigma_b n\omega_m}$	$\sqrt{n^2k^2 + j\mu_b\sigma_b\omega_e}$

The rotor flux, Φ_r, normal to the surface of each pole is used to determine the flux through the stator pole and base. The complex amplitude of the normal B field at the surface of the stator is

$$\hat{B}_{zn}^{(3)} = jnk\hat{A}_{xn}^{(3)} = jnk\alpha_{3n}\hat{A}_{xn(m)}^{(1)}. \tag{2-163}$$

From Figure 2-29, the rotor flux into a stator pole is the integral of $\hat{B}_{zn}^{(s)}$ over a quarter wavelength

$$\hat{\Phi}_{rn(m)} = \int_{-\lambda/8}^{\lambda/8} \hat{B}_{zn}^{(s)} e^{-jnky}\,dy = -j2\sin\left(\frac{n\pi}{4}\right)\alpha_{3n}\hat{A}_{xn(m)}^{(1)}. \tag{2-164}$$

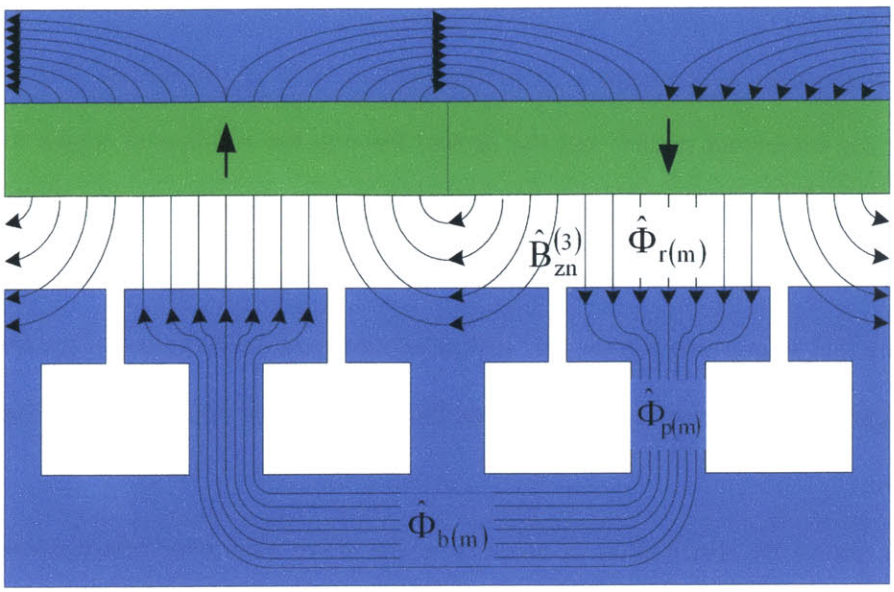

Figure 2-30: Flux paths for rotor flux through stator.

2.3.2 Rotor/Air gap Continuum Model for Stator Currents

The stator currents will produce a tangential H field at the surface of the stator whose harmonics, $H_{yn(J)}^{(3)}$, are inputs to the rotor model. Making use of the β parameters from Section 2.2.1 the vector potential at interface ⑥ due to the stator currents is

$$\hat{A}_{xn(J)}^{(6)} = -\frac{1}{\beta_{6n}}\hat{H}_{yn(J)}^{(3)}. \tag{2-167}$$

The vector potential at the surface of the stator is

$$\hat{A}_{xn(J)}^{(3)} = \beta_{5n}\hat{A}_{xn(J)}^{(6)} = -\frac{\beta_{5n}}{\beta_{6n}}\hat{H}_{yn(J)}^{(3)}. \tag{2-168}$$

Referring back to Figure 2-29, the total flux incident on the surface of a pole due to the stator currents

$$\hat{\Phi}_{r(J)} = \sum_n \hat{\Phi}_{rn(J)} = j2\sum_n \sin\left(\frac{n\pi}{4}\right)\frac{\beta_{5n}}{\beta_{6n}}\hat{H}_{yn(J)}^{(3)}. \tag{2-169}$$

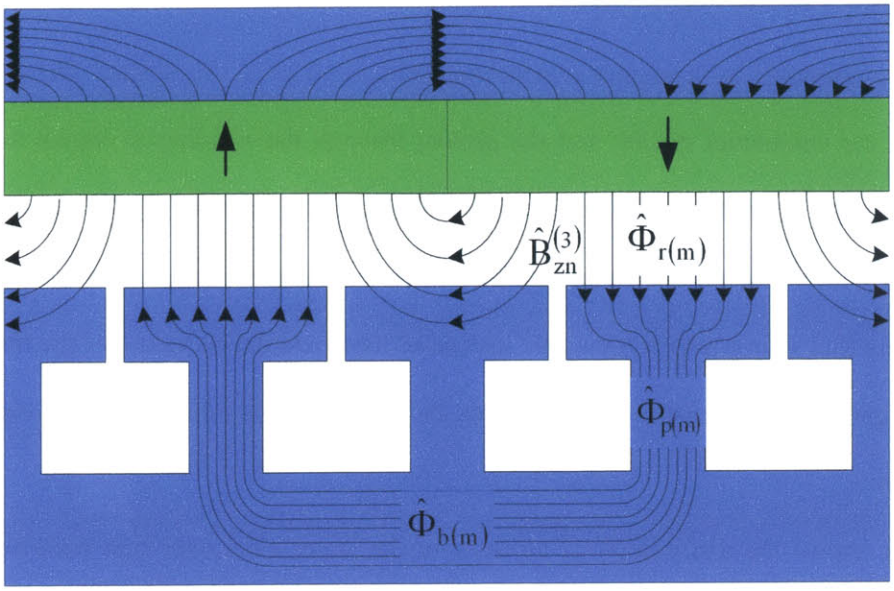

Figure 2-30: Flux paths for rotor flux through stator.

2.3.2 Rotor/Air gap Continuum Model for Stator Currents

The stator currents will produce a tangential H field at the surface of the stator whose harmonics, $H^{(3)}_{yn(J)}$, are inputs to the rotor model. Making use of the β parameters from Section 2.2.1 the vector potential at interface ⑥ due to the stator currents is

$$\hat{A}^{(6)}_{xn(J)} = -\frac{1}{\beta_{6n}}\hat{H}^{(3)}_{yn(J)}. \tag{2-167}$$

The vector potential at the surface of the stator is

$$\hat{A}^{(3)}_{xn(J)} = \beta_{5n}\hat{A}^{(6)}_{xn(J)} = -\frac{\beta_{5n}}{\beta_{6n}}\hat{H}^{(3)}_{yn(J)}. \tag{2-168}$$

Referring back to Figure 2-29, the total flux incident on the surface of a pole due to the stator currents

$$\hat{\Phi}_{r(J)} = \sum_n \hat{\Phi}_{rn(J)} = j2\sum_n \sin\left(\frac{n\pi}{4}\right)\frac{\beta_{5n}}{\beta_{6n}}\hat{H}^{(3)}_{yn(J)}. \tag{2-169}$$

2.3.3 Lumped Parameter Stator Model

The stator is modeled as a magnetic reluctance circuit. It uses the normal flux over each pole, computed from the continuum model, and the current through the winding as inputs to determine the leakage flux through the stator teeth gaps. This leakage flux is divided by the area of the teeth to determine the H field through the teeth gaps. The reluctance circuit is simpler than the one used in [26]. There is only one flux source over a rotor pole instead of three and the curvature of the flux paths around a stator slot is ignored. In contrast to [26], however, the effects of eddy currents in the stator laminations are included here.

Figure 2-31 shows the distribution of currents in the stator slots over one wavelength. Each slot contains a coil from phase A and a coil from phase B. Phase A is driven with current $I_o\cos(\omega t)$ while phase B has is driven with current $I_o\sin(\omega t)$. The current in slot 1 is

$$-\sqrt{2}I_o\cos\left(\omega t-\frac{\pi}{4}\right)=\mathrm{Re}\left\{-\sqrt{2}I_o e^{-j\frac{\pi}{4}}e^{j\omega t}\right\}=\mathrm{Re}\left\{\hat{I}e^{j\omega t}\right\}. \tag{2-170}$$

The current in slot 1 is designated to be in the –x direction so that the tangential H at the teeth gap above the slot is in the +y direction. The currents in slots 2, 3 and 4 have the same magnitude but are shifted in phase by $\pi/2$, π, and $3\pi/2$, respectively. The $\pi/2$ symmetry between successive slots will be exploited when analyzing the stator reluctance circuit.

Since the reluctance of each tooth gap is much larger than the reluctance of the hat, pole and base, most of the MMF drop around the leakage flux path will be dropped across the gap. Therefore, the flux across the teeth gap will be proportional to and in phase with the current in the slot beneath it. The current distribution in the slots leads to the tangential H field distribution shown in Figure 2-31. The tangential H field peaks in the region of the teeth gaps and can be represented in the following form

$$H^{(3)}_{y(J)}(y,t)=\mathrm{Re}\left\{\hat{H}^{(3)}_{y(J)}(y)e^{j\omega t}\right\}. \tag{2-171}$$

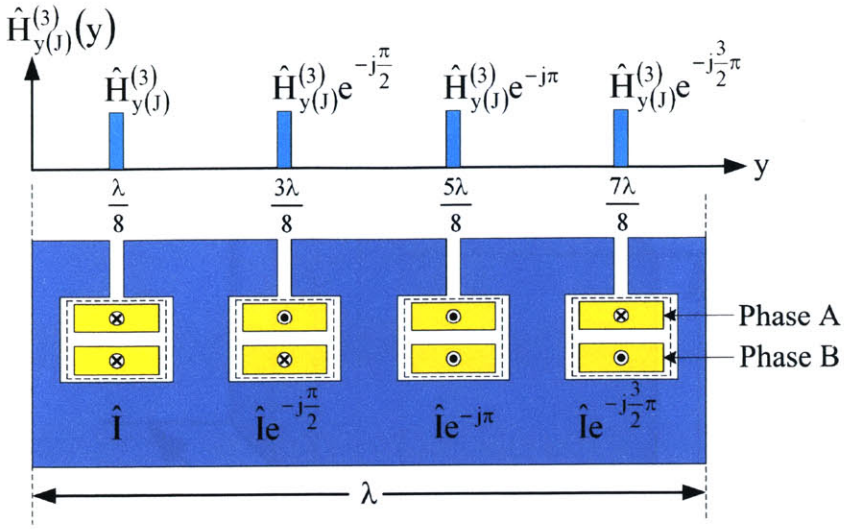

Figure 2-31: Current distribution in the stator slots and corresponding tangential H field at the surface of the stator.

This spatial distribution $\hat{H}^{(3)}_{y(J)}(y)$ can be decomposed into its spatial harmonic components

$$\hat{H}^{(3)}_{y(J)}(y) = \sum_{n=-\infty}^{\infty} \hat{H}^{(3)}_{yn(J)} e^{-jnky} \quad . \tag{2-172}$$

The complex magnitude of each spatial harmonic is [26]

$$\hat{H}^{(3)}_{yn(J)} = \frac{4}{n\pi} \sin\left(n\pi \frac{L_g}{\lambda}\right) e^{j\frac{n\pi}{4}} \hat{H}^{(3)}_{y(J)}, \text{ for n = 1,-3, 5,-7, 9...} \tag{2-173}$$

2.3.3.1 Laminated Stator Reluctances

The laminations for the slotted stator are a series of thin concentric shells just as in the case for the surface wound machine. The cross section of the flux paths through the stator are long in the azimuthal (T_{hat}, T_{base}) and axial direction (T_{pole}) but short in the radial direction (W). Thus the eddy currents generated in the laminations flow mainly in a single direction along T_{hat}, T_{pole} and T_{base}. The analysis of Section 2.2.6 will be used to determine the complex reluctance of the laminated stator.

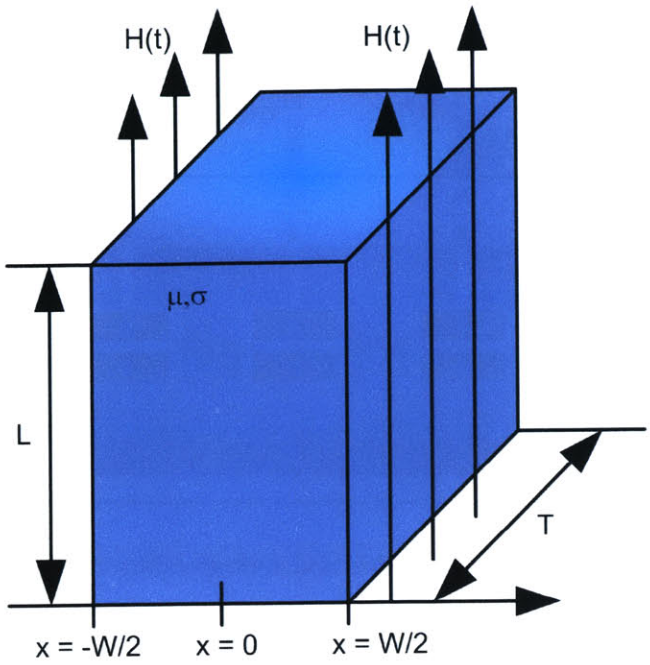

Figure 2-32: Eddy currents in a lamination of thickness W. The lightly shaded region represents minimum flux penetration.

Figure 2-32 shows a lamination of length L, width W and height H, with a permeability of μ and a conductivity of σ. Equation (2-82) describes the flux through such a lamination as a function of the applied H field, H(t). Equation (2-82) can be rewritten as

$$\hat{\Phi} = \frac{2\mu T H_0}{\alpha}\tanh\left(\alpha\frac{W}{2}\right)\times\frac{WL}{WL} = \left(\frac{\mu TW}{L}\right)\times\left(H_0 L\right)\times\left(\frac{2}{\alpha W}\right)\tanh\left(\alpha\frac{W}{2}\right). \tag{2-174}$$

The first term in (2-174) is the DC permeance of the lamination

$$P = R^{-1} = \frac{\mu TW}{L}. \tag{2-175}$$

The second term is the MMF drop across the lamination,

$$(Ni) = H_0 L. \tag{2-176}$$

The third term describes how induced eddy currents affect the reluctance of the lamination. Note that the eddy currents not only increase the magnitude of the reluctance but also create a phase lag between the applied MMF and the flux through the lamination because the reluctance is complex.

A new function F(Q) is defined to represent the eddy current effects on the reluctance

$$F(Q)=\frac{Q}{\tanh(Q)}, \tag{2-177}$$

where the parameter Q, defined in (2-84) of Section 2.2.6, is

$$Q=\frac{1+j}{2}\frac{W}{\delta}. \tag{2-178}$$

The complex reluctance, R, of a lamination is then

$$R=\frac{L}{\mu TW}F(Q). \tag{2-179}$$

Note that the rotor is continuous over its entirety. The rotor continuum model determines the H and B fields in the air gap over an incremental radial span, dr. These incremental fields are integrated over the radial span of the machine to find the flux, torque, voltage, etc... The stator on the other hand consists of a finite number of laminations and, therefore, a finite number of reluctance circuits. In order to couple the stator's finite number of laminations to the continuous model of the rotor an incremental reluctance circuit for the laminated stator is needed so that the field solutions will be a continuous function of radius.

As shown previously in Figure 2-14 of Section 2.2.7, the flux from the rotor over a radial span of W+S will flow into a lamination of radial span W, where S is the width of the insulation layer between laminations. From the standpoint of the rotor, the reluctances in the stator will be proportional to

$$R\propto\frac{L}{\mu Tp_f(W+S)}, \tag{2-180}$$

where the packing factor, p_f, is defined to be

$$p_f=\frac{W}{W+S}. \tag{2-181}$$

The equivalent reluctance over an incremental radial span Δ is then proportional to

$$R\propto\frac{L}{\mu Tp_f\Delta}. \tag{2-182}$$

The stator teeth gap, pole and base are each modeled by a separate reluctance: R_g, R_p and R_b, respectively. The incremental reluctances for the hat, pole and base are

$$R_p = \frac{L_p}{\mu_p T_p p_f \Delta} F(Q_p), \tag{2-183}$$

$$R_b = \frac{\lambda/4}{\mu_b T_{sb} p_f \Delta} F(Q_b), \tag{2-184}$$

where $Q_i \propto \frac{1}{\delta(\mu_i)}$ for i = p or b. The flux through the teeth gap is not constrained to a lamination width but will instead flow through the entire radial span of the teeth gap. From Figure 2-33, the width of the path for the flux through the teeth gap for each lamination is W+S. The incremental reluctance of the teeth gap is

$$R_g = \frac{L_g}{\mu_0 T_h \Delta}. \tag{2-185}$$

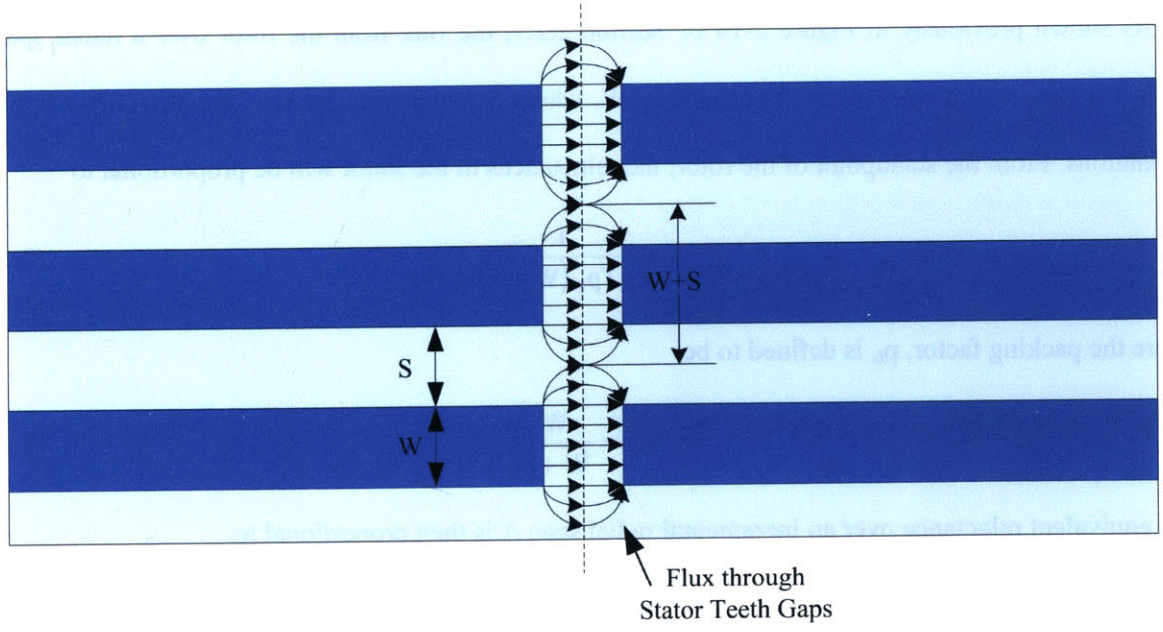

Figure 2-33: Flux through the stator teeth gaps are not constrained to flow through a lamination width, W, but will instead diverge into the space between laminations.

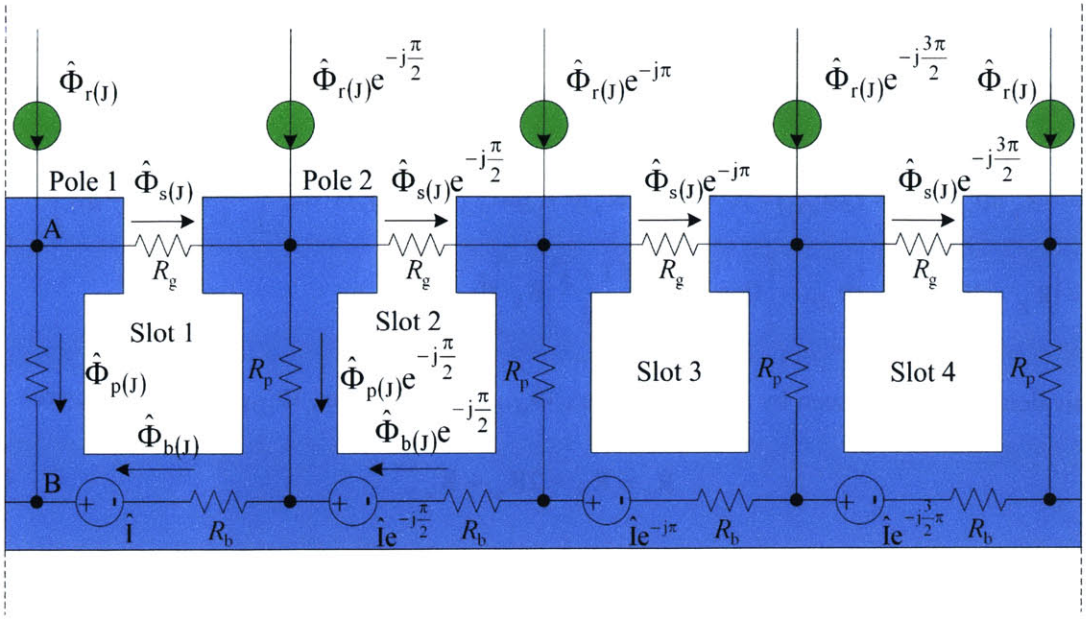

Figure 2-34: Stator magnetic reluctance circuit.

2.3.3.2 Stator Reluctance Circuit

The stator circuit consists of a network of reluctances driven by MMF and flux sources as shown in Figure 2-34. The MMF sources represent the current enclosed in a slot, while the flux sources represent the flux from the rotor above a given stator pole due to the stator currents. The goal is to determine the magnitude of the H field through the teeth gap as a function of the applied current. This analysis will make use of Kirchoff's Current Law (KCL) and Kirchoff's Voltage Law (KVL) for the reluctance circuit.

Using KCL and summing the fluxes at node A in Figure 2-34, the flux through a pole is

$$\hat{\Phi}_{p(J)} = \hat{\Phi}_{r(J)} + (j-1)\hat{\Phi}_{s(J)}, \tag{2-186}$$

while, summing the fluxes at node B, the flux through the stator base is

$$\hat{\Phi}_{b(J)} = (-j)\hat{\Phi}_{b(J)} + (-j)\hat{\Phi}_{r(J)} + (1+j)\hat{\Phi}_{s(J)}. \tag{2-187}$$

Rearranging the terms in (2-187), the flux through the stator base is

$$\hat{\Phi}_{b(J)} = \frac{1}{j-1}\hat{\Phi}_{r(J)} + \hat{\Phi}_{s(J)}. \tag{2-188}$$

The next step is to determine flux through the teeth gap, $\hat{\Phi}_{s(J)}$, in terms of $\hat{I}$ and $\hat{\Phi}_{r(J)}$. This can be done using KVL around the Slot 1. The MMF drop across Slot 1 is

$$\begin{aligned}\hat{I} &= -R_p\left(\hat{\Phi}_{r(J)} + (j-1)\hat{\Phi}_{s(J)}\right) + R_g\hat{\Phi}_{s(J)} + R_p\left((1+j)\hat{\Phi}_{s(J)} - j\hat{\Phi}_{r(J)}\right) + R_b\left(\frac{1}{j-1}\hat{\Phi}_{r(J)} + \hat{\Phi}_{s(J)}\right) \\ &= \left[R_g + 2R_p + R_b\right]\hat{\Phi}_{s(J)} - \left[(1+j)R_p + \left(\frac{1+j}{2}\right)R_b\right]\hat{\Phi}_{r(J)}\end{aligned} \quad (2\text{-}189)$$

The equivalent reluctances seen by the leakage flux, $\hat{\Phi}_{s(J)}$, and rotor flux, $\hat{\Phi}_{r(J)}$, respectively, are

$$R_s = R_g + 2R_p + R_b, \quad (2\text{-}190)$$

$$R_r = (1+j)R_p + \left(\frac{1+j}{2}\right)R_b. \quad (2\text{-}191)$$

Equation (2-189) can now be written as

$$R_s\hat{\Phi}_{s(J)} - R_r\hat{\Phi}_{r(J)} = \hat{I}. \quad (2\text{-}192)$$

The flux through a tooth gap is

$$\hat{\Phi}_{s(J)} = \mu_0 T_{hat}\hat{H}^{(3)}_{y(J)}, \quad (2\text{-}193)$$

while the rotor flux over one stator pole, derived in the rotor modeling section, is

$$\hat{\Phi}_{r(J)} = j2\sum_n \sin\left(\frac{n\pi}{4}\right)\frac{\beta_{5n}}{\beta_{6n}}\hat{H}^{(3)}_{yn(J)}. \quad (2\text{-}194)$$

Substituting Equation (2-173) for $\hat{H}^{(3)}_{yn(J)}$ into (2-194) gives

$$\hat{\Phi}_{r(J)} = j2\left[\sum_n \text{sinc}\left(\frac{n}{4}\right)\left(\frac{\beta_{5n}}{\beta_{6n}}\right)\sin\left(n\pi\frac{L_g}{\lambda}\right)e^{j\frac{n\pi}{4}}\right]\hat{H}^{(3)}_{y(J)}. \quad (2\text{-}195)$$

By substituting (2-193) and (2-195) into (2-192) the complex amplitude of the magnetic field through the teeth gap as a function of the current through a slot can be found

$$\mu_0 T_{hat} R_s\hat{H}^{(3)}_{y(J)} - j2\left[\sum_n \text{sinc}\left(\frac{n}{4}\right)\left(\frac{\beta_{5n}}{\beta_{6n}}\right)\sin\left(n\pi\frac{L_g}{\lambda}\right)e^{j\frac{n\pi}{4}}\right]R_r\hat{H}^{(3)}_{y(J)} = \hat{I}. \quad (2\text{-}196)$$

Defining an equivalent "teeth gap" length to be

$$L_{eq} = \mu_0 T_{hat} R_s - j2\left[\sum_n \text{sinc}\left(\frac{n}{4}\right)\left(\frac{\beta_{5n}}{\beta_{6n}}\right)\sin\left(n\pi\frac{L_g}{\lambda}\right)e^{j\frac{n\pi}{4}}\right]R_r, \tag{2-197}$$

the complex amplitude of the tangential H field at the surface of the stator slot is

$$\hat{H}^{(3)}_{y(J)} = \frac{\hat{I}}{L_{eq}}. \tag{2-198}$$

The equivalent teeth gap length is proportional to the stator reluctances and is therefore inversely proportional to the incremental radial span Δ. Since L_{eq} is in the denominator of (2-198), the tangential H field at the surface of the stator is proportional to Δ. The tangential H field can be integrated over the radial span of the machine by letting $\Delta \rightarrow dr$.

2.3.4 Saturation and Hysteresis loss

Saturation effects in the slotted machine are handled using the same iterative approach used in the surface wound machine. A permeability is assigned to the stator pole, stator base and rotor core so that the magnitudes of the B fields in those parts lie on the core material's B-H curve. The magnitudes of the peak B fields in the stator pole and base are

$$B_{maxp} = \left|\frac{\Phi_p}{F(Q_p)T_{pole}p_f}\right|, \tag{2-199}$$

$$B_{maxb} = \left|\frac{\Phi_b}{F(Q_b)T_{base}p_f}\right|. \tag{2-200}$$

The RMS value for the B field at the bottom surface of the rotor core is used

$$B_{rms,r} = \sqrt{\frac{1}{2}\sum_{n=1,odd}^{\infty}\left(\left|B^{(5)}_{yn}\right|^2 + \left|B^{(5)}_{zn}\right|^2\right)}, \tag{2-201}$$

Note that the flux through the pole, base and rotor core is the sum of the fluxes generated by the rotor PM and the stator currents (i.e. $\Phi_p = \Phi_{p(m)} + \Phi_{p(J)}$). The output of the iteration procedure will determine μ_r, μ_p μ_b to determine the α and β parameters for the rotor continuum model. The effective permeabilities can

then be used to determine the effective conductivity of the stator pole and base using Equation (2-86) in Section 2.2.6. The effective conductivity of the stator pole and base are defined as

$$\sigma_p = \sigma_s\left(1 - \left|\frac{\tanh(Q_p)}{Q_p}\right|\right), \tag{2-202}$$

$$\sigma_b = \sigma_s\left(1 - \left|\frac{\tanh(Q_b)}{Q_b}\right|\right). \tag{2-203}$$

The hysteresis loss in the laminated stator core is determined by calculating the core loss in the hat, pole and base at the radius of each lamination

$$P_{coreh} = \frac{\omega_m}{2\pi} WT_h \sum_{i=1}^{N_{lam}} (L_{sb,i} - L_g)\rho_{core}\left(B_{maxh}\big|_{r=r_{lam,i}}\right), \tag{2-204}$$

$$P_{corep} = \frac{\omega_m}{2\pi} WL_{pe} \sum_{i=1}^{N_{lam}} T_{p,i}\rho_{core}\left(B_{maxp}\big|_{r=r_{lam,i}}\right), \tag{2-205}$$

$$P_{coreb} = \frac{\omega_m}{2\pi} WT_{sb} \sum_{i=1}^{N_{lam}} L_{sb,i}\rho_{core}\left(B_{maxb}\big|_{r=r_{lam,i}}\right). \tag{2-206}$$

For Equation (2-204) the peak B field in the hat is given by

$$B_{maxh} = \frac{T_{pole}}{L_{base} - L_{gap}} B_{maxp}. \tag{2-207}$$

The total core loss for the stator is

$$P_{core,s} = 2PN(P_{core,h} + P_{core,p} + P_{core,b}). \tag{2-208}$$

In the case of an induction machine where the frequency of the stator currents is not synchronous with the machine speed, the rotor will experience a time varying field. This will produce hysteresis loss in the rotor core given by

$$P_{core} = \frac{|s|\omega_e}{2}\left(R_o^2 - R_i^2\right)\int_0^{T_{rc}} \rho_{core}(B_1(z))dz. \tag{2-209}$$

Notice that the core loss depends only on the magnitude of the slip. The peak B field, as function of z, in the rotor core is given by

$$B_1(z) = \max_{\theta}\left(\sqrt{B_y^2(z,\theta) + B_z^2(z,\theta)}\right), \tag{2-210}$$

where,

$$B_y(z,\theta) = \mathrm{Re}\left\{\mu_r \sum_{n=-\infty}^{\infty}\left(\frac{\gamma_n}{\mu_0}\frac{\sinh(\gamma_{rn}z)}{\sinh(\gamma_{rn}T_{rc})} + \beta_{2n}\frac{\sinh(\gamma_{rn}(T_{rc}-z))}{\sinh(\gamma_{rn}T_{rc})}\right)\hat{A}_{xn(J)}^{(6)} e^{jn\theta}\right\}, \tag{2-211}$$

$$B_z(z,\theta) = \mathrm{Re}\left\{\sum_{n=1,\mathrm{odd}}^{\infty}\left(\frac{\sinh(\gamma_{rn}z)}{\sinh(\gamma_{rn}T_{rc})} + \beta_{1n}\frac{\sinh(\gamma_{rn}(T_{rc}-z))}{\sinh(\gamma_{rn}T_{rc})}\right)\hat{A}_{xn(J)}^{(6)} e^{jn\theta}\right\}. \tag{2-212}$$

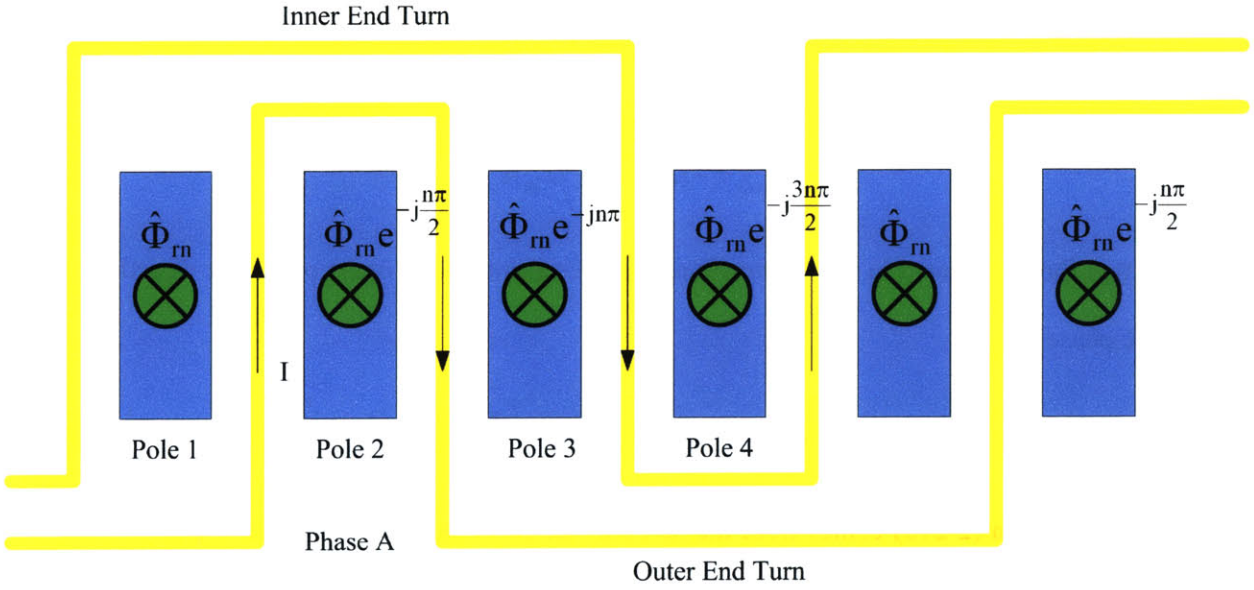

Figure 2-35: Winding diagram for phase A. The flux through Pole 4 is linked by the two outer end turns and contributes to the open-circuit voltage.

2.3.5 Equivalent Circuit Model

2.3.5.1 Open-Circuit Voltage

The spinning multi-pole PM rotor creates a time-varying flux that induces a voltage, V_{oc}, on each phase of the stator windings governed by Faraday's Law,

$$V_{oc} = \frac{d\lambda_m}{dt}, \tag{2-213}$$

where λ_m is the total flux from the rotor PM linked by a single phase. In order to determine the open-circuit voltage, the flux through the poles linked by a single phase of the stator windings must be found. Figure 2-35 shows the winding pattern for a 2-turn pole winding. The two outer end turns link the flux through Pole 4 twice for each pole pair, P, of the machine. On the other hand, the flux through Pole 1 and 3 are 180° out of phase with each other and therefore cancel while the flux through Pole 2 is not link by any of the outer end turns. The harmonic components of the incremental flux through Pole 4, due to the rotor PM, are

$$\hat{\Phi}_{pn(4)} = \hat{\Phi}_{rn(m)} e^{-j\frac{3n\pi}{2}} = \hat{\Phi}_{rn(m)} e^{j\frac{n\pi}{2}}, \tag{2-214}$$

where

$$\hat{\Phi}_{rn(m)} = -j2\sin\left(\frac{n\pi}{4}\right)\alpha_{3n}\hat{A}^{(1)}_{xn(m)}. \tag{2-215}$$

Note that this flux is oriented in the –z direction. The incremental flux, in the positive z direction, linked by a single phase is

$$\hat{\Phi}_{zn,coil(m)} = -PN\hat{\Phi}_{rn(m)} e^{j\frac{n\pi}{2}} = j2PN\sin\left(\frac{n\pi}{4}\right)\alpha_{3n}\hat{A}^{(1)}_{xn(m)} e^{j\frac{n\pi}{2}}. \tag{2-216}$$

The sin(nπ/4) term in (2-216) comes from the fact that the two outer end turns in Figure 2-35 both link flux over a quarter wavelength. The outer end turn that loops around Pole 4 is short-pitched by design while the other outer end turn is effectively short-pitched because the flux through Poles 1 and 3 cancel. Integrating over the radial span of the machine, the flux linked by a single phase for each harmonic is

$$\hat{\lambda}_{n,coil(m)} = \int_{r=R_i}^{r=R_o} \hat{\Phi}_{zn,coil(m)} dr. \tag{2-217}$$

The harmonic amplitudes of the open-circuit voltage induced by this flux is

$$\hat{V}_{ocn} = \frac{d}{dt}\hat{\lambda}_{n,coil(m)} = jn\omega_m \hat{\lambda}_{n,coil(m)}. \tag{2-218}$$

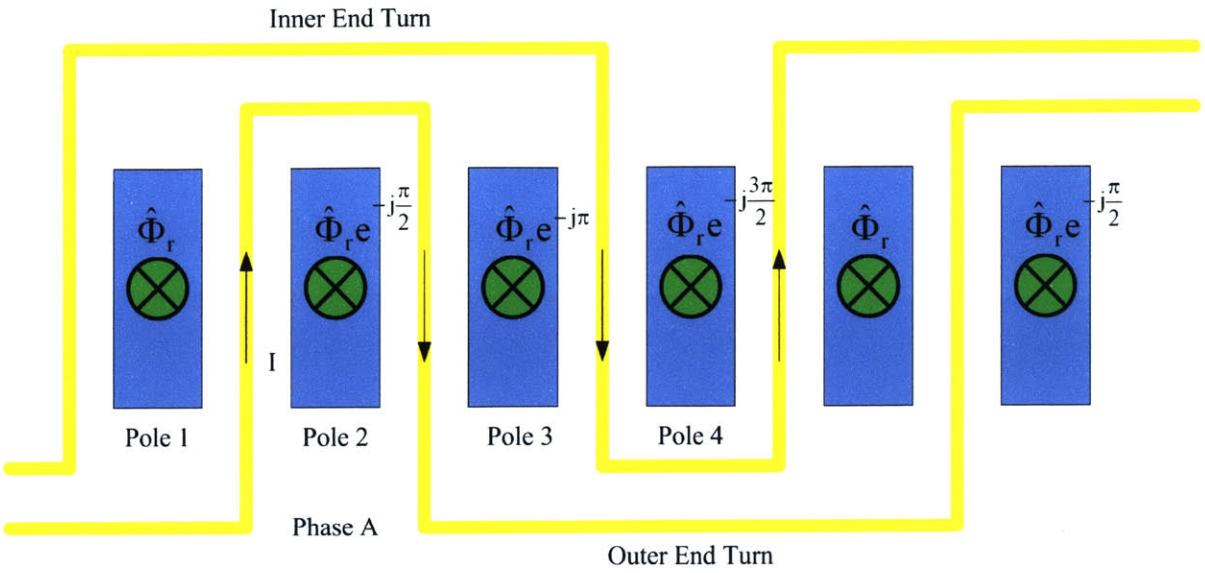

Figure 2-36: Winding diagram for phase A. The flux through Pole 4 is linked by the two outer end turns and contributes to the stator inductance.

2.3.5.2 Stator Inductance

The stator inductance can be computed by finding the total flux generated by the stator currents and linked by a single phase of the machine. This flux is found by integrating the incremental flux through the stator poles linked by a single phase over the radial span of the machine. Figure 2-35 is redrawn in Figure 2-36 showing the $-\pi/2$ symmetry for all spatial harmonics of the stator currents. Referring to the stator reluctance circuit in Figure 2-34, the flux through Pole 1 is

$$\hat{\Phi}_{p(J)} = \hat{\Phi}_{r(J)} + (j-1)\hat{\Phi}_{s(J)}. \tag{2-219}$$

Just as in the case for the open-circuit voltage calculation, the stator winding links the flux through Pole 4 NP times. The incremental flux, in the positive z direction, linked by a single phase is then

$$\hat{\Phi}_{coil(J)} = -jPN\left(\hat{\Phi}_{r(J)} + (j-1)\hat{\Phi}_{s(J)}\right). \tag{2-220}$$

Integrating over the radial span of the machine, the total flux linked by a single phase is

$$\hat{\lambda}_{coil(J)} = \int_{r=R_i}^{r=R_o} \hat{\Phi}_{coil(J)} dr\,. \tag{2-221}$$

Unlike in the three-phase case for the surface wound machines, the windings of the two phase machine do not link flux produced by the other phase. Therefore, the stator phase inductance, L_s, will be

$$L_s = \frac{\mathrm{Re}\{\hat{\lambda}_{coil(J)}\}}{I_0}. \tag{2-222}$$

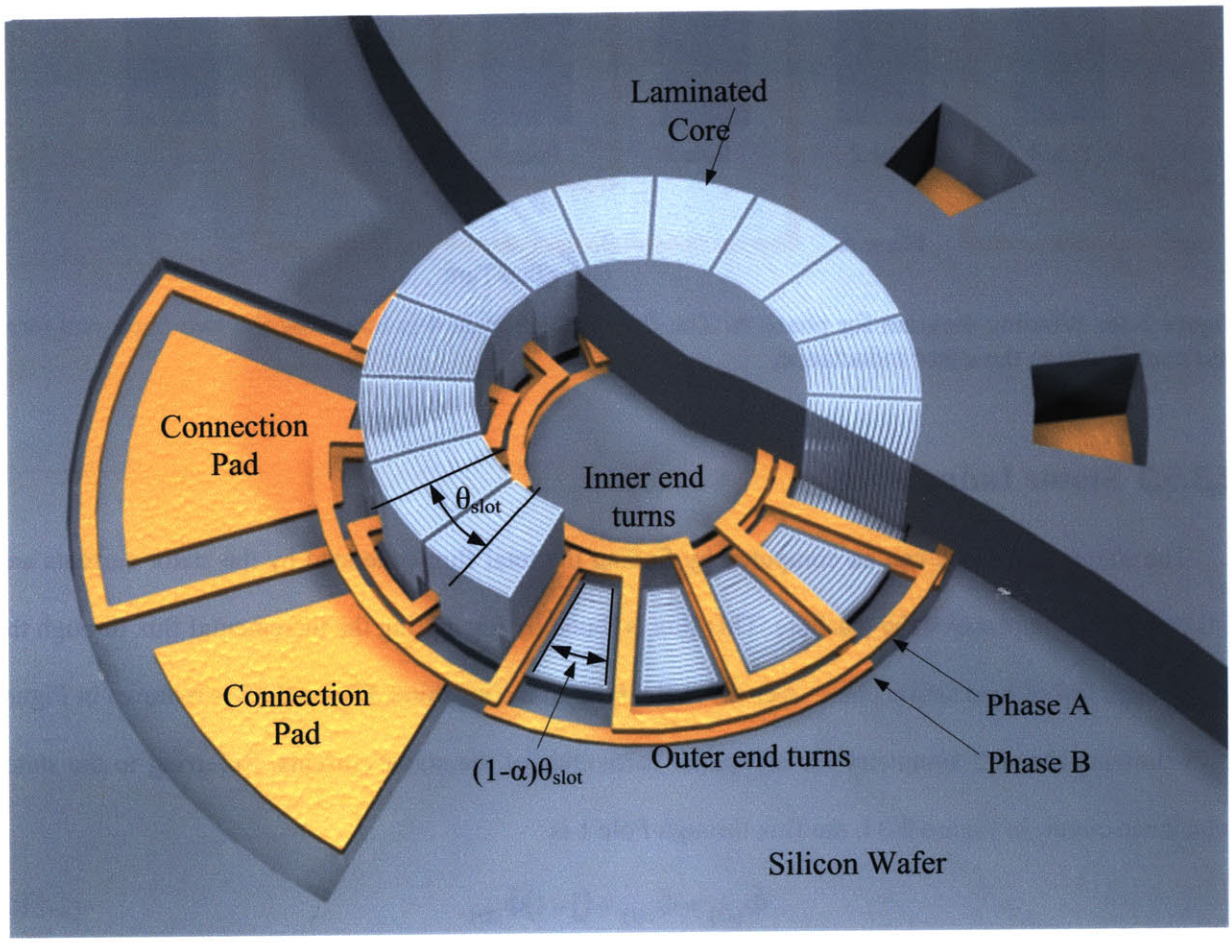

Figure 2-37: Winding pattern for 2-turn/pole concentric wound slotted stator.

2.3.5.3 Stator Resistance

There are only two phases in a slotted stator machine. Each phase is on a separate layer and fills each slot of the stator. This is due to fabrication constraints. The slotted stators have concentric windings as shown in Figure 2-37. There are 2PN conductors in a single phase. The angle spanned by a single slot is

$$\theta_{slot} = \frac{2\pi}{2PN} = \frac{\pi}{PN}. \tag{2-223}$$

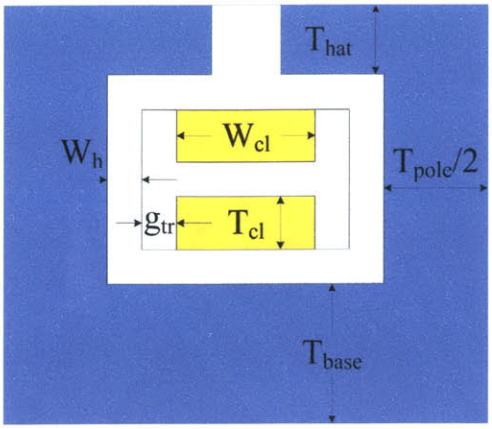

Figure 2-38: Radial conductors are buried in a slot and isolated from the stator core by a silicon frame of thickness of W_h.

The pole spans some fraction $(1-\alpha)$ of a slot,

$$\theta_{pole} = (1-\alpha)\frac{\pi}{PN}, \tag{2-224}$$

where α is the fraction left over for the conductors in the slot. The machines considered here have laminations embedded in a silicon frame. The silicon frame imposes constraints on the width and spacing of the windings in the slot. Figure 2-38 shows a radial conductor in a slot. The width of the winding in a slot is

$$W_{cl}(r) = \frac{\alpha\pi r}{PN} - g_{tr} - W_h, \tag{2-225}$$

where g_{tr} is the spacing between the conductor and the silicon side wall and W_h is the thickness of the side wall. The corresponding resistance of the radial conductor is

$$R_{conductor} = \frac{PN}{\alpha\pi\sigma_c T_{cl}} \ln\left(\frac{W_{cl}(R_o)}{W_{cl}(R_i)}\right), \tag{2-226}$$

while the total resistance of all the radial conductors in a single phase is

$$R_{radial} = \frac{2(PN)^2}{\alpha\pi\sigma_c T_{cl}} \ln\left(\frac{W_{cl}(R_o)}{W_{cl}(R_i)}\right). \tag{2-227}$$

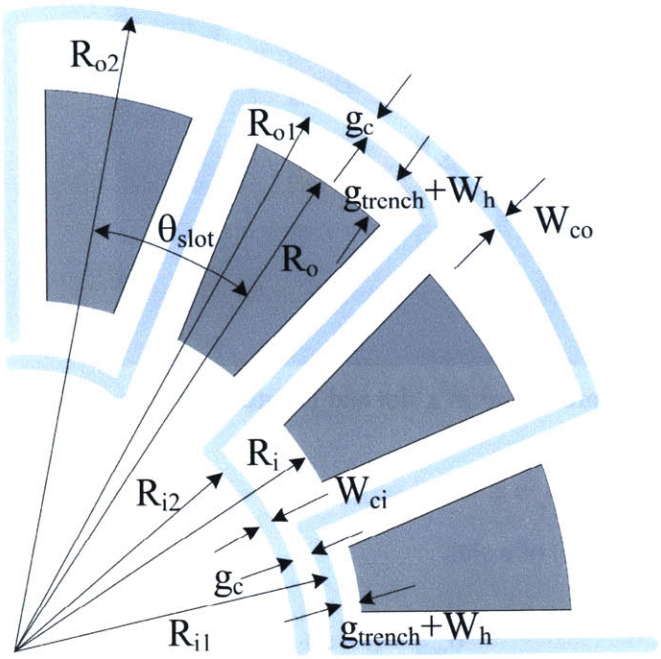

Figure 2-39: End turn connections for a 2-turn pole concentric wound slotted stator.

The end turns for the slotted stator are handled in the same manner as in the concentric surface wound stator. Figure 2-39 shows a 2-turn/pole winding. The short pitched winding spans an angle of π/PN (θ_{slot}) while the long pitched winding spans 3π/PN ($3\theta_{slot}$). The resistance of the outer end turn for each phase is

$$R_{outer} = \frac{\pi}{\sigma_c T_{co} W_{co}} \left(\frac{R_{o1} + 3R_{o2}}{2} \right), \tag{2-228}$$

where

$$R_{o1} = R_o + \frac{W_{co}}{2} + g_{coil}, \tag{2-229}$$

$$R_{o2} = R_o + \frac{3W_{co}}{2} + 2g_{coil}. \tag{2-230}$$

Similarly the resistance of the inner end turn is

$$R_{inner} = \frac{\pi}{\sigma_c T_{ci} W_{ci}} \left(\frac{R_{i1} + 3R_{i2}}{2} \right), \tag{2-231}$$

where

$$R_{i1} = R_i - \frac{W_{ci}}{2} - g_{coil}, \tag{2-232}$$

$$R_{i2} = R_i - \frac{3W_{ci}}{2} - 2g_{coil}, \tag{2-233}$$

For the general case of an N-turns/pole concentric winding, the arc lengths of the n^{th} inner and outer end turns are

$$L_{in} = \frac{(2n-1)\pi R_{in}}{PN}, \tag{2-234}$$

$$L_{on} = \frac{(2n-1)\pi R_{on}}{PN}, \tag{2-235}$$

where

$$R_{in} = R_i - \frac{2n-1}{2} W_{ci} - ng_{coil}, \tag{2-236}$$

$$R_{on} = R_o + \frac{2n-1}{2} W_{co} + ng_{coil}. \tag{2-237}$$

The resulting resistances of the inner and outer end turns are

$$R_{ci} = P\sum_{n=1}^{N} \frac{L_{in}}{\sigma_c T_{ci} W_{ci}} = \frac{\pi}{\sigma_c N T_{ci} W_{ci}} \sum_{n=1}^{N} (2n-1) R_{in}, \tag{2-238}$$

$$R_{co} = P\sum_{n=1}^{N} \frac{L_{on}}{\sigma_c T_{co} W_{co}} = \frac{\pi}{\sigma_c N T_{co} W_{co}} \sum_{n=1}^{N} (2n-1) R_{on}. \tag{2-239}$$

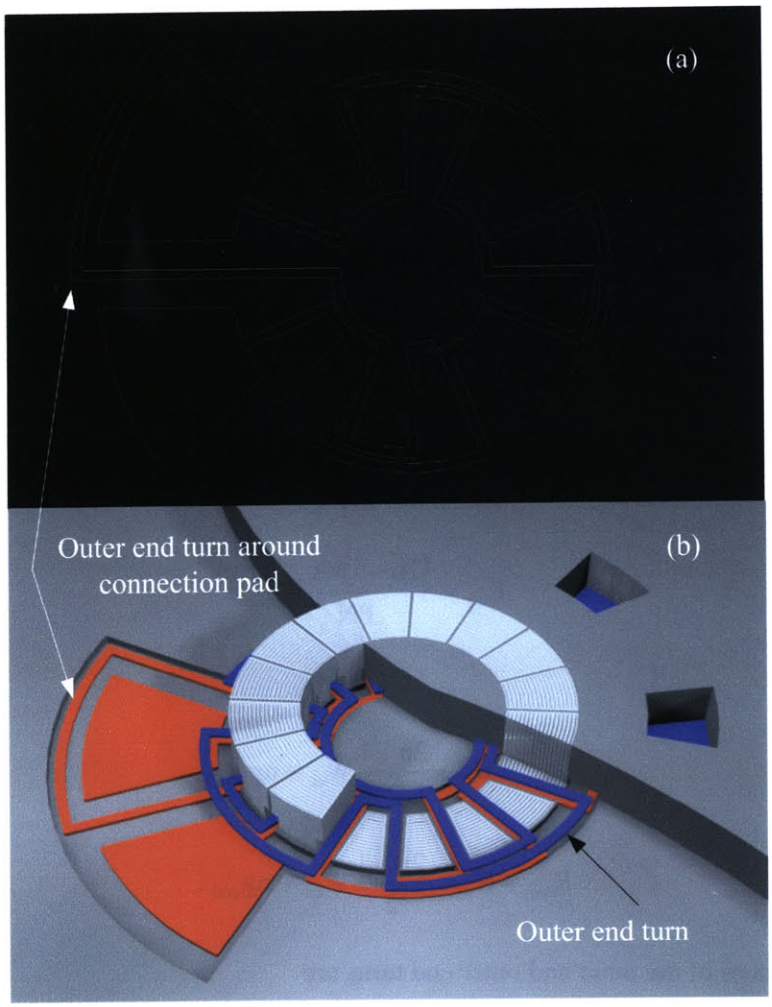

Figure 2-40: Winding pattern for slotted machine (a) mask layout and (b) placement of windings in laminated stator (Phase A in blue, Phase B in red). (Courtesy of David Arnold, GIT [28]).

The previous calculation for the outer end turn resistance assumed that the end turns for each pole pair is the same. However, for a concentric winding in which the entire coil occupies a single layer, the end turns around the connection pads will be different from the others as shown in Figure 2-40. The end turn around the connection pad has longer radial conductors, R_{op}, and a longer outer end turn path length, L_{op}. However, the resistance due to this one longer end turn is about the same as the resistance due to the sum of the two end turns for the other pole pairs so that Equation (2-239) for outer end turn resistance can still be used.

2.4 Model verification with FEA Analysis

To verify that the analytical model can accurately predict open-circuit voltages, 3D FEA simulations of a prototype surface wound PM machine are done using FEMLAB (version 3.1) by collaborators at GIT. The rotor consists of an annular PM and back iron with an outer diameter of 9.525 mm, inner diameter 5.525 mm and each with a thickness of 500 μm. The rotor is suspended 300 μm above the stator core, which is modeled as a large disk that extends well beyond the outer radius of the rotor. This is done because initial PM machines will be fabricated on ferromagnetic wafers. The 300 μm gap between the rotor and stator emulates the 100 μm physical air gap and 200 μm thick surface windings.

In the model, the rotor-stator assembly is surrounded by air, and periodic boundary conditions are imposed. Due to the symmetry of the system, only 1/2P of the assembly is modeled, as shown in Figure 2-41(a). Hiperco 50 is used as the rotor back iron material and Moly Permalloy is used as the stator core material. The annular PM has an ideal square wave magnetization profile with B_r set to 1 T and a permeability of μ_0 to simulate a SmCo magnet.

Using the nonlinear B-H curves for both the Moly Permalloy and Hiperco 50, a 3D, magneto-static FEA model is used as input into a nonlinear solver, and the magnetic fields in the machine for a stationary rotor are calculated. The resulting axial (z-direction) B field distribution 100 μm above the stator core (half the height of the stator windings) is then extracted, as shown in Figure 2-41(b) for an 8-pole machine. The z-directed B field is then input into a MATLAB script. The script solves for the voltage induced on a winding of arbitrary shape by solving for the time-derivative of the flux through a predefined contour as the magnetic field pattern is rotated at the synchronous speed.

The contour over which the B field is integrated is varied in order to simulate various winding patterns. For instance, the winding can have the same radial span as the rotor PM or it can extend beyond the inner and outer radii of the PM by some distance in order to capture the fringing flux, and thus maximize the voltage. Figure 2-42 shows the variation in the open-circuit voltage as a function of the radial extension beyond the PM annulus. A contour that is concentric with the PM (i.e. same radial span)

encloses 86% of the flux that can be obtained if all the fringing flux is linked. Therefore, there is very little radial fringing in the magnetic fields even with an air gap as large as 300 μm. For a winding extending only 0.25 mm beyond both the inner and outer radii, 96.7% of the maximum flux is captured, whereas a winding extending 1 mm is assumed to capture all of the fringing flux. Thus, the 1 mm extension is used for comparison to the 2D analytical model, because the 2D model does not capture radial fringing flux.

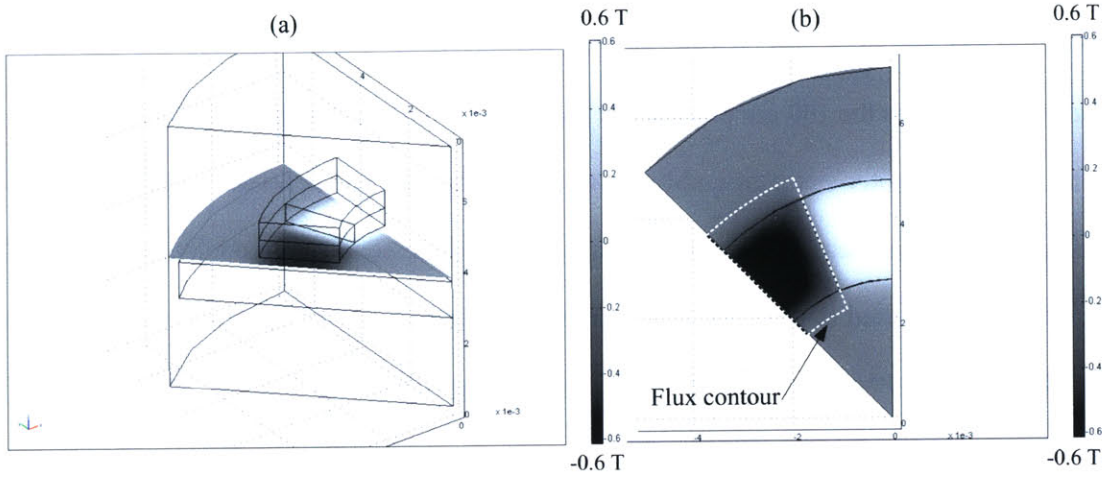

Figure 2-41: 8-pole axial magnetic flux density 100 μm above surface of a planar PM machine stator: (a) perspective view and (b) top view.

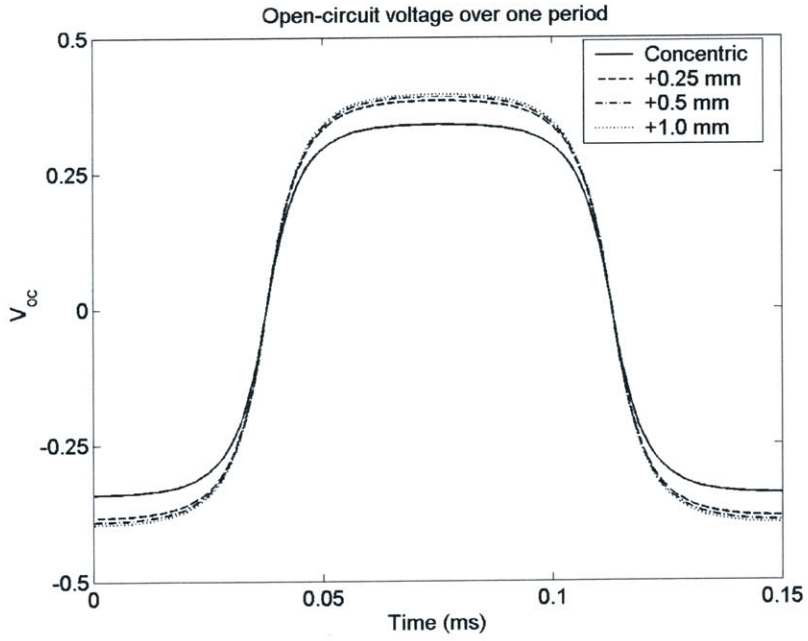

Figure 2-42: Open-circuit voltage for different radial spans of the magnetic flux integration contour.

The stator core is not an annulus but instead a large wafer as discussed in Chapter 4, the flux from the rotor PM will have more area to flow horizontally through the stator. This will lead to a smaller flux density in the stator than if it were only an annulus of ferromagnetic material. From the 3D FEA analysis, a stator winding that has a radial span 1.25 times that of the rotor captures 96.7% of the maximum flux possible. Therefore, the "effective" radial span of the stator will be 1.25 times the radial span of the rotor so that the average B field in the stator is taken to be 80% of the value calculated by (2-92).

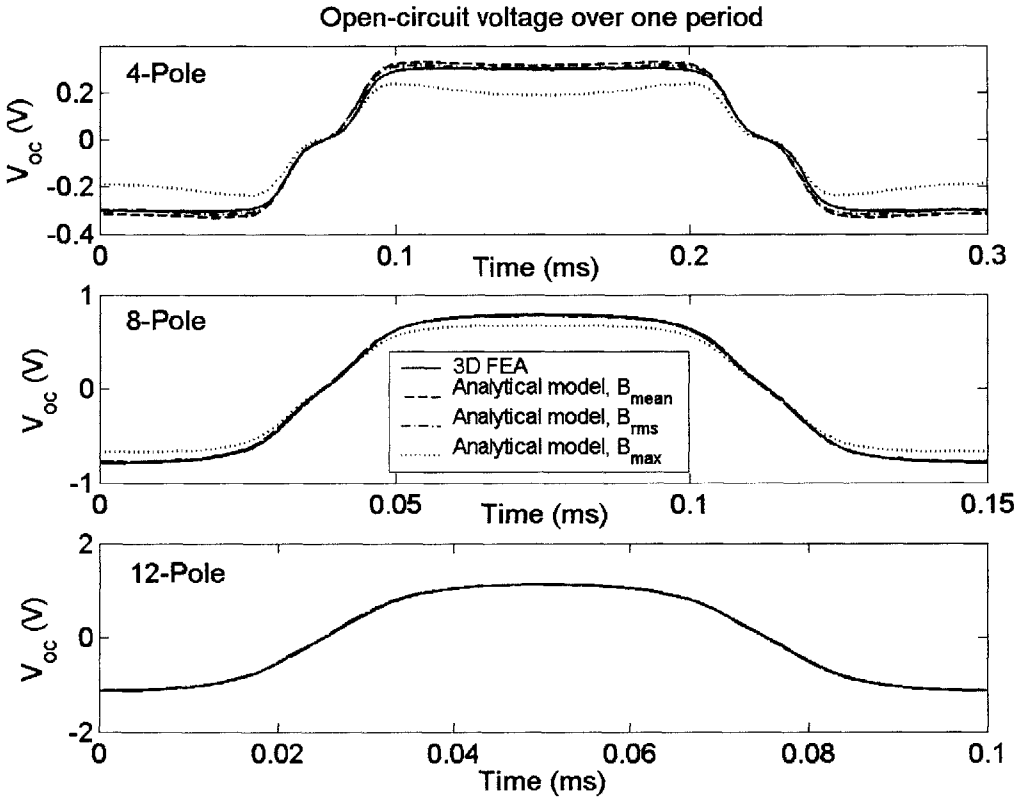

Figure 2-43: Open-circuit voltage over one period for the 4-, 8- and 12-pole machines.

Figure 2-43 shows a comparison of open-circuit voltage waveforms predicted by the analytical model to the FEA results for machines with different number of poles, all with 2-turns/pole and with the rotor spinning at 100 krpm. Notice that for a 4-pole machine, using B_{mean} to determine the relative permeabilities of the rotor and stator core leads to an over prediction of the open-circuit voltage while using B_{max} under predicts the open-circuit voltage. Using B_{rms} also over predicts the open-circuit voltage

but the error is much smaller. For an 8-pole machine, the rotor and stator cores are less saturated and the open-circuit voltage predicted using B_{mean} and B_{rms} converge to the same answer while the open circuit voltage predicted by using B_{max} is still smaller then the FEA result. With a 12-pole machine, the B fields in the rotor and stator cores are far from the saturation limit and all three B field values converge to the same open-circuit voltage. This makes sense since B_{mean} will give an optimistic value for the relative permeability while B_{max} will give a conservative estimate. Since B_{rms} is always larger then B_{mean} but less then B_{max}, using the RMS of the B field will predict an open-circuit voltage in between the values predicted by using the other two metrics and so is likely the best choice in all cases.

The RMS voltage as a function of pole count is shown in Figure 2-44. For a 2-pole machine the errors in open-circuit voltages between the FEA and analytical results using B_{mean}, B_{rms} and B_{max} are 18%, 7% and -37 %, respectively. For a 4-pole machine, the errors are 7%, 2.5% and –28% while an 8-pole machine the errors are 1%, 1% and -13%. For higher pole counts, using any the B field values matches the FEA result. From Figure 2-44 it can be seen that using B_{rms} to compute the effective permeabilities for the rotor and stator core give the most accurate result over the widest range of machine poles.

Notice that for a small number of poles (2-8), the increase in voltage is somewhat linear while for larger pole counts (12+), there are diminishing returns. To understand why the voltage does not increase linearly with pole number in Figure 2-44, recall that the magnetic fields in the air gap decay away from the rotor PM with an exponential rate proportional to P, the number of pole pairs. For small P, the decay rate is small, and therefore the magnetic fields produced by the rotor PM are not significantly diminished as they reach the stator surface. For large values of P, the decay rate is large enough that magnetic fields at the stator surface are greatly reduced. From a physical standpoint, as the number of poles increases, the width of each pole decreases since the circumference of the PM annulus is constant. When the poles become tightly packed the flux lines between adjacent north and south poles are short enough that they connect to each other without passing through the stator core. Thus the flux linked by the stator windings decreases.

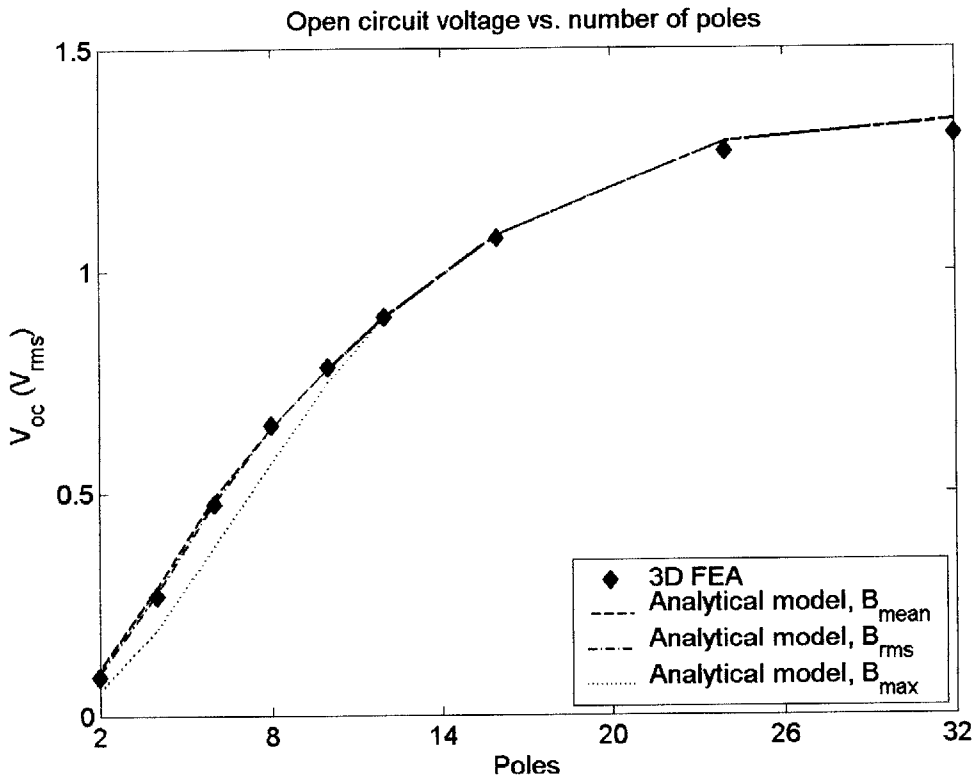

Figure 2-44: Open circuit voltage vs. number of poles.

Figure 2-45 shows open-circuit voltage waveforms for an 8 pole machine at 100 krpm with 2-, 4- and 6-turn/pole stators. The analytical model uses B_{rms} resulting in a good match between the FEA and analytical results. Figure 2-46 shows the RMS voltage vs. turn/pole. The open-circuit voltages obtained by using B_{mean} and B_{rms} produce the same results so the two curves lie on top of one another. Notice that the analytical model shows a relatively linear slope, which means that the spatial offset in adjacent turns of a multiple turn/pole machine have a small effect on the open-circuit voltage.

Figure 2-47 shows open-circuit voltage as a function of air gap for an 8-pole, 2-turn/pole machine at 100 krpm. The voltage decreases exponentially with air gap, as expected. Using B_{max} under predicts the open-circuit voltage at an air gap of 100 μm. As the air gap increases the flux density in the rotor and stator cores decrease and the cores become unsaturated. This leads to a convergence of the analytical model using the three different B field values. The analytical predictions agree extremely well with the FEA results.

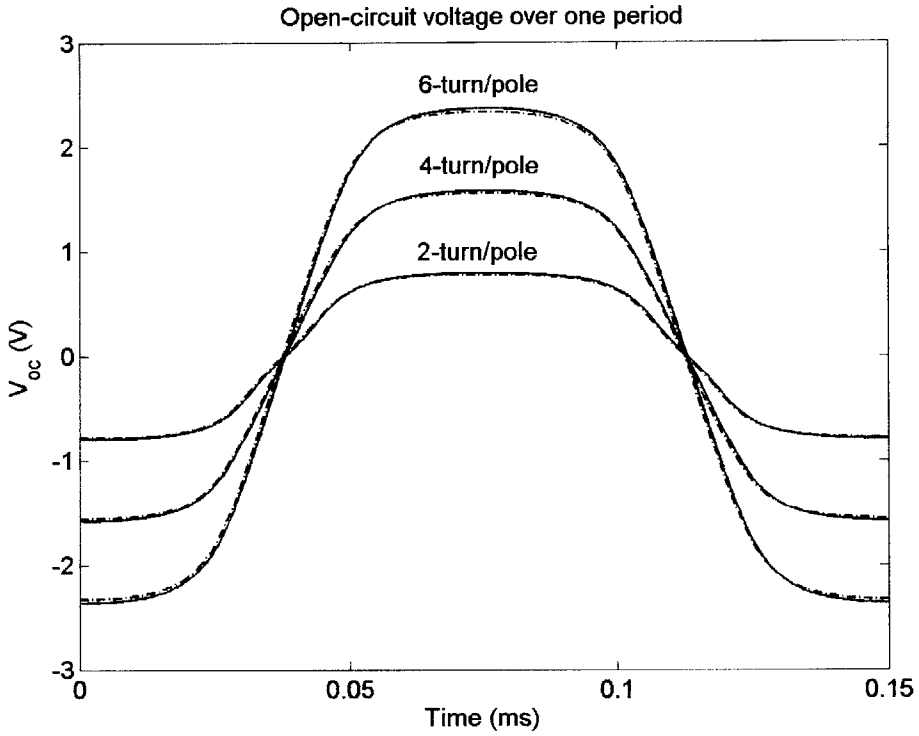

Figure 2-45: Open-circuit voltage over one period for 2-, 4- and 6-turn/pole machines. Solid lines represent FEA; dotted lines represent analytical model using B_{rms} to compute effective permeabilities.

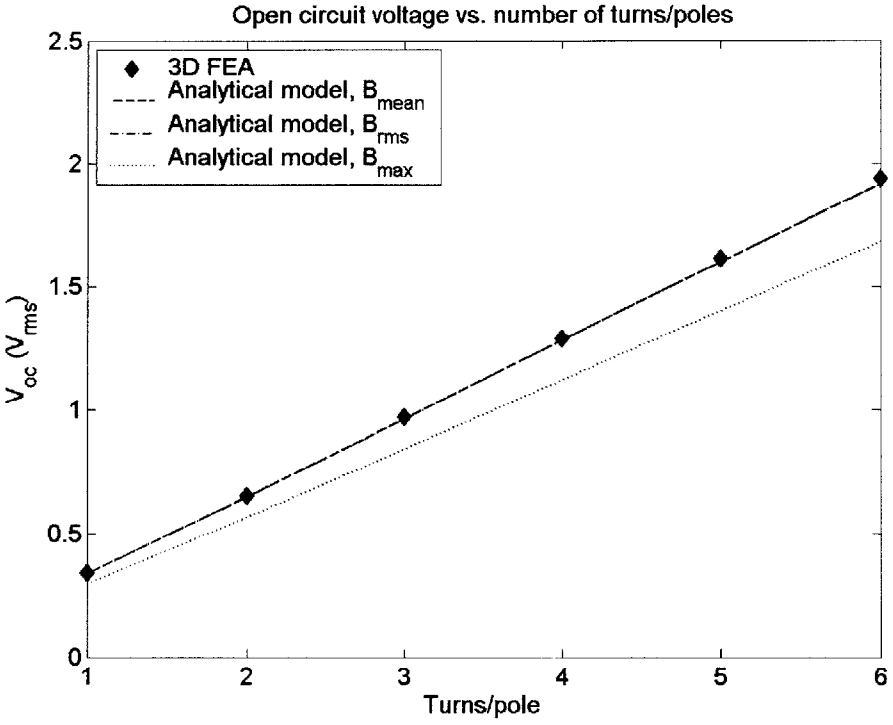

Figure 2-46: Open-circuit voltage vs. turns/pole.

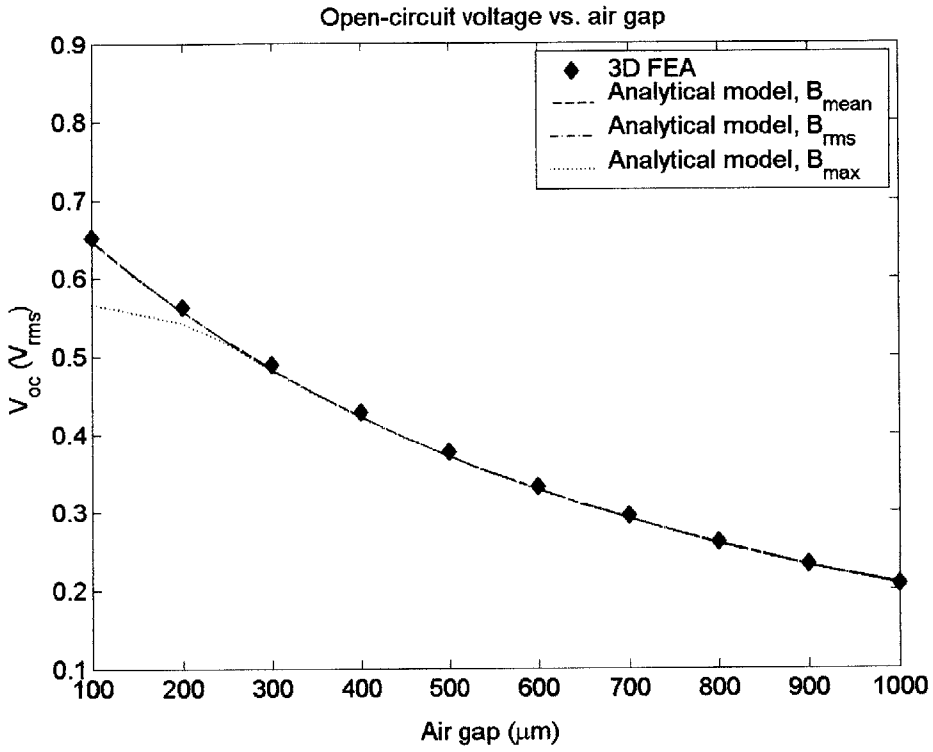

Figure 2-47: Open-circuit voltage vs. air gap.

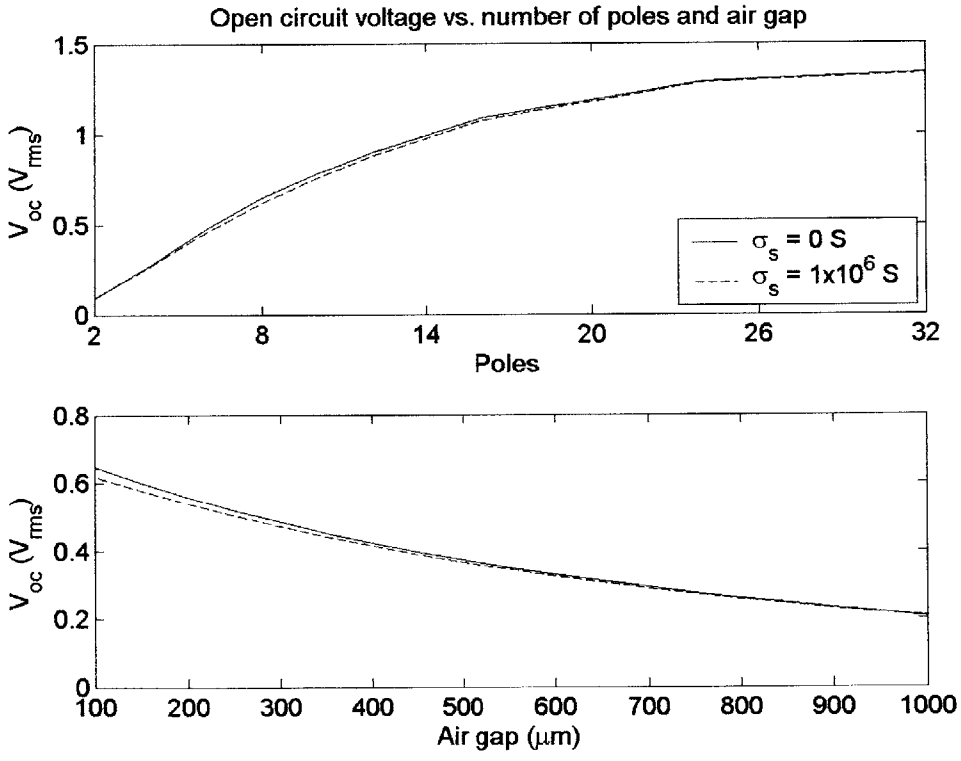

Figure 2-48: Open-circuit voltage vs. poles and air gap for conductive and non-conductive stators.

Note that the FEMLAB simulations solve a static problem. The resulting magnetic field solutions do not incorporate the effects of eddy currents in the stator that would be present due to a spinning PM rotor. In the analytical model, there is only a small discrepancy between the open-circuit voltages predicted from machines with conducting and non-conducting stators (Figure 2-48). The eddy currents generated in the conductive stator, due to the spinning PM, create their own magnetic fields that try to prevent the PM flux from coupling to the stator. However, due to the large air gap, the magnetic fields generated are very small and have negligible effects on the open-circuit voltage.

Using B_{rms} to compute the relative permeabilities in the rotor and stator cores and setting $\sigma_s = 1.6\times10^6$ S for a Moly Permalloy stator, an 8-pole machine has a 4.7% difference in the open-circuit voltages between conductive and non-conductive stators. As the number of poles decrease the two curves converge because the stator core begins to saturate and the induced eddy currents become smaller. At higher pole counts, the permeability of the stator core is so high that the reduced reluctance in the stator core due to the presence of eddy currents produces a negligible effect on the open-circuit voltage.

The discrepancy between the open-circuit voltage of conductive and non-conductive stators also decreases with air gap (Figure 2-48). The eddy currents increase the flux density in the stator core by constraining the flux to flow with the penetration depth γ_{sn}. This results in a lower permeability for the stator and therefore a lower RMS voltage. As the air gap increases, the reluctance of the air gap increases which reduces the impact of the lower permeability in the stator and makes the RMS voltages for the conducting and non-conducting converge.

2.5 Summary

Analytical models of magnetic machines with surface wound and slotted stators have been developed in this chapter. These models can be used to model both synchronous (PM) and asynchronous (induction) machines. The surface wound machine model is presented first and consists of a continuum field analysis of planar layers. The 3D field solutions for the machine were constructed by integrating 2D Cartesian

coordinated solutions over the radial span of the machine. The main continuum model consists of Equations (2-27), (2-28), (2-36), (2-37) and Tables 2-1 and 2-2. The vector potential solutions due to the rotor active layer and stator currents consist of Equations (2-48), (2-49), (2-55), (2-57), (2-66), (2-67), (2-75) and (2-76).

The effects of eddy currents/laminations and saturation are incorporated into the model through the use of effective conductivities (2-84), (2-86) and permeabilities, (2-87), (2-88), (2-93) and (2-94), respectively. Equations (2-95) – (2-100) are used to compute hysteresis loss using the BH curve of the core material while electromechanical torque and eddy current losses are computed using the Maxwell Stress Tensor in Equations (2-105) – (2-111).

An equivalent per-phase circuit model is then derived from the field solutions. It consists of an open-circuit voltage (2-114), (2-118) – (2-120); stator inductance (2-122) – (2-126) and resistance (2-128) – (2-134) and (2-145) – (2-150). Proximity eddy current losses in the stator windings can be computed using (2-157) and (2-160) – (2-162).

These same calculations were the repeated for the slotted stator magnetic machine. The slotted machines used a combination of a full continuum analysis for the rotor magnetization and a hybrid continuum/lumped parameter model for the stator currents. The continuum model for the PM consists of (2-162), (2-165), (2-166) and Table 2-3, in addition to the main continuum model for the surface wound stator. The rotor continuum model for the stator currents consist of (2-167) – (2-169).

The stator lumped parameter model consists of (2-170) – (2-173), (2-186), (2-188), (2-190), (2-191), (2-197) and (2-198). The complex reluctances for the lumped parameter model are given in (2-177), (2-178), (2-183) – (2-185). Saturation and hysteresis loss can be computed using (2-199) – (2-203) and (2-204) – (2-212), respectively.

The per-phase equivalent circuit for the slotted stator machine is computed using (2-216) – (2-218) for the open-circuit voltage, (2-219) – (2-222) for the phase inductance and (2-227), (2-234) – (2-239) for the phase resistance.

The model for the surface wound PM machine is compared to FEA analysis and agrees extremely well with the numerical results over a wide variation in the number of poles, turns/pole and air gap. It was found that using the RMS values for the B fields in the rotor and stator core to compute relative permeabilities provided the most accurate results over the widest range of machine dimensions and should be used in most cases.

Chapter 3 builds on the models to determine power and efficiency of the various machines as function of speed, material properties, dimensions, and input excitation. In particular this chapter makes use of equations for computing output power, torque, eddy current loss, hysteresis loss, proximity loss and stator conduction loss. Chapters 4 and 5 make use of the equivalent circuit model for the surface wound machine so that the generator can be coupled to the power electronics models for power generation system simulation and design.

3 Machine Comparisons

Initial investigations into magnetic machines suitable for generator applications in the microengine focused on induction machines [26] due to the operating temperature requirement of 700 °C. The induction machines consisted of a slotted stator with two-phase 2-turn/pole concentric windings. Induction machines with laminated stators incorporated into two fusion bonded silicon wafers were reported in [28]. With the reduction in the operating temperature to 300 °C, PM machines were considered as possible magnetic generators. Certain rare earth PMs such as SmCo and CoPt have Curie temperatures above 300 °C and therefore can operate inside the revised microengine.

This chapter compares the slotted stator induction machine (SLIM), slotted stator PM machine (SLPM) and surface wound PM machine (SWPM) within the context of the microengine. The constraints posed by the microengine will be presented first in Section 3.1, followed by a discussion of the design parameters over which the three machines will be compared in Section 3.2. The scripts used to obtain the results in this chapter are given in Appendix B. Since the induction machine used a slotted stator, the SLIM and SLPM will be compare against each other first in Section 3.3. The comparison will show that the SLPM can produce more power at a higher efficiency than the SLIM for a given input current, number of poles, and surface area. This is because the PM produces much more magnetic flux in the air gap than do the stator currents in the induction machine.

Once induction machines are eliminated, PM machines with slotted and surface wound stators are compared in Section 3.4. The resulting comparison will show that the SWPM produces more power at a higher efficiency than the SLPM for a give input current, number of poles, and surface area. This is because the SLPM uses a two-phase concentric wound stator that does not link all the flux from the rotor PM (Section 2.3.5). The use of such a stator is imposed by fabrication constraints that require an entire phase winding to occupy a single coil layer. The SWPM machine on the other hand uses a three-phase winding that does link all the flux. The three-phase windings occupy two coil layers using end turns that cross over one another.

The initial comparison between the three machines in Sections 3.3 and 3.4 are done at room temperature because, at the time of the comparison, the focus was on low temperature air powered turbine generators which would be used a stepping stone to high temperature generators in the future and because data on the high temperature performance of the materials used was not available. Section 3.5 compares the three machines using recently available data on the remanence of the PM and stator winding resistance vs. temperature. The results of the high temperature comparison reinforce the conclusion arrived at in Sections 3.3 and 3.4.

Note that surface wound induction machines (SWIM) can be simulated using the models developed in Chapter 2. However, induction machines rely on small air gaps to create strong magnetic fields that couple the rotor and stator to produce torque. The air gaps of surface wound machines are too large for the stator currents to produce magnetic fields strong enough to produce significant torque. Therefore the surface wound induction machine will not be considered here.

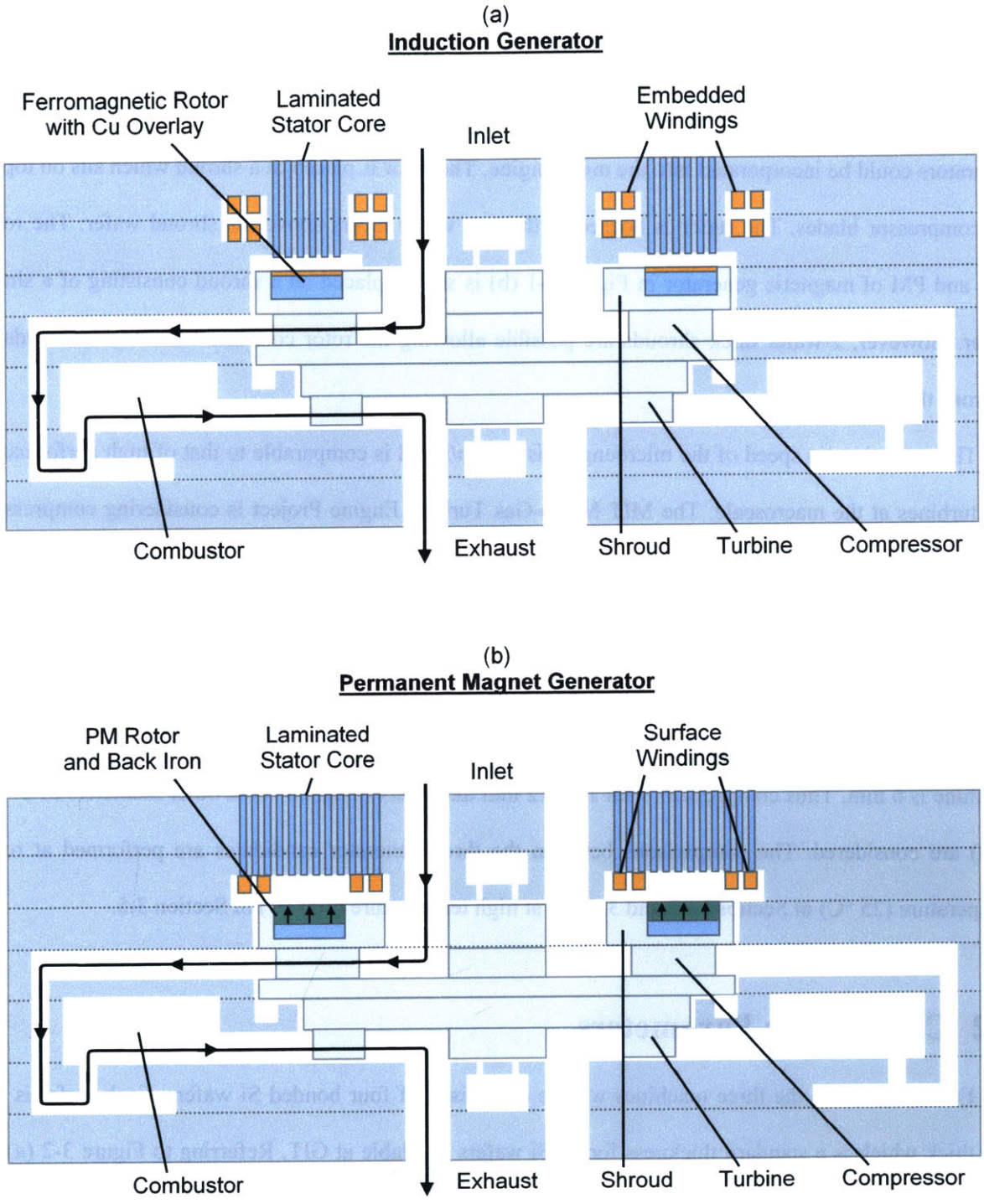

Figure 3-1: Conceptual drawing of (a) induction and (b) permanent-magnet generators integrated into a multi-wafer Si microengine (Courtesy of David Arnold, GIT [49]).

3.1 Microengine Constraints

The microengine consists of a multi-wafer Si stack with the thicknesses of the wafers varying between 500 μm (4" wafer) and 650 μm (6" wafer). Figure 3-1 depicts how both induction and PM generators could be incorporated into the microengine. The rotor is placed in a shroud which sits on top of the compressor blades. The stator is housed in the two wafer layers above the shroud wafer. The rotor core and PM of magnetic generator in Figure 3-1 (b) is shown placed on a shroud consisting of a single wafer. However, 2-wafer thick shrouds are possible allowing the rotor core and PM to be hundreds of microns thick.

The operating tip speed of the microengine is 500 m/s and is comparable to that of high performance gas turbines at the macroscale. The MIT Micro-Gas Turbine Engine Project is considering compressors with diameters of 8, 10 and 12 mm. For a 12 mm rotor, the rotational velocity at a 500 m/s tip speed is 800,000 rpm. The shroud includes a retaining ring to prevent the magnetic core of the rotor from breaking apart at high speeds. The thickness of this retaining ring is 1 mm. The outer diameter of the air inlet hole is 4 mm. The inner end turns are given 1 mm of radial space so that the inner diameter of the machine is 6 mm. Thus compressors with 10 – 12 mm diameters (magnetic core outer diameters of 8 – 10 mm) are considered. The comparisons between the three generator candidates are performed at room temperature (25 °C) in Sections 3.3 and 3.4 and at high temperature (300 °C) in Section 3.5.

3.2 Comparison Parameters

For comparison, the three machines will be comprised of four bonded Si wafers. Each wafer is 550 μm thick which is a standard thickness for 4" Si wafers available at GIT. Referring to Figure 3-2 (a) for the slotted stator machines, the rotor consists of a single wafer where the sum of the active layer and rotor core thicknesses is no more than 500 μm. The air gap, hats, poles and part of the base make up two wafers. The fourth wafer is use to add extra thickness to the stator base to prevent it from saturating. This is important for a planar machine where the surface area of the machine is much wider than the stator

base thickness. To keep the overall machine thickness the same, the SWPM machine also uses four wafers. Referring to Figure 3-2 (b) the rotor comprises two wafers, allowing for both the rotor core and active layer (i.e. PM) to be hundreds of microns thick. However, the practical limitation to the thickness of either the rotor core or active layer is 500 μm. The outer end turns are 500 μm wide and width of the inner end turns is dictated by how much of the 1 mm radial space is taken up by the silicon sidewall, W_h, trench gap, g_{tr}, and coil spacing g_{cl}. Table 3-1 summarizes the constraints placed on the dimensions shown in Figure 3-2.

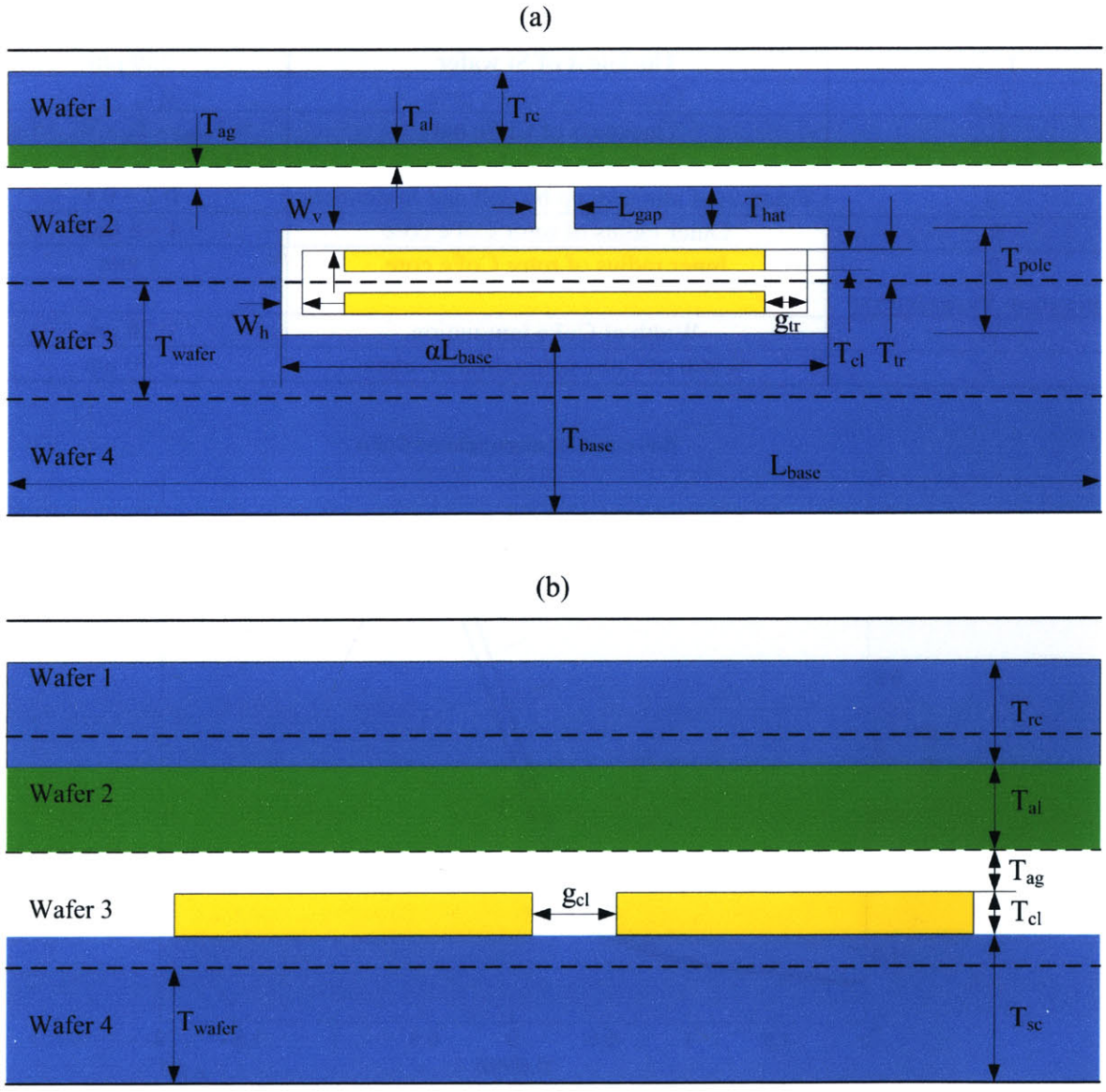

Figure 3-2: 4-wafer Si stack for (a) slotted stator and (b) surface wound stator.

Table 3-1: Surface wound and slotted stator dimension constraints.

Coil Parameters:	Description	Value
T_{tr}	Thickness of Si trench	≤ 150 μm
g_{tr}	Gap between trench sidewall and coil	$\geq (t_{trench} / 3)$
W_{cl}	Width of coils in a slot	$\geq t_{trench}$
T_{cl}	Thickness of coil in a slot	$\leq (t_{trench} - 25\ \mu m)$
g_{cl}	Gap between two adjacent coils	$\geq (t_{trench} / 5)$
W_{ci}	Width of inner end turn coil	$\frac{1}{2}$ (1 mm - $(W_h+2g_{tr}+g_{cl})$)
T_{ci}	Thickness of inner end turn coil	T_{cl}
W_{co}	Width of outer end turn coil	500 μm
T_{co}	Thickness of outer end turn coil	T_{cl}
Structural Parameters:		
W_h	Width of horizontal Si structural dividers	100 μm
W_v	Width of vertical Si structural dividers	100 μm
Core Parameters:		
T_{wafer}	Thickness of Si wafer	550 μm
T_{pole}	Thickness of CoFe pole	$= 2(T_{tr} + W_v)$
T_{hat}	Thickness of CoFe hat	$= T_{wafer} - T_{tr} - W_v - T_{ag}$
T_{base}	Thickness of CoFe base	$= 2T_{wafer} - T_{tr} - W_v$
α	Fraction of slot take up by coil and Si dividers	0.2 – 0.8
R_o	Outer radius of rotor CoFe core	4 – 5 mm
R_i	Inner radius of rotor CoFe core	3 mm
Lamination Parameters:		
W	Width of CoFe lamination	≥ 20 μm
S	Width of CoFe lamination dividers	≥ 20 μm

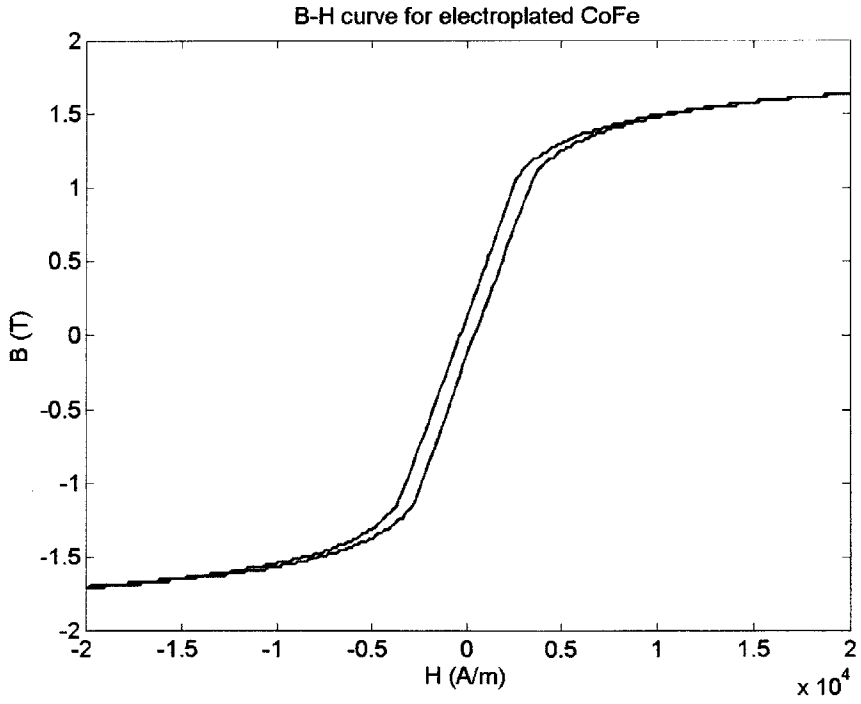

Figure 3-3: B-H curve for electroplated CoFe (Courtesy of GIT).

An annular rotor PM with an approximate square wave magnetization (c_m = 1 μm) and a remanence of 1 T (SmCo) is used for both the SLPM and SWPM. Electroplate CoFe, developed by GIT, is used for the rotor and stator core. It has a conductivity of 5×10^6 Siemens, saturation flux density, B_{sat}, of 1.72 T and a coercivity, H_c of 437.7 A/m. The B-H curve for CoFe is shown in Figure 3-3. Electroplated CoFe laminations, as thin as 20 μm, can be made with Si divider thicknesses of 20 μm [28]. Thicker laminations can be used for increased packing density and lower core loss but will lead to higher eddy current losses.

Figure 3-4 shows the power flow for all three generators. The converted power out, P_{elect}, is the electromechanical power converted across the air gap of the machine. In a PM machine it is equal to

$$P_{elect} = 1.5 V_{ocl} I_o . \tag{3-1}$$

The output power, P_{out}, from the machine is the converted power out minus the conduction loss, P_{cond},

$$P_{out} = P_{elect} - P_{cond} . \tag{3-2}$$

The hysteresis, $P_{hysteresis}$, and eddy current, P_{eddy}, losses in the stator and rotor core are upstream of the converted power. The proximity eddy current loss, P_{prox}, in the stator windings is only present in the surface wound machines. These losses do not affect output power but do decrease efficiency because mechanical torque must be provided by the microengine to overcome these losses. The efficiency is defined as

$$\text{Efficiency} = \frac{P_{out}}{P_{out} + P_{cond} + P_{eddy} + P_{hysteresis} + P_{prox}} . \tag{3-3}$$

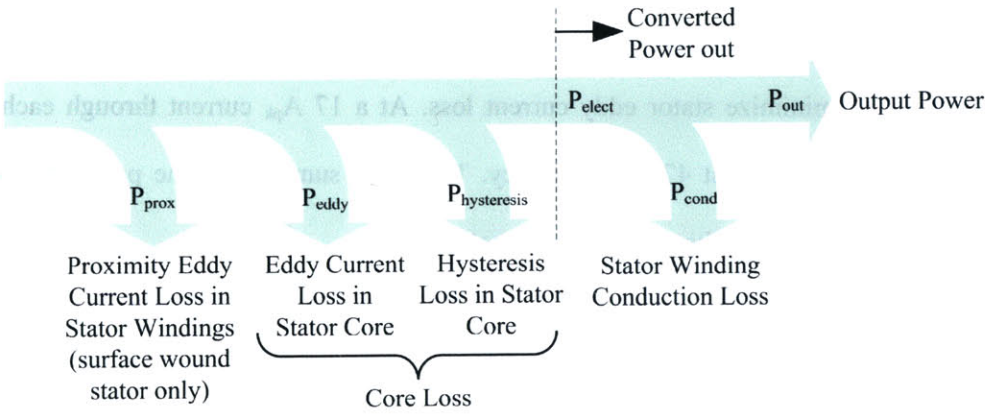

Figure 3-4: Power flow diagram for magnetic machine.

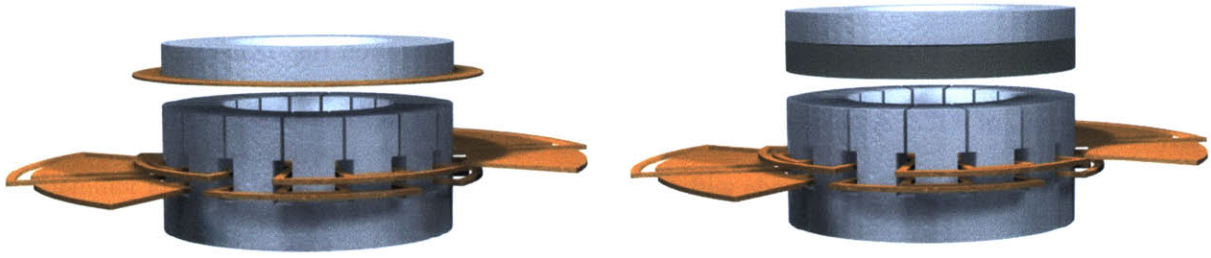

(a) (b)

Figure 3-5: Renderings of (a) induction and (b) permanent-magnet machines used for comparison. Note the axial direction has been elongated for clarity.

3.3 Induction Machines vs. PM machines

The layout for the SLIM and SLPM is shown in Figure 3-5. The induction machine is optimized over the stator dimensions, air gap, active layer and rotor core thicknesses, slip, number of poles and input current to determine the most efficient machine that can generate at least 10 W of power. The air gap is varied between 25 – 75 μm, which is the range used in [26], and the rotor active layer of the induction machine is swept between 10 – 100 μm, keeping $T_{al} + T_{rc} = 500$ μm. The slip was varied between 0 and -0.2, the number of poles between 4 – 16 and phase current, I_o, between 5 – 30A. The most efficient SLIM that delivers 10 W has 10 Poles, 20 μm active layer thickness and has a slip of -0.1. The fraction of the slot taken up by the coils and silicon sidewall, α, is 0.65 to widen the coils and the thickness of the trench is 150 μm to maximize the coil height and minimize resistance. The laminations are 30 μm wide and the dividers are 20 μm to minimize stator eddy current loss. At a 17 A_{pk} current through each phase, the machine can generate 10.26 W at 47.3% efficiency. Table 3-2 summarizes the parameters over which optimization was done as well as the optimum parameters.

Figures 3-6 and 3-7 show how output power and efficiency vary with slip and active layer thickness at 17 A_{pk} phase current. The output power and efficiency peak at T_{al} = 20 μm. As the active layer thickness increases distance between the rotor and stator cores increase, reducing the strength of the

magnetic fields in the air gap generated by the stator currents. The power and efficiency increase as slip increases, reaching a maximum around s = -0.1. They then decrease with increasing slip as the induced eddy currents in the active layer begin to prevent flux generated by the stator currents from linking the rotor.

Table 3-2: Induction machine optimization parameters.

Parameter	Range	Optimum Value
T_{tr}	50 – 150 μm	**150 μm**
T_{al}	10 – 100 μm	**20 μm**
T_{ag}	25 – 75 μm	**25 μm**
Slip	0 – -0.2	**-0.1**
Poles	4-16	**10**
I_o	5 – 30 A	**17 A**
α	0.2 – 0.8	**0.65**
W	20 – 50 μm	**30 μm**
R_o	4 – 5 mm	**5 mm**

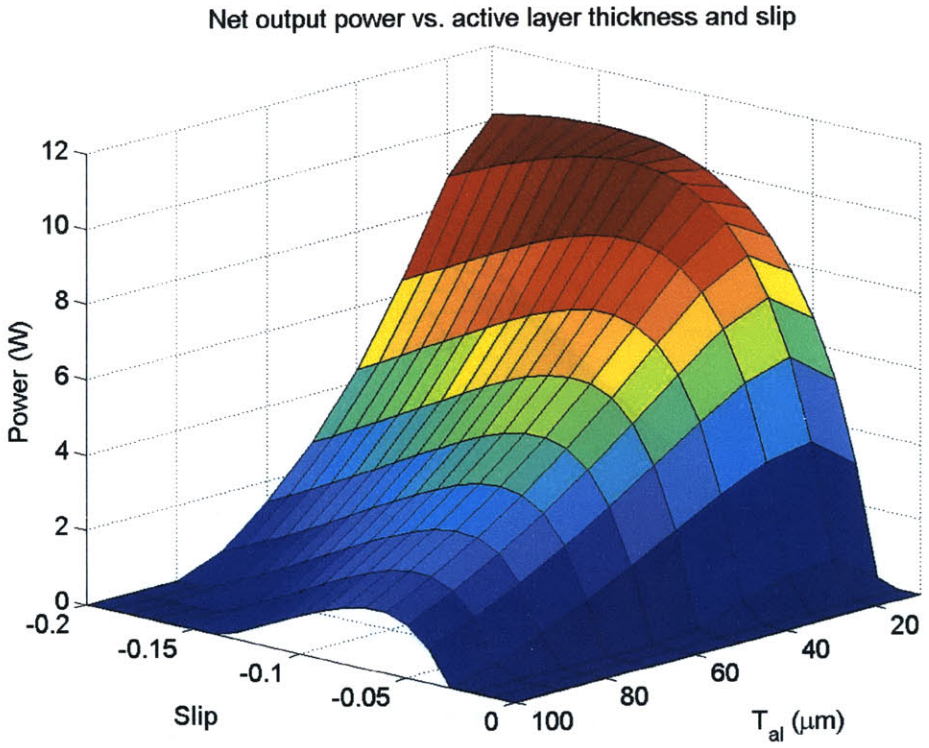

Figure 3-6: Output power vs. active layer thickness and slip for the induction machine at 17 A phase current.

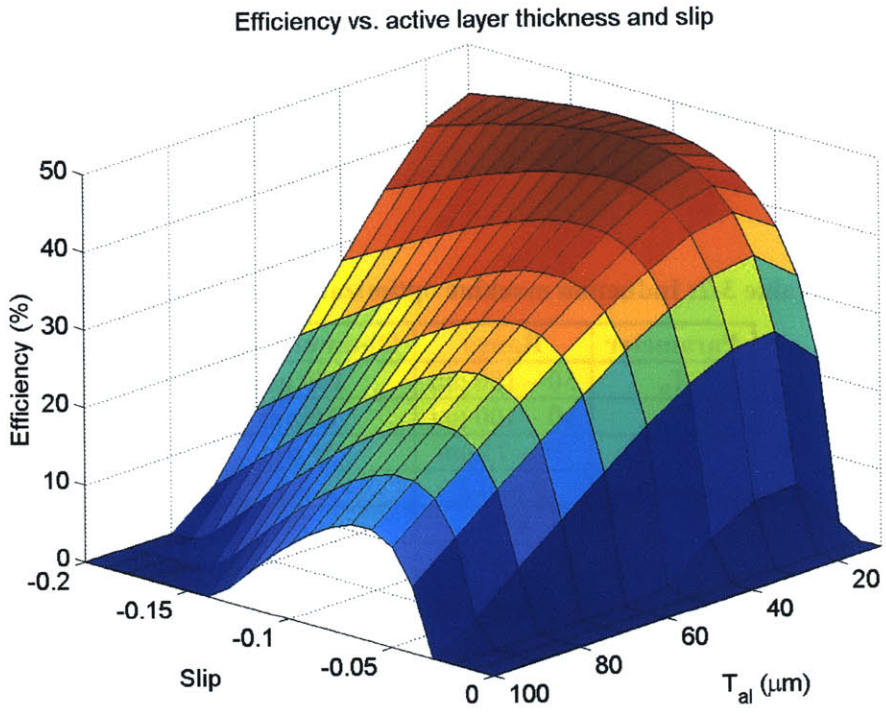

Figure 3-7: Efficiency vs. active layer thickness and slip for the induction machine at 17 A phase current.

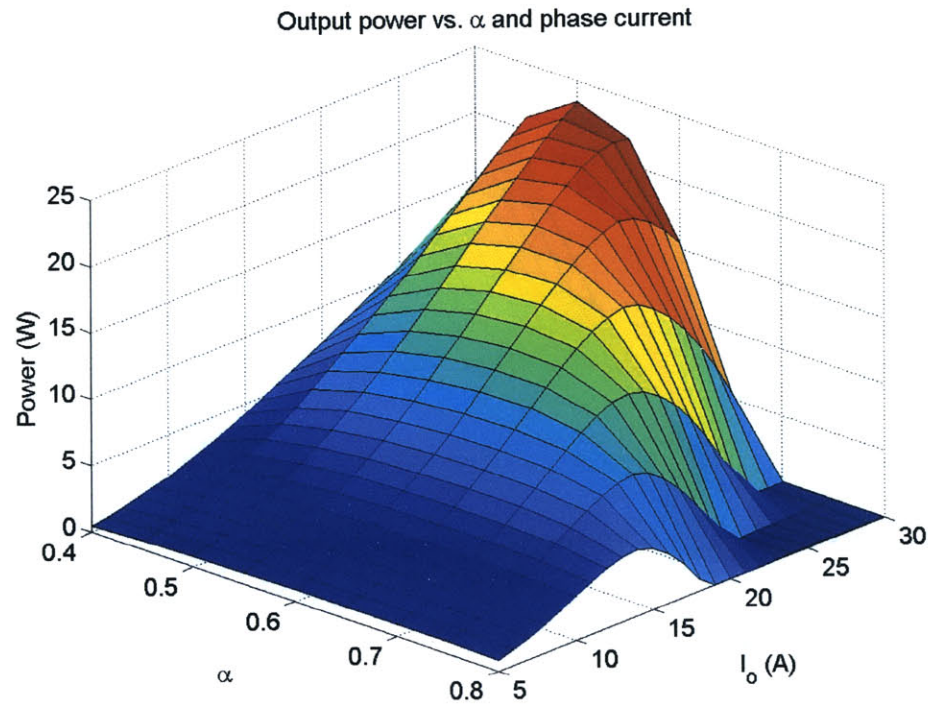

Figure 3-8: Output power vs. α and phase current for the induction machine at s = -0.1 and T_{al} = 20 μm.

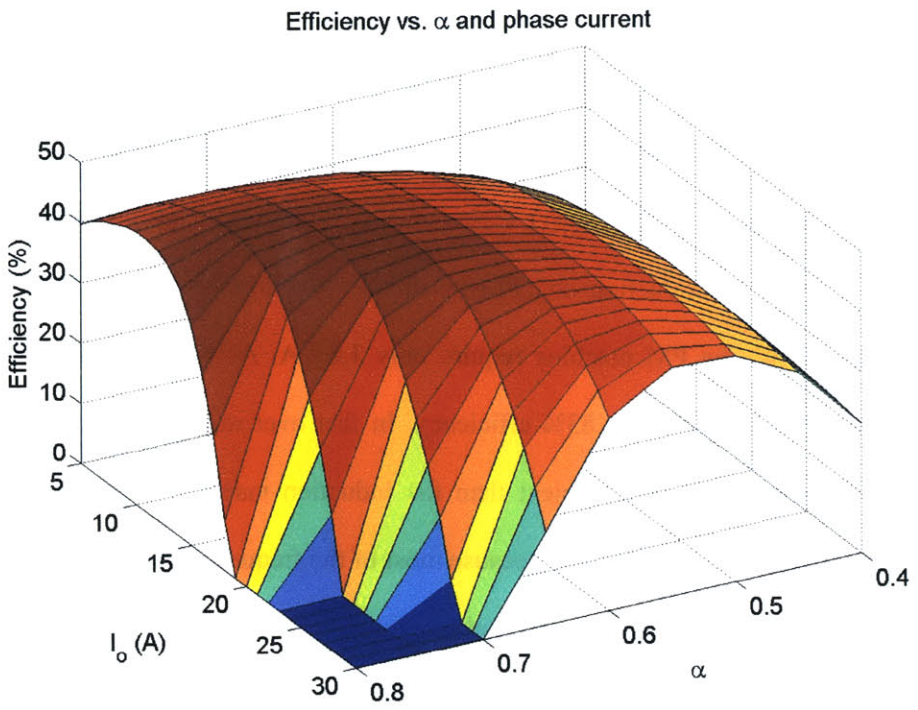

Figure 3-9: Efficiency vs. α and phase current for the induction machine at s = -0.1 and T_{al} = 20 μm.

Figures 3-8 and 3-9 show how output power and efficiency vary with phase current and α. Power increases as the square of the input current until the machine saturates. Once this occurs, torque increases linearly while conduction loss continues to grow as current squared. A further increase in current leads to a net decrease in the output power. Note that the current at which the output power begins to fall decreases with increasing α. For small α, the coils take up a small percentage of the slot. As the α increases, the coils become wider, making the stator poles narrow and saturate at lower phase currents.

For comparison, a 10-Pole, 2-turn/pole SLPM machine is used to keep the number of turns equal. The rotor has a 50 μm thick active layer and 50 μm thick air gap. Decreasing the air gap or increasing the active layer thickness would cause the stator base to saturate. The fraction of the slot taken up the coils and silicon dividers is 0.5 to keep the stator poles wide enough to prevent saturation yet still keep the resistance of the radial conductors to a minimum. The other stator dimensions are same as the induction machine.

Figure 3-10 compares the output power and efficiency of the two machines as a function of phase current. The torque in an induction machine goes as the current squared, so for a fixed speed, power varies quadratically with the current. The torque in the SLPM machine is proportional to the rotor PM flux times the current and therefore the power varies linearly with current for a fixed speed. Notice the huge discrepancy between the induction and PM machines. Whereas it takes 17 A for the induction machine to generate 10 W, the PM machine require only 1.85 A. At 17 A, the PM machine has the potential to generate 83 W of power at 83% efficiency. In fact over most of the current range the PM machine is approximately 35% more efficient than the induction machine. The efficiency of the PM machine increases with phase current. This is because most of the frequency dependent losses (Hysteresis, eddy current) are due to the spinning rotor PM and remain constant at a fixed speed. By increasing the phase current the output power increases while the frequency dependent losses remain the same, increasing efficiency. This is true until the conduction loss, which rises quadraticaly with current, begins to dominate and starts to decrease overall efficiency. This occurs around 18 A.

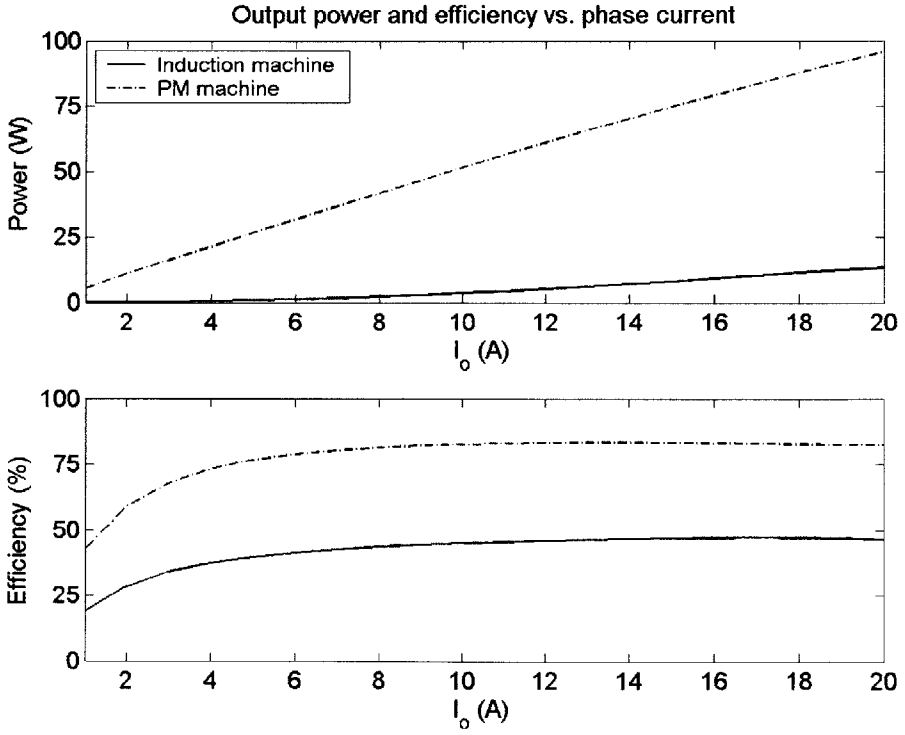

Figure 3-10: Output power and efficiency vs. phase current for the induction and PM machines.

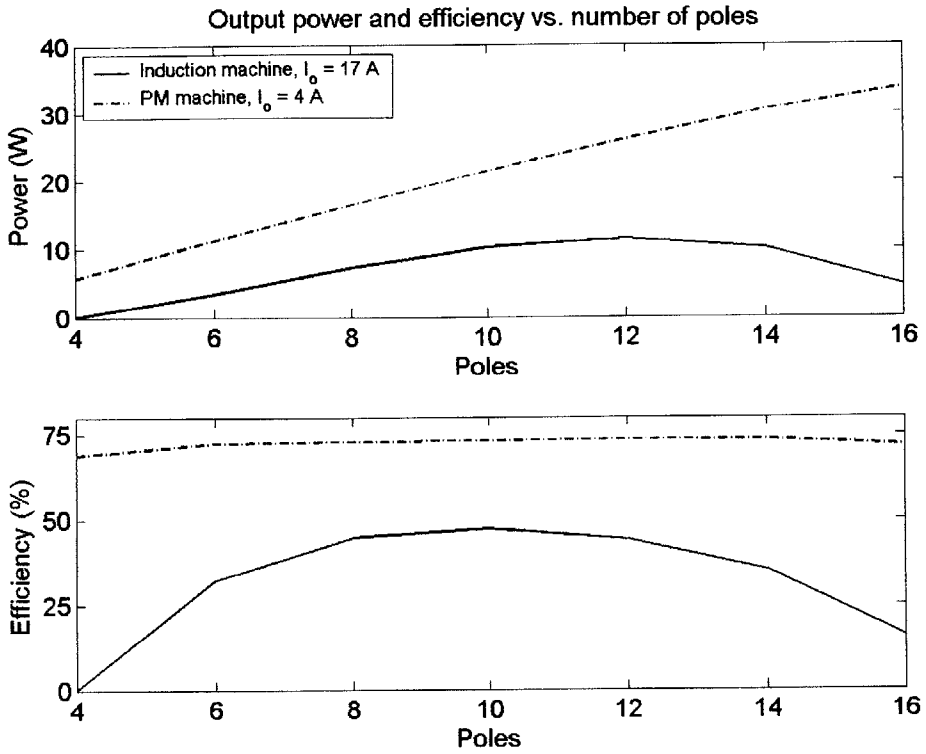

Figure 3-11: Output power and efficiency vs. number of poles for the induction and PM machines.

Figure 3-11 compares the induction and PM machines as function of pole count at a fixed input phase current. Again, the PM machine outperforms the induction machine by a considerable margin. Between 4 and 10 poles, the induction machine power and efficiency rise because the eddy currents induced in the rotor active layer increase with increasing slip frequency which is proportional to the number of poles. The conduction loss, which dominates, also increases as the increasing number of poles increases the resistance. The resistance of the radial conductors rises faster than P^2 because of the minimum values for W_h and g_{tr} which remain fixed. At 12 poles, the induced currents in the active layer begin to prevent flux from linking the rotor. The output power increases but not as fast as the conduction loss, so that efficiency begins to drop. At 14 poles, the width of the stator poles is so thin that they saturate, especially near the inner radius. This limits the output power further while the conduction loss continues to increase.

The increase in power of PM machine is approximately linear, because the voltage goes linearly with the number of poles. The hysteresis loss does not quite go linearly with the number of poles. At low pole

count the base is saturated and since it makes up the bulk of the slotted stator by volume, the core loss density within the machine is at its maximum. As the number of poles increases, the stator electrical frequency increases but the peak flux density in the stator base decreases so that the net increase is less than linear. At 4 poles, the core loss is 2 W, at 8 poles it is 3.42 W while at 12 poles it is only 4 W. The eddy current loss, on the other hand, grows slightly faster than the number of poles squared. The eddy current loss is only 0.33 W for a 4-pole machine because the base is saturated, which leads to a small effective permeability and a large skin depth. At 10 poles, the eddy current loss is 3.8 Watts since, not only has the frequency increased, but the stator base is no longer saturated. The conduction loss also rises rapidly but at 4 A, the loss is below a Watt until a 14 pole machine. The net result is that the efficiency stays more or less constant around 72% over the pole range with a minimum at 68% for a 4-pole machine and a maximum of 73% for a 12 pole machine.

The performance of the two machines is compared as function of rotor core outer radius in Figure 3-12 at a fixed phase current of 17 A for the induction machine and 4 a for the PM machine. The torque for both machines is proportional to the square of the area. However, as the radius decreases the angular velocity increase to keep the tip speed constant at 500 m/s. Therefore, output power for both machines increases linearly with the outer radius due to the fixed tip speed constraint. The efficiency drops in the induction machine because the resistance of the windings does not decrease as fast as the surface area. A 4 mm outer radius reduces the radial conductor length by 20% but decreases the active area of the machine by 56%. The conduction loss for a machine with a 5 mm outer radius is 7.7 W. A machine with an outer radius of 4 mm has 44% of the surface area but 77% of the conduction loss (5.9 W).

For the PM machine, the hysteresis loss is proportional to frequency and surface area (for a fixed stator thickness) just like the output power and thus should grow linearly with radius. However, as the outer radius increases, the width of the rotor PM pole increases while the thickness of the stator base remains the same. Consequently, the flux density in the stator base increases with radius and hysteresis loss grows slightly faster than the output power. The eddy current loss in the stator is also proportional to the surface area (for a fixed stator thickness) but goes as frequency squared. At an outer radius of 5 mm,

the eddy current loss and hysteresis loss are about 17% (3.8 W) of the output power (~22 W) while at a radius of 4 mm, the eddy current loss grows to 19.4% of output power while the hysteresis loss falls to 15.8%. The increase in eddy current loss more than offsets the decrease in hysteresis loss and the result is a decreasing efficiency with decreasing outer radius for a fixed tip speed. Note that even at less than ¼ the current, the PM machine can generate more power and at a higher efficiency than the induction machine over wide range of pole count and outer radii.

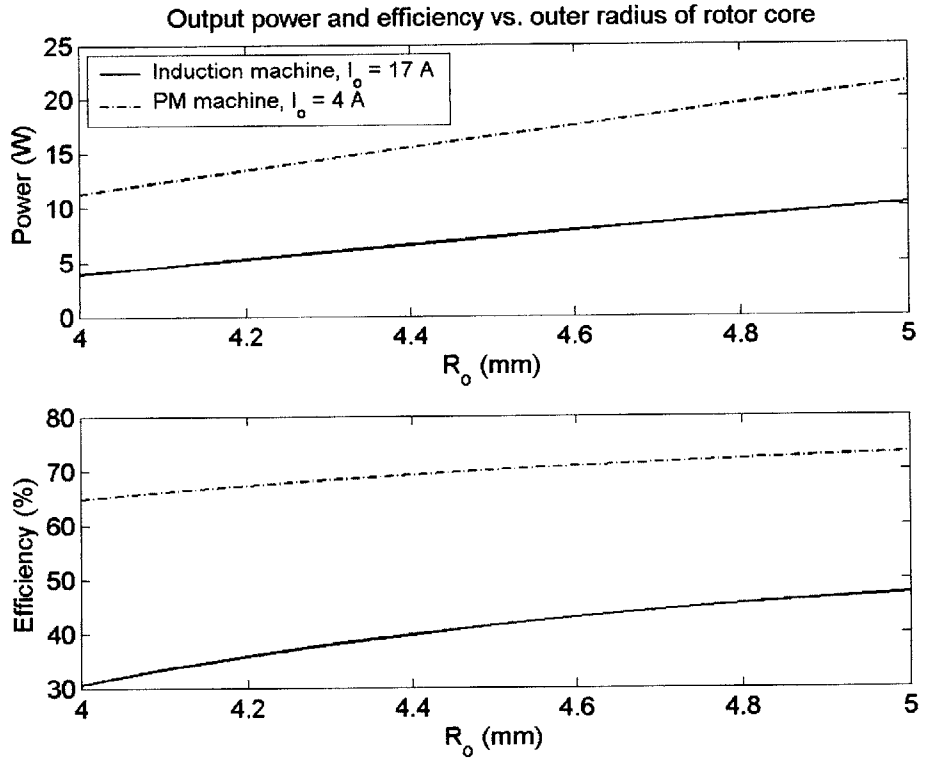

Figure 3-12: Output power and efficiency vs. outer radius of rotor core for the induction and PM machines.

To understand the difference in performance between the induction and PM machines, Table 3-3 lists the loss break down and operating parameters. Notice that the voltage, eddy current and core loss are all much larger in the PM machine. This is because the PM produces a rotor flux that is much larger than what can be produced by stator currents through the mutual inductance in the induction machine. The total flux linked by a phase in the PM machine is 13.2 μWb where as the flux linked by a phase in the

induction machine is 5 μWb at a stator current of 17 A and at half the air gap. The efficiency of the induction machine is greatly reduced by the large conduction loss which is an order of magnitude larger than PM machine considered here.

The flux linked by a phase in the PM machine is proportional to the turns/pole, N, but in an induction machine it is proportional to N^2. In a macroscale machine, N may be as large as 20 but in a microscale machine N is limited to 2 – 4 due to fabrication constraints as be will discussed in Chapter 4. If the microscale slotted stator had 20-turns/pole, the flux linked in the PM machine would increase to 132 μWb but would increase to 500 μWb in the induction machine. It would take only 4.5 A to produce 132 μWb with such a stator at a 25 μm air gap. This would reduce the conduction loss to about 1/16 its current value. It is primarily the limitation in the number of turns in a phase winding that limits the performance of the induction machine as the scale is reduced. The conclusion is that for high power and high efficiency operation PM machines are a much better choice than induction machines at the microscale given current and likely future fabrication limitations.

Table 3-3: Power Breakdown and operating parameters for the induction and PM machines.

Parameter	Induction Machine	PM Machine
P	5	5
I_o	17 A	4 A
Efficiency	47.3%	72.6%
P_{out}	10.26 W	21.43 W
P_{cond}	7.69 W	0.54 W
$P_{hysteresis}$	1.72 W	3.76 W
P_{eddy}	0.23 W	3.8 W
V_{oc1}	1.9 V	5.49 V
f_e	60 kHz	66.3 kHz
Flux linkage	5 μWb	13.2 μWb

3.4 Surface Wound vs. Slotted Stator PM Machines

Now that induction machines have been eliminated, the type of PM machine to build must be analyzed. Macroscale PM machines come in two different varieties of stator types, slotted stators and surface wound stators as shown in Figure 3-13. With a suitably thick magnet, the rotor–stator air gap can

be made large (250+ μm) to reduce windage loss while maintaining high magnetic flux in the air gap. Thus, the stator windings can be designed to occupy space in the air gap on the surface of the stator substrate rather than being embedded in slots and closed over with hats.

Surface wound stators offer several design advantages over slotted stators. First, fabrication of windings on the flat stator surface is much simpler. In fact, the absence of slots allows the fabrication of three-phase windings that produce significantly more output power than the two phase windings in the slotted stator. The slotted stator structure is formed by etching trenches into two silicon wafers. The coils are electroplated in these trenches and then the two wafers are fusion bonded [49]. Due to the difficulty of making a phase winding that partially resides on both wafers, an entire phase winding must occupy a single wafer. This limits the slotted stator to two phases with concentric windings. Since the surface wound stator has no slots, a three-phase winding can be constructed using two coil layers and cross over conductors on the outer end turns shown in Figure 3-13(b). Also, there is more surface area for the windings, which can reduce conduction loss. Furthermore, cogging, where the poles of the PM tend to align themselves with the gaps between the stator hats, producing torque pulsations and associated loss, is avoided. There are also no pole face eddy current losses in the surface wound stator either.

Finally, when the generator is connected to a load, its AC voltages will produce AC currents through the stator windings. The currents will produce their own magnetic fields (armature reaction) in the air gap. These magnetic fields will have higher order spatial harmonics that interact asynchronously with the rotor PM producing eddy currents. These rotor eddy currents reduce the overall efficiency, and in some cases, the heat produced can demagnetize the rotor PM [48]. Due to the large air gap in a surface wound stator, the magnetic fields produced by the stator currents are very weak, making the eddy current losses in the rotor PM negligible.

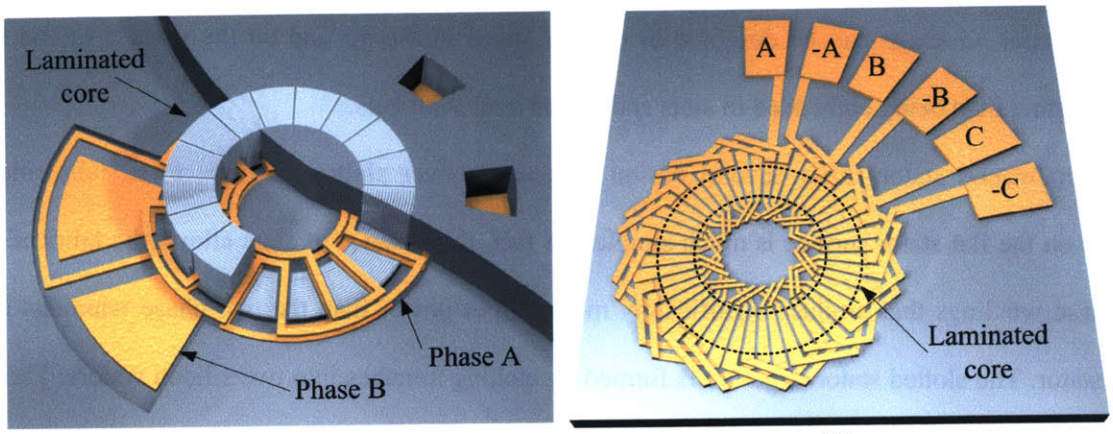

(a) (b)

Figure 3-13: Renderings of (a) slotted stator and (b) surface wound stator with 8-poles, 2-turns/pole.

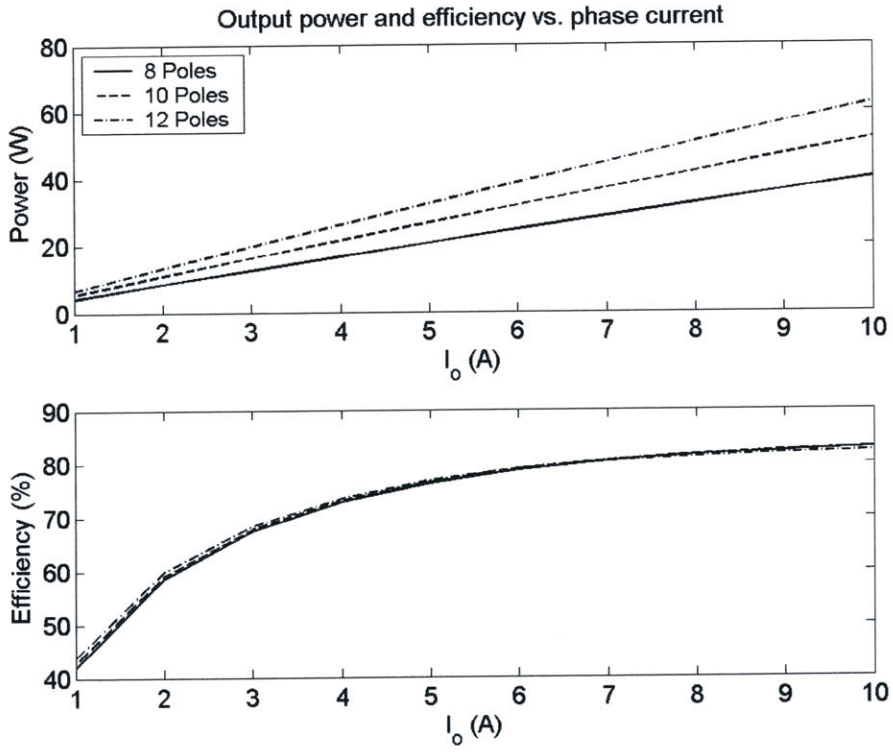

Figure 3-14: Output power and efficiency for the slotted stator PM machine vs. phase current for different number of poles.

For the comparison, a 12-Pole, 2-turn/pole slotted stator machine is used with the same rotor and stator dimensions used in the previous section. This machine produces higher output power than an 8- or 10-pole machine while achieving the same over efficiency over a 1 – 10 A current range as shown in Figure 3-14. The surface wound machine will be a three-phase 8-pole, 3-turn/pole machine with full pitched coils. This is done to keep the number of turns per phase constant between the machines.

An 8-pole, 3-turn/pole stator is chosen over a 12-pole, 2-turn/pole stator because the former has much lower frequency dependent losses and is more efficient. In addition, the radial conductors have two laminations each (C_{lam} = 2) and g_{cl} is set to 75 μm to minimize the sum of the conduction loss and proximity eddy current losses in the windings. The inner end turns are 200 μm thick and extend 1 mm inward (R_{il}) from the inner radius of the stator core while the outer end turns are 500 μm thick and extend 1.5 mm (R_{ol}) outward from the outer radius of the stator core. Since the trenches are no longer present, the surface wound coils can be made up to 200 μm thick. An air gap of 50 μm is used for both machines. To keep the rotor flux generated by the PM the same in both cases the active layer of the surface wound machine is 250 μm thick and is backed by a 500 μm thick rotor core. This also keeps the overall thicknesses of the SWPM and SLPM equal.

Figure 3-15 compares the surface wound and slotted stator PM machines as a function of phase current. The surface wound stator produces about twice as much power as the slotted stator machine with efficiencies varying from 60% at I_o = 1 A to 84% at I_o = 6 A with an efficiency of 83% at I_o = 10 A. The slotted stator achieves efficiencies of 44% at 1 A, and up to 82% at 10 A. Efficiency for a given output power is compared in Figure 3-16. The two machines have comparable efficiencies at the lower power levels but the surface wound machine becomes more efficient over an output power range of 40 – 100 W.

Comparison between the two stators as function of pole count, at 5 A input phase current, is shown in Figure 3-17. The output power of the surface wound machine is about double that of slotted stator machine. The peak efficiency for the surface wound machine is at 8 poles while the peak efficiency for the slotted stator machine is at 12 poles.

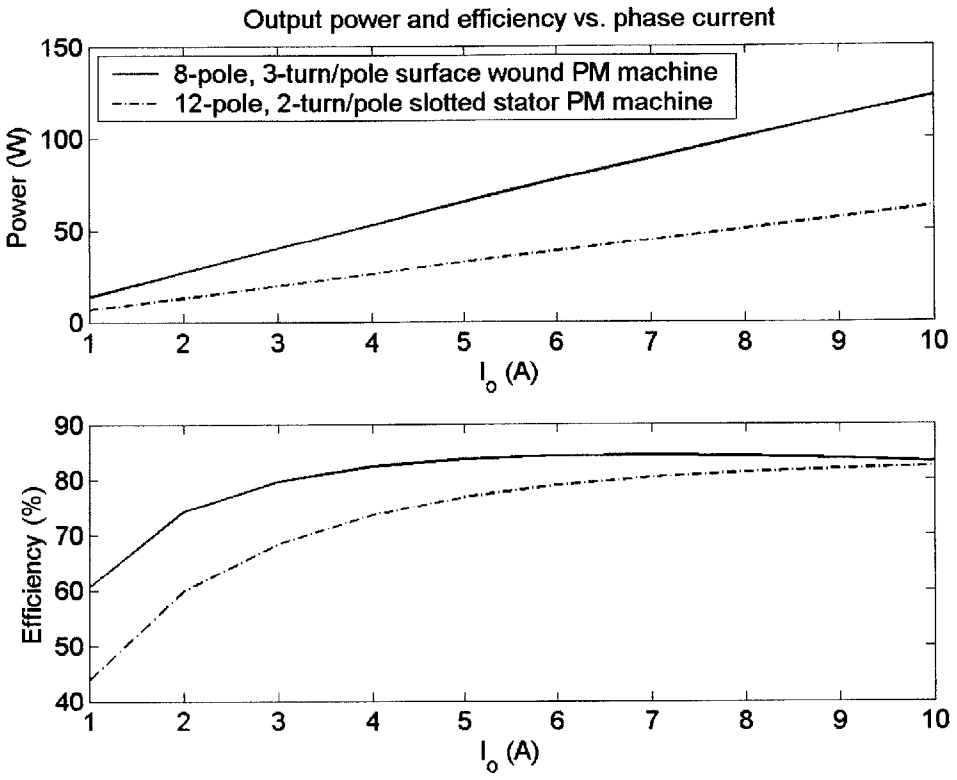

Figure 3-15: Output power and efficiency vs. phase current for the surface wound and slotted stator PM machines.

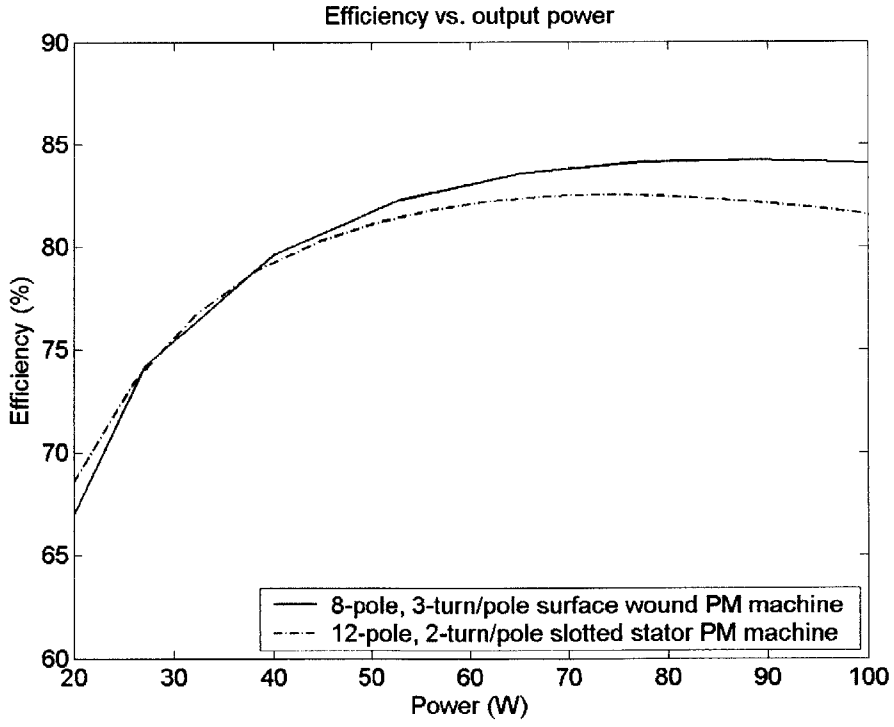

Figure 3-16: Efficiency vs. output power for the surface wound and slotted stator PM machines.

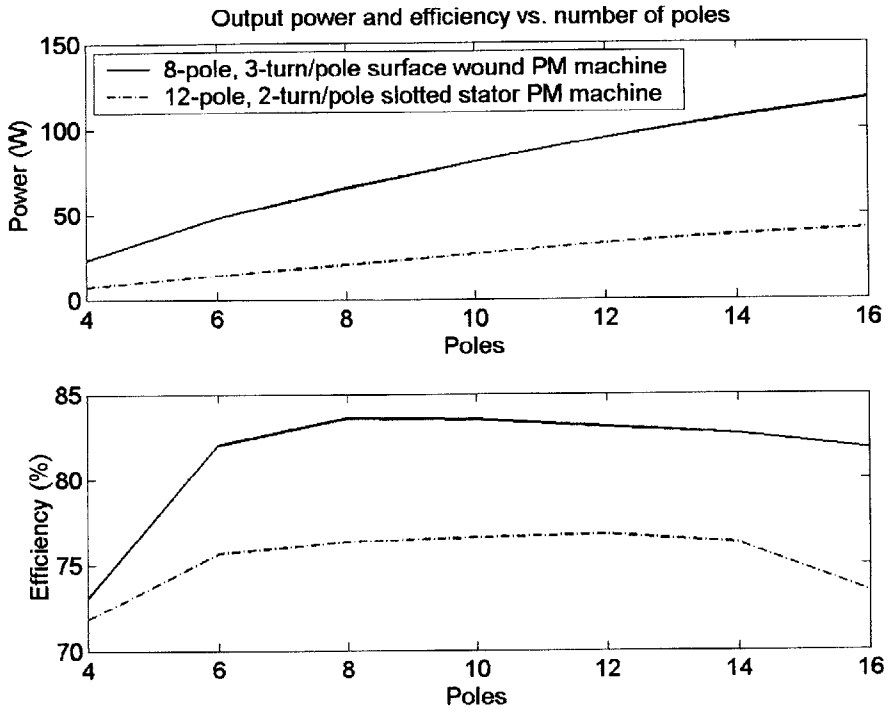

Figure 3-17: Output power and efficiency vs. pole count for the surface wound and slotted stator PM machines at 5 A phase current.

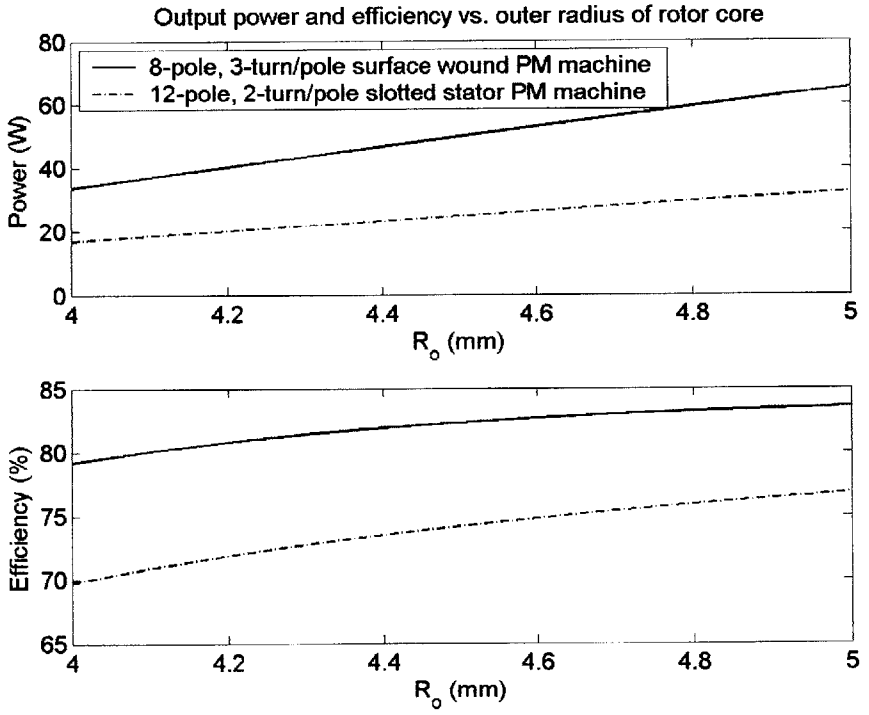

Figure 3-18: Output power and efficiency vs. outer radius of the rotor core for the surface wound and slotted stator PM machines at 5 A phase current.

Comparison between the two PM machines as a function of the outer radius of the rotor core is shown in Figure 3-18. The decrease in output power is linear with radius for fixed tip speed as explained in Section 3-2. The output power for a surface wound machine with an outer radius of 4 mm has about half the output power (34 W) of a machine with an outer radius of 5 mm (65 W) while the efficiency is only 4.4% lower (79.2% vs. 83.6%). This is because the proximity eddy current losses in the surface windings have decreased from 3.91 W at R_o = 5 mm to 1 W at R_o = 4 mm. This drastic reduction is due to the fact that the width of the radial conductors increases with radius and the proximity eddy current losses go as width cubed. The reduction in core loss and conduction loss by 46% and 33%, respectively, at R_o = 4 mm also keeps the efficiency high. The surface wound stator is 9.4% more efficient than the slotted stator at R_o = 4 mm, and is 6.8% more efficient at R_o = 5 mm.

To get a better understanding of the performance differences between slotted and surface wound stators Table 3-5 lists the power breakdown and relevant machine parameters for the two machines at a phase current of 5 A. Notice that for the same PM flux, the surface wound machine has only 20% of the eddy current loss of the slotted stator machine. This is due to both the increased volume of the slotted stator and the fact that the electrical frequency is much higher (80 kHz vs. 53 kHz). However, the reduced eddy current loss in the stator core of the surface wound machine is more than made up by the proximity eddy current loss in the stator windings so that the total loss in the stator due to eddy currents is about the same (4.91 W for the surface wound stator, 4.79 W for the slotted stator).

The dominant losses for the surface wound stator are conduction loss and proximity eddy current loss in the windings. In the surface wound stator, the radial conductors of all three phases occupy the same coil layer and the radial conductors have been laminated to reduce proximity eddy current losses. The resistance of each phase of the surface wound PM machine is 105.9 mΩ while the phase resistance for the slotted stator is only 49.3 mΩ. The slotted machine has less resistance not only because its radial conductors are unlaminated but each winding occupies its own layer. Even with the space taken up by the poles of the stator core and the silicon structural dividers, the overall phase resistance of the slotted stator is less.

Table 3-4: Power Breakdown and operating parameters for the surface wound and slotted stator PM machines.

Parameter	Surface Wound PM Machine	Slotted Stator PM Machine
P	4	6
N	3	2
I_o	5 A	5 A
Efficiency	83.6%	76.3%
P_{out}	65.2 W	32.4 W
P_{cond}	3.97 W	1.23 W
$P_{hysteresis}$	3.93 W	4.03 W
P_{eddy}	1 W	4.79 W
P_{prox}	3.91 W	–
V_{oc1}	9.22 V	6.72 V
f_e	53 kHz	80 kHz
Flux linkage	27.7 μWb	13.4 μWb

There is also a discrepancy between the voltages produced by the two machines. Both machines have 24 turns per phase. However, the slotted stator has a concentric winding that links the flux over a single pole twice. This essentially creates two short pitched windings that link flux over a quarter wavelength rather than over a half wavelength in the full pitched windings of the surface wound machine. The harmonic components of the open-circuit voltage for a quarter wavelength short pitched coil are $\sin(\pi/4) = 0.7071$ times that of a full pitched coil. This accounts for the smaller open-circuit voltage. The three-phase surface wound machine power is $1.5V_{oc1}I_o$ while the two-phase slotted stator power is $V_{oc1}I_o$. Since the open circuit voltage of the slotted stator is 0.7071 that of the surface wound machine, it produces $0.7071\times 2/3 \approx ½$ the power. As a result the surface wound machine can generate more power for given input phase current at a higher efficiency than the slotted stator machine.

The total loss in the two different types of stators is about the same (12.81 W in the surface wound stator and 10.05 w in the slotted stator). It is the ability to fabricate three-phase, full pitched windings that give the surface wound stator a higher output power and efficiency than a slotted stator for the same rotor PM flux. Thus the surface wound machines are the better candidate for electromechanical energy conversion within the microengine.

3.5 High Temperature Comparison

As the operating temperature increases two key factors in the performance of the machines must be taken into account. The first is the increasing resistance of the stator windings as well as the resistance of the rotor conductor in the induction machine. Figure 3-19 plots the stator resistance versus temperature normalized to the stator resistance at room temperature (25 °C) which was done by colleagues at GIT. A surface wound stator is heated up to 225 °C on a hotplate and the resistance is measured using a four-point probe measurement system. The theoretical plot corresponds to the following temperature dependence of copper,

$$R_s(T) = R_s(25^\circ C)[1 - 0.0039(T - 25)], \tag{3-4}$$

The experimental data is somewhat higher then the predicted resistance. Using a least-squares curve fit the extrapolated increase in temperature at 300 °C is 2.14 times its room temperature value while the theory predicts an increase by a factor of 2.07.

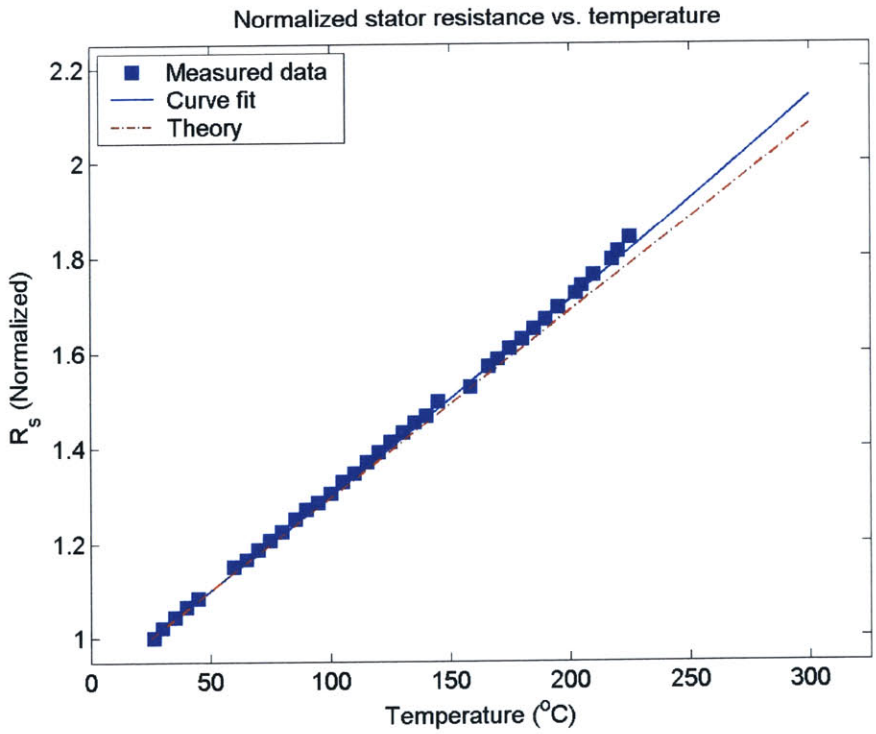

Figure 3-19: Temperature dependence of the resistance of a surface wound stator normalized to its value at room temperature. (Courtesy of Florian Herreault, GIT)

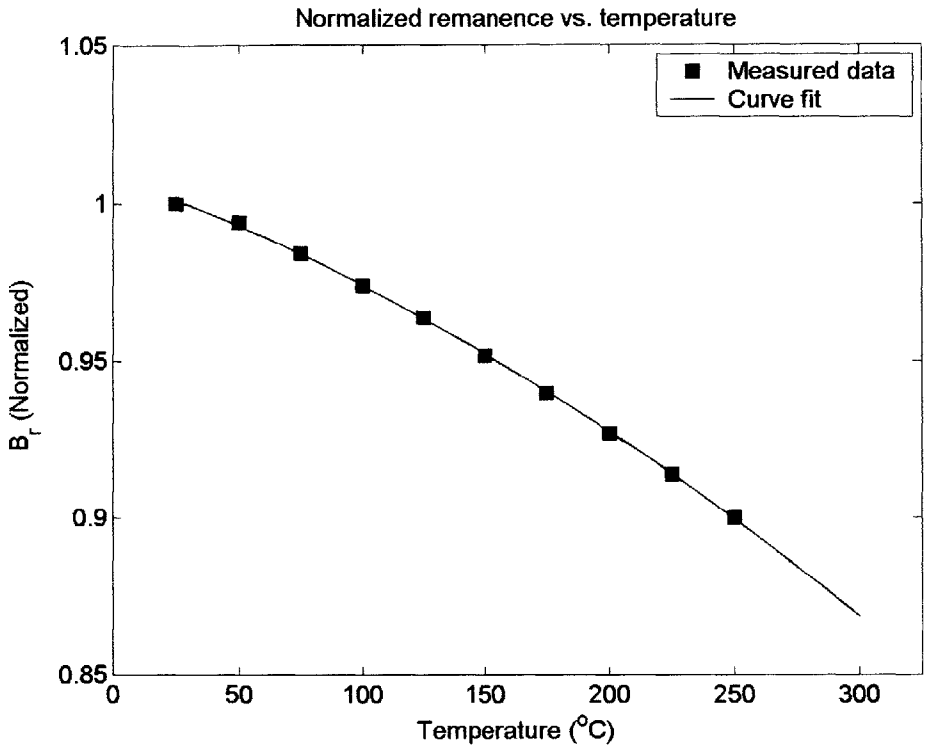

Figure 3-20: Temperature dependence of the remanence of a SmCo PM normalized to its value at room temperature. (Courtesy of Iulica Zana, GIT)

The second key factor is the reduction in the remanence of the rotor PM with temperature. The remanence versus temperature, normalized to room temperature, is shown in Figure 3-20 for the Sm_2Co_{17} PMs that are used in the PM machines. These experiments were conducted using a vibrating sample magnetometer up to a maximum temperature of 250 °C by colleagues at GIT. Using the curve fit the remanence of the SmCo PM at 300 °C is predicted to be 87% of its room temperature value.

The induction machine was simulated at 300 °C with the same parameter sweeps used in Section 3.3. It was found that the induction machine does not produce any net power over the range of the parameters considered. The increased resistance of the rotor conductor at high temperature reduces the amount of torque produced for a given stator current. In addition, the conduction loss at 300 °C is more than double its room temperature value for the same stator current. These two effects degrade the performance of the induction machine to the point that it can no longer produce any net power so that, not only do induction machines scale poorly as the size is reduced, they scale poorly as the operating temperature increases.

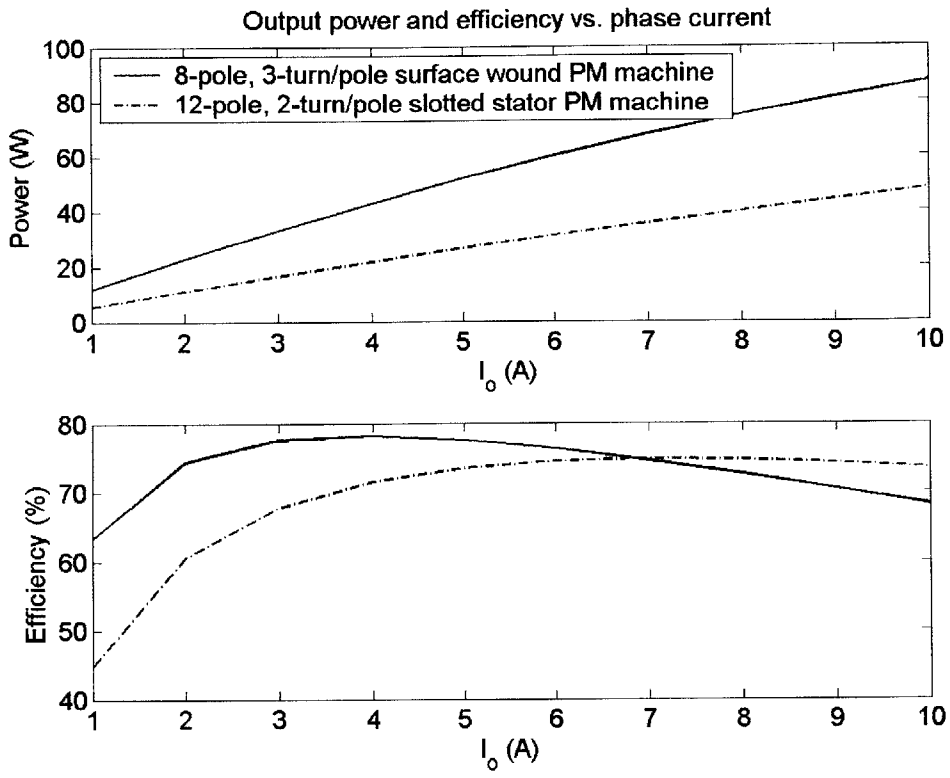

Figure 3-21: Output power and efficiency vs. phase current for the surface wound and slotted stator PM machines at 300 °C.

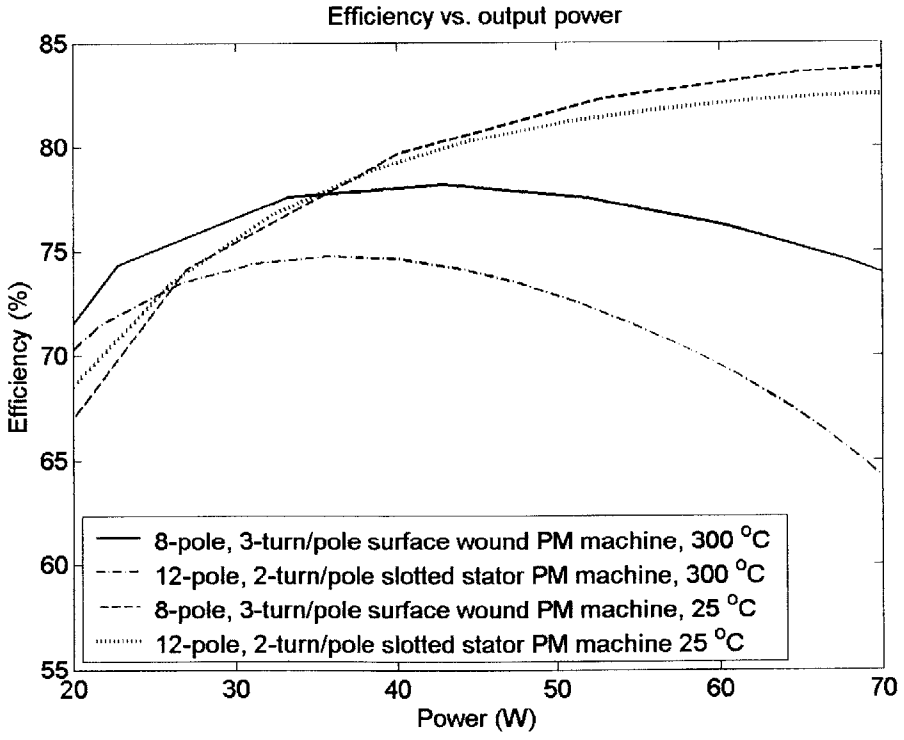

Figure 3-22: Efficiency vs. output power for the surface wound and slotted stator PM machines.

The slotted stator and surface wound PM machines were also simulated at 300 °C. Figure 3-21 plots the output power and efficiency as function of phase current. The surface wound PM machine still provides twice the output power of the slotted stator PM machine but becomes less efficient at phase currents above 7 A. However, from the standpoint of efficiency at a given output power, the surface wound stator still outperforms the slotted stator as shown in Figure 3-22. In fact, the difference in performance is larger at 300 °C than at room temperature.

The power breakdown and relevant machine parameters are listed in Table 3-5 for the surface wound and slotted stator PM machines with 5 A per phase at both high temperature and room temperature. The surface wound stator still delivers twice the output power of the slotted stator and at a higher efficiency. Note that while the conduction loss of both machines doubles, the proximity eddy current losses in the stator windings significantly decrease. This is due to both the reduced remanence of the rotor PM as well as the increased resistivity of the stator windings. In fact, it is the reduction in proximity eddy current losses at high temperature, which is mainly due to the increased stator resistance, that leads to a larger difference in the relative performance of the surface wound and slotted stators in Figure 3-22. Therefore, not only are surface wound stators better than slotted stators for low temperature generators, they are still the best choice for high temperature power generation within the microengine.

Table 3-5: Power Breakdown and operating parameters for the surface wound and slotted stator PM machines.

Parameter	Surface Wound PM Machine (25 °C | 300 °C)		Slotted Stator PM Machine (25 °C | 300 °C)	
P	4		6	
N	3		2	
I_o	5 A		5 A	
Efficiency	83.6%	77.5%	76.3%	73%
P_{out}	65.2 W	52 W	32.4 W	29.2 W
P_{cond}	3.97 W	8.49 W	1.23 W	2.63 W
$P_{hysteresis}$	3.93 W	3.87 W	4.03 W	3.47 W
P_{eddy}	1 W	1.31 W	4.79 W	3.69 W
P_{prox}	3.91 W	1.39 W	–	–
V_{ocl}	9.22 V	8.05 V	6.72 V	5.84 V
f_e	53 kHz	53 kHz	80 kHz	80 kHz
Flux linkage	27.7 μWb	24.2 μWb	13.4 μWb	11.6 μWb

3.6 Summary

This chapter provides a comparison of slotted stator induction, slotted stator PM and surface wound PM machines within the dimensional constraints and operating speed and temperature of the microengine. The induction and PM machines with slotted stators were compared first at room temperature. It was found that most efficient induction machine had a 10-pole, 2-turn/pole stator and could generate 10.26 W at 47.35% efficiency with 17 A through each phase. In contrast, the slotted stator PM machine could generate 21.43 W at 72.6% efficiency with only 4 A per phase. This is with a 50 μm thick active layer and 50 μm thick air gap. The PM machine generates more power at a higher efficiency than the induction machine for a given phase current, pole count and outer radius of the rotor core. The PM produces a rotor flux that is much larger than what can be produced by stator currents through the mutual inductance of an induction machine. This inductance is insufficient to match the flux from the PM machine because of the small number of turns/pole, N, used in the stator which is a fabrication limitation. Since the mutual inductance is proportional to N^2, the power capability of the induction machine decreases significantly at the microscale.

Given the superior performance of the PM machine over the induction machine, Section 3.4 compared PM machines with slotted and surface wound stators at room temperature. A 12-pole, 2-turn/pole slotted stator PM machine was compared to an 8-pole, 3-turn/pole surface wound machine. The surface wound stator had 200 μm thick coils, a 50 μm thick air gap and a 250 μm thick active layer (PM) to keep the flux density in the air gap the same as in the slotted stator machine.

The surface wound machine was found to be more efficient over a wide range of phase currents, pole counts and outer radii of the rotor core. For a given output power, the surface wound machine was found to be more efficient. With a phase current of 5 A, the surface wound machine can generate 65.2 W at 83.6% efficiency while the slotted stator machine could only generate 32.4 W at 76.3% efficiency. The difference in performance was because the surface wound machine consisted of three-phase, full pitched

windings that maximized flux linkage. The slotted stator, on the other hand, had only two phases that linked 50% of the maximum flux.

The slotted stator is limited to two phases due to its fabrication process. A single phase winding is electroplated inside the trenches of each of the two silicon wafers that are fusion bonded to create the slots for the slotted stator. The entire winding is forced to occupy a single wafer due to the difficulty of making a phase winding that partially resides on both wafers. Since no cross over conductors are allowed, the slotted stator must have concentric windings which do not link the maximum amount of flux. These fabrication limitations for the slotted stator are very challenging to overcome and therefore, it is unlikely that in the future a three-phase microscale slotted stator PM machine could be built using two silicon wafers.

Interestingly enough it was found that the phase resistance of the windings in the slotted stator was less than half of the surface wound stator. This is because the radial conductors of all three phases occupy the same coil layer in the surface wound stator and are laminated to reduce proximity eddy current loss. The windings in the slotted stator machine occupy their own coil layer which more than makes up for the reduced surface area due the stator core poles and silicon structural dividers.

The three machines were compared at 300 °C using recently available data on the temperature dependence of the stator windings and rotor PM remanence. At high temperature, it was found that the induction machine is unable to generate any output power due to the combination of increase stator resistance and reduced rotor conductivity. The surface wound PM machine still outperformed the slotted stator PM machine. With a phase current of 5 A, the surface wound machine can generate 52 W at 77.5% efficiency while the slotted stator machine can only generate 29.2 W at 73% efficiency. In terms of efficiency versus output power the surface wound stator had a higher relative performance than the slotted stator at high temperature than at low temperature. This is because, while the conduction loss of both stators increases with temperature, the proximity eddy current loss in the windings of the surface wound stator decreases due to the increased resistivity of the copper windings and the reduced remanence of the rotor PM.

The surface wound PM machine generates the most power and at the highest efficiency among the three types of magnetic machines considered here at both room temperature and high temperature. It is therefore the most suited for power generation within the microengine. The following chapters of this thesis will focus on the design, fabrication and testing of surface wound PM machines, and their associated power electronics, capable of generating and delivering multi-Watt DC power to a load.

4 First Generation Surface Wound PM Generators

Surface wound PM machines were chosen as the best candidate for efficient, high power generation in the microengine. This chapter focuses on the design of surface wound, microscale PM machines capable of generating and delivering Watt-level power at speeds of approximately 100,000 rpm. The emphasis will be on DC power generation via power electronics that rectify the AC voltages of the generators. Since integration issues are not dealt with at this stage, silicon wafers and electroplated core materials will not be used. Instead, a ferromagnetic wafer will be used as the stator core. Since this wafer will not be laminated, eddy current losses will degrade efficiency but will not affect output power provided that the turbine that spins the rotor provides sufficient mechanical power to overcome the added losses (which it does).

Section 4.1 will discuss important scaling laws used to optimize the dimensions of the PM machine. A simplified model of the PM machine, derived from the continuum model in Section 2.2 will be presented and used to derive the scaling laws. Section 4.2 presents the design of the first generation PM generators. Section 4.3 will discuss the fabrication of the PM machines with emphasis on the rotor magnetization process, rotor assembly and stator winding fabrication process. The spinning rotor test stand (SRTS) used to spin the rotors at high speeds (100,000+ rpm) is discussed in Section 4.4 while the design of the first generation power electronics for DC power generation is discussed in Section 4.5. This Chapter concludes with the test results of the first generation PM machines in Section 4.6. Electrical characterization of the machines in terms of its circuit parameters is presented first followed by power generation tests.

The PM machines described in this chapter were built and tested in collaboration with colleagues at GIT who were responsible for the rotor magnetization process, stator fabrication process and spinning rotor test stand assembly. For more information on these topics the reader is referred to [49]. The author of this thesis was responsible for the system level design of the PM machines, the design and actual

fabrication of the stator windings as well as the design and construction of the power electronics. Testing and characterization of the PM machines was a group effort.

4.1 Simplified model and scaling laws

The continuum model in Section 2.2 is very fast and accurate, but to derive some analytical insight into how various parameters affect the open-circuit voltage, the continuum model can be simplified. To do so, let the magnetization profile approache an ideal square wave ($c_m \rightarrow 0$). Also, assume that the rotor and stator cores and rotor active layer (PM) are ideal: μ_r and $\mu_s \rightarrow \infty$ and σ_r, σ_s, and $\sigma_a = 0$. In addition, assume that the wavelength is much larger than the thicknesses of the air gap, stator windings, rotor PM and rotor and stator cores: $\gamma_n T_i << 1$ (for i = sc, rc, al, cl, and ag). This last approximation means that the exponential decay of the fields in the machine can be ignored. In addition, the B and H fields are assumed to be independent of radius. The period of the rotor PM is also independent of the radius and the wave number, k, is evaluated at the mean radius

$$k = \frac{P}{R_m} = \frac{2P}{R_o + R_i}. \tag{4-1}$$

Given these approximations, the vector potential due to the rotor PM, using Equation (2-57), is

$$\hat{A}_{xn(m)} = \frac{4}{n\pi}\frac{B_r}{nk}\sin\left(\frac{n\pi}{2}\right) = \frac{2B_r}{n^2\pi}\frac{(R_o + R_i)}{P}\sin\left(\frac{n\pi}{2}\right). \tag{4-2}$$

$A^{(l)}_{xn(m)}$ simplifies to

$$\hat{A}^{(l)}_{xn(m)} = -j\frac{\gamma_{an}}{\mu_a}\left[\frac{\beta_{4n} - \beta_{2n}}{\alpha_{8n}\beta_{4n} - \alpha_{6n}\beta_{2n}}\right]\sinh(\gamma_{an}T_{al})\hat{A}_{xn(m)} = -j\left(\frac{T_{al}}{T_{al} + T_{cl} + T_{ag}}\right)\hat{A}_{xn(m)}. \tag{4-3}$$

The vector potential evaluated at half the thickness of the stator winding layer now becomes

$$\hat{A}_{xn,coil(m)} = \hat{A}^{(l)}_{xn(m)} = -j\frac{(R_o + R_i)}{P}\left(\frac{T_{al}}{T_{al} + T_{cl} + T_{ag}}B_r\right)\frac{2}{n^2\pi}\sin\left(\frac{n\pi}{2}\right). \tag{4-4}$$

To simplify things further, the spatial offset in the multiple turns of an N-turn/pole stator is ignored and so the incremental flux/phase reduces to

$$\hat{\Phi}_{zn,coil(m)} = 2PN\hat{A}_{xn,coil(m)}e^{j\frac{n\pi}{2}} = (R_o + R_i)\left(\frac{T_{al}}{T_{al}+T_{cl}+T_{ag}}B_r\right)N\frac{4}{n^2\pi}. \tag{4-5}$$

Since (4-5) is independent of the radius, the flux linked by a phase becomes

$$\hat{\lambda}_{n,coil(m)} = (R_o - R_i)\hat{\Phi}_{zn,coil(m)} = (R_o^2 - R_i^2)\left(\frac{T_{al}}{T_{al}+T_{cl}+T_{ag}}B_r\right)N\frac{4}{n^2\pi}, \tag{4-6}$$

while the harmonic amplitudes of the open-circuit voltage are

$$\hat{V}_{ocn} = jn\omega_m\hat{\lambda}_{n,coil(m)} = j(R_o^2 - R_i^2)\left(\frac{T_{al}}{T_{al}+T_{cl}+T_{ag}}B_r\right)NP\Omega_m\frac{4}{n\pi}. \tag{4-7}$$

The voltage harmonics can be added to generate the total open-circuit voltage

$$V_{oc}(t) = Re\left\{\sum_{n=1,odd}^{\infty}\hat{V}_{n,coil(m)}e^{jn\omega_m t}\right\} = V_o\sum_{n=1,odd}^{\infty}-\frac{4}{n\pi}\sin(\omega_m t), \tag{4-8}$$

where

$$V_o = (R_o^2 - R_i^2)\left(\frac{T_{al}}{T_{al}+T_{cl}+T_{ag}}B_r\right)NP\Omega_m. \tag{4-9}$$

The term inside the summation of (4-8) is the Fourier components of a square wave. Therefore the open-circuit voltage due to a square wave magnetization is also a square wave with magnitude V_o. The first term in parentheses in (4-9) shows how the open-circuit voltage scales with the active area of the machine. The second term in parentheses is the B field in the air gap and shows that the thickness of the rotor PM should be larger than the thickness of the coil layer and physical air gap combined in order to maximize the flux generated from the rotor PM. Lastly, the open-circuit voltage scales linearly with B_r, N, P and Ω_m.

From Section 2.2.9, the total resistance per phase is $R_{radial} + R_{inner} + R_{outer}$. Utilizing Equations (2-130), (2-132) and (2-134) for a full pitched winding, the total resistance per phase is equal to

$$R_s = \frac{6(PNC_{lam})^2}{\pi\sigma_c T_{cl}} \ln\left(\frac{W_{cl}(R_o)}{W_{cl}(R_i)}\right) + \frac{2NPL_{outer}}{\sigma_c T_{co} W_{co}} + \frac{2NPL_{inner}}{\sigma_c T_{ci} W_{ci}} \propto \frac{1}{T_{cl}}. \quad (4\text{-}10)$$

The resistance is inversely proportional to the thickness of the radial conductors that make up the coil layer. (4-10) assumes the thickness of the inner and outer end turns are some constant fraction of the coil layer. The output power capability of a PM generator is approximately proportional to

$$P_{out} \propto \frac{V_{oc}^2}{R_s} \propto \left(\frac{T_{al}}{T_{al} + T_{ag} + T_{cl}}\right)^2 T_{cl}. \quad (4\text{-}11)$$

Equation (4-11) contains important information about the relative thicknesses of the active layer, air gap and coil layer in order to maximize output power. First, the air gap should be made as small as possible. Second, for a given coil layer and air gap thickness, power is maximized as the term inside the parentheses goes to unity. Finally, taking the derivative of (4-11) with respect to T_{cl}, the maximum output power for a fixed air gap and active layer thickness is

$$T_{cl} = T_{al} + T_{ag}. \quad (4\text{-}12)$$

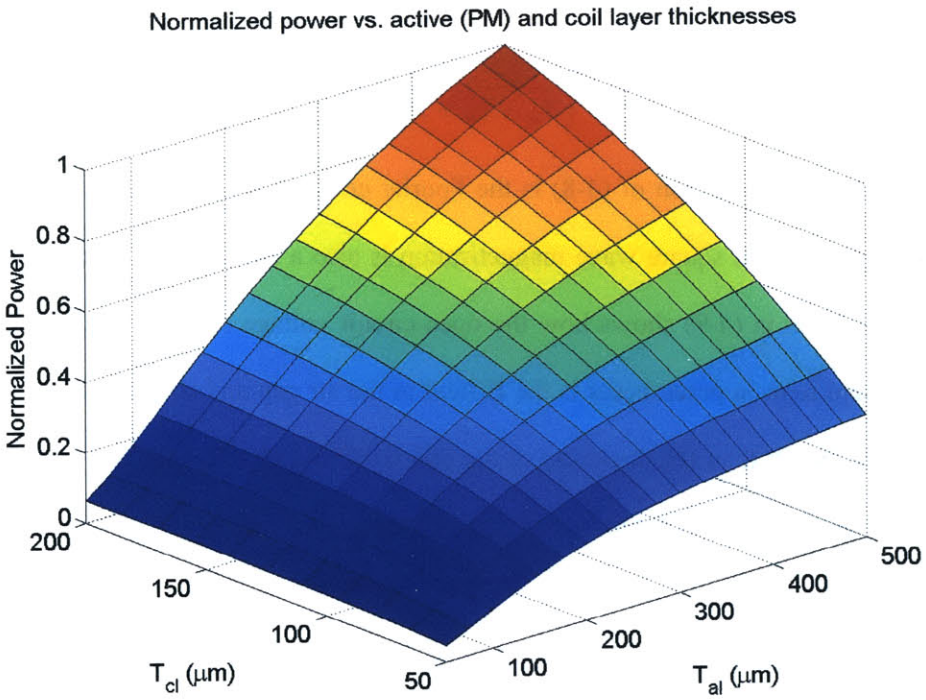

Figure 4-1: Normalized power vs. PM and coil layer thicknesses.

So for a fixed air gap and active layer thickness, the coil layer should equal the sum of the two. The maximum thickness for the rotor PM is 500 μm, set by the microengine constraint. The maximum height of the coil layer is 200 μm due to fabrication constraints. So for any given coil thickness the maximum power is achieved by setting T_{al} to its maximum value, while for a given rotor PM thickness, the maximum power is achieved by setting T_{cl} to it maximum. Thus, the maximum power is achieved when T_{al} is set to 500 μm and T_{cl} is set to 200 μm as illustrated in Figure 4-1.

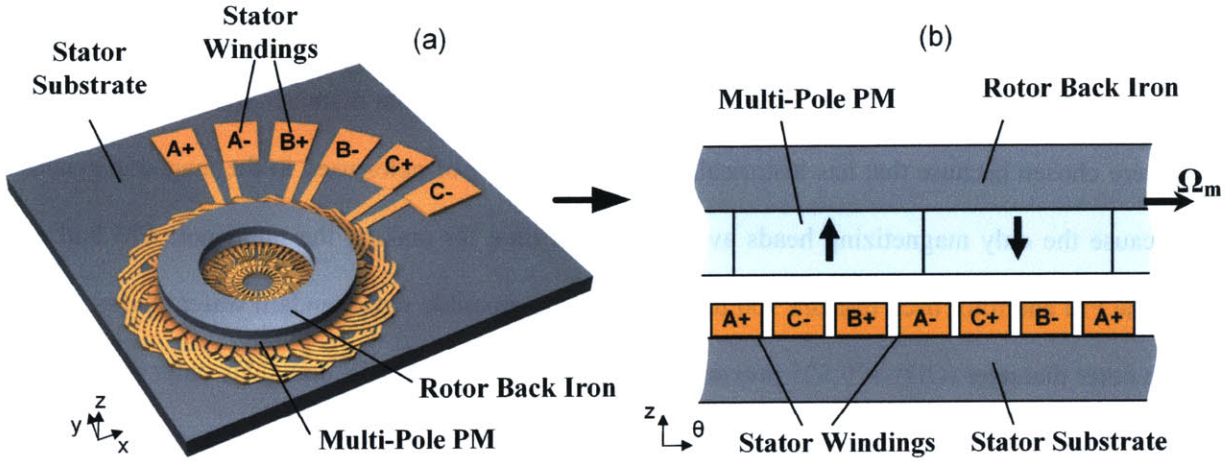

Figure 4-2: Conceptual drawing of the PM generator: (a) perspective view and (b) cross-section. (Courtesy of David Arnold, GIT [49])

4.2 PM Machine Design

The first generation generators are three-phase, 8-pole, axial-air-gap, synchronous machines [41]. Each machine consists of a rotor with an annular PM and ferromagnetic back iron and a stator with multi-turn windings on the surface of a ferromagnetic substrate, which serves as the stator back iron, as shown in Figure 4-2. During operation, the rotating multi-poled PM rotor creates a time-varying magnetic flux in the rotor-stator air gap, which induces AC voltages at the terminals of the stator windings. The magnetic flux generated by the PM can be concentrated in the rotor-stator air gap by using back irons with very large permeabilities. By using rare earth PMs, which have large remanences (~1 T), strong magnetic fluxes can be generated in the air gap. In fact, by using high-performance magnetic materials (PM, rotor

and stator back iron) and a suitably thick magnet (~500 μm), the actual rotor-stator air gap can be made relatively large (300–500 μm) to reduce windage loss while maintaining high magnetic flux in the air gap. Thus, the stator windings can be hundreds of microns thick and occupy space in the air gap on the surface of the stator substrate.

4.2.1 Rotor Design

The rotor contains an 8-pole, annular, pressure-formed (sintered) Sm_2Co_{17} PM and a ferromagnetic $Fe_{49}Co_{49}V_2$ (Hiperco 50) back iron, as shown in Figure 4-3. The rotor components are mounted in a poly(methyl methacrylate) (PMMA) adaptor for assembly onto a 1.6 mm diameter shaft for testing. Eight poles were chosen because that has historically been the number of poles used in the magnetic generator and because the only magnetizing heads available at the time for making the multi-pole PM had eight poles. The PM and rotor back iron are 500 μm thick to be compatible with standard wafer thicknesses and have an outer diameter (OD) of 9.525 mm and inner diameter (ID) of 3.175 mm. This outer diameter was chosen because it was the closest match to the 10 mm OD of the microengine generator. To keep the radial span the same as in the microengine generator an inner diameter of 5.525 mm was chosen. However, at the time the stators were fabricated, PMs with an ID of 3.175 mm were used because magnets of these dimensions were commercially available in small quantities, without the need for custom (and costly) manufacturing.

SmCo was selected for its combination of high energy product ($BH_{max} \sim 240$ kJ/m^3) for high energy conversion, and high operating temperatures ($T_{max} \sim 300$°C) [50]. Although NdFeB has a higher energy product ($BH_{max} \sim 400$ kJ/m^3), it does not provide the necessary operating temperatures ($T_{max} \sim 150$°C) for integration with the combustion-driven microengine [50]. However, it would be suitable for a low-temperature turbine generator. Hiperco 50 was selected for the rotor back iron for its combination of a reasonably high permeability ($\mu_r > 3000$), and for its high saturation flux density ($B_s \sim 2.4$ T) to minimize the thickness of the back irons while avoiding magnetic saturation [51]. Note the fields in the rotor back iron are nearly time-invariant, so the coercivity of the rotor back iron is not a major concern.

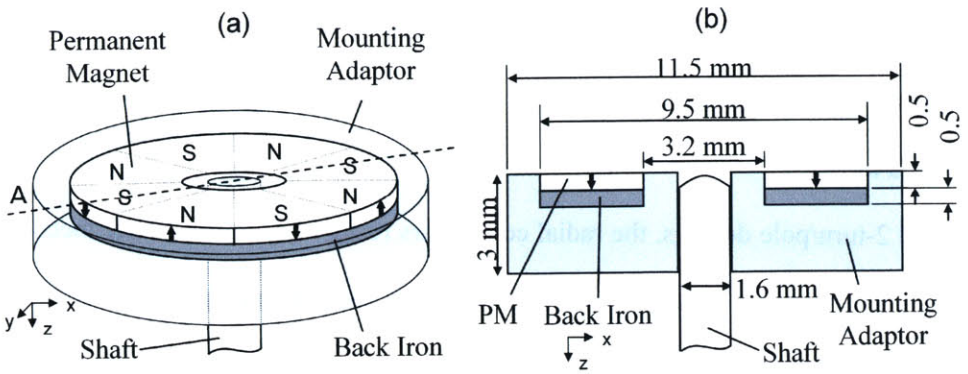

Figure 4-3: Schematic (a) perspective view and (b) cross-section of the PM machine rotors. Note that the rotor is shown upside down. (Courtesy of David Arnold, GIT [49])

4.2.2 Stator Design

The stator uses interleaved, three-phase, multi-turn, full pitched electroplated Cu windings that are dielectrically isolated from a 1-mm thick $Ni_{80}Fe_{15}Mo_5$ (Moly Permalloy) substrate by a 3 μm spin-on-glass layer and/or 5 μm polyimide layer. The active area of the stator has an OD of 9.525 mm and an ID of 5.525 mm. NiFeMo is selected as the stator back iron (substrate) material for its combination of high permeability ($\mu_r > 1x10^4$), low coercivity ($H_c \sim 0.16$ A/m) to minimize hysteresis losses, and commercial availability in sheets of suitable thickness [51].

The microfabricated coils, with small interconductor gaps, variable width geometries, and complex interleaved structures, are a key enabling technology for achieving high power density in miniaturized PM generators. The winding patterns are designed for minimal resistance to ensure optimal generator performance. Increasing the number of turns results in higher induced voltages for better compatibility with the associated power electronics. However, certain fabrication constraints (e.g. minimum feature size, highest aspect ratio, etc.) limit the geometry and overall fabrication precision. The radial conductors are unlaminated since the proximity eddy current loss in the windings at rotational speeds near 100,000 rpm is only 50 – 100 mW and is much smaller than the eddy current losses in the stator core.

To explore tradeoffs in output voltage and power versus fabrication complexity, three different winding patterns were developed (1-, 2- and 4-turn/pole), as shown in Figures 4-4 and 4-5. By

interleaving the coils, three distinct winding phases are possible using only two layers of metallization. The radial conductors (located directly beneath the PM rotor) are connected using appropriately arranged inner and outer end turns.

For the 1- and 2-turn/pole designs, the radial conductors reside only on the lower metallization layer, and a mesh of lower and upper level "crossovers" is used to form the end turns. In contrast, the radial conductors on the 4-turn/pole design occupy both the lower and upper metal layers and are connected by more complicated end turns. In the case of the 4-turn/pole design, the pattern is a complete double-layer winding, similar to what is used in macroscale machines [52].

For all three winding patterns, the radial conductors vary in width from 225 μm at the ID to 550 μm at the OD, with a 130 μm gap between adjacent radial conductors. The end turns of the 1-and 2-turn/pole machines have a minimum feature size of 100 μm and a minimum interconductor gap of 160 μm, while the end turns of the 4-turn/pole machine have a minimum feature size of 40 μm and a minimum interconductor gap of 40 μm. The number of vias is proportional to the number of turns, and the 1-, 2-, and 4-turn/pole designs use 16, 32, and 64 vias per phase, respectively.

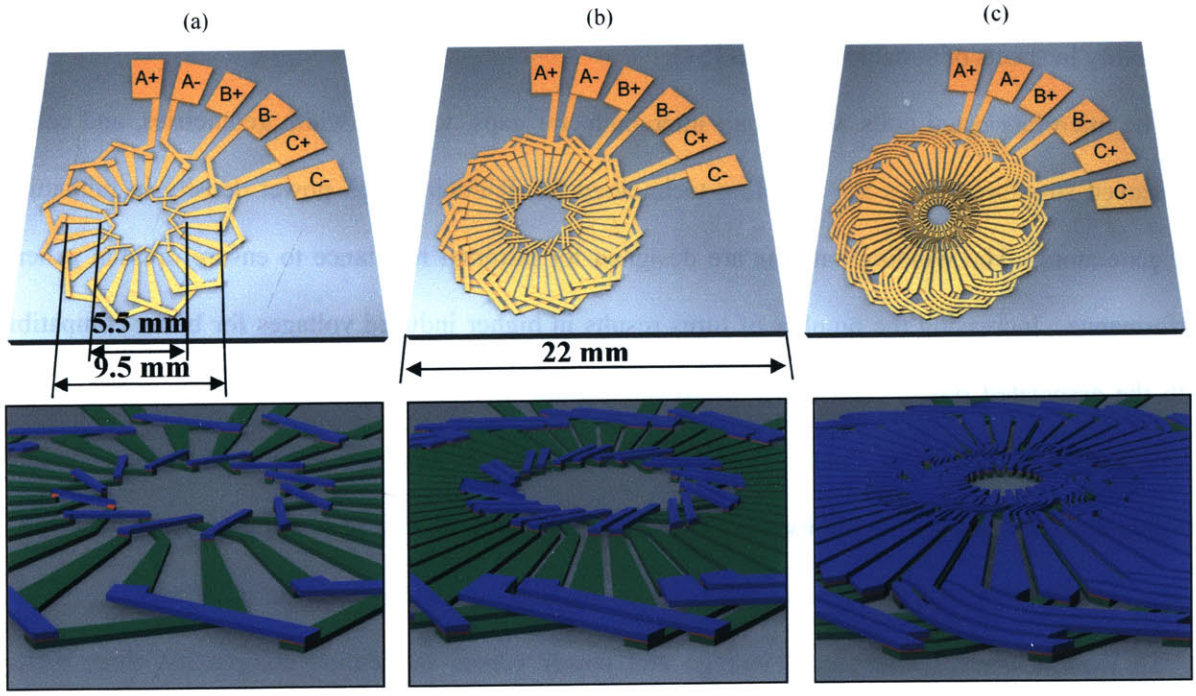

Figure 4-4: Renderings of the stator winding patterns for (a) 1-turn/pole, (b) 2-turn/pole, and (c) 4-turn/pole designs. (Courtesy of David Arnold, GIT [49])

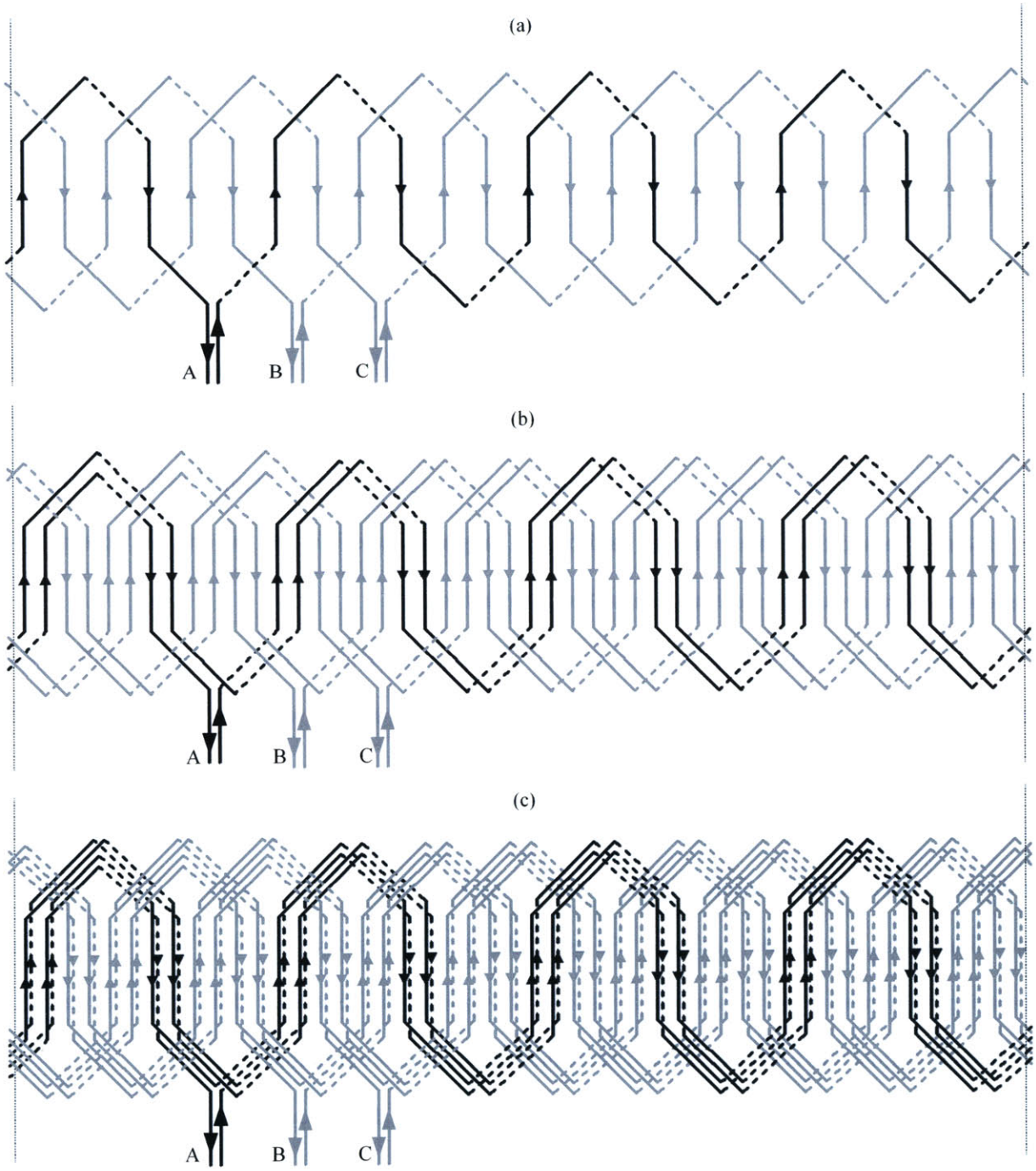

Figure 4-5: Schematic winding diagrams for the (a) 1-, (b) 2-, and (c) 4-turn/pole designs. Solid line represents layer 1 and dashed line, layer 2. Phase A is darkened for reference.

4.3 Device Fabrication

MEMS fabrication technologies impose several design constraints for microscale rotating magnetic machines not typically seen at the macroscale. The machines are typically limited to a planar geometry due the constraints of surface/bulk micromachining techniques, whereas their macroscale counterparts often employ a thee-dimensional cylindrical geometry. Macroscale permanent magnet (PM) machines use discrete permanent magnets while microscale machines, such as the ones presented here, use a multi-poled PM annulus. The annulus contains "transition regions" where the rotor magnetization smoothly transitions between north and south poles. The size of these "transition regions" can be on the order of a magnetic pole width, resulting in non-ideal magnetization patterns, and thus, reduced voltages induced in the windings. In addition, incorporating hard or soft magnetic materials into the process flow requires subsequent microfabrication steps to occur at low temperature.

The difficulty of using microfabrication to bury windings in slots and closing them over with hats, as is typical in the stators of macroscale magnetic machines, makes surface wound stators preferable at the microscale. PM machines with slotted stators and therefore small air gaps are also prone to demagnetizing the rotor PM, which is not an issue with surface wound stators due to their small armature reactance. Furthermore, macroscale machines typically have many turns/pole, (~ 20-turns/pole). However, due to space limitations, microscale machines will generally have only a few turns/pole (~ 2–4-turns/pole). Increasing the number of turns/pole would significantly increase the resistance of the stator windings due to minimum feature size constraints, and correspondingly reduce power output.

Microfabrication also limits the thickness of the windings due to constraints on the aspect ratio between winding width and thickness. Inner and outer end turns make up a small percentage of the overall size of macroscale machines. In microscale machines, these inner and outer end turns can take up considerable area and typically account for a large proportion of the overall winding resistance. The space required for the inner end turns of a planar machine limits the minimum radius of the active area, while the space required for the outer end turns can double the surface area of the stator.

In contrast to the associated design constraints, MEMS fabrication technologies can improve the performance of microscale magnetic machines. The stator windings can be photolithographically defined which permits optimized winding patterns with variable-width conductors. In addition, high-resolution features can help reduce certain losses; skin effects can be reduced by using windings with small cross-sections and eddy current losses in both the windings and magnetic core can be reduced by using laminations of micron scale thicknesses.

The ratio of surface area to volume decreases as the length scale is reduced. Heat conduction is proportional to surface area while heat production is proportional to volume. Microfabrication can be used to create flat conductors which have a larger surface area to volume ratio than round conductors. By placing these flat conductors in intimate contact to their substrate, cooling via thermal conduction greatly improves. This allows for much higher current densities in the windings than possible in macroscale machines. Current densities of up to 10^9 A/m^2 have been achieved in microscale magnetic machines while their macroscale counterparts are limited to 10^7 A/m^2 [23]. Microscale magnetic machines can also match the linear tip speeds of their macroscale counterparts by spinning much faster, near 100,000 – 1,000,000 rpm. This, combined with the higher current densities allowable in the windings, enables microscale machines with very high power densities.

4.3.1 Rotor Fabrication

The required eight-pole magnetization pattern for the SmCo is formed using a pulse magnetizer using a two-step process. First, the rotor is uniformly magnetized in the axial direction to saturation using a high intensity magnetic field pulse. Then, selected regions are magnetically reversed using a magnetizing head, machined out of $Fe_{49}Co_{49}V_2$ (Hiperco 50). As shown in Figure 4-6(a), the magnetizing head has four pole pieces, which during the reversal step act to concentrate the fields across certain regions while shielding other regions. The areas of the PM between the head pole pieces are thus reversed due to the high magnetic fields, while the other areas experience some leakage flux but do not reverse.

In practice, this method requires careful selection of the magnitude of the field reversal pulse. A very small pulse will not overcome the coercivity of the already magnetized structure, resulting in little or no reversal. Conversely, a very large pulse will reverse all areas of the magnet, presumably due to leakage flux and/or saturation of the magnetizing head. These effects were not fully explored, but instead, the magnetizing process was repeated until balanced north and south poles were achieved, as measured using a Hall-effect Gauss probe. The resulting 8-pole rotor magnet is shown in Figure 4-6(b) using magnetic viewing paper. The rotor back iron and mounting adaptor are conventionally milled from sheets of Hiperco 50 and PMMA, respectively. The PM and rotor back iron are then glued into the mounting adaptor, which is fit onto a 1.6 mm (1/16 in.) shaft for testing, as shown in Figure 4-6(c).

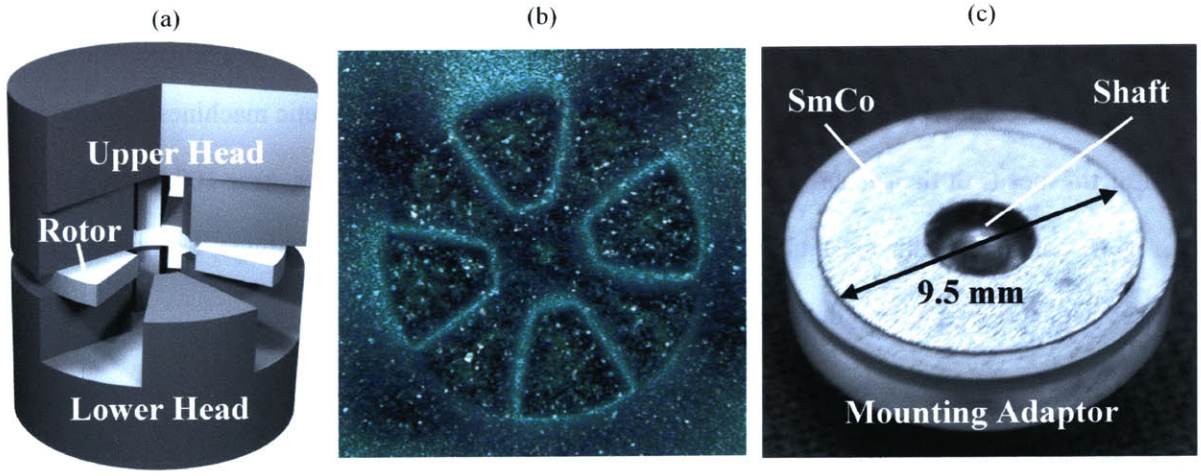

Figure 4-6: (a) Cutaway view of PM rotor in magnetizing head, (b) magnetic pole pattern using magnetic viewing paper, and (c) 500-μm thick PM rotor and back iron mounted onto shaft. (Courtesy of David Arnold, GIT [49])

4.3.2 Stator Fabrication

The stators are fabricated using electroplated windings on 100-mm and 75-mm diameter magnetic substrates cut from 1-mm thick sheets of $Ni_{80}Fe_{15}Mo_5$. The complete winding fabrication process flow is shown in Figure 4-7. First, to isolate the coils from the substrate, a dielectric layer is deposited (Figure 4-7a). Initially, a spin-on-glass (SOG) process was used, where a 1 μm PECVD SiO_2 adhesion layer was

deposited, followed by ~2 μm of Accuglass T-12 SOG, and finally, a 1 μm PECVD SiO_2 capping layer. It was later found that this layer sometimes suffered from cracking and/or pin-hole defects, resulting in shorts from the coils to the substrate, which reduced the yield. Therefore, this process is supplemented or replaced by the deposition of ~5 μm of PI-2611 polyimide.

The stator windings are constructed using a two-layer electroplating process [53,54], identical for the three different winding patterns. First, a Ti/Cu seed layer is sputter deposited, and Futurrex NR9-8000P negative photoresist is used to pattern a ~100-μm thick mold for layer 1 (Figure 4-7b). Cu is then electroplated up to the thickness of the mold (Figure 4-7c). Next, the resist is stripped using Futurrex RR4 resist remover, and the seed layers are removed by wet etching. The Cu etching uses "blue etch" (NH_4OH saturated with $CuSO_4$), and the Ti etching uses diluted HF acid (Figure 4-7d). Then, SU-8 2025 photosensitive epoxy is used to pattern the via layer, encapsulating layer 1 except for the via openings (Figure 4-7e). Then, a new Ti/Cu seed layer is sputter deposited, and layer 2 is patterned using NR9-8000P photoresist (Figure 4-7f). Cu is plated to form layer 2, with the vias connecting to layer 1 (Figure 4-7g). Finally, the Futurrex resist is stripped, and the seed layers are etched as before (Figure 4-7h). The remaining SU-8 provides additional mechanical support, but in the case of a high-temperature device for a microturbine, the SU-8 could be removed using oxygen rich reactive ion etching (RIE), provided an inorganic dielectric layer was used (e.g. SOG). For more details the reader is referred to [49].

Figure 4-8 shows examples of the three winding patterns after fabrication. Note that with an increasing number of turns, the patterns, particularly the inner end turns, become quite complex, and hence more difficult to fabricate. The thicknesses of the final windings were measured optically by ablating some of the SU8 using an excimer laser system. Only the thickness of layer 1, T_1, and the total thickness, T_{cl}, were measured, as shown in Figure 4-9.

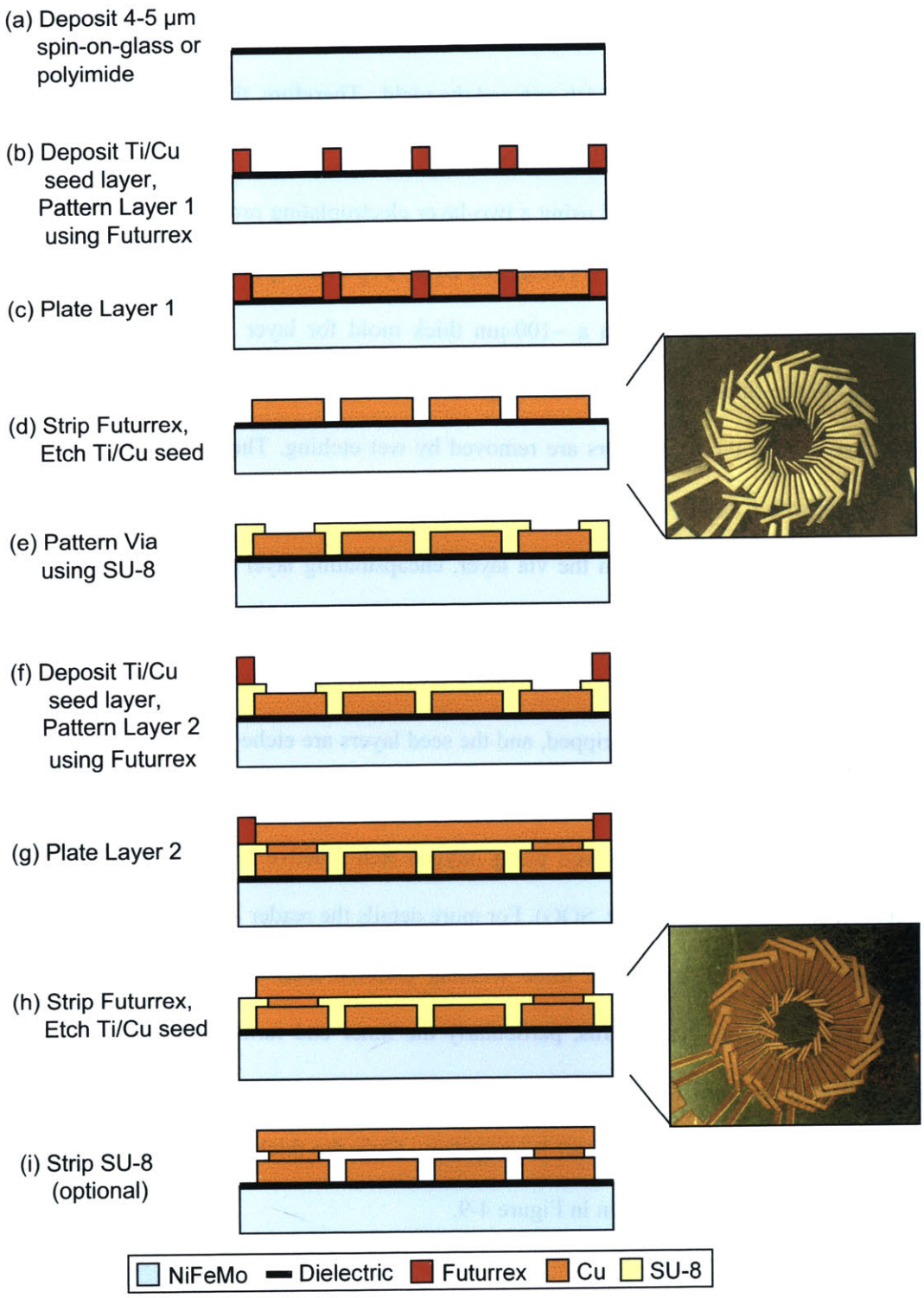

Figure 4-7: Stator winding fabrication process flow. (Courtesy of David Arnold, GIT [49])

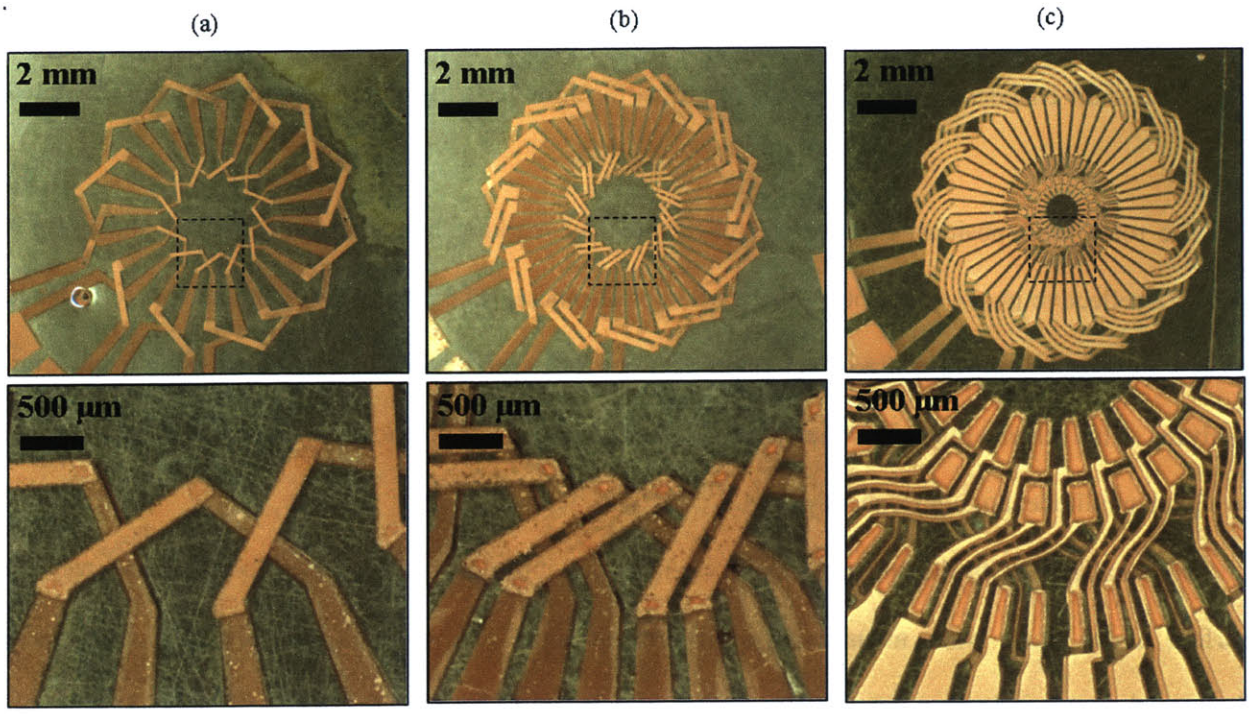

Figure 4-8: Fabricated stator windings: (a) 1-turn/pole, (b) 2-turn/pole and (c) 4-turn/pole machines.

Device	T_1	T_{cl}
1-turn/pole	~125 µm	~245 µm
2-turn/pole	~100 µm	~190 µm
2-turn/pole	~80 µm	~170 µm

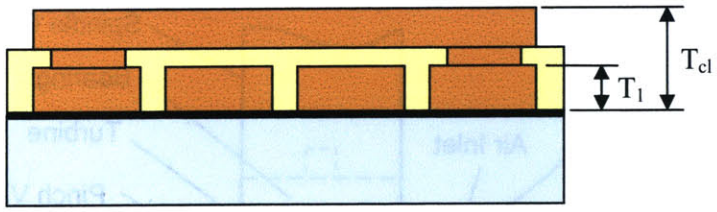

Figure 4-9: Measured winding thicknesses for various PM machines.

4.4 Spinning Rotor Test Stand

For characterization, a test stand was developed to support spinning rotors in order to demonstrate electrical power generation while avoiding the design and fabrication complexities of integrated high-speed bearings. The test stand comprises a high-speed, air-driven spindle (High Speed Carving and Engraving Products) to spin rotors with a controllable air gap over the surface of the stators, as depicted in Figure 4-10. Powered by compressed nitrogen, the spindle provides rotational speeds in excess of

350,000 rpm. The rotor/shaft assembly is mounted in the spindle, and the rotation speed is measured with an optical shaft encoder or, in the case of electrical machine tests, using the frequency of the generated output.

The rotor shaft position encoder is implemented by marking half of the shaft black and using a GP2L22 reflective photo-interrupter (Sharp Microelectronics). The alternating high and low reflectance creates an output signal with frequency dependent on shaft speed, which is monitored using a spectrum analyzer. This scheme minimizes the sensitivity to sensor range or position, which would cause a change in signal amplitude, but not frequency.

One challenge with the spinning rotor system is the ability to precisely position the rotor over the surface of the stator while maintaining a uniform air gap. This requires not only good registration between the rotor and stator, but also fine control over the angle between the rotor and stator. In practice, the stator is clamped to an xyz-micropositioner stage, having ±5 μm resolution in all three directions. Rotors are mounted to a shaft and inserted into the spindle, which is attached to an articulating arm providing translation and rotation in all directions. For more details the reader is referred to [49].

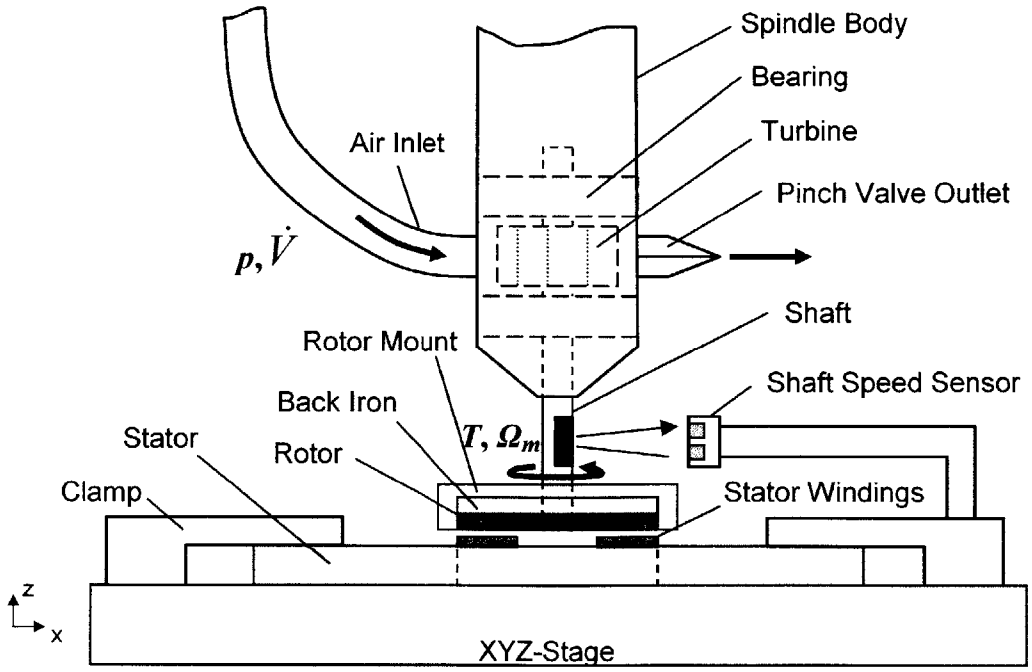

Figure 4-10: Spinning rotor test stand, depicting the air-powered spindle spinning a magnetic rotor over the surface of the stator. (Courtesy of David Arnold, GIT [49])

4.5 Power Electronics

To provide power to modern electronic devices that operate using a DC voltage, the AC generator voltages are first stepped up using a three-phase Δ/wye-connected transformer (N_1:N_2 = 1:6 turns ratio) and then converted to DC using a three-phase diode bridge rectifier. The circuit diagram is shown in Figure 4-11. The bridge rectifier uses Schottky diodes, which are selected for their small forward voltage drops (0.3 – 0.4 V). The generator windings are connected in a wye configuration and tied to the Δ-connected primary side of the transformer. This gives an additional factor of three increase from the line-to-neutral voltage of the machine (V_{oc}) to the line-to-line voltage of the transformer secondary side for an overall step-up ratio of 18, minimizing the effects of the diode voltage drops.

The generator and power electronics are modeled in PSpice to predict the output power as a function of rotational speed and load. The generator model consists of a voltage source (V_{oc}), stator resistance and inductance. An additional ~30 mΩ of contact resistance between the machine windings, breadboard, and transformer windings is added in series with the stator winding resistance. PSpice models for the B320A Schottky diodes were obtained from Diodes Inc.

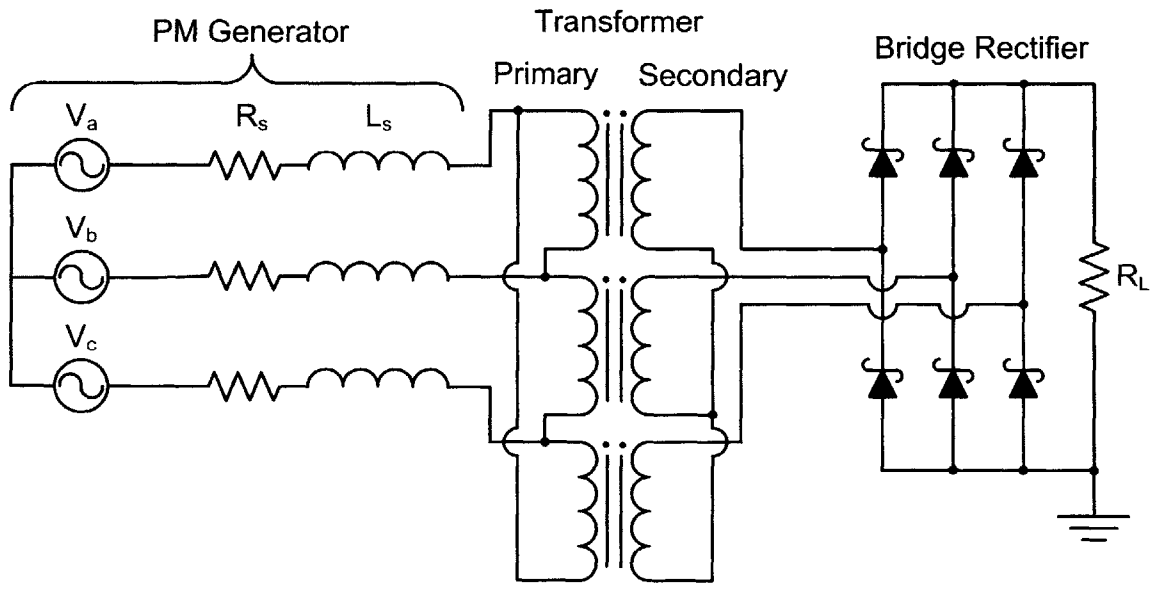

Figure 4-11: Three-phase rectification circuit for DC power generation tests.

The transformer uses three stacked EI cores (PC40EI16 from TDK), as shown in Figure 4-12. The primary side consists of 10 turns of 22-gauge wire in single layer, while the secondary has 60 turns of 25-gauge wire distributed over five winding layers. The completed transformer measures 43 mm long, 25 mm wide, and 11 mm thick. Figure 4-13 shows the fully constructed power electronic circuit.

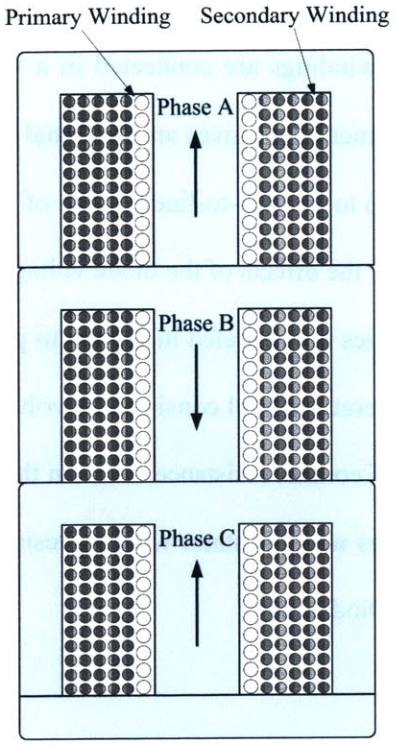

Figure 4-12: Three-phase transformer core and phase windings.

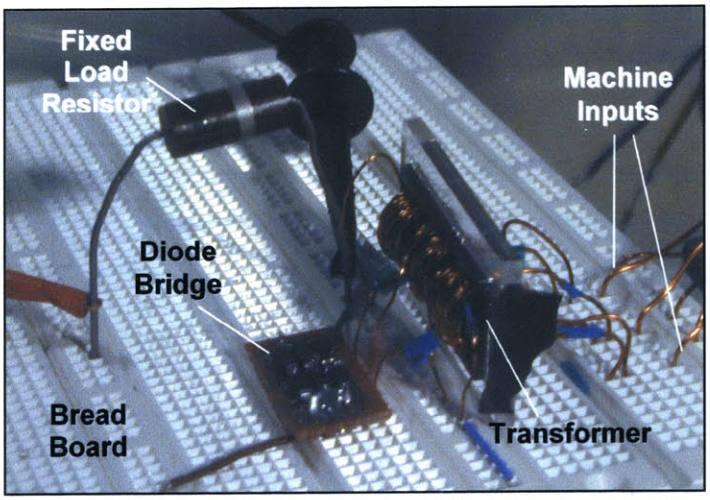

Figure 4-13: Photograph of power electronics used for DC power generation with the PM generators.

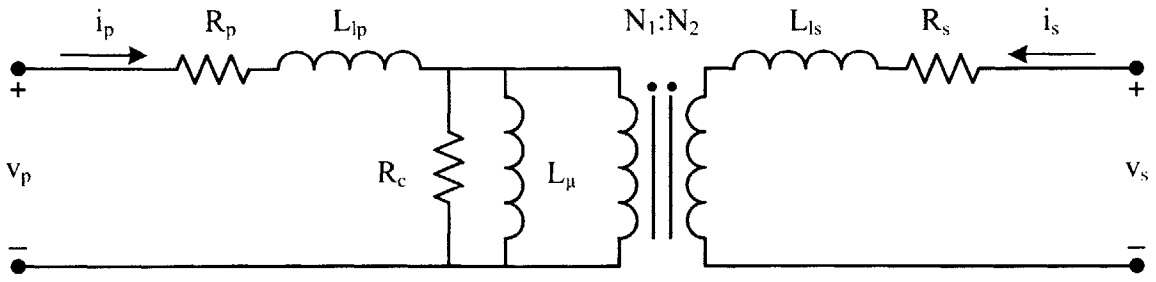

Figure 4-14: Circuit model of a single phase of the transformer.

The transformer model, shown in Figure 4-14, takes into account winding resistance (R_p, R_s), core loss through an effective resistance (R_c), leakage inductance (L_{lp}, L_{ls}), and magnetizing (L_μ) inductance. Proximity and skin effects, which increase the resistance of the transformer windings, are also taken into account [55]. The primary and secondary winding layers are converted to foils of thickness h_i, where

$$h_i = \sqrt{\frac{\pi}{4}} D_i . \tag{4-13}$$

The subscript i stands for either the (p)rimary or (s)econdary winding. The porosity factor, η_i, for a winding layer is the total height of the coils in a layer divided by the height of the winding window, l_w,

$$\eta_i = \frac{N_i h_i}{l_w} . \tag{4-14}$$

The ratio of the effective foil thickness to skin depth, Q_i, is given by

$$Q_i = \sqrt{\eta_i}\,\frac{h_i}{\delta}, \tag{4-15}$$

where,

$$\delta = \sqrt{\frac{2}{\omega_m \mu_0 \sigma_c}} . \tag{4-16}$$

Defining M_i to be the number of coil layers (M_p = 1, M_s = 5), the AC resistance of the transformer windings due to proximity effect is $\kappa_{proxeff,i}$ times the DC resistance, R_i, where

$$\kappa_{proxeff,i} = Q_i \left[\frac{\sinh(2Q_i) + \sin(2Q_i)}{\cosh(2Q_i) - \cos(2Q_i)} \right] + \frac{2\left(M_i^2 - 1\right)}{3} \left[\frac{\sinh(Q_i) - \sin(Q_i)}{\cosh(Q_i) + \cos(Q_i)} \right] . \tag{4-17}$$

The winding resistances, leakage inductances, and magnetizing inductances are found using an impedance analyzer. The primary and secondary resistances increase by 1.1% and 7%, respectively, over their DC values at a frequency of 6.67 kHz (corresponding to 100,000 rpm). The primary leakage is too small to accurately measure, so an approximate value is used.

The core loss in the transformer is modeled as a resistor in parallel with the magnetizing inductance [47]. In order to determine the value of this resistance, the flux density in the transformer is needed. The flux linked by the transformer core approximately equals the first harmonic of the line-to-line voltage divided by the electrical frequency,

$$\lambda_{core} = N_1 A_{core} B_{core} \approx \frac{\sqrt{3} V_{oc1}}{\omega_e}, \tag{4-18}$$

where V_{oc1} is the first harmonic of V_{oc}, N_1 is the number of primary turns, A_{core} is the area of the core, and B_{core} is the flux density in the core. Note that this is the upper bound on the core flux linkage since the voltage applied to the core will decrease as current flows through the stator windings, and a voltage drop develops across the winding resistance. Rearranging (4-18) and using the fact that $V_{oc1} = \lambda_{m1}\omega_e$, B_{core} is

$$B_{core} \approx \frac{\sqrt{3}\lambda_{m1}}{N_1 A_{core}}. \tag{4-19}$$

Interestingly, the peak flux density in the core is independent of the speed of the generator. The core loss density is determined from core material data sheet (PC40EI16 from TDK) using B_{core}. The total core loss, P_{core}, is the core loss density times the volume of the core. The core resistance is then

$$R_c = \frac{\left(\sqrt{3} V_{oc1}\right)^2}{2P_{core}} \propto \frac{f_e^2}{f_e} = f_e. \tag{4-20}$$

Equation (4-20) shows that the core loss is approximately linear in frequency [47], so that the core resistance can be easily recomputed for power generation tests at different speeds. The results of the transformer parameter measurements and calculations are summarized in Table 4-1 using the open-circuit voltage of the 2-turn/pole machine at 100,000 rpm. The mismatch in the magnetizing inductances occurs because the "I" portions of the EI cores for phases A and B are not used.

Table 4-1: Transformer Parameters.

Property	Primary	Secondary
Num. turns	10	60
Wire gage	22	25
R_x @ DC	18 mΩ	225 mΩ
R_x @ 6.67 kHz	18.3 mΩ	241 mΩ
Magnetizing Inductance, Lμ	A: 56 μH B: 67 μH C: 114 μH	A: 2.0 mH B: 2.4 mH C: 4.1 mH
Leakage Inductance, L_l	A: ~0.01 μH B: ~0.01 μH C: ~0.01 μH	A: 16 μH B: 8.8 μH C: 17 μH
R_c @ 6.67 kHz	90Ω	

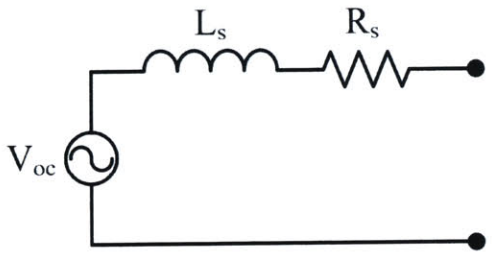

Figure 4-15: Per-phase equivalent circuit of PM machine.

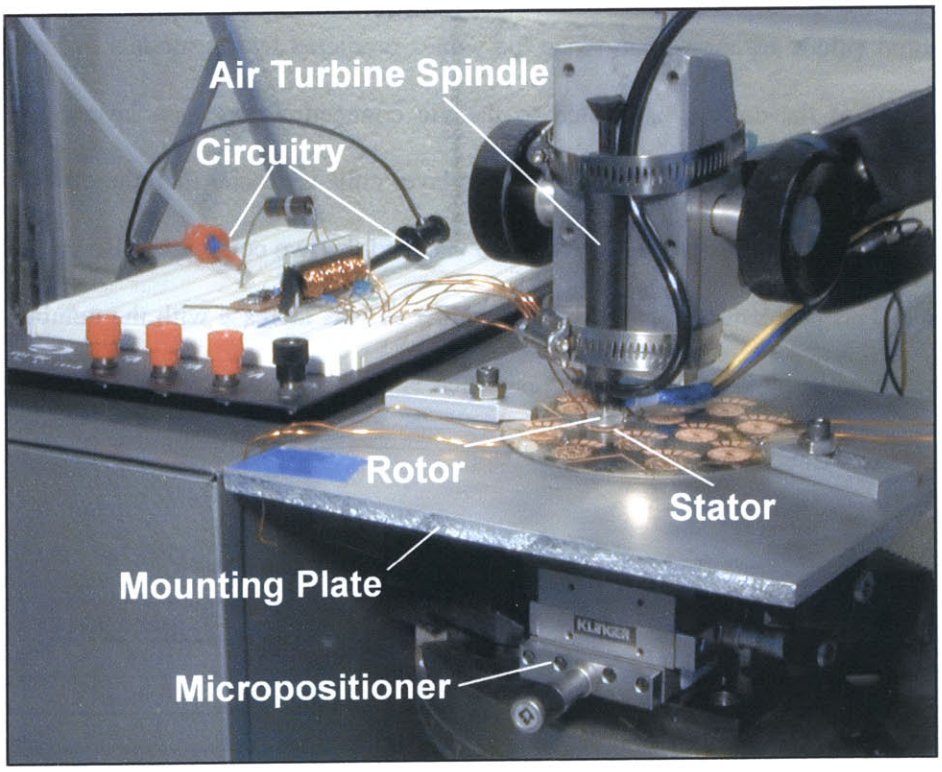

Figure 4-16: Photograph of test setup for characterization of the PM generators.

4.6 Test Results

The stators are first characterized in terms of their equivalent circuit parameters: phase resistance, R_s, phase inductance, L_s, and open-circuit voltage, V_{oc} (Figure 4-15). The machines are then connected to power electronics for power generation tests, which are conducted at varying load resistances and speeds with the rotor-stator air gap set to 100 μm. The test setup for these measurements is shown in Figure 4-16.

4.6.1 Electrical Characterization

The line-to-neutral resistances and inductances (at 100 μm rotor-stator air gap) for the stators are summarized in Table 4-2. The resistance of the 2-turn/pole machine is about twice that of the 1-turn/pole machine, which is expected since a winding in a 2-turn/pole machine is twice as long as that in a 1-turn/pole machine yet has the same cross-sectional area. The 4-turn/pole machine has a much higher resistance than the 2-turn/pole machine because the inner end turns have a much smaller cross-sectional area due to limited space in the center region of the machine.

The measured values are more than twice the values predicted by the models in Section 2.2.9. The increase resistance of the coils is attributed to the via connections between layers. The via layer is approximately 40 μm high so the thickness of the top layer coils is thinner than the difference of $T_{cl} - T_1$ from Figure 4-9. The contact resistance between the vias and the two coil layers also contributes a higher phase resistance. This problem gets worse as the number of vias increase with the number of turns/pole. Minimizing the number of vias to decrease resistance is addressed in Chapter 5 where 2nd generation machines are designed and tested.

Table 4-2: Per-phase electrical parameters.

Device	R_s (model)	R_s (measured)	L_s (model)	L_s (measured)
1-turn/pole	18 mΩ	41 mΩ	0.023 μH	0.18 μH
2-turn/pole	36 mΩ	98 mΩ	0.093 μH	0.34 μH
4-turn/pole	240 mΩ	690 mΩ	0.371 μH	1.0 μH

The phase inductance is also much larger than predicted by the analytical model. The radial span of the rotor (R_o = 4.76 mm, R_i = 1.59 mm) is used for the integration bounds to compute the flux in Equation (2-124). The continuum model does not take into account the leakage inductance from the inner or outer end turns which become quite intricate as the number of turns/pole increases (Figure 4-8). The leakage inductance of a macroscale machine is typically a small fraction of magnetizing inductance [41]. In macroscale surface wound PM machines, the leakage can be on the same order of magnitude as the magnetizing inductance. In the microscale surface wound PM machines presented here, however, the leakage inductance dominates the over all stator inductance. In fact the surface area taken up by the outer end turns is 61.5 mm^2 is about the same as the active area of the machine (R_o = 4.76 mm, R_i = 1.59 mm), which is 63 mm^2.

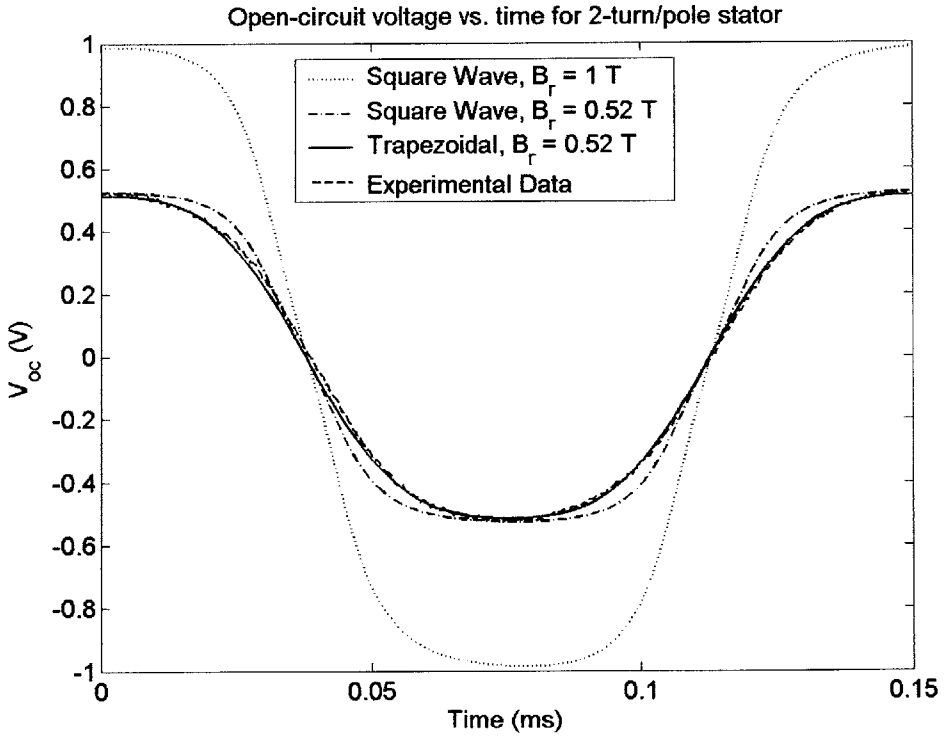

Figure 4-17: Effects of smaller B_r and 1 mm transition region on open-circuit voltage waveforms. Experimental data is from an 8-pole, 2-turn/pole machine at 100 krpm.

The open-circuit voltage, V_{oc}, of each machine is measured as a function of speed with the air gap set to 100 μm. A sample time waveform for the 2-turn/pole machine at a speed of 100 krpm is shown in Figure 4-17, along with various theoretical curves, as predicted from the analytical continuum model from Section 2.2. The ideal square wave magnetization with a B_r of 1T is seen to over predict the experimental results. A closer fit is obtained if the remanence used in the analytical model is reduced to 0.52 T. Further improvement, is made by introducing a 1 mm linear magnetization transition region between north and south poles. This trapezoidal profile yields a more sinusoidal shape, and more likely represents the physical magnetization pattern.

It is believed that the selective pulse magnetization process used to pattern the rotor does not fully saturate the material, resulting in a reduced remanence. Also, transition regions between poles are possible due to saturation of the magnetized heads at the edges of the magnetizer poles and the resulting leakage flux. Nevertheless, using a B_r of 0.52 T and a 1 mm transition region, the experimental measurements of V_{oc} agree well with the analytical model of the machines over a wide range of speeds, turns/pole and air gaps.

Sample time waveforms for the 1-, 2- and 4-turn/pole machine at a speed of 100 krpm and an air gap of 100 μm are shown in Figure 4-18, along with the theoretical predictions using a B_r of 0.52 T and a 1 mm transition region in the analytical model. Note the sinusoidal shape and low harmonic content of V_{oc}, which is a result of the large air gap. Figure 4-19 shows the RMS of V_{oc} varying linearly with speed and number of turns per pole as expected. The open-circuit voltage is also measured as a function of air gap. Figure 4-20 shows the open-circuit voltage for the same three machines at a rotor speed of 100,000 rpm. The open-circuit voltage is a decreasing function of air gap due to the exponential decay of rotor flux in the air gap.

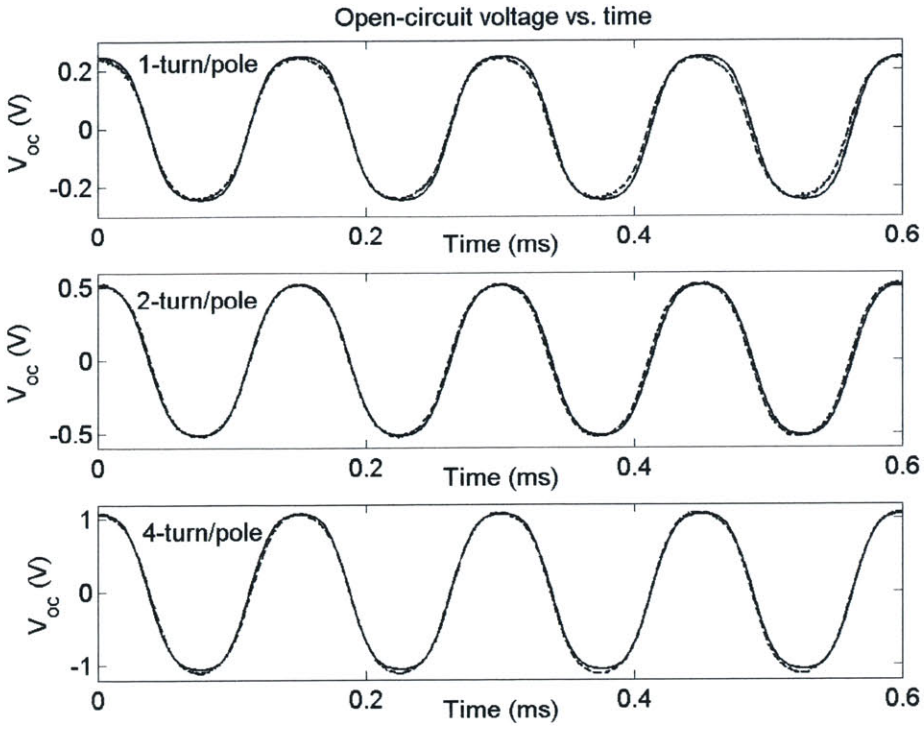

Figure 4-18: Open-circuit voltage vs. time for the 1-, 2- and 4-turn/pole machines at speed of 100 krpm and an air gap of 100 μm. Dotted lines represent measurement; solid lines represent analytical model.

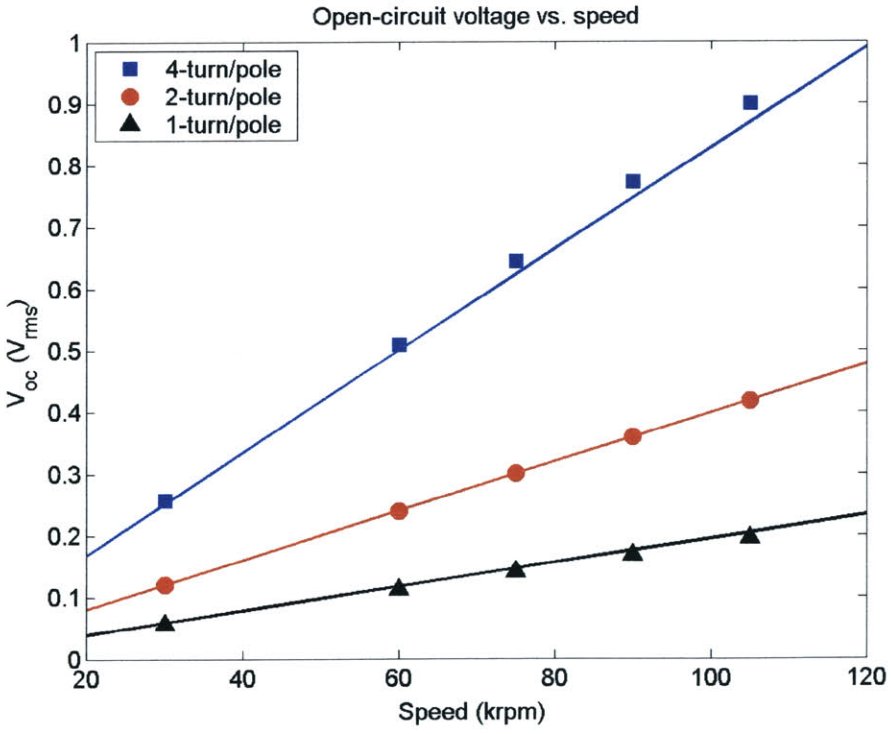

Figure 4-19: Open-circuit RMS voltages vs. rotational speed for 100 μm air gap. Points represent measurements; curves represent analytical model.

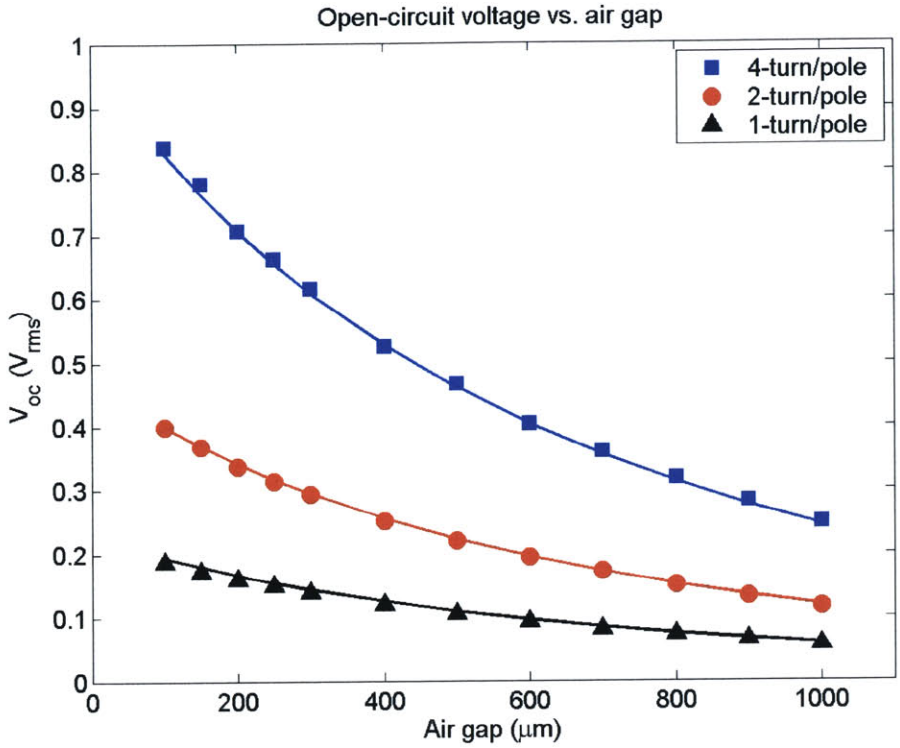

Figure 4-20: Open-circuit RMS voltages vs. air gap at 100,000 rpm. Points represent measurements; curves represent analytical model.

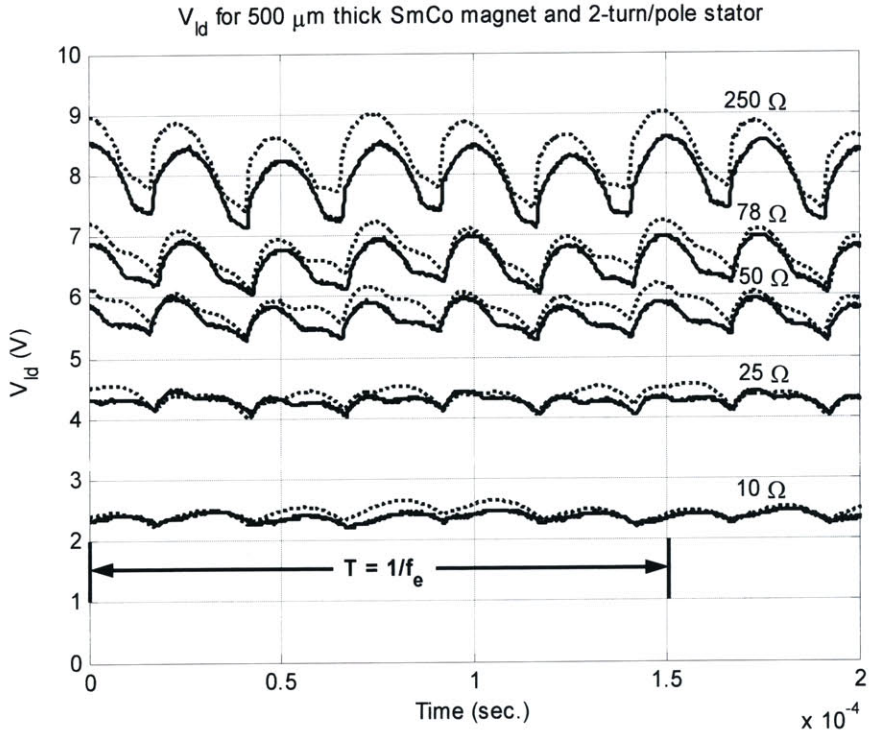

Figure 4-21: Voltage across load resistor for different resistances for 2-turn/pole machine at 100 μm air gap and 100,000 rpm. Solid lines represent measurements; dashed lines represent PSpice model.

4.6.2 DC power generation

Using the power electronics described in Section 4.5, the rectified voltage measured across the load resistor for the 2-turn/pole machine is shown in Figure 4-21 for different load resistances. The ripple voltage is uneven because the magnetizing inductances, L_μ, of the three-phase transformer are all different due to the core structure. This leads to different voltage divider ratios between the primary winding resistance and L_μ, producing slightly unbalanced voltages in the transformer secondary windings.

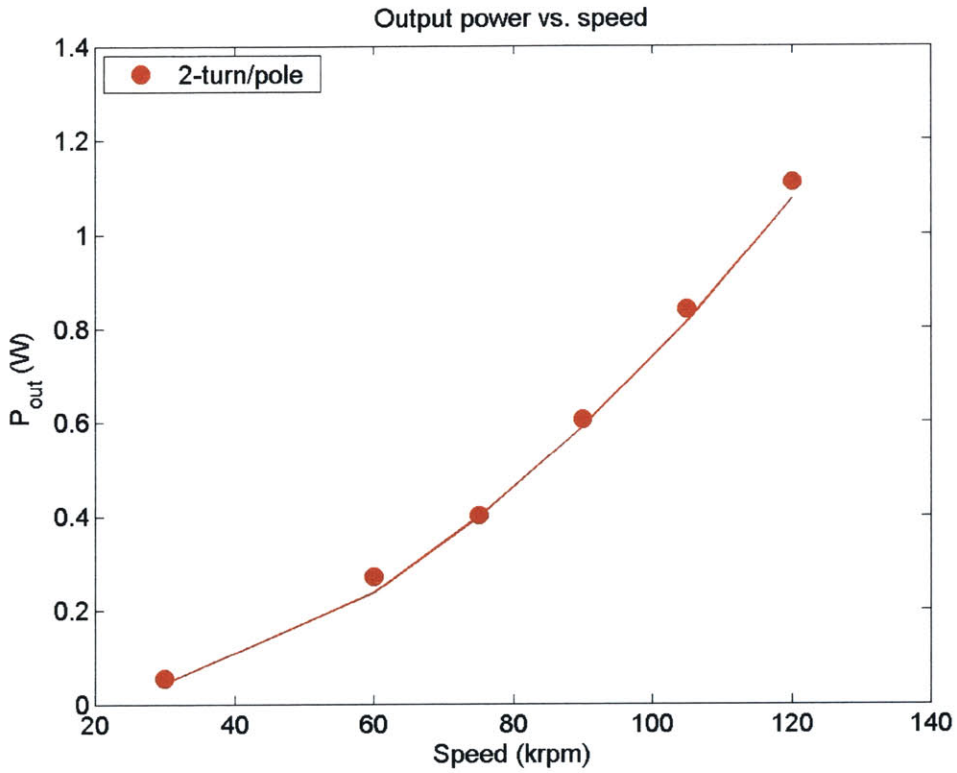

Figure 4-22: DC output power across the load resistor for 2-turn/pole machine at 100 μm air gap vs. rotational speed for 30 Ω load. Points represent measurements; curves represent PSpice model.

Figure 4-22 plots the DC output power for the 2-turn/pole machine as a function of speed for a fixed load of 30 Ω and confirms the expected quadratic dependence on speed up to 120,000 rpm. Figure 4-23 shows the DC power delivered to the load as a function of load resistance (10–250 Ω) from the 2-turn/pole machine at 80,000, 100,000, and 120,000 rpm. At the three different rotation speeds, the

generator delivers a maximum power of 0.46, 0.76 and 1.1 W, respectively. The machine shows the expected power transfer characteristics, with output power maximized under a matched load condition of $R_l \approx 25\ \Omega$. It should be noted that even though the 4-turn/pole machine produces a higher voltage than the 2-turn/pole machine, it delivers less power because of its much larger phase resistance.

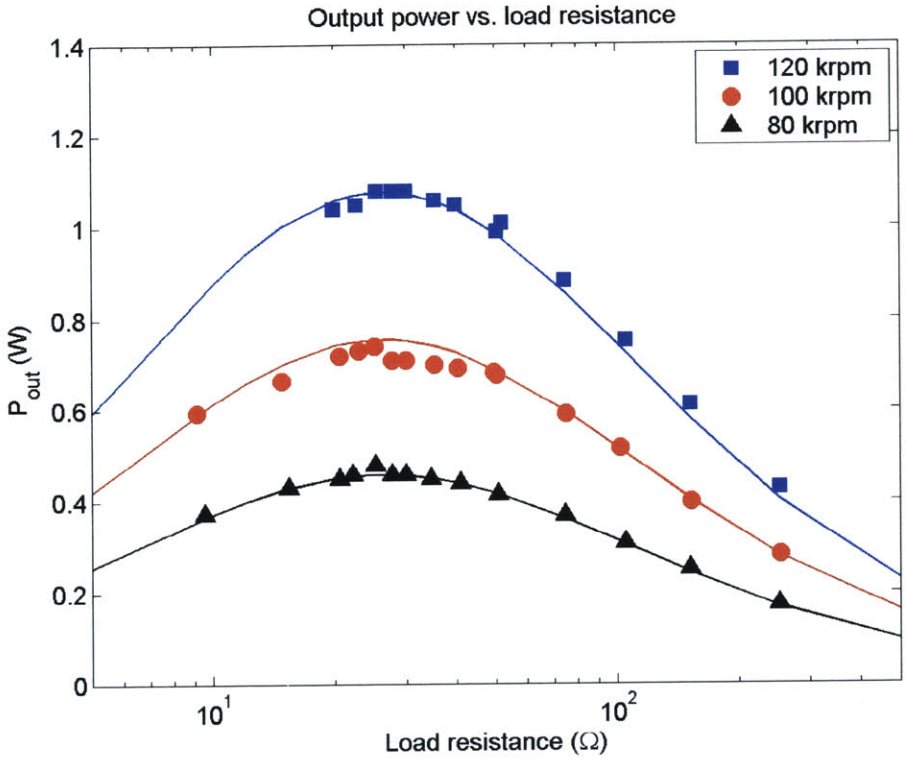

Figure 4-23: DC output power across the load resistor for 2-turn/pole machine at 100 μm air gap vs. load resistance at 80, 100, and 120 krpm. Points represent measurements; curves represent PSpice model.

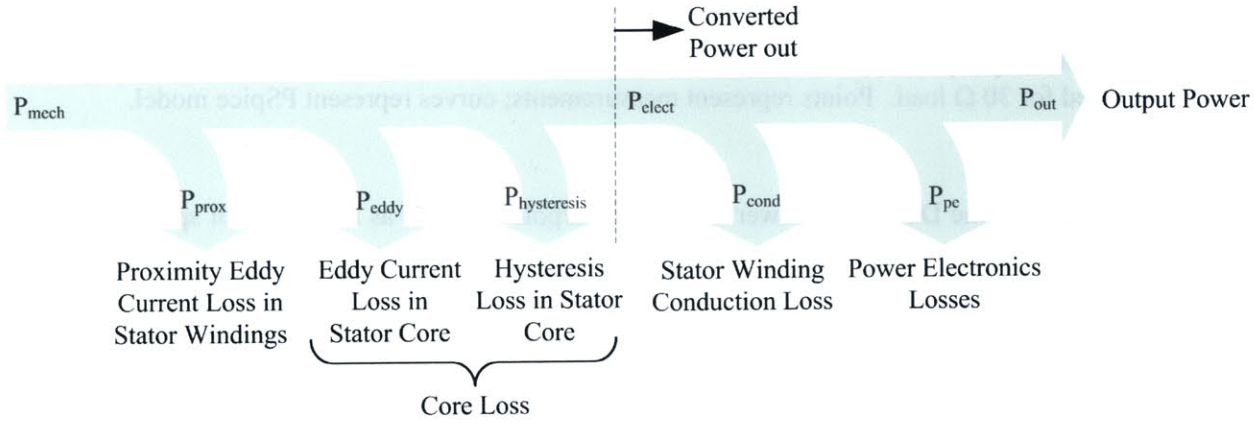

Figure 4-24: Power flow diagram for PM generator system.

Machine efficiency is also an important consideration in the generator design. The power flow diagram for the generator is shown in Figure 4-24. The total generator system efficiency, η_g, and electrical system efficiency, η_e, are defined as

$$\eta_g = \frac{P_{out}}{P_{mech}}, \tag{4-21}$$

$$\eta_e = \frac{P_{out}}{P_{elect}}. \tag{4-22}$$

Direct experimental measurement of the total generator system efficiency is not possible because of the difficulty in measuring the input mechanical power, P_{mech}. Instead, the total input mechanical power is estimated by summing the proximity loss, core loss and converted power, $P_{mech} = P_{prox} + P_{core} + P_{elect}$. The core loss, P_{core}, and proximity loss, P_{prox}, are computed in Section 2.2.7–8 and 2.2.10 respectively. The core loss consists of both eddy current and hysteresis losses. The converted power, P_{elect}, is power available from the open-circuit voltage in the equivalent circuit model and is extracted from the PSpice model. P_{elect} consists of stator winding conduction loss, P_{cond}, power electronics losses, P_{pe}, and power delivered to the load, P_{out}.

The core and proximity losses in the stator are shown in Table 4-3. The proximity loss is small due to the relatively slow rotational speeds (at least compared to microengine speeds) while the hysteresis loss is small because of the low coercivity of the Moly Permalloy wafer used for the stator core. The eddy current loss, on the other hand, is quite large (1.5–3 W), suggesting the need for stator laminations to minimize this loss. Figure 4-25 shows the electrical and generator system efficiencies for the 2-turn/pole machine as functions of load resistance and speed. The generator system efficiency is substantially lower than the electrical system efficiency due to the large eddy current losses in the stator core.

Table 4-3: Hysteresis and eddy current losses in the stator.

Speed (rpm)	$P_{hysteresis}$	P_{eddy}	P_{prox}
80,000	0.097 W	1.57 W	0.047 W
100,000	0.120 W	2.24 W	0.073 W
120,000	0.144 W	3.00 W	0.104 W

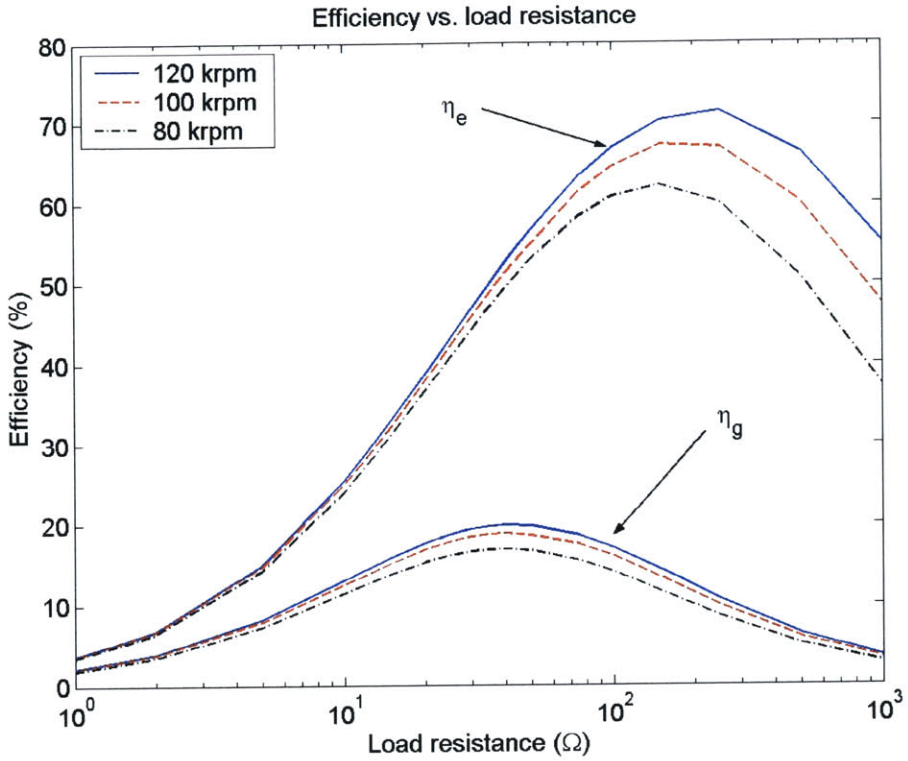

Figure 4-25: Electrical system efficiency, η_e, and generator system efficiency, η_g, for the 2-turn/pole machine at 100 μm air gap.

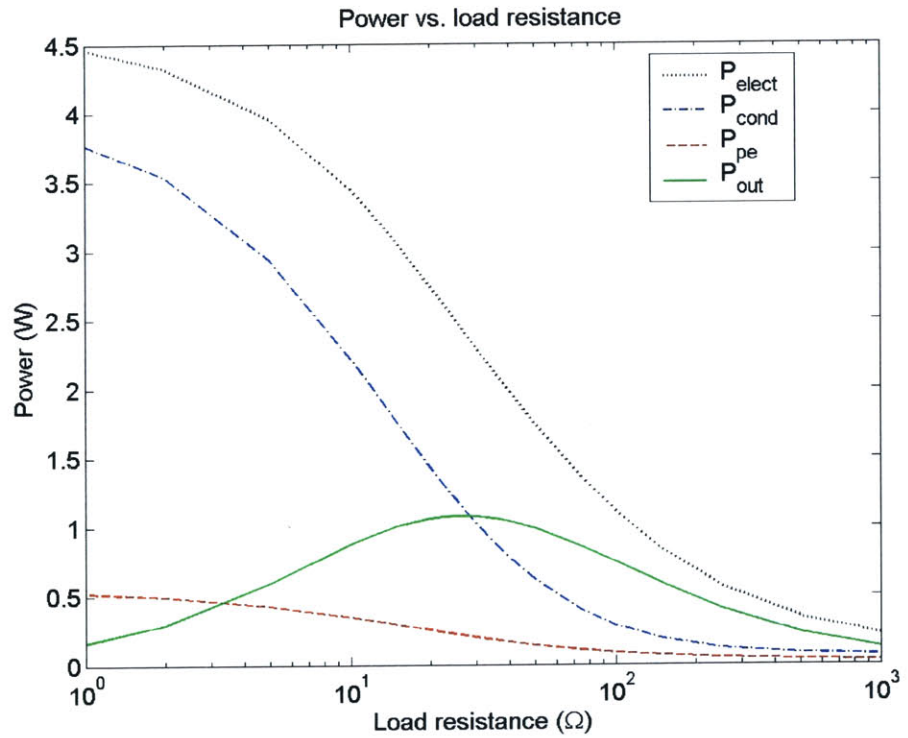

Figure 4-26: Power breakdown for the 2-turn/pole PM machine as a function of load resistance at 120,000 rpm and 100 μm air gap.

At the matched load condition of $R_l \approx 25\ \Omega$, the machine at 120,000 rpm shows an electrical system efficiency of 43% and a generator system efficiency of 19%. Thus, it requires 5.75 W of mechanical power, of which 2.5 W is converted by the machine to electrical power, to deliver the 1.1 W output power. The electrical power breakdown of the generator, at 120,000 rpm, as function of load resistance is shown in figure 4-26. The output power, conduction loss and power electronics losses all increase as load resistance decreases, until the matched load condition is reached and maximum power is delivered to the load. Decreasing the resistance further reduces output power but conduction and power electronics losses increase as the current through the generator and power electronics continues to increase.

The efficiency of the power electronics, η_{pe}, is shown in Figure 4-27, where

$$\eta_{pe} = \frac{P_{out}}{P_{out} + P_{pe}}. \tag{4-23}$$

The power electronics efficiency for the matched load condition ($R_l \approx 25\ \Omega$) at 120,000 rpm is 83% while at 80,000 rpm, it is 78%. The efficiency decreases as the load resistance increases beyond 100 Ω because as the output power decreases, the core loss and diode capacitive losses stay constant. Similarly, the efficiency decreases as the load resistance decreases beyond the matched load condition because the output power drops while the conduction loss in the windings of the transformer continues to increase. Note that both the electrical system and power electronics efficiencies are dependent on the speed. The output power increases as speed squared but the hysteresis loss in the transformer core and the capacitive loss in the Schottky diodes increase linearly with speed. The conduction loss in the stator and transformer windings will increase with speed squared since the current through the machine is proportional to the voltage. However, the diode conduction loss is proportional the current through the diode (proportional to speed) times the diode forward drop, which is roughly constant. Therefore the diode loss only goes up linearly with speed. Since some of the power electronics losses grow slower than speed squared, the efficiency increases with speed.

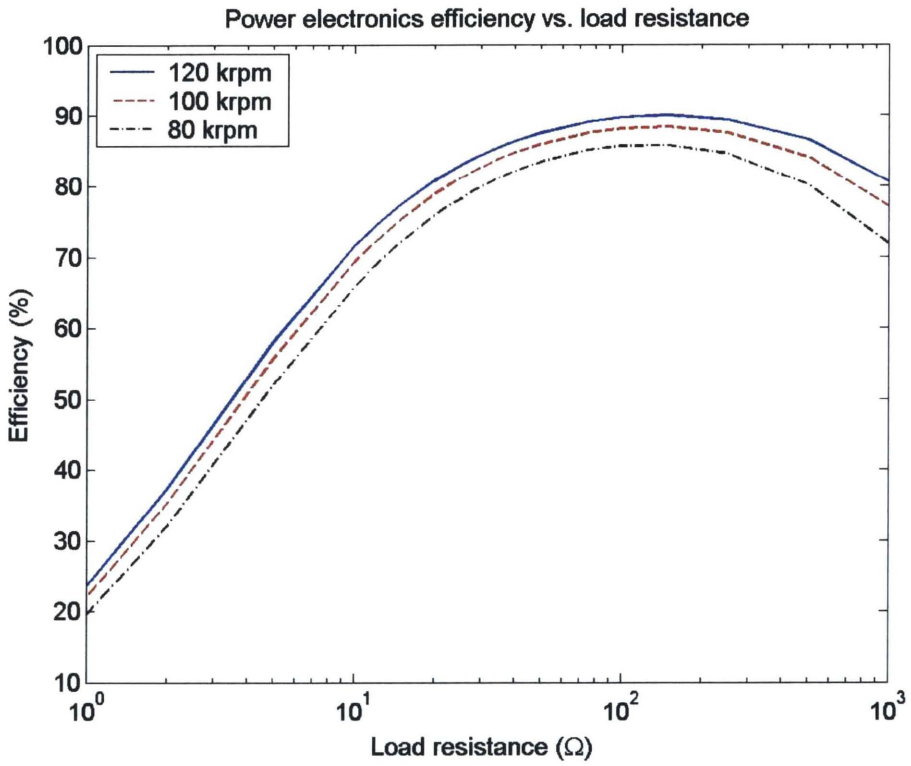

Figure 4-27: Power electronics efficiency, η_{pe}, for the 2-turn/pole machine at 100 μm air gap.

4.7 Summary

This chapter presented the design, fabrication and testing of the first generation PM machines designed for Watt-level power generation. The generators are three-phase, 8-pole, axial-air-gap, synchronous machines. The rotor consists of a 500 μm SmCo PM and Hiperco 50 core. The stator consisted of 1-, 2- and 4-turn/pole windings placed on the surface of a 1 mm thick Moly Permalloy stator core. A simplified model of the machine was presented and used to show that the maximum power in the PM machine is achieved by making the PM as thick as possible and the coils equal to the sum of the air gap and PM thickness. If that coil thickness is not achievable due to fabrication limitations, maximum power is achieved by making the coils as thick as possible. The PM generators were designed and fabricated using a combination of microfabrication and precision machining/assembly.

The machines were then characterized using an air-driven spindle. The measured resistances were higher than those predicted by the analytical models due to via contact resistance. The measured

inductances where higher than predicted due to end turn leakage inductances, which was found to dominate the overall inductance of microscale surface wound PM machines. The measured open-circuit voltages deviated from a PM with an ideal square wave magnetization and 1 T remanence. In order to match the experimental data, B_r was set to 0.52 T and a 1 mm transition region between the rotor PM poles was used in the analytical continuum model. Once this adjustment was made, the experimental and theoretical values for the open-circuit voltage were well matched for various speeds, air gaps, and turns/pole.

The PM machines were connected to power electronics for power generation tests. At 120,000 rpm, the 2-turn/pole machine demonstrated 2.5 W of mechanical-to-electrical power conversion and delivered 1.1 W of DC power to a resistive load. The current in the stator windings when delivering 1.1 W to the load is 2.83 A_{pk}, which translates to a peak current density of $\sim 2\times10^8$ A/m^2. This is one to two orders of magnitude higher than the current density found in a macroscale machine. For an active machine volume of 110 mm^3 (9.5 mm OD, 5.5 mm ID, 2.3 mm thick), the 1.1 W output power corresponds to a power density of 10 MW/m^3. A typical 1000 MW turbine generator with an active volume of 60 m^3 (8.4 m long, 3 m stator core outer diameter) has a power density of 17 MW/m^3. The power density of the microscale PM machine is comparable to its macroscale counterpart due to its high rotation speeds and current densities.

These results prove that Watt-level power generation and delivery is achievable using miniaturized magnetic machines and demonstrates the viability of scaled PM generators for portable power applications. However, despite the impressive performance of this power system, there is room for improvement. The stator resistance is much larger than predicted due to the large number of vias and cross-over conductors used in the end turns, which limits output power. In addition, the transformer and diode bridge circuit is much larger than the generator and does not provide either a regulated DC output voltage nor power factor correction. These issues will be addressed in the next chapter which presents the design of improved generators and power electronics.

5 Second Generation Surface Wound PM Generators and Power Electronics

The first generation microscale PM machines reported here demonstrated the ability to generate and deliver one Watt of power to a resistive load. The next step is to increase the performance of these machines to enable multi-Watt delivery at a regulated DC output voltage. The goal is to design a PM machine capable of delivering 10 W of power to a load.

To increase the output power, a number of things can be done. First, the machine can be spun faster to increase the open-circuit voltage. Second, better PMs could be found to increase the flux density in the air gap. Third, improvements in the stator windings and power electronics would lead to reduced losses. Finally, increasing the area of the machine would increase the flux linked by a phase and increase power. Table 5-1 summarizes these improvements and their benefits. Referring to Table 5-1, the biggest increase comes from increasing the speed. Higher remanence in the PMs is difficult to create from the selective poling process discussed in Section 4.3 and increasing the radial span of the machines makes them larger than the proposed microengine compressor designs at this time. Therefore, the best path to increase output power is to increase rotational speed while improving the stator winding design and power electronics.

Unloaded, the spindle used in the SRTS can spin up to 400,000 rpm. Using the PMMA retaining ring, the rotor core/PM assembly can spin up to 230,000 RPM before breaking apart. Speeds of up to 325,000 rpm have been demonstrated by housing the rotor core and PM inside a Titanium retaining ring in high speed rotor tests performed by colleagues at GIT and CAU [56]. This was achieved with a PM that had the same active area as the stator (5.525 mm ID, 9.525 mm OD) and had recently become available. Therefore, the decision is made to target 10 Watts of power generation at 300,000 rpm. Since increasing the speed from 120,000 rpm to 300,000 rpm only increases the output power to about 6.8 W, an improved PM machine is also needed. The necessary optimization and design of the second generation PM machines is described in Sections 5.1.1 and 5.1.2. The optimization is performed using the open-circuit voltage predictions from the models in Chapter 2 in conjunction with a new concentric winding design

and resistance model developed by colleagues at GIT. The characterization of these machines is presented in section 5.1.3. The design, construction and testing of switch-mode power electronics for delivering power at a regulated output voltage is described in section 5.2 along with a comparison with the first generation power electronics. The author of this thesis is solely responsible for design and construction of the second generation power electronics. Again, testing of the new generators and power electronics is a group effort.

Table 5-1: Power improvements for the PM generator.

Parameter	Change	Increase in power
Speed, Ω_m	120 krpm → 360 krpm	9× improvement
Better PM's	B_r: 0.5 T → 1T	4× improvement
Optimize R_s	20% reduction	1.25× improvement
Reduce P_{pe}	10–20%	1.15× improvement
Increase R_o, R_i	150%	2.25× improvement

5.1 Second Generation Surface-Wound PM Machines

5.1.1 Power and Efficiency Scaling

The amount of power that a PM generator can deliver is a function of its open-circuit voltage, resistance and inductance and, the equivalent resistance and inductance of any power electronics that connect the generator to its load. A simplified model of the generating system is shown in Figure 5-1, where the generator is modeled with a voltage source, V_{oc}, stator resistance, R_s, and inductance, L_s. The power electronics is modeled, for simplicity, with an equivalent resistor and inductance R_{pe} and L_{pe}, respectively. The resistance, R_{pe}, represents both the conduction and magnetic core losses in the power electronics while the inductance could represent, for example, the leakage and magnetizing inductance of a transformer as seen from the stator terminals. The generator is driving a load resistor, R_{load}. R_s and R_{pe} are combined to form an equivalent source resistance, R_{source}, and L_s and L_{pe} are combined to form an equivalent source inductance, L_{source} for the generator system. R_{pe} can be dependent on voltage, current and/or frequency.

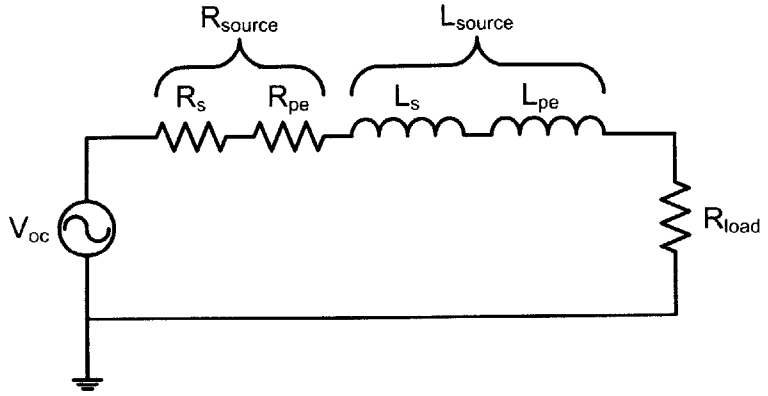

Figure 5-1: Simplified equivalent circuit of the PM generator and power electronics driving a load resistor.

Referring to Figure 5-1, the maximum power delivered to the load, P_{out}, is proportional to

$$P_{out} \propto \frac{V_{oc}^2}{R_{source}\left[1+\sqrt{1+(\omega_m \tau_{source})^2}\right]}, \tag{5-1}$$

which occurs when R_{load} equals the magnitude of the source impedance, Z_{source},

$$R_{load} = |Z_{source}| = R_{source}\sqrt{1+(\omega_m \tau_{source})^2}, \tag{5-2}$$

where

$$\tau_{source} = \frac{L_{source}}{R_{source}}. \tag{5-3}$$

The resistance of the radial conductors and end turns in R_s are both dependent on N and P,

$$R_s = \frac{6(PNC_{lam})^2}{\pi \sigma_c T_{cl}} \ln\left(\frac{W_{cl}(R_o)}{W_{cl}(R_i)}\right) + \frac{2PNL_{outer}}{\sigma_c T_{co} W_{co}} + \frac{2PNL_{inner}}{\sigma_c T_{ci} W_{ci}} \propto k_1 (PN)^2 + k_2 PN. \tag{5-4}$$

The radial conductors grow as PN squared while the end turns grow linearly with PN. Even though the end turn resistance grows slower, it can make up a large fraction of the over all resistance.

The losses in the power electronics can be independent of frequency, such as conduction loss in the on-state resistance of a power MOSFET, proportional to the square root of the frequency, such as skin depth losses in the windings of high frequency transformers, or linear with frequency, such as in the switching loss of a power MOSFET. The frequency dependent component is the most important because

it scales with both the speed and number of pole pairs of the machine. R_{pe} will be assumed to be proportional to $P\Omega_m$, because the fastest growing frequency-dependent component scales linearly,

$$R_{pe} \approx k_3 P\Omega_m . \tag{5-5}$$

Referring back to Equation (4-9), the open-circuit voltage is proportional to N, P and Ω_m. Equation (5-1) can now be expressed in terms of N, P and Ω_m,

$$P_{out} \propto \frac{(PN\Omega_m)^2}{\left(k_1(PN)^2 + k_2 PN + k_3 P\Omega_m\right)\left[1+\sqrt{1+(P\Omega_m \tau_{source})^2}\right]} . \tag{5-6}$$

By making N large, both the open-circuit voltage and stator resistance increase while dissipation in the power electronics and the effect of source reactance remains the same leading to higher output power. In addition, for large N, P_{out} will be independent of both P and N, and scale with the square of the rotational speed. In reality, the minimum feature size constraint will limit the gap between adjacent radial conductors and a large number of turns/pole will lead to thin inner and outer end turns. Both effects make R_{stator} increase slightly faster than N^2. Therefore, to maximize output power, the number of turns/pole should be maximized subject to stator fabrication and surface area limitations.

The total generator system efficiency can be expressed as

$$\eta_g = \frac{P_{out}}{P_{out} + P_{prox} + P_{core} + P_{source}}, \tag{5-7}$$

where P_{core} is the sum of the stator core eddy current and hysteresis losses. The eddy current loss is either proportional to frequency squared (skin depth > core/lamination thickness) or linear with frequency (skin depth < core/lamination thickness). The hysteresis loss is linear with frequency. In the worst case scenario,

$$P_{core} \propto k_4 (P\Omega_m)^2 + k_5 P\Omega_m . \tag{5-8}$$

Generator system efficiency can be increased by making P small. However, doing so will make the rotor PM poles wide. Consequently, the rotor and stator cores must be made thicker to prevent them from saturating. The proximity skin effect losses are approximately independent of P (from the analysis carried out in Section 2.2.10) and scale as speed squared. However, proximity losses decrease as N squared.

Therefore, to maximize efficiency, the number of poles should be minimized subject to rotor and stator core thickness limitations while the number of turns/pole should be maximized subject to stator fabrication and surface area limitations.

5.1.2 Stator Optimization and Design

Figure 5-2 plots the output power as a function of P and N for different values of R_{pe}. The machine is spinning at 100,000 rpm with an air gap of 100 μm. The open-circuit voltage is computed using the PM used in the first generation PM generators. The white regions in Figure 5-2 denote combinations of N and P that are too difficult to fabricate. Note that as R_{pe} increases, the maximum output power occurs at higher values of N and/or P.

To choose an appropriate value for N and P, an estimate of the power electronics resistance at the intended operating condition is needed. At 300,000 rpm, the stator electrical frequency is between 20 – 30 kHz for 8 to 12 pole machines. Since the switch-mode rectifier design had not yet been started at the time of this optimization, the resistance of the transformer, from in Section 4.5, as seen from the stator terminal is used. Recall that the secondary is connected in a wye configuration while the primary is configured in a delta configuration. The reflected secondary resistance will be $3/n^2$ smaller, where n is the turns ratio. The stator windings are in a wye configuration and are connected to the delta configured primary. To get a line-to-neutral, or wye equivalent, resistance both the primary and reflected secondary resistances are divide by three (Δ→Y transformation). Therefore the equivalent power electronics resistance will be,

$$R_{pe} \approx \frac{R_{primary}}{3} + \frac{R_{secondary}}{n^2}. \tag{5-9}$$

At 20 kHz, the primary and secondary resistances of the transformer are 20 mΩ and 360 mΩ, respectively, while at 30 kHz, they are 22 mΩ and 542 mΩ, respectively. Note that the secondary resistance increases faster with frequency because its 60 turns are distributed over five layers, which increase the effects of proximity eddy currents in the transformer windings. R_{pe} will be approximately 17 mΩ at 20 kHz and 22 mΩ at 30 kHz. Looking at power out vs. P and N for R_{pe} = 25 mΩ, the 12-pole, 2-

turn/pole and 8-pole, 3-turn/pole machines achieve the highest output power for a minimum number of total turns per phase. The minimum number of turns is used to increase the probability of fabricating a working device on the first try. Given the discussion of power and efficiency scaling in the previous section, the 8-pole, 3-turn/pole machine is chosen as the second generation device.

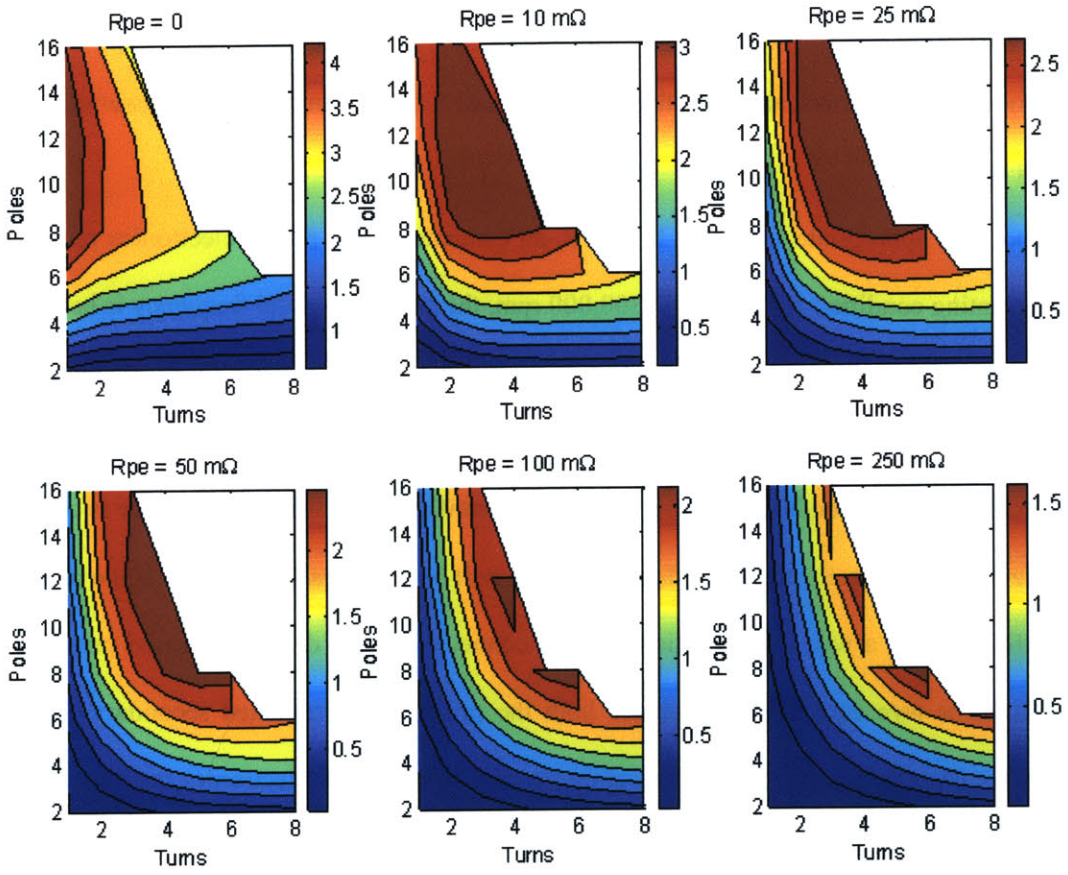

Figure 5-2: PM machine output power as function of poles and turns/pole for different values of the equivalent power electronics resistance, R_{pe}.

A 2nd generation 8-pole, 3-turn/pole stator is shown in Figure 5-3. These stators use a single layer for the radial conductors that is 200 μm thick. The end turns occupy two layers and are each 80 μm thick. There is a 40 μm thick SU8 insulation layer between the top and bottom end turns. The winding pattern for these machines is shown in Figure 5-4. The stators use concentric windings in which a complete end turn occupies a single layer. This eliminates the need for cross-over conductors like the ones used in the 1st generation stators. In fact, the only cross-over conductors needed are for connections to the pads. With fewer crossovers the number of vias is drastically reduced. In addition, by using concentric windings, the end turns can be made to be circular arcs. This makes much more efficient use of the surface area of the inner and outer regions of the stator than the triangular end turns used in the 1st generation devices. Furthermore, variable width coils are used with the gaps between adjacent radial conductors and end turns equal to 50 μm rather than 130 μm. The combination of the reduced number of vias, better end turn design and more aggressive fabrication leads to a predicted stator resistance of 100 mΩ. This resistance is about the same as that of a 1st generation 2-turn/pole machine. In fact, the predicted output power capability is increased by a factor of 2.25 over the 2-turn/pole machines presented in Chapter 4 due to the improved stator resistance.

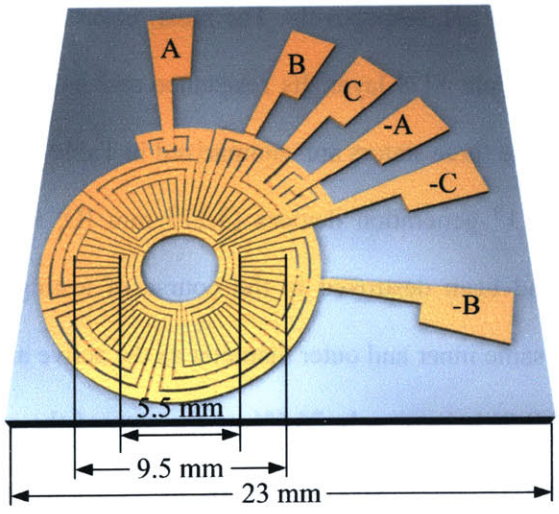

Figure 5-3: 8-pole, 3-turn/pole concentric wound stator.

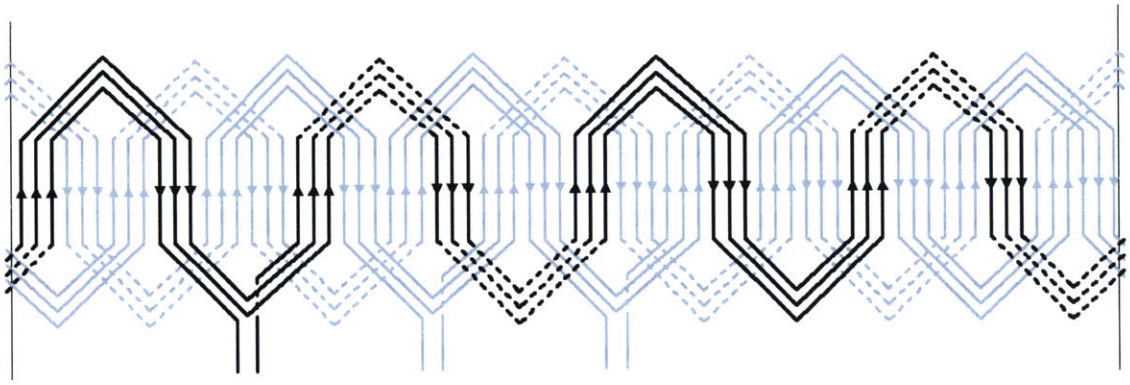

Figure 5-4: Winding diagram for the 3-turn/pole concentric wound stator. Solid lines represent end turns on the top layer while dashed lines represent end turns on the bottom layer. The radial conductors, marked with arrows, occupy both coil layers. Phase A is darkened for reference.

5.1.3 Stator Characterization

Figure 5-5 shows a fabricated 3-turn/pole stator. Three working stators have been built and tested. The first stator, designated stator #1, has radial conductors with an average thickness of 205 μm. There is a layer of SU8 over the coils to protect them and is approximately 16 μm thick. The measured phase resistance is 136 mΩ, which is only 36% higher than predicted. The measured phase inductance is 0.31 μH, which is more than double the 0.138 μH predicted by the continuum model. The second working 3-turn/pole stator, stator #2, has 188 μm thick radial conductors and no SU8 layer. Its measured resistance and inductance is 160 mΩ and 0.3 μH, respectively. The most recent stator, stator #3, also has coils that are 188 μm thick and has a ~50 μm SU8 layer. Its resistance and inductance is 145 mΩ and 0.34 μH, respectively. The properties of the three stators are summarized in Table 5-2.

The magnets used for the 1st generation devices (3.175 mm ID, 9.525 mm OD) were no longer available since all of them had been destroyed in the course of testing the generators. Instead, PMs became available that had the same inner and outer diameter as the active area of the stator (5.525 mm ID, 9.525 mm OD). These "small" PMs have only 74.6% of the area of the ones used in the 1st generation devices, which means the open-circuit voltage is reduced by 25.4% (assuming equal remanences) and power is approximately cut in half. Stator #1 was only tested with a small PM before being destroyed when the rotor crashed into the stator. Later, "large" PMs had been found that have an inner diameter of 5

mm and an outer diameter of 10 mm. These PMs produce 93% of the voltage of the PMs used in the 1st generation devices (again assuming equal remanences) and 86.5% of the power. Stator #2 and #3 are tested with the large PMs.

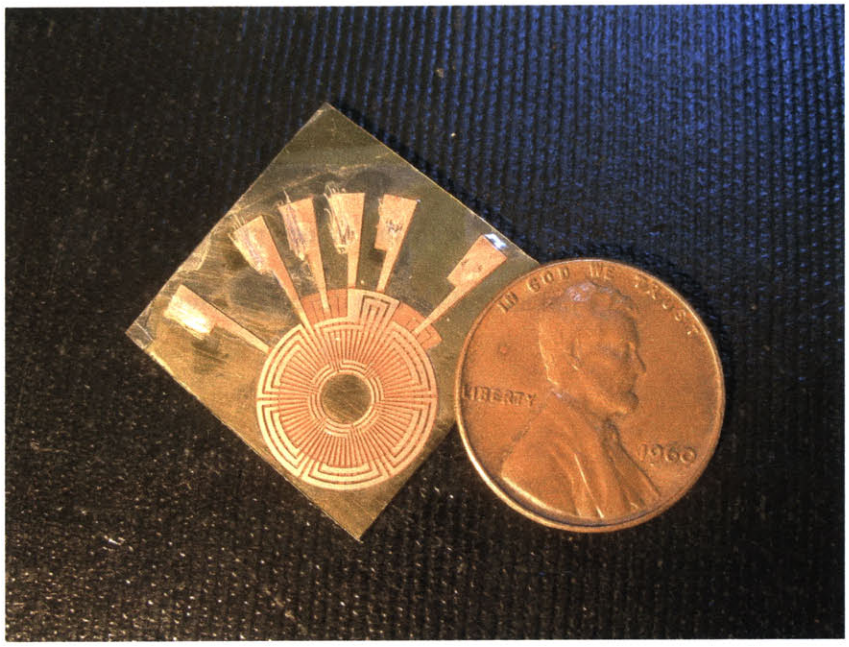

Figure 5-5: Fabricated 3-turn/pole concentric wound stator is shown along side a penny for size comparison.

Table 5-2: Fabricated 3-turn/pole Stator Parameters.

Stator	R_s (mΩ)	L_s (μH)	T_{cl} (μm)	T_{SU8} (μm)
#1	136	0.31	205	~15
#2	160	0.30	188	0
#3	145	0.34	188	~50

Figure 5-6 shows the open-circuit voltage waveforms for stator #1 with the small PM and stator #2 with the large PM at an air gap of 100 μm and a speed of 100 krpm. A remanence, B_r, of 0.54 T and a transition length, c_m, of 1.5 mm is used to match the data for the small PM, while B_r and c_m for the large PM are 0.52 T and 1.2 mm, respectively. Given the 20% variation in open-circuit B fields among the various magnets measured by colleagues at GIT [49], the minor variations in the remanences of the two PMs are not surprising.

The open-circuit voltage as function of speed, at an air gap of 100 μm, is shown in Figure 5-7 for both stator #1 with the small PM and stator #2 with the large PM. The open-circuit voltages as function of air gap for these two rotor/stator combinations is shown in Figure 5-8 for a speed of 100 krpm. The open-circuit voltage for stator #3 with the large PM is shown as function of speed and air gap in Figures 5-9 and 5-10, respectively. The open-circuit voltage as function of speed is taken at an air gap of 100 μm and 250 μm while the voltage vs. air gap is taken at 50, 100 and 150 krpm. For stator #1 and #3, the thickness of the SU8 layer is added to the air gap thickness. Notice that, once B_r and c_m are set at a single speed and air gap, the experimental data agree very well with the values predicted by the analytical continuum model in Section 2.2 for both the small and large PMs with different stators.

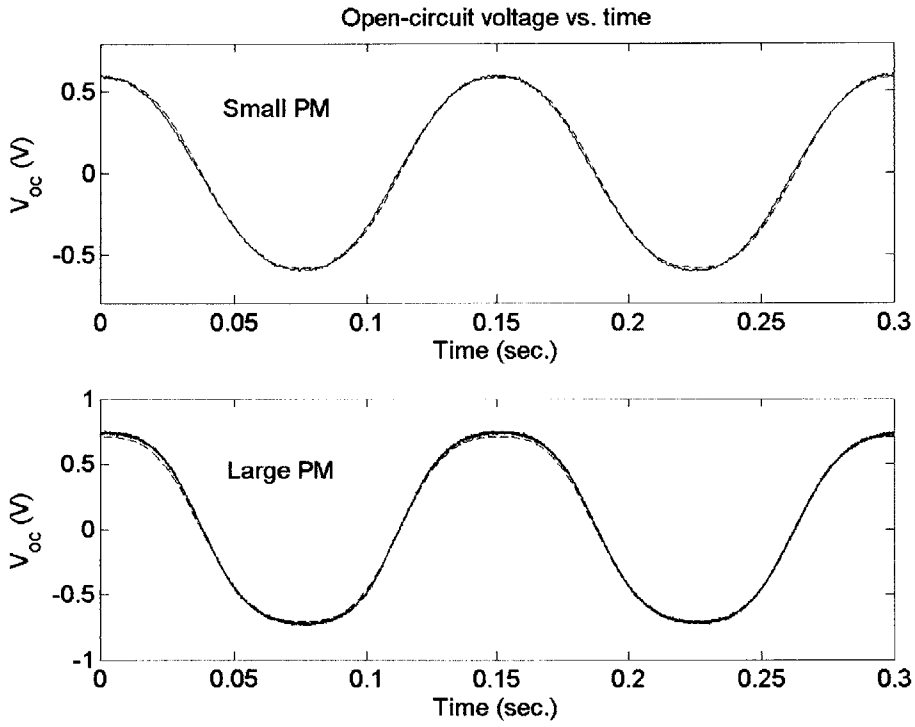

Figure 5-6: Open circuit voltage vs. time for stator #1 with a small PM and stator #2 with a large PM at a 100 μm air gap and a speed of 100 krpm Solid lines represent measurements; dashed lines represent analytical model.

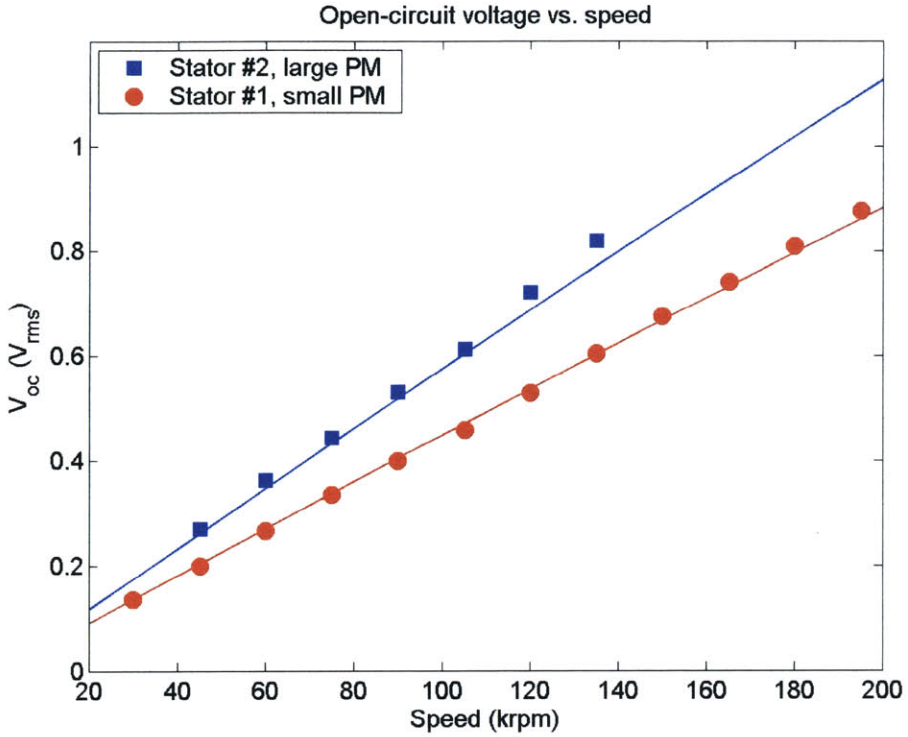

Figure 5-7: Open-circuit voltages vs. rotational speed for 100 μm air gap. Points represent measurements; curves represent analytical model.

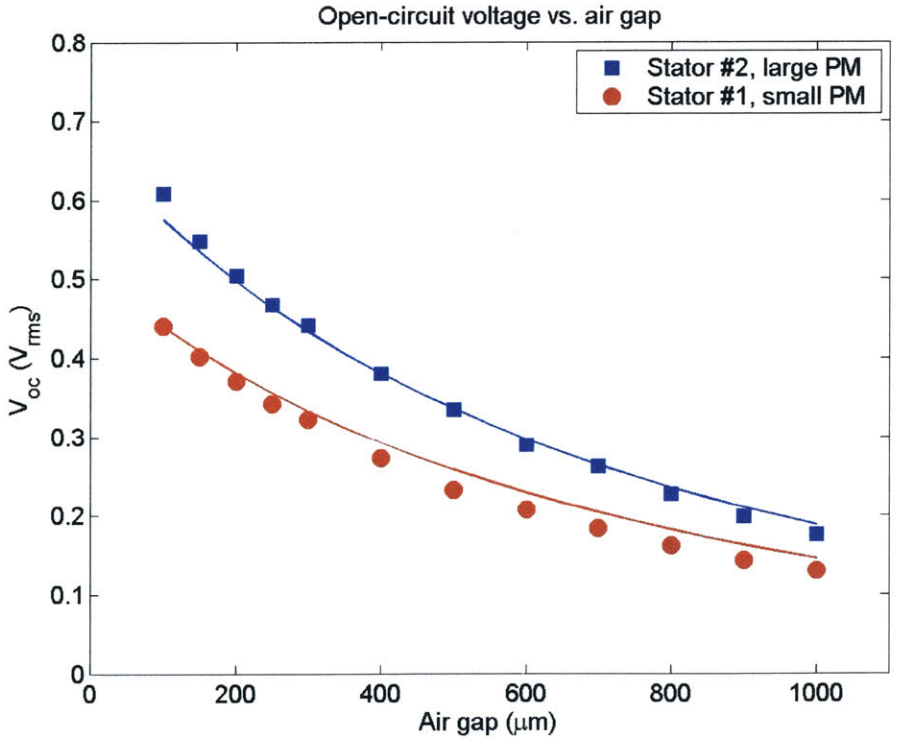

Figure 5-8: Open-circuit voltages vs. air gap at 100,000 rpm. Points represent measurements; curves represent analytical model.

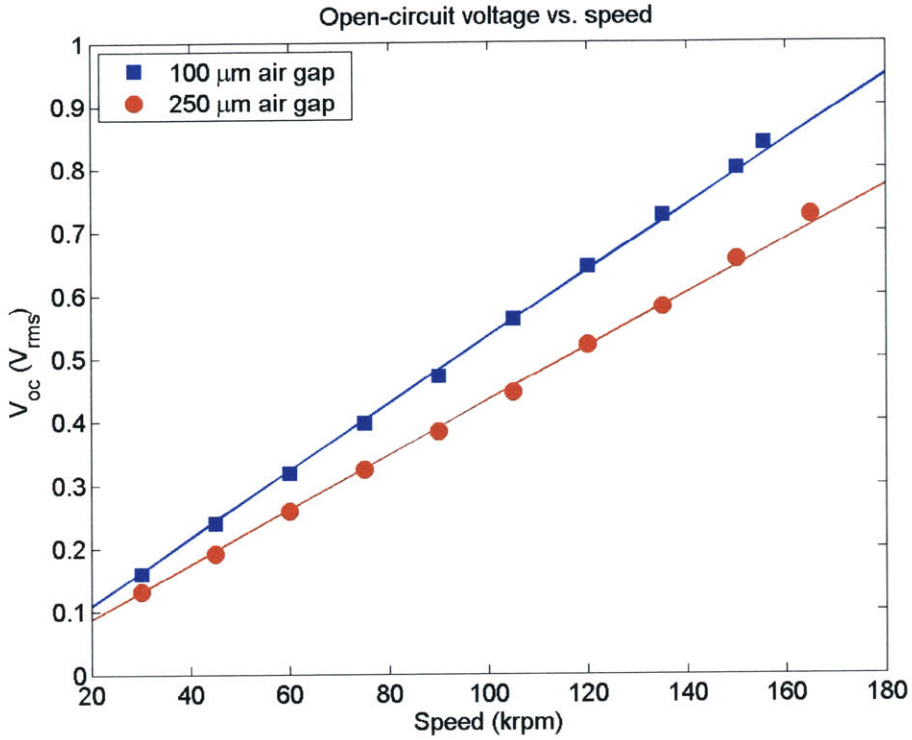

Figure 5-9: Open-circuit voltages vs. rotational speed for stator #3 at different air gaps. Points represent measurements; curves represent analytical model.

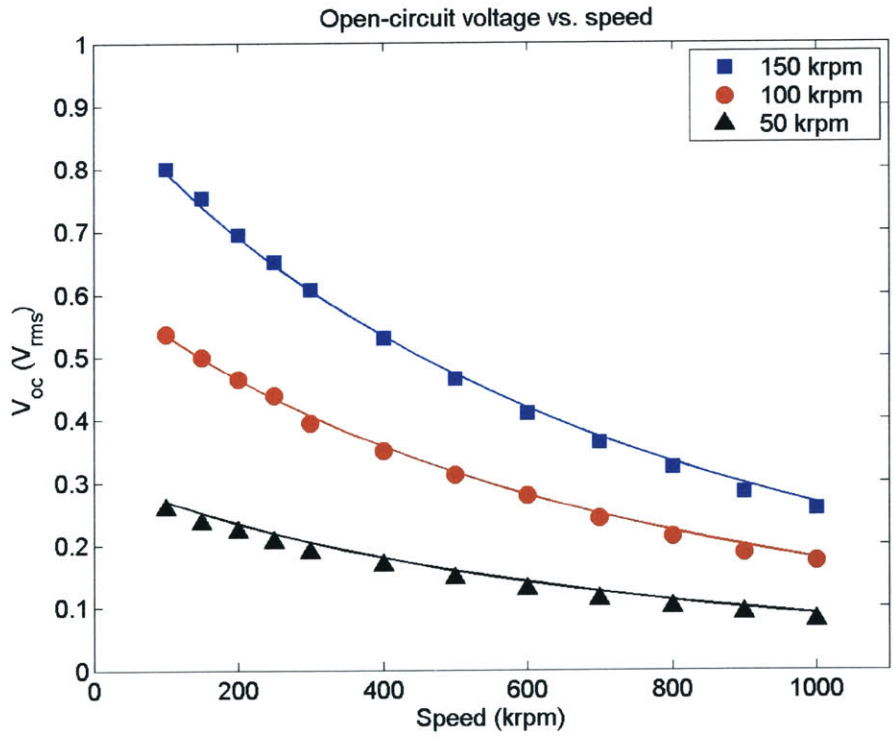

Figure 5-10: Open-circuit voltages vs. air gap at different speeds for stator #3. Points represent measurements; curves represent analytical model.

The three stators are tested using the transformer and diode bridge rectifier from Section 4.5. Testing focuses on delivering maximum power to the load resistor vs. speed. The matched load condition is set by varying the load resistance at a speed of 100 krpm and an air gap of 100 μm. The resistor value that achieves maximum power transfer is then used for power vs. speed measurements. Note that as the power delivered is increased, the load resistor will begin to heat up. The resistance of the load resistor is measured at each speed where power is measured to insure accuracy.

Stator #1 is tested with the small PM. At a speed of 180 krpm it delivered 2.45 W to a load resistance of 35 Ω as shown in Figure 5-11. The converted electrical power, computed from the PSpice model, is 5.15 W. The estimated electrical system efficiency, defined in Equation (4-22) in Section 4.6.2, is 47.6%. At a speed of 185 krpm, the rotor shaft loosened itself from the spindle and crashed into the stator, shorting the coils of two phases together.

Stator #2 is tested with the large PM and demonstrates 3.54 W of power delivered to a 35 Ω load as shown in Figure 5-11. This is achieved at a speed of 210 krpm. With an estimated converted electrical power of 7.75 W, the electrical system efficiency of this machine is 45.7%. For stator #2, the air gap had accidentally been set to 150 μm and thus produces about 12.5% less power than it would at a 100 μm air gap. Tests at higher speeds could not be conducted because the rotor crashed into the stator in subsequent testing.

Figure 5-11 also shows the predicted power to the load resistor that a 1st generation 2-turn/pole stator would deliver with both the small and large PMs. The stator resistance is 100 mΩ and the air gap is 100 μm. At a speed of 180 krpm, the 2-turn/pole stator would deliver 1.3 W to a 30 Ω load with the small PM, which is approximately the matched load power (Section 4.6). Stator #1 produces 88% more output power than a comparable 2-turn/pole stator. Similarly, the 2-turn/pole stator can deliver 2.6 W at 210 krpm with the large PM. Stator #2 with the large PM produces only 36% more output power due to its larger air gap (150 μm) and phase resistance (160 mΩ).

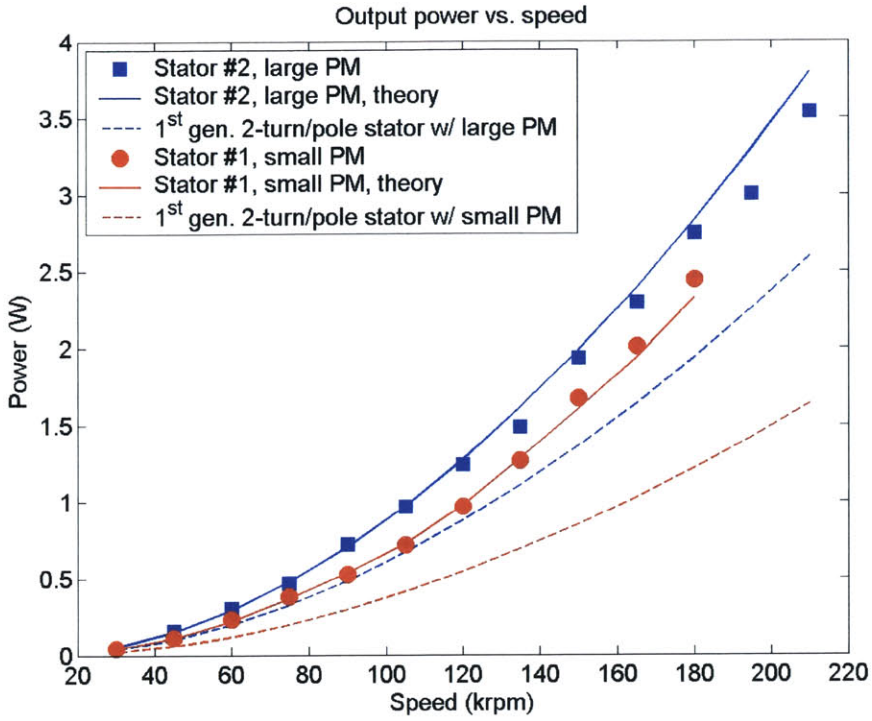

Figure 5-11: DC output power across the load resistor for different machines at 100 μm air gap vs. rotational speed. Points represent measurements; curves represent PSpice model.

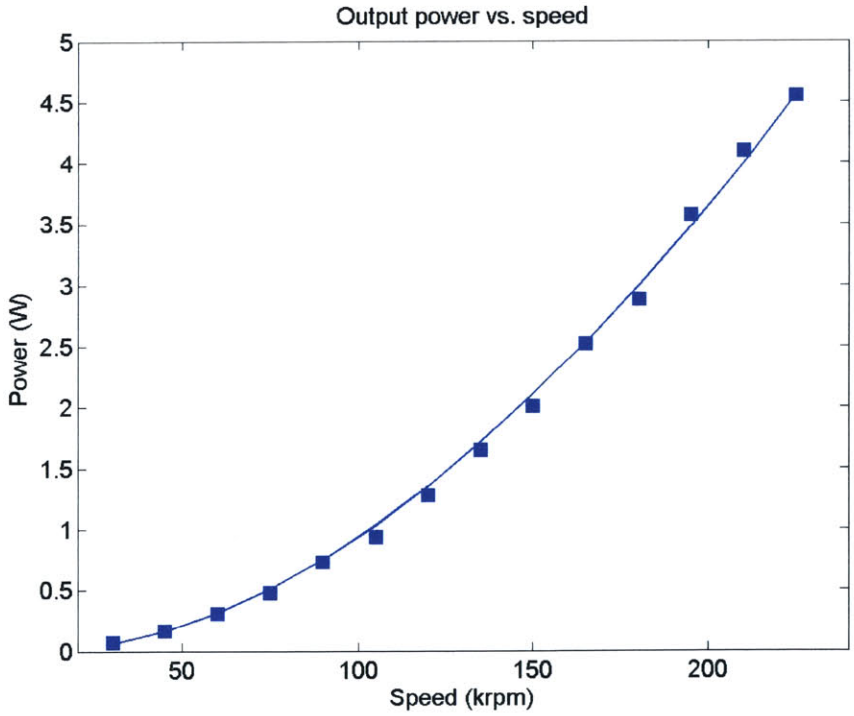

Figure 5-12: DC output power across the load resistor for stator #3 vs. rotational speed for a 41 Ω load at 100 μm air gap. Points represent measurements; curves represent PSpice model.

Output power vs. speed for stator #3 is shown in Figure 5-12 for a 41 Ω load. At 225 krpm, this stator demonstrates 4.55 W of power delivery at an estimated electrical system efficiency of 50.6%. Due to the 50 μm SU8 layer, the effective air gap is the same as in the stator #2 power vs. speed tests. At 210 krpm, stator #3 deliveres 4.1 W due to its smaller stator resistance, corresponding to a 58% improvement in power delivery over a 1st generation 2-turn/pole stator.

The output power vs. load resistance, at a speed of 100 krpm, is shown in Figure 5-13 and shows a peak output power at approximately 37 Ω. Stator #3 is tested again, this time with the 37 Ω load. The output power vs. speed is shown in Figure 5-14. This time the rotor is spun up to 305 krpm and delivers 8 W of DC power to the load resistor at an estimated electrical system efficiency of 49.2%. This corresponds to 16.27 W of mechanical-to-electrical power conversion. There is 7.46 W dissipated in the stator windings and 0.81 W dissipated in the transformer and diode bridge rectifier. The hysteresis loss in the stator core and the proximity eddy current loss in the stator windings are 0.37 W and 0.92 W, respectively, while the stator core eddy current loss is 12.56 W. The resulting generator system efficiency, defined in Equation (4-21) in Section 4.6.2, is only 26.6%. The power breakdown for the 8 W test is summarized in Table 5-3. For all three stators, the measured values correspond well with the PSpice model of the generator and power electronics. As in the case of the 1st generation machine testing, a contact resistance of 30 mΩ is assumed in the breadboard used for the power electronics.

The predicted electrical, η_e, and generator, η_g, system efficiencies are shown in Figure 5-15 as a function of speed. The electrical system efficiency approaches the matched load value of 50% as the speed increases because the transformer core loss and diode voltage drops become negligible with increasing speed. The generator system efficiency is much smaller than the electrical system efficiency due to the substantial eddy current loss in the stator core.

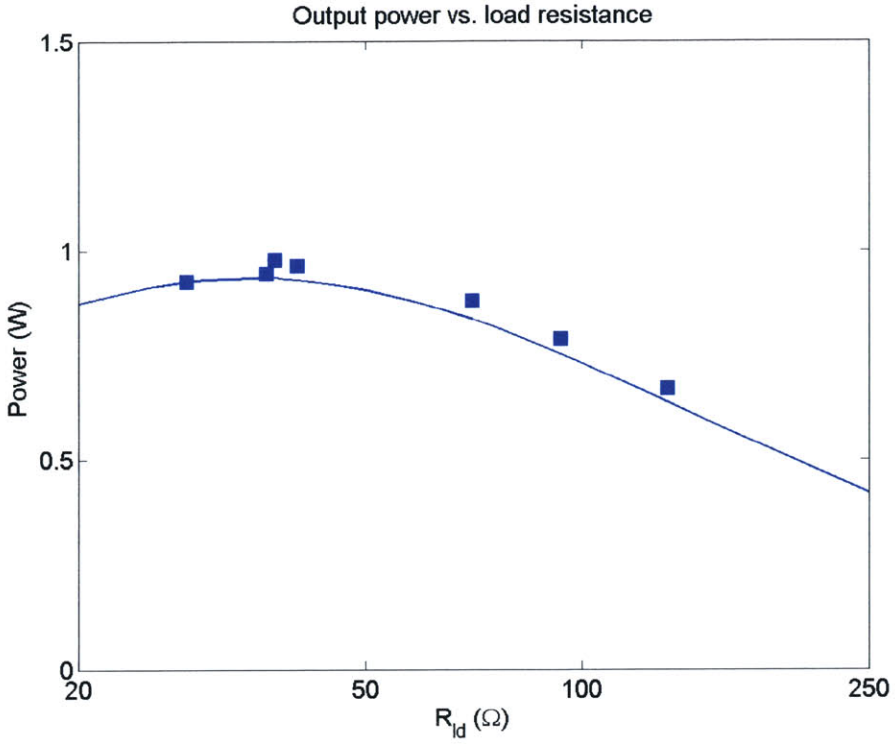

Figure 5-13: DC output power across the load resistor for stator #3 vs. load resistance at an air gap of 100 μm and a speed of 100 krpm. Points represent measurements; curves represent PSpice model.

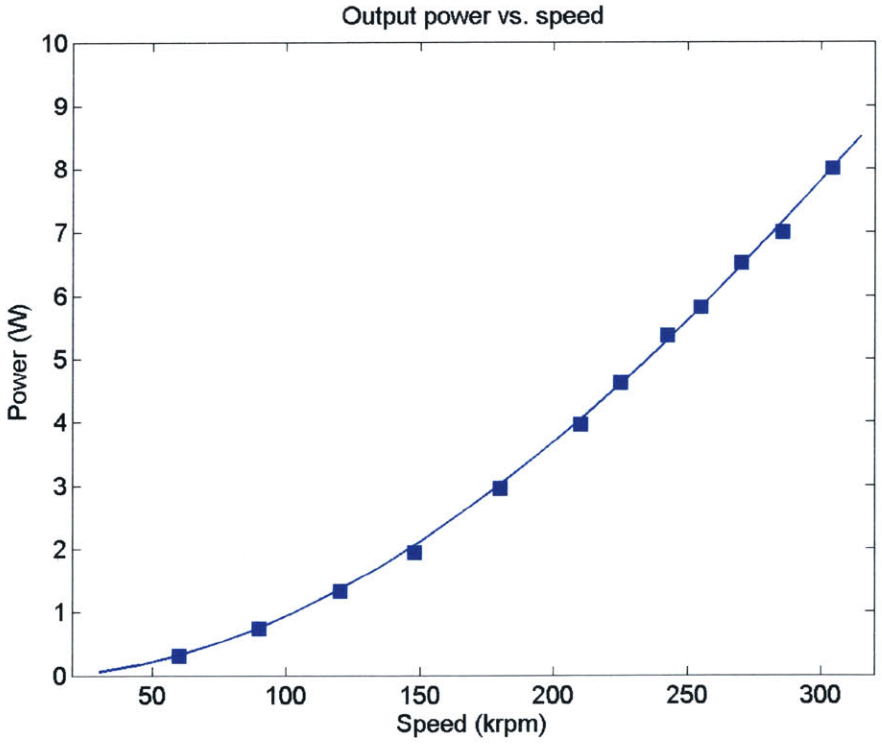

Figure 5-14: DC output power across the load resistor for stator #3 vs. speed for a 37 Ω load at a 100 μm air gap. Points represent measurements; curves represent PSpice model.

Table 5-3: Power breakdown for stator #3 at 300 krpm and a 37 Ω load.

	Stator #3
P_{mech}	30.12 W
P_{prox}	0.92 W
P_{eddy}	12.56 W
$P_{hysteresis}$	0.37 W
P_{elect}	16.27 W
P_{cond}	7.46 W
P_{pe}	0.81 W
P_{out}	8 W
η_e	49.2%
η_g	26.6%

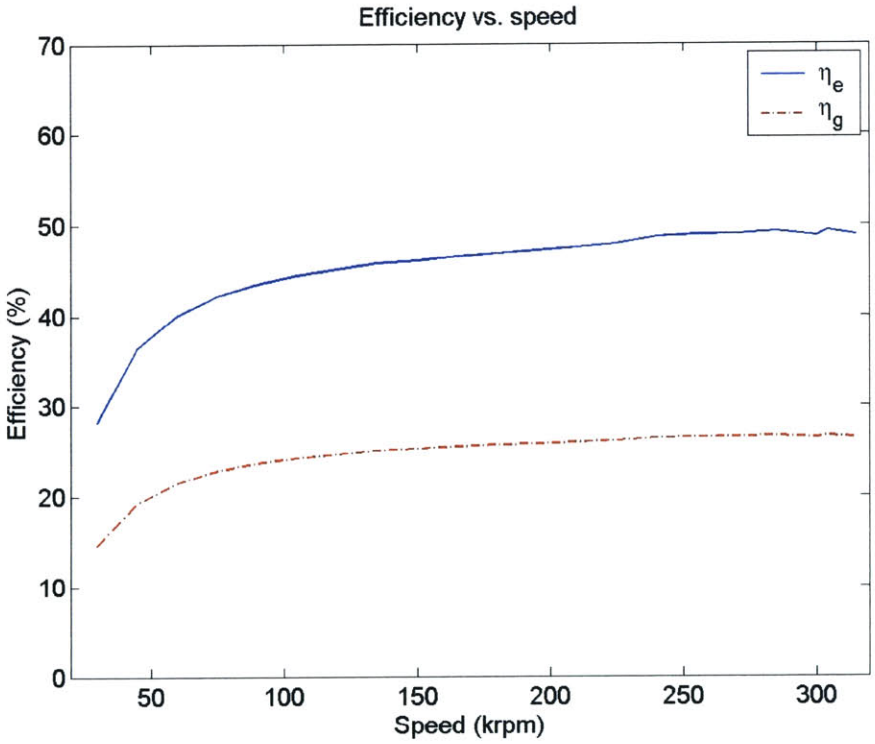

Figure 5-15: Electrical system efficiency, η_e, and generator system efficiency, η_g, for stator #3 vs. speed at a 100 μm air gap.

The power breakdown as function of load, at 300 krpm, is shown in Figure 5-16. Note that the sum of the core and proximity effect losses are larger than the output power, conduction loss and power electronics losses even at matched load conditions. Referring to Table 5-3, the dominant loss is the eddy current loss in the stator core which can be reduced significantly by using a laminated stator. The

proximity eddy current loss in the stator windings can be reduced by laminating the radial conductors. However, since the conduction loss is eight times as large as the proximity loss, it is better to leave the windings unlaminated to keep the winding resistance to a minimum.

The resulting electrical and generator system efficiencies from Figure 5-16 are plotted in Figure 5-17. At large load resistance values the electrical system efficiency reaches 80%, while the overall generator system efficiency falls due to the fixed core and proximity losses. Both η_e and η_g converge for very small values of the load resistance as conduction loss in the stator windings dominate all other losses.

At 305 krpm, stator #3 met the same fate as the other two 3-turn/pole stators. A piece of the rotor PM broke off and ripped up the coils as shown in Figure 5-18(a). The rotor assembly with the broken PM is shown in Figure 5-18(b).

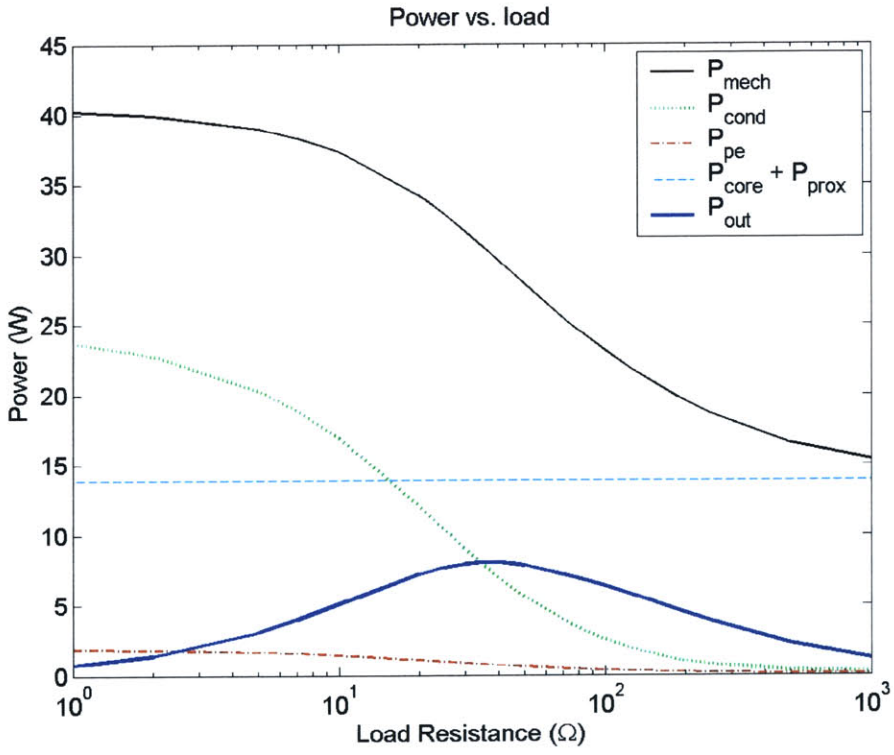

Figure 5-16: Power Breakdown for stator #3 as a function of load resistance at 300 krpm for an air gap of 100 μm.

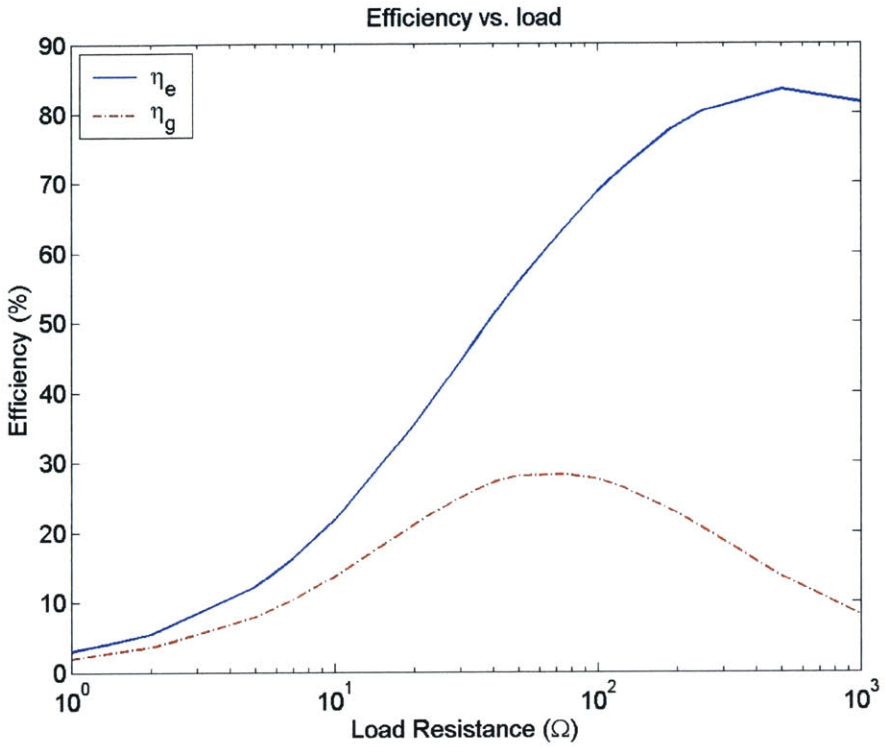

Figure 5-17: Electrical system efficiency, η_e, and generator system efficiency, η_g, for stator #3 vs. load resistance at a 100 μm air gap and 300 krpm.

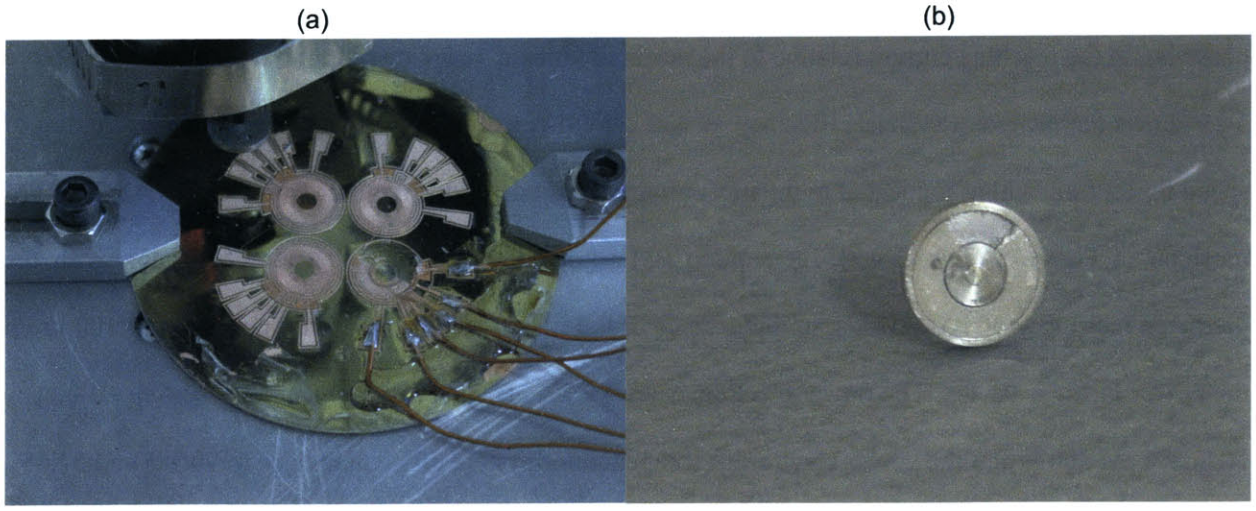

Figure 5-18: Generator destruction at 300 krpm (a) stator #3 and (b) rotor PM.

5.2 Second Generation Power Electronics

For the microengine to truly be a battery replacement it must provide a constant DC output voltage. The magnetic generators presented in the previous section all produce a three-phase AC voltage. If the microengine is to replace the BA5590, which has a 12 V DC output, then power electronics are needed to rectify and boost the AC voltages from the generator and operate under closed loop control to provide a regulated output voltage.

PM generators allow the use of both passive and active electronics to create a DC output voltage. One possible solution is to use the transformer and diode bridge rectifier presented Section 4.5 to provide the voltage step up and rectification followed by a linear regulator to provide a constant output voltage. However, passive electronics tend to be large and bulky. Transformers designed for use in the stator electrical frequency range of 10-20 kHz can be very large compared to the PM machine. The three-phase transformer in Section 4.5 is 43 mm × 25 mm × 11 mm. A stator "die" is a 23 mm square that is at most 1.2 mm thick (with the stator coils) while the stator windings themselves have a 13 mm diameter with the outer end turns included. The transformer has more than eight times the volume of the stator die. In addition, the transformer/diode bridge combination cannot provide power factor correction. Power factor correction is important at high speeds where the machine and transformer inductances will start to create a phase lag in the machine current relative to the machine voltage, reducing output power capability. Figure 5-19 shows the generator system efficiency, power electronics efficiency and power factor as function of speed for a PM machine connected to the transformer and diode bridge rectifier from Section 4.5. The PM machine in Figure 5-19 uses a 1^{st} generation PM rotor and an ideal 2^{nd} generation stator, with the predicted resistance of 100 mΩ and an inductance of 0.3 μH, at an air gap of 100 μm. At only 100 krpm the power factor is 93.4%. The power electronics are 85.7% efficient and the generator system efficiency is 46.8%. At 300 krpm, the power electronics and generator system efficiencies rise to 90.7% and 51.5%, respectively. However the power factor drops to 90% while at 500 krpm the power factor is only 82.6%. Clearly, as the speed rises, passive power electronics become a poor choice for power conversion.

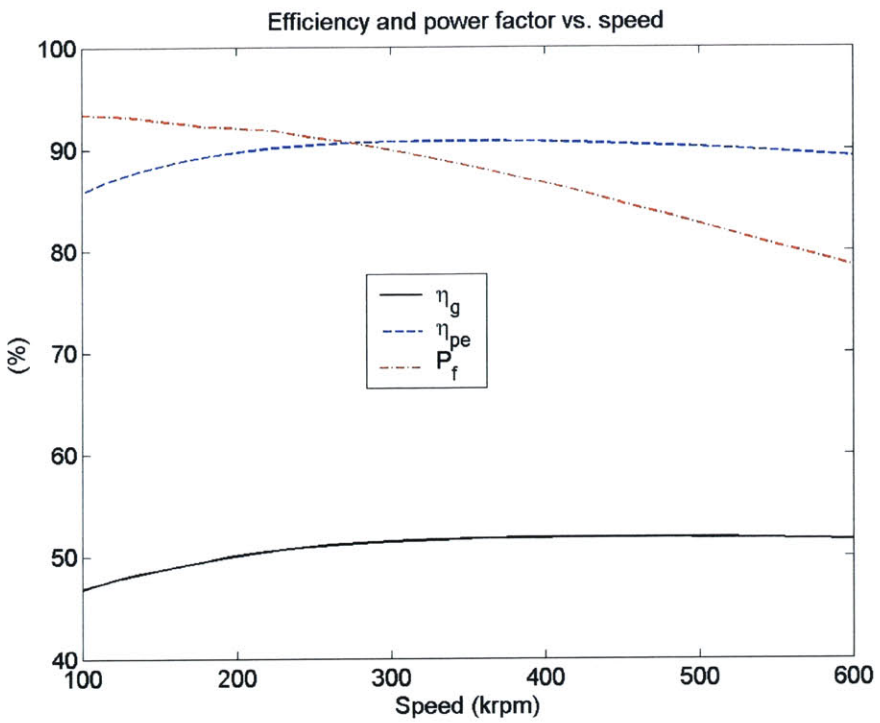

Figure 5-19: Generator system efficiency (η_g), power electronic efficiency (η_{pe}) and power factor (P_f) vs. speed for a 3-turn/pole stator connected to the transformer and diode bridge rectifier.

Additionally, using a linear regulator is a simple way to achieve output voltage regulation but they tend to be inefficient. The efficiency of a linear regulator is approximately its output voltage divided by its input voltage. To deliver maximum power the voltage across the diode bridge, at no load, needs to be more than twice the desired output voltage of the linear regulator. This is because when maximum power is being delivered, the voltage across the diode bridge will be half the no-load voltage and a linear regulator typically requires at least a 0.5 – 1 V difference between its input and output voltage to operate properly. At light loads, the linear regulator will be approximately 50% efficient. As the load increases, the voltage into the linear regulator drops and its efficiency improves, but the generator system efficiency decreases.

Switch-mode power electronics can eliminate the transformer, diode bridge and linear regulator and provide all four functions (power factor correction, rectification, voltage step-up, and regulation) in a much more compact and efficient way. Given their high rotational speed of 100,000+ rpm, microscale magnetic machines operate at electrical frequencies one to two orders of magnitude larger than typical

macroscale machines, typically in the kHz to tens of kHz range. The high operating electrical frequencies lead to smaller passive filtering components in switch-mode power electronic circuits that drive them as motors or generators. The small size of these PM machines also leads to low stator inductances. This allows for both generators and motor drive systems with fast transient responses, but also requires very high switching frequencies (hundreds of kHz to low MHz) in their associated power electronics.

Power electronics for macroscale PM machines often require speed and/or position sensing to determine the position of the magnetic poles on the rotor. This information is used to keep the stator currents in phase with the voltage to achieve maximum energy/power conversion. There are a number of ways of determining the position of the rotor. A hall effect sensor is commonly used in macroscale PM machines. However, these sensors are impractical to use in the microscale PM machines presented in this thesis not only due the complexity involved in integrating the sensor into the machine but also due to the operation temperatures (~ 300 °C).

An alternate way is to use "sensor-less" techniques to estimate the rotor position from current and terminal voltage measurements. These techniques are computationally intensive, often requiring the use of high-performance microprocessors or digital signal processors (DSP). These techniques are used in macroscale machines that spin much slower than 100,000 rpm and whose stator electrical frequencies are in the tens to hundreds of Hz. The PWM signal generated by the microprocessor or DSP is typically no higher than a few tens of kHz. Real time processing of current and voltage information to determine the proper turn-on and turn-off times of the power transistors would be difficult achieve for the high speeds in the microscale PM machines.

This section presents the design of a compact switch-mode rectifier that can provide a 12 V DC output from the microscale PM machine with near unity power factor. The rectifier operates without the need for any direct sensing of the rotor position/speed or terminal voltage/currents. The converter turns the PM machine into a current source that can be controlled with a voltage control loop implemented using an off-the-shelf pulse-width-modulated (PWM) control IC. Several topologies are first presented in Section 5.2.1 followed by their comparison in Section 5.2.2. A switch-mode rectifier based on the boost

semi-bridge topology is chosen because it is the most compact and efficient. Next, the modeling, design and control of the boost rectifier are presented in Section 5.2.3 followed by component selection in Section 5.2.4. Characterization of the switch-mode rectifier and PM generator is given in Section 5.2.5. Finally, a comparison between the switch-mode rectifier and the transformer/diode bridge circuit of Section 4.5 in terms of efficiency, power density and power factor is given in Section 5.2.6.

5.2.1 Switch-mode Rectifier Topology

Design of the rectifier is based on the following assumptions: the generator is an 8-pole, 3-turn/pole stator using the same PM used in the 1st generation machines (3.175 mm ID, 9.525 mm OD) with a stator resistance of 100 mΩ and a inductance of 0.3 – 0.5 μH. The fundamental of the open-circuit voltage in the machine is 2.5 V_{pk} at 20 kHz. The goal is to design a boost rectifier that can efficiently deliver 10 W to a load with the PM machine spinning at 300,000 rpm. The surface area taken up by the power stage of the rectifier should be no larger than 23 mm × 23 mm, which is the "die" area of the 2nd generator stator.

Switch-mode power converters for macroscale PM machines operate in continuous-conduction-mode (CCM) where the currents through the machine inductances are continuous sinusoids with small ripple at the switching frequency of the converter. The switching frequency will be proportional to the applied DC voltage, V_o, the duty ratio, D, of the PWM signal and inversely proportional to the stator inductance, L_s, and desired ripple current, $I_{ripple,pk-pk}$,

$$f_{sw} \propto \frac{V_o D}{L_s I_{ripple,pk-pk}}. \tag{5-10}$$

The output voltage is 12 V, while the stator open-circuit voltage is much smaller and is ignored for the purpose of this analysis. The machine inductance can vary from 0.3 – 0.5 μH. For a stator inductance of 0.5 μH, a duty ratio 0.5 and a desired ripple current of 1 A_{pk-pk}, the switching frequency will be 12 MHz. Such a high switching frequency is difficult to implement in PWM converters because of the small delays needed in the control circuitry. In addition, gate drive, switching transition and output capacitive losses become excessive large at these high switching frequencies.

One way to provide active rectification and eliminate the transformer and diode bridge is to use a MOSFET bridge. The output of the bridge can be connected to a CCM boost converter to provide step and regulation of the rectified voltage as shown in Figure 5-20. The MOSFET bridge switches at the stator electrical frequency. To properly gate the MOSFETs the position of the rotor is needed. Alternatively, the terminal voltages and currents can be used. This is a "sensorless" technique that is not computationally complex and requires only comparators and simple logic gates to implement. The terminal currents can be measured by making the low-side switches (Q2, Q4, Q6) current sense MOSFETs. Current sense MOSFETS, such as the Si4730EY from Vishay Siliconix (www.vishay.com), use a current mirror to measure the current through the transistor.

The MOSFET bridge is controlled so that it mimics the behavior of an ideal diode bridge. V_{an}, V_{bn} and V_{cn} are the line-to-neutral open-circuit voltages of phases A, B and C, respectively. When V_{an} is greater than zero and is greater than V_{bn} and V_{cn} MOSTEFT Q_1 is on. When V_{bn} (>0) becomes larger than V_{an} and V_{cn} then MOSFET Q_3 conducts. Only two phases have currents through them at any given time and conduct for only 2/3 of every cycle.

This rectification strategy uses the terminal voltages and currents to determine when the MOSFETS will be switched on and off. The line-to-neutral terminal voltages are V_{at}, V_{bt}, and V_{ct} and include the voltage drops due to phase resistance and inductance. Figure 5-21 illustrates a high-side switching transition and a low side switching transition. In 5-21(a) phases A and C are conducting. At some point V_{bn} will become larger than V_{an}. When this occurs the current through the machine will be as shown in Figure 5-21(b). The transition point can be determined from the terminal currents and voltages. Since there is no current in phase B before the switching transition, $V_{bn} = V_{bt}$. The open-circuit voltage of phase A can be computed from

$$V_{an} = V_{at} - \left(\sqrt{R_s^2 + \omega_e^2 L_s^2}\right) I_a = V_{at} + \left(\sqrt{R_s^2 + \omega_e^2 L_s^2}\right) I_c . \qquad (5\text{-}11)$$

The next transition will be a low-side transition and occurs when V_{an} becomes more negative than V_{cn}, at which point current will flow through phases A and B. This is illustrated in 5-21(c). There is no current

through phase A before the transition so V_{an} equals V_{at}. The open-circuit voltage of phase C is computed from

$$V_{cn} = V_{ct} - \left(\sqrt{R_s^2 + \omega_e^2 L_s^2}\right) I_c , \tag{5-12}$$

The MOSFET rectifier acts like an ideal diode bridge which conducts only 2/3 of the cycle. Using the current sensing MOSFETs can make the displacement factor close to unity. However, the partial conduction of the rectifier MOSFETs leads to higher distortion factor and lower power factor. In addition, the stator inductance creates commutation effects that create lag in the phase currents. This can negate the benefits of using the current sense MOSFETs to determine the open-circuit voltages.

The 12 V output from the CCM boost converter can be used to power the MOSFET rectifier. Since the output voltage, V_o, is much larger than the rectified voltage, V_r, low side gate drives can be used for all six MOSFETs. Current sensing of the boost current will be necessary for current-mode control of the boost converter if good dynamic response is desired. Therefore, the boost MOSFET could also be a current sensing MOSFET. This topology requires seven MOSFETs, seven gate drives and up to seven Shottky diodes. While the switching frequency of the MOSFET rectifier is low (20 kHz), the switching frequency of the boost FET must be high (~1 MHz) to keep the size of boost inductor small.

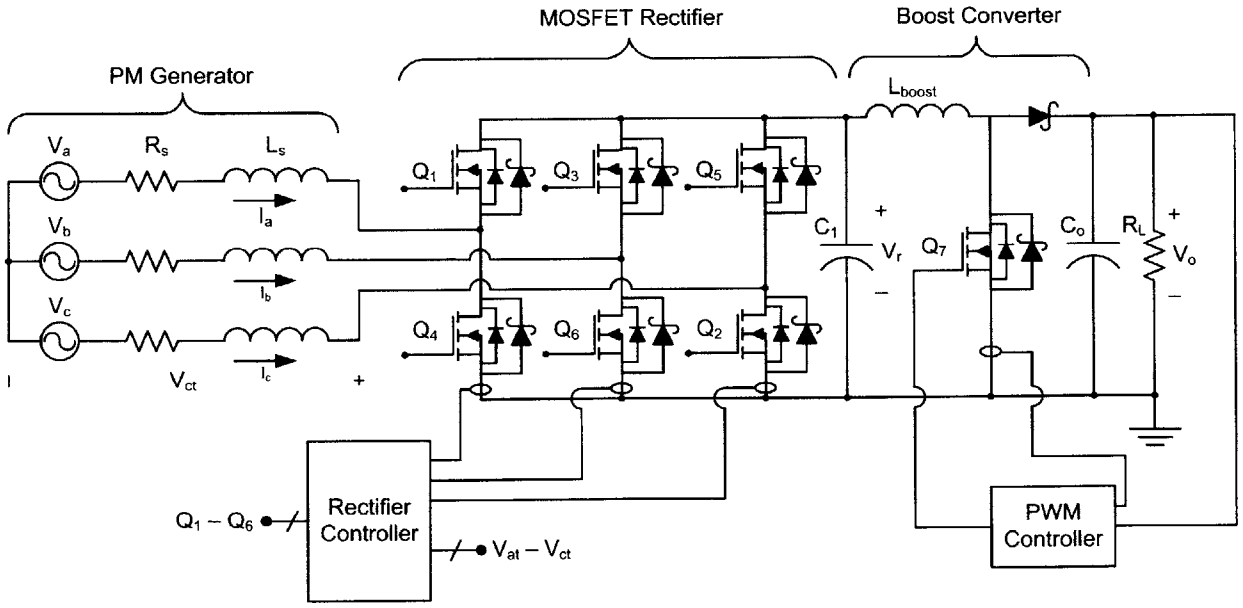

Figure 5-20: MOSFET Rectifier and CCM boost converter.

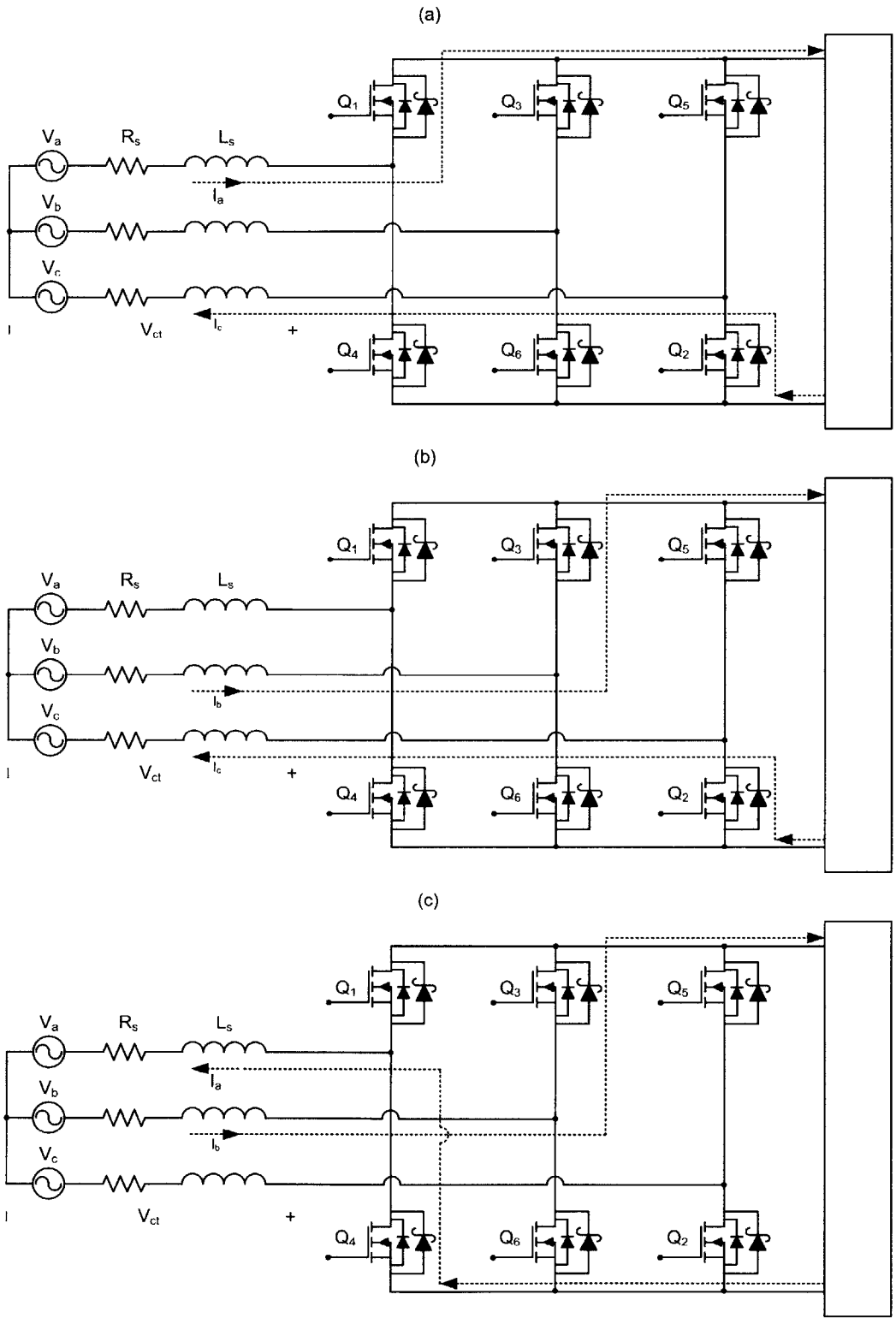

Figure 5-21: MOSFET rectifier switching sequence.

An alternative way of providing rectification and voltage step up is to operate in discontinuous-conduction-mode (DCM). In DCM, the inductor current will be discontinuous over a stator electrical period. One possible topology is the three-phase DCM boost rectifier [57-59] shown in Figure 5-22. This topology is typically used in 60 Hz line applications and provides near unity power factor and low harmonic rectification without the need for large low-frequency passive magnetic components [57]. A low-pass filter is used to attenuate the ripple current from the boost inductors so that the line voltage only sees a sinusoidal current at the line frequency. Unlike the CCM boost converter, there are no turn-on gate drive or diode reverse recovery losses. In addition the DCM converter can operate at lower switching frequencies (~500 kHz) and while there are three inductors in the DCM converter, the total volume of the magnetics is smaller. The DCM converter does have higher current stress in the switch than a CCM converter [58], which limits it application at high power levels (1+ kW) but is perfectly suitable for low power applications like the microscale PM generator where the currents are in the 2–5 A range.

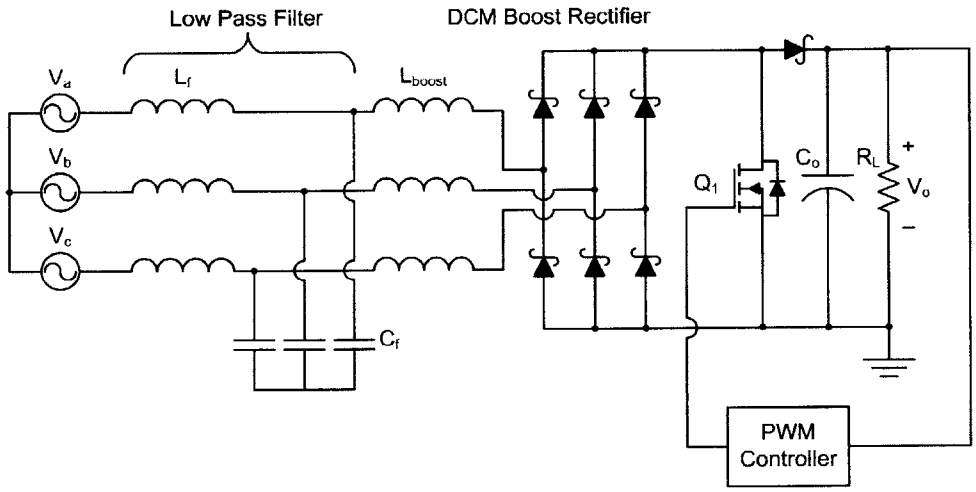

Figure 5-22: Three-phase DCM boost rectifier.

The forward voltage drops in the diode bridge are negligible in line applications where the voltages are 115 V_{rms} – 270 V_{rms} [58,59] but are substantial compared to voltages produces by the microscale PM machines. One way to overcome this is to use the MOSFET rectifier in place of the diode bridge as shown in Figure 5-23. This topology also uses seven MOSFETs and seven gate drives. The MOSFET rectifier

has partial conduction so that for 1/3 of the cycle, the phase currents conduct through the body diode or a free wheeling Schottky diode, if that is used, which leads to higher losses.

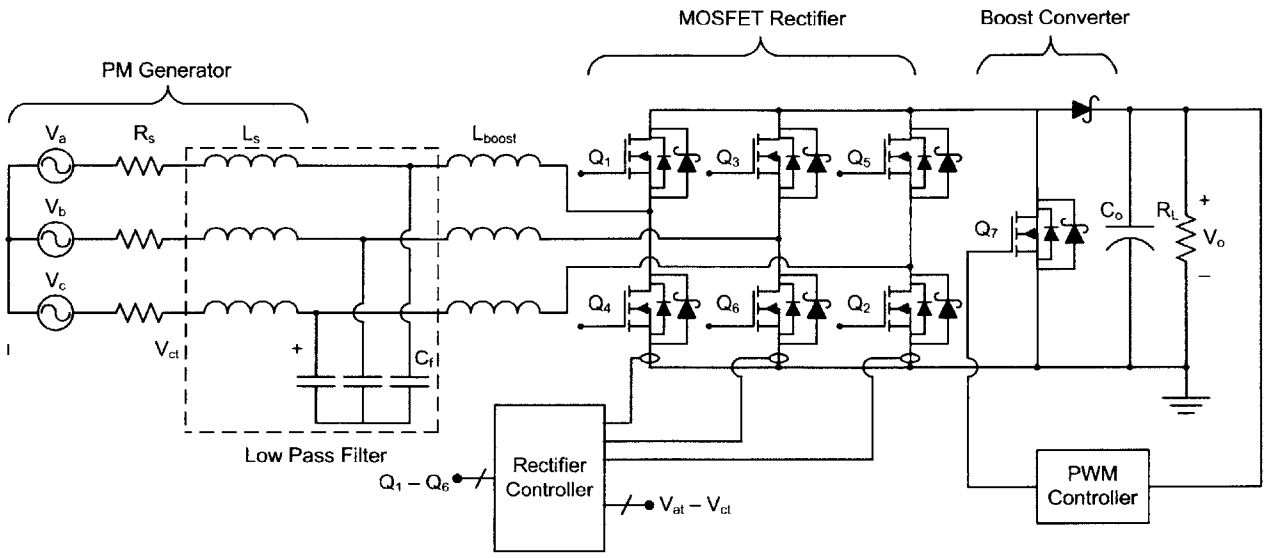

Figure 5-23: DCM boost rectifier with the diode bridge replaced by a MOSFET bridge. The machine inductance, L_s, and external capacitance, C_f, filter out switching ripple in the boost inductor currents.

The rectifier proposed for the microscale PM machine uses a variant based on the boost semi-bridge topology [60] shown in Figure 5-24. The three power MOSFETs are driven from the same control signal and are turned on/off at a constant switching frequency much higher than the stator electrical frequency. Independent control of all three phases, as well as direct position, speed, current or voltage sensing is not needed to align the stator currents with the line-to-neutral voltages due to DCM nature of circuit [60]. In addition, using three switches instead of one reduces average current stress in each switch by 30% [60]. The DCM boost rectifier using the boost semi-bridge topology uses only three MOSFETs, three gate drives and six Schottky diodes. The efficiency of this boost semi-bridge circuit can be improved by using synchronous rectification shown in Figure 5-25. When current through the boost inductor is negative the MOSFET is kept on, so that the low side free wheeling diode doesn't conduct. This can eliminate the three low side free wheeling diodes. The diode conduction loss, turn-off switching transition loss and gate drive losses are reduced by 50% because the MOSFETs are turning on and off at the switching frequency half the time. Though synchronous rectification requires current sensing, only the direction of the current

is needed. The boost MOSFETs need not be current sense MOSFETs. A small current sense resistor, level shifting amplifier and a comparator could be used instead.

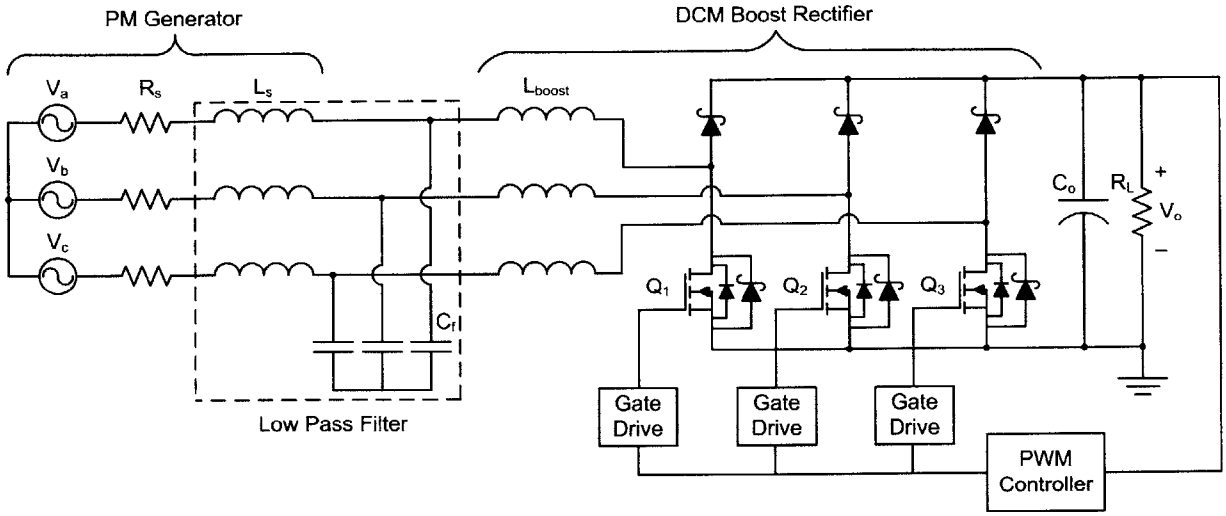

Figure 5-24: DCM rectifier based on the boost semi-bridge topology.

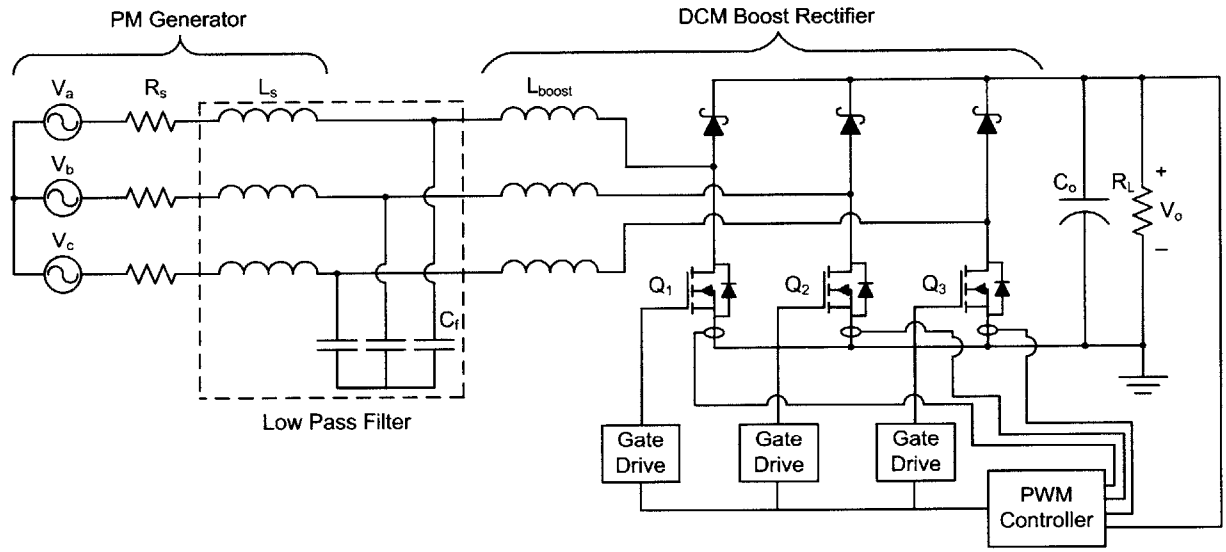

Figure 5-25: DCM rectifier using the boost semi-bridge topology with synchronous rectification.

Figure 5-26 shows the currents through the DCM boost rectifier, of Figure 5-24, and PM machine over a switching period. The voltage in phase A, V_a, is positive while the voltage on phases B and C, V_b and V_c, respectively, are negative for illustration purposes. At the beginning of each switching period the three MOSFETs are turned on and the currents through the boost inductors rise to a value proportional to

their respective open-circuit line-to-neutral voltages as shown Figure 5-26(a). The duty cycle determines the fraction of the switching period that the switches remain on and consequently the peak current in the boost inductor. When the MOSFETs are turned off the currents will flow through the diode bridge shown in Figure 5-26(b). If the current through the boost inductor is positive (phase A), then current will flow through the high side (or boost) diode. If currents are negative (phases B, C), they will flow through the free wheeling diode in parallel with the MOSFET. The current in phase A will decrease according to

$$\frac{dI_a}{dt} = \frac{1}{L_{boost}}\left(V_a - \frac{2}{3}V_o\right), \tag{5-13}$$

while the currents in phases B and C will rise according to

$$\frac{dI_b}{dt} = \frac{1}{L_{boost}}\left(V_b + \frac{1}{3}V_o\right), \tag{5-14}$$

$$\frac{dI_c}{dt} = \frac{1}{L_{boost}}\left(V_c + \frac{1}{3}V_o\right). \tag{5-15}$$

Equations (5-13) – (5-15) will hold until the current in one of the phases goes to zero, which is phase C in this example. At this point only two diodes are conducting as shown in Figure 5-26(c). The current in phase A during this portion of the switching period will decrease according to

$$\frac{dI_a}{dt} = \frac{1}{2L_{boost}}\left(V_a - V_b - V_o\right). \tag{5-16}$$

The current in phase B will rise at an equal and opposite rate of the current of phase A. In Figure 5-26(d) the currents through phase A and B return to zero before the beginning of the next switching period.

To illustrate the operation of the rectifier the boost inductor currents in the rectifier over a few switching periods are shown in Figure 5-27 while the currents in the MOSFETs and diodes are shown in Figure 5-28. The rectifier has been simulated in PSIM for its ability to easily simulate switch-mode power electronics. The currents flow from the drain to the source of the MOSFET is designated as positive while the current through the diode flows from anode to cathode which is always positive.

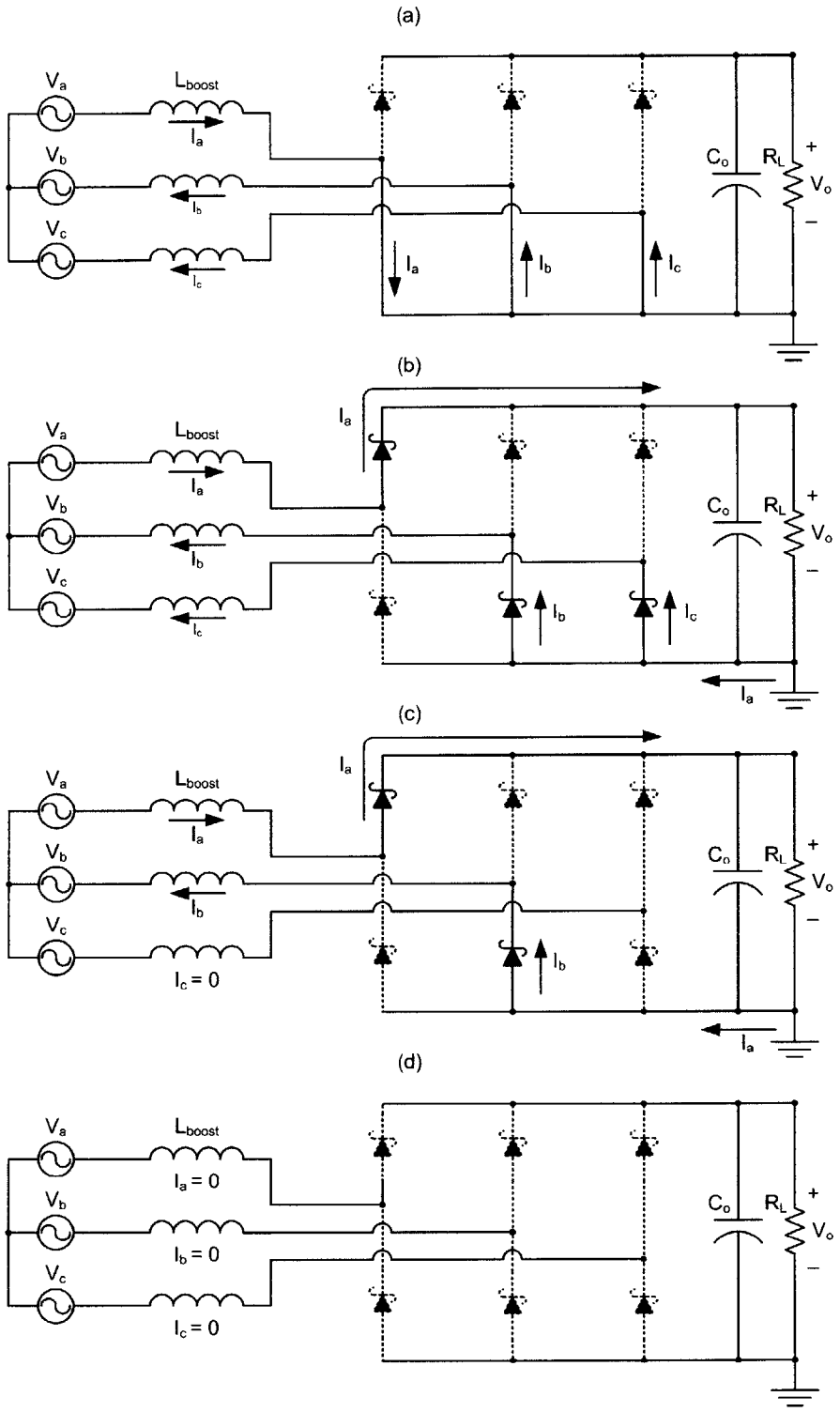

Figure 5-26: Currents through the PM machine and boost rectifier over a switching period: (a) at the beginning of the period all thee MOSFETs turn on, (b) MOSFET turn off and currents flow through diode bridge, (c) phase C current returns to zero and (d) all three phase current return to zero before the next period begins. The current through phase A is positive while the current through phases B and C are negative.

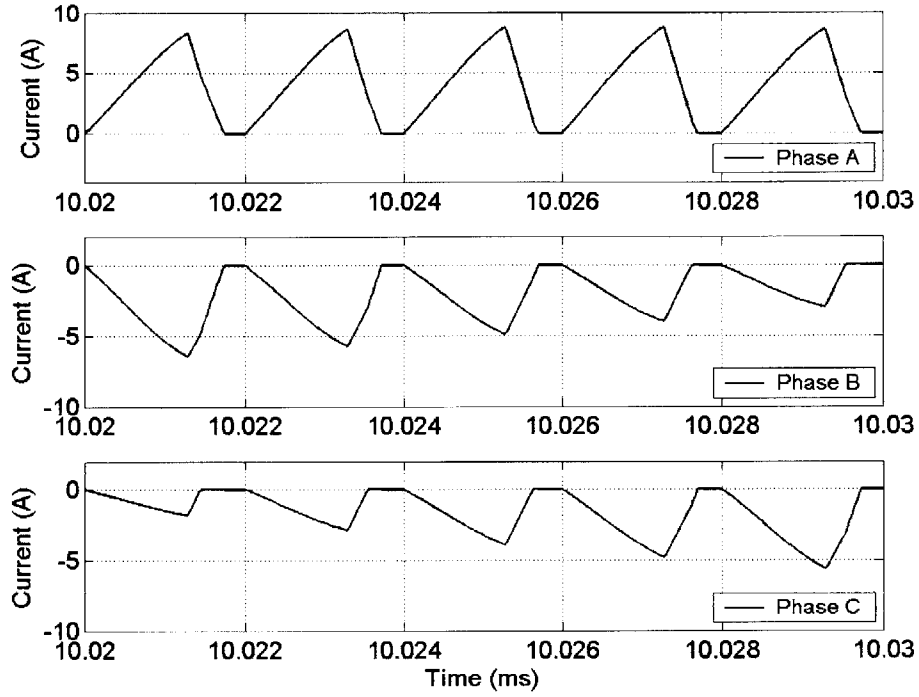

Figure 5-27: Boost inductor currents in all three phases over several switching periods corresponding to Figure 5-26.

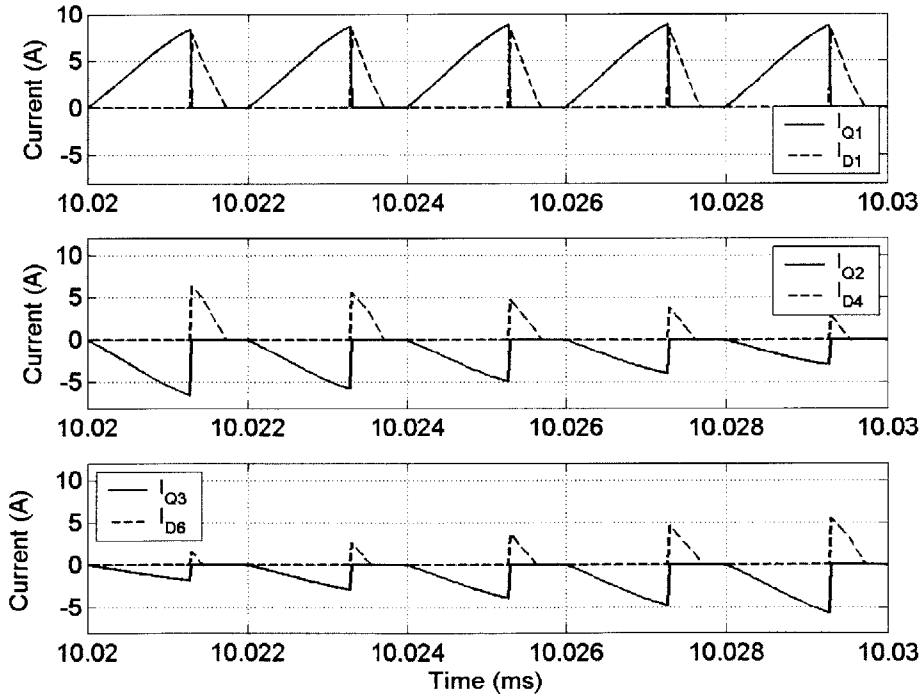

Figure 5-28: Currents through the MOSFETs and diodes over several switching periods corresponding to Figure 5-26.

The peak boost inductor current is proportional to the average value of the line-to-neutral voltage during the on time of the MOSFET. This average value varies sinusoidally. Since the current in the boost inductor returns to zero each period, the variation in the average value of the current over a switching period will also be approximately sinusoidal and will be in phase with the open-circuit voltage. The boost inductor currents have a component at the stator electrical frequency as well as a component near the switching frequency [58]. For a DC output voltage much larger than the open-circuit voltage, such as in the case for the microscale PM machines, the time it takes the boost inductor current to return to zero is much shorter than the on time of the switch. Therefore the average current over a switching period is almost independent of the output voltage leading to low harmonic distortion of the current waveform [60]. This is illustrated in Figure 5-29 which shows a PSIM simulation of the rectifier over two electrical periods of the stator. The open-circuit voltage is sinusoidal with small 3^{rd} and 5^{th} harmonic components. The boost inductor current is in phase and its envelope varies with the open-circuit voltage. The filtered current in the stator winding is mainly composed of the fundamental component of the boost inductor current. It has no 3^{rd} harmonic component because the generator is a balanced three-phase machine.

The boost inductors are separate external inductors while the machine inductance and resistance, along with an external capacitor, act as a damped low-pass LC filter. By using separate inductors, the high frequency, high ripple currents are localized on the printed circuit board to minimize electromagnetic interference (EMI). The LC filter reduces the high frequency ripple component of the boost inductor current so that the currents through the stator windings are composed mainly of a fundamental harmonic at the stator electrical frequency with a small ripple component at the switching frequency. Because the ripple component is much smaller, the RMS of the stator currents is primarily due to the fundamental harmonic. This leads to low harmonic distortion and reduced conduction loss is the stator windings. Even though the RMS currents are larger in the boost inductor, its resistance is much smaller than the stator resistance (by design) so the conduction loss in the inductor is a small fraction of the overall conduction loss.

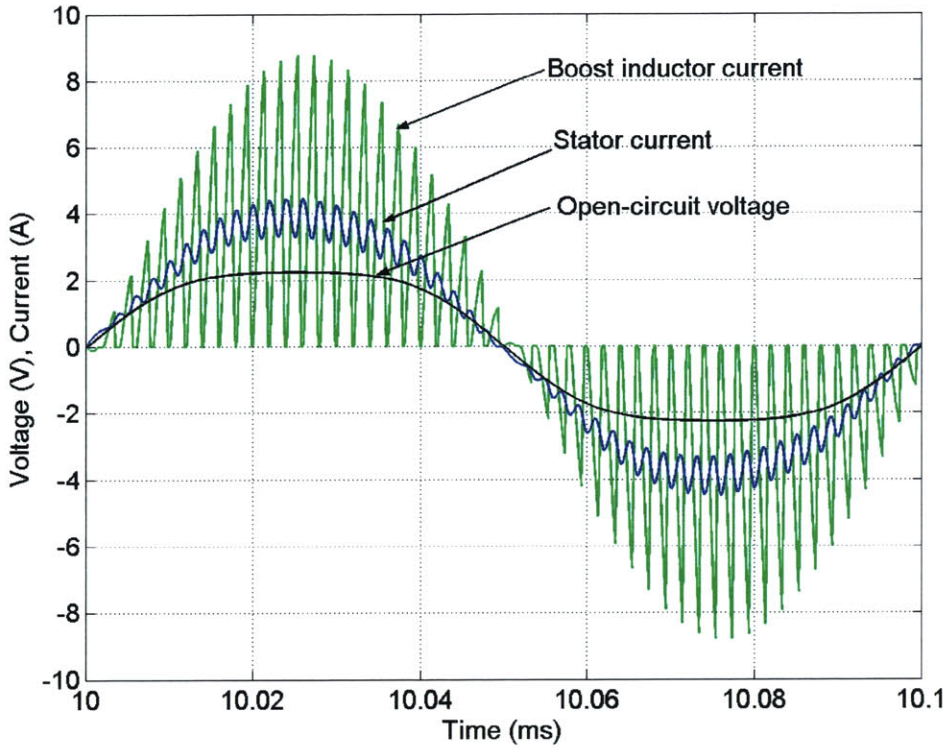

Figure 5-29: PSIM simulation of the open-circuit voltage, boost inductor current and stator current of phase A for two stator electrical periods.

In typical line applications the electrical frequency is only 60 Hz and the switching frequency is 20 – 40 kHz [57], which is thee orders of magnitude larger than the line frequency. This makes filtering the high frequency ripple current easy. In this thesis, the PM machine electrical frequency is 10 – 20 kHz. The switching frequency will be 500 – 600 kHz which is only one order of magnitude higher. This makes filtering more challenging. However, significant attenuation of the ripple is not needed. High frequency ripple currents in the stator windings produce negligible loss in the rotor and stator cores due to the large air gap of the machine. The machine acts as a surface wound induction machine with very large slip due to the huge difference between the machine speed and the switching frequencies. The ripple component and the line component have approximately the same order of magnitude. Reducing the ripple component by a factor of 5–10 means the RMS current is primarily due to the component at the stator electrical frequency since the relative contributions go as the square of the magnitudes. The high frequency ripple would only contribute 0.5 – 2 % to the RMS current and 0.25% – 4% of the stator conduction loss.

5.2.2 Topology Comparison

The four topologies considered in the last section are the MOSFET rectifier/CCM boost converter, the DCM boost MOSFET-rectifier and the DCM boost semi-bridge rectifier with and without synchronous rectification. These four topologies are simulated in PSIM which is used for its ease of implementing switch-mode power electronics with various control strategies. They are compared in terms of their power electronics efficiency, electrical system efficiency and power factor when connected to a second generation stator and delivering 10 W of power to a load resistor. The rotor PM is the same as the one used in the first generation machines since those were the only ones available at the time of this analysis. However, the choice of the rotor PM does not make a big difference when comparing the relative performance of the power electronics. The stator resistance and inductance is assumed to be 100 mΩ and 0.3 μH, respectively. The rotor stator air gap is 100 μm and the rotational speed is 300 krpm. The details of the components used and loss calculations for the rectifiers can be found in Appendix C.

For the MOSFET rectifier/CCM boost converter topology current sensing MOSFETs are used for the boost switch and the low side switches on the rectifier. The high side switches use a normal power MOSFET. The boost converter has a switching frequency of 1 MHz and uses a 1.5 μH D03316P-152 surface mount power inductor with a DC resistance of 10 mΩ from Coilcraft. The inductor core is 8.4 mm in diameter and is 5.2 mm tall for a volume of 287 mm^3 while the base is 13 mm by 9.4 mm. This topology can deliver 10 W to load at a power electronics efficiency of 78% and electrical system efficiency of 62%. The power factor for this topology is 92%. The stator current is shown in Figure 5-30. The fact that the current only conducts for 2/3 of every cycle leads to distortion in the input current waveform reducing power factor. In addition, the commutation effects of the stator inductance on the MOSFET rectifier introduce a slight phase lag that further degrades power factor.

All three DCM rectifiers switch at 500 kHz and use three 0.33 μH D01813H-331 surface mount power inductors from Coilcraft. The inductor core is 4.6 mm in diameter and is 5 mm tall while the base is 8.8 mm by 6.1 mm. The total volume of all three inductors used in the DCM rectifiers is 249 mm^3

which is smaller than the inductor used in the CCM boost converter. The DC resistance of these inductors is only 4 mΩ but at 500 kHz the resistance is 38 mΩ. The DCM boost MOSFET rectifier uses the same MOSFETs in the rectifier as the CCM converter but uses a normal power MOSFET as the boost switch. The boost semi-bridge rectifier uses only normal power MOSFETs as the boost switches. For synchronous rectification a 10 mΩ resistor is placed in series with the MOSFETs to sense the direction of the current.

Figure 5-31 shows waveforms for the boost semi-bridge rectifier. The boost inductor current is at the limit between DCM and CCM operation. The stator current and voltages are in phase as desired and the output voltage is 12 V with 60 mV of peak-to-peak ripple. Figure 5-32 shows the harmonic components of the boost inductor and stator currents. Both currents have a 20 kHz component of 4.5 A. The boost inductor current has harmonic components at 480 kHz and 520 kHz with magnitudes of 2 A and 1.82 A, respectively. The magnitudes of these harmonic components in the stator current waveforms are only 0.33 A and 0.25 A, respectively. The higher order harmonic components beyond 520 kHz in the boost inductor current are almost completely filtered out by the stator input filter. Total harmonic distortion (THD) of the stator currents is only 9.7% while the THD of the boost inductor current is 64%.

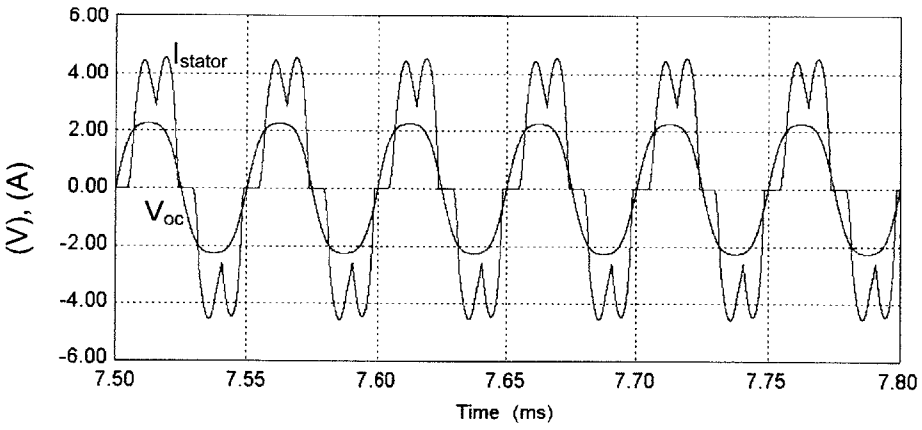

Figure 5-30: Open-circuit voltage and stator current for the MOSFET Rectifier/CCM boost converter.

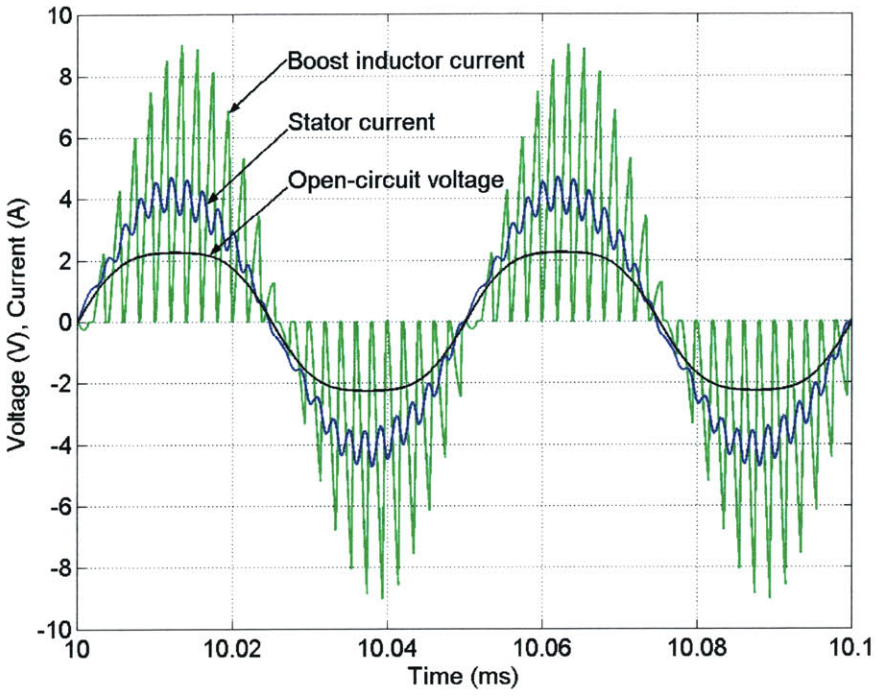

Figure 5-31: Open circuit voltage, boost inductor current and stator current for the DCM boost semi-bridge rectifier when delivering 10 W to the load at 300 krpm.

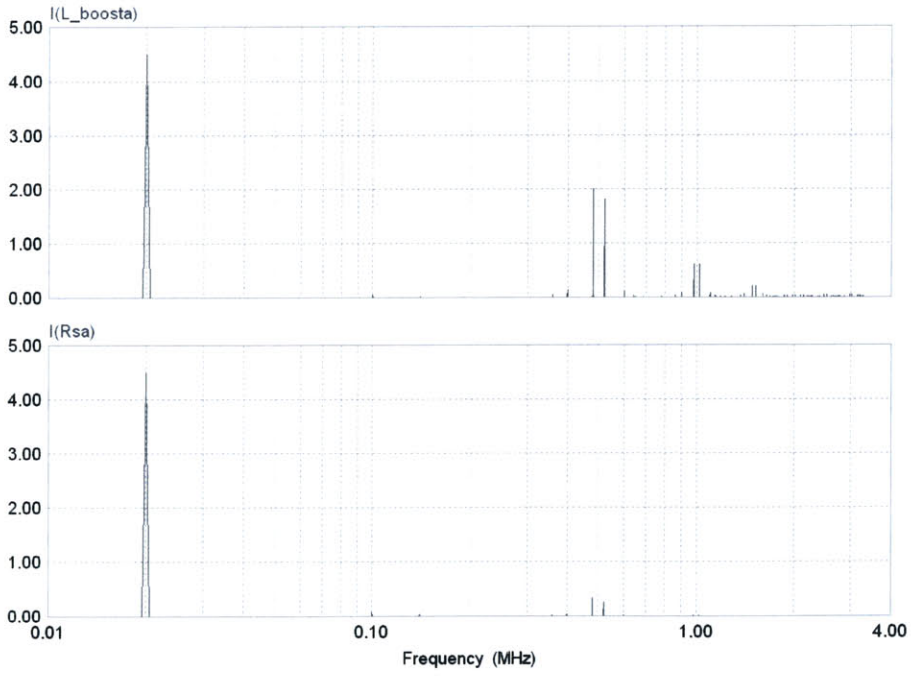

Figure 5-32: Harmonic content of boost inductor and stator currents.

As a final comparison the same 3-turn/pole generator, when connected to the transformer/diode bridge circuit, can deliver 10 W at 71.6% efficiency with the power electronics efficiency at 94.7%. This, however, is misleading. The passive circuit provides no output voltage regulation. Suppose the diode bridge is connected to a DC/DC converter that can deliver 10 W of power at 85% efficiency. This means that the power out from the diode bridge must be 11.76 W. This requires the PM machine to generate 18.318 W, of which 5.744 W is dissipated in the stator resistance. The transformer and diode bridge dissipate 0.814 W. The electrical system efficiency is 55% while the power electronics efficiency (transformer + diode bridge + DC/DC converter) is 80% efficient. In addition the power factor is only 89% while in the boost rectifier it is 99%. Table 5-4 summarizes the predicted performance of the generator with different power electronics.

For the four topologies considered the power electronics and electrical system efficiencies are very similar. The CCM boost converter uses a much larger inductor than the DCM converter and requires seven MOSFETs and gate drives. The DCM boost MOSFET rectifier also requires seven MOSFETs and gate drives. The boost semi-bridge rectifier requires only three MOSFETs and gate drives and with synchronous rectification provides the highest overall electrical system efficiency in the most compact size. At this point the two topologies using the MOSFET rectifier are no longer considered.

The breakdown of the loss in the DCM boost semi-bridge rectifier without synchronous rectification is shown in Table 5-5. The largest contributor to the loss is the conduction loss in the boost inductors. The boost inductor conduction loss is primarily due to skin effects in the thick wire used that makes the resistance at 500 kHz 34 mΩ larger than its DC value. The skin effect can be reduced by using Litz wire instead of a single thick solid wire. Table 5-6 shows the estimated performance improvements in the boost semi-bridge topology assuming the use of Litz wire were to increase the resistance by only 17 mΩ at 500 kHz. The boost semi-bridge rectifier has both its power electronics and electrical system efficiency increased by 4% to 77% and 64% respectively. With synchronous rectification the power electronics become over 80% efficient while the electrical system efficiency approaches 70%.

Table 5-4: Performance breakdown of generator system with different power electronics.

Property	MOSFET rectifier/ CCM boost converter	DCM boost MOSFET rectifier	DCM boost semi-bridge rectifier	DCM boost semi-bridge rectifier with synch. rect.	Transformer/ diode bridge/ DC-DC converter
P_{elect}	16.05 W	16.33 W	16.78 W	15.95	18.32 W
P_{cond}	3.17 W	2.91W	3.066 W	2.75 W	5.75 W
P_{pe}	2.88 W	3.42 W	3.714 W	3.2 W	2.57 W
P_{out}	10 W	10 W	10 W	10 W	10 W
η_e	78%	75%	73%	76%	80%
η_{pe}	62%	61%	60%	63%	55%
P_f	92%	98%	99%	99%	89%

Table 5-5: Loss breakdown of boost rectifier.

Loss Component	Power Loss
Boost inductor conduction loss	1.628 W
Boost inductor core loss	184 mW
MOSFET conduction loss	353 mW
MOSFET switching transition loss	198 mW
Diode conduction loss	855 mW
MOSFET & Diode capacitive losses	97 mW
Control IC & gate drives	399 mW
Total	**3.714W**

Table 5-6: Estimated performance of DCM boost semi-bridge rectifiers with Litz wire inductors.

Property	DCM boost semi-bridge rectifier	DCM boost semi-bridge rectifier with synch. rect.
P_{elect}	15.54 W	14.74 W
P_{cond}	2.59 W	2.34 W
P_{pe}	2.95 W	2.4 W
P_{out}	10 W	10 W
η_e	77%	81%
η_{pe}	64%	68%
P_f	99%	99%

The DCM boost semi-bridge rectifier with synchronous rectification using boost inductors with Litz wire would be the best choice terms of size and efficiency. However, the first switch-mode rectifier will be a DCM boost semi-bridge rectifier without synchronous rectification because its control can be easily implemented with an off-the-shelf voltage-mode PWM control IC. The implementation of the synchronous rectification and the use of Litz wire inductors is left for future work. From now on the term the DCM boost rectifier using the semi-bridge topology will be simply referred to as the boost rectifier.

5.2.3 Modeling, Design and Control

Figure 5-33 shows a simplified model of the power generation system. The input side is shown on a per-phase line-to-neutral basis. Assuming an ideal lossless converter, the power in will equal the output power

$$\frac{3}{2}V_1 I_1 = V_o I_o = P_o, \tag{5-17}$$

where, V_1 is the peak line-to-neutral voltage after the stator resistance and I_1 is the peak fundamental component of the current through a single boost inductor. The input power from the generator will be

$$\frac{3}{2}V_{oc} I_1 = \frac{3}{2}I_1^2 R_s + P_o. \tag{5-18}$$

Solving (5-18) for I_1, the required current in each phase to deliver P_o to the output is

$$I_1 = \frac{V_{oc}}{2R_s}\left(1 - \sqrt{1 - \frac{P_o}{P_{max}}}\right). \tag{5-19}$$

where,

$$P_{max} \equiv \frac{3V_{oc}^2}{8R_s}. \tag{5-20}$$

P_{max} is the power the three phase generator can deliver to a matched resistive three phase load. The input voltage to the power converter, on a line-to-neutral basis will be

$$V_1 = V_{oc} - I_1 R_s = \frac{V_{oc}}{2}\left(1 + \sqrt{1 - \frac{P_o}{P_{max}}}\right). \tag{5-21}$$

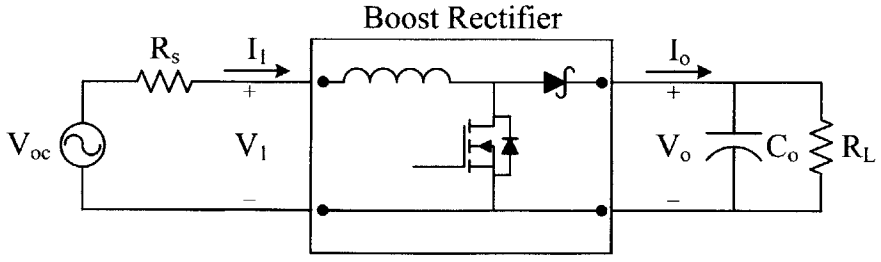

Figure 5-33: Simplified model of the boost rectifier and PM generator. The input circuit is shown on a per-phase line-to-neutral basis.

In [61] the input and output currents as a function of input voltage, output voltage, duty ratio, boost inductance and switching frequency were derived for the three-phase DCM boost rectifier. The terms in [61] are modified using the voltage after the machine resistance, V_1, rather than the input voltage, V_{oc}. The average output current for the boost rectifier is

$$I_o = \frac{1.46}{2L_{boost}f_{sw}} \frac{V_1^2 D^2}{(V_o - 1.67V_1)}. \tag{5-22}$$

The per-phase input current to the converter can be found using (5-17) and (5-22) and is equal to

$$I_1 = \frac{0.973}{2L_{boost}f_{sw}} \frac{V_o V_1 D^2}{(V_o - 1.67V_1)}. \tag{5-23}$$

To deliver 10 W at an output voltage of 12 V, I_o must be 833 mA. Under the assumptions in Section 5.2 (V_{oc} = 2.5 V, R_s = 100 mΩ) P_{max} equals 23.44 W. Using (5-21), V_1 is 2.196 V. Equation (5-22) can be used as guide to determine the desired boost inductor value and duty ratio. Rewriting (5-22),

$$\frac{L_{boost}}{D^2} = \frac{1.46}{2I_o f_{sw}} \frac{V_1^2}{(V_o - 1.67V_1)}. \tag{5-24}$$

A switching frequency of 500 kHz is chosen to minimize frequency dependent losses. Since the output voltage is much larger than the input voltage, a large duty can be chosen and still keep the boost inductor current discontinuous. A larger duty ratio typically leads to a smaller RMS value for the boost current, minimizing conduction loss. However, since the converter is not lossless, any duty ratio set by (5-24) will under predict the actual duty ratio. This is because the converter must draw extra power to overcome its own losses which it does by increasing the inductor current. The duty ratio is set to 0.5 which corresponds to a boost inductor value of 0.36 μH. The closest standard value available is 0.33 μH and the resulting nominal duty ratio is 0.57. Simulations of the boost rectifier confirm that the inductor current remains discontinuous at maximum output power.

To design a control system for the boost rectifier, a small signal model of the converter is needed. A small signal model based on the current injected equivalent circuit method was derived in [61] for the

three-phase DCM boost rectifier. To determine the small signal model parameters, the currents, voltages and duty ratio are broken into a large signal component and a small signal component,

$$\begin{aligned} V_o &= V_O + \tilde{v}_o \\ I_o &= I_O + \tilde{i}_o \\ V_1 &= V_I + \tilde{v}_1 \\ I_1 &= I_I + \tilde{i}_o \\ d &= D + \tilde{d} \end{aligned} \quad . \tag{5-25}$$

The output parameters can be found by substituting small signal perturbations into the rearranged form of (5-22),

$$(V_o - 1.67V_1)I_o = \frac{1.46}{2L_{boost}f_{sw}} V_I^2 D^2 \, . \tag{5-26}$$

The small signal output current can be written as a function of the input and output voltage and duty ratio [55]

$$\tilde{i}_o = G_2 \tilde{v}_1 + K_O \tilde{d} - \frac{\tilde{v}_o}{R_O} \, . \tag{5-27}$$

where,

$$G_2 = \left(\frac{2V_O - 1.67V_I}{V_O - 1.67V_I} \right) \frac{I_O}{V_I} \, . \tag{5-28}$$

$$K_O = \frac{2I_O}{D} \, . \tag{5-29}$$

$$R_O = \frac{V_O}{I_O} \left(1 - \frac{1.67V_I}{V_O} \right) . \tag{5-30}$$

Similarly the input parameters can be found by substituting the small signal perturbations into the rearranged form of (5-23)

$$(V_O - 1.67V_1)I_I = \frac{0.973}{2L_{boost}f_{sw}} V_O V_I D^2 \, . \tag{5-31}$$

The small signal input current can be written as a function of the input and output voltage and duty ratio [55]

$$\tilde{i}_I = G_I \tilde{v}_o + K_I \tilde{d} + \frac{\tilde{v}_o}{R_I}. \tag{5-32}$$

where,

$$G_I = \left(\frac{-1.67V_I}{V_O - 1.67V_I} \right) \frac{I_I}{V_O}. \tag{5-33}$$

$$K_I = \frac{2I_I}{D}. \tag{5-34}$$

$$R_I = \frac{V_I}{I_I} \left(1 - \frac{1.67V_O}{V_O} \right). \tag{5-35}$$

The complete small signal model is shown in Figure 5-34.

The rectifier acts like a controlled current source. This is typical of switch-mode power converters operating in discontinuous conduction mode [47]. The average output current is controlled by the duty ratio. This current is proportional to the square of the duty ratio. The transfer functions between the input voltage, duty ratio and load current can be found with the aid of the (5-27). The voltage on the output capacitor, C_o, is the only state variable so the dynamics of the converter are first order. By summing the currents at the output, the stator equation the capacitor current is the Laplace domain is

$$sC_o \tilde{v}_o = G_2 \tilde{v}_I + K_O \tilde{d} - \frac{\tilde{v}_o}{R_O} - \frac{\tilde{v}_o}{R_L} - \tilde{i}_L. \tag{5-36}$$

Rearranging (5-36), the output voltage as function of input voltage, duty ratio and perturbations in the load current is

$$\tilde{v}_o(s) = \frac{G_2 R_{eq}}{\tau_o s + 1} \tilde{v}_I + \frac{K_o R_{eq}}{\tau_o s + 1} \tilde{d} - \frac{R_{eq}}{\tau_o s + 1} \tilde{i}_L. \tag{5-37}$$

where,

$$R_{eq} = R_O \| R_L, \tag{5-38}$$

$$\tau_o = R_{eq} C_o. \tag{5-39}$$

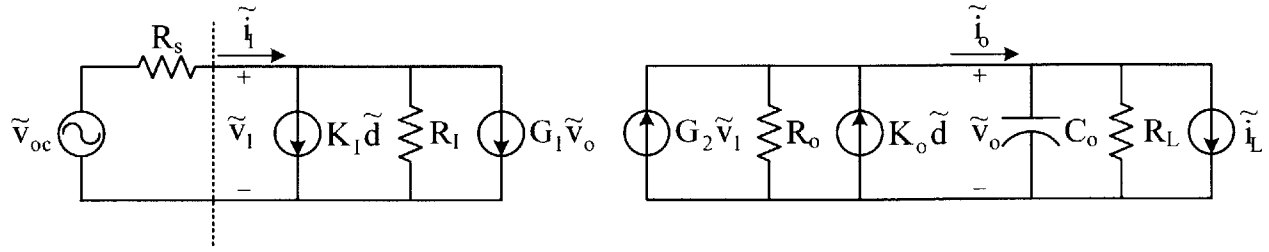

Figure 5-34: Small signal model for DCM boost rectifier. Input circuit is on a per-phase line-to-neutral basis.

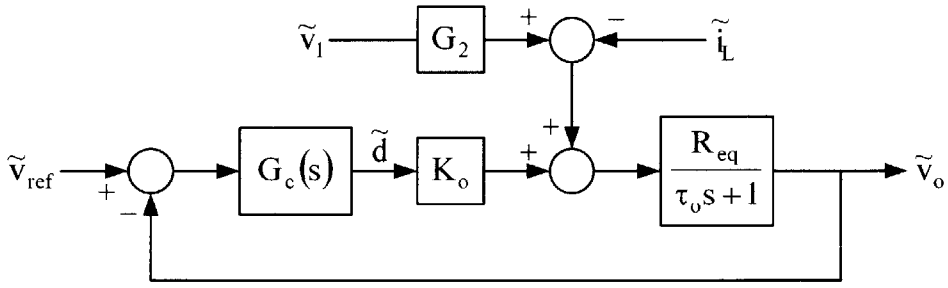

Figure 5-35: Control system block diagram for boost rectifier.

An outer voltage control loop is used to control the duty ratio to regulate the output voltage as shown in Figure 5-35. The rectifier is placed in a feedback loop in which the difference between output voltage and reference voltage is sent to a compensator $G_c(s)$. The output of the compensator determines the duty ratio of the converter. A proportional plus integral (PI) compensator is used

$$G_c(s)=\frac{K_c(\tau_c s+1)}{s}. \tag{5-40}$$

The closed-loop transfer function from the reference to output voltage is

$$\frac{\tilde{v}_o}{v_{ref}}(s)=M(s)=\frac{K_c K_o R_{eq}(\tau_c s+1)}{\tau_o s^2+(1+K_c K_o R_{eq}\tau_c)s+K_c K_o R_{eq}}. \tag{5-41}$$

Equation (5-41) can be rearranged and put into the standard second order model form [62]

$$M(s)=\frac{\left(\frac{K_c K_o}{C_o}\right)(\tau_c s+1)}{s^2+\left(\frac{1}{\tau_o}+\frac{K_c K_o \tau_c}{C_o}\right)s+\left(\frac{K_c K_o}{C_o}\right)}=\frac{\omega_n^2(\tau_c s+1)}{s^2+2\zeta\omega_n s+\omega_n^2}, \tag{5-42}$$

where

$$\omega_n^2 = \left(\frac{K_c K_o}{C_o}\right), \tag{5-43}$$

$$\zeta = \frac{1}{2}\left(\frac{1}{\tau_o \omega_n} + \omega_n \tau_c\right). \tag{5-44}$$

The closed loop bandwidth of the converter can be found by calculating at what frequency the magnitude of M(jω) is equal to 0.7071. After some algebraic manipulation the, closed loop bandwidth is

$$\omega_h = \omega_n\left(\upsilon - 2\zeta^2 + \sqrt{1 - 4\zeta^2\upsilon + \upsilon^2 + 4\zeta^4}\right), \tag{5-45}$$

where,

$$\upsilon = 1 + (\tau_c \omega_n)^2. \tag{5-46}$$

The following compensator is chosen to provide a closed loop bandwidth of 20 kHz with 83° of phase margin,

$$G_c(s) = \frac{20000\left(4.4 \times 10^{-5} s + 1\right)}{s}. \tag{5-47}$$

The bode plots for the loop transmission, L(jω), defined as the open loop transfer function from V_{ref} to V_o, and M(jω), the closed loop transfer function from V_{ref} to V_o, is shown in Figure 5-36. A 7.5 W – 10 W – 7.5 W load step is shown in Figure 5-37. The peak over/undershoot of the output voltage is ~60 mV with a settling time of 1.5 ms. The inductor current changes rapidly to bring the output voltage back to 12 V.

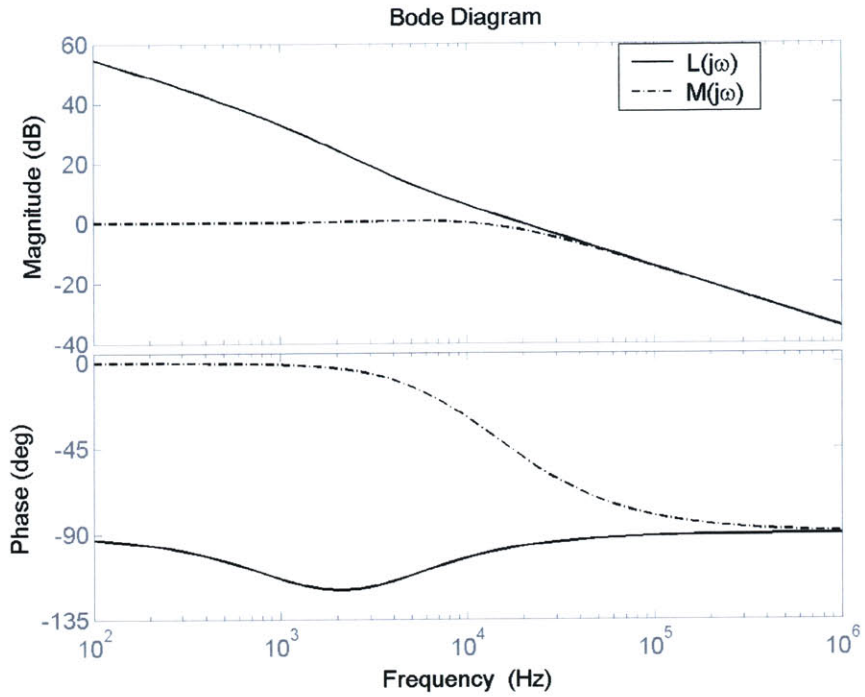

Figure 5-36: Bode plot of open loop and closed loop transfer functions L(jω) and M(jω) from V_{ref} to V_o.

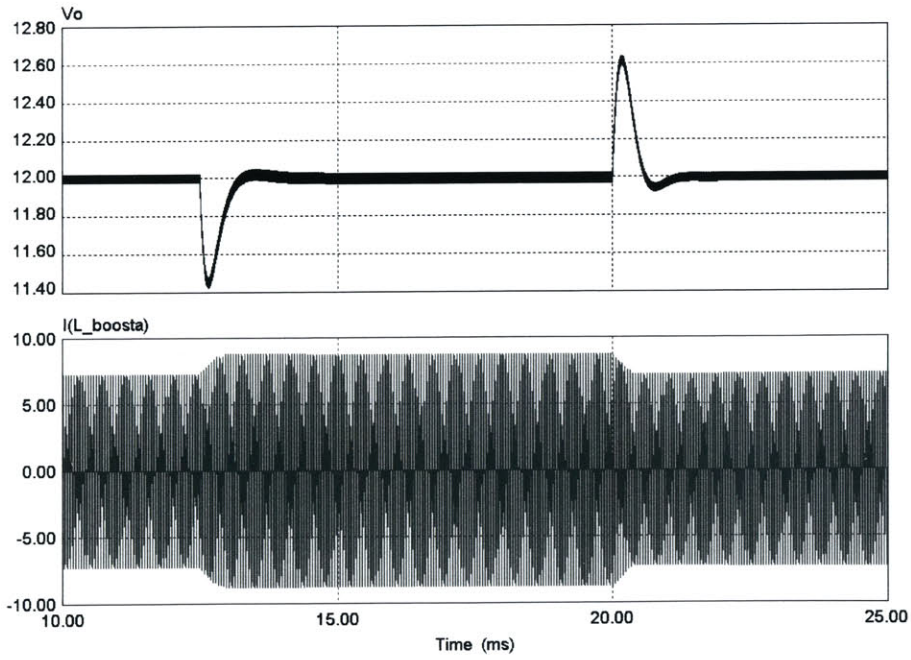

Figure 5-37: Transient response of the output voltage and boost inductor current during a 7.5 W – 10 W – 7.5 W load step.

The interaction between the input filter and the closed loop converter can change the transient response of the closed loop system and may even make the system unstable. The output impedance of the input filter affects the control-to-output and line-to-output transfer functions. If the unity gain cross over frequency of the loop transfer function is greater than or equal to the resonant frequency of the input filter then instability can occur if the output impedance of the filter is larger than the input impedance of the rectifier. To determine the effects of the input filter on the closed loop system, the Middlebrook Extra Element Theorem is used [55]. The theorem determines how a transfer function is modified by the addition of external impedances to a network without having to solve the system all over again.

The control-to-output transfer function without the input filter is

$$G_{vd}(s)=\frac{\tilde{v}_o}{\tilde{d}}(s)\bigg|_{\tilde{v}_1=0}=\frac{K_O R_{eq}}{\tau_o s+1}, \tag{5-48}$$

while the line-to-output transfer function is

$$\frac{\tilde{v}_o}{\tilde{v}_1}(s)\bigg|_{\tilde{d}=0}=\frac{G_2 R_{eq}}{\tau_o s+1}. \tag{5-49}$$

Using the Middlebrook Extra Element Theorem, the control-to-output transfer function with the input filter present is [55]

$$G_{vd}(s)=G_{vd}(s)\big|_{Z_o=0}\left(\frac{1+\frac{Z_o}{Z_N}}{1+\frac{Z_o}{Z_D}}\right). \tag{5-50}$$

The term outside the parentheses is the control-to-output transfer function when there is no input filter and is given in (5-48). Z_o is the output impedance of the input filter. The small signal input circuit in Figure 5-38 is on a line-to-neutral basis. The filter capacitors, C_f, are connected in a Δ configuration. The equivalent line-to-neutral filter capacitance, C_s, can be found by converting the Δ-connected capacitors into their equivalent wye configuration values. The line to neutral capacitance C_s will be $3C_f$. The output impedance of the input filter is then

$$Z_o(s) = \frac{R_s + L_s s}{1 + R_s C_s s + L_s C_s s^2}. \tag{5-51}$$

The converter input impedance under the condition that the perturbations in the duty cycle is zero, Z_D, is

$$Z_D(s) = Z_i(s)\big|_{\tilde{d}=0}. \tag{5-52}$$

Figure 5-39(a) shows the small signal model of the converter with the perturbations in the duty ratio equal to zero. A test current is applied to the input circuit. The output current is

$$\tilde{i}_o = G_2 \tilde{v}_t. \tag{5-53}$$

The output voltage will be

$$\tilde{v}_o(s) = G_2 Z_L \tilde{v}_t = \frac{G_2 R_{eq}}{\tau_o s + 1} \tilde{v}_t. \tag{5-54}$$

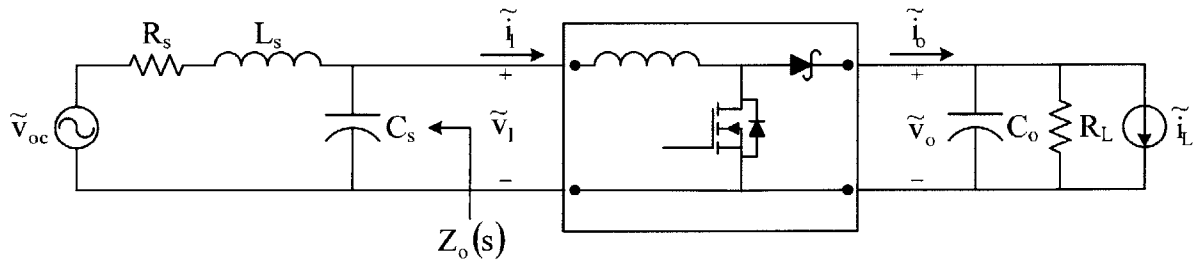

Figure 5-38: Small signal model of boost rectifier showing equivalent line-to-neutral input filter with output impedance $Z_o(s)$.

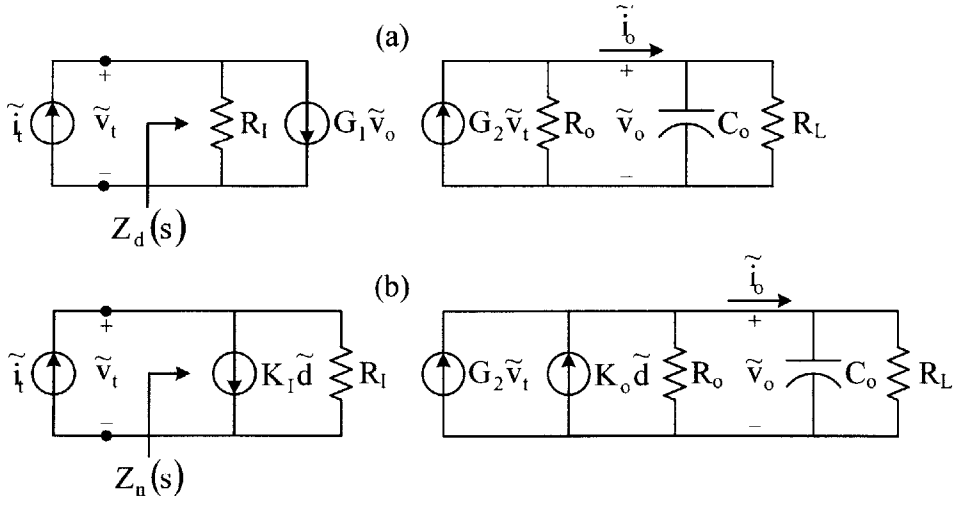

Figure 5-39: Small signal model of boost rectifier with (a) perturbations in duty cycle = 0 for calculating $Z_D(s)$ and (b) perturbations in the output voltage → 0 for calculating $Z_N(s)$.

The test current will equal the sum of the current through the input resistor, R_I, and the current source G_1,

$$\tilde{i}_t = \frac{\tilde{v}_t}{R_I} + G_1 G_2 Z_L \tilde{v}_t . \tag{5-55}$$

The resulting input impedance is

$$Z_D(s) = \frac{\tilde{v}_t}{\tilde{i}_t} = \frac{R_I}{1 + G_1 G_2 Z_L R_I} . \tag{5-56}$$

After some algebraic manipulation (5-56) can be written as

$$Z_D(s) = \frac{V_1}{I_1} \frac{(\tau_o s + 1)}{(\tau_1 s + 1)} . \tag{5-57}$$

where,

$$\tau_1 = \frac{R_I^2}{R_I + R_o} C_o . \tag{5-58}$$

The impedance, Z_N, is the input impedance of the rectifier under the assumption that the perturbation in the output voltage go to zero,

$$Z_N(s) = Z_i(s)\big|_{\tilde{v}_o \to 0} . \tag{5-59}$$

This is impedance of the converter under perfect control in which the duty cycle is varied such that the output voltage is held constant [55]. It can be found with the aid of Figure 5-39(b). A test current is again applied to the input circuit of the boost rectifier. If the perturbation in the output voltage is zero then the small signal output current must also go to zero. The current sourced by the duty ratio must exactly cancel out the output current generated by the input voltage through G_1. Under these conditions the duty ratio is

$$\tilde{d} = -\frac{G_2}{K_o} \tilde{v}_t . \tag{5-60}$$

The input current will equal the sum of the current through the input resistance and the current from the duty ratio current source,

$$\tilde{i}_t = -\frac{K_I G_2}{K_o} \tilde{v}_t + \frac{\tilde{v}_t}{R_I} . \tag{5-61}$$

The resulting input impedance is

$$Z_N(s) = \frac{\tilde{v}_t}{\tilde{i}_t} = -\frac{K_o R_I}{K_I R_I G_2 - K_o}. \tag{5-62}$$

After extensive algebraic manipulation (5-62) can be written as

$$Z_N(s) = -\frac{V_1}{I_1}. \tag{5-63}$$

In order for the input filter to have a negligible effect on the system transfer functions, the magnitude of Z_o should be much smaller than the magnitudes of Z_N and Z_D. Figure 5-40 plot Z_N, Z_D and Z_o from 100 Hz to 25 kHz. The stator (input filter) inductance is 0.3 μH. A filter capacitance of 0.83 μF is chosen to attenuate the boost inductor ripple current by a factor of six while keeping the resonant frequency of the filter (184 kHz) high enough so that it introduces little phase shift at 20 kHz. The unity gain cross over frequency of loop transmission $L(s) = G_c(s)G_{vd}(s)$ is 19 kHz. Up to this frequency the impedance of the input filter has negligible affect on the control-to-output and line-to-output transfer functions as desired.

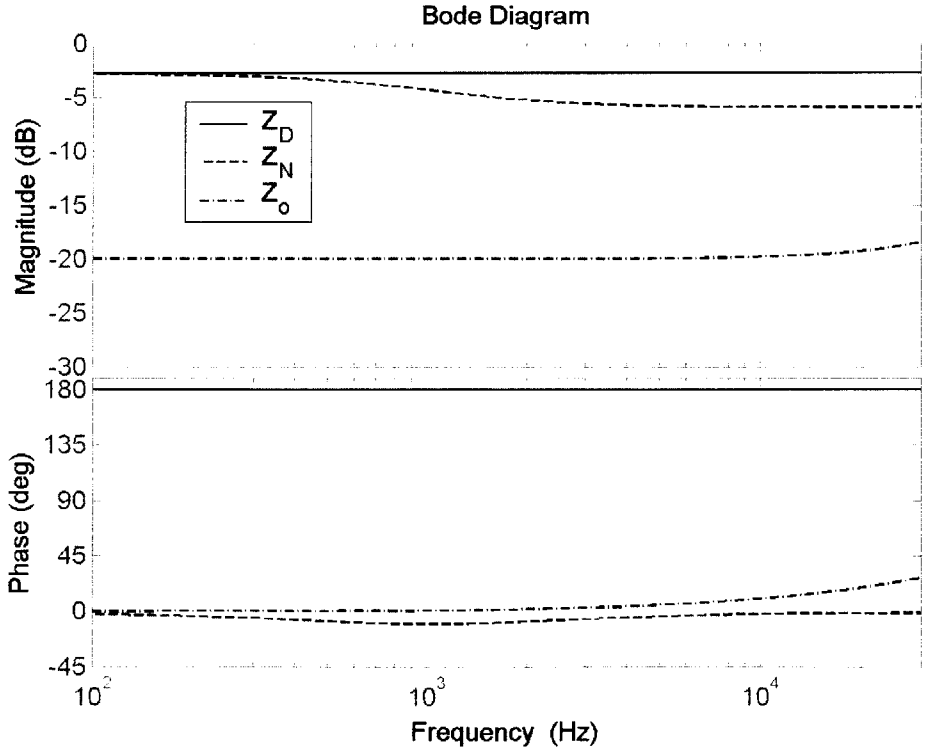

Figure 5-40: Bode plot of Z_D, Z_N and Z_o.

5.2.4 Component Selection

This section describes the components used in the DCM boost rectifier. The complete circuit schematic of the rectifier is shown in Figure 5-41. The list of components used in the rectifier is shown in Table 5-7. The control section of the rectifier is discussed first followed by the power stage component selection. A standard off-the-shelf voltage-mode PWM control IC is used the boost rectifier. A simple SPICE macro-model for the PWM controller has been found [63] so that the boost rectifier can be modeled in PSpice. This is done because PSIM does not model switching or capacitive losses in the MOSFET or diodes. For the rectifier comparison in Section 5.2.2 these losses were computed using analytical models in Appendix C but required some iteration in the simulations. The iteration was acceptable only because a single output power was simulated.

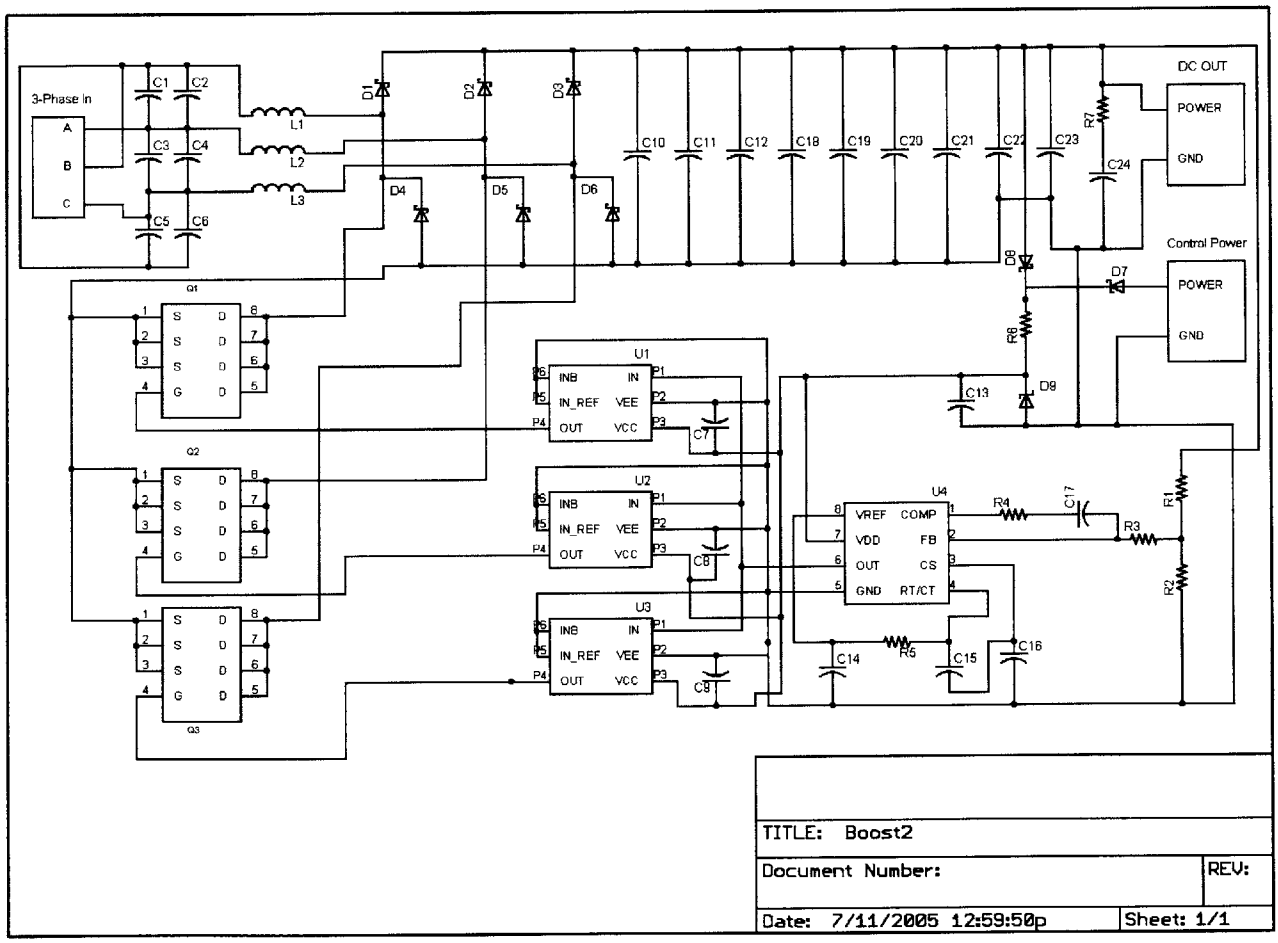

Figure 5-41: Circuit schematic of DCM boost rectifier.

Table 5-7: Boost Rectifier Components.

Component	Value	Part Number	Description
R_1	91 kΩ		1/10W 0.1% 0805 SMD
R_2	24 kΩ		1/10W 0.1% 0805 SMD
R_3	8.87 kΩ		1/8W 1% 0805 SMD
R_4	7.87 kΩ		1/8W 1% 0805 SMD
R_5	3.9 kΩ		1/8W 1% 0805 SMD
R_6	10 Ω		1/8W 1% 0805 SMD
R_7	15 Ω		1/8W 1% 0805 SMD
C_1, C_3, C_5	0.68 µF		CERAMIC 10% 25V X5R 0805
C_2, C_4, C_6	0.15 µF		CERAMIC 10% 25V X7R 0805
$C_7 - C_{12}$	0.47 µF		CERAMIC 10% 25V X7R 0805
C_{13}	1 µF		CERAMIC 10% 25V X5R 0805
C_{14}	0.1 µF		CERAMIC 10% 50V X7R 0805
C_{15}	1200 pF		CERAMIC 10% 50V X7R 0805
C_{16}	2200 pF		CERAMIC 10% 50V X7R 0805
C_{17}	5600 pF		CERAMIC 10% 50V X7R 0805
C_{18}, C_{19}, C_{20}	4.7 µF		CERAMIC 10% 25V X5R 1206
C_{21}, C_{22}, C_{23}	2.2 µF		CERAMIC 10% 25V X5R 1206
C_{24}	33 µF		TANTALUM 16V 10% SMD
L_1, L_2, L_3	0.33 µH	DO1813H-331	SMD Power Inductor, 10 A I_{sat}, 7 A I_{rms}
$D_1 - D_6$		DFLS130L	30V 1A SCHOTTKY DIODE POWERDI123
D_7, D_8		B0520WS	20V 200MW SCHOTTKY DIODE SOD-323
D_8		1N4743A	13V 1W ZENER DIODE 5% DO-41
Q_1, Q_2, Q_3		IRF7413Z	30 V 13 A MOSFET SO-8
U_1, U_2, U_3		LM5112	14.5 V 3A/7A GATE DRIVE LLP-6
U_4		UCC28C40	PWM CONTROL IC 8-MSOP

5.2.4.1 Control Section

The control section of the boost rectifier is shown in Figure 5-42. It consists of one active circuit, the UCC28C40 (U_4) and various passive components. The UCC28C40 (Texas Instruments) is a current mode control IC that comes in a MSOP-8 package that is 3.05 mm × 3.05 mm (5 mm with pins) and is 1 mm high. It is intended for high frequency power supplies for 12 V systems and has a maximum switching frequency of 1 MHz. The maximum rated supply voltage for the control IC is 20 V. It can starts up from a minimum supply voltage of 7 V and its under voltage lockout (UVLO) is 6.6 V, which means that once the converter is running, the control IC shuts off when its supply voltage is at 6.6 V rather than at 7 V.

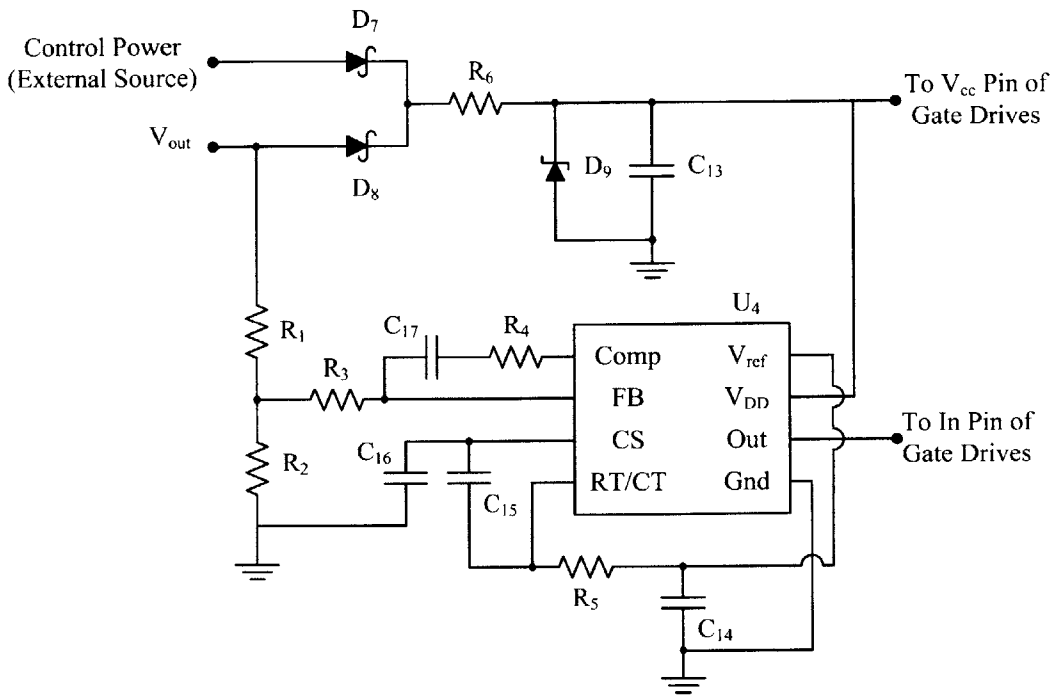

Figure 5-42: Boost rectifier control section.

The UCC28C40's error amplifier has 90 dB of DC gain and a gain-bandwidth product (GBW) of 1.5 MHz (typical values). The FB pin is the inverting input to the error amplifier while the non-inverting input is connected to a 2.5 V reference. The reference voltage is accurate to ±2% over its operating temperature range of –40 °C to 105 °C. The Comp pin is the output of the error amplifier. The 12 V output voltage is divided down to match the 2.5 V reference using R_1 and R_2, which are 91 kΩ and 24 kΩ, respectively, with a tolerance of 0.1%. The voltage across R_2 is fed to the compensation network consisting of R_3, R_4 and C_{17}. R_3 and R_4 are 8.87 kΩ and 7.87 kΩ, respectively, and have 1% tolerance. C_{17} is 5600 pF ceramic capacitor with 10% tolerance. The network implements the following PI compensator transfer function

$$G_c(s) = \frac{20000\left(4.4\times10^{-5}s+1\right)}{s}. \tag{5-64}$$

The V_{ref} pin is a 5 V reference that is used to charge up a time capacitor through the timing resistor, R_5. The timing capacitor charges up to 3 V at which point an internal current sink of 8.4 mA discharges the capacitor through the RT/CT pin. When the voltage drops down to 0.7 V, the current sink turns off

and C_T is charged up again. The CS pin is the current sense signal pin and is connected to the non-inverting input of the PWM comparator. To use the UCC28C40 as a voltage-mode controller, a 0 – 1 V saw tooth ramp needs to be fed into the CS pin [64]. This ramp voltage is compared to the output of the error amplifier to determine the duty ratio of the output pulses. This ramp can be generated by using a fraction of the C_T ramp voltage. This is implemented by a capacitive voltage divider through timing capacitors C_{15} and C_{16} which are 1200 pF and 2200 pF, respectively. C_{16} will have 35% of the total voltage across the two capacitors and the peak ramp voltage will be 1.06 V. The equivalent timing capacitance is 776 pF. From the UCC28C40 data sheet, to generate a 500 kHz switching frequency with a timing capacitance of 776 pF, a 3.9 kΩ resistor is needed. This timing resistance is bypassed with a 0.1 μF capacitor (C_{14}) to ground.

The operating supply current at 500 kHz is 4 mA. At a supply voltage (VDD) of 12 V, the control IC only consumes 48 mW of power, far below the maximum power dissipation rating of the MSOP-8 package of 350 mW. The IC's junction-to-ambient thermal resistance, θ_{ja}, is 269 °C/W, leading to a modest 13 °C rise in the junction temperature above the ambient temperature at maximum power dissipation.

The control IC (and gate drives) can be powered either from an external power supply through D_7 or from the output voltage through D_8. To start up the converter, an external supply raises the V_{DD} pin to 7 V, at which point the converter turns on and starts to bring up the output voltage. When the output voltage becomes larger than the external supply voltage, the converter powers itself up to 12 V. D_7 and D_8 are 200 mW, 20 V B0520WS Schottky diodes from Diodes Inc. and provide an OR-ing function for the two power sources. If self-sustained operation is not desired, then D8 can be removed and the external power source can be set to 12 V. The sense resistor, R_6, is used to measure the power consumed by the control IC and gate drives and has a value of 10 Ω. A 1 μF capacitor (C_{13}) is used for supply bypassing of the UCC28C40's V_{DD} pin. D_9 is a 13 V Zener diode and is used to clamp the supply voltage to protect the gate drives, which are rated to 14 V, from over voltage transients.

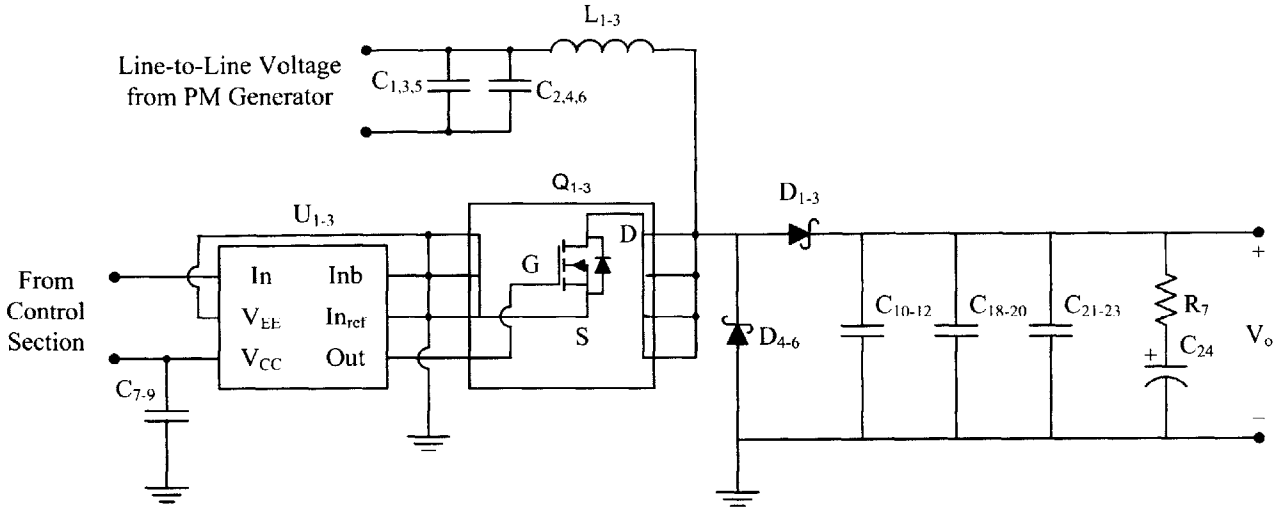

Figure 5-43: Boost rectifier power stage.

5.2.4.2 Power Stage

A single phase of the rectifier's power stage is shown in Figure 5-43. The only exception is the damping leg composed of R_7 and C_{24} of which there is only one. The passive components (L, C, D) and their losses, are discussed first. Next the gate drive (U_1 – U_3) selection is presented followed by the selection and loss calculation of the power MOSFETs (Q_1 – Q_3).

Boost Inductors

A 0.33 μH inductor was chosen in Section 5.2.3. Using the model derived in that section the peak current in the boost inductor will be

$$I_{pk} = \frac{V_1 D}{L_{boost} f_{sw}} = 7.6A\,. \tag{5-65}$$

The corresponding RMS current through the boost inductor is 3.8 A which is found from the simulation model. The D01813H-331 from Coilcraft is a 0.33 μH (±20% tolerance) surface mount power inductor designed for high current applications. It is chosen as the boost inductor due to its high saturation (10 A) and RMS (7 A) current ratings, small size and its easy availability. The inductor is essentially a small ferrite core wrapped with a few turns of thick wire and has a self resonance frequency of 600 MHz. The inductor is 5.84 mm by 6.1 mm and 5 mm high (8.89 mm with end connections).

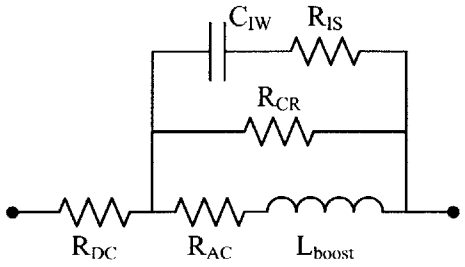

Figure 5-44: Equivalent circuit of boost inductor.

The equivalent circuit model for the inductor is shown in Figure 5-44. The SPICE model for the D01813H-331 is available from www.Coilcraft.com. The DC resistance of the inductor, R_{DC}, is only 4 mΩ while the interwinding capacitance, C_{IW}, and the isolation resistance, R_{IS}, are 14 pF and 50 kΩ, respectively. The AC resistance, R_{AC}, core resistance, R_{CR}, and high frequency inductance (in μH), L_{boost}, can be found using

$$R_{AC}(f_{sw}) = K_1\sqrt{f_{sw}}, \tag{5-66}$$

$$R_{CR}(f_{sw}) = K_2\sqrt{f_{sw}}, \tag{5-67}$$

$$L_{boost}(f_{sw}) = K_3 - K_4\log(K_5 f_{sw}), \tag{5-68}$$

where $K_1 = 4.85\times10^{-5}$, $K_2 = 0.146$, $K_3 = 0.33$, $K_4 = 7.96\times10^{-3}$ and $K_5 = 1.02\times10^{-5}$. At a switching frequency of 500 kHz, $R_{AC} = 34$ mΩ, $R_C = 104$ Ω and $L_{boost} = 0.324$ μH. The AC resistance of the inductor windings is substantially larger than the DC resistance and contributes a significant amount of loss in the inductor. This is expected due to the thickness of the wire used. In the future, the single thick wire can be replaced by multiple thinner wires, or even Litz wire, to reduce skin effect.

Input/Output filter capacitors

The input filter capacitors are composed of a 0.68 μF capacitor (C_1, C_3, C_5) in parallel with a 0.15 μF (C_1, C_3, C_5) for a total filter capacitance of 0.83 μF. This value is chosen because the filter attenuates the boost inductor ripple current by a factor of six while keeping its resonant frequency (184 kHz) high enough so that it introduces little phase shift at 20 kHz. The two capacitors come in EIA 0805 packages.

In order to have no more than 100 mV of peak-to-peak ripple voltage on the output voltage at an output power of 10 W, the output filter capacitance, C_o, needs to be at least 20 μF. Multilayer ceramic capacitors are used for filtering and bypassing. The output filter capacitor is made up of multiple 0.47 μF ($C_{10} - C_{12}$), 4.7 μF ($C_{18} - C_{20}$) and 2.2 μF ($C_{21} - C_{23}$) capacitors rather than a single 22 μF capacitor (closest standard value to 20 μF). This is to improve the high frequency behavior of the filter capacitance by using multiple capacitors with a high self resonant frequency (SRF). The 2.2 and 4.7 μF capacitors come in an EIA 1206 package with an equivalent series inductance (ESL) of 1.1 – 1.4 nH [65]. The SRF of these capacitors is 2 – 3.2 MHz. The 0.47 μF capacitors come in an EIA 0805 package with an ESL of 0.6 – 0.9 nH and a SRF of 7.7 – 9.5 MHz. Using multiple capacitors also allows them to be placed near the three power stages of the boost rectifier. This is important because the power stage handles high frequency switch currents which are sourced and sinked by the output filter capacitors.

Damping Leg

The compensator transfer function is designed using a small signal model of the rectifier assuming maximum output power operating conditions. The load and operating conditions can wide vary. A smaller load corresponds to a larger load resistance as well as a larger output resistance of the rectifier. This moves the pole in the transfer function inward reducing phase margin and causes the transient response to a load step to exhibit oscillatory behavior. To prevent this oscillatory response a damping leg, consisting of a 15 Ω resistor (R_7) and a 33 μF tantalum capacitor (C_{24}), is used. From a transient point of view the damping leg looks like a 17 Ω load (15 Ω + 2 Ω capacitor ESR) but does not dissipate any DC power.

Diode Bridge

The diodes used in the bridge ($D_1 - D_6$) are 30 V, 1 A DFLS130L surface mount Schottky diode from Diodes Inc. These diodes have very low forward voltages and junction capacitances. The forward voltage is only 0.36 V with 1.5 A through the diode and the total capacitance is 70 pF at a reverse voltage of 12 V. Each comes in a PowerDi123 package that is 3 mm long, 2 mm wide, and 1 mm high and is capable of dissipating 556 mW of power. The SPICE model for the DFLS130L can be found at www.diodes.com.

Gate Drives

The LM5112 gate driver IC from National semiconductor (U_1 – U_3) is used to drive the power MOSFETS and comes in a leadless LLP-6 (SOT-23) package that is 3 mm × 3mm and 0.8 mm high. The gate drive has both an inverting (INB) and non-inverting (IN) input. Since the inverting input is not needed it is tied to ground. The LM5112 has two separate ground connections, one for the input (IN_{REF}) and one for the output (V_{EE}). This allows the input signal to be ground referenced while the gate drive can be pulled down to a voltage below ground by making V_{EE} negative. Since this feature is not necessary for the boost rectifier, both INREFF and V_{EE} are tied to ground.

The gate drive is capable of sourcing 3 A and sinking 7 A with a propagation delay of 25 ns. The output resistance of the gate drive is 30 Ω when sourcing current and 1.4 Ω when sinking current. Asymmetric current source/sink capability is desired. The gate drive for the MOSFET typically includes an external resistor to limit the rise time of the gate-to-source voltage, V_{gs}. This is done to reduce EMI. The external resistor also prevents oscillations in the MOSFET gate voltage due to interaction between the input capacitance of the MOSFET and any parasitic trace inductance between the driver and the FET. The external resistor adds extra dissipation in the gate drive circuit. It also increases the turn-on transition time which increases the turn-on switching transition loss. However, because the rectifier operates in discontinuous conduction mode, the boost inductor current starts at zero at the beginning of every cycle. There is no turn-on transition loss so a slow turn-on of the MOSFET is not a problem. The high output resistance of the gate drive when sourcing current eliminates the need for an external resistor, saving board space. There will be a turn-off transition loss as the current in the boost inductor transitions from the flowing through the power MOSFET to the high side diode. Reducing the turn-off transition time will minimize this loss. The high current sink capability and low output resistance allows the MOSFET to turn of quickly, minimizing the turn-off transition loss. Note that when the boost inductor current is negative, current switches from the power MOSFET to the free wheeling diode. Since the drain to source voltage of the MOSFET is equal to the forward voltage of the Schottky diode (~0.4 V), the turn-off transition loss is much lower than when the current is positive.

The gate drive can operate from a 3.5 – 14 V supply. A 0.47 μF multilayer ceramic capacitor (C_7 – C_9) is used for supply bypassing due to its small ESR and ESL. The input supply current is 1 mA (2 mA max). Gate drive loss is equal to the sum of the quiescent power lost, the power consumed charging and discharging the gate of the MOSFET and the transient loss in the gate drive which occurs when the output switches state,

$$P_{gd} = V_{gd} I_q + V_{gd} Q_g f_{sw} + 0.889 Q_g f_{sw} . \tag{5-69}$$

V_{gd} is the gate drive voltage (either the output voltage or 10 – 12 V from an external supply). Q_g is the total gate charge on the MOSFET when $V_{gs} = V_{gd}$. The total gate charge required to put a certain voltage across the gate and source is usually specified because the input capacitance is nonlinear [66]. It is 14 nC at V_{gs} = 10 V and 16.3 nC at V_{gs} = 12 V for the MOSFETs used.

Power MOSFET

The IRF7413Z (Q_1 – Q_3) from International Rectifier is a 30 V, 13 A power MOSFET intended for notebook processor power applications. It comes in an SOIC-8 package that is 5 mm long, 4 mm wide (6 mm with pins) and 1.75 mm high. The maximum power dissipation is 2.5 W at 25 °C and 1.6 W at 70 °C. The IRF7413Z has a maximum on-state resistance, $R_{ds,on}$, of 10 mΩ at a gate-to-source voltage of 10 V at 25 °C. The on-state resistance will vary with temperature. From the IRF7413Z data sheet this dependence is approximately

$$R_{ds,on}(T) = R_{ds,on}\big|_{25^\circ C}\left[1 + 0.00385(T - 25)\right]. \tag{5-70}$$

The maximum RMS current through the MOSFET will be 4 A at 10W. The junction-to-ambient thermal resistivity, θ_{ja}, of the SOIC-8 package is 50 °C/W. At an ambient temperature of 40 °C, the junction temperature of the MOSFET will be 48.8 °C the on state resistance will be 11 mΩ and the power dissipation will be 176 mW. The gate drives will be powered from the 12 V output voltage. Since $R_{ds,on}$ decreases with increasing V_{gs}, the actual resistance of the MOSFET will be less than 11 mΩ even at maximum power dissipation. The SPICE model for the IRF7413Z is available at www.irf.com.

5.2.5 Boost Rectifier Characterization

This section presents the characterization of the DCM boost rectifier with the components specified in Section 5.2.4. The rectifier is shown in Figure 5-45 along with a 3-turn/pole stator for size comparison. The rectifier power stage is 24 mm × 22.5 mm and has about the same surface area as the stator die. The PCB is 1.6 mm thick and most of the components are 1.75 mm in height or less with the boost inductors being 5 mm tall. The output filter capacitors and free wheeling diodes are placed on the bottom side of the power stage. The control section is only 11 mm × 10 mm. The size of the control section could be made smaller by using EIA 0603 size packages for all the passives. This is not done in the first pass due to the difficulty of soldering such small components.

The boost rectifier is first tested with a 1st generation 2-turn/pole stator that has a phase resistance of 220 mΩ to verify its operation. The control section is powered from an external 12 V source. Figure 5-46 shows the boost inductor current, stator current and open-circuit voltage at a speed of 150 krpm. Both the boost inductor and stator currents are in phase with the open-circuit voltage, verifying that the converter works properly. The converter delivers 0.85 W to a load resistor. Figure 5-47 shows the boost inductor current, V_{ds} of Q_1 and the output voltage over a couple of switching periods. The ringing in the drain-to-source voltage and the inductor current is due to the LC tank created by the boost inductor and the output capacitance of Q_1. The output voltage also exhibits ringing when the MOSFET turns on and off. However, the magnitude is much smaller than the ringing on V_{ds} due to the output filter capacitor, C_o.

The next step in characterizing the boost rectifier is to check that the output voltage of the converter can power the control electronics to produce self-sustained operation. The converter is loaded with a series combination of 6 LEDs (2 blue, 2 white and 2 red). The generator is spun up to 150 krpm. A 9 V battery is connected temporarily to the control power terminal block. The converter can power itself to 12 V almost instantaneously. The test setup for this demonstration is shown in Figure 5-48. Since the LEDS have a small viewing angle, Figure 5-49 shows the test setup from the top to bettor show the brightness of LEDs. The control section of the rectifier consumes 0.48 W of power. This is 20% larger than predicted

but it not surprising. In computing the gate drive losses, typical values for gate charge from the data sheet is used. If the maximum gate charge value is used then the gate drives alone would consume 0.52 W so the measured control power is well within the range.

The converter is then connected to the second-generation stator #3, with the large PM, to first characterize the power stage of boost rectifier in terms of its input stator current, efficiency and power factor as function of speed and load. An external 12 V supply is used to power the control circuitry. After the power stage is characterized the boost rectifier is spun at high speeds to deliver Watt-level power at a regulated output voltage. A nitrogen tank that can provide more than 100 psi is used to spin the rotor to speeds in excess of 300 krpm. All tests are done at an air gap of 100 μm.

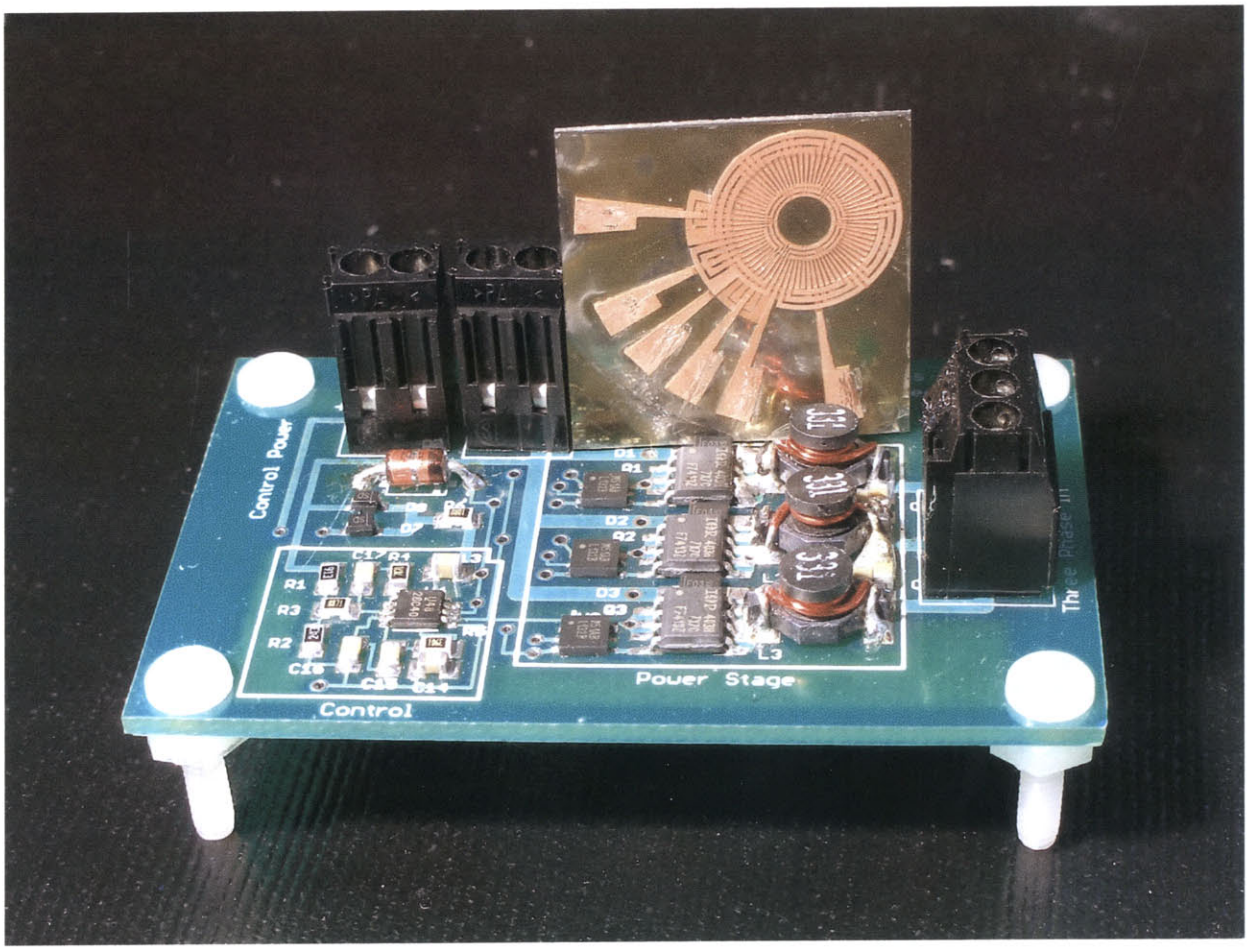

Figure 5-45: Boost rectifier board shown with the 3-turn stator for size comparison.

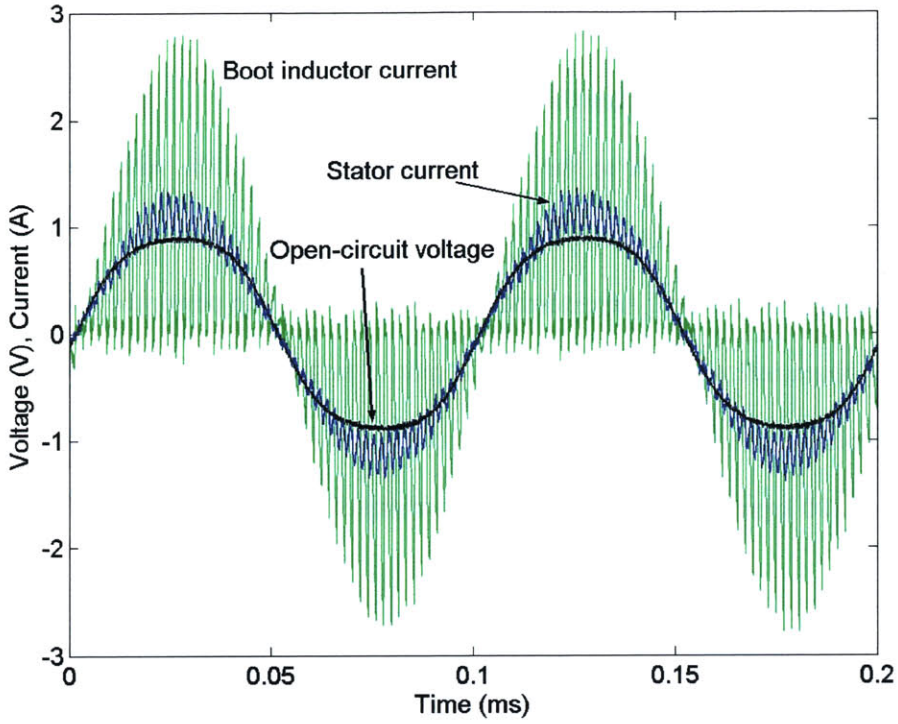

Figure 5-46: Boost rectifier waveforms over two stator electrical periods at generator speed of 150 krpm.

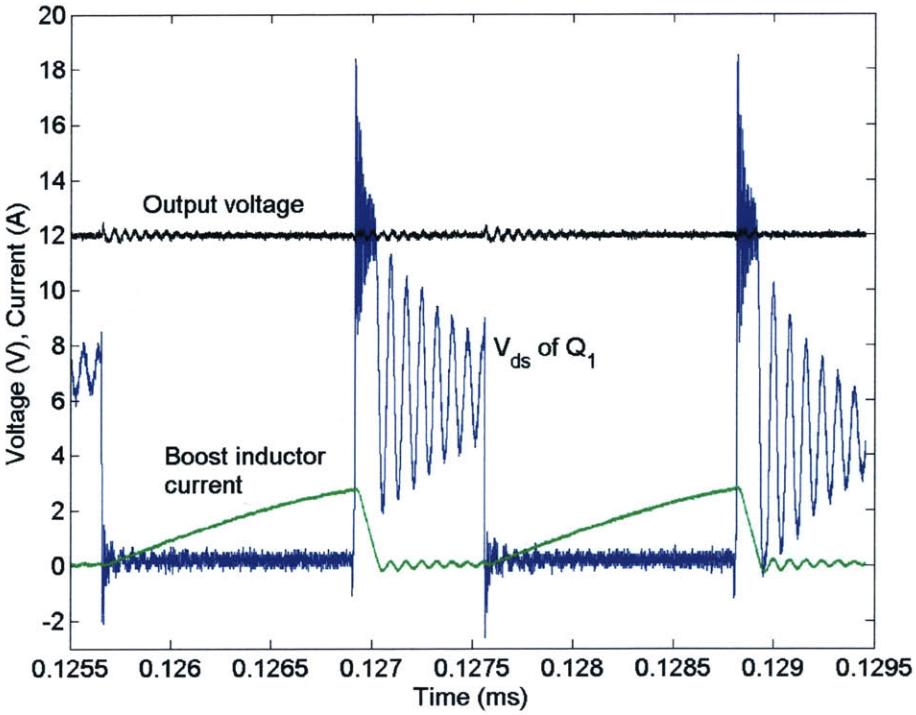

Figure 5-47: Boost rectifier waveforms over two switching periods.

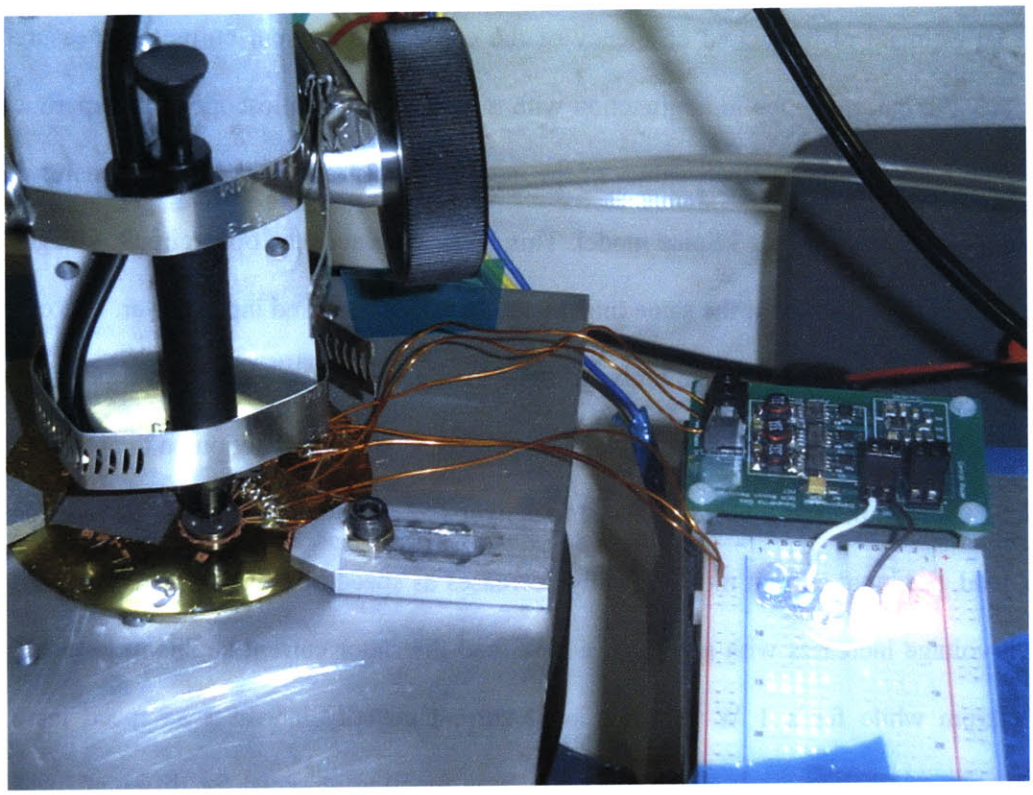

Figure 5-48: Test setup for self-sustained operation. Boost rectifier is powering six LEDs.

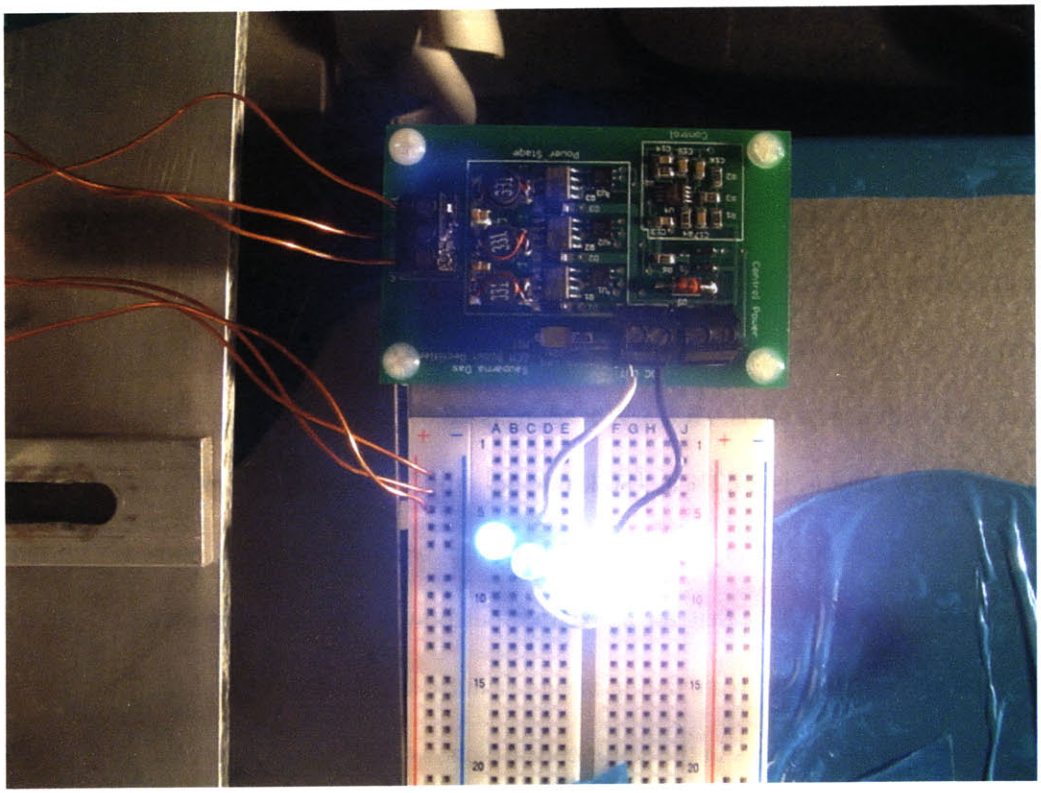

Figure 5-49: Boost rectifier powering six LEDs in series.

To get an estimate of the actual efficiency of the converter the input current is measured using a Tektronix TCP202 current probe in conjunction with a TDS3034B oscilloscope. The experimental input power is found by multiply the RMS values of the measured open-circuit voltage and stator currents by the power factor predicted by the PSpice model. This is done because the open-circuit voltage and stator currents could not be measured at the same time to compute the measured input power. The output power is measured in real time with a voltage probe across a load potentiometer, a current probe around a wire connecting the potentiometer to the rectifier and using the channel math function on the oscilloscope.

Figure 5-50 shows the stator current needed to deliver 1, 2 and 3 W to the load as a function of speed. For a 3 W load, the input current monotonically decreases as speed increases. This is expected since the open-circuit voltage increases with speed. At a 2 W load the stator current begins to level off at speeds above 240 krpm while for a 1 W load the input current actually increases as speed increases. The electrical system and power electronics efficiencies as a function of speed for different fixed loads are shown in Figure 5-51. For a 3 W load, both η_e and η_{pe} increase with speed and are 75.5% and 83.4% at 282 krpm respectively. For a 2 W load, η_e and η_{pe} increase until 240 krpm at which point they level off at 76% and 83%, respectively. At an output power of 1 W, η_e and η_{pe} increase up 75.8% and 81% at 220 krpm and then decreases 71.6% and 78.3% at 272 krpm, respectively.

Figure 5-52 shows the generator system efficiency as a function of speed for 1, 2, and 3 W loads. The points are computed from the measured input power in conjunction with the analytical model of Section 2.2 to determine the proximity, eddy current and hysteresis losses in the stator. The curves are computed from PSpice and analytical models. At a 3 W load, η_g is 26.6% at 180 krpm and decreases to only 17% at 300 krpm. For a 2 W load η_g is 24.2% at 180 krpm and only 12.4% at 300 krpm while for a 1 W load, η_g is 15% and 6.7% at 180 and 300 krpm, respectively. The proximity, hysteresis and eddy current losses in the stator increase with speed so that for a fixed output power, the overall generator system efficiency decreases as the speed increases. Note that η_g is significantly smaller than η_e and η_{pe}. This is primarily due to the significant eddy current loss in the stator core which is 4.7 W at 180 krpm and 12.2 W at 300 krpm. For all three power levels, the measured data correspond well with the PSpice simulations.

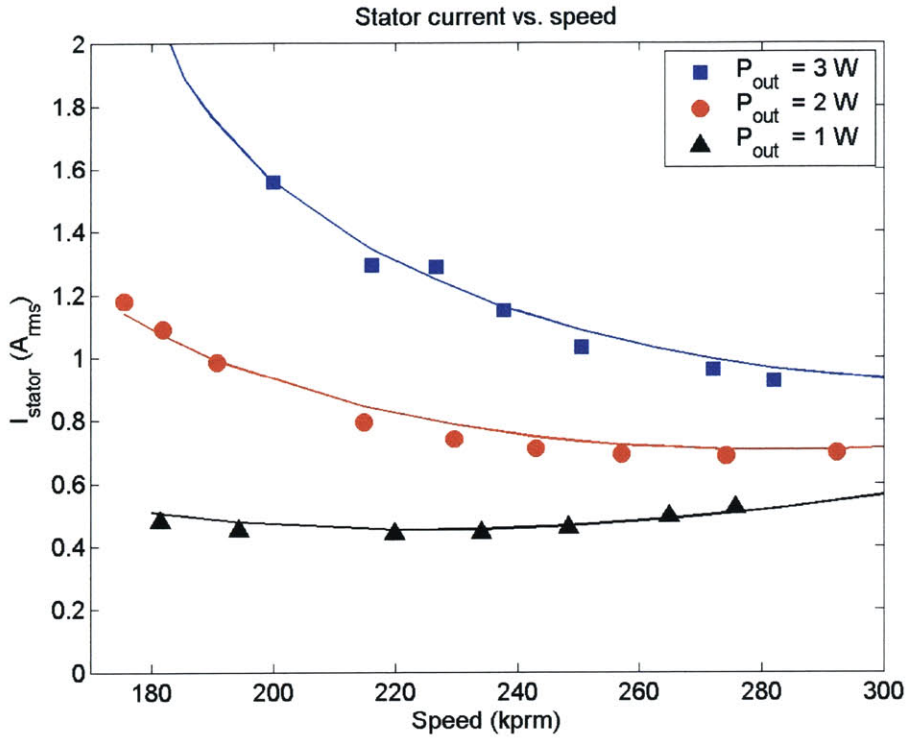

Figure 5-50: Stator current vs. speed for 1, 2 and 3 W loads. Points represent measurements; curves represent PSpice model.

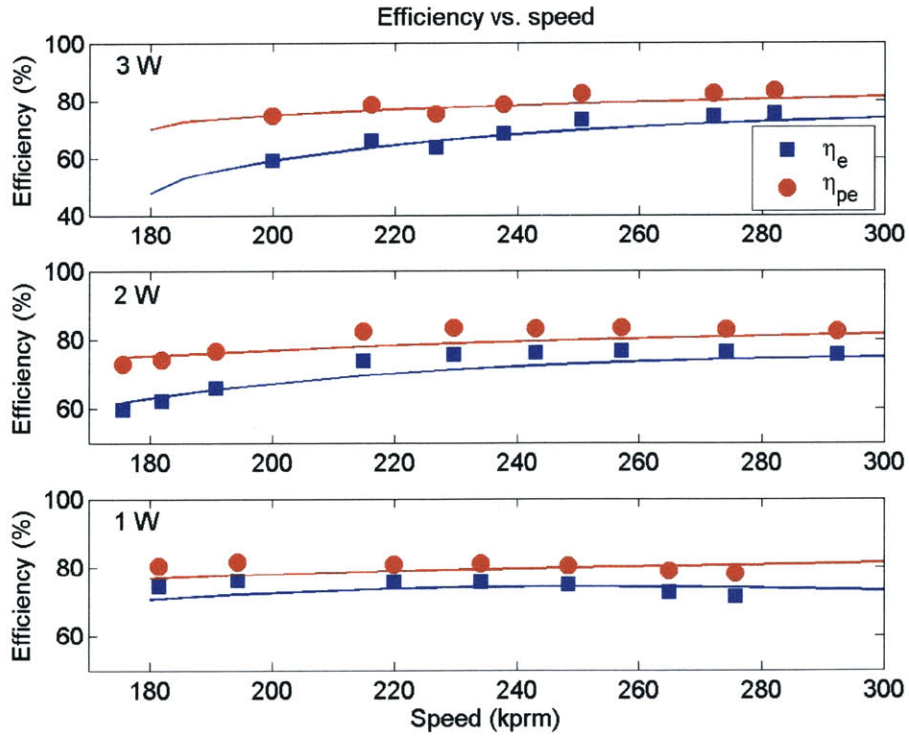

Figure 5-51: Electrical system efficiency, η_e, and power electronics efficiency, η_{pe}, vs. speed for 1, 2 and 3 W loads. Points represent measurements; curves represent PSpice model.

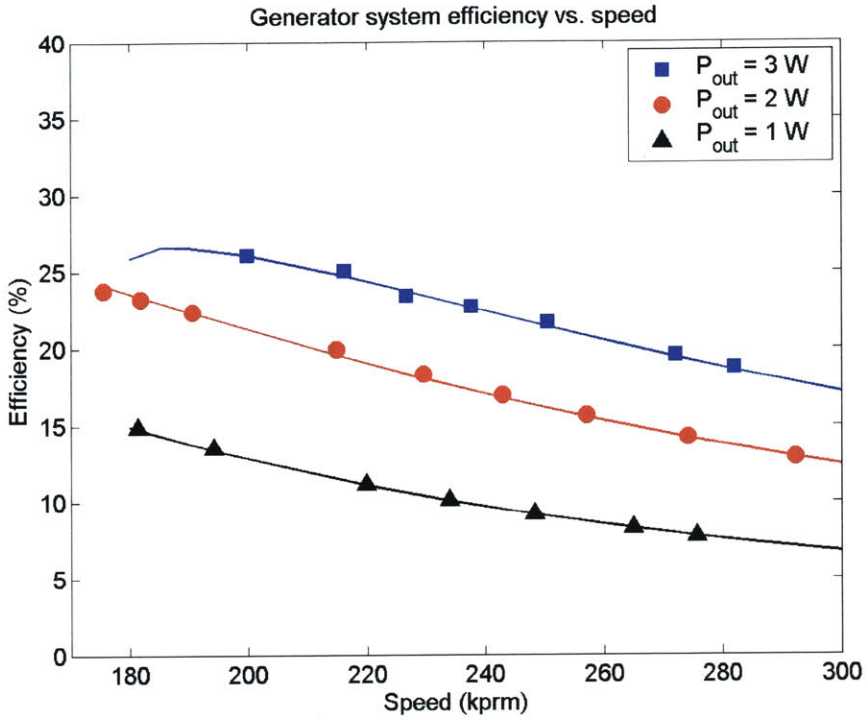

Figure 5-52: Generator system efficiency vs. speed 1, 2 and 3 W loads. Points represent measurements /analytical model; curves represent PSpice/analytical model.

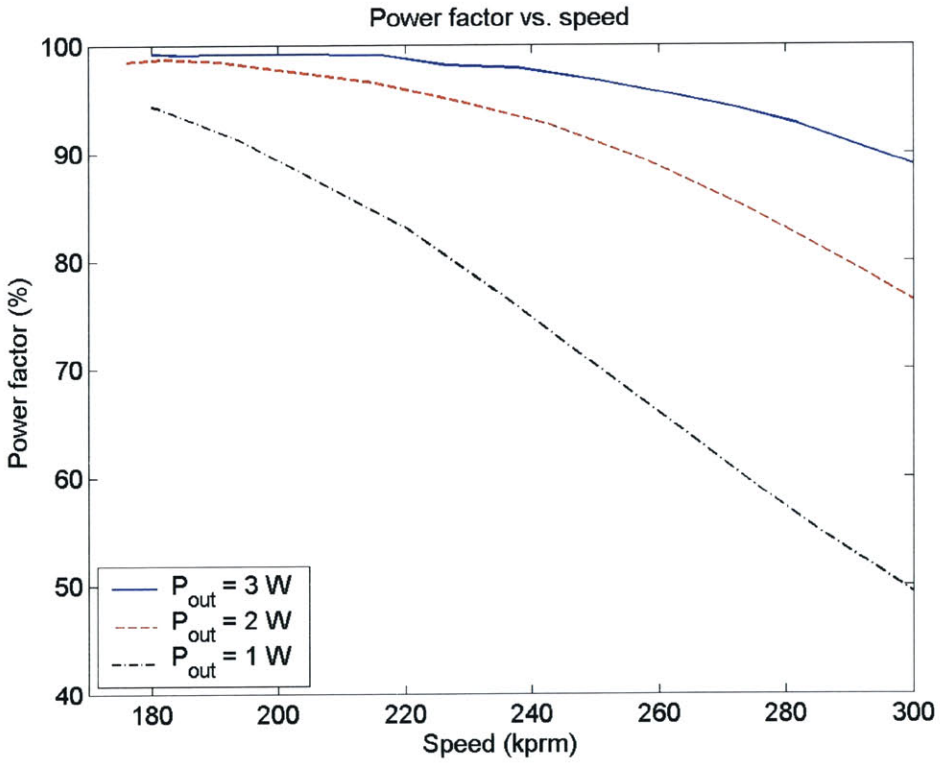

Figure 5-53: Power factor vs. speed for 1, 2 and 3 W loads.

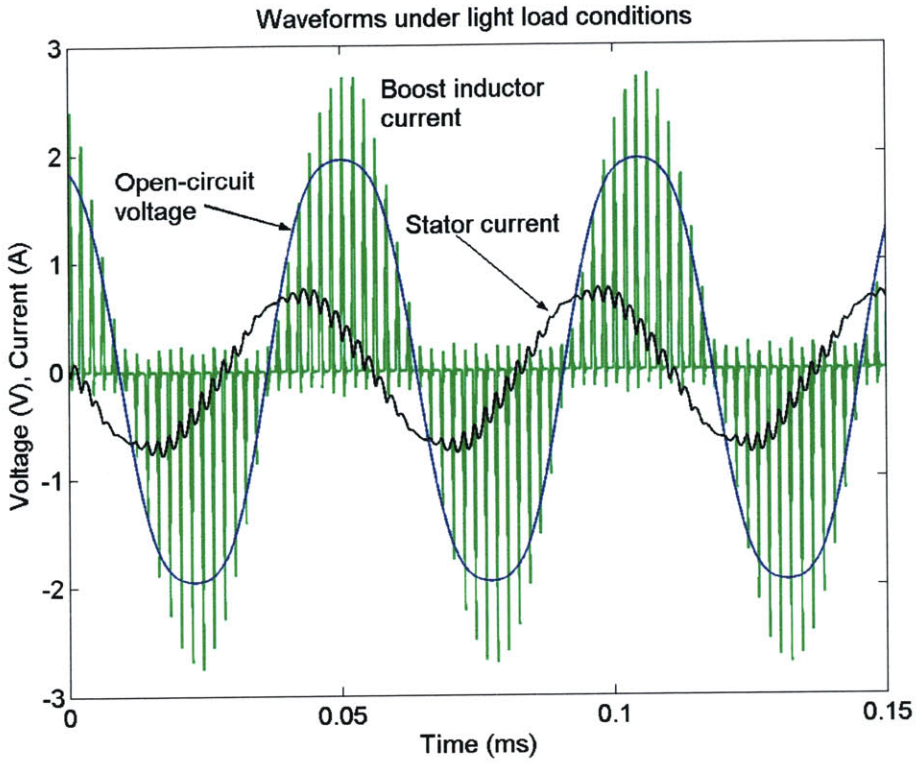

Figure 5-54: Open-circuit voltage, stator current and boost inductor current under light load conditions.

Power factor as function of speed for a fixed output power is shown in Figure 5-53. At low speeds, when a large input current is needed to provide the necessary output power, high power factor (>90%) is achieved. As the speed increases the power factor decreases. For a 3 W load, the power factor is 99% for speeds less 220 krpm and greater than 95% for speeds less than 270 krpm. For a 2 W load, the power factor remains above 90% for speeds below 250 krpm but decreases to 76% at 300 krpm. At 1 W, the power factor is greater than 80% for speeds below 225 krpm but reduces to only 49% at 300 krpm.

The increase in the stator current and the decrease in efficiency and power factor at high speeds and light loads are due to the filter capacitors. From the stator terminals the filter capacitors look like a Δ-connected load in parallel with the power stage of the boost rectifier. At high output power, the input impedance of the boost rectifier's power stage is small compared to the filter capacitors. The generator is essentially driving a resistive load with most of the stator current flowing through the boost rectifier. At light loads, the input impedance of the rectifier is large compared to the impedance of the filter capacitor.

The generator is essentially driving a capacitive load which leads to poor power factor. The impedance of the filter capacitors decreases as the speed increases. This leads to higher stator currents when the output power is low (1 – 2 W). As the speed further increases the stator current needed for a 3 W output will also start to increase just like the 1 W curve in Figure 5-50. The filter capacitors also lead to a lower power factor at light loads as more of the stator current flows through the filter capacitors. Figure 5-54 shows a PSpice simulation of the open-circuit voltage, stator current and boost inductor current for a rectifier delivering 1 W at 276 krpm. Note that while the boost inductor current is in phase with the open-circuit voltage, the stator current actually leads the open-circuit voltage due to the current through the filter capacitors.

The required stator current as a function of load power is shown in Figure 5-55 at a speed of 240 krpm. Notice that the stator current levels off at light load because of the current through the filter capacitors. The power electronics, electrical system and generator system efficiencies as a function of load power are shown in Figure 5-56. Both η_{pe} and η_e increase with decreasing load power as the conduction losses in the stator windings, boost inductor windings, power MOSFETs and diodes decrease. On the other hand, η_g increases as the output power increases because the proximity, hysteresis and eddy current losses in the stator are fixed at a given speed and are independent of the load. The power stage is 75% – 82% efficiency over a 1 – 4.5 W load range while the electrical system efficiency is 59% – 75% efficient. The generator system efficiency is 9.7% at 1 W and increases to 27% at 4.5W. The large discrepancy between the η_e and η_g is due to the 8 W of eddy current loss in the stator core at 240 krpm. The proximity and hysteresis losses are only 0.58 and 0.29 W respectively.

Below 1 W, η_{pe} starts to decrease again as the output capacitive losses in the power MOSFETs and diodes start to dominate the overall loss. The electrical system efficiency also decreases below 1 W because, in addition to the reduced power electronics efficiency, the current through the stator is primarily composed of the current through the filter capacitor which is independent of output power. The predicted power factor as a function of load is shown in Figure 5-57. The power factor is 99% at 4.5 W and is more than 98% down to 3 W. The power factor decreases to 90% at 1.7 W out and is only 49% at 0.5 W out.

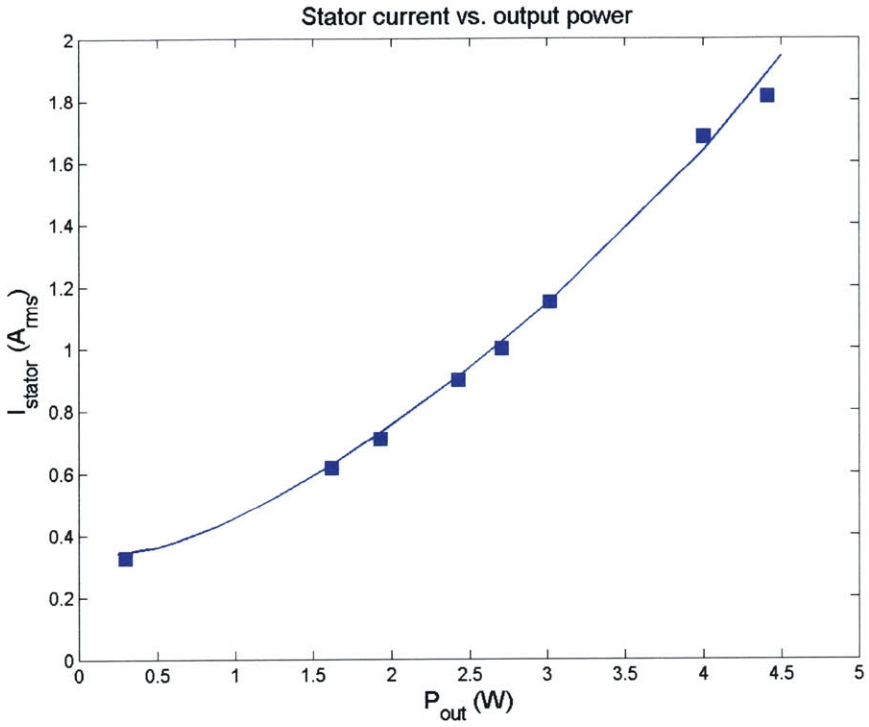

Figure 5-55: Stator current vs. output power at 240 krpm. Points represent measurements; curve represent PSpice model.

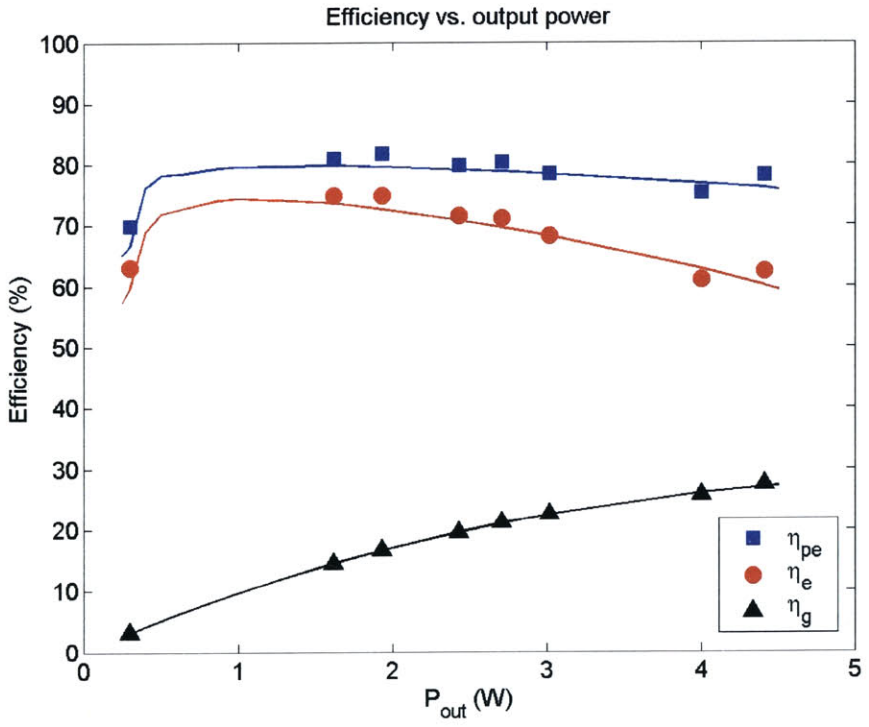

Figure 5-56: Power electronics, η_{pe}, electrical system, η_e, and generator system, η_g, efficiencies vs. output power at 240 krpm. For η_{pe} and η_e, points represent measurements; curves represent PSpice model. For η_g, points represent measurements/analytical model; curves represent PSpice/analytical model.

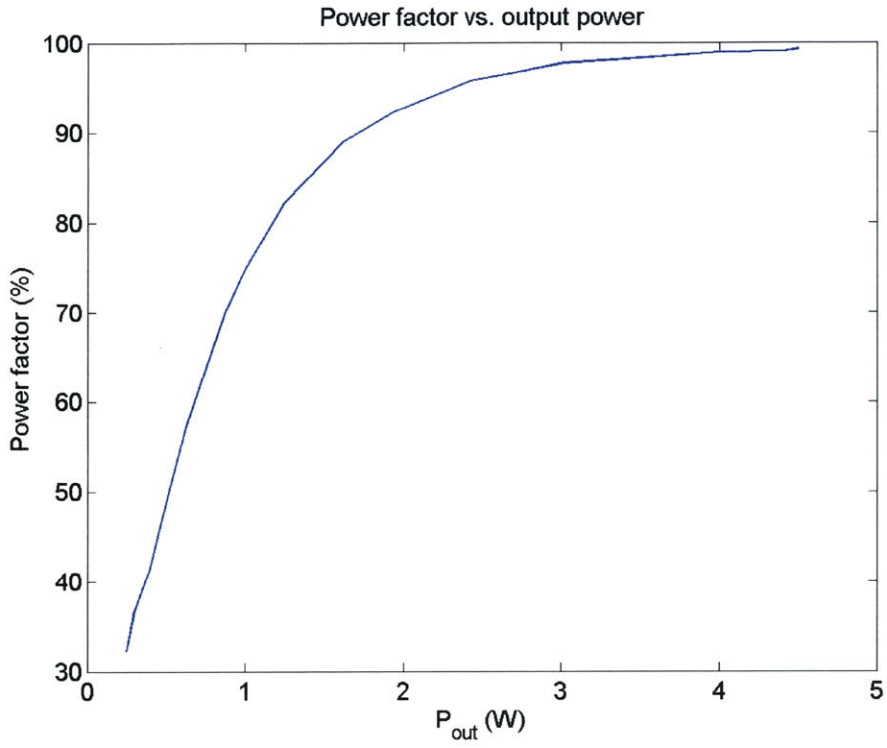

Figure 5-57: Predicted power factor vs. output power at 240 krpm.

Since the output voltage of the rectifier is fixed, maximum output power at a given speed could be found by adjusting the potentiometer load resistance until the output voltage just starts to fall. However, when the load resistance is being adjusted the speed changes, requiring the pressure supply from the nitrogen tank to also be adjusted. The pressure knob on the tank allows only very coarse control of the pressure so that adjusting both the tank pressure and load resistance is difficult. Alternatively, the load resistance can be fixed to some value and the pressure from the nitrogen tank can be increased until the output voltage reaches 12 V. If the speed is too low to provide a 12 V output at some load resistance then the PWM chip operates in a duty cycle limited mode. The stator current and boost inductor current during the duty cycle limited operation is shown in Figure 5-58. Note that the input stator current is less sinusoidal than in Figure 5-46 due to the presence of additional harmonics. This phenomenon is not observed in the PSpice model of the rectifier. Once there is sufficient pressure to provide a 12 V output, the PWM chip gets out of its duty cycle limited operation at which point the speed would significantly rise and the input stator current would decrease and have the same form shown in Figure 5-46. When the

speed settles to its final value the output voltage would be at 12 V but the power delivered to the load is not necessarily the maximum power achievable at that speed because the load is no longer matched.

Figure 5-59 shows output power at different speeds for both a self-sustaining converter and a converter with a 12 V external control power supply. Note that this is not the maximum output power achievable at these speeds but just what is achieved using the coarse pressure control knob on the nitrogen tank. Also plotted in Figure 5-59 is the input stator current needed to achieve the output power at different speeds. The externally powered boost rectifier demonstrates 5.47 W of power delivery at a speed of 298 krpm while the self-sustaining boost rectifier delivers 5.52 W at 303 krpm. These two data points were achieved by fixing the load resistance and then increasing the pressure to achieve a 12 V output voltage. When the pressure became sufficient for the rectifier to come out of duty cycle limited operation the rotor suddenly sped up to ~300 krpm. The measurements were then recorded and the pressure decreased to slow down the rotor. Attempts were not made to adjust the load potentiometer to find the maximum power due to concerns about rotor structural integrity at these speeds.

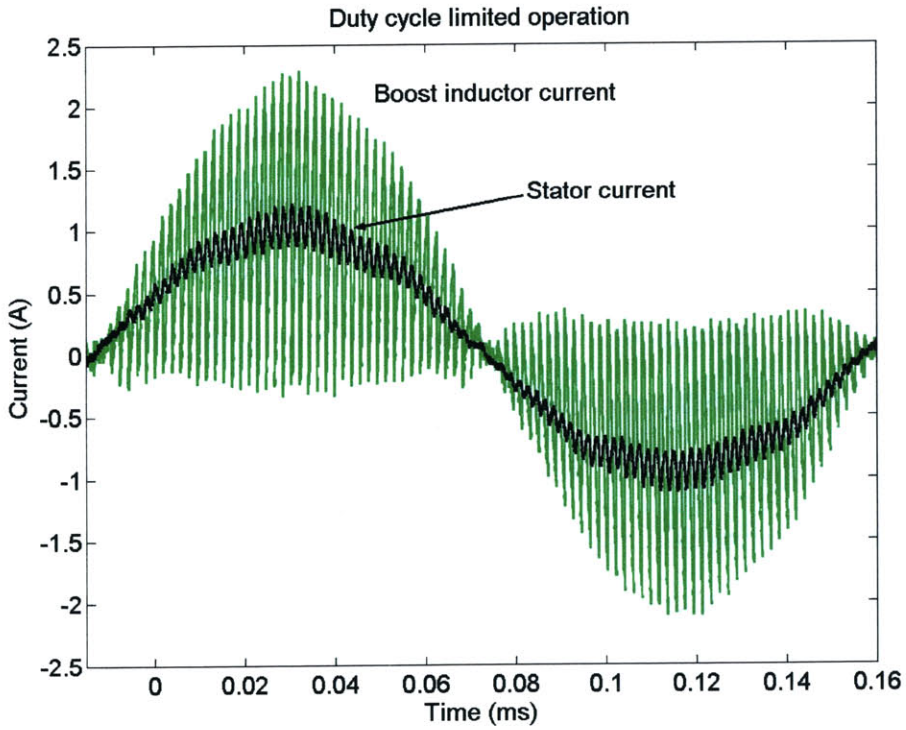

Figure 5-58: Measured stator and boost inductor current under duty cycle limited operation.

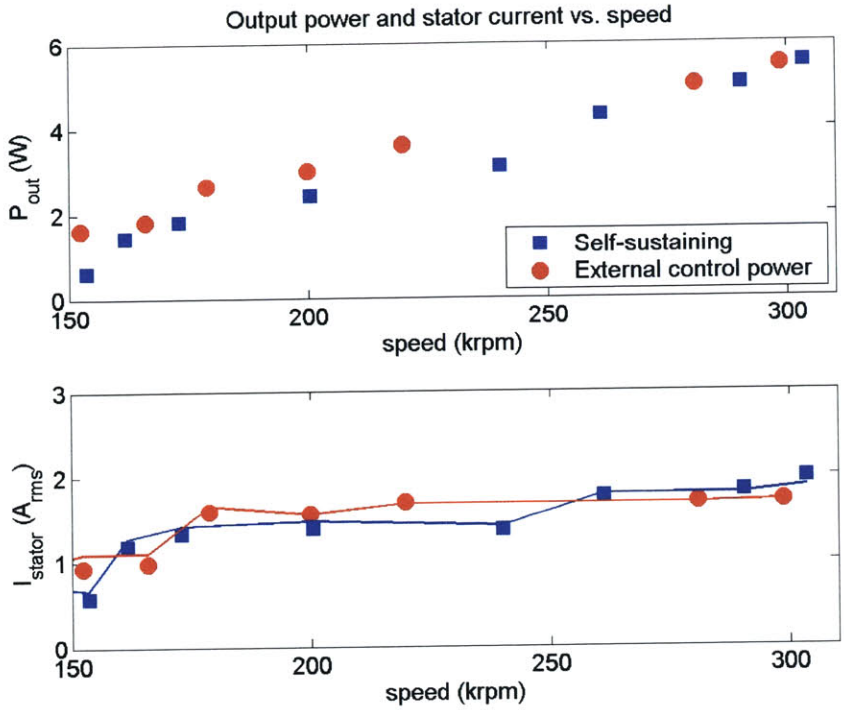

Figure 5-59: Power and stator current vs. speed for the boost rectifier with and without external control power. Points represent measurements; curves represent PSpice model.

The power electronics, electrical system and generator system efficiencies for the self-sustaining boost rectifier are shown in Figure 5-60. The power electronics efficiency varies between 40% at low speed/power to 70% at high speeds/power. This is because, as the as the speed increases, the output power delivered increases making the fixed losses in the control IC and gate drives a smaller fraction of the input power. At 303 krpm the self sustaining rectifier delivered 5.52 W at 69% power electronics efficiency with an electrical system efficiency of 57%. Including the predicted core and proximity losses in the stator core of 13.72 W, the overall generator system efficiency is 23.6%. The power electronics, electrical system and generator system efficiencies for the externally powered boost rectifier are shown in Figure 5-61. The externally powered rectifier achieved an 85% power electronics efficiency at 152 krpm when delivering 1.62 W, while the self-sustaining rectifier delivered 0.61 W at a power electronics efficiency of 48%. At 298 krpm, the externally controlled rectifier delivered 5.47 W at a power electronics efficiency of 79% and an electrical system efficiency of 67%, about 10% higher than the self-sustaining rectifier.

The overall generator system efficiency is 25.5%. In fact the externally powered boost rectifier is able to maintain a generator system efficiency of about 25% throughout the speed range because gate drive losses are not counted while the self-sustaining rectifier has a generator system efficiency of only 11% at 150 krpm. The power factor for the output powers in Figure 5-59 is 98% – 99.5%.

The output voltage of the self-sustaining boost rectifier at 303 krpm is plotted in Figure 5-62. The output voltage has a low frequency variation which is due to wobble in the rotor at high speeds. This wobble leads to variation in the open-circuit voltage from period to period. This variation can also be seen in the input stator current which is also plotted in Figure 5-62. This is the current through the stator when the self-sustaining rectifier is delivering 5.52 W. The measured current matches well with the PSpice prediction except for the variation in the amplitude of the current from period to period. The THD of the current is 15%.

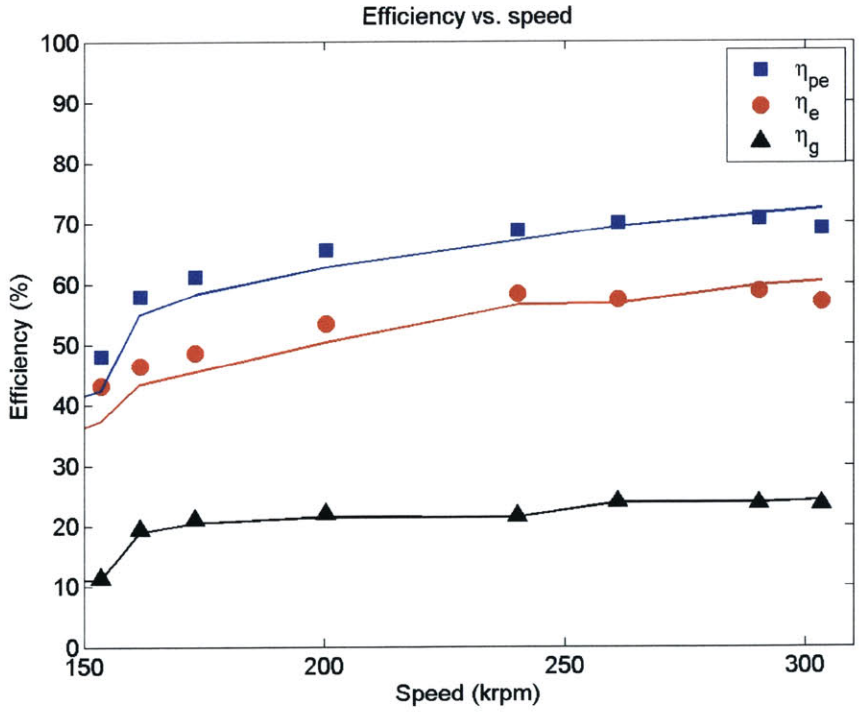

Figure 5-60: Power electronics, η_{pe}, electrical system, η_e, and generator system, η_g, efficiencies vs. speed for the self-sustaining boost rectifier. For η_{pe} and η_e, points represent measurements; curves represent PSpice model. For η_g, points represent measurements/analytical model; curves represent PSpice/analytical model.

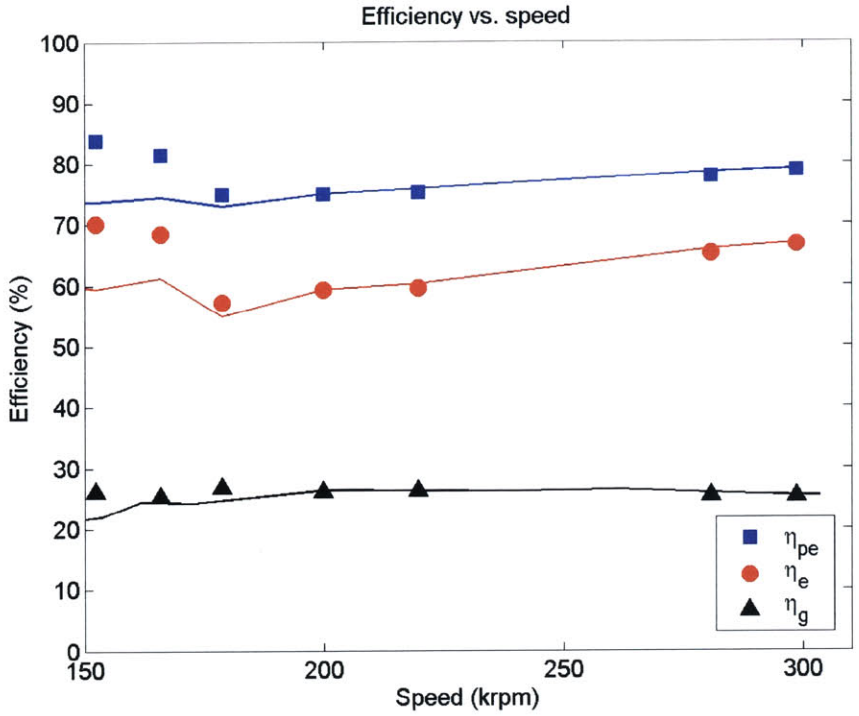

Figure 5-61: Power electronics, η_{pe}, electrical system, η_e, and generator system, η_g, efficiencies vs. speed for the boost rectifier with external control power. For η_{pe} and η_e, points represent measurements; curves represent PSpice model. For η_g, points represent measurements/analytical model; curves represent PSpice/analytical model.

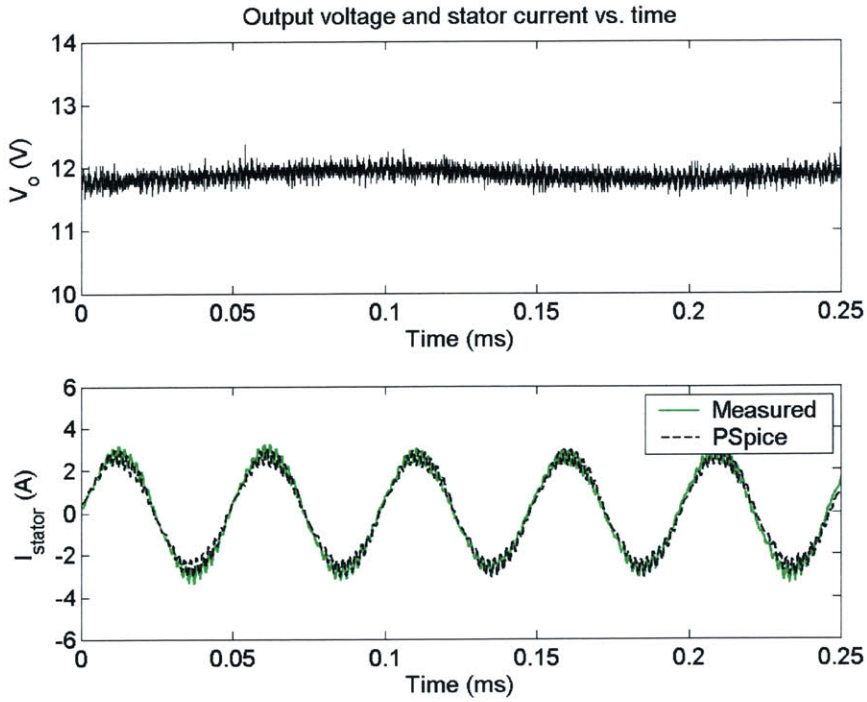

Figure 5-62: Output voltage of the self-sustaining boost rectifier and current through stator #3 at a speed of 303 krpm and an output power of 5.52 W.

5.2.6 Comparison between the first and second generation power electronics

The passive and active power electronics were designed with different constraints and with different objectives. The goal of the passive power electronics was to maximize output power by efficiently stepping up and rectifying the generator's AC voltages with no constraints on the size of the circuit. In addition, output voltage regulation and power factor correction were not needed for the low speed power generation tests in Chapter 4. With no size constraint, a very large transformer was used to make the passive electronics highly efficient. The boost rectifier, on the other hand, was designed with size being an important consideration. Unlike the passive circuit, the boost rectifier provides power factor correction and voltage regulation in addition to stepping up and rectifying the generator's AC voltages. The goal was to efficiently deliver power at a regulated DC voltage with high power factor in a compact size. The size of the boost rectifier's power stage is limited to the size of a stator die. The passive and active power electronics are shown in Figure 5-63. The transformer in the passive circuit is much larger than the power stage of the boost rectifier and the bridge rectifier in the passive circuit is larger than the control section of the boost rectifier. The black terminal blocks in Figure 5-63 are used so that the generator can be easily connected and disconnected to the power electronics.

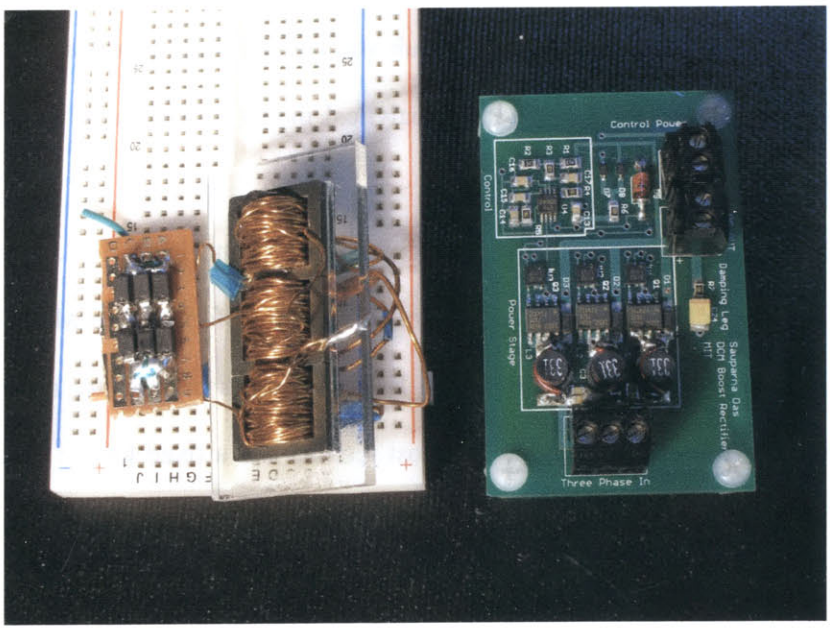

Figure 5-63: Size comparison of the passive (left) and active (right) power electronics.

Figure 5-64 compares the output power vs. speed for the second-generation stator #3 connected to the passive and active power electronics. The boost rectifier data in Figure 5-64 is from the self-sustaining converter. The generator with the passive circuit delivers more power to the load but remember that the power vs. speed for the boost rectifier is not under matched load conditions. This is evident from the electrical system efficiency vs. speed in Figure 5-65, which shows that the generator with the boost rectifier is operating at efficiencies above 50%. The generator with the passive electronics, on the other hand, has an electrical system efficiency of 46 – 49%.

The overall generator system efficiencies of the PM machine with the passive and active power electronics is shown in Figure 5-66. The generator system efficiency of the PM machine with the passive circuit is about 25% – 27% over a 160 – 320 krpm speed range while the PM machine with the boost rectifier is 20% – 24% efficient. Note that, at the same speed, the core and proximity losses in the stator are same for both machine/power electronics combinations. Since the boost rectifier provides less output power at a given speed, its overall generator system efficiency is less than the PM machine with the passive circuit. The curves in Figure 5-66 are generated using the PSpice model for the generator and power electronics to determine the stator conduction and power electronics losses and the analytical model from Section 2.2 to determine the proximity and core losses in the stator. The data points in Figure 5-65 are computed by using the measured open-circuit voltage and stator currents to determine the stator conduction and power electronics losses and the analytical model to determine the proximity and core losses in the stator.

The power electronics efficiency of the two circuits is shown in Figure 5-67. The passive circuit is 20–30% more efficient than boost rectifier because of its large transformer size which dwarfs the size of the boost rectifier's power stage. In addition, the boost inductors chosen are not the most efficient possible due to its thick solid wires. Finally, the boost rectifier has a fixed loss of 0.48 W in the control section that the output of the boost rectifier must power in addition to the load. Since both circuits provide voltage step-up and rectification, one can think of the 0.48 W of fixed loss as the cost of providing output voltage regulation and power factor correction.

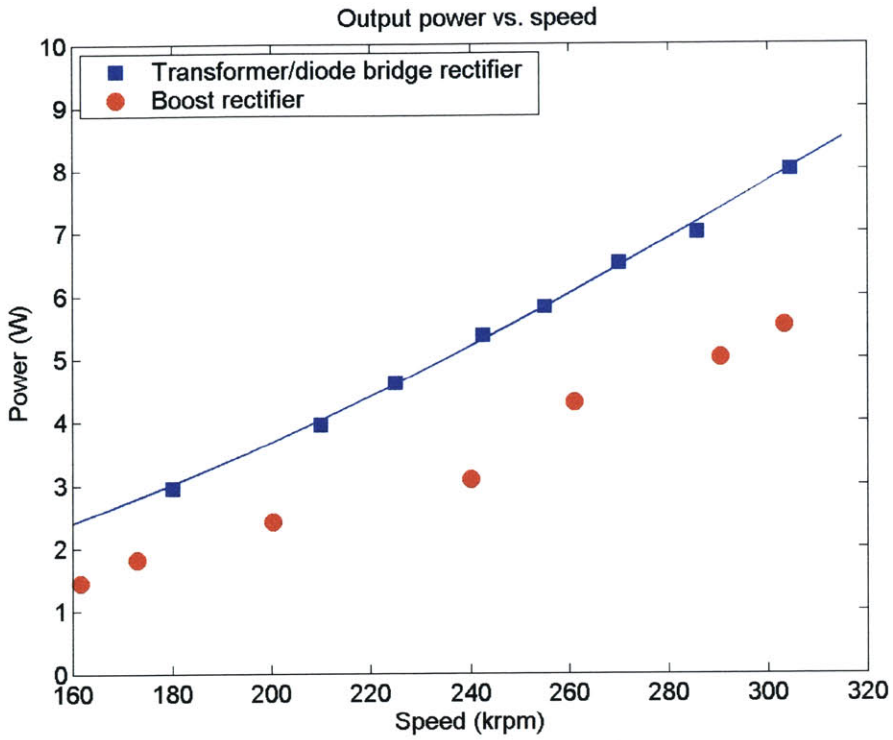

Figure 5-64: Output power vs. speed for the transformer/diode bridge and boost rectifier. Points represent measurements; curves represent PSpice model.

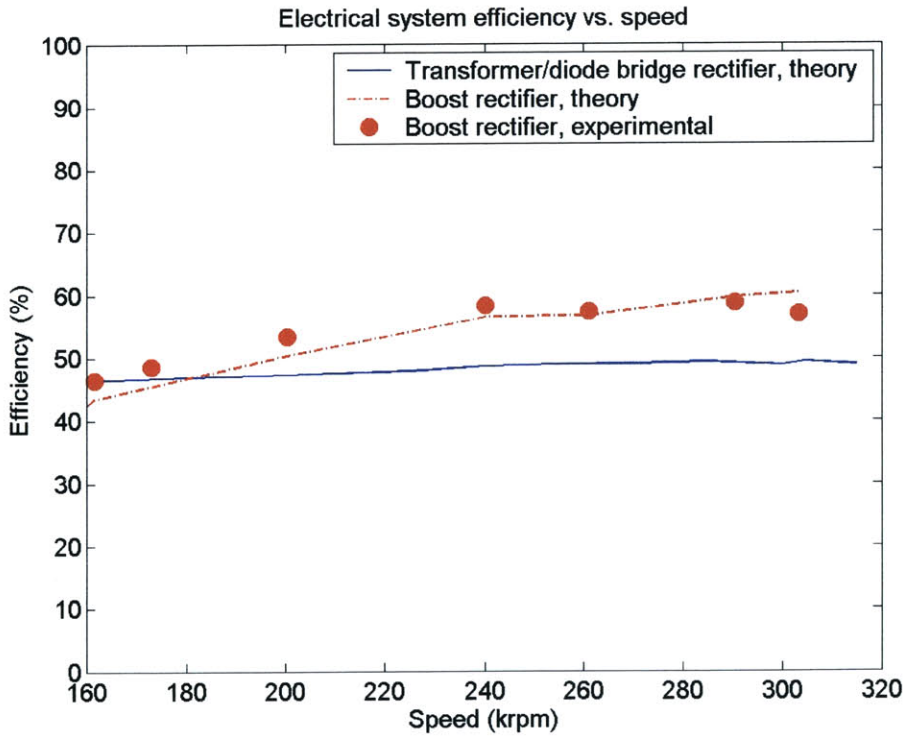

Figure 5-65: Electrical system efficiency vs. speed for the transformer/diode bridge rectifier and boost rectifier. Points represent measurements; curves represent PSpice model.

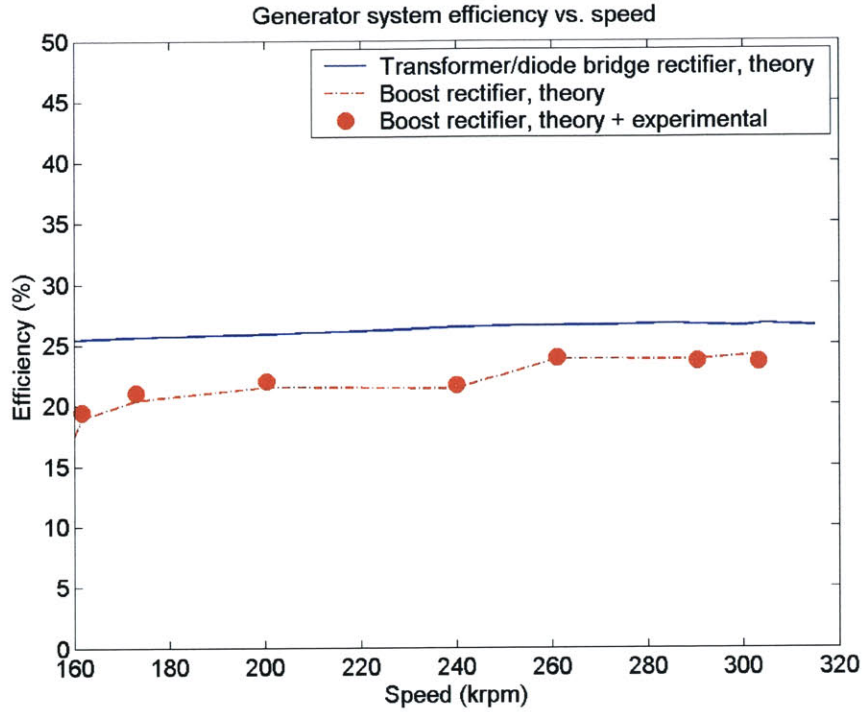

Figure 5-66: Generator system efficiency vs. speed for the transformer/diode bridge rectifier and boost rectifier. Points represent measurements/analytical model; curves represent PSpice/analytical model.

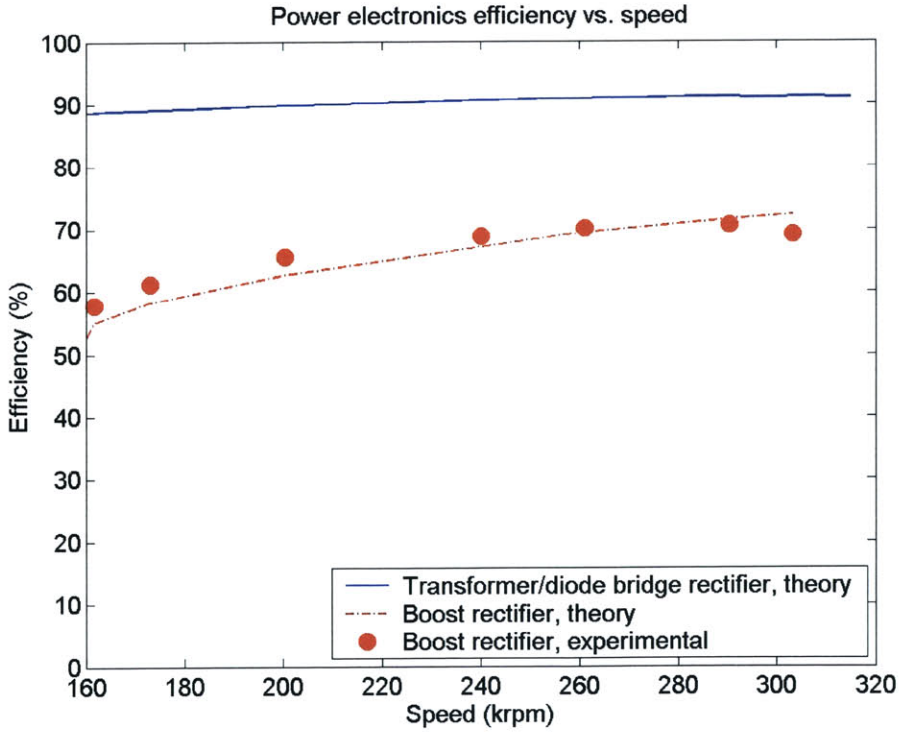

Figure 5-67: Power electronics efficiency vs. speed for the transformer/diode bridge and boost rectifier. Points represent measurements; curves represent PSpice model.

Table 5-8: Performance breakdown of the second generation PM machine with first and second generation power electronics.

Property	Transformer/ diode bridge rectifier	Self-sustaining boost rectifier	Self-sustaining boost rectifier power stage
Speed	305 krpm	303 krpm	303 krpm
P_{mech}	30.12 W	23.4 W	23.4 W
P_{prox}	0.92 W	0.91 W	0.91 W
P_{eddy}	12.56 W	12.45 W	12.45 W
$P_{hysteresis}$	0.37 W	0.36 W	0.36 W
P_{elect}	16.27 W	9.68 W	9.68 W
P_{cond}	7.46 W	1.71 W	1.71W
P_{pe}	0.81 W	2.46 W	1.98 W
P_{out}	8 W	5.52 W	6 W
η_{pe}	90.8%	69%	78%
η_e	49.2%	57%	62%
η_g	26.6%	23.6%	25.6%
Power factor	89.2%	98.3%	98.3%
Volume	5017 mm^3	1190 mm^3	1080 mm^3
Power density	1.59 MW/m^3	4.64 MW/m^3	5.56 MW/m^3

Table 5-8 give a breakdown of the performance of the PM machine with the passive and active power electronics. At 305 krpm, the PM machine with the transformer and diode bridge rectifier can deliver 8 W at an electrical system efficiency of 49.2% and overall generator system efficiency of 26.6%. The passive power electronics is 90.8% efficient but the generator has significant conduction loss (7.46 W) which is an order of magnitude larger than the losses in the power electronics. The power factor for the passive circuit is 89.2%. At 303 krpm, the PM machine with the boost rectifier can deliver 5.52 W at 57% electrical system efficiency and 23.6% generator system efficiency. The power factor of 98.3% is very close to unity. The boost rectifier is 69% efficient and the power lost in the circuit (2.46 W) is actually larger than the stator conduction loss (1.71 W). In both cases, the 12+ W of eddy current loss in the stator core leads to generator system efficiencies that are significantly lower than the electrical system efficiencies.

A better performance comparison may be between the transformer/diode bridge rectifier and the power stage of the boost rectifier. At 303 krpm, the power stage delivers 6 W out, of which 0.48 W is fed back to power the control circuitry. The electrical system efficiency in this case is 62% and the power

stage is 78% efficient. The generator system efficiency in this case is only 1% less than the PM machine with the passive circuit.

Another important metric for the power electronics is power density. The frame of the transformer is 43 mm long, 25 mm wide and 3 mm thick. The windings are cylinders that extend 4 mm beyond the thickness of the frame in each direction and are 10 mm long each. The volume of the transformer is 4833 mm^3. The six diodes are 2.9 mm × 4.6 mm × 2.3 mm each for a bridge rectifier volume of 184 mm^3. The total volume of the passive power electronics is 5017 mm^3 and the power density is 1.59 MW/m^3 when delivering 8 W to the load. The power stage of the boost rectifier is 24 mm × 22.5 mm. The tallest components are the boost inductors which are 5 mm high. The other components are 1 – 1.75 mm in height. The bypass and filter capacitors on the bottom side of the PCB can easily fit in the empty spaces on the top side of power stage area. For a mean height of about 2 mm the volume of the power stage is 1080 mm^3. The control section is 11 mm × 10 mm and the average component height is 1 mm for a volume of 110 mm^3. The total power electronics volume is 1190 mm^3. At an output power of 5.52 W the boost rectifier has a power density of 4.64 MW/m^3, which is nearly three times the power density of the passive power electronics. Considering only the power stage of the boost rectifier, the power density is 5.56 M W/m^3 for 5.52 W of output power (6 W from the power stage). This is more than three and a half times larger than the passive power electronics.

The size of the power electronics could be further reduced by integrating the control IC, gate drives and power MOSFETs onto a single chip. In fact, a large percentage of the volume of the MOSFET is taken up by the SO-8 package. The semiconductor die of each of the three MOSFETS could probably fit into a single SO-8 package. A fully integrated boost rectifier chip could be as small as 7 mm × 7 mm with a height of only 0.75 mm. This would be similar in size to the 4-phase, 10 W fully integrated LTC3425 boost converter from Linear Technology (www.linear.com). With this amount of integration, the total volume of the boost rectifier could be as small as half the size of the current power stage, or about 500 mm^3, with little degradation in performance. This would increase the power density to six times that of the passive power electronics.

5.3 Summary

This chapter began by looking into ways of increasing output power beyond one Watt from the microscale PM generators. The best way to achieve multi-Watt power delivery was to increase the rotational speed and improve the design of the stators. From the scaling laws for the machine power and efficiency, it was found that to increase both efficiency and power the number of turns/pole should be maximized subject to minimum feature size constraints while the number of poles should be minimized subject to maximum rotor/stator core thickness limitations. Optimization of the stator led to an 8-pole, 3-turn/pole machine with concentric windings. Three of these 2nd generation stators were built and tested and one delivered 8 W of DC power to a load resistor at 305 krpm using the transformer and diode bridge rectifier. The stator current was 5.36 A peak corresponding to a current density of ~6×10^{8} A/m^2, which is three time larger than what was achieved in the first generation stator and two orders of magnitude larger than what is possible in a macroscale machine. For an active machine volume of 138.4 mm^3, (10 mm OD, 5 mm ID, 2.35 mm thick), the 8 W output power corresponds to a power density of 57.8 MW/m^3, which is more than three times the power density of a 1000 MW turbine generator.

The estimated electrical and generator system efficiencies are 49.2% and 26.6%, respectively, when the generator is delivering 8 W to the load. The difference between the two efficiency metrics is due to the eddy current loss in the stator core. In fact, the 12.56 W lost due to eddy currents in the stator core is larger than either the output power or the sum of all the other losses in the system (9.56 W). This means that laminating the stator will be necessary to increase the overall generator system efficiency. The proximity eddy current loss in the stator windings could be reduced by laminating the stator. However, because the conduction loss in the stator winding is substantially larger (7.46 W vs. 0.92 W) it is better to use solid radial conductors to minimize the resistance of the stator.

The transformer/diode bridge rectifier used for power generation tests does not provide power at a constant output voltage. In addition, it has lagging power factor at high speeds and is quite bulky compared to the compact PM machines. The second part of this chapter focused on the design of a

switch-mode rectifier that could deliver power at a constant output voltage of 12 V with near unity power factor. Several topologies were looked at. Two topologies used a three-phase MOSFET bridge rectifier in conjunction with either a continuous-conduction-mode boost converter or a discontinuous-conduction-mode boost rectifier. Neither of these topologies were chose because they required seven active devices and gate drives and had large magnetic components. The rectifier chosen used a boost semi-bridge topology operating in discontinuous-conduction-mode. Synchronous rectification of the power stage and the use of Litz wire inductors would improve the efficiency of the rectifier but was left for future work.

A boost rectifier without synchronous rectification and using commercially available inductors was built and tested. The power stage of the rectifier takes up the same area as a stator die and is much more compact than the transformer/diode bridge rectifier. The rectifier demonstrated the ability for self-sustained operation by having the output voltage power the control circuitry while lighting up six LEDs. When connected to a 2nd generation stator, the self-sustaining boost rectifier delivered 5.52 W to a load resistor at a regulated output voltage of 12 V and at a speed of 303 krpm. The power electronics was 69% efficient and had a power factor of 98.3%. The electrical and generator system efficiencies were 57% and 23.6%, respectively, with the discrepancy due to the large eddy current loss in the stator core.

The power density of the boost rectifier is 4.64 MW/m^3, which is three times the power density of the transformer/diode bridge, even though it is less efficient than the passive circuit. The power density of the boost rectifier can be further increased by integrating the control IC, gate drives and power MOSFETs into a single chip. Integration could lead to a switch-mode rectifier that is half the size of the discrete design and have six times the power density of the transformer/diode bridge rectifier. These results demonstrate the viability of compact electric power generation systems, consisting of a microscale PM machine and a near unity power factor switch-mode rectifier, for delivering multi-Watt electric power to a load at a regulated output voltage.

6 Concluding Remarks

6.1 Summary

This thesis presented the modeling, design, fabrication and testing of microscale PM machines and power electronics capable of generating and delivering Watt-level DC power to a load. These machines were also compared to microscale induction machines developed earlier in the MIT Micro-Engine Program. Chapter 2 developed analytical models for asynchronous (Induction) and synchronous (PM) planar magnetic machines with slotted and surface wound stators. The surface wound machines can be modeled as a set of planar continuum layers by solving Maxwell's equations in the Magneto-quasi-static (MQS) domain. For the slotted stator magnetic machine, a hybrid continuum/lumped parameter model was used. The field solutions were solved in the spatio-temporal frequency domain, which allowed complicated winding patterns and rotor magnetization profiles to be modeled by decomposing them into their respective Fourier components and then solving for fluxes, voltages, currents, etc., for each harmonic component. The effects of eddy currents, laminations and saturation were incorporated into the model through the use of effective conductivities and permeabilities. Hysteresis and eddy current losses in rotor and stator cores and proximity eddy current losses in the coils of the surface wound stator, as well as torque and pull-in force on the rotor can be computed from the field solutions. In addition, the models were used to derive a per-phase equivalent circuit for the PM machine consisting of an inductance and an open-circuit voltage. This general field theory approach to machine modeling was computationally very fast and agreed well with both FEA analysis of the surface wound PM machine as well as experimental data from the first- and second-generation PM generators. These fast, accurate analytical models are an important contribution to the modeling and design MEMS magnetic machines. In Chapter 4, a simplified model of the PM machine was derived from the continuum model in Chapter 2 by assuming ideal properties for the materials used. This model was used to gain insight into how speed, geometry and the number of poles and turns/pole affect the output power capability of the machine.

With an operating temperature of 300 °C, the four magnetic machine candidates for microengine power generation were the slotted stator induction, slotted stator PM, surface wound induction and surface wound PM machines. The surface wound induction machine generates negligible amounts of power due to the large rotor-stator air gap and was readily dismissed as a viable candidate. The other three machines were compared to one another in terms of output power capability and efficiency within the dimensional constraints and operating speeds of the microengine in Chapter 3 at both room temperature and at 300 °C. In Section 3.3, both PM machines were found to generate more power at a higher efficiency than the induction machine over a wide range of input currents, pole counts and outer radii of the rotor core at room temperature. This was because the rotor magnet in a PM machine produced a rotor flux that was much larger than what could be produced by stator currents through the mutual inductance in an induction machine at the microscale. This is an important result for MEMS designers. High-density electromechanical power conversion is better achieved through the interaction between currents and flux generated by permanent magnets rather than electromagnets. Further, it was also shown in Section 3.4 that the surface wound PM machine could generate more output power at a higher efficiency than a PM machine with a slotted stator. The difference in performance was because the surface wound stator consisted of three phases with full pitched windings that maximized flux linkage. The slotted stator was limited to two phases that link 50% of the maximum flux due to its fabrication process, which required that an entire phase winding occupy a single wafer. This fabrication constraint is not likely to be overcome in the near future. In Section 3.5 the three magnetic machines were compared at 300 °C using recently available high temperature data for the remanence of the SmCo PM and the stator winding resistance. It was found that due to the increased resistivity of the stator windings and rotor conductor the induction machine was incapable of generating net electrical power at high temperature. The surface wound and slotted PM machines were able to generate power at high temperature with only a small degradation in performance. The surface wound stator still outperformed the slotted stator in terms of output power and efficiency at 300 °C. Therefore, the surface wound PM machine was the best candidate for electric power generation within the microengine and was the focus of the rest of this thesis.

Chapter 4 presented the design, fabrication and testing of the first-generation PM machines designed for Watt-level power generation. The generators were three-phase, 8-pole, axial-air-gap, synchronous machines. The rotor consisted of a 500 μm SmCo PM and Hiperco 50 core. The stator consisted of 1-, 2- and 4-turn/pole windings placed on the surface of a 1 mm thick Moly Permalloy stator core. The PM generators were designed and fabricated using a combination of microfabrication and precision machining/assembly. The machines were then characterized using an air-driven spindle which, when powered by compressed nitrogen, provided rotational speeds in excess of 350,000 rpm. The measured open-circuit voltages deviated from a PM with an ideal square wave magnetization and 1 T remanence. It is believed that the selective pulse magnetization process used to pattern the rotor did not fully saturate the magnet, resulting in a reduced remanence. Also, transition regions between poles were possible due to saturation of the magnetized heads at the edges of the magnetizer poles and the resulting leakage flux. In order to match the experimental data, the remanence was set to 0.52 T and a 1-mm transition region between poles was used in the analytical model developed in Chapter 2. Once this adjustment was made, the experimental and theoretical values for the open-circuit voltage and output power were well matched for various speeds, air gaps, and turns/pole, as seen in Figures 4-18 through 4-23 in Section 4.6.

To provide DC power to a load, the AC generator voltages were first stepped up using a three-phase Δ/wye-connected transformer and then converted to DC using a three-phase diode bridge rectifier. At 120,000 rpm, the 2-turn/pole machine demonstrated 2.5 W of mechanical-to-electrical power conversion and delivered 1.1 W of DC power to a resistive load. This was the first ever demonstration of Watt-level power delivered by a power MEMS device and proved the viability of scaled PM machines for practical power applications. The electrical system efficiency, defined as the output power divided the converted power, is 43%. There was an additional 3.25 W lost in the stator due to eddy currents in the stator core and windings and hysteresis the stator core. The input mechanical power is 5.75 W, making the overall generator system efficiency 19%. Given its active machine volume of 110 mm^3 (9.5 mm OD, 5.5 mm ID, 2.3 mm thick), the 1.1 W of output power corresponded to a power density of 10 MW/m^3; note that a typical 1000 MW turbine generator with an active volume of 60 m^3 (8.4 m long, 3 m stator core outer

diameter) has a power density of 17 MW/m^3. The currents in the stator windings when delivering 1.1 W to the load were 2.83 A_{pk}, which translated to a peak current density of ~2×10^8 A/m^2. This was one to two orders of magnitude higher than the current density found in a macroscale machine.

Despite these impressive results there was still room for improvement. The stator resistance was much larger than predicted due to the large number of vias and cross-over conductors used in the end turns which limits output power. In addition, the transformer and diode bridge circuit were much larger than the generator and did not provide either a regulated DC output voltage nor power factor correction. Improvements in the PM machines and power electronics were presented in Chapter 5. Using the power and efficiency scaling laws derived in Section 5.1.1, it was found that to increase both efficiency and power, the number of turns/pole should be maximized subject to minimum feature size constraints, while the number of poles should be minimized subject to maximum rotor/stator core thickness limitations. Optimization of the stator led to an 8-pole, 3-turn/pole machine with concentric windings. The end turns of the concentric wound stator were circular arcs that occupied a single layer. This made more efficient use of the inner and outer regions of the stator and eliminated the need for cross-over conductors like the ones used in the 1st generation stators. With fewer crossovers, the number of vias was drastically reduced and, along with the better end turn design and more aggressive fabrication, it led to a stator that could produce 58% – 88% more power than a 8-pole, 2-turn/pole 1st generation stator, assuming the same rotor PM was used.

One of these 2nd generation PM machines, when connected to the transformer and diode bridge rectifier, delivered 8 W of DC power to a load resistor at a speed of 305,000 rpm. This was the first demonstration of multi-Watt power delivery, and is the highest power ever delivered by a power MEMS device to date. The 8 Watts represents more than a 7× increase in power with only a 2.5× increase in the speed from the first generation design. The estimated electrical system efficiency is 49.2% which corresponds to 16.27 W of mechanical-to-electrical power conversion. The overall generator system efficiency was 26.6% due to the additional 13.85 W dissipated in stator due to eddy currents and hysteresis. For an active machine volume of 138.4 mm^3, (10 mm OD, 5 mm ID, 2.35 mm thick) this

corresponded to a power density of 57.8 MW/m^3, which is more than three times larger than the 17 MW/m^3 power density of a macroscale turbine generator. Again, this was due to the very high current densities and high rotor tip speeds of the microscale generators.

Unlike most work on microscale generators, this thesis addressed the issue of not only power generation but also power delivery. High output power from a generator is useless if it cannot be efficiently converted into a form that the end-user requires. Towards that end, a switch-mode rectifier based on the boost semi-bridge topology operating in discontinuous-conduction-mode was designed in Section 5.2 to provide power at a regulated DC output voltage with near unity power factor. Power factor correction is achieved without the need for direct rotor position/speed or stator current/voltage sensing. The power stage of the rectifier took up the same area as a stator die and was much more compact than the transformer/diode bridge rectifier. Switch-mode power electronics specifically designed for MEMS-scaled magnetic machines is a unique contribution of this thesis. This switch-mode rectifier demonstrated the ability for self-sustained operation by having its output voltage power its control circuitry while lighting up six LEDs. When connected to a 2^{nd} generation stator, the self-sustaining boost rectifier delivered 5.52 W at a regulated output voltage of 12 V to a load resistor at 303,000 rpm. This was at a power factor of 98.3%, electrical system efficiency of 57% and, an overall generator system efficiency of 23.6%.

6.2 Conclusions

The work presented in this thesis proves that microscale axial-flux PM machines and power electronics are capable of generating and delivering multi-Watt DC power to a load and are a viable compact power generation system for portable power applications. With the transformer and diode bridge rectifier, a maximum of 8 W, at a generator system efficiency of 26.6%, was delivered to a resistive load at 300,000 rpm. Also at 300,000 rpm, a maximum of 5.52 W was delivered with the switch-mode rectifier at a generator system efficiency of 23.6% W and at a power density three times that of the passive circuit.

From the comparison of axial-flux induction and PM machines in Chapter 3 it is found that a high performance permanent magnet such as SmCo produces a rotor flux that is much larger than what can be produced by stator currents through the mutual inductance. This inductance is insufficient to match the flux from the PM machine because of the small number of turns/pole, N, used in the stator. Since the mutual inductance is proportional to N^2, the power capability of the induction machine decreases significantly as the number of turns/pole decreases. Macroscale machines typically have many turns/pole (~20-turns/pole). However, due to space limitations, microscale machines will generally have only a few turns/pole (~2–4-turns/pole). Increasing the number of turns/pole would significantly increase the resistance of the stator windings due to minimum feature size constraints. Thus, high power density is better achieved through the interaction of stator currents with flux generated from a permanent magnet rather than an electromagnet at the microscale.

In addition, the inner and outer end turns make up a small percentage of the overall size of macroscale machines. In microscale machines, these inner and outer end turns can take up considerable area and typically account for a large proportion of the overall winding resistance. The space required for the inner end turns of a planar machine limits the minimum radius of the active area of the machine, while the space required for the outer end turns can double the surface area of the stator. Furthermore, the leakage inductance of the microscale surface wound PM machines presented here dominates the over all stator inductance because the surface area taken up by the outer end turns is comparable to the active area of the machine. However, despite the effects of the leakage inductance, the overall impendence of the PM machines is resistance dominated. This is because the time constant of the magnetic machine, equal to the stator inductance divided by the stator resistance, scales as length squared and becomes very small at the microscale.

The difficulty of using microfabrication to bury windings in slots and closing the slots over with hats, as is typical in the stators of macroscale magnetic machines, makes surface wound stators preferable at the microscale. In fact, it is the absence of slots that allow for the fabrication of more complex interleaved winding patterns of the surface wound PM machines which allow for higher flux linkage than in the

slotted stator PM machines. The stator windings can be photolithographically defined, which permits optimized winding patterns with variable-width conductors. In addition, high-resolution features can help reduce certain losses; eddy current losses in the windings can be reduced by using laminations of micron scale thicknesses. Microfabrication can be used to create flat conductors which have a larger surface area to volume ratio than round conductors. By placing these flat conductors in intimate contact to their substrate, cooling via thermal conduction greatly improves. In fact it is the microfabricated coils, with small interconductor gaps, variable width geometries, complex interleaved structures and enhanced heat transfer capabilities, that are the key enabling technology for achieving high current density in miniaturized PM generators. Current densities of $\sim 10^9$ A/m^2 have been achieved in the second generation stators when delivering 8 W to a load and, along with the high rotational speeds, lead to power densities that are three times that of a macroscale turbine generator.

The biggest loss in the PM machines is due to eddy currents in the conductive stator core. In fact, at 305,000 rpm the eddy current loss (12.56 W) is larger than either the output power (8 W) or the sum of all the other losses (9.56 W). This means that the PM machines must have laminated stators in order to improve their overall system efficiency. The proximity eddy current loss in the stator windings are on the order of 1 W at 305,000 rpm. At higher speeds, this will increase significantly and it may be necessary to laminate the radial conductors of the stator windings. However, because the PM machine is expected to operate at 300 °C, conductivity of the stator windings will drop by more than a factor of two. The resulting decrease in conductivity will partially offset the increased loss due to higher rotational speeds. The increase in conduction loss due to higher temperatures may require that the radial conductors be unlaminated to minimize the sum of the conduction and proximity losses.

PM machines allow the use of both passive and active power electronics to deliver DC power. Passive electronics, particularly the transformers, are very large relative to the PM machine and do not provide output voltage regulation. However, they can be made arbitrarily large so as to improve efficiency. A regulated output voltage is necessary for powering most modern portable electronic equipment. In addition, passive electronics do not provide power factor correction which is important at speeds of

300,000 rpm and above. Active power electronics, such as the switch-mode boost rectifier can provide both output voltage regulation and power factor correction in a much more compact form. In fact, the power stage of the boost rectifier is about the same size as the stator die. The control IC and gate drives and even the power MOSFETs can be integrated into a single package, further reducing the overall size of the power electronics without degradation in efficiency. Integration could lead to active power electronics with a total volume of ~500 m^3. This would be half the volume of the power stage of the discrete implementation and over six times smaller than the transformer/diode bridge circuit.

Using active power electronics with high speed microscale PM machines requires that two important issues be addressed. The first is that given their high rotational speed, these machines operate at electrical frequencies one to two orders of magnitude larger than typical macroscale machines, typically in the kHz to tens of kHz range. The high operating electrical frequencies lead to smaller passive filtering components in switch-mode power electronic circuits. However, the small size of these PM machines also leads to low stator inductances which can require very high switching frequencies. In fact, using the stator inductance as the primary magnetic component in the switch-mode rectifier would require switching frequencies of ~10 MHz if continuous-conduction-mode operation with small current ripple is desired. This leads to very high switching losses and poor efficiency in the converter.

The second issue that must be addressed is that for active rectification to work, the position/speed of the poles of the rotor PM must typically be known. This information is used to keep the stator currents in phase with the voltage to achieve maximum energy/power conversion. It could be done by direct measurement using a Hall sensor but that is not feasible due to the temperature constraints for the PM machine. Alternatively, "sensorless" techniques could be used by measuring the terminal currents and voltages of the machine. This solution is computationally intensive, often requiring the use of high-performance microprocessors or digital signal processors (DSP). It is difficult to implement given the high rotational speeds and switching frequencies required.

These issues are resolved in this thesis by using a switch-mode rectifier operating in discontinuous-conduction-mode (DCM) with an external inductor as the primary magnetic energy storage element. The

external inductors are operated in DCM with the stator inductance, along with an external capacitor, acting as a filter so that the currents in the machine comprise mainly of the fundamental harmonic. This DCM operation provides automatic power factor correction at a reduced switching frequency of 500 kHz without the need for direct rotor position/speed or stator current/voltage sensing. In addition the DCM operation of the rectifier turns the generator into a controlled current source so that only a single feedback loop is necessary to regulate the output voltage.

To predict the performance of the surface wound PM machine within the microengine environment assume that a 2nd generation stator is used with a large PM (5 mm ID, 10 mm OD) at a 50 μm air gap. The stator resistance is assumed to be 136 mΩ, which is the minimum achieved so far. The PM has a remanence of 0.52 T and a 1.2 mm transition region, which are values used to fit the continuum model to the measure data in Section 5.1.3. At 300 °C the remanence of SmCo will be 87% of its room temperature value while the stator resistance will be 214% of its room temperature value. The stator resistance will become 291 mΩ and the fundamental of the open circuit voltage at 500,000 rpm is 3.4 V. That stator consists of 50 μm thick lamination and 50 μm thick lamination dividers. The rotor and stator cores use the electroplated CoFe from Chapter 3 and are 500 μm and 800 μm thick, respectively. Under these conditions 10 W of output power is achievable with an overall generator system efficiency (η_g) of 50% assuming a switch-mode rectifier that is 80% (η_{pe}). The radial conductors of the stator windings are not laminated because the conduction loss (3.5 A) is much higher than the proximity eddy current loss (1.37 W). The laminated stator core has only 0.78 W of eddy current loss. Without these laminations the eddy current loss would be over 40 W. This is summarized in Table 6-1.

If the annular PM is replaced with discrete PMs that are fully magnetized to a remanence of 1 T at room temperature, the fundamental of the open-circuit voltage becomes 6.78 V. 10 W can be delivered to a load at an overall generator system efficiency of 56% for a switch-mode rectifier that is 80% efficient. Due to the increase flux in the air gap, each radial conductor is composed of two laminations which increase the stator resistance to 675 mΩ. The proximity eddy current loss is reduced to 0.68 W while the conduction loss in the stator is 2.05 W. The eddy current loss is much smaller than in the case of the

Annular PM because the higher remanence of the PM leads to heavier saturation in the stator core. This leads to a lower effective permeability and a larger skin depth.

Using the same discrete PMs this generator is predicted to deliver 20 W of output power at a speed of 500,000 rpm with an overall generator system efficiency of 58.7% for a switch-mode rectifier that is 80% efficient. It takes about twice as much current to generate 20 W than to generate 10 W. This means that the conduction loss goes up by a factor of four. To make the generator system 58.7% efficient, the radial conductors have been left unlaminated to minimize conduction loss. The interconductor gaps have been increased from 50 μm to 100 μm to reduce proximity eddy current losses in the stator windings with a minimal (8%) increase in the stator winding resistance.

Table 6-1: Predicted generator system performance at 300 °C and 500,000 rpm.

Property	Annular PM	Discrete PM	Discrete PM
P_{mech}	20.04 W	17.89 W	34.15 W
P_{prox}	1.37 W	0.68 W	2.71 W
P_{eddy}	0.78 W	0.24 W	0.27 W
$P_{hysteresis}$	1.89 W	2.42 W	2.42 W
P_{elect}	16 W	14.55 W	28.75 W
P_{cond}	3.5 W	2.05 W	3.75W
P_{pe}	2.5 W	2.5 W	2.5 W
P_{out}	10 W	10 W	20 W
η_g	50%	56%	58.7%

6.3 Recommendations for Future Work

The next logical step is to demonstrate the performance of the PM machines at high temperature. The resistance of the stator windings is predicted to be 214% its room temperature value when heated to 300 °C. The remanence of SmCo at 300 °C is 87% of its room temperature value. Therefore the matched load power is expected to drop to about 35% of what was achieved at room temperature. To maintain the generator system efficiency at its room temperature value, the output power would have to be even lower.

The maximum speed attainable with a SmCo magnet is 325,000 rpm when housed in a titanium retaining ring [56]. Further work must be done on the structural integrity of the rotor assembly to bring the operating speed up to the 500,000 rpm – 1 Mrpm speeds of the microengine. This might require the

use of discrete "pie piece" magnets in a spoke wheel rotor. The poling process used to create the multi-pole PM annulus led to a suboptimal magnetization of ~0.5 T. The use of discrete PM pieces with the full remanence of 1 T would create a higher flux in the air gap and increase output power by a factor of four. This would more than offset the reduced output power due to the higher stator resistance at 300 °C.

Along with high temperature characterization and structural improvements, integration of the PM machines into the silicon microengine must be done. This involves carrying over the electroplating process done on a ferromagnetic wafer over to a silicon wafer. In addition, laminations in the stator windings and the stator core will be needed to limit eddy current losses in these parts of the machine. Also, incorporating hard or soft magnetic materials into the process flow of the microengine will require subsequent microfabrication steps to occur at low temperature. Furthermore, integration of the PM machine will rely heavily on the design of high speed air bearings capable of supporting a much more massive rotor than is currently supported. This may require a much more uniformly fabricated rotor PM and rotor core to reduce imbalance and/or the use of active balancing techniques.

The biggest losses in the boost rectifier are the conduction losses in the boost inductors and diode bridge. Improved inductors wound with Litz wire can reduce high frequency AC resistance and reduce conduction loss in the inductors. Using synchronous rectification, in which the MOSFET is kept on during half the stator electrical period when the voltage is negative, would reduce diode conduction loss in half by not having to turn on the free-wheeling diodes. This would also cut switching losses in half since the PWM switching of the MOSFET would occur only when stator line-to-neutral voltage is positive. This would require sensing the MOSFET current or possibly the terminal voltage but note that only the magnitude is needed to implement synchronous rectification. With synchronous rectification and the use of Litz wire inductors, the boost rectifier is expected to be ~80% efficient or roughly 10% more efficient than the current design.

The final issue to be addressed is the startup of the boost rectifier. Currently an external power source brings the V_{DD} pin of the control IC up to 7 V at which point the IC turns on and brings the output voltage up to 12 V. The output voltage then powers the IC and gate drives. When the machine is spinning, it

creates a low (1 – 3 V) DC voltage across the diode bridge. This voltage can be boosted up using a charge pump to 7 V to turn-on the control IC creating a self starting rectifier.

Appendix A: Planar Layer with Magnetization

This appendix derives the convection-diffusion equation for a planar layer with a spatially varying magnetization used to model the rotor permanent magnet in Chapter 2. Consider a medium with magnetization $\overline{M}$, permeability μ, and conductivity σ moving with constant velocity, $\overline{v}$. The constitutive relation for this medium is $\overline{B} = \mu(\overline{H} + \overline{M})$. Since the divergence of $\overline{B}$ is zero, it can written as the curl of some vector

$$\nabla \cdot \overline{B} = 0 \rightarrow \overline{B} = \nabla \times \overline{A}, \tag{A-1}$$

where $\overline{A}$ is known as the magnetic vector potential. Ampere's law in this medium is

$$\nabla \times \overline{H} = \sigma(\overline{E} + \overline{v} \times \overline{B}). \tag{A-2}$$

Multiplying both sides of Equation (A-2) by μ and substituting in the constitutive law gives

$$\nabla \times (\overline{B} - \mu\overline{M}) = \mu\sigma(\overline{E} + \overline{v} \times \overline{B}). \tag{A-3}$$

Taking the curl of both sides of (A-3) gives

$$\nabla \times \nabla \times (\overline{B} - \mu\overline{M}) = \mu\sigma(\nabla \times \overline{E} + \nabla \times \overline{v} \times \overline{B}). \tag{A-4}$$

The electric field can now be substituted with the $\overline{B}$ field using Faraday's law,

$$\nabla \times \overline{E} = -\frac{\partial \overline{B}}{\partial t}. \tag{A-5}$$

Doing so reduces (A-4) to

$$\nabla \times \nabla \times (\overline{B} - \mu\overline{M}) = \mu\sigma\left(-\frac{\partial \overline{B}}{\partial t} + \nabla \times \overline{v} \times \overline{B}\right). \tag{A-6}$$

Substituting (A-1) into equation (A-6) gives

$$\nabla \times \nabla \times (\nabla \times \overline{A} - \mu\overline{M}) = \mu\sigma\left(-\nabla \times \frac{\partial \overline{A}}{\partial t} + \nabla \times \overline{v} \times \nabla \times \overline{A}\right). \tag{A-7}$$

Equation (A-7) can be rewritten as

$$\nabla \times \left[\nabla \times \left(\nabla \times \overline{A} - \mu \overline{M} \right) + \mu\sigma \left(\frac{\partial \overline{A}}{\partial t} - \overline{v} \times \nabla \times \overline{A} \right) \right] = 0 . \tag{A-8}$$

Using the identity $\nabla \times \nabla \phi = 0$, the expression within the bracket in Equation (A-8) can be set equal to the gradient of some scalar potential

$$\nabla \times \left(\nabla \times \overline{A} - \mu \overline{M} \right) + \mu\sigma \left(\frac{\partial \overline{A}}{\partial t} - \overline{v} \times \nabla \times \overline{A} \right) = -\nabla \phi , \tag{A-9}$$

which further simplifies to

$$\nabla \left(\nabla \cdot \overline{A} \right) - \nabla^2 \overline{A} - \nabla \times \mu \overline{M} + \mu\sigma \left(\frac{\partial \overline{A}}{\partial t} - \overline{v} \times \nabla \times \overline{A} \right) = -\nabla \phi . \tag{A-10}$$

Using the following gauge condition

$$\nabla \left(\nabla \cdot \overline{A} + \phi \right) = 0 , \tag{A-11}$$

Equation (A-10) reduces to

$$\nabla^2 \overline{A} + \nabla \times \mu \overline{M} + = \mu\sigma \left(\frac{\partial \overline{A}}{\partial t} - \overline{v} \times \nabla \times \overline{A} \right) . \tag{A-12}$$

For a planar layer with a magnetization $M_z(y)$ moving uniformly with velocity U_y, as shown in Figure A-1, will have a vector potential with only one component, A_x. For such a layer, Equation (A-12) becomes

$$\nabla^2 A_x + \mu \frac{\partial M_z}{\partial y} = \mu\sigma \left(\frac{\partial A_x}{\partial t} + U_y \frac{\partial A_x}{\partial y} \right) . \tag{A-13}$$

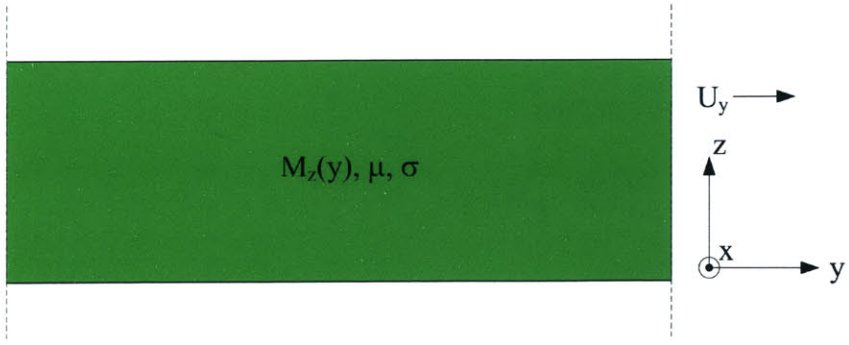

Figure A-1: Lossy magnetic media moving in the y direction with velocity U_y.

Appendix B: Matlab code for Chapter 3

This appendix contains the Matlab scripts used in the comparison of the slotted stator induction machine, slotted stator PM machine and surface wound PM machine in Chapter 3. For each machine there is a script that contains all the parameters used; a script that computes the effective permeabilities and hysteresis loss in the stator core; a script that computes the torque, open-circuit voltage and inductance; a script that computes the stator resistance and a main script that runs all the other scripts. For the slotted stator inducton machine there is an additional script that computes the hysteresis loss in the rotor core. For the surface wound PM machine there is an additional script that computes the proximity eddy current loss in the stator windings. For the high temperature comparison in Section 3.5, the rotor conductivity is divided by 2.14 and the remenance of the rotor PM is reduced to 87% of its room temperature value.

```
%%%%%%%%%%%%%%%%%%%%%%%%%%%%%%%%%%%%%%%%%%%%%%%%%%%
%%%% SLotted stator Induction Machine system (SLIM_system) calls the other SLIM_*          %%%%
%%%% scripts to compute power and efficiency vs. speed, input current, pole pairs ...       %%%%
%%%% SLIM_parameters is called first to initialize all the variables followed by            %%%%
%%%% SLIM_fields which computes the effective permiabilities of the machine.                %%%%
%%%% SLIM_power, SLIM_hysteresis and SLIM_resistance are then called to compute the         %%%%
%%%% output power, efficiency and various losses in the slotted sator induction machine.    %%%%
%%%%%%%%%%%%%%%%%%%%%%%%%%%%%%%%%%%%%%%%%%%%%%%%%%%

global T_rc T_al T_ag T_cl g_cl L_gap L_pole T_hat T_base R_im R_om
global u_0 u_a sigma_r sigma_c sigma_a v M P N w_e W S N_lam pf alpha

SLIM_parameters

%%% To get output power, loss, efficiency at a single speed, current ... %%%

[U_r U_p U_b R_mr Core_loss_s] = SLIM_fields(w_m,I_o,Href,Bref,Ba,Core_loss_density);
[Fp Torque V_o L_s] = SLIM_power(w_m,I_o,U_r,U_p,U_b,R_mr);
[R_s] = SLIM_resistance(W_ci,W_co,T_ci,T_co,g_tr,W_h);
[Core_loss_r] = SLIM_hysteresis(w_m,I_o,U_r,U_p,U_b,R_mr,Ba,Core_loss_density,s);
P_mech = Torque*Omega_m;
P_elect = I_o*real(V_o);
P_cond = R_s*I_o^2;
P_core = Core_loss_s + Core_loss_r;
```

```
P_out = P_elect + P_cond;
Eff = (P_elect + P_cond)/(P_mech - P_core);

%%%%%%%%%%%%%%%%%%%%%%%%%%%%%%%%%%%%%%%%
%%% Optimzation with respect to slip and active layer thickness %%%
%%%%%%%%%%%%%%%%%%%%%%%%%%%%%%%%%%%%%%%%

slip = -1*[0:.01:.2];
active_layer = [10:10:100];
P_omax = 0;
Eff_max = 0;
for e = 1:length(slip)
        s = slip(e)
        w_e = w_m/(1-s);

        for f = 1:length(active_layer)
                T_al = active_layer(f)*1e-6;
                [U_r U_p U_b R_mr Core_loss_s] = SLIM_fields(w_m,I_o,Href,Bref,Ba,Core_loss_density);
                [Fp Torque V_o L_s] = SLIM_power(w_m,I_o,U_r,U_p,U_b,R_mr);
                [R_s] = SLIM_resistance(W_ci,W_co,T_ci,T_co,g_tr,W_h);
                [Core_loss_r] = SLIM_hysteresis(w_m,I_o,U_r,U_p,U_b,R_mr,Ba,Core_loss_density,s);
                P_mech = Torque*Omega_m;
                P_elect = I_o*real(V_o);
                P_cond = R_s*I_o^2;
                P_core = Core_loss_s + Core_loss_r;
                P_out(e,f) = max(0,-(P_elect + P_cond));
                Eff(e,f) = max(0,(P_elect + P_cond)/(P_mech - P_core));

                 if Eff(e,f) > Eff_max
                        Eff_max = Eff(e,f);
                        P_omax = P_out(e,f);
                        slip_max = s;
                        al_max = T_al;
                end

        end

end

figure(1)
surf(active_layer,slip,P_out)
xlabel('Thickness of active layer (\mum)')
ylabel('Slip')
zlabel('Power (W)')
title('Net output power vs. active layer thickness and slip')

figure(2)
surf(active_layer,slip,Eff*100)
xlabel('Thickness of active layer (\mum)')
ylabel('Slip')
zlabel('Efficiency (%)')
title('Efficiency vs. active layer thickness and slip')
```

```
%%%%%%%%%%%%%%%%%%%%%%%%%%%%%%%%%%%%%%%
%%% Optimzation with respect to phase current and alpha %%%
%%%%%%%%%%%%%%%%%%%%%%%%%%%%%%%%%%%%%%%

I_phase = [5:30];
alpha_parameter = [0.4:.05:.8];
P_omax = 0;
Eff_max = 0;

for e = 1:length(I_phase)
        I_o = I_phase(e)

        for f = 1:length(alpha_parameter)
                alpha = alpha_parameter(f);
                [U_r U_p U_b R_mr Core_loss_s] = SLIM_fields(w_m,I_o,Href,Bref,Ba,Core_loss_density);
                [Fp Torque V_o L_s] = SLIM_power(w_m,I_o,U_r,U_p,U_b,R_mr);
                [R_s] = SLIM_resistance(W_ci,W_co,T_ci,T_co,g_tr,W_h);
                [Core_loss_r] = SLIM_hysteresis(w_m,I_o,U_r,U_p,U_b,R_mr,Ba,Core_loss_density,s);
                P_mech = Torque*Omega_m;
                P_elect = I_o*real(V_o);
                P_cond = R_s*I_o^2;
                P_core = Core_loss_s + Core_loss_r;
                P_out(e,f) = max(0,-(P_elect + P_cond));
                Eff(e,f) = max(0,(P_elect + P_cond)/(P_mech - P_core));

                if (Eff(e,f) > Eff_max) & (P_out(e,f) >= 10)
                        Eff_max = Eff(e,f);
                        P_omax = P_out(e,f);
                        I_max = I_o;
                        a_max = alpha;
                end

        end

end

figure(3)
surf(alpha_parameter,I_phase,P_out)
xlabel('\alpha')
ylabel('I_o (A)')
zlabel('Power (W)')
title('Output power vs. \alpha and phase current')

figure(4)
surf(alpha_parameter,I_phase,Eff*100)
xlabel('\alpha')
ylabel('I_o (A)')
zlabel('Efficiency (%)')
title('Efficiency vs. \alpha and phase current')
```

```
%%%%%%%%%%%%%%%%%%%%%%%%%%%%%%%%%%%%
%%% Output power and efficiency vs. # of pole pairs %%%
%%%%%%%%%%%%%%%%%%%%%%%%%%%%%%%%%%%%

Pole_pairs = [2:8];
for e = 1:length(Pole_pairs)
        P = Pole_pairs(e)
        w_m = P*Omega_m;                % angular velocity of rotor (rad/s)
         s = -.1;                       % slip
        w_e = w_m/(1-s);                % electrical angular frequency (rad/s)
        [U_r U_p U_b R_mr Core_loss_s] = SLIM_fields(w_m,I_o,Href,Bref,Ba,Core_loss_density);
        [Fp Torque V_o L_s] = SLIM_power(w_m,I_o,U_r,U_p,U_b,R_mr);
        [R_s] = SLIM_resistance(W_ci,W_co,T_ci,T_co,g_tr,W_h);
        [Core_loss_r] = SLIM_hysteresis(w_m,I_o,U_r,U_p,U_b,R_mr,Ba,Core_loss_density,s);
        P_mech = Torque*Omega_m;
        P_elect = I_o*real(V_o);
        P_cond = R_s*I_o^2;
        P_core = Core_loss_s + Core_loss_r;
        P_out(e) = max(0,-(P_elect + P_cond));
        Eff(e) = max(0,(P_elect + P_cond)/(P_mech - P_core));
 end

figure(5)
subplot(2,1,1)
plot(2*Pole_pairs,P_out,'k')
xlabel('Poles')
ylabel('Power (W)')
title('Output power and efficiency vs. number of Poles ')
hold on
subplot(2,1,2)
plot(2*Pole_pairs,Eff*100,'k')
xlabel('Poles')
ylabel('Efficiency (%)')
hold on


%%%%%%%%%%%%%%%%%%%%%%%%%%%%%%%%%%%%
%%% Output power and efficiency vs. phase current %%%
%%%%%%%%%%%%%%%%%%%%%%%%%%%%%%%%%%%%

I_phase = [1:20];
for e = 1:length(I_phase)
        I_o = I_phase(e)
        [U_r U_p U_b R_mr Core_loss_s] = SLIM_fields(w_m,I_o,Href,Bref,Ba,Core_loss_density);
        [Fp Torque V_o L_s] = SLIM_power(w_m,I_o,U_r,U_p,U_b,R_mr);
        [R_s] = SLIM_resistance(W_ci,W_co,T_ci,T_co,g_tr,W_h);
        [Core_loss_r] = SLIM_hysteresis(w_m,I_o,U_r,U_p,U_b,R_mr,Ba,Core_loss_density,s);
        P_mech = Torque*Omega_m;
        P_elect = I_o*real(V_o);
        P_cond = R_s*I_o^2;
        P_core = Core_loss_s + Core_loss_r;
        P_out(e) = max(0,-(P_elect + P_cond));
        Eff(e) = max(0,(P_elect + P_cond)/(P_mech - P_core));

end
```

```
figure(6)
subplot(2,1,1)
plot(I_phase,P_out,'b')
xlabel('I_o (A)')
ylabel('Power (W)')
title('Output power and efficiency vs. Phase Current')
hold on
subplot(2,1,2)
plot(I_phase,Eff*100,'b')
xlabel('I_o (A)')
ylabel('Efficiency (%)')
hold on

%%%%%%%%%%%%%%%%%%%%%%%%%%%%%%%%%%%%%%%%%%%%%
%%% Output power and efficiency vs. outer radius of magnetic core %%%
%%%%%%%%%%%%%%%%%%%%%%%%%%%%%%%%%%%%%%%%%%%%%

Outer_Radius = [4:.1:5];
for e = 1:length(Outer_Radius)
        R_om = Outer_Radius(e)*1e-3
        Omega_m = 500/(R_om+1e-3);
        w_m = P*Omega_m;                % angular velocity of rotor (rad/s)
        s = -.1;                        % slip
        w_e = w_m/(1-s);                % electrical angular frequency (rad/s)
        [U_r U_p U_b R_mr Core_loss_s] = SLIM_fields(w_m,I_o,Href,Bref,Ba,Core_loss_density);
        [Fp Torque V_o L_s] = SLIM_power(w_m,I_o,U_r,U_p,U_b,R_mr);
        [R_s] = SLIM_resistance(W_ci,W_co,T_ci,T_co,g_tr,W_h);
        [Core_loss_r] = SLIM_hysteresis(w_m,I_o,U_r,U_p,U_b,R_mr,Ba,Core_loss_density,s);
        P_mech = Torque*Omega_m;
        P_elect = I_o*real(V_o);
        P_cond = R_s*I_o^2;
        P_core = Core_loss_s + Core_loss_r;
        P_out(e) = max(0,-(P_elect + P_cond));
        Eff(e) = max(0,(P_elect + P_cond)/(P_mech - P_core));

end

figure(7)
subplot(2,1,1)
plot(Outer_Radius,P_out,'k')
xlabel('Outer Radius (mm)')
ylabel('Power (W)')
title('Output power and efficiency vs. outer radius of rotor core')
hold on
subplot(2,1,2)
plot(Outer_Radius,Eff*100,'k')
xlabel('Outer Radius (mm)')
ylabel('Efficiency (%)')
hold on
```

```
%%%%%%%%%%%%%%%%%%%%%%%%%%%%%%%%%%%%%%%%%%%%%%%%%%%%%%%%%%%%%%%%%%%%%%%%%%%%%%%%
%%%%% SLotted stator Induction Machine parameters (SLIM_parameters) initializes the %%%%%
%%%%% variables for the machine dimensions, material properties and electrical inputs %%%%%
%%%%% used in SLIM_fields, SLIM_power, SLIM_hysteresis and SLIM_resistance. (MKS units) %%%%%
%%%%%%%%%%%%%%%%%%%%%%%%%%%%%%%%%%%%%%%%%%%%%%%%%%%%%%%%%%%%%%%%%%%%%%%%%%%%%%%%

global T_rc T_al T_ag T_cl g_cl L_gap L_pole T_hat T_base R_im R_om
global u_0 u_a sigma_r sigma_c sigma_a v M P N w_e W S N_lam pf alpha

% Rotor Dimenstions (meters)

    T_rc = 500e-6;                          % thickness of rotor core
    T_al = 20e-6;                           % thickness of rotor conductor
    T_ag = 25e-6;                           % air gap

% Stator Dimensions (meters)

    T_tr = 150e-6;                          % thickness of Si trench
    g_tr = T_tr/3;                          % gap between trench sidewall and coil
    T_cl = T_tr - 25e-6;                    % thickness of Cu coil
    T_ci = T_cl;                            % thickness of inner end turn
    T_co = T_cl;                            % thickness of outer end turn
    alpha = 0.65;                           % fraction of slot taken up by coil and Si dividers
    g_cl = T_tr/5;                          % gap between two adjacent coils
    W_h = 100e-6;                           % width of horizontal Si structural dividers
    W_v = 100e-6;                           % width of vertical Si structural dividers
    W_ci = 0.5*(1e-3 - (W_h+2*g_tr+g_cl));  % width of inner end turn coils
    W_co = 500e-6;                          % width of outer end turn coils
    T_wafer = 550e-6;                       % thickness of Si wafer
    L_gap = 50e-6;                          % length of stator tooth gap
    T_hat = T_wafer - T_tr - W_v - T_ag;    % thickness of stator hat
    T_base = 2*T_wafer - T_tr - W_v;        % thickness of stator base
    L_pole = 2*(T_tr + W_v);                % length of stator pole
    R_im = 0.003;                           % magnetic core inner radius
    R_om = 0.005;                           % magnetic core outer radius

% Material Properties

    Temp = 300;                             % temperature (degrees C)
    u_0 = 4*pi*1e-7;                        % permeability of free space (henry/m)
    u_a = 1*u_0;                            % permeability of active layer (henry/m)
    sigma_r = 5e6;                          % conductivity of electroplated CoFe (siemens)
    sigma_c = 5.8e7/(1+3.9e-3*(Temp-25));   % conductivity of Cu (siemens)
    sigma_a = sigma_c;                      % conductivity of rotor active layer (siemens)
    v = 2e-5;                               % viscosity of air

    load CoFe_data.mat                      % B-H data for CoFe from GIT
    Href1 = max(Ho) + [3e6:-1e4:1e4];       % extenstion of B-H curve
    Bref1 = max(Bo) + (Href1-max(Ho))*u_0;  % using permeability u_0
    Href = [Ho Href1];                      % B-H curve used in SLIM_fields
    Bref = [Bo Bref1];

% Electrical Parameters

    I_o = 20;                               % Phase current (A)
    M = 1;                                  % number of harmonics solved for
```

```
Speed = 795774.7;                       % speed (RPM)
Omega_m = 500/(R_om+1e-3);              % speed (rad/s)
P = 5;                                  % number of pole pairs
N = 2;                                  % number of turns/pole
w_m = P*Omega_m;                        % angular velocity of rotor (rad/s)
s = -.1;                                % slip
w_e = w_m/(1-s);                        % electrical angular frequency (rad/s)

% Lamination Parameters

W = 30e-6;                              % lamination thickness (m)
S = 20e-6;                              % insulation thickness (m)
N_lam = round((R_om - R_im)/(W+S));     % number of laminations
pf = W/(W+S);                           % packing factor
```

```
function [u_r,u_p,u_b,R_mr,Core_loss_s] = SLIM_fields(w_m,I_o,Href,Bref,Ba,Core_loss_density)

%%%%%%%%%%%%%%%%%%%%%%%%%%%%%%%%%%%%%%%%%%%%%%%%%%%%%%%%%%%%%%%%%%%%%%%%%%%
%%%%% SLotted stator Induction Machine fields (SLIM_fields) computes the permeability of %%%%%
%%%%% the rotor core (u_r), stator pole (u_p) and stator base (u_b) using a nonlinear B-H %%%%%
%%%%% curve. The starting value for u_r, u_p and u_b is 200*u_0. The script iteratively %%%%%
%%%%% solves for the peak B fields in the rotor & stator until u_r, u_p and u_b are found %%%%%
%%%%% such that the maximum B lies on the B-H curve. The script also computes the resulting %%%%%
%%%%% core loss in the stator. (MKS units)                                          %%%%%
%%%%%%%%%%%%%%%%%%%%%%%%%%%%%%%%%%%%%%%%%%%%%%%%%%%%%%%%%%%%%%%%%%%%%%%%%%%

global T_rc T_al T_ag T_cl g_cl L_gap L_pole T_hat T_base R_im R_om
global u_0 u_a sigma_r sigma_c sigma_a v M P N w_e W S N_lam pf alpha

Z = N_lam+1;
dr = (R_om - R_im)/(Z-1);               % radial increment (m)
u_r = ones(1,Z)*200*u_0;                % initial rotor permeability (henry/m)
u_p = ones(1,Z)*200*u_0;                % initial stator pole permeability (henry/m)
u_b = ones(1,Z)*200*u_0;                % initial stator base permeability (henry/m)
B_maxr = ones(1,Z)*5;                   % initial B_maxr (T)
B_mr = ones(1,Z)*2;                     % initial B_mr on B_H curve (T)
B_maxp = ones(1,Z)*5;                   % initial B_maxp (T)
B_mp = ones(1,Z)*2;                     % initial B_mp on B_H curve (T)
B_maxb = ones(1,Z)*5;                   % initial B_maxb (T)
B_mb = ones(1,Z)*2;                     % initial B_mb on B_H curve (T)

for k = 1:Z

    r(k) = R_im + (k-1)*dr;             % rotor radius (m)
    lambda = 2*pi*r(k)/P;               % wave length (m)
    L_base = lambda/4;                  % base length = 1/4 of a wavelength (m)
    T_pole = (1-alpha)*L_base;          % thickness of stator pole (m)

    V_pole = 2*P*N*T_pole*L_pole*W;     % volume of all the stator poles at radius r (m^3)
    V_base = 2*P*N*T_base*L_base*W;     % volume of all the stator bases at radius r (m^3)
    V_hat = 2*P*N*T_hat*(L_base-L_gap)*W; % volume of all the stator hats at radius r (m^3)

    sigma_p = sigma_r;                  % conductivity of the stator pole (siemens)
    sigma_b = sigma_r;                  % conductivity of the stator base (siemens)
```

```
delta_p = sqrt(2/(u_p(k)*sigma_p*w_e));          % magnetic skin depth of stator pole (m)
Q_p = .5*(1+j)*W/delta_p;                        % ratio of lamination thickness to skin depth
FQ_p = Q_p/tanh(Q_p);                            % eddy current reluctance factor

delta_b = sqrt(2/(u_b(k)*sigma_p*w_e));          % magnetic skin depth of stator base (m)
Q_b = .5*(1+j)*W/delta_b;                        % ratio of lamination thickness to skin depth
FQ_b = Q_b/tanh(Q_b);                            % eddy current reluctance factor

Rg = L_gap/(u_0*T_hat);                          % reluctance of teeth gap
Rp = FQ_p*L_pole/(u_p(k)*T_pole*pf);             % reluctance of stator pole
Rb = FQ_b*(L_base-T_pole)/(u_b(k)*T_base*pf);    % reluctance of stator base

R_s = Rg + 2*Rp + Rb;                            % reluctance seen by 1 stator tooth gap
R_r = (1+j)*Rp + .5*(1+j)*Rb;                    % reluctance seen by 1 rotor flux source

while (abs(B_maxb(k) - B_mb(k)) > 1e-4) | (abs(B_maxp(k) - B_mp(k)) > 1e-4) | (abs(B_maxr(k) -
B_mr(k)) > 1e-4),


      for m = 1:M

            n = (2*m - 1) * (-1)^(m-1);                % harmonic number
            k_n = n*P/r(k);                            % wave number (1/m)

            gamma_0n = abs(k_n);                       % magnitude of wave number (1/m)
            gamma_an = sqrt((k_n)^2+i*u_a*sigma_a*(w_e - n*w_m));
                                                       % rotor conductor diffusion constant (1/m)
            gamma_rn = sqrt((k_n)^2+i*u_r(k)*sigma_r*(w_e - n*w_m));
                                                        % rotor core diffusion constant (1/m)

             %%% rotor transfer relation constants %%%

beta_1n = (u_r(k)/gamma_rn) * gamma_0n/u_0 * sinh(gamma_rn*T_rc)  + 1* cosh(gamma_rn*T_rc);
beta_2n = (gamma_rn/u_r(k)) * 1 * sinh(gamma_rn*T_rc)  + gamma_0n/u_0 * cosh(gamma_rn*T_rc);
beta_3n = (u_a/gamma_an) * beta_2n * sinh(gamma_an*T_al)  + beta_1n * cosh(gamma_an*T_al);
beta_4n = (gamma_an/u_a) * beta_1n * sinh(gamma_an*T_al)  + beta_2n * cosh(gamma_an*T_al);
beta_5n = (u_0/gamma_0n) * beta_4n * sinh(gamma_0n*T_ag)  + beta_3n * cosh(gamma_0n*T_ag);
beta_6n = (gamma_0n/u_0) * beta_3n * sinh(gamma_0n*T_ag)  + beta_4n * cosh(gamma_0n*T_ag);

      %%%%%%%%%%%%%%%%%%%%%%%%%%%%%%%%%%%%%%%%%%%%%%%%%%%%%%%%

            Hyn3 = 4 * exp(j*n*pi/4)* sin(n*pi*L_gap/lambda) / (n*pi);
            Axn6 = -Hyn3/beta_6n;                            % vector potential at surface of stator
            G_beta(m) = sinc(n/4)*(beta_5n/beta_6n)*sin(n*pi*L_gap/lambda)*exp(j*n*pi/4);

            Byn5(m) = -u_r(k)*beta_2n*Axn6;  % harmonic components of tangential B at rotor core
            Bzn5(m) = j*k_n*beta_1n*Axn6;    % harmonic components of normal B at rotor core

      end

      L_eq = L_gap - j*2*R_r*sum(G_beta);        % effective length of stator teeth gap (m)
       H_y3 = (1-j)*I_o/L_eq;                    % tangential H at surface of stator (A/m)

      Phi_s = u_0*T_hat*H_y3;                    % leakage flux through stator tooth (Wb)
      Phi_r = j*2*sum(G_beta)*H_y3;              % magentizing flux (Wb)
```

```
            Phi_p = Phi_r + (j-1)*Phi_s;                % flux through stator pole (Wb)
            Phi_b = Phi_s + Phi_r/(j-1);                % flux through stator base (Wb)


            B_r = sqrt(0.5*sum(abs(Byn5).^2+abs(Bzn5).^2))*abs(H_y3);
                                                        % magnitude of B through rotor core (T)
            B_g = abs(u_0*H_y3);                        % magnitude of B through stator teeth (T)
            B_p = abs(Phi_p/T_pole);                    % magnitude of B through stator pole (T)
            B_b = abs(Phi_b/T_base);                    % magnitude of B through stator base (T)

            B_maxr(k) = B_r;                            % update B_maxr
            H_maxr(k) = B_maxr(k)/u_r(k);               % compute corresponding H_maxr using current u
            B_mr(k) = interp1(Href,Bref,H_maxr(k));     % update B_mr using nonlinear B-H curve
            u_r(k) = B_mr(k)/H_maxr(k);                 % update rotor permeability

             B_maxp(k) = B_p;                           % update B_maxp
             H_maxp(k) = B_maxp(k)/u_p(k);              %  compute corresponding H_maxp using current u
            B_mp(k) = interp1(Href,Bref,H_maxp(k));     % update B_mp using nonlinear B-H curve
            u_p(k) = B_mp(k)/H_maxp(k);                 % update stator pole permeability

            B_maxb(k) = B_b;                            % update B_maxb
            H_maxb(k) = B_maxb(k)/u_b(k);               % compute corresponding H_maxb using current u
            B_mb(k) = interp1(Href,Bref,H_maxb(k));     % update B_mb using nonlinear B-H curve
            u_b(k) = B_mb(k)/H_maxb(k);                 % update stator base permeability

        end

        R_mr(k) = r(k);                                 % rotor radius (m)
        B_h = B_p*T_pole/(L_base-L_gap);                % magnitude of B through rotor core (T)

        %%% Compute hysteresis loss in slotted stator lamination at radius r %%%

        if B_h >= 1.72 % 0.7 T for Moly Permalloy (NiFeMo), 1.72 T for electroplated CoFeNi
                cl_h = V_hat*max(Core_loss_density);
        else
                cl_h = V_hat*interp1(Ba,Core_loss_density,B_h);
        end

        if B_p >= 1.72 % 0.7 T for Moly Permalloy (NiFeMo), 1.72 T for electroplated CoFeNi
                cl_p = V_pole*max(Core_loss_density);
        else
                cl_p = V_pole*interp1(Ba,Core_loss_density,B_p);
        end

        if B_b >= 1.72 % 0.7 T for Moly Permalloy (NiFeMo), 1.72 T for electroplated CoFeNi
                cl_b = V_base*max(Core_loss_density);
        else
                cl_b = V_base*interp1(Ba,Core_loss_density,B_b);
        end

        dCL_s(k) = cl_h + cl_p + cl_b;

end

Core_loss_s = w_e*sum(dCL_s)/(2*pi);  % Total hysteresis loss in stator (W)
```

```
function [Fp,Torque,V_o,L_s] = SLIM_power(w_m,I_o,U_r,U_p,U_b,R_mr)

%%%%%%%%%%%%%%%%%%%%%%%%%%%%%%%%%%%%%%%%%%%%%%%%%%%%%%%%%%%%%%%%%%%%%%%%%%%%%%%
%%%% SLotted stator Induction Machine power (SLIM_power) computes the pull-in force,     %%%%%
%%%% torque, induced voltage and stator phase inductance for the slotted stator           %%%%%
%%%% induction machine using the effective permeability for the rotor core, stator pole   %%%%%
%%%% and stator base from SLIM_fields. (MKS units)                                        %%%%%
%%%%%%%%%%%%%%%%%%%%%%%%%%%%%%%%%%%%%%%%%%%%%%%%%%%%%%%%%%%%%%%%%%%%%%%%%%%%%%%

global T_rc T_al T_ag T_cl g_cl L_gap L_pole T_hat T_base R_im R_om
global u_0 u_a sigma_r sigma_c sigma_a v M P N w_e W S N_lam pf alpha

dr = (R_om-R_im)/500;                          % incremental radiul distance (m)

for x = 1:501

    r = R_im + (x-1)*dr;                       % radius (m)
    lambda = 2*pi*r/P;                         % wave length (m)
    L_base = lambda/4;                         % base length = 1/4 of a wavelength (m)
    T_pole = (1-alpha)*L_base;                 % thickness of stator pole (m)

    u_r = interp1(R_mr,U_r,r);                 % rotor permeability (henry/m)
    u_p = interp1(R_mr,U_p,r);                 % stator pole permeability (henry/m)
    u_b = interp1(R_mr,U_b,r);                 % stator base permeability (henry/m)

    sigma_p = sigma_r;                         % conductivity of the stator pole (siemens)
    sigma_b = sigma_r;                         % conductivity of the stator base (siemens)

    delta_p = sqrt(2/(u_p*sigma_p*w_e));       % magnetic skin depth of stator pole (m)
    Q_p = .5*(1+j)*W/delta_p;                  % ratio of lamination thickness to skin depth
    FQ_p = Q_p/tanh(Q_p);                      % eddy current reluctance factor

    delta_b = sqrt(2/(u_b*sigma_b*w_e));       % magnetic skin depth of stator base (m)
    Q_b = .5*(1+j)*W/delta_b;                  % ratio of lamination thickness to skin depth
    FQ_b = Q_b/tanh(Q_b);                      % eddy current reluctance factor

    Rg = L_gap/(u_0*T_hat);                    % reluctance of teeth gap
    Rp = FQ_p*L_pole/(u_p*T_pole*pf);          % reluctance of stator pole
    Rb = FQ_b*(L_base)/(u_b*T_base*pf);        % reluctance of stator base

    R_s = Rg + 2*Rp + Rb;                      % reluctance seen by 1 stator tooth gap
    R_r = (1+j)*Rp + .5*(1+j)*Rb;              % reluctance seen by rotor flux over stator tooth

    for m = 1:M

        n = (2*m - 1) * (-1)^(m-1);            % harmonic number
        k_n = n*P/r;                           % wave number (1/m)

        gamma_0n = abs(k_n);                   % magnitude of wave number (1/m)
        gamma_an = sqrt((k_n)^2+i*u_a*sigma_a*(w_e - n*w_m));
                                               % rotor conductor diffusion constant (1/m)
        gamma_rn = sqrt((k_n)^2+i*u_r*sigma_r*(w_e - n*w_m));
                                               % rotor core diffusion constant (1/m)

        %%% rotor transfer relation constants %%%
```

```
        beta_1n = (u_r/gamma_rn) * gamma_0n/u_0 * sinh(gamma_rn*T_rc)  + 1 * cosh(gamma_rn*T_rc);
        beta_2n = (gamma_rn/u_r) * 1 * sinh(gamma_rn*T_rc)  + gamma_0n/u_0 * cosh(gamma_rn*T_rc);
        beta_3n = (u_a/gamma_an) * beta_2n * sinh(gamma_an*T_al)  + beta_1n * cosh(gamma_an*T_al);
        beta_4n = (gamma_an/u_a) * beta_1n * sinh(gamma_an*T_al)  + beta_2n * cosh(gamma_an*T_al);
        beta_5n = (u_0/gamma_0n) * beta_4n * sinh(gamma_0n*T_ag)  + beta_3n * cosh(gamma_0n*T_ag);
        beta_6n = (gamma_0n/u_0) * beta_3n * sinh(gamma_0n*T_ag)  + beta_4n * cosh(gamma_0n*T_ag);

                %%%%%%%%%%%%%%%%%%%%%%%%%%%%%%%%%%%%%%%%%%%%%%%%%%%%%%%

                Hyn3 = 4 * exp(j*n*pi/4)* sin(n*pi*L_gap/lambda) / (n*pi);
                Axn6 = -Hyn3/beta_6n;                   % vector potential at surface of stator
                G_beta(m) = sinc(n/4)*(beta_5n/beta_6n)*sin(n*pi*L_gap/lambda)*exp(j*n*pi/4);

                Hyn4 = -beta_4n*Axn6;    % harmonic components of tangential H at the rotor conductor surface
                Bzn4 = j*k_n*beta_3n*Axn6;
                                              % harmonic components of normal B at the rotor conductor surface

                zeta1(m) = 0.25*((abs(Bzn4))^2/u_0 + u_0*(abs(Hyn4))^2);
                                                  % harmonic component of pull-in force
                zeta2(m) = 0.5*real(Bzn4 * Hyn4');        % harmonic components of torque

  end

        L_eq = L_gap - j*2*R_r*sum(G_beta);           % effective length of stator teeth gap (m)
        H_y3 = (1-j)*I_o/L_eq;                        % tangential H at surface of stator (A/m)

        Phi_s = u_0*T_hat*H_y3;                       % leakage flux through stator tooth (Wb)
        Phi_r = j*2*sum(G_beta)*H_y3;                 % magentizing flux (Wb)
        Phi_p = Phi_r + (j-1)*Phi_s;                  % flux through stator pole (Wb)

        dFp(x) = sum(zeta1) * dr * r * (abs(H_y3))^2;     % pull-in force over region [r,r+dr] (N)
        dT(x) = sum(zeta2) * dr * r^2 * (abs(H_y3))^2;    % total torque over region [r,r+dr] (N-m)
        dPhi_m(x) = dr*(-j*Phi_r);                    % magnetizing flux over region [r,r+dr] (Wb)
        dPhi(x) = dr*(-j*Phi_p);                      % total flux over region [r,r+dr] (Wb)
end

Fp = -2*u_0*pi*sum(dFp);                              % pull-in force acting rotor (N)
Torque = -2*pi*sum(dT);                               % torque on rotor (N-m)
V_o = j*w_e*P*N*sum(dPhi_m);                          % induced voltage (V)
L_s = P*N*real(sum(dPhi))/I_o;                        % stator inductance (H)
```

```
function [Core_loss_r] = SLIM_hysteresis(w_m,I_o,U_r,U_p,U_b,R_mr,Ba,Core_loss_density,s)

%%%%%%%%%%%%%%%%%%%%%%%%%%%%%%%%%%%%%%%%%%%%%%%%%%%%%%%%%%%%%%%%%%%%%%%%%%
%%%%% SLotted stator Induction Machine hysteresis (SLIM_hysteresis) computes the    %%%%%
%%%%% hysteresis loss in the rotor core of the slotted stator induction machine     %%%%%
%%%%% using the effective permeability for the rotor core, stator pole and stator   %%%%%
%%%%% base from SLIM_fields. (MKS units)                                            %%%%%
%%%%%%%%%%%%%%%%%%%%%%%%%%%%%%%%%%%%%%%%%%%%%%%%%%%%%%%%%%%%%%%%%%%%%%%%%%

global T_rc T_al T_ag T_cl g_cl L_gap L_pole T_hat T_base R_im R_om
global u_0 u_a sigma_r sigma_c sigma_a v M P N w_e W S N_lam pf alpha
```

```
r = (R_om+R_im)/2;                          % radius (m)

lambda = 2*pi*r/P;                          % wave length (m)
L_base = lambda/4;                          % base length = 1/4 of a wavelength (m)
T_pole = (1-alpha)*L_base;                  % thickness of stator pole (m)

u_r = interp1(R_mr,U_r,r);                  % rotor permeability (henry/m)
u_p = interp1(R_mr,U_p,r);                  % stator pole permeability (henry/m)
u_b = interp1(R_mr,U_b,r);                  % stator base permeability (henry/m)

sigma_p = sigma_r;                          % conductivity of the stator pole (siemens)
sigma_b = sigma_r;                          % conductivity of the stator base (siemens)

delta_p = sqrt(2/(u_p*sigma_p*w_e));        % magnetic skin depth of stator pole (m)
Q_p = .5*(1+j)*W/delta_p;                   % ratio of lamination thickness to skin depth
FQ_p = Q_p/tanh(Q_p);                       % eddy current reluctance factor

delta_b = sqrt(2/(u_b*sigma_b*w_e));        % magnetic skin depth of stator base (m)
Q_b = .5*(1+j)*W/delta_b;                   % ratio of lamination thickness to skin depth
FQ_b = Q_b/tanh(Q_b);                       % eddy current reluctance factor

Rg = L_gap/(u_0*T_hat);                     % reluctance of teeth gap
Rp = FQ_p*L_pole/(u_p*T_pole*pf);           % reluctance of stator pole
Rb = FQ_b*(L_base)/(u_b*T_base*pf);         % reluctance of stator base

R_s = Rg + 2*Rp + Rb;                       % reluctance seen by 1 stator tooth gap
R_r = (1+j)*Rp + .5*(1+j)*Rb;               % reluctance seen by rotor flux over stator tooth

for m = 1:M

        n = (2*m - 1) * (-1)^(m-1);                                 % harmonic number
        k_n = n*P/r;                                                % wave number (1/m)

        gamma_0n = abs(k_n);                                        % magnitude of wave number (1/m)
        gamma_an = sqrt((k_n)^2+i*u_a*sigma_a*(w_e - n*w_m));       % rotor conductor diffusion constant (1/m)
        gamma_rn = sqrt((k_n)^2+i*u_r*sigma_r*(w_e - n*w_m));       % rotor core diffusion constant  (1/m)


        %%% rotor transfer relation constants %%%

        beta_1n = (u_r/gamma_rn) * gamma_0n/u_0 * sinh(gamma_rn*T_rc) + 1  * cosh(gamma_rn*T_rc);
        beta_2n = (gamma_rn/u_r) * 1 * sinh(gamma_rn*T_rc) + gamma_0n/u_0 * cosh(gamma_rn*T_rc);
        beta_3n = (u_a/gamma_an) * beta_2n * sinh(gamma_an*T_al) + beta_1n * cosh(gamma_an*T_al);
        beta_4n = (gamma_an/u_a) * beta_1n * sinh(gamma_an*T_al) + beta_2n * cosh(gamma_an*T_al);
        beta_5n = (u_0/gamma_0n) * beta_4n * sinh(gamma_0n*T_ag) + beta_3n * cosh(gamma_0n*T_ag);
        beta_6n = (gamma_0n/u_0) * beta_3n * sinh(gamma_0n*T_ag) + beta_4n * cosh(gamma_0n*T_ag);

        %%%%%%%%%%%%%%%%%%%%%%%%%%%%%%%%%%%%%%%%%%%%%%%%%%%%%%%%%%%%%%%%%%%%%%%%%%%%

        Hyn3 = 4 * exp(j*n*pi/4)* sin(n*pi*L_gap/lambda) / (n*pi);
        Axn6 = -Hyn3/beta_6n;                                       % vector potential at surface of stator
        G_beta(m) = sinc(n/4)*(beta_5n/beta_6n)*sin(n*pi*L_gap/lambda)*exp(j*n*pi/4);
        B_yr(m) = -u_r*Axn6*gamma_0n/u_0;                           % harmonic components of tangential B at rotor core
        B_ya(m) = -u_r*beta_2n*Axn6;                                % harmonic components of normal B at rotor core

end
```

```
        L_eq = L_gap - j*2*R_r*sum(G_beta);          % effective length of stator teeth gap (m)
        H_y3 = (1-j)*I_o/L_eq;                       % tangential H at surface of stator (A/m)


%%%% Compute hysteresis loss in rotor core %%%%

theta = [0:0.04:1]*2*pi;                             % wavelength in radians
V_rotor = 2*pi*r*T_rc*(R_om - R_im);                 % volume of rotor

for e = 1:100
        z = .01*(e-.5)*T_rc;
        for m = 1:M

                n = (2*m - 1) * (-1)^(m-1);          % harmonic number
                gamma_rn = sqrt((k_n)^2+i*u_r*sigma_r*(w_e - n*w_m)); % rotor core diffusion constant (1/m)

                for q = 1:25
                        Byrot(m,q) = H_y3*(B_yr(m)*sinh(gamma_rn*z)/sinh(gamma_rn*T_rc)+B_ya(m)
                        *sinh(gamma_rn*(T_rc-z))/sinh(gamma_rn*T_rc))*exp(-j*n*theta(q));
                end

         end

        if M == 1
                B_rot(e) = max(real(Byrot));
        else
                B_rot(e) = max(real(sum(Byrot)));
        end

        if B_rot(e) >= 1.72 % 0.7 T for Moly Permalloy (NiFeMo), 1.72 T for electroplated CoFeNi
                cl_r(e) = 0.005*V_rotor*max(Core_loss_density);
        else
                cl_r(e) = 0.005*V_rotor*interp1(Ba,Core_loss_density,B_rot(e));
        end
end

Core_loss_r = abs(s)*w_e*sum(cl_r)/(2*pi);           % total hysteresis loss in rotor core
```

```
function [R_s] = SLIM_resistance(W_ci,W_co,T_ci,T_co,g_tr,W_h)

%%%%%%%%%%%%%%%%%%%%%%%%%%%%%%%%%%%%%%%%%%%%%%%%%%%%%%%%%%%%%%%%%%%%%%%%%%%%
%%%% SLotted stator Induction Machine resistance  (SLIM_resistance) computes the      %%%%
%%%% resistance of a single phase of the slotted stator induction machine. (MKS units)      %%%%
%%%%%%%%%%%%%%%%%%%%%%%%%%%%%%%%%%%%%%%%%%%%%%%%%%%%%%%%%%%%%%%%%%%%%%%%%%%%

global T_rc T_al T_ag T_cl g_cl L_gap L_pole T_hat T_base R_im R_om u_0 u_a c_m delta_m
global sigma_r sigma_c sigma_a sigma_s B_rm v M P N w_e W S N_lam pf alpha

%%% Resistance of radial conductors %%%

W_cl_ri = alpha*pi*R_im/(P*N) - 2*(W_h + g_tr);
W_cl_ro = alpha*pi*R_om/(P*N) - 2*(W_h + g_tr);
R_radial = (2*(P*N)^2/(alpha*pi*sigma_c*T_cl)) * log(W_cl_ro/W_cl_ri);
```

```
%%% Resistance of inner and outer end turns %%%

for n = 1:N
        R_i(n) = R_im - 0.5*(2*n-1)*W_ci - (n-1)*g_cl - (W_h + g_tr);
        R_o(n) = R_om + 0.5*(2*n-1)*W_co + (n-1)*g_cl + (W_h + g_tr);
        L_i(n) = (2*n-1)*pi*R_i(n)/(P*N);
        L_o(n) = (2*n-1)*pi*R_o(n)/(P*N);
end

R_inner = P*sum(L_i)/(sigma_c*T_ci*W_ci);
R_outer = P*sum(L_o)/(sigma_c*T_co*W_co);

%%% Total resistance of a single phase %%%

R_s = R_radial + R_inner + R_outer;
```

```
%%%%%%%%%%%%%%%%%%%%%%%%%%%%%%%%%%%%%%%%%%%%%%%%%%%%%%%%%%%%%%
%%%% SLotted stator PM machine system (SLPM_system) calls the other SLPM_* scripts to     %%%%
%%%% compute power and efficiency vs. speed, input current, pole pairs ...                %%%%
%%%% SLPM_parameters is called first to initialize all the variables followed by          %%%%
%%%% SLPM_fields which computes the effective permiabilities of the machine.              %%%%
%%%% SLPM_power, SLPM_hysteresis and SLIM_resistance are then called to compute the       %%%%
%%%% output power, efficiency and various losses in the PM machine.                       %%%%
%%%%  NOTE: SLIM_resistance is used for both the slotted stator inductiona and PM machine %%%%
%%%%%%%%%%%%%%%%%%%%%%%%%%%%%%%%%%%%%%%%%%%%%%%%%%%%%%%%%%%%%%%%

global T_rc T_al T_ag T_cl g_cl L_gap L_pole T_hat T_base R_im R_om u_0 u_a c_m delta_m
global sigma_r sigma_c sigma_a sigma_s B_rm v M P N w_e W S N_lam pf alpha


SLPM_parameters

%%% To get output power, loss, efficiency at a single speed, current ... %%%

[U_r U_p U_b R_mr Core_loss] = SLPM_fields(w_m,I_o,Href,Bref,Ba,Core_loss_density);
[Fp Torque V_o L_s] = SLPM_power(w_m,I_o,U_r,U_p,U_b,R_mr);
[R_s] = SLIM_resistance(W_ci,W_co,T_ci,T_co,g_tr,W_h);
P_elect = I_o*real(V_o(1));
P_mech =  I_o*real(V_o(1)) + sum(Torque*Omega_m);
P_cond = R_s*I_o^2;
P_core = Core_loss;
P_out = P_elect + P_cond;
Eff = (P_elect + P_cond)/(P_mech - P_core);
sum(Torque*Omega_m);
```

```
%%%%%%%%%%%%%%%%%%%%%%%%%%%%%%%%%%%%%%%%%%%%%%%%
%%%% Output power and efficiency vs. phase current %%%
%%%%%%%%%%%%%%%%%%%%%%%%%%%%%%%%%%%%%%%%%%%%%%%%

I_phase = [1:10];

for e = 1:length(I_phase)
        I_o = I_phase(e)
        [U_r U_p U_b R_mr Core_loss] = SLPM_fields(w_m,I_o,Href,Bref,Ba,Core_loss_density);
        [Fp Torque V_o L_s] = SLPM_power(w_m,I_o,U_r,U_p,U_b,R_mr);
        [R_s] = SLIM_resistance(W_ci,W_co,T_ci,T_co,g_tr,W_h);
        P_elect = I_o*real(V_o(1));
        P_mech = P_elect + Torque(1)*Omega_m;
        P_cond = R_s*I_o^2;
        P_core = Core_loss;
        P_out(e) = max(0,-(P_elect + P_cond));
        Eff(e) = max(0,(P_elect + P_cond)/(P_mech - P_core));

end

figure(1)
subplot(2,1,1)
plot(I_phase,P_out,'k-.')
xlabel('I_o (A)')
ylabel('Power (W)')
title('Output power and efficiency vs. phase current')
hold on
subplot(2,1,2)
plot(I_phase,Eff*100,'k-.')
xlabel('I_o (A)')
ylabel('Efficiency (%)')
hold on

figure(2)
plot(P_out,Eff*100,'k:')
xlabel('Power (W)')
ylabel('Efficiency (%)')
title('Efficiency vs. output power')


%%%%%%%%%%%%%%%%%%%%%%%%%%%%%%%%%%%%%%%%%%%%%%%%
%%%% Output power and efficiency vs. # of pole pairs %%%
%%%%%%%%%%%%%%%%%%%%%%%%%%%%%%%%%%%%%%%%%%%%%%%%

Pole_pairs = [2:8];
for e = 1:length(Pole_pairs)
        P = Pole_pairs(e)
        w_m = P*Omega_m;                % angular velocity of rotor (rad/s)
        w_e = w_m;                      % electrical angular frequency (rad/s)
        [U_r U_p U_b R_mr Core_loss] = SLPM_fields(w_m,I_o,Href,Bref,Ba,Core_loss_density);
        [Fp Torque V_o L_s] = SLPM_power(w_m,I_o,U_r,U_p,U_b,R_mr);
        [R_s] = SLIM_resistance(W_ci,W_co,T_ci,T_co,g_tr,W_h);
        P_elect = I_o*real(V_o(1));
        P_mech = P_elect + Torque(1)*Omega_m;
        P_cond = R_s*I_o^2;
```

```
        P_core = Core_loss;
        P_out(e) = max(0,-(P_elect + P_cond));
        Eff(e) = max(0,(P_elect + P_cond)/(P_mech - P_core));

end

figure(3)
subplot(2,1,1)
plot(2*Pole_pairs,P_out,'k-.')
xlabel('Poles')
ylabel('Power (W)')
title('Output power and efficiency vs. number of poles ')
hold on
subplot(2,1,2)
plot(2*Pole_pairs,Eff*100,'k-.')
xlabel('Poles')
ylabel('Efficiency (%)')
hold on

%%%%%%%%%%%%%%%%%%%%%%%%%%%%%%%%%%%%%%%%%%%%%%%%%%%%%%%%%%%%
%%% Output power and efficiency vs. outer radius of magnetic core %%%
%%%%%%%%%%%%%%%%%%%%%%%%%%%%%%%%%%%%%%%%%%%%%%%%%%%%%%%%%%%%

Outer_Radius = [4:.1:5];
for e = 1:length(Outer_Radius)
        R_om = Outer_Radius(e)*1e-3
        Omega_m = 500/(R_om+1e-3);
        w_m = P*Omega_m;                        % angular velocity of rotor (rad/s)
        w_e = w_m;                              % electrical angular frequency (rad/s)
        [U_r U_p U_b R_mr Core_loss] = SLPM_fields(w_m,I_o,Href,Bref,Ba,Core_loss_density);
        [Fp Torque V_o L_s] = SLPM_power(w_m,I_o,U_r,U_p,U_b,R_mr);
        [R_s] = SLIM_resistance(W_ci,W_co,T_ci,T_co,g_tr,W_h);
        P_elect = I_o*real(V_o(1));
        P_mech = P_elect + Torque(1)*Omega_m;
        P_cond = R_s*I_o^2;
        P_core = Core_loss;
        P_out(e) = max(0,-(P_elect + P_cond));
        Eff(e) = max(0,(P_elect + P_cond)/(P_mech - P_core));

end

figure(4)
subplot(2,1,1)
plot(Outer_Radius,P_out,'k-.')
xlabel('R_o (mm)')
ylabel('Power (W)')
title('Output power and efficiency vs. outer radius of rotor core')
hold on
subplot(2,1,2)
plot(Outer_Radius,Eff*100,'k-.')
xlabel('R_o (mm)')
ylabel('Efficiency (%)')
hold on
```

```
%%%%%%%%%%%%%%%%%%%%%%%%%%%%%%%%%%%%%%%%%%%%%%%%%%%%%%%%
%%%% SLotted stator PM machine parameters (SLPM_parameters) initializes the variables        %%%%
%%%% for the machine dimensions, material properties and electrical inputs used in           %%%%
%%%% SLPM_fields, SLPM_power, SLPM_hysteresis and SLIM_resistance. (MKS units)               %%%%
%%%%%%%%%%%%%%%%%%%%%%%%%%%%%%%%%%%%%%%%%%%%%%%%%%%%%%%%

global T_rc T_al T_ag T_cl g_cl L_gap L_pole T_hat T_base R_im R_om u_0 u_a c_m delta_m
global sigma_r sigma_c sigma_a sigma_s B_rm v M P N w_e W S N_lam pf alpha


% Rotor Dimenstions (meters)

        T_rc = 450e-6;                          % thickness of rotor core
        T_al = 50e-6;                           % thickness of rotor conductor
        T_ag = 50e-6;                           % air gap
        c_m = 0.000001;                         % transition region length

% Stator Dimensions (meters)

         T_tr = 150e-6;                         % thickness of Si trench
        g_tr = T_tr/3;                          % gap between trench sidewall and coil
        T_cl = T_tr - 25e-6;                    % thickness of Cu coil
        T_ci = T_cl;                            % thickness of inner end turn
        T_co = T_cl;                            % thickness of outer end turn
        alpha = 0.5;                            % fraction of slot taken up by coil and Si dividers
        g_cl = T_tr/5;                          % gap between two adjacent coils
        W_h = 100e-6;                           % width of horizontal Si structural dividers
        W_v = 100e-6;                           % width of vertical Si structural dividers
        W_ci = 0.5*(1e-3 - (W_h+2*g_tr+g_cl));  % width of inner end turn coils
        W_co = 500e-6;                          % width of outer end turn coils
         T_wafer = 550e-6;                      % thickness of Si wafer
        L_gap = 50e-6;                          % length of stator tooth gap
        T_hat = T_wafer - T_tr - W_v - T_ag;    % thickness of Ni-Fe hat
        T_base = 2*T_wafer - T_tr - W_v;        % thickness of Ni-Fe base
        L_pole = 2*(T_tr + W_v);                % length of Ni-Fe pole
        R_im = 0.003;                           % magnetic core inner radius
        R_om = 0.005;                           % magnetic core outer radius


% Material Properties

        Temp = 25;                              % temperature (degrees C)
        u_0 = 4*pi*1e-7;                        % permeability of free space (henry/m)
        u_a = 1*u_0;                            % permeability of active layer (henry/m)
        sigma_r = 5e6;                          % conductivity of CoFe (siemens)
        sigma_c = 5.8e7;                        % conductivity of Cu (siemens)
        sigma_a = 1e7;                          % conductivity of rotor active layer (siemens)
        sigma_s = 5e6;                          % conductivity of CoFe (siemens)
        B_rm = 1;                               % remanence of rotor PM (T)
        v = 2e-5;                               % dynamic viscosity of air (N-s/m)

        load CoFe_data.mat                      % B-H data for CoFe from GIT
        Href1 = max(Ho) + [5e6:-1e4:1e4];       % extension of B-H curve
        Bref1 = max(Bo) + (Href1-max(Ho))*u_0;  % using permeability u_0
        Href = [Ho Href1];                      % B-H curve used in SLIM_fields
        Bref = [Bo Bref1];
```

```
% Electrical Parameters

    I_o = 5;                                % Phase current (A)
    delta_m = pi/2;                         % Phase difference between rotor flux and stator current
    M = 5;                                  % number of harmonics solved for in MIMF and MIMRP
    P = 6;                                  % number of pole pairs
    N = 2;                                  % number of turns/pole
    Speed = 795774.7;                       % speed (RPM)
    Omega_m = 500/(R_om+1e-3);              % speed (rad/s)
    w_m = P*Omega_m;                        % angular velocity of rotor (rad/s)
    w_e = w_m;                              % electrical angular frequency (rad/s)

% Lamination Parameters

    W = 30e-6;                              % lamination thickness (m)
    S = 20e-6;                              % insulation thickness (m)
    N_lam = round((R_om - R_im)/(W+S));     % number of laminations
    pf = W/(W+S);                           % packing factor
```

```
function [u_r,u_p,u_b,R_mr,Core_loss_s] = SLPM_fields(w_m,I_o,Href,Bref,Ba,Core_loss_density)

%%%%%%%%%%%%%%%%%%%%%%%%%%%%%%%%%%%%%%%%%%%%%%%%%%%%%%%%%%%%%%%%%%%%%%%%%%%%%%%
%%%%% SLotted stator PM machine fields (SLPM_fields) computes the permeability of the      %%%%%
%%%%% rotor core (u_r), stator pole (u_p) and stator base (u_b) using a nonlinear B-H      %%%%%
%%%%% curve. The starting value for u_r, u_p and u_b is 200*u_0. The script iteratively    %%%%%
%%%%% solves for the peak B fields in the rotor & stator until u_r, u_p and u_b are found  %%%%%
%%%%% such that the maximum B lies on the B-H curve. The script also computes the resulting %%%%%
%%%%% core loss in the stator. (MKS units)                                                 %%%%%
%%%%%%%%%%%%%%%%%%%%%%%%%%%%%%%%%%%%%%%%%%%%%%%%%%%%%%%%%%%%%%%%%%%%%%%%%%%%%%%

global T_rc T_al T_ag T_cl g_cl L_gap L_pole T_hat T_base R_im R_om u_0 u_a c_m delta_m
global sigma_r sigma_c sigma_a sigma_s B_rm v M P N w_e W S N_lam pf alpha


Z = N_lam+1;
dr = (R_om - R_im)/(Z-1);               % radial increment (m)
u_r = ones(1,Z)*200*u_0;                % initial rotor permeability (henry/m)
u_p = ones(1,Z)*200*u_0;                % initial stator pole permeability (henry/m)
u_b = ones(1,Z)*200*u_0;                % initial stator base permeability (henry/m)
B_maxr = ones(1,Z)*5;                   % initial B_maxr (T)
B_mr = ones(1,Z)*2;                     % initial B_mr on B_H curve (T)
B_maxp = ones(1,Z)*5;                   % initial B_maxp (T)
B_mp = ones(1,Z)*2;                     % initial B_mp on B_H curve (T)
B_maxb = ones(1,Z)*5;                   % initial B_maxb (T)
B_mb = ones(1,Z)*2;                     % initial B_mb on B_H curve (T)

T_sl = T_hat + L_pole;                  % thickness of slot layer (m)
T_sb = T_base;                          % thickness of base layer (m)

for k = 1:Z

    r(k) = R_im + (k-1)*dr;             % rotor radius (m)
    lambda = 2*pi*r(k)/P;               % wave length (m)
    L_base = lambda/4;                  % base length = 1/4 of a wavelength (m)
```

```
T_pole = (1-alpha)*L_base;                  % thickness of stator pole (m)
lm = (pi*r(k)/P) - c_m;                     % length of region of constant remanence (m)
V_pole = 2*P*N*T_pole*L_pole*W;             % volume of all the stator poles at radius r (m^3)
V_base = 2*P*N*T_base*L_base*W;             % volume of all the stator bases at radius r (m^3)
V_hat = 2*P*N*T_hat*(L_base-L_gap)*W;       % volume of all the stator hats at radius r (m^3)


delta_p = sqrt(2/(u_p(k)*sigma_s*w_e));     % magnetic skin depth of stator pole (m)
Q_p = .5*(1+j)*W/delta_p;                   % ratio of lamination thickness to skin depth
FQ_p = Q_p/tanh(Q_p);                       % eddy current reluctance factor

delta_b = sqrt(2/(u_b(k)*sigma_s*w_e));     % magnetic skin depth of stator base (m)
Q_b = .5*(1+j)*W/delta_b;                   % ratio of lamination thickness to skin depth
FQ_b = Q_b/tanh(Q_b);                       % eddy current reluctance factor

Rg = L_gap/(u_0*T_hat);                     % reluctance of teeth gap
Rp = FQ_p*L_pole/(u_p(k)*T_pole*pf);        % reluctance of stator pole
Rb = FQ_b*(L_base-T_pole)/(u_b(k)*T_base*pf); % reluctance of stator base

R_s = Rg + 2*Rp + Rb;                       % reluctance seen by 1 stator tooth gap
R_r = (1+j)*Rp + .5*(1+j)*Rb;               % reluctance seen by 1 rotor flux source

sigma_p = sigma_s*(1-abs(1/FQ_p));          % conductivity of the stator slot layer (siemens)
sigma_b = sigma_s*(1-abs(1/FQ_b));          % conductivity of the stator base layer (siemens)

while (abs(B_maxb(k) - B_mb(k)) > 1e-4) | (abs(B_maxp(k) - B_mp(k)) > 1e-4) | (abs(B_maxr(k) -
B_mr(k)) > 1e-4),

        for m = 1:M

                n = (2*m - 1) * (-1)^(m-1);             % harmonic number for stator currents
                k_n = n*P/r(k);                         % wave number (1/m)

                gamma_0n = abs(k_n);                    % magnitude of wave number (1/m)
                gamma_an = sqrt((k_n)^2+i*u_a*sigma_a*(w_e - n*w_m));
                                                        % rotor conductor diffusion constant (1/m)
                gamma_rn = sqrt((k_n)^2+i*u_r(k)*sigma_r*(w_e - n*w_m));
                                                        % rotor core diffusion constant (1/m)

        %%% rotor transfer relation constants for stator currents %%%

beta_1n = (u_r(k)/gamma_rn) * gamma_0n/u_0 * sinh(gamma_rn*T_rc) + 1* cosh(gamma_rn*T_rc);
beta_2n = (gamma_rn/u_r(k)) * 1* sinh(gamma_rn*T_rc) + gamma_0n/u_0 * cosh(gamma_rn*T_rc);
beta_3n = (u_a/gamma_an) * beta_2n * sinh(gamma_an*T_al) + beta_1n * cosh(gamma_an*T_al);
beta_4n = (gamma_an/u_a) * beta_1n * sinh(gamma_an*T_al) + beta_2n * cosh(gamma_an*T_al);
beta_5n = (u_0/gamma_0n) * beta_4n * sinh(gamma_0n*T_ag) + beta_3n * cosh(gamma_0n*T_ag);
beta_6n = (gamma_0n/u_0) * beta_3n * sinh(gamma_0n*T_ag) + beta_4n * cosh(gamma_0n*T_ag);

        %%%%%%%%%%%%%%%%%%%%%%%%%%%%%%%%%%%%%%%%%%%%%%%%%%%%%%%%%%%%%%%%%%%%%%%%%%%%%%%

                Hyn3 = j*4 * exp(j*n*pi/4)* sin(n*pi*L_gap/lambda) / (n*pi);
                Axn6 = -Hyn3/beta_6n;                   % vector potential at surface of stator
                G_beta(m) = sinc(n/4)*(beta_5n/beta_6n)*sin(n*pi*L_gap/lambda)*exp(j*n*pi/4);
```

```
        B_yn5j(m) = -u_r(k)*beta_2n*Axn6;
                                        % harmonic components of tangential B at rotor core
        B_zn5j(m) = j*k_n*beta_1n*Axn6;
                                        % harmonic components of normal B at rotor core

end

L_eq = L_gap - j*2*R_r*sum(G_beta);     % effective length of stator teeth gap (m)
H_y3 = (1-j)*I_o/L_eq;                  % tangential H at surface of stator (A/m)


for m = 1:M

        n = (2*m - 1);                  % harmonic number for rotor magnetization
        k_n = n*P/r(k);                 % wave number (1/m)

        gamma_0n = k_n;                 % magnitude of wave number (1/m)
        gamma_an = k_n;                 % rotor conductor diffusion constant (1/m)
        gamma_rn = k_n;                 % rotor core diffusion constant (1/m)
        gamma_pn = sqrt(k_n^2+j*u_p(k)*sigma_p*n*w_m);
                                        % stator slot diffusion constant (1/m)
        gamma_bn = sqrt(k_n^2+j*u_b(k)*sigma_p*n*w_m);
                                        % stator base diffusion constant (1/m)

        %%% rotor transfer relation constants for rotor magnetization %%%

    alpha_1n(m) = (u_b(k)/gamma_bn)*gamma_0n/u_0*sinh(gamma_bn*T_sb)+1*cosh(gamma_bn*T_sb);
    alpha_2n(m) = (gamma_bn/u_b(k))*1*sinh(gamma_bn*T_sb)+gamma_0n/u_0*cosh(gamma_bn*T_sb);
alpha_3n(m) = (u_p(k)/gamma_pn)*alpha_2n(m)*sinh(gamma_pn*T_sl)+alpha_1n(m)*cosh(gamma_pn*T_sl);
alpha_4n(m) = (gamma_pn/u_p(k))*alpha_1n(m)*sinh(gamma_pn*T_sl)+alpha_2n(m)*cosh(gamma_pn*T_sl);
 alpha_5n(m) = u_0/gamma_0n)*alpha_4n(m)*sinh(gamma_0n*T_ag)+alpha_3n(m)*cosh(gamma_0n*T_ag);
alpha_6n(m) = (gamma_0n/u_0)*alpha_3n(m)*sinh(gamma_0n*T_ag)+alpha_4n(m)* cosh(gamma_0n*T_ag);
 alpha_7n(m) = (u_a/gamma_0n)*alpha_6n(m)*sinh(gamma_0n*T_al)+alpha_5n(m)* cosh(gamma_0n*T_al);
 alpha_8n(m)  = (gamma_0n/u_a)*alpha_5n(m)*sinh(gamma_0n*T_al)+alpha_6n(m)* cosh(gamma_0n*T_al);

   beta_1n(m) = (u_r(k)/gamma_rn) * gamma_0n/u_0 * sinh(gamma_rn*T_rc) + 1 * cosh(gamma_rn*T_rc);
   beta_2n(m) = (gamma_rn/u_r(k)) * 1 * sinh(gamma_rn*T_rc) + gamma_0n/u_0 * cosh(gamma_rn*T_rc);
   beta_3n(m) = (u_a/gamma_an)*beta_2n(m)*sinh(gamma_an*T_al)+beta_1n(m) * cosh(gamma_an*T_al);
   beta_4n(m) = (gamma_an/u_a)*beta_1n(m)*sinh(gamma_an*T_al)+ beta_2n(m)* cosh(gamma_an*T_al);
   beta_5n(m) = (u_0/gamma_0n)*beta_4n(m)*sinh(gamma_0n*T_ag)+beta_3n(m)* cosh(gamma_0n*T_ag);
   beta_6n(m) = (gamma_0n/u_0)*beta_3n(m)*sinh(gamma_0n*T_ag)+beta_4n(m)* cosh(gamma_0n*T_ag);
   beta_7n(m) = (u_p(k)/gamma_pn)*beta_6n(m)*sinh(gamma_pn*T_sl)+beta_5n(m)*cosh(gamma_pn*T_sl);
   beta_8n(m) = (gamma_pn/u_p(k))*beta_5n(m)*sinh(gamma_pn*T_sl)+beta_6n(m)*cosh(gamma_pn*T_sl);

        %%%%%%%%%%%%%%%%%%%%%%%%%%%%%%%%%%%%%%%%%%%%%%%%%%%%%%%%%%%%

        B_m = (8/(n*pi))*(B_rm/c_m)*cos(.5*k_n*lm)*exp(j*n*delta_m);
        A_xnm = B_m/k_n^2;              % vector potential due to rotor magnetization

cmb = (beta_4n(m)  - beta_2n(m))  / (beta_4n(m)*alpha_8n(m) - beta_2n(m)*alpha_6n(m));
cmt = (alpha_8n(m) - alpha_6n(m)) / (beta_4n(m)*alpha_8n(m) - beta_2n(m)*alpha_6n(m));

        %%% vector potential due to rotor PM %%%
        A_xnm1 = -j*cmb*(gamma_an/u_a)*sinh(gamma_an*T_al)*A_xnm;
        A_xnm6 = -j*cmt*(gamma_an/u_a)*sinh(gamma_an*T_al)*A_xnm;
```

```
            B_zn5m(m) = j*k_n*beta_1n(m)*A_xnm6;
                                % harmonic components of tangential B at interface 5
            B_yn5m(m) = -u_r(k)*(k_n/u_0)*A_xnm6;
                                % harmonic components of normal B at interface 5
            Phi_rnm(m) = -j*2*sin(n*pi/4)*alpha_3n(m)*A_xnm1;
                                % rotor flux source from permenent magnet

        end

        B_yn5 = B_yn5m + B_yn5j*H_y3;          % tangential B at interface 5 from I_o and B_rm
        B_zn5 = B_zn5m + B_zn5j*H_y3;          % normal B at interface 5 from I_o and B_rm

        Phi_s = u_0*T_hat*H_y3;                        % leakage flux through stator tooth (Wb)
        Phi_r = j*2*sum(G_beta)*H_y3;                  % magentizing flux (Wb)
        Phi_p = Phi_r + (j-1)*Phi_s+ sum(Phi_rnm);     % flux through stator pole (Wb)
        Phi_b = Phi_s + Phi_r/(j-1)+ sum(Phi_rnm);     % flux through stator base (Wb)


        B_r = sqrt(0.5*sum(abs(B_yn5).^2+abs(B_zn5).^2));
        B_g = abs(u_0*H_y3);                           % magnitude of B through stator teeth (T)
        B_p = abs(Phi_p/T_pole);                       % magnitude of B through stator pole (T)
        B_b = abs(Phi_b/T_base);                       % magnitude of B through stator base (T)

        B_maxr(k) = B_r;                               % update B_maxr
        H_maxr(k) = B_maxr(k)/u_r(k);          % compute corresponding H_maxr using current u
        B_mr(k) = interp1(Href,Bref,H_maxr(k));        % update B_mr using nonlinear B-H curve
        u_r(k) = B_mr(k)/H_maxr(k);                    % update rotor permeability

        B_maxp(k) = B_p;                               % update B_maxp
        H_maxp(k) = B_maxp(k)/u_p(k);          % compute corresponding H_maxp using current u
        B_mp(k) = interp1(Href,Bref,H_maxp(k));        % update B_mp using nonlinear B-H curve
        u_p(k) = B_mp(k)/H_maxp(k);                    % update stator pole permeability

        B_maxb(k) = B_b;                               % update B_maxb
        H_maxb(k) = B_maxb(k)/u_b(k);          % compute corresponding H_maxb using current u
        B_mb(k) = interp1(Href,Bref,H_maxb(k));        % update B_mb using nonlinear B-H curve
        u_b(k) = B_mb(k)/H_maxb(k);                    % update stator base permeability

end

R_mr(k) = r(k);                                        % rotor radius (m)
B_h = B_p*T_pole/(L_base-L_gap);                       % magnitude of B through rotor core (T)

 if B_h >= 1.72 % 0.7 T for Moly Permalloy (NiFeMo), 1.72 T for electroplated CoFeNi
        cl_h = V_hat*max(Core_loss_density);
else
        cl_h = V_hat*interp1(Ba,Core_loss_density,B_h);
end

if B_p >= 1.72 % 0.7 T for Moly Permalloy (NiFeMo), 1.72 T for electroplated CoFeNi
        cl_p = V_pole*max(Core_loss_density);
else
        cl_p = V_pole*interp1(Ba,Core_loss_density,B_p);
end

 if B_b >= 1.72 % 0.7 T for Moly Permalloy (NiFeMo), 1.72 T for electroplated CoFeNi
```

```
            cl_b = V_base*max(Core_loss_density);
        else
            cl_b = V_base*interp1(Ba,Core_loss_density,B_b);
        end

        dCL_s(k) = cl_h + cl_p + cl_b;

end

Core_loss_s = w_e*sum(dCL_s)/(2*pi);        % Total hysteresis loss in stator (W)
```

```
function [Fp,Torque,V_oc,L_s] = SLPM_power(w_m,I_o,U_r,U_p,U_b,R_mr)

%%%%%%%%%%%%%%%%%%%%%%%%%%%%%%%%%%%%%%%%%%%%%%%%%%%%%%%%%%%%%%%%%%%%%%%%
%%%% SLotted stator PM machine power (SLPM_power) computes the pull-in force, torque,    %%%%%
%%%% open-circuit voltage and stator phase inductance for the slotted stator PM           %%%%%
%%%% machine using the effective permeability for the rotor core, stator pole            %%%%%
%%%% and stator base from SLPM_fields. (MKS units)                                       %%%%%
%%%%%%%%%%%%%%%%%%%%%%%%%%%%%%%%%%%%%%%%%%%%%%%%%%%%%%%%%%%%%%%%%%%%%%%%

global T_rc T_al T_ag T_cl g_cl L_gap L_pole T_hat T_base R_im R_om u_0 u_a c_m delta_m
global sigma_r sigma_c sigma_a sigma_s B_rm v M P N w_e W S N_lam pf alpha

T_sl = T_hat + L_pole;                          % thickness of slot layer (m)
T_sb = T_base;                                  % thickness of base layer (m)
dr = (R_om-R_im)/500;                           % incremental radiul distance (m)

for x = 1:501

        r = R_im + (x-1)*dr;                    % radius (m)
        lambda = 2*pi*r/P;                      % wave length (m)
        L_base = lambda/4;                      % base length = 1/4 of a wavelength (m)
        T_pole = (1-alpha)*L_base;              % thickness of stator pole (m)
        lm = (pi*r/P) - c_m;                    % length of region of constant remanence
        u_r = interp1(R_mr,U_r,r);              % rotor permeability (henry/m)
        u_p = interp1(R_mr,U_p,r);              % stator pole permeability (henry/m)
        u_b = interp1(R_mr,U_b,r);              % stator base permeability (henry/m)


        delta_p = sqrt(2/(u_p*sigma_s*w_e));    % magnetic skin depth of stator pole (m)
        Q_p = .5*(1+j)*W/delta_p;               % ratio of lamination thickness to skin depth
        FQ_p = Q_p/tanh(Q_p);                   % eddy current reluctance factor

        delta_b = sqrt(2/(u_b*sigma_s*w_e));    % magnetic skin depth of stator base (m)
        Q_b = .5*(1+j)*W/delta_b;               % ratio of lamination thickness to skin depth
        FQ_b = Q_b/tanh(Q_b);                   % eddy current reluctance factor

        sigma_p = sigma_s*(1-abs(1/FQ_p));      % conductivity of stator slot layer (siemens)
        sigma_b = sigma_s*(1-abs(1/FQ_b));      % conductivity of stator base layer (siemens)

        Rg = L_gap/(u_0*T_hat);                 % reluctance of teeth gap
        Rp = FQ_p*L_pole/(u_p*T_pole*pf);       % reluctance of stator pole
        Rb = FQ_b*(L_base)/(u_b*T_base*pf);     % reluctance of stator base

        R_s = Rg + 2*Rp + Rb;                   % reluctance seen by 1 stator tooth gap
```

```
R_r = (1+j)*Rp + .5*(1+j)*Rb;                    % reluctance seen by 1 rotor flux source

for m = 1:M

        n = (2*m - 1) * (-1)^(m-1);              % harmonic number for rotor magetization
        k_n = n*P/r;                             % wave number (1/m)

        gamma_0n = abs(k_n);                     % magnitude of wave number (1/m)
        gamma_an = abs(k_n);                     % inverse of rotor conductor skin depth (m)
        gamma_rn = abs(k_n);                     % inverse of rotor core skin depth (m)

        %%% rotor transfer relation constants for stator currents%%%

beta_1n = (u_r/gamma_rn) * gamma_0n/u_0 * sinh(gamma_rn*T_rc) + 1* cosh(gamma_rn*T_rc);
beta_2n = (gamma_rn/u_r) * 1 * sinh(gamma_rn*T_rc) + gamma_0n/u_0 * cosh(gamma_rn*T_rc);
beta_3n = (u_a/gamma_an) * beta_2n * sinh(gamma_an*T_al) + beta_1n * cosh(gamma_an*T_al);
beta_4n = (gamma_an/u_a) * beta_1n * sinh(gamma_an*T_al) + beta_2n * cosh(gamma_an*T_al);
beta_5n = (u_0/gamma_0n) * beta_4n * sinh(gamma_0n*T_ag) + beta_3n * cosh(gamma_0n*T_ag);
 beta_6n = (gamma_0n/u_0) * beta_3n * sinh(gamma_0n*T_ag) + beta_4n * cosh(gamma_0n*T_ag);

        %%%%%%%%%%%%%%%%%%%%%%%%%%%%%%%%%%%%%%%%%%%%%%%%%%%%%%%%%%%%%%%%%%%%%%%%%%%%%%%%

        Hyn3 = j*4*exp(j*n*pi/4)*sin(n*pi*L_gap/lambda)/(n*pi);
        Axn6 = -Hyn3/beta_6n;                    % vector potential at surface of stator
        G_beta(m) = sinc(n/4)*(beta_5n/beta_6n)*sin(n*pi*L_gap/lambda)*exp(j*n*pi/4);

end

L_eq = L_gap - j*2*R_r*sum(G_beta);              % effective length of stator teeth gap (m)
H_y3 = (1-j)*I_o/L_eq;                           % tangential H at surface of stator (A/m)
Phi_s = u_0*T_hat*H_y3;                          % leakage flux through stator tooth (Wb)
Phi_r = j*2*sum(G_beta)*H_y3;                    % magentizing flux (Wb)
Phi_p = Phi_r + (j-1)*Phi_s;                     % flux through stator pole (Wb)


for m = 1:M

        n = (2*m - 1);                           % harmonic number for rotor magnetization
        k_n = n*P/r;                             % wave number (1/m)

        gamma_0n = k_n;                          % magnitude of wave number (1/m)
        gamma_an = k_n;                          % rotor conductor diffusion constant (1/m)
        gamma_rn = k_n;                          % rotor core diffusion constant (1/m)
        gamma_pn = sqrt(k_n^2+j*u_p*sigma_p*n*w_m);  % stator slot diffusion constant (1/m)
        gamma_bn = sqrt(k_n^2+j*u_b*sigma_p*n*w_m);  % stator base diffusion constant (1/m)

        %%% rotor transfer relation constants for rotor magnetization %%%

  alpha_1n(m) = (u_b/gamma_bn) * gamma_0n/u_0 * sinh(gamma_bn*T_sb) + 1 * cosh(gamma_bn*T_sb);
  alpha_2n(m) = (gamma_bn/u_b) * 1 * sinh(gamma_bn*T_sb) + gamma_0n/u_0 * cosh(gamma_bn*T_sb);
alpha_3n(m) = (u_p/gamma_pn)*alpha_2n(m)*sinh(gamma_pn*T_sl)+alpha_1n(m)*cosh(gamma_pn*T_sl);
alpha_4n(m) = (gamma_pn/u_p)*alpha_1n(m)*sinh(gamma_pn*T_sl)+alpha_2n(m)*cosh(gamma_pn*T_sl);
alpha_5n(m) = (u_0/gamma_0n)*alpha_4n(m)*sinh(gamma_0n*T_ag)+alpha_3n(m)*cosh(gamma_0n*T_ag);
alpha_6n(m) = (gamma_0n/u_0)*alpha_3n(m)*sinh(gamma_0n*T_ag)+alpha_4n(m)*cosh(gamma_0n*T_ag);
alpha_7n(m) = (u_a/gamma_an)*alpha_6n(m)*sinh(gamma_an*T_al)+alpha_5n(m)*cosh(gamma_an*T_al);
alpha_8n(m) = (gamma_an/u_a)*alpha_5n(m)*sinh(gamma_an*T_al)+alpha_6n(m)*cosh(gamma_an*T_al);
```

```
beta_1n(m) = (u_r/gamma_rn) * gamma_0n/u_0 * sinh(gamma_rn*T_rc) + 1 * cosh(gamma_rn*T_rc);
beta_2n(m) = (gamma_rn/u_r) * 1* sinh(gamma_rn*T_rc) + gamma_0n/u_0 * cosh(gamma_rn*T_rc);
beta_3n(m) = (u_a/gamma_an)*beta_2n(m)*sinh(gamma_an*T_al)+beta_1n(m)*cosh(gamma_an*T_al);
beta_4n(m) = (gamma_an/u_a)*beta_1n(m)*sinh(gamma_an*T_al)+beta_2n(m)*cosh(gamma_an*T_al);
beta_5n(m) = (u_0/gamma_0n)*beta_4n(m)*sinh(gamma_0n*T_ag)+beta_3n(m)*cosh(gamma_0n*T_ag);
beta_6n(m) = (gamma_0n/u_0)*beta_3n(m)*sinh(gamma_0n*T_ag)+beta_4n(m)*cosh(gamma_0n*T_ag);
beta_7n(m) = (u_p/gamma_pn)*beta_6n(m)*sinh(gamma_pn*T_sl)+beta_5n(m) * cosh(gamma_pn*T_sl);
beta_8n(m) = (gamma_pn/u_p)*beta_5n(m)*sinh(gamma_pn*T_sl)+beta_6n(m) * cosh(gamma_pn*T_sl);

        %%%%%%%%%%%%%%%%%%%%%%%%%%%%%%%%%%%%%%%%%%%%%%%%%%%%%%%%%%%%

        B_m = (8/(n*pi))*(B_rm/c_m)*cos(.5*k_n*lm)*exp(j*n*delta_m);
        A_xnm = B_m/k_n^2;                      % vector potential due to rotor magnetization

        cmb = (beta_4n(m)  - beta_2n(m))  / (beta_4n(m)*alpha_8n(m) - beta_2n(m)*alpha_6n(m));
        cmt = (alpha_8n(m) - alpha_6n(m)) / (beta_4n(m)*alpha_8n(m) - beta_2n(m)*alpha_6n(m));

        A_xnm1 = -j*cmb*(gamma_an/u_a)*sinh(gamma_an*T_al)*A_xnm;
                                                % vector potential at interface 1

        %%%%%%%%%%%%%%%%%%%%%%%%%%%%%%%%%%%%%%%%%%%%%%%%%%%%%%%%%%%%
        %%% To get mechanicail input power set m == 1              %%%
        %%% If just the eddy current loss is desired, set m == -1,  %%%
        %%% mechanical input power = P_eddy + P_elect.              %%%
        %%%%%%%%%%%%%%%%%%%%%%%%%%%%%%%%%%%%%%%%%%%%%%%%%%%%%%%%%%%%

        if m == -1
                A_xnj6 = 4*exp(-j*pi/4)*sin(pi*L_gap/lambda)*H_y3/(beta_6n(1)*pi);
                                                % vector potential at interface 6 due to rotor PM
        else
                A_xnj6 =  0;
        end

        B_zn4 = j*k_n*(alpha_5n(m)*A_xnm1 + beta_3n(m)*A_xnj6);
                                % harmonic components of tangential H at the rotor conductor surface
        H_yn4 = alpha_6n(m)*A_xnm1 - beta_4n(m)*A_xnj6;
                                % harmonic components of normal B at the rotor conductor surface

        zeta1(m) = 0.5*real(B_zn4*H_yn4');              % harmonic components of torque
        zeta2(m) = 0.25*((1/u_0) * (abs(B_zn4))^2 - u_0*(abs(H_yn4))^2);
                                                % harmonic components of pull-in force

        dPhi_zncoilm(x,m) = j*2*P*N*sin(n*pi/4)*alpha_3n(m)*A_xnm1;
                                                % flux from rotor PM over region [r,r+dr] (Wb)
        dV(x,m) = exp(j*n*pi/2)*n*w_m*dPhi_zncoilm(x,m)*dr;
                                        % incremental voltage from PM over region [r,r+dr] (V)
        dT(x,m) = zeta1(m) * dr * r^2;          % total torque over region [r,r+dr] (N-m)
    end

    dFp(x) = sum(zeta2)* dr * r;                % pull-in force over region [r,r+dr] (N)
    dPhi(x) = dr*(-j*Phi_p);                    % flux from stator current over region [r,r+dr] (Wb)

end

Fp = -2*u_0*pi*sum(dFp);                        % pull-in force acting rotor (N)
```

```
Torque = -2*pi*sum(dT);                    % torque on rotor (N-m)
V_oc = sum(dV);                            % open-circuit voltage (V)
L_s = P*N*real(sum(dPhi))/I_o;             % stator phase inductance (H)
```

```
%%%%%%%%%%%%%%%%%%%%%%%%%%%%%%%%%%%%%%%%%%%%%%%%%%%%%%%%%%%%%%%%%%%%%%%%%%%%%%%
%%%%% Surface Wound PM machine system (SWPM_system) calls the other SWPM_* scripts to %%%%%
%%%%% compute power and efficiency vs. speed, input current, pole pairs ...          %%%%%
%%%%% SWPM_parameters is called first to initialize all the variables followed by     %%%%%
%%%%% SWPM_fields which computes the effective permiabilities of the machine.         %%%%%
%%%%% SWPM_power, SWPM_hysteresis and SWPM_resistance are then called to compute the  %%%%%
%%%%% output power, efficiency and various losses in the PM machine.                  %%%%%
%%%%%%%%%%%%%%%%%%%%%%%%%%%%%%%%%%%%%%%%%%%%%%%%%%%%%%%%%%%%%%%%%%%%%%%%%%%%%%%

global T_rc T_al T_ag T_sc T_cl g_cl c_m W S pf N_lam T_cl H_refr B_refr H_refs B_refs
global R_im R_om u_0 u_a sigma_c sigma_a sigma_r sigma_s B_rm v M P N w_e delta_m

SWPM_parameters

%%% To get output power, loss, efficiency at a single speed, current ... %%%

[U_r U_s R_mr B_rotor B_stator Core_loss] = SWPM_fields(w_m,I_o,Ba,Core_loss_density);
[Fp Torque V_o L_s B_coil] = SWPM_power(w_m,I_o,U_r,U_s,R_mr);
[Core_loss] = SWPM_hysteresis(w_m,I_o,U_r,U_s,R_mr,Ba,Core_loss_density);
[R_s] = SWPM_resistance(W_ci,W_co,T_ci,T_co,R_o1,R_i1,winding,C_lam);
[P_prox B_eddy] = SWPM_proximity(C_lam,B_coil);
P_elect = 1.5*I_o*real(V_o(1))
P_mech = sum(Torque)*Omega_m
P_core = Core_loss
P_cond = 1.5*R_s*I_o^2
P_prox
P_out = P_elect + P_cond
Eff = (P_elect + P_cond)/(P_mech - P_core - P_prox)


%%%%%%%%%%%%%%%%%%%%%%%%%%%%%%%%%%%%%%%%%%%%%%%%%%%%%%%%%%%%%%%%%%%%%%%%%%%%%%%
%%% Output power and efficiency vs. phase current %%%
%%%%%%%%%%%%%%%%%%%%%%%%%%%%%%%%%%%%%%%%%%%%%%%%%%%%%%%%%%%%%%%%%%%%%%%%%%%%%%%

I_phase = [1:10];
for e = 1:length(I_phase)
        I_o = I_phase(e)
        [U_r U_s R_mr B_rotor B_stator Core_loss] = SWPM_fields(w_m,I_o,Ba,Core_loss_density);
        [Fp Torque V_o L_s B_coil] = SWPM_power(w_m,I_o,U_r,U_s,R_mr);
        [Core_loss] = SWPM_hysteresis(w_m,I_o,U_r,U_s,R_mr,Ba,Core_loss_density);
        [R_s] = SWPM_resistance(W_ci,W_co,T_ci,T_co,R_o1,R_i1,winding,C_lam);
        [P_prox B_eddy] = SWPM_proximity(C_lam,B_coil);
        P_elect = 1.5*I_o*real(V_o(1));
        P_mech = sum(Torque)*Omega_m;
        P_cond = 1.5*R_s*I_o^2;
        P_core = Core_loss;
        P_out(e) = P_elect + P_cond;
        Eff(e) = (P_elect + P_cond)/(P_mech - P_core - P_prox);

end
```

```
figure(1)
subplot(2,1,1)
plot(I_phase,-P_out,'k--')
xlabel('I_o (A)')
ylabel('Power (W)')
title('Output power and efficiency vs. phase current')
hold on
subplot(2,1,2)
plot(I_phase,Eff*100,'k--')
xlabel('I_o (A)')
ylabel('Efficiency (%)')
hold on

figure(2)
plot(-P_out,Eff*100,'k--')
hold on
xlabel('Power (W)')
ylabel('Efficiency (%)')
title('Efficiency vs. output power')

%%%%%%%%%%%%%%%%%%%%%%%%%%%%%%%%%%%%
%%% Output power and efficiency vs. # of pole pairs %%%
%%%%%%%%%%%%%%%%%%%%%%%%%%%%%%%%%%%%

Pole_pairs = [2:8];
for e = 1:length(Pole_pairs)
        P = Pole_pairs(e)
        w_m = P*Omega_m;                    % angular velocity of rotor (rad/s)
        w_e = w_m;                          % electrical angular frequency (rad/s)
        g_cl = 75e-6*4/P;
        [U_r U_s R_mr B_rotor B_stator Core_loss] = SWPM_fields(w_m,I_o,Ba,Core_loss_density);
        [Fp Torque V_o L_s B_coil] = SWPM_power(w_m,I_o,U_r,U_s,R_mr);
        [Core_loss] = SWPM_hysteresis(w_m,I_o,U_r,U_s,R_mr,Ba,Core_loss_density);
        [R_s] = SWPM_resistance(W_ci,W_co,T_ci,T_co,R_o1,R_i1,winding,C_lam);
        [P_prox B_eddy] = SWPM_proximity(C_lam,B_coil);
        P_elect = 1.5*I_o*real(V_o(1));
        P_mech = sum(Torque)*Omega_m;
        P_cond = 1.5*R_s*I_o^2;
        P_core = Core_loss;
        P_out(e) = P_elect + P_cond;
        Eff(e) = (P_elect + P_cond)/(P_mech - P_core - P_prox);

end

figure(3)
subplot(2,1,1)
plot(2*Pole_pairs,-P_out,'k')
xlabel('Poles')
ylabel('Power (W)')
title('Output power and effieciency vs. number of poles ')
hold on
subplot(2,1,2)
plot(2*Pole_pairs,Eff*100,'k')
xlabel('Poles')
ylabel('Efficiency (%)')
hold on
```

```
%%%%%%%%%%%%%%%%%%%%%%%%%%%%%%%%%%%%%%%%%%
%%%% Output power and efficiency vs. outer radius of magnetic core %%%
%%%%%%%%%%%%%%%%%%%%%%%%%%%%%%%%%%%%%%%%%%

Outer_Radius = [4:.1:5];
for e = 1:length(Outer_Radius)
        R_om = Outer_Radius(e)*1e-3
        Omega_m = 500/(R_om+1e-3);
        w_m = P*Omega_m;                        % angular velocity of rotor (rad/s)
        w_e = w_m;                        % electrical angular frequency (rad/s)
        [U_r U_s R_mr B_rotor B_stator Core_loss] = SWPM_fields(w_m,I_o,Ba,Core_loss_density);
        [Fp Torque V_o L_s B_coil] = SWPM_power(w_m,I_o,U_r,U_s,R_mr);
        [Core_loss] = SWPM_hysteresis(w_m,I_o,U_r,U_s,R_mr,Ba,Core_loss_density);
        [R_s] = SWPM_resistance(W_ci,W_co,T_ci,T_co,R_o1,R_i1,winding,C_lam);
        [P_prox B_eddy] = SWPM_proximity(C_lam,B_coil);
        P_elect = 1.5*I_o*real(V_o(1));
        P_mech = sum(Torque)*Omega_m;
        P_cond = 1.5*R_s*I_o^2;
        P_core = Core_loss;
        P_out(e) = P_elect + P_cond;
        Eff(e) = (P_elect + P_cond)/(P_mech - P_core - P_prox);
end

figure(4)
subplot(2,1,1)
plot(Outer_Radius,-P_out,'k')
xlabel('R_o (mm)')
ylabel('Power (W)')
title('Output power and efficiency vs. outer radius of rotor core')
hold on
subplot(2,1,2)
plot(Outer_Radius,Eff*100,'k')
xlabel('R_o (mm)')
ylabel('Efficiency (%)')
hold on

%%%%%%%%%%%%%%%%%%%%%%%%%%%%%%%%%%%%%%%%%%%
%%%% Output power and efficiency vs. active and coil layer thickness %%%
%%%%%%%%%%%%%%%%%%%%%%%%%%%%%%%%%%%%%%%%%%%

Eff_max = 0;
coil_layer = [50:10:200];
active_layer = [100:25:500];
for e = 1:length(coil_layer)
        T_cl = coil_layer(e)*1e-6
        T_ci = T_cl/2;
        T_co = T_cl/2;

        for f = 1:length(active_layer)
                T_al = active_layer(f)*1e-6;
                [U_r U_s R_mr B_rotor B_stator Core_loss] = SWPM_fields(w_m,I_o,Ba,Core_loss_density);
                [Fp Torque V_o L_s] = SWPM_power(w_m,I_o,U_r,U_s,R_mr);
                [Core_loss] = SWPM_hysteresis(w_m,I_o,U_r,U_s,R_mr,Ba,Core_loss_density);
                [R_s] = SWPM_resistance(W_ci,W_co,T_ci,T_co,R_o1,R_i1,winding);
                P_elect = 1.5*I_o*real(V_o(1));
                P_mech = sum(Torque)*Omega_m;
```

```
                P_cond = 1.5*R_s*I_o^2;
                P_core = Core_loss;
                P_out(e,f) = max(0,-(P_elect + P_cond));
                Eff(e,f) = max(0,(P_elect + P_cond)/(P_mech - P_core));

                if (Eff(e,f) > Eff_max) & (P_out(e,f) >= 10)
                        Eff_max = Eff(e,f);
                        P_omax = P_out(e,f);
                        al_max = T_al;
                        cl_max = T_cl;
                end
        end

end

figure(5)
surf(active_layer,coil_layer,P_out)
xlabel('Active layer thickness (\mum)')
ylabel('Coil layer thickness (\mum)')
zlabel('Power (W)')
title('Output power vs. active and coil layer thicknesses')

figure(6)
surf(active_layer,coil_layer,Eff*100)
xlabel('Active layer thickness (\mum)')
ylabel('Coil layer thickness (\mum)')
zlabel('Efficincy (%)')
title('Efficiency vs. active and coil layer thicknesses')
```

```
%%%%%%%%%%%%%%%%%%%%%%%%%%%%%%%%%%%%%%%%%%%%%%%%%%%%%%%%%%%%%%%%%%%%%%%%%%%%%%%
%%%% Surface Wound PM machine parameters (SWPM_parameters) initializes the variables     %%%%
%%%% for the machine dimensions, material properties and electrical inputs used in        %%%%
%%%% SWPM_fields, SWPM_power, SWPM_hysteresis and SWPM_resistance. (MKS units)    %%%%
%%%%%%%%%%%%%%%%%%%%%%%%%%%%%%%%%%%%%%%%%%%%%%%%%%%%%%%%%%%%%%%%%%%%%%%%%%%%%%%

global T_rc T_al T_ag T_sc T_cl g_cl c_m W S pf N_lam T_cl H_refr B_refr H_refs B_refs
global R_im R_om u_0 u_a sigma_c sigma_a sigma_r sigma_s B_rm v M P N w_e delta_m


% Rotor Dimenstions (meters)

        T_rc = 500e-6;                  % thickness of rotor core
        T_al = 250e-6;                  % thickness of rotor magnets
        T_ag = 50e-6;                   % air gap
        c_m = 0.000001;                 % transition region length


% Stator Dimensions (meters)

        T_wafer = 550e-6;               % thickness of Si wafer
        winding = 'full pitched';       % winding type, either 'full pitched' or ' concentric '
        T_cl = 200e-6;                  % thickness of Cu coil
        T_sc = 2*T_wafer - T_cl - T_ag; % thickness of stator core
        T_ci = T_cl/2;                  % thickness of inner end turn
```

```
T_co = T_cl/2;                          % thickness of outer end turn
g_cl = 75e-6;                           % gap between two adjacent coils
W_ci = 200e-6;                          % width of inner end turn coils
W_co = 500e-6;                          % width of outer end turn coils
R_im = 3e-3;                            % magnetic core inner radius
R_om = 5e-3;                            % magnetic core outer radius
R_o1 = R_om+1.5e-3;                     % outer radius of outer end turn (full pitched coils only)
R_i1 = 2e-3;                            % inner radius of inner end turn (full pitched coils only)

% Material Properties

Temp = 300;                             % temperature (degrees C)
u_0 = 4*pi*1e-7;                        % permeability of free space (henry/m)
u_a = 1*u_0;                            % permeability of active layer (henry/m)
sigma_c = 5.8e7;                        % conductivity of Cu (siemens)
sigma_a = 1e7;                          % conductivity of rotor active layer (siemens)
sigma_r = 5e6;                          % conductivity of CoFe (siemens)
sigma_s = 5e6;                          % conductivity of CoFe (siemens)
B_rm = 1;                               % remanence of rotor PM (T)
 v = 2e-5;                              % dynamic viscosity of air (N-s/m)

load CoFe_data.mat                      % B-H data for CoFe from GIT
H1 = max(Ho) + [2e6:-1e4:1e4];          % extension of B-H curve
B1 = max(Bo) + (H1-max(Ho))*u_0;        % using permeability u_0
H_refr = [Ho H1];                       % B-H curve used in SLIM_fields
B_refr = [Bo B1];
H_refs = [Ho H1];
B_refs = [Bo B1];

% Electrical Parameters

I_o = 5;                                % Phase current (A)
delta_m = pi/2;                         % Phase difference between rotor flux and stator current
M = 5;                                  % number of harmonics solved for
P = 4;                                  % number of pole pairs
N = 3;                                  % number of turns per pole
speed = 79577.47;                       % angular velocity of rotor (RPM)
Omega_m = 500/(R_om+1e-3);              % angular velocity of rotor (rad/s)
w_m = P*Omega_m;                        % angular velocity of rotor (rad/s)
w_e = w_m;                              % electrical angular frequency (rad/s)

% Lamination Parameters

W = 30e-6;                              % lamination thickness (m)
S = 20e-6;                              % insulation thickness (m)
N_lam = round((R_om - R_im)/(W+S));     % number of laminations
pf = W/(W+S);                           % packing factor
C_lam = 2;                              % number of coil laminations
```

```
function [u_r,u_s,R_mr,B_rotor,B_stator,Core_loss] = SWPM_fields(w_m,I_o,Ba,Core_loss_density)

%%%%%%%%%%%%%%%%%%%%%%%%%%%%%%%%%%%%%%%%%%%%%%%%%%%%%%%%%%%%%%%%%%%%%%%%%%%%
%%%%% Surface Wound PM machine fields (SWPM_fields) computes the permeability of the      %%%%%
%%%%% rotor  core (u_r) and stator core (u_s) using a nonlinear B-H curve. The starting value for %%%%%
%%%%% u_r and u_s is 200*u_0. The script iteratively solves for the RMS B fields in the      %%%%%
%%%%% rotor & stator until u_r and u_s are found such that the RMS B fields lie on the B-H   %%%%%
%%%%% curve. The script also computes the resulting core loss in the stator. (MKS units)     %%%%%
%%%%%%%%%%%%%%%%%%%%%%%%%%%%%%%%%%%%%%%%%%%%%%%%%%%%%%%%%%%%%%%%%%%%%%%%%%%%

global T_rc T_al T_ag T_sc T_cl g_cl c_m W S pf N_lam T_cl H_refr B_refr H_refs B_refs
global R_im R_om u_0 u_a sigma_c sigma_a sigma_r sigma_s B_rm v M P N w_e delta_m


if N_lam == 1
        E = 1;
        dr = (R_om - R_im);                          % radial increment for unlaminated stator (m)
else
        E = N_lam+1;
        dr = (R_om - R_im)/(E-1);                    % radial increment for laminated stator (m)
end

u_r = ones(1,E)*200*u_0;                             % initial rotor permeability (henry/m)
u_s = ones(1,E)*200*u_0;                             % initial stator pole permeability (henry/m)
B_maxr = ones(1,E)*5;                                % initial B_maxr (T)
B_mr = ones(1,E)*2;                                  % initial B_mr on B_H curve (T)
B_maxs = ones(1,E)*5;                                % initial B_maxs (T)
B_ms = ones(1,E)*2;                                  % initial B_ms on B_H curve (T)


for k = 1:E

        if N_lam ==1
                r(k) = R_im + 0.5*dr;                % rotor radius for unlaminated stator (m)
        else
                r(k) = R_im + (k-1)*dr ;             % rotor radius for laminated stator (m)
        end

        lm = (pi*r(k)/P) - c_m;                      % length of region of constant remanence (m)
        lambda = 2*pi*r(k)/P;                        % wave length (m)
        V_stator = 2*pi*r(k)*T_sc*W;                 % incremental volume of the stator core (m^3)

        if w_e == 0
                FQ_s = 1;
        else
                delta_s = sqrt(2/(u_s(k)*sigma_s*w_e));   % magnetic skin depth of stator core (m)
                Q_s = .5*(1+j)*W/delta_s;            % ratio of lamination thickness to skin depth
                FQ_s = Q_s/tanh(Q_s);                % eddy current reluctance factor
        end

        sigma_seff = sigma_s*(1-abs(1/FQ_s));        % effective conductivity of stator core (siemens)
        K = P/r(k);                                  % wave number of fundamental harmonic (1/m)


        while (abs(B_maxr(k) - B_mr(k)) > 1e-4) | (abs(B_maxs(k) - B_ms(k)) > 1e-4),
```

```
for m = 1:M

        n = (2*m - 1);                  % harmonic number
        k_n = n*P/r(k);                 % wave number (1/m)

        gamma_0n = k_n;                 % magnitude of wave number (1/m)
        gamma_an = k_n;                 % rotor activel layer diffusion constant (1/m)
        gamma_rn = k_n;                 % rotor core diffusion constant (1/m)
        gamma_sn = sqrt(k_n^2+j*u_s(k)*sigma_seff*n*w_m);
                                        % stator core diffusion constant (1/m)

    %%% rotor transfer relation constants %%%

  alpha_1n(m) = (u_s(k)/gamma_sn)*gamma_0n/u_0 * sinh(gamma_sn*T_sc) + 1 * cosh(gamma_sn*T_sc);
  alpha_2n(m) = (gamma_sn/u_s(k))* 1* sinh(gamma_sn*T_sc) + gamma_0n/u_0 * cosh(gamma_sn*T_sc);
alpha_3n(m) = (u_0/gamma_0n)*alpha_2n(m)*sinh(gamma_0n*T_cl)+alpha_1n(m)*cosh(gamma_0n*T_cl)
alpha_4n(m) = (gamma_0n/u_0)*alpha_1n(m)*sinh(gamma_0n*T_cl)+alpha_2n(m)*cosh(gamma_0n*T_cl);
alpha_5n(m) = (u_0/gamma_0n)*alpha_4n(m)*sinh(gamma_0n*T_ag)+alpha_3n(m)*cosh(gamma_0n*T_ag);
alpha_6n(m) = (gamma_0n/u_0)*alpha_3n(m)*sinh(gamma_0n*T_ag)+alpha_4n(m)*cosh(gamma_0n*T_ag);
alpha_7n(m) = (u_a/gamma_0n)*alpha_6n(m)*sinh(gamma_0n*T_al)+alpha_5n(m)*cosh(gamma_0n*T_al);
alpha_8n(m) = (gamma_0n/u_a)*alpha_5n(m)*sinh(gamma_0n*T_al)+alpha_6n(m)*cosh(gamma_0n*T_al);

  beta_1n(m) = (u_r(k)/gamma_rn) * gamma_0n/u_0 * sinh(gamma_rn*T_rc) + 1* cosh(gamma_rn*T_rc);
  beta_2n(m) = (gamma_rn/u_r(k)) * 1 * sinh(gamma_rn*T_rc) + gamma_0n/u_0 * cosh(gamma_rn*T_rc);
  beta_3n(m) = (u_a/gamma_an)*beta_2n(m)*sinh(gamma_an*T_al)+beta_1n(m) * cosh(gamma_an*T_al);
  beta_4n(m) = (gamma_an/u_a)*beta_1n(m)*sinh(gamma_an*T_al)+beta_2n(m) * cosh(gamma_an*T_al);
  beta_5n(m) = (u_0/gamma_0n)*beta_4n(m)*sinh(gamma_0n*T_ag)+beta_3n(m)* cosh(gamma_0n*T_ag);
  beta_6n(m) = (gamma_0n/u_0)*beta_3n(m)*sinh(gamma_0n*T_ag)+beta_4n(m)*cosh(gamma_0n*T_ag);
  beta_7n(m) = (u_0/gamma_0n)*beta_6n(m)*sinh(gamma_0n*T_cl)+beta_5n(m) * cosh(gamma_0n*T_cl);
  beta_8n(m) = (gamma_0n/u_0)*beta_5n(m)*sinh(gamma_0n*T_cl)+beta_6n(m) * cosh(gamma_0n*T_cl);

%%%%%%%%%%%%%%%%%%%%%%%%%%%%%%%%%%%%%%%%%%%%%%%%%%%%%%%%%%%%%%%%%%%%%%%%%%%%%%%

        B_m = (8/(n*pi))*(B_rm/c_m)*cos(.5*k_n*lm)*exp(j*n*delta_m);
        A_xnm = B_m/k_n^2;              % vector potential due to rotor magnetization

    cmb = (beta_4n(m)  - beta_2n(m))  / (beta_4n(m)*alpha_8n(m) - beta_2n(m)*alpha_6n(m));
    cmt = (alpha_8n(m) - alpha_6n(m)) / (beta_4n(m)*alpha_8n(m) - beta_2n(m)*alpha_6n(m));
    cjb = (beta_8n(m)  - beta_6n(m))  / (alpha_4n(m)*beta_8n(m) - alpha_2n(m)*beta_6n(m));
    cjt = (alpha_4n(m) - alpha_2n(m)) / (alpha_4n(m)*beta_8n(m) - alpha_2n(m)*beta_6n(m));

        %%% vector potentials due to rotor PM %%%
        A_xnm1 = -j*cmb*(gamma_an/u_a)*sinh(gamma_an*T_al)*A_xnm;
         A_xnm6 = -j*cmt*(gamma_an/u_a)*sinh(gamma_an*T_al)*A_xnm;

        %%% harmonic components of tangential and normal B at interfaces 1, 2 and 5 %%%
        B_zn2(m) = j*k_n*alpha_1n(m)*A_xnm1;
        B_zn1(m) = j*k_n*A_xnm1;
        B_yn2(m) = u_s(k)*alpha_2n(m)*A_xnm1;
         B_yn1(m) = u_s(k)*(k_n/u_0)*A_xnm1;
        B_zn5(m) = j*k_n*beta_1n(m)*A_xnm6;
        B_yn5(m) = -u_r(k)*(k_n/u_0)*A_xnm6;

    end
```

```
        B_s = sqrt(0.5*sum(abs(B_yn2).^2+abs(B_zn2).^2));          % RMS B field in stator core (T)
        B_r = sqrt(0.5*sum(abs(B_yn5).^2+abs(B_zn5).^2));          % RMS B field in rotor core (T)

        B_maxr(k) = B_r;                                           % update B_maxr
        H_maxr(k) = B_maxr(k)/u_r(k);                % compute corresponding H_maxr using current u
        B_mr(k) = interp1(H_refr,B_refr,H_maxr(k));          % update B_mr using nonlinear B-H curve
        u_r(k) = B_mr(k)/H_maxr(k);                            % update rotor permeability

        B_maxs(k) = max(B_s);                                      % update B_maxp
        H_maxs(k) = B_maxs(k)/u_s(k);                % compute corresponding H_maxp using current u
        B_ms(k) = interp1(H_refs,B_refs,H_maxs(k));           % update B_mp using nonlinear B-H curve
        u_s(k) = B_ms(k)/H_maxs(k);                            % update stator pole permeability

end

B_rotor(k) = B_r;                                  % RMS B through rotor core at radius r (T)
B_stator(k) = B_s/pf;                              % RMS B through stator core at radius r (T)
H_stator(k) = interp1(B_refs,H_refs,B_stator(k));  % corresponding H in stator core (A/m)
H_rotor(k) = interp1(B_refr,H_refr,B_rotor(k));    % corresponding H in rotor core (A/m)
u_s(k) = B_stator(k)/H_stator(k);                  % effective permeability of the stator core (henry/m)
u_r(k) = B_rotor(k)/H_rotor(k);                    % effective permeability of the rotor core (henry/m)

R_mr(k) = r(k);                                    % rotor radius (m)

%%%% Compute hysteresis loss in stator core %%%%

theta = [0:0.04:1]*2*pi;                           % wavelength in radians

for x = 1:50
        z = .02*(x-.5)*T_sc;
        for m = 1:M

                n = (2*m - 1);                             % harmonic number
                k_n = n*P/r(k);                            % wave number (1/m)
                gamma_sn = sqrt(k_n^2+j*u_s(k)*sigma_seff*n*w_m);
                                                           % stator core diffusion constant (m)

                %%% Comput By and Bz in stator core %%%

                for q = 1:25
                        Bystat(m,q) = B_yn2(m)*sinh(gamma_sn*z)/sinh(gamma_sn*T_sc)+
                        B_yn1(m)*sinh(gamma_sn* (T_sc-z))/sinh(gamma_sn*T_sc))
                        *exp(-j*n*theta(q));
                        Bzstat(m,q) = (B_zn2(m)*sinh(gamma_sn*z)/sinh(gamma_sn*T_sc)+
                        B_zn1(m)*sinh(gamma_sn* (T_sc-z))/sinh(gamma_sn*T_sc))
                        *exp(-j*n*theta(q));

                end

        end

        B_1(x) = (1/pf)*max(sqrt((real(sum(Bystat))).^2 + (real(sum(Bzstat))).^2));
                                        % peak B field in the stator core (T)

        if B_1(x) >= 0.7  % 0.7 T for Moly Permalloy (NiFeMo), 1.72 T for electroplated CoFeNi
                cl_s(x) = 0.02*V_stator*max(Core_loss_density);
```

```
        else
                cl_s(x) = 0.02*V_stator*interp1(Ba,Core_loss_density,B_1(x));
        end

    end
    dCL_s(k) = sum(cl_s);                   % hysteresis loss in incremental strip at radius r (W)

end

Core_loss = sum(dCL_s)*w_e/(2*pi);          % total hysteresis loss in rotor core (W)
```

```
function [Fp,Torque,V_oc,L_s,B_coil] = SWPM_power(w_m,I_o,U_r,U_s,R_mr)

%%%%%%%%%%%%%%%%%%%%%%%%%%%%%%%%%%%%%%%%%%%%%%%%%%%%%%%%%%%%%%%%%%%%%%%%
%%%%% Surface Wound PM machine power (SWPM_power) computes the pull-in force, torque, %%%%%
%%%%% open-circuit voltage and stator phase inductance for the surface wound PM        %%%%%
%%%%% machine using the effective permeability for the rotor core and stator core from  %%%%%
%%%%% SWPM_fields. It also computes the B field in the stator windings so that the      %%%%%
%%%%% proximity eddy current loss can be found. (MKS units)                            %%%%%
%%%%%%%%%%%%%%%%%%%%%%%%%%%%%%%%%%%%%%%%%%%%%%%%%%%%%%%%%%%%%%%%%%%%%%%%

global T_rc T_al T_ag T_sc T_cl g_cl c_m W S pf N_lam T_cl H_refr B_refr H_refs B_refs
global R_im R_om u_0 u_a sigma_c sigma_a sigma_r sigma_s B_rm v M P N w_e delta_m

dr = (R_om-R_im)/500;                       % incremental radiul distance (m)

for x = 1:501

    r = R_im + (x-1)*dr;                    % radius (m)
    lambda = 2*pi*r/P;                      % wave length (m)
    L_base = lambda/4;                      % base length = 1/4 of a wavelength (m)
    lm = (pi*r/P) - c_m;                    % length of region of constant remanence (m)
    W_cl = pi*r/(3*P*N) - g_cl;             % width of coil at radius r (m)

    if N_lam == 1
        u_r = U_r;                          % permeability of rotor core  (henry/m)
        u_s = U_s;                          % permeability of stator core  (henry/m)
    else
        u_r = interp1(R_mr,U_r,r);          % permeability of rotor core  (henry/m)
        u_s = interp1(R_mr,U_s,r);          % permeability of stator core  (henry/m)
    end


    if w_e == 0
        FQ_s = 1;
    else
        delta_s = sqrt(2/(u_s*sigma_s*w_e));    % magnetic skin depth of stator base (m)
        Q_s = .5*(1+j)*W/delta_s;               % ratio of lamination thickness to skin depth
        FQ_s = Q_s/tanh(Q_s);                   % eddy current reluctance factor
    end

    sigma_seff = sigma_s*(1-abs(1/FQ_s));   % effective conductivity of stator core (siemens)

    K = P/r;                                % wave number of fundamental harmonic (1/m)
```

```
J_o = I_o/(W_cl*T_cl);                          % current density in coil (A/m^2)

%%% vector potential due to rotor magnetization %%%
% A_xj = (6/pi)*(u_0*J_o/K^2)*sin(pi*W_cl/lambda)*sum(exp(-j*pi*(2*N+1:2:4*N-1)/(6*N)));

A_xj = 6*(u_0*J_o/K^2)*W_cl/lambda*sum(exp(-j*pi*(2*N+1:2:4*N-1)/(6*N)));
                                                % long wavelength approximation
for m = 1:M

        n = (2*m - 1);                          % harmonic number
        k_n = n*P/r;                            % wave number (1/m)

        gamma_0n = k_n;                         % magnitude of wave number (1/m)
        gamma_an = k_n;                         % rotor conductor diffusion constant (1/m)
        gamma_rn = k_n;                         % rotor core diffusion constant (1/m)
        gamma_sn = sqrt(k_n^2+j*u_s*sigma_seff*n*w_m);      % stator core diffusion constant (1/m)

        %%% rotor transfer relation constants %%%

alpha_1n(m) = (u_s/gamma_sn) * gamma_0n/u_0 * sinh(gamma_sn*T_sc) + 1 * cosh(gamma_sn*T_sc);
alpha_2n(m) = (gamma_sn/u_s) * 1 * sinh(gamma_sn*T_sc) + gamma_0n/u_0 * cosh(gamma_sn*T_sc);
alpha_3n(m) = (u_0/gamma_0n)*alpha_2n(m)*sinh(gamma_0n*T_cl)+alpha_1n(m)*cosh(gamma_0n*T_cl);
alpha_4n(m) = (gamma_0n/u_0)*alpha_1n(m)*sinh(gamma_0n*T_cl)+alpha_2n(m)*cosh(gamma_0n*T_cl);
alpha_5n(m) = (u_0/gamma_0n)*alpha_4n(m)*sinh(gamma_0n*T_ag)+alpha_3n(m)*cosh(gamma_0n*T_ag);
alpha_6n(m) = (gamma_0n/u_0)*alpha_3n(m)*sinh(gamma_0n*T_ag)+alpha_4n(m)*cosh(gamma_0n*T_ag);
alpha_7n(m) = (u_a/gamma_an)*alpha_6n(m)*sinh(gamma_an*T_al) + alpha_5n(m) * cosh(gamma_an*T_al);
alpha_8n(m) = (gamma_an/u_a)*alpha_5n(m)*sinh(gamma_an*T_al) + alpha_6n(m) * cosh(gamma_an*T_al);

beta_1n(m) = (u_r/gamma_rn) * gamma_0n/u_0 * sinh(gamma_rn*T_rc) + 1 * cosh(gamma_rn*T_rc);
beta_2n(m) = (gamma_rn/u_r) * 1 * sinh(gamma_rn*T_rc) + gamma_0n/u_0 * cosh(gamma_rn*T_rc);
beta_3n(m) = (u_a/gamma_an) * beta_2n(m) * sinh(gamma_an*T_al) + beta_1n(m) * cosh(gamma_an*T_al);
beta_4n(m) = (gamma_an/u_a) * beta_1n(m) * sinh(gamma_an*T_al) + beta_2n(m) * cosh(gamma_an*T_al);
beta_5n(m) = (u_0/gamma_0n) * beta_4n(m)* sinh(gamma_0n*T_ag) + beta_3n(m) * cosh(gamma_0n*T_ag);
beta_6n(m) = (gamma_0n/u_0) * beta_3n(m)* sinh(gamma_0n*T_ag) + beta_4n(m) * cosh(gamma_0n*T_ag);
beta_7n(m) = (u_0/gamma_0n) * beta_6n(m) * sinh(gamma_0n*T_cl) + beta_5n(m) * cosh(gamma_0n*T_cl);
beta_8n(m) = (gamma_0n/u_0) * beta_5n(m) * sinh(gamma_0n*T_cl) + beta_6n(m) * cosh(gamma_0n*T_cl);

        %%%%%%%%%%%%%%%%%%%%%%%%%%%%%%%%%%%%%%%%%%%%%%%%%%%%%%%%%%%%%%%%%%%%%%%%

        B_m = (8/(n*pi))*(B_rm/c_m)*cos(.5*k_n*lm)*exp(j*n*delta_m);
        A_xnm = B_m/k_n^2;                      % vector potential due to rotor magnetization

        cmb = (beta_4n(m)  - beta_2n(m))  / (beta_4n(m)*alpha_8n(m) - beta_2n(m)*alpha_6n(m));
        cmt = (alpha_8n(m) - alpha_6n(m)) / (beta_4n(m)*alpha_8n(m) - beta_2n(m)*alpha_6n(m));
        cjb = (beta_8n(m)  - beta_6n(m))  / (alpha_4n(m)*beta_8n(m) - alpha_2n(m)*beta_6n(m));
        cjt = (alpha_4n(m) - alpha_2n(m)) / (alpha_4n(m)*beta_8n(m) - alpha_2n(m)*beta_6n(m));

        %%% vector potentials due to rotor PM %%%
        A_xnm1 = -j*cmb*(gamma_an/u_a)*sinh(gamma_an*T_al)*A_xnm;
        A_xnm6 = -j*cmt*(gamma_an/u_a)*sinh(gamma_an*T_al)*A_xnm;

        %%% vector potentials due to stator current %%%
        if m == 1
                A_xnj1 =  cjb*(gamma_0n/u_0)*sinh(gamma_0n*T_cl)*A_xj;
                A_xnj6 =  cjt*(gamma_0n/u_0)*sinh(gamma_0n*T_cl)*A_xj;
        else
```

```
            A_xnj1 = 0;
            A_xnj6 = 0;
        end

        B_zn4 = j*k_n*(alpha_5n(m)*A_xnm1 + beta_3n(m)*A_xnj6);
                                % harmonic components of tangential H at the rotor PM surface
        H_yn4 = alpha_6n(m)*A_xnm1 - beta_4n(m)*A_xnj6;
                                % harmonic components of normal B at the rotor PM surface

        zeta1(m) = 0.5*real(B_zn4*H_yn4');      % harmonic components of torque
        zeta2(m) = 0.25*((1/u_0) * (abs(B_zn4))^2 - u_0*(abs(H_yn4))^2);
                                % harmonic components of pull-in force

    A_xncoilm(m) = A_xnm1*(alpha_3n(m) + lpha_1n(m))*sinh(.5*gamma_0n*T_cl)/sinh(gamma_0n*T_cl);
                                % vector potential at stator coil due to rotor PM
A_xncoilj(m) = (A_xnj6*beta_5n(m)+A_xnj1*alpha_1n(m))*sinh(.5*gamma_0n*T_cl)/sinh(gamma_0n*T_cl);
                                % vector potential at stator coil 1 due to stator current
        B_coilm(x,m) = j*k_n*A_xncoilm(m);      % B field at stator coil due to rotor PM

        dV(x,m) = j*n*w_m*2*P*A_xncoilm(m)*sum(exp(j*n*pi*(2*N+1:2:4*N-1)/(6*N)))*dr;
                                % voltage from PM over region [r,r+dr] (V)
        dPhi(x,m) = 2*P*A_xncoilj(m)*sum(exp(j*n*pi*(2*N+1:2:4*N-1)/(6*N)))*dr;
                                % flux from stator current over region [r,r+dr] (Wb)
        dT(x,m) = zeta1(m) * dr * r^2;          % total torque over region [r,r+dr] (N-m)

    end

    dFp(x) = sum(zeta2)* dr * r;                % pull-in force over region [r,r+dr] (N)

end

Fp = -2*pi*sum(dFp);                            % pull-in force acting rotor (N)
Torque = -2*pi*sum(dT);                         % torque on rotor (N-m)
V_oc = sum(dV);                                 % open-circuit voltage (V)
Flux = sum(dPhi);                               % total flux from stator currents (H)
L_s = (2/3)*real(sum(Flux))/I_o;                % stator phase inductance (H)
B_coil = mean(abs(B_coilm));                    % average B at stator coil over radial span of the machine (T)
```

```
function [Core_loss] = SWPM_hysteresis(w_m,I_o,U_r,U_s,R_mr,Ba,Core_loss_density)

%%%%%%%%%%%%%%%%%%%%%%%%%%%%%%%%%%%%%%%%%%%%%%%%%%%%%%%%%%%%%%%%%%%%%%%%%%%%%%%
%%%%% Surface Wound PM machine hystersis (SWPM_hysteresis) computes the hysteresis     %%%%%
%%%%% loss in the rotor core of the slotted stator induction machine using the          %%%%%
%%%%% effective permeability for the rotor core and stator core from SWPM_fields.       %%%%%
%%%%% (MKS units)                                                                      %%%%%
%%%%%%%%%%%%%%%%%%%%%%%%%%%%%%%%%%%%%%%%%%%%%%%%%%%%%%%%%%%%%%%%%%%%%%%%%%%%%%%

global T_rc T_al T_ag T_sc T_cl g_cl c_m W S pf N_lam T_cl H_refr B_refr H_refs B_refs
global R_im R_om u_0 u_a sigma_c sigma_a sigma_r sigma_s B_rm v M P N w_e delta_m

if N_lam == 1
    E = 1;
    dr = (R_om - R_im);                         % radial increment for unlaminated stator (m)
else
```

```
        E = N_lam+1;
        dr = (R_om - R_im)/(E-1);                    % radial increment for laminated stator (m)
end

for k = 1:E

        if N_lam ==1
                r(k) = R_im + 0.5*dr;                % rotor radius for unlaminated stator (m)
        else
                r(k) = R_im + (k-1)*dr ;             % rotor radius for laminated stator (m)
        end

        lm = (pi*r(k)/P) - c_m;                      % length of region of constant remanence (m)
        lambda = 2*pi*r(k)/P;                        % wave length (m)
        V_stator = 2*pi*r(k)*T_sc*W;                 % incremental volume of the stator core (m^3)

        if N_lam == 1
                u_r(k) = U_r;                        % permeability of rotor core  (henry/m)
                u_s(k) = U_s;                        % permeability of stator core  (henry/m)
        else
                u_r(k) = interp1(R_mr,U_r,r(k));     % permeability of rotor core  (henry/m)
                u_s(k) = interp1(R_mr,U_s,r(k));     % permeability of stator core  (henry/m)
        end

        if w_e == 0
                FQ_s = 1;
        else
                delta_s = sqrt(2/(u_s(k)*sigma_s*w_e));  % magnetic skin depth of stator base (m)
                Q_s = .5*(1+j)*W/delta_s;            % ratio of lamination thickness to skin depth
                FQ_s = Q_s/tanh(Q_s);                % eddy current reluctance factor
        end

        sigma_seff = sigma_s*(1-abs(1/FQ_s));        % effective conductivity of stator core (siemens)
        K = P/r(k);                                  % wave number of fundamental harmonic (1/m)

        for m = 1:M

                n = (2*m - 1);                       % harmonic number
                k_n = n*P/r(k);                      % wave number (1/m)

                gamma_0n = k_n;                      % magnitude of wave number (1/m)
                gamma_an = k_n;                      % rotor conductor diffusion constant (1/m)
                gamma_rn = k_n;                      % rotor core diffusion constant (1/m)
                gamma_sn = sqrt(k_n^2+j*u_s(k)*sigma_seff*n*w_m);
                                                     % stator core diffusion constant (1/m)

                %%% rotor transfer relation constants %%%

alpha_1n(m) = (u_s(k)/gamma_sn) * gamma_0n/u_0 * sinh(gamma_sn*T_sc) + 1 * cosh(gamma_sn*T_sc);
alpha_2n(m) = (gamma_sn/u_s(k)) * 1 * sinh(gamma_sn*T_sc) + gamma_0n/u_0 * cosh(gamma_sn*T_sc);
alpha_3n(m) = (u_0/gamma_0n)*alpha_2n(m) *sinh(gamma_0n*T_cl)+alpha_1n(m) * cosh(gamma_0n*T_cl);
alpha_4n(m) = (gamma_0n/u_0)*alpha_1n(m)* sinh(gamma_0n*T_cl)+ alpha_2n(m)*cosh(gamma_0n*T_cl);
alpha_5n(m) = (u_0/gamma_0n)*alpha_4n(m)*sinh(gamma_0n*T_ag)+alpha_3n(m)*cosh(gamma_0n*T_ag);
alpha_6n(m) = (gamma_0n/u_0)*alpha_3n(m)*sinh(gamma_0n*T_ag)+alpha_4n(m)* cosh(gamma_0n*T_ag);
alpha_7n(m) = (u_a/gamma_0n)*alpha_6n(m)*sinh(gamma_0n*T_al)+alpha_5n(m)*cosh(gamma_0n*T_al);
alpha_8n(m) = (gamma_0n/u_a)*alpha_5n(m)*sinh(gamma_0n*T_al)+alpha_6n(m)*cosh(gamma_0n*T_al);
```

```
beta_1n(m) = (u_r(k)/gamma_rn)*gamma_0n/u_0*sinh(gamma_rn*T_rc) + 1* cosh(gamma_rn*T_rc);
beta_2n(m) = (gamma_rn/u_r(k)) * 1* sinh(gamma_rn*T_rc) + gamma_0n/u_0 * cosh(gamma_rn*T_rc);
beta_3n(m) = (u_a/gamma_an)*beta_2n(m)* sinh(gamma_an*T_al) + beta_1n(m) * cosh(gamma_an*T_al);
beta_4n(m) = (gamma_an/u_a) * beta_1n(m) * sinh(gamma_an*T_al) + beta_2n(m) * cosh(gamma_an*T_al);
beta_5n(m) = (u_0/gamma_0n) * beta_4n(m) * sinh(gamma_0n*T_ag) + beta_3n(m)* cosh(gamma_0n*T_ag);
beta_6n(m) = (gamma_0n/u_0) * beta_3n(m) * sinh(gamma_0n*T_ag) + beta_4n(m)* cosh(gamma_0n*T_ag);
beta_7n(m) = (u_0/gamma_0n) * beta_6n(m) * sinh(gamma_0n*T_cl) + beta_5n(m) * cosh(gamma_0n*T_cl);
beta_8n(m) = (gamma_0n/u_0) * beta_5n(m) * sinh(gamma_0n*T_cl) + beta_6n(m) * cosh(gamma_0n*T_cl);

%%%%%%%%%%%%%%%%%%%%%%%%%%%%%%%%%%%%%%%%%%%%%%%%%%%%%%%%%%%%%%%%%%%%%%%%%%%%%%%%

        B_m = (8/(n*pi))*(B_rm/c_m)*cos(.5*k_n*lm)*exp(j*n*delta_m);
        A_xnm = B_m/k_n^2;                          % vector potential due to rotor magnetization

        cmb = (beta_4n(m)  - beta_2n(m))  / (beta_4n(m)*alpha_8n(m) - beta_2n(m)*alpha_6n(m));
        cmt = (alpha_8n(m) - alpha_6n(m)) / (beta_4n(m)*alpha_8n(m) - beta_2n(m)*alpha_6n(m));
        cjb = (beta_8n(m)  - beta_6n(m))  / (alpha_4n(m)*beta_8n(m) - alpha_2n(m)*beta_6n(m));
        cjt = (alpha_4n(m) - alpha_2n(m)) / (alpha_4n(m)*beta_8n(m) - alpha_2n(m)*beta_6n(m));

        %%% vector potentials due to rotor PM %%%
        A_xnm1 = -j*cmb*(gamma_an/u_a)*sinh(gamma_an*T_al)*A_xnm;
        A_xnm6 = -j*cmt*(gamma_an/u_a)*sinh(gamma_an*T_al)*A_xnm;

        %%% harmonic components of tangential and normal B at interfaces 1, 2 and 5 %%%

        B_zn2(m) = j*k_n*alpha_1n(m)*A_xnm1;
        B_zn1(m) = j*k_n*A_xnm1;
        B_yn2(m) = u_s(k)*alpha_2n(m)*A_xnm1;
        B_yn1(m) = u_s(k)*(k_n/u_0)*A_xnm1;
        B_zn5(m) = j*k_n*beta_1n(m)*A_xnm6;
        B_yn5(m) = -u_r(k)*(k_n/u_0)*A_xnm6;
end

theta = [0:0.04:1]*2*pi;                            % wavelength in radians

for x = 1:50
        z = .02*(x-.5)*T_sc;
        for m = 1:M

                n = (2*m - 1);                      % harmonic number
                k_n = n*P/r(k);                     % wave number (1/m)
                gamma_sn = sqrt(k_n^2+j*u_s(k)*sigma_seff*n*w_m);
                                                    % stator core diffusion constant (m)

        %%% Comput By and Bz in stator core %%%

                for q = 1:25
                        Bystat(m,q) = B_yn2(m)*sinh(gamma_sn*z)/sinh(gamma_sn*T_sc)+B_yn1(m)
                        *sinh(gamma_sn* (T_sc-z))/sinh(gamma_sn*T_sc))*exp(-j*n*theta(q));
                        Bzstat(m,q) = (B_zn2(m)*sinh(gamma_sn*z)/sinh(gamma_sn*T_sc)+B_zn1(m)
                        *sinh(gamma_sn*(T_sc-z))/sinh(gamma_sn*T_sc))*exp(-j*n*theta(q));
                end

        end
```

```
            B_1(x) = (1/pf)*max(sqrt((real(sum(Bystat))).^2 + (real(sum(Bzstat))).^2));
                                                % peak B field in the stator core (T)

            if B_1(x) >= 0.7  % 0.7 T for Moly Permalloy (NiFeMo), 1.72 T for electroplated CoFeNi
                  cl_s(x) = 0.02*V_stator*max(Core_loss_density);
            else
                  cl_s(x) = 0.02*V_stator*interp1(Ba,Core_loss_density,B_1(x));
            end
      end
      dCL_s(k) = sum(cl_s);                     % hysteresis loss in incremental strip at radius r (W)

end

Core_loss = sum(dCL_s)*w_e/(2*pi);              % total hysteresis loss in rotor core (W)
```

```
function [P_prox,B_eddy] = SWPM_proximity(C_lam,B_coil)

%%%%%%%%%%%%%%%%%%%%%%%%%%%%%%%%%%%%%%%%%%%%%%%%%%%%%%%%%%%%%%%%%%%%%%%%%%%%%%%
%%%%% Surface Wound PM machine proximity (SWPM_proximity) computes the proximity      %%%%%
%%%%% effect eddy current loss in the stator windigns of the surface wound PM machine  %%%%%
%%%%% using the B field in the coils computed in SWPM_power. (MKS units)               %%%%%
%%%%%%%%%%%%%%%%%%%%%%%%%%%%%%%%%%%%%%%%%%%%%%%%%%%%%%%%%%%%%%%%%%%%%%%%%%%%%%%

global T_rc T_al T_ag T_sc T_cl g_cl c_m W S pf N_lam T_cl H_refr B_refr H_refs B_refs
global R_im R_om u_0 u_a sigma_c sigma_a sigma_r sigma_s B_rm v M P N w_e delta_m


W_cl_ri = pi*R_im/(3*P*N*C_lam) - g_cl;         % width of radial conductor at the inner radius (m)
W_cl_ro = pi*R_om/(3*P*N*C_lam) - g_cl;         % width of radial conductor at the outer radius (m)

harm = [1:2:(2*M-1)];

P_prox = 6*P*N*C_lam*(sigma_c/96)*w_e^2*sum((harm.^2).*(B_coil.^2))*T_cl*
      (0.75*P*N*C_lam/pi)*(W_cl_ro^4 - W_cl_ri^4);

I_eddy = 0.25*sigma_c*w_e*B_coil(1)*T_cl*(0.5*W_cl_ro)^2;      % induced current (A)

B_eddy = u_0*I_eddy/(T_al+T_ag+T_cl);                          % resulting B field due to I_eddy (T)
```

```
function [R_s] = SWPM_resistance(W_ci,W_co,T_ci,T_co,R_o1,R_i1,winding,C_lam)

%%%%%%%%%%%%%%%%%%%%%%%%%%%%%%%%%%%%%%%%%%%%%%%%%%%%%%%%%%%%%%%%%%%%%%%%%%%%%%%
%%%%% Surface Wound PM machine resistance  (SWPM_resistance) computes the resistance  %%%%%
%%%%% of a single phase of the surface wound PM machine with either full pitched or    %%%%%
%%%%% concenctric windings. (MKS units)                                                %%%%%
%%%%%%%%%%%%%%%%%%%%%%%%%%%%%%%%%%%%%%%%%%%%%%%%%%%%%%%%%%%%%%%%%%%%%%%%%%%%%%%

global T_rc T_al T_ag T_sc T_cl g_cl c_m W S pf N_lam T_cl H_refr B_refr H_refs B_refs
global R_im R_om u_0 u_a sigma_c sigma_a sigma_r sigma_s B_rm v M P N w_e delta_m
```

```
%%% Resistance of radial conductors %%%
W_cl_ri = pi*R_im/(3*P*N*C_lam) - g_cl;
W_cl_ro = pi*R_om/(3*P*N*C_lam) - g_cl;
R_radial = (6*(P*N*C_lam)^2/(pi*sigma_c*T_cl)) * log(W_cl_ro/W_cl_ri);

%%% Resistance of inner and outer end turns %%%
if winding == 'full pitched'
        L_inner = sqrt((.5*pi*R_im/P)^2 + (R_im - R_i1)^2);
        L_outer = sqrt((.5*pi*R_om/P)^2 + (R_o1 - R_om)^2);
        R_inner = 2*N*P*L_inner/(pi*sigma_c*T_ci*W_ci);
        R_outer = 2*N*P*L_outer/(pi*sigma_c*T_co*W_co);
elseif winding == ' concentric '
        for n = 1:N
                R_i(n) = R_im - 0.5*(2*n-1)*W_ci - n*g_cl;
                R_o(n) = R_om + 0.5*(2*n-1)*W_co + n*g_cl;
                L_i(n) = (2*(N+n)-1)*pi*R_i(n)/(3*P*N);
                L_o(n) = (2*(N+n)-1)*pi*R_o(n)/(3*P*N);
        end

        R_inner = P*sum(L_i)/(sigma_c*T_ci*W_ci);
        R_outer = P*sum(L_o)/(sigma_c*T_co*W_co);
end

%%% Total resistance of a single phase %%%
R_s = R_radial + R_inner + R_outer;
```

Appendix C: PSIM Models and Loss Calculations for Chapter 5

This appendix describes the modeling and loss calculations used in comparing the different switch-mode rectifier topologies in Section 5.2.2. The four topologies considered are the MOSFET rectifier/CCM boost converter, the DCM boost MOSFET-rectifier and the DCM boost semi-bridge rectifier with and without synchronous rectification. These four topologies are simulated in PSIM because of the ease in which various control strategies can be implemented. However, PSIM models the MOSFET as an ideal switch with a drain-to-source resistance and body diode. The diodes are modeled with only a constant forward voltage. The gate drive, capacitive turn-off, and switching transition losses in the MOSFET, as well as the capacitive losses in the diodes, are not accounted for in the PSIM model. To accurately predict the efficiencies of the various topologies these losses must be accounted for.

In addition, the losses in the boost inductors must also be accurately modeled. An equivalent circuit is used to model the high frequency winding resistance and core loss of the inductors. The values used in the equivalent circuit are computed using the SPICE models of the inductors from Coilcraft.

C.1 MOSFET Losses

For the MOSFET rectifier/CCM boost converter topology current sensing MOSFETs are used for the boost switch and the low side switches on the rectifier. The high side switches use a normal power MOSFET. The DCM boost MOSFET rectifier uses the same MOSFETs in the rectifier as the CCM converter but uses a normal power MOSFET as the boost switch. The boost semi-bridge rectifier uses only normal power MOSFETs as the boost switches.

The Si4730EY, from Vishay Siliconix, is used for the current sense MOSFETs while all the other MOSFETs are the IRF7413Z from International rectifier. For the DCM rectifiers, the LM5112 is used to drive the gate of the IRF7413Z. It has a low-side output resistance of 1.4 Ω while the gate resistance of the IRF7413Z is 2.3 Ω. For the CCM boost converter, the boost FET is the Si4730EY. No gate resistance is specified in the data sheet. A generic gate driver is used and the sum of the gate resistance and the

output resistance of the gate driver is assumed to be 5 Ω. The properties for the two power MOSFETs with their respective gate drivers are shown in Table C-1.

The main losses in the MOSFET are conduction loss, gate drive loss, output capacitive loss and switching transition loss. The maximum drain-to-source resistance, $R_{ds,on}$, of the power MOSFET at a gate-to-source voltage of 10 V and at 40 °C ambient temperature is used for the on-state resistance in the PSIM model. These values can be obtained from the MOSFET data sheet. For the Si4730EY, $R_{ds,on}$ is 20 mΩ and for the IRF7413Z, $R_{ds,on}$ is 10 mΩ.

The gate drive loss is the power consumed charging and discharging the gate of the MOSFET and is given by

$$P_{gd} = V_{gd} Q_g f_{sw} . \tag{C-1}$$

V_{gd} is the gate drive voltage and is 12 V for all the topologies. Q_g is the total gate charge on the MOSFET when $V_{gs} = V_{gd}$. The total gate charge required to put a certain voltage across the gate and source is usually specified because the input capacitance is nonlinear [66]. At a V_{gd} of 12 V, Q_g is 41 nC for the Si4730EY and 16.3 nC for the IRF7413Z.

Table C-1: MOSFET and gate drive parameters.

	IRF7413Z	Si4730EY
$R_{ds,on}$ (@ V_{gs} = 10 V)	10 mΩ	20 mΩ
Q_g (@ V_{gs} = 12 V)	16.3 nC	41 nC
C_{iss} (@ V_{ds} = 12 V)	1300 pF	2700 pF
C_{iss} (@ V_{ds} = 0 V)	1210 pF	2050 pF
$R_g + R_{oh}$	–	5 Ω
$R_g + R_{ol}$	3.7 Ω	5 Ω

The energy lost in the output capacitance of the MOSFET depends on the size of capacitance and the maximum voltage applied. This capacitance is charged when the MOSFET turns off and is discharged when it is turned on. Figure C-1 shows the output capacitance, C_{oss}, as a function of drain-to-source voltage, V_{ds} for the IRF7413Z. The data points have been fitted to the following analytical function

$$C_{oss}(V_{ds}) \approx \frac{650\text{pF}}{(1 + V_{ds})^{0.35}} . \tag{C-2}$$

The energy dissipated charging and discharging the output capacitance over a switching cycle is equal to the peak V_{ds} times the charge on the output capacitor at peak V_{ds}.

$$E_{cout}(V_{ds}) = V_{ds} Q_{oss}(V_{ds}) = V_{ds} \int_0^{V_{ds}} C_{oss}(V) dV . \tag{C-3}$$

The corresponding output capacitive loss in the boost MOSFET for the CCM boost converter and DCM boost MOSFET-rectifier is

$$P_{cout} = f_{sw} E_{cout}(V_o) = f_{sw} V_o \int_0^{V_o} C_{oss}(V_{ds}) dV_{ds} . \tag{C-4}$$

Note that when the boost inductor current in the semi-bridge topology is positive, the current will flow through the high side diode so that the peak value of V_{ds} is V_o. V_{ds} is much smaller than V_o when the boost current is negative and the resulting energy loss is much smaller than when the current is positive and can be ignored. Therefore, the power lost in the output capacitance of each power MOSFET is half of that in Equation (C-4).

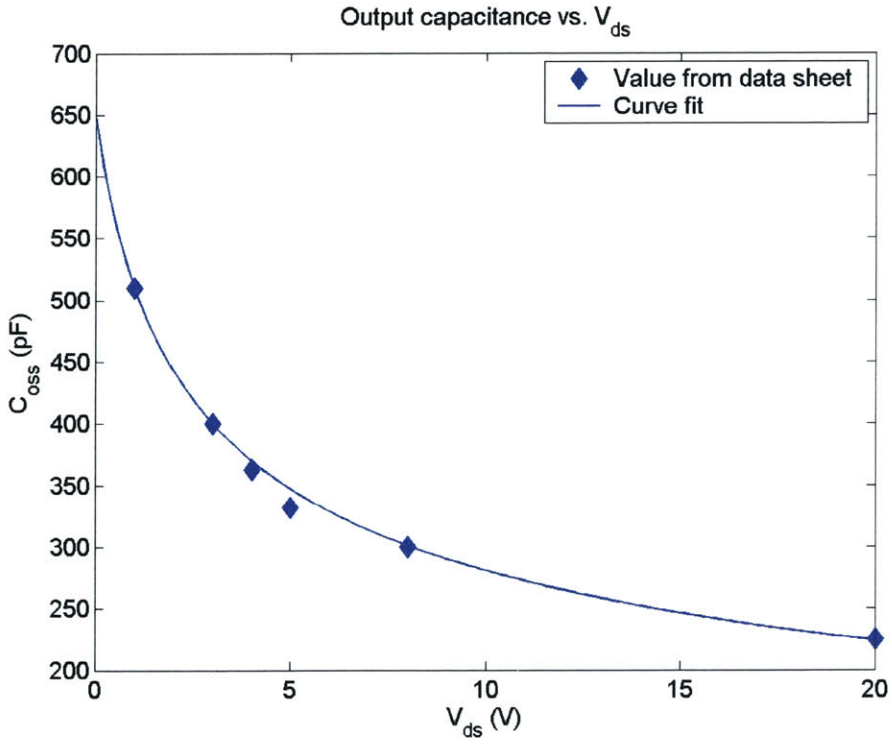

Figure C-1: Output capacitance vs. drain-to-source voltage for the IRF7413Z power MOSFET. Points represent data sheet values; curve represents analytical model.

The switching transition losses are due to currents flowing through the MOSFET when their drain-to-source voltage rises and falls [47]. The smaller the input capacitance the less charge it takes to reach the turn-on gate voltage and the shorter the time in which there is current through the FET while a large voltage is across the drain and source. The power dissipated in the switching transition loss depends on frequency and current through the MOSFET. Note that only the CCM boost converter has both a turn-on and turn-off switching transition loss while the DCM boost rectifiers have only a turn-off transition loss.

Figure C-2 shows the stages of the MOSFET turn-on sequence used to determine turn-on transition time. A V_{gs} vs. Q_g curve is shown in Figure C-2(a). When the MOSFET is about to turn on, the switch current is zero and V_{ds} is equal to V_r for the rectifier MOSFETs and V_o for the boost MOSFET. The gate drive must charge the input capacitance, C_{iss}, through the series combination of the gate resistor, R_g, and gate drive source resistance, R_{oh} as shown in Figure C-2(b). The time it takes for the gate voltage to go form the threshold voltage to the Miller plateau voltage, T_{f1}, can be computed from

$$T_{r1} = \tau_{r1} \mathrm{Ln}\left(\frac{V_{gd} - V_{th}}{V_{gd} - V_{gs,m}} \right). \tag{C-5}$$

where,

$$\tau_{r1} = C_{iss}\left(V_{ds} = V_o\right)\left(R_g + R_{oh}\right). \tag{C-6}$$

During this period the MOSFET current rises.

Once the Miller plateau voltage is reached, the MOSFET gate acts like a constant voltage source while the charge in the gate-to-drain capacitance, Q_{gd}, is discharged (Figure C-2(c)). The drain-source voltage falls to ~0V during this period. The time it takes this charge to discharge is the time it takes for V_{ds} to rise from ~0 to V_o. This time is

$$T_{r2} = \frac{Q_{gd}\left(R_g + R_{oh}\right)}{V_{gd} - V_{gs,m}}. \tag{C-7}$$

Once Q_{gd} is charged, the gate-to-source capacitance, C_{gs}, charges up as shown in Figure C-2(d). The time it takes for V_{gs} to reach V_{gd} is

$$T_{r3} \approx 3\tau_{r3}. \tag{C-8}$$

where,

$$\tau_{r3} = C_{iss}(V_{ds} = 0)(R_g + R_{oh}). \tag{C-9}$$

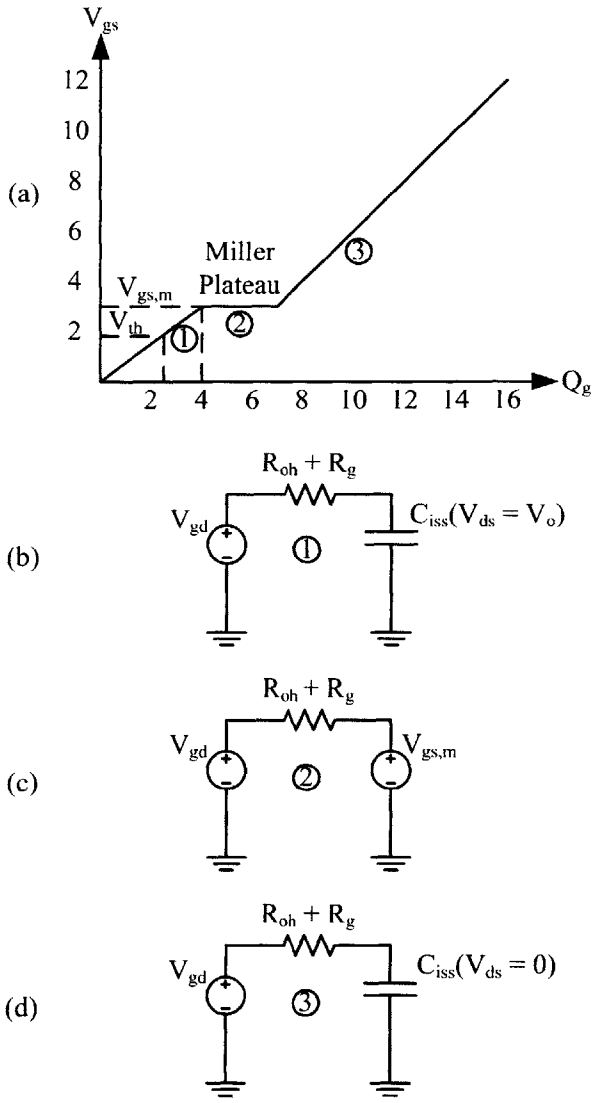

Figure C-2: MOSFET turn-on gate charging sequence and equivalent circuits.

The power dissipated in the turn-on transition loss for the CCM boost converter is [47]

$$P_{swtr,on} = 0.5 f_{sw} I_{ds,pk} V_{ds,pk} T_r. \tag{C-10}$$

The fall time, T_r, is equal to $T_{r1} + T_{r2}$. T_{r3} does not contribute to the transition loss because the current through the MOSFET is constant during that time. For the boost MOSFET $V_{ds,pk}$ will equal V_o while $I_{ds,pk}$ can be found from the PSIM simulation.

The turn-off transition uses the reverse sequence in Figure C-2 and is shown in Figure C-3. When the MOSFET is about to turn off, it switch current is at some peak value and V_{ds} is ~0 V. The gate drive must discharge the input capacitance, C_{iss}, through the series combination of the gate resistor, R_g, and gate drive sink resistance, R_{ol} as shown in Figure C-3(b). The time it takes for the gate voltage to drop to the Miller plateau voltage, T_{f1}, can be computed from

$$T_{f1} = \tau_{f1} \mathrm{Ln}\left(\frac{V_{gd}}{V_{gs,m}}\right). \tag{C-11}$$

where,

$$\tau_{f1} = C_{iss}\left(V_{ds} = 0\right)\left(R_g + R_{ol}\right). \tag{C-12}$$

Once the Miller plateau voltage is reached, the MOSFET gate acts like a constant voltage source while the charge in the gate-to-drain capacitance, Q_{gd}, is discharged (Figure C-3(c)). The time it takes this charge to discharge is the time it takes for V_{ds} to rise from ~0 to V_o. This time is

$$T_{f2} = \frac{Q_{gd}\left(R_g + R_{ol}\right)}{V_{gs,m}}. \tag{C-13}$$

Once Q_{gd} is discharged, the gate-to-source capacitance, C_{gs}, discharges as shown in Figure C-3(d). During the period the MOSFET current falls until V_{gs} equals the threshold voltage, V_{th}. When V_{gs} equals V_{th} the current is zero. The time it takes for this to happen is

$$T_{f3} = \tau_{f3} \mathrm{Ln}\left(\frac{V_{gs,m}}{V_{th}}\right). \tag{C-14}$$

where,

$$\tau_{f3} = C_{iss}\left(V_{ds} = V_o\right)\left(R_g + R_{ol}\right). \tag{C-15}$$

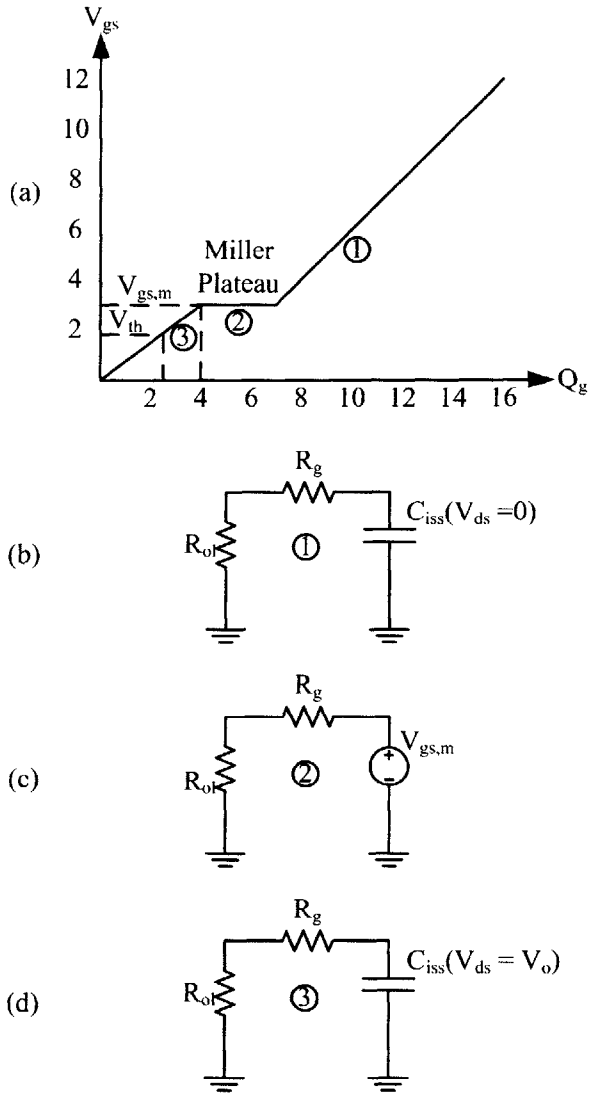

Figure C-3: MOSFET turn-off gate charging sequence and equivalent circuits.

The energy dissipated in a single transition is

$$E_{swtr} = 0.5 I_{ds,pk} V_{ds,pk} T_f . \tag{C-16}$$

The fall time, T_f, is equal to $T_{f2} + T_{f3}$. T_{f1} does not contribute to the transition loss because V_{ds} is still zero during that time. For the boost MOSFET in the CCM converter and DCM boost MOSFET rectifier $V_{ds,pk}$ will equal V_o while $I_{ds,pk}$ can be found from the PSIM simulation. The switching transition loss will be

$$P_{swtr,off} = 0.5 f_{sw} I_{ds,pk} V_o T_f . \tag{C-17}$$

When the boost inductor current in the semi-bridge rectifier is positive, $V_{ds,pk}$ will rise to $V_o + V_f + R_f I_{ds,pk}$. When the current is negative, V_{ds} is equal to $V_f + R_f I_{ds,pk}$ of the free wheeling diode. The energy dissipated a single transition when the currents are positive and negative, respectively, are

$$E_{swtr} = 0.5T_f\left[(V_o + V_f)I_{ds,pk} + R_f I_{ds,pk}^2\right], \tag{C-18}$$

$$E_{swtr} = 0.5T_f\left[V_f I_{ds,pk} + R_f I_{ds,pk}^2\right]. \tag{C-19}$$

The peak switch current in the MOSFET over a switching period, $I_{ds,pk}$, will vary sinusoidally. This peak switch current over stator electrical period can be approximated as

$$I_{ds,pk}(k) \approx I_{pk}\sin(k\theta_k) \approx \frac{V_{oc1}DT_{sw}}{L_{boost}}\sin(k\theta_k), \tag{C-20}$$

where I_{pk} is the peak switch current over a stator electrical period. The angle θ_k is equal to $2\pi/K$, where K is f_{sw}/f_e. V_{oc1} is the peak value of the fundamental component of the open-circuit voltage. The switching transition energy over a stator electrical period will be

$$E_{swtr}\big|_{T_e} = \frac{1}{2}T_f\sum_{k=1}^{K}\left[(0.5V_o + V_f)I_{pk}\left|\sin(k\theta_k)\right| + R_f I_{pk}^2\sin^2(k\theta_k)\right]. \tag{C-21}$$

The turn-off switching transition power dissipated in a single MOSFET is

$$P_{swtr,off} = f_e E_{swtr}\big|_{T_e} = \frac{f_{sw}}{K}E_{swtr}\big|_{T_e} = \frac{f_{sw}T_f}{2}\frac{1}{K}\sum_{k=1}^{K}\left[\left(\frac{V_o}{2} + V_f\right)I_{pk}\left|\sin(k\theta_k)\right| + R_f I_{pk}^2\sin^2(k\theta_k)\right]. \tag{C-22}$$

Since the switching frequency is much larger than the stator electrical frequency, (C-22) can be approximated as

$$P_{swtr,off} \approx \frac{1}{4}f_{sw}T_f\left[(V_o + 2V_f)\left(\frac{2I_{pk}}{\pi}\right) + R_f I_{pk}^2\right]. \tag{C-23}$$

The capacitive turn-off loss and gate drive loss are fixed losses. They can be modeled as a resistance in parallel with the load resistor. The switching transition loss varies with the peak boost inductor current which itself varies with output power. Since the comparison of the converter topologies is done at a fixed output power of 10 W, the switching transition loss can also be modeled as a resistor in parallel with the

load for simplicity. The switching transition loss can be found iteratively by simulating the circuit and using the resulting I_{pk} in (C-10), (C-17) or (C-23). The loss can be added to the gate drive and output capacitive loss to determine fixed resistance, R_{fixed}, in parallel with the load resistor,

$$R_{fixed} = \frac{V_o^2}{P_{gd} + P_{cout} + P_{swtr} + P_{ct}}. \tag{C-24}$$

P_{ct} in Equation (C-24) is the diode capacitive loss which is computed in the next section. The circuit can simulated again to see if the peak transistor currents change significantly. If they do, then the new values of the peak switch currents can be used to recalculate R_{fixed} until the peak transistor currents vary by less then 1% from the previous iteration.

C.2 Diode Losses

The diodes used in the comparison are DFLS130L surface mount Schottky diode from Diodes Inc. The diodes are modeled as a voltage source, $V_f = 0.272$ V, in series with resistor, $R_f = 54.7$ mΩ, using the data sheet values of the forward voltage drop vs. forward current (Figure C-4).

The loss due to the junction capacitance is found by calculating the energy dissipated charging and discharging the diode capacitance over a switching cycle. This will be equal to the peak reverse voltage, V_r, across the diode times the charge on the diode capacitance at the peak V_r. The capacitance vs. reverse voltage of the diode is shown in Figure C-5. It is difficult to fit this curve to an analytical expression so interpolation is used to determine values between data points.

The power lost in the diode capacitance in the DCM rectifier is

$$P_{ct} = f_{sw} V_o \int_0^{V_o} C_t(V_r) dV_r . \tag{C-25}$$

The voltage across the diode changes from 0 to $-V_o$ only when the current through the boost inductor is positive which occurs during half the electrical period of the stator. The total loss in all the diodes is $3P_{ct}$. The capacitive loss in the diodes of the MOSFET rectifier used with the CCM boost converter is ignored because the reverse voltage is only a few volts and the switching frequency of the rectifier is only 20 kHz.

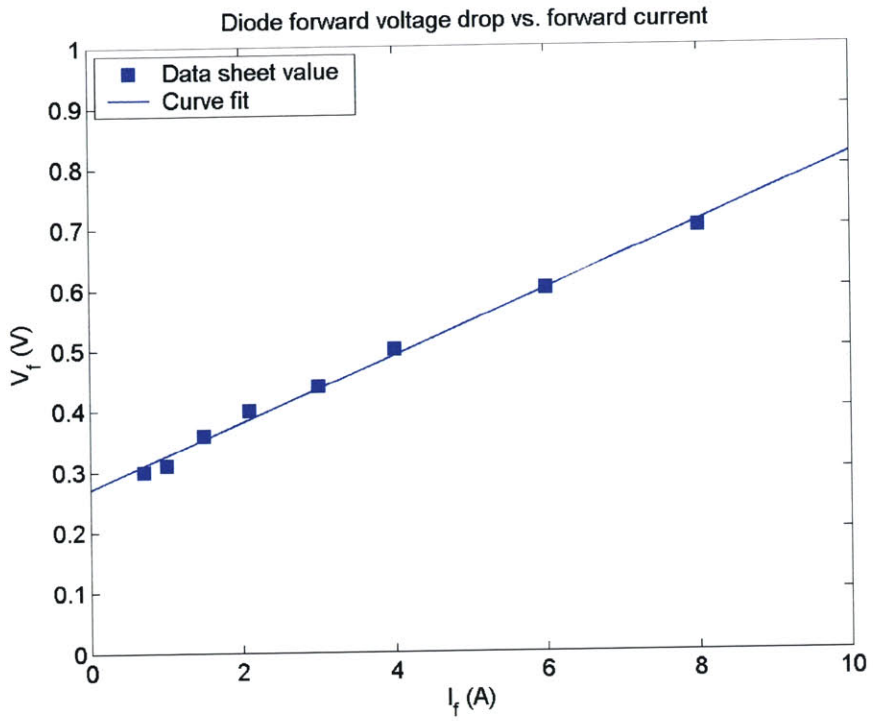

Figure C-4: Forward voltage vs. forward current for the DFLS130L Schottky diode.

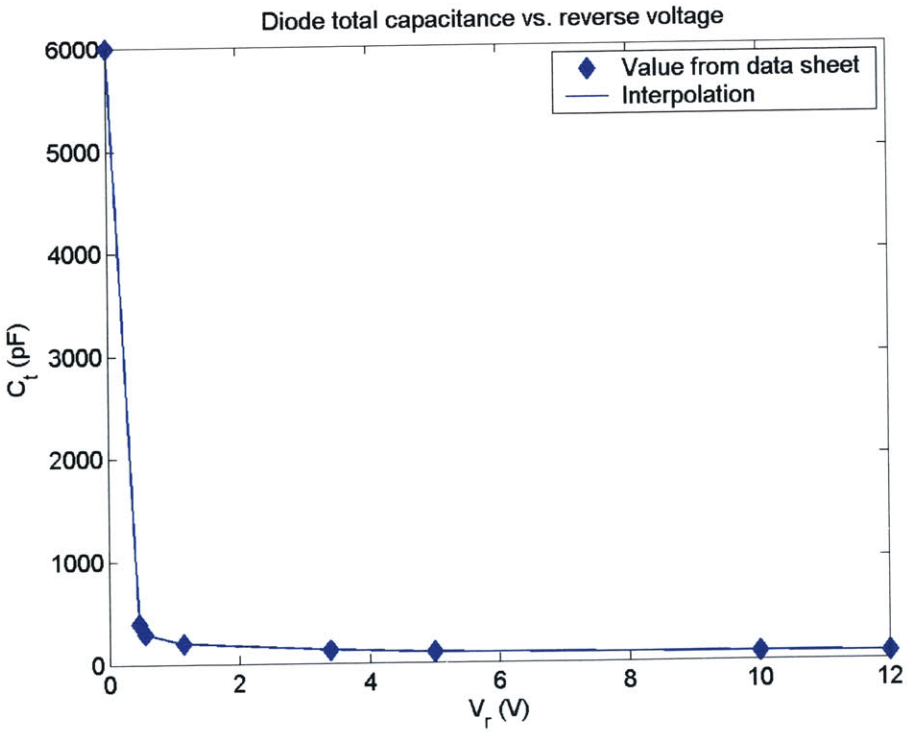

Figure C-5: Total capacitance vs. reverse voltage for the DFLS130L Schottky diode.

C.3 Boost Inductor Losses

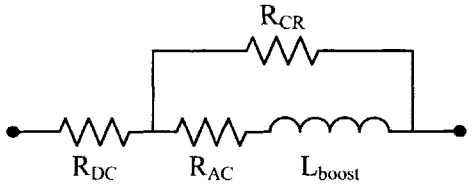

Figure C-6: Equivalent circuit of boost inductor.

Coil craft inductors are used in the topology comparisons. The inductors used in the DCM rectifiers are the 0.33 μH D01813H-331 while the inductor used in the CCM boost converter is the 1.5 μH D03316P-152. The equivalent circuit model for the inductors is shown in Figure C-6 and the SPICE models are available from www.Coilcraft.com. The inductors are modeled with a DC resistance, R_{DC}, AC resistance, R_{AC}, core resistance, R_{CR}, and high frequency inductance (in μH), L_{boost}, which can be found using

$$R_{AC}(f_{sw}) = K_1\sqrt{f_{sw}}\,, \tag{C-26}$$

$$R_{CR}(f_{sw}) = K_2\sqrt{f_{sw}}\,, \tag{C-27}$$

$$L_{boost}(f_{sw}) = K_3 - K_4\log(K_5 f_{sw}). \tag{C-28}$$

The AC resistance of the inductor used in the CCM boost inductor is ignored since the RMS current through the inductor is dominated by the DC current. The AC resistance for the boost inductors in the DCM rectifiers will be substantial since its current is an AC waveform at the switching frequency and so cannot be ignored. The values for the parameters in (C-26)–(C-28) are given in Table C-2 for both inductors. At a switching frequency of 500 kHz, R_{AC} = 34 mΩ, R_{CR} = 104 Ω and L_{boost} = 0.324 μH for the D01813H-331. At a switching frequency of 1 MHz, R_{CR} = 677 Ω and L_{boost} = 1.45 μH for the D03316P-152.

Table C-2: Boost inductor SPICE model parameters.

	K_1	K_2	K_3	K_4	K_5	f_{sw}	R_{DC}	R_{AC}	R_{CR}	L_{boost}
D01813H-331	4.85×10^{-5}	0.146	0.33	7.96×10^{-3}	1.02×10^{-5}	500 kHz	4 mΩ	34 mΩ	104 Ω	0.324 μH
D03316P-152	5.03×10^{-5}	0.677	1.48	3.48×10^{-2}	6.2×10^{-6}	1 MHz	10 mΩ	–	677 Ω	1.45 μH

References

[1] http://www.defenselink.mil/speeches/1997/t19970311-lynn.html

[2] S. A. Jacobson and A. H. Epstein, "An informal survey of power MEMS," ISMME 2003.

[3] A. H. Epstein and S. D. Senturia, "Macro power from micro machinery;" *Science*, vol. 276, no. 5316, p. 1211, May 1997.

[4] A. H. Epstein, S. D. Senturia, et al., "Power MEMS and microengines," in *Digest Tech. Papers Transducers '97 Conference*, Chicago, June 16-19, 1997, pp. 753-756.

[5] Epstein, A.H., "Millimeter-Scale, MEMS Gas Turbine Engines," *ASME J. of Eng. For Gas Turbines and Power*, Vol. 126, No. 2, April 2004, pp. 205-226.

[6] L. G. Frèchette, et al., "Demonstration of a microfabricated high-speed turbine supported on gas bearings," *Tech. Dig. Solid-State Sensor and Actuator Workshop* (Hilton Head 2000), June 2000, pp. 43-7.

[7] L. G. Frèchette, "Development of a microfabricated silicon motor-driven compressor system," Ph.D. Dissertation, Massachusetts Institute of Technology, Cambridge, MA, Aug. 2000.

[8] A. Mehra, A. A. Ayon, I. A. Waitz, and M. A. Schmidt, "Microfabrication of high temperature silicon devices using wafer bonding and deep reactive ion etching;" *J. Microelectromech. Syst.*, vol. 8, no. 2, pp. 152-60, June 1999.

[9] A. Mehra, "Development of a high power density combustion system for a silicon micro gas turbine engine;" Ph.D. Dissertation, Massachusetts Institute of Technology, Cambridge, MA, Feb. 2000.

[10] A. Mehra, et al., "A six-wafer combustion system for a silicon micro gas turbine engine," *J. Microelectromech. Syst.*, vol. 9, pp. 517-27, 2000.

[11] K. Lohner, K-S. Chen, A. A. Ayon, and S. M. Spearing, "Microfabricated silicon carbide microengine structures" *Proc. Symposium. Mater. Res. Soc., Materials Science of Microelectromechanical Systems (MEMS) Devices,* 1999, pp. 85-90.

[12] K-S. Chen, "Materials characterization and structural design of ceramic micro turbomachinery," Ph.D. Dissertation, Massachusetts Institute of Technology, Cambridge, MA, Feb. 1999.

[13] K-S. Chen, A. Ayon, and S. M. Spearing, "Controlling and testing the fracture strength of silicon on the mesoscale," *J. Amer. Ceramic Soc.*, vol. 83, no. 6, pp. 1476-1484, June 2000.

[14] A. A. Ayón, et al., "Characterization of a time multiplexed inductively coupled plasma etcher," *J. Electrochem. Soc.*, vol. 146, pp. 339-349, Jan. 1999.

[15] A. A. Ayón, X. Zhang, and R. Khanna, "Anisotropic silicon trenches 300-500 μm deep employing time multiplexed deep etching (TMDE)," *Sens. Actuators: Phys. A*, vol. 91, pp. 381-385, 2001.

[16] A. A. Ayón, et al., "Characterization of silicon wafer bonding for power MEMS applications," *Sens. Actuators: Phys. A*, vol. 103, pp. 1-8, 2003.

[17] N. Miki, et al., "Multi-stack silicon-direct wafer bonding for 3D MEMS manufacturing," *Sens. Actuators: Phys. A*, vol. 103, pp. 194-201, 2003.

[18] S. F. Nagle and J. H. Lang; "A micro-scale electric-induction machine for a micro gas-turbine generator;" *Proc. 27th Meeting Electrostatics Soc. Amer.*, June 1999, pp. 57-66.

[19] S. F. Nagle, "Analysis, design, and fabrication of an electric induction micromotor for a micro gas-turbine generator," Ph.D. Dissertation, Massachusetts Institute of Technology, Cambridge, MA, Oct. 2000.

[20] C. Livermore, et al., "A high-power MEMS electric induction motor," *J. Microelectromech. Syst.*, vol. 13, no. 3, pp. 465-471, June 2004.

[21] Steyn, J.L. et al: Generating Electric Power with a MEMS ElectroQuasiStatic Induction Turbine-Generator, to be presented at the *18th IEEE International Conference on Micro Electro Mechanical Systems MEMS 2005*, Miami, FL.

[22] L. Steyn, "A microfabricated electroquasistatic induction turbine generator" Ph.D. Dissertation, Massachusetts Institute of Technology, Cambridge, MA, June 2005.

[23] H. Koser, F. Cros, M. G. Allen, and J. H. Lang, "A High Torque Density Magnetic Induction Machine," in *Digest Tech. Papers Transducers '01 Conference*, Munich, Germany, June 10-14, 2001, pp. 284-287.

[24] F. Cros., "Developpement d'une micromachine a induction magnetique – developpement de Techniques de microfabrication pour micro-electroaimants," Ph.D. Dissertation, Ecole Doctorale de Toulouse, France, Sept. 2002.

[25] F. Cros, et al., "Micro-magnetic induction machines for portable power applications," *Proc. Army Research LabCollaborative Technology Alliances, Power and Energy*, April 2003, pp. 17-21.

[26] H. Koser, "Development of Magnetic Induction Machines for Micro Turbo Machinery," *Ph.D. Thesis*, Massachusetts Institute of Technology, Cambridge, MA, June 2002.

[27] H. Koser, F. Cros, M. G. Allen, and J. H. Lang, "Magnetic diffusion modeling in nonlinear micro-media: A modified finite-difference time-domain approach," *Proc. 6th Int. Conf. Model. Sim. of Microsyst.* (MSM 2003), Feb. 2003, pt. 2, vol.2, pp. 408-411.

[28] D. P. Arnold, et al., "Magnetic Induction Machines Embedded in Fusion-Bonded Silicon," in *Digest Tech. Papers Hilton Head '04 Conference*, Hilton Head Island, June 6-10, 2004, pp.129-132.

[29] H. Koser and J. H. Lang, "Magnetic induction micro machine – Part I: Design and analysis," *J. Microelectromech. Syst.*, (submitted for review).

[30] F. Cros, H. Koser, M. G. Allen, and J. H. Lang, "Magnetic induction micro machine – Part II: Fabrication and testing," *J. Microelectromech. Syst.*, (submitted for review).

[31] H. Koser, F. Cros, M. G. Allen, and J. H. Lang, "Magnetic induction micro machine – Part III: Eddy currents and nonlinear effects," *J. Microelectromech. Syst.*, (submitted for review).

[32] R. M. Bozorth, *Ferromagnetism*, New York: IEEE Press, Reissue, 1993.

[33] O. Cugat, J. Delamare, and G. Reyne, "Magnetic Micro-Actuators and Systems (MAGMAS)," *J. Microelectromech. Syst.*, vol. 39, no. 5, pp. 3607-3612, Nov. 2003.

[34] B. Wagner, M. Kreutzer, and W. Benecke, "Permanent Magnet Micromotors on Silicon Substrates," *J. Microelectromech. Syst.*, vol. 2, no. 1, pp. 23-29, Mar. 1993.

[35] K.-P. Kamper, et al., "Electromagnetic permanent magnet micromotor with integrated micro gear box," *Proc. 5th Int. Conf. New Actuators* (Actuator '96), June 1996, pp. 429-432.

[36] U. Berg, et al., "Series production and testing of a micro motor," *Proc. 6th Int. Conf. New Actuators* (Actuator '98), June 1998, pp. 552-555.

[37] P.-A.Gilles, J. Delamare, O. Cugat, and J.-L. Schanen, "Design of a Permanent Magnet Planar Synchronous Micromotor," *Proc. 35th Mtg. IEEE Industry Appl. Soc.*, Oct. 2000, vol. 1, pp. 223-227.

[38] C. Yang, et al., "An Axial Flux Electromagnetic Micromotor," *J. Micromech. Microeng.*, vol. 11, pp. 113-117, 2001.

[39] A. S. Holmes, G. Hong, and K. R. Buffard, "Axial-flux Permanent Magnet Machines for Micropower Generation," *J. Microelectromech. Syst.*, vol. 14, no. 1, pp. 54-62, Feb. 2005.

[40] H. Raisigel, et al., "Magnetic planar micro generator," in *Digest Tech. Papers Transducers '05 Conference*, Seoul, South Korea, June 10-14, 2005, pp.757-761.

[41] A.E. Fitzgerald, C. Kingsley, Jr., S. D. Umans, *Electric Machinery*, 6th Ed., New York: McGraw Hill, 2002.

[42] J.R. Melcher, Continuum Electromechanics, Cambridge: MIT Press, 1981.

[43] J.L. Kirtley Jr. and H.W. Beaty, Electric Motor Handbook, New York: McGraw-Hill, 1998.

[44] D.L. Trumper, W.-J. Kim, and M.E. Williams, "Design and Analysis Framework for Linear Permanent-Magnet Machines," Trans. on Industry App., vol. 32, no. 2, pp. 371-379, Mar./Apr. 1996.

[45] M. Zahn, Electromagnetic Field Theory: A Problem Solving Aprroach, Malabar: Kreiger, 1979.

[46] H.H. Woodson and J.R. Melcher, Electromechanical Dynamics, New York: John Wiley & Sons, 1968.
[47] J.G. Kassakian, M.F. Schlecht, and G.C. Verghese, Principles of Power Electronics, Reading: Addison Wesley, 1991.
[48] J.L. Kirtley Jr. and E. Lovelace, "Drag Loss in Retaining Rings of Permanent Magnet Motors," in Digest Tech. Papers International Electric Machines and Drives Conference, Madison, WI, June 1-4, 2004.
[49] D. P. Arnold, "Magnetic Machines for Microengine Power Generation," Ph.D. Thesis, Georgia Institute of Technology, Atlanta, GA, December 2004.
[50] "MMPA Standard No. 0100-00, Standard Specifications for Permanent Magnet Materials," published by International Magnetics Association (formerly Magnetic Materials Producers Association), Available: http://www.intl-magnetics.org/pdfs/0100-00.pdf.
[51] R. M. Bozorth, *Ferromagnetism*, New York: IEEE Press, Reissue, 1993.
[52] M. S. Sarma, *Electric Machines*, New York: West, 2nd Ed., 1994.
[53] J.-W. Park and Mark G. Allen, "Ultra Low-Profile Micromachined Power Inductors with Highly Laminated Ni/Fe Cores: Application to Low-Megahertz DC-DC Converters," *IEEE Trans. Magn.*, vol. 39, no. 5, pp. 3184-3186, Sept. 2003.
[54] M. G. Allen, "MEMS Technology for the Fabrication of RF Components," *IEEE Trans. Magn.*, vol. 39, no. 5, pp. 3073-3078, Sept. 2003.
[55] R.W. Erickson and D. Maksimovic, *Fundamental of Power Electronics*, Norwell: Kluwer, 1999.
[56] David P. Arnold, et al., "High-Speed Characterization and Mechanical Modeling of Microscale, Axial-Flux, Permanent-Magnet Generators," in *Digest Tech. Papers Transducers '05 Conference*, Seoul, South Korea, June 10-14, 2005, pp. 284-287.
[57] A. R. Prasad, P. D. Ziogas, and S. Manias, "An Active Power Factor Correction Technique for Three-Phase Diode Rectifiers," IEEE Trans. Power Electron., vol. 6, pp. 83-92, Jan. 1991.
[58] J. W. Kolar, H. Ertl, and F. C. Zach, "A Comprehensive Design Approach for a Three-Phase High-Frequency Single-Switch Discontinuous-Mode Boost Power Factor Corrector based on Analytically Derived Normalized Converter Component Ratings," IEEE Trans. Ind. Applicat., vol. 31, no. 3, pp. 569-82, May/June 1995.
[59] J. W. Kolar, H. Ertl, and F. C. Zach, "Space Vector-Based Analytical Analysis of the Input Current Distortion of a Three-Phase Discontinuous-Mode Boost Rectifier System," IEEE Trans. Power Electron., vol. 10, pp. 733-744, Nov. 1995.
[60] E. H. Ismail and R. Erickson, "Single-Switch 3-Phase PWM Low Harmonic Rectifiers," IEEE Trans. Power Electron., vol. 11, no. 2, pp. 338-346, Mar. 1996.
[61] D. Simonetti, J. L. Vieira, and G. Sousa, " Modeling of the High-Power-Factor Discontinuous Boost Rectifiers," IEEE Trans. Ind. Electron., vol. 46, no. 4, pp. 788-795, Aug. 1999.
[62] B.C. Kuo, *Automatic Control Systems*, New Delhi: Prentice Hall, 2003.
[63] C. Basso, "Write your own generic SPICE power supplies controller models," www.intusoft.com/tech.htm.
[64] The UCC38C42 Family of High-Speed, BiCMOS Current Mode PWM Controllers: Application Note. www.ti.com
[65] S. Das, "A Low Noise, Low Power DC/DC Converter for Cell Phone Power Applications," M.Eng. Thesis, Massachusetts Institute of Technology, Cambridge, MA, June 2002.
[66] D.A. Grant and J. Gowar, *Power MOSFETs, Theory and Applications*, New York: John Wiley and Sons, 1989.